Measurement of Higgs boson properties using the diphoton decay channel at the Compact Muon Solenoid experiment

Shameena Bonomally

Imperial College London
Department of Physics

A thesis submitted to Imperial College London
for the degree of Doctor of Philosophy
August 2021

Abstract

Measurements of the Higgs boson production cross-sections via the decay of the Higgs boson to two photons are reported. The measurements are made using data collected in the period 2016-2018 by the Compact Muon Solenoid detector at the Large Hadron Collider in proton-proton collisions at a centre-of-mass energy of 13 TeV, amounting to an integrated luminosity of 137 fb^{-1}. The production modes are measured in kinematic regions defined by the simplified template cross-section framework. Analysis categories targeting Higgs boson events, produced via vector boson fusion, vector boson associated production (where the vector boson decays hadronically), and a single top quark associated production (where the top quark decays hadronically), are specifically discussed. The total Higgs boson signal strength, relative to the Standard Model prediction, is measured to be $1.14^{+0.11}_{-0.10}$. Other properties of the Higgs boson are measured, including Standard Model signal strength modifiers, production cross-sections, and its couplings to other particles. The observed upper limit on the tH cross-section as a ratio to the Standard Model expectation is 9.47. All results are found to be in agreement with Standard Model predictions.

To Nana

Declaration

The work contained in this thesis is my own. It was produced by building upon existing studies from members of the Compact Muon Solenoid (CMS) Collaboration, as detailed below. Where the work of others is used in the text, it is referenced appropriately.

Chapter 1 introduces the work of this thesis and relevant prior results in the field of particle physics in my own words.

Chapter 2 explains the theoretical framework of the Standard Model and Higgs boson phenomenology, which is entirely the work of others, in my own words. Higgs boson measurements in the simplified template cross-section framework are summarised, including my own work on the $H \to \gamma\gamma$ analysis using data collected by the CMS detector in 2016-2018 [1].

Chapter 3 describes the Large Hadron Collider and the CMS detector, located at the *Centre Européen pour la Recherche Nucléaire*, in my own words.

Chapter 4 describes the use of precision timing in the High Granularity Calorimeter of the CMS detector, which is my own work, produced together with Arabella Martelli and Chris Seez [2]. The trackster iterative clustering framework, used as a tool in this study, is the work of others.

Chapter 5 firstly describes the reconstruction of collision events from the CMS detector, which is solely the work of others in the collaboration, in my own words. The main focus of this chapter is the categorisation of events in the $H \to \gamma\gamma$ analysis in the vector boson fusion, Higgs strahlung, and single top quark associated production channels, which is my own work. The data-driven method for background modelling was initially developed by Yacine Haddad, but has been modified and implemented by myself in this analysis.

Chapter 6 describes the building of signal and background models and the treatment of uncertainties in the analysis. The final observed results are also reported. This represents my own work, although the techniques used were initially developed by others. The treatment of uncertainties is identical to that in previous $H \to \gamma\gamma$ analyses [1, 3].

Chapter 7 summarises the work of this thesis and a combination of my own future development considerations and future work planned by the CMS Collaboration.

Shameena Bonomally

Acknowledgements

I owe my deepest gratitude to Imperial College London for being my home for the last five years and for having allowed me to have an enriching academic journey through both my masters and doctoral degrees. I offer my special thanks to members of the Imperial HEP administration team, not only for having been seamless in all our interactions, but more so for their perpetual and sincere words of motivation. I am ever grateful to my supervisor, Gavin Davies, for his endless patience and continued kindness towards me as a father figure and for his words of counsel and encouragement whenever I needed them. I am also thankful to my supervisor, Paul Dauncey, for his invaluable contribution to editing this thesis and for his guidance during my studies. Particularly helpful to me during my time at CERN was Chris Seez who I thank for his unparalleled insights and constructive criticism. I cannot begin to express my thanks to Arabella Martelli for having been the most remarkable mentor during my time at CERN and for having helped and cared ever since. I am deeply indebted to Edward Scott for his belief in me and for his unwavering support during my journey, both as a dear friend and mentor. From the Imperial College Business School, I thank Esma Koca and Gokhan Yildirim for their most sincere encouragement and for their profound faith in my abilities. From my HEP cohort, I thank Ryan Newcombe and Vilius Čepaitis for having gifted me with the most genuine friendship I could wish for. I am deeply grateful to my non-academic mentors Surabhi Shukla and Diego Solarte for their powerful teachings and life lessons. I further thank my secondary school teachers Pretty Ruhee and Benu Servansingh for having first kindled my interest in physics. I extend my special thanks to Fay Dowker and Saad Nabeebaccus who taught me everything I know about theoretical physics in the most elegant way I can imagine. I cannot forget to thank my family, Mum, Dad, Aunty Dariny, Uncle Mahen, Nikhil, Nani and Nana for always being by my side no matter what. Lastly, I thank Ramy Rezkalla for being the one constant in my life that never changes and for whom I hold the utmost admiration.

There are things known and there are things unknown,
and in between are the doors of perception.

- Aldous Huxley

Contents

List of Tables

List of Figures

Chapter 1

Introduction

Fundamental constituents of matter, fermions, and mediators of the forces of nature, bosons, may be described in a mathematical framework called the Standard Model (SM) [4–9], introduced in the early 1970s. Over the past few decades, precision measurements and experimental observations of weak neutral currents, gauge bosons and the top quark amongst others [10–19], have helped to test SM predictions and gradually establish the SM as the present leading model of high-energy physics. Interactions of the different particle fields in the SM allow fermions and bosons to acquire mass through Yukawa couplings [5] and the Higgs mechanism [20–25] respectively, both of which involve the Higgs field. The Higgs mechanism in the SM leads to the prediction of the Higgs boson which was discovered in 2012 at the Large Hadron Collider (LHC) [26] by the ATLAS and CMS experiments [27, 28]. The discovery of the Higgs boson was deemed a sufficient proof of the Higgs mechanism for which François Englert and Peter Higgs were awarded the 2013 Nobel Prize in Physics.

However, several anomalies relating to the mechanism still remain unexplained. Primarily, the SM does not offer an explanation for the gravitational force, which as yet remains not unified with other SM forces. Furthermore, owing to its multiple interactions with other SM particles, the SM Higgs boson theoretically ought to be much heavier than observed [29]. Similarly, the Higgs field has an energy density several orders of magnitude higher than the critical energy density of space as given by the cosmological constant [30]. Among the other shortcomings of the SM is the absence of an explanation for dark matter and dark energy which account for 25% and 70% of the universe respectively [31]. Additionally, for several decades, neutrinos were assumed to be massless in the SM, a property which helps to explain why only left-handed neutrinos are observed. However, experimental measurements of neutrino oscillations confirm that neutrinos have mass [32]. The above-mentioned missing elements of the SM have been addressed by theories providing extensions to the SM theory. These "beyond the SM" (BSM) theories postulate new mechanisms which may give rise to new particles and, in some cases, new interactions involving the Higgs boson. It is the aim of the LHC high luminosity (HL-LHC) [33–36] phase to make more precise measurements of the Higgs boson interactions and to search for evidence of BSM physics that could explain the missing elements in the SM.

This thesis is dedicated to precise measurements of the Higgs boson cross-sections via the decay of the Higgs boson to two photons at the CMS experiment. The data used to derive the results of this thesis is from LHC proton-proton collisions at $\sqrt{s} = 13\,\text{TeV}$ in the years 2016, 2017 and 2018 with integrated luminosities of 35.9, 41.5, and $59.4\,\text{fb}^{-1}$ respectively. The full Run II dataset therefore contains data amounting to an integrated luminosity of $137\,\text{fb}^{-1}$. The CMS detector [37, 38], operating in the LHC ring, measures particles produced in proton-proton collisions and was designed to discover the Higgs boson. In particular, the CMS electromagnetic calorimeter (ECAL) [39] is designed to provide an excellent energy resolution to increase sensitivity to the $H \to \gamma\gamma$ decay. The final result of this thesis is the measurement of the Higgs boson cross-sections within the simplified template cross-section (STXS) framework [40]. The STXS framework represents an improved method of conducting Higgs boson cross-section, signal strength and coupling measurements whereby theoretical model and uncertainty dependence is reduced, and theoretical interpretations are more easily derived. Granular measurements made with the STXS framework can therefore be updated in the long-term as theory predictions are improved. These measurements simultaneously help to precisely test the SM and constrain BSM theories. Measurements in the STXS *Stage 1.0* framework (Section 2.3.1) were first presented in Ref. [3] with data taken in the years 2016 and 2017. Since, the STXS framework has been updated to *Stage 1.2*. This thesis primarily presents some of the improvements made in Ref. [1] with the Stage 1.2 framework over the Ref. [3] analysis. Additional measurements, beyond what is included in Ref. [1], are also presented.

The structure of the thesis is as follows.

Chapter 2 describes the mathematical framework for studying gauge-invariant field theories and hence the laws which govern fundamental particles and their interactions. Emphasis is placed on the Higgs mechanism and on the phenomenology and measurements of the Higgs boson at the LHC. The status of the measurements of the Higgs boson properties, including those made in the STXS frameworks, are summarised.

Chapter 3 is dedicated to describing the general functioning of the LHC facility, the requirements and design of the CMS detector, and the future of the LHC and the CMS experiment. The luminosity upgrade of the present LHC ring is discussed, together with the foreseen upgrades of the CMS detector. In this context, the high granularity endcap calorimeter (HGCAL) [41–43] upgrade is discussed in detail.

Chapter 4 reports on the progress made in the study and applications of precision timing in the HGCAL reconstruction chain since the publication of the HGCAL Technical Design Report (TDR) [44]. The chapter outlines the current status and the prospective use of precision timing at the various stages of the HGCAL reconstruction of a complete shower.

Chapter 5 first presents a brief introduction to the reconstruction of $H \to \gamma\gamma$ events. Emphasis is placed on the reconstruction of photons and jets. The main aim of the chapter is to describe the the improvements made in Ref. [1] (over Ref [3]) in the categorisation of VBF events, including VH processes where the vector boson decays hadronically. This chapter further presents techniques to categorise *hadronic* tHq events.

Chapter 6 describes the construction of models for the signal and background contributions to the diphoton invariant mass spectra in the STXS analysis categories. The treatment of systematic uncertainties in the analysis is detailed. The chapter then presents the

statistical fitting procedure used to extract the final results of the analysis and the associated uncertainties. The measured Higgs boson cross-sections at two levels of granularity within the STXS framework are presented, and comparisons are made to the corresponding SM predictions.

Chapter 7 states the conclusions drawn from the results of the analysis, and details possible future avenues.

Chapter 2

Theory

2.1 The Standard Model of particle physics

2.1.1 Introduction

Particle physics seeks to establish the properties of subatomic particles, and the phenomenology of their interactions. The SM [4–9] describes three generations of fermions (six quarks and six leptons, and their anti-particles) as the fundamental constituents of matter. While gravitational interactions are not considered between high-energy elementary particles, quarks and leptons may undergo weak, electromagnetic or strong interactions. These interactions may be explained through gauge symmetric field theories (Section 2.1.2) whereby quantum numbers or charges are conserved. The electric charge, the colour charge and weak isospin charge are respectively conserved in electromagnetic, strong and weak interactions. In the SM gauge theory, the $W^{\pm}$ and Z bosons, the photon (γ), and the gluon (g) are the virtual force carriers or gauge bosons exchanged between particles to convey weak, electromagnetic and strong forces respectively.

The SM electroweak theory (Section 2.1.2) provides a common picture for the weak and electromagnetic interactions, without unifying them. Over the past few decades, precision measurements and the experimental observations of weak neutral currents, gauge bosons and the top quark amongst others, have helped to test SM predictions and gradually establish the SM as the present leading model of high-energy physics [10–19]. One of the early challenges in particle physics was to explain the range of the weak force, of the order 10^{-18} m, as compared to the infinite range of the electromagnetic force. It was proposed that the mediators of the weak force could have a shorter range of action if they were massive. The measurement of $W^{\pm}$ and Z boson masses [12–14] emphasised the need for a mechanism to generate mass terms for weak gauge bosons in the SM Lagrangian while preserving gauge invariance and ensuring renormalisability of the theory. It is important to note here that massless boson fields only possess two degrees of freedom which correspond to horizontal and transverse polarisations, while massive boson fields possess an extra degree of freedom

which corresponds to a longitudinal polarisation.

The Higgs mechanism [20–25] causes spontaneous breaking of SM electroweak gauge symmetry (EWSB) (Section 2.1.3) through interactions of the gauge fields ($W^{\pm}$ and Z) and the four components of the Higgs field. The $W^{\pm}$ and Z bosons, originally massless in a free field theory, acquire an extra degree of freedom and become massive. Fluctuations of the Higgs field around the vacuum expectation value result in a fundamental massive scalar (spin-0) particle, called the Higgs boson, which is the remaining degree of freedom. Fermions also gain mass from the Higgs field, through Yukawa interactions [5] described in Section 2.1.3. Although results of early experimental studies [45] indirectly advocated the existence of the Higgs field for several decades after the SM was introduced, the Higgs boson was only discovered in 2012 [27, 28].

The next sections briefly describe the mathematical framework for studying gauge invariant field theories and hence the laws which govern fundamental particles and their interactions. Emphasis is placed on the EWSB mechanism and on the phenomenology of the Higgs boson at the LHC, including state-of-the-art frameworks for conducting precision measurements.

2.1.2 Quantum fields and gauge invariance

Relativistic Quantum Field Theory (QFT) [46] builds upon the concept of wave-particle duality and describes every particle as an excitation of a quantum field, similar to a ripple in a still body of water after it is disturbed. If provided with sufficient energy, the energy of a quantum field may increase from its value in the vacuum of empty space, resulting in the creation of a wave-like particle. The energy E involved in creating a real massive particle at rest is given by

$$E = mc^2 \ , \tag{2.1}$$

where m is the mass of the particle and c is the speed of light. For a massless particle, the energy involved is proportional to the frequency f of the field as

$$E = hf \ , \tag{2.2}$$

where h denotes Plank's constant.

The fermions described in Section 2.1.1 may interact through the fundamental forces by the exchange of bosons which exist as virtual particles when the energy available in the interaction is insufficient for their creation. The creation of virtual particles from vacuum state fluctuations is allowed by Werner Heisenberg's energy-time uncertainty principle [47]; energy may be borrowed from the vacuum of spacetime and used to create virtual particles for a short period of time. The heavier the virtual particle, the greater is the amount of energy borrowed from the vacuum. The decay time of the virtual particles influences the range of the fundamental force being mediated. The amplitude of an interaction occurring is therefore inversely proportional to the mass of the virtual particles involved. In sub-dominant interactions, virtual particles may themselves interact through the exchange of other virtual particles, producing loops in the corresponding Feynman diagrams.

In classical mechanics, the Euler-Lagrange equation for motion in a direction x,

$$\frac{d}{dt}\left(\frac{\partial L}{\partial \dot{x}}\right) = \frac{\partial L}{\partial x} \ , \tag{2.3}$$

stems from the principle that a physical system follows the path for which the action is minimised or, more generally, is stationary. Equations of motion are derived by applying the Euler Lagrange equation to a Lagrangian [48] of the form

$$L = T - V \ , \tag{2.4}$$

where T and V represent the kinetic and potential energy terms. In the case of a horizontally oscillating mass attached to a spring, the Lagrangian bears a potential energy term $V(x)$ of the form $\frac{1}{2}kx^2$, where k is the spring constant and x is the displacement of the mass from its equilibrium position. It is useful to note the shape of the potential energy function of this system. At the minimum of the parabola, the system is in equilibrium. In cases where $V(x)$ is negative, an inverted parabola gives rise to an unstable equilibrium position at the maximum. The latter situation is problematic and analogously arises in the Lagrangian density of the Higgs field as described in Section 2.1.3.

This chapter explores the nature and interactions of three different types of fields, namely Dirac fields which produce spin $\frac{1}{2}$ fermions, vector boson fields which produce spin 1 bosons, and scalar boson fields which produce spin 0 bosons.

Formulated in 1928, the Dirac field theory [49] was the first theory to combine special relativity and quantum mechanics. The Dirac Lagrangian density for a free fermion field ψ is given by

$$\mathcal{L} = i\bar{\psi}\gamma^\mu\partial_\mu\psi - m\bar{\psi}\psi \ , \tag{2.5}$$

where the kinetic term contains partial derivatives of the field with respect to the four spacetime coordinates μ with $\mu = t, x, y, z$, the Pauli adjoint $\bar{\psi}$ of ψ, and the Dirac matrices γ^μ which represent four 4×4 matrices obeying $\{\gamma^\mu, \gamma^\nu\} = 2g^{\mu\nu}$. The potential energy term contains the mass m of the particle produced from the excitation of the Dirac field ψ. The Lagrangian method may be applied to the Lagrangian density of the Dirac field to obtain the Dirac equation,

$$i\gamma^\mu\partial_\mu\psi - m\psi = 0 \ , \tag{2.6}$$

which is obeyed by all fermions. The significance of the mass term in the Dirac equation is further discussed in Section 2.1.3.

When applied to the electromagnetic field A_μ in the Lagrangian density

$$\mathcal{L} = -\frac{1}{4}F_{\mu\nu}F^{\mu\nu} + \frac{1}{c}j_\mu A^\mu \ , \tag{2.7}$$

(where $A^\mu = (\phi, A^x, A^y, A^z)$, $F_{\mu\nu}$ is the field strength tensor, j is the electric current density

vector), the Lagrangian method yields Maxwell's equations,

$$\mathbf{B} = \nabla \times \mathbf{A} \ , \tag{2.8}$$

$$\mathbf{E} = -\nabla\phi - \frac{\partial \mathbf{A}}{\partial t} \ , \tag{2.9}$$

which describe the effect of changing $\mathbf{A}$, short for A^i, on the observable magnetic $\mathbf{B}$ and electric $\mathbf{E}$ fields [50]. Notably, certain transformations, known as gauge transformations, of the field A^μ do not result in changes in the observables $\mathbf{B}$ and $\mathbf{E}$. It can be shown that the transformations

$$\phi \to \phi - \frac{\partial \alpha}{\partial t} \ , \tag{2.10}$$

$$A_i \to A_i + \nabla\alpha \ , \tag{2.11}$$

(with $\alpha(t, x, y, z)$), when applied simultaneously, keep the electromagnetic Lagrangian density invariant. The idea of gauge invariance [51–53] may be applied to any type of field to give a gauge field theory, where the Lagrangian density is invariant under a continuous group of *local* transformations of the field. The act of changing the field by the same quantity at every point in spacetime signifies a global transformation while a local transformation results in different variations of the field at different points. Given the choice of gauge transformation does not affect the observables in a gauge invariant theory, it is often mathematically convenient to choose a particular gauge. As per Nöther's theorem [54], the continuous symmetry of a field theory under a gauge transformation implies the existence of a conserved current from which one can construct conserved charges or quantum numbers. It is useful to think of a field theory as being invariant or symmetric under a group of transformations called a *Lie group*. For every generator (basis vector) in a Lie group, there arises a corresponding gauge field. If the Lie group generators commute, the gauge theory is *Abelian*. The Standard Model bears symmetries of the unitary non-Abelian product group $SU(3) \times SU(2) \times U(1)$.

The following sections apply the Lagrangian method to the gluon fields, photon and W and Z fields, the Higgs field and Dirac fermion fields to deduce the nature of the fields and the particles created from their excitations. It will be shown that gauge invariance of the Lagrangian density of the free vector boson fields and fermion fields requires that the vector bosons and fermions be massless. By studying the Lagrangian density of several fields in a single gauge theory such as the SM, interactions between the fields may be further deduced. In this context, mechanisms that allow vector bosons and fermions to acquire mass through interactions with the Higgs field will be described. The Lagrangian density of the Standard Model $\mathcal{L}_{SM}$ takes the form

$$\mathcal{L}_{SM} = \mathcal{L}_{gauge} + \mathcal{L}_{fermion} + \mathcal{L}_{Higgs} - \mathcal{L}_{Yuk} \ , \tag{2.12}$$

where $\mathcal{L}_{Yuk}$, $\mathcal{L}_{gauge}$, $\mathcal{L}_{fermion}$ and $\mathcal{L}_{Higgs}$ denote the Lagrangian density of the Yukawa interaction, the gauge fields, the fermion fields and the Higgs field respectively.

Strong interactions

Quantum chromodynamics (QCD) [55, 56] is the fundamental theory of strong interactions between quarks and gluons. The QCD Lagrangian density is

$$\mathcal{L}_{QCD} = -\frac{1}{4}F^a_{\mu\nu}F^{\mu\nu}_a + \sum_{f=1}^{n_f}\bar{\psi}^{(f)}(i\gamma^\mu D_\mu - m_f)\psi^{(f)} \ , \tag{2.13}$$

where $\psi^{(f)}$ is a 4-component Dirac spinor representing a quark q of flavour f, with $q_f \in \{u, d, s, ...\}$. Quarks in QCD are distinguished only by their differing masses m_f.

The QCD lagrangian density is a sum of quark (second term) and gluon (first term) contributions and is required to be invariant under the gauge transformation $\psi(x) \to \psi'(x) = U\psi(x)$, where U,

$$U = \exp(i\sum_a \theta^a(x)\lambda^a/2) \ , \tag{2.14}$$

are 3×3 unitary matrices acting on the colour index and forming a fundamental representation of $SU(3)$ symmetry whereby the colour charge is preserved.

The matrices $\lambda_a/2$ with $(a = 1, ..., 8)$ are 3×3 Hermitian matrices, which are the generators of $SU(3)$, with λ^a being the Gell-Mann matrices in the fundamental representation. The f^{abc} terms are the totally antisymmetric structure constants of $SU(3)$ with $[\frac{1}{2}\lambda^a, \frac{1}{2}\lambda^b] = if^{abc}\frac{1}{2}\lambda^c$. The θ^a terms are real-valued functions of x^μ. The covariant derivative D^μ is given by

$$D_\mu\psi^{(f)} = \partial_\mu\psi^{(f)} + ig_sA^a_\mu\frac{1}{2}\lambda^a\psi^{(f)} \ , \tag{2.15}$$

where g_s is the strong coupling constant. The vector fields A^a_μ represent eight gluon fields. A mass term of the form $\frac{1}{2}m_g^2A^\mu_aA^a_\mu$ is not gauge invariant and, therefore, gluons are predicted to be massless.

The gluon part of the Lagrangian density is the kinetic term containing the anti-symmetric field strength tensor $F^a_{\mu\nu}$. For the whole Lagrangian density to be gauge invariant under $SU(3)$, the field strength tensor is required to transform as $F^a_{\mu\nu} \to UF^a_{\mu\nu}U^\dagger$. This may be accomplished by choosing $F^a_{\mu\nu}$ as

$$F^a_{\mu\nu} = \partial_\mu A^a_\nu - \partial_\nu A^a_\mu - g_s[A^a_\mu, A^a_\nu] \ , \tag{2.16}$$

where the commutator term $[A^a_\mu, A^a_\nu]$ is equal to $f^{abc}A^b_\mu A^c_\nu$. This term is a direct result of a non-Abelian theory, where $f^{abc} \neq 0$. The non-commutation of the gluon fields implies three and four-point gluon self-interactions. Furthermore, the QCD Lagrangian density is symmetric under rotations of left and right-handed fermion fields in the left and right isospaces, implying that the QCD Lagrangian density has chiral symmetry $U(2)_L \times U(2)_R$.

Quarks and gluons are not observed as free particles in nature but are confined in colour-neutral hadrons that transform as singlets in $SU(3)$. The colour singlets are quark-antiquark pairs (mesons) and triple-quark states (baryons). The mechanism of confinement arises because gluons possess colour charge; self-interactions in gluon fields render the force stronger at shorter distances. This phenomenon is known as *vacuum screening*. The strong coupling

constant may be parameterised by the energy scale μ of a process as

$$\alpha_s(\mu) = \frac{2\pi}{\beta_0 \ln(\mu/\Lambda_{QCD})} \ , \tag{2.17}$$

where $g_s = \sqrt{4\pi\alpha_s}$. The parameter Λ_{QCD} sets a scale at which the coupling constant becomes large and the physics becomes non-perturbative. The function β_0 is defined by $(11n - 2f)/3$, where n is the number of colours and f is the number of quark flavours. The $11n$ term represents the gluon self-coupling effect while the $2f$ term corresponds to quark-antiquark pair effects.

The constant is large for scales $< 1\,\text{GeV}$, explaining the *confinement* of quarks and gluons into composite states, and it grows weaker with increasing scales, leading to *asymptotic freedom* [57, 58]. Quark confinement at energies $< 1\,\text{GeV}$ does not allow quark masses to be directly measured. In high-energy interactions, such as deep inelastic scattering, quarks and gluons may act as quasi-free particles, partons [59, 60]. These intractions may be used to study the distribution of partons in the hadron and hence derive parton distribution functions (PDFs).

Electroweak interactions

Interactions between gauge bosons and fermions are described by the Lagrangian density

$$\mathcal{L}_{\text{gauge}} = -\frac{1}{4}\sum_{A=1}^{3} F^A_{\mu\nu}F^{A\mu\nu} - \frac{1}{4}B_{\mu\nu}B^{\mu\nu} + \bar{\psi}_{\text{L}}\text{i}\gamma^\mu D_\mu\psi_{\text{L}} + \bar{\psi}_{\text{R}}\text{i}\gamma^\mu D_\mu\psi_{\text{R}} \ , \tag{2.18}$$

which is the Yang-Mills Lagrangian [61] for the gauge group $SU(2)_L \times U(1)_Y$ with fermion matter fields. Weak isospin and weak hypercharge Y are the quantum numbers associated with $SU(2)$ and $U(1)_Y$ symmetries respectively. The gauge field B_μ, given by

$$B_{\mu\nu} = \partial_\mu B_\nu - \partial_\nu B_\mu \ , \tag{2.19}$$

relates to $U(1)_Y$ theory while the W^A_μ fields, given by

$$F^A_{\mu\nu} = \partial_\mu W^A_\nu - \partial_\nu W^A_\mu - g\epsilon_{ABC}\, W^B_\mu W^C_\nu \ , \tag{2.20}$$

correspond to $SU(2)$ theory which has the 2×2 Pauli matrices [62] as generators. In $SU(2)$, the group structure constants ϵ_{ABC} coincide with the totally antisymmetric Levi-Civita tensor.

As described later in Section 2.1.3, the left and right-handed ψ_L and ψ_R spinors behave differently and mass terms for fermions are forbidden in the free Dirac Lagrangian density. Thus the vector interactions in the electroweak Lagrangian do not mix ψ_L and ψ_R fields. Furthermore, evidence from beta decays in the Wu experiment [63] showed that the weak force violates parity conservation. Later, with the development of the *V-A* theory [64, 65], it was shown that the weak force couples to left-handed fermions, not to right-handed ones, hence the 'L' subscript in $SU(2)_L$ theory. Couplings of the weak force to right-handed

fermions are not omitted in the following equations. The covariant derivatives $D_{\psi L,R}$ are

$$D_\mu \psi_{\mathrm{L,R}} = \left(\partial_\mu + \mathrm{i}g \sum_{A=1}^{3} \tau^A_{\mathrm{L,R}} W^A_\mu + \mathrm{i}g' \frac{1}{2} Y_{\mathrm{L,R}} B_\mu \right) \psi_{\mathrm{L,R}} \ , \tag{2.21}$$

where the spinors $\psi_{L,R}$ span reducible representations of $SU(2) \times U(1)$, and $\tau^A_{L,R}$ and $Y_{L,R}/2$ are the $SU(2)$ and $U(1)$ generators in the reducible representations $\psi_{L,R}$. Commutation relations of the $SU(2)$ generators are given by

$$\left[\tau^A_{\mathrm{L}}, \tau^B_{\mathrm{L}}\right] = \mathrm{i}\epsilon_{ABC} t^C_{\mathrm{L}} \ , \quad \left[\tau^A_{\mathrm{R}}, \tau^B_{\mathrm{R}}\right] = \mathrm{i}\epsilon_{ABC} \tau^C_{\mathrm{R}} \ . \tag{2.22}$$

The electric charge generator is given by

$$Q = \tau^3_{\mathrm{L}} + \frac{1}{2} Y_{\mathrm{L}} = \tau^3_{\mathrm{R}} + \frac{1}{2} Y_{\mathrm{R}} \ . \tag{2.23}$$

Furthermore, g' and g are the independent coupling constants relating to $SU(2)$ and $U(1)$ respectively.

The couplings of gauge bosons and fermions may be derived from Equations 2.18 and 2.21. The charged W_μ fields are combinations of $W^{1,2}_\mu$, while the photon A_μ and weak neutral gauge boson field Z_μ are combinations of W^3_μ and B_μ. The $W^{1,2}_\mu$ fields may be written in terms of the $W^\pm_\mu$ fields as

$$\begin{array}{rcl} g(\tau^1 W^1_\mu + \tau^2 W^2_\mu) & = & g\left[\frac{1}{\sqrt{2}}(\tau^1 + \mathrm{i}\tau^2)\frac{1}{\sqrt{2}}(W^1_\mu - \mathrm{i}W^2_\mu) + \mathrm{h.c.}\right] \\ & = & g\left(\frac{1}{\sqrt{2}}\tau^+ W^-_\mu + \mathrm{h.c.}\right) \ , \end{array} \tag{2.24}$$

by using the relationship $t^\pm = t^1 \pm it^2$ and the relation

$$W^\pm = (W^1 \pm \mathrm{i}W^2)/\sqrt{2} \ . \tag{2.25}$$

This relationship may be extended to the left and right fermion fields to obtain the charged current gauge coupling $V_{\bar{\psi}\psi W}$ given by

$$V_{\bar{\psi}\psi W} = g\bar{\psi}\gamma_\mu \left[\frac{1}{\sqrt{2}} \tau^+_{\mathrm{L}} \frac{1}{2}(1 - \gamma_5) + \frac{1}{\sqrt{2}} \tau^+_{\mathrm{R}} \frac{1}{2}(1 + \gamma_5) \right] \psi W^-_\mu + \mathrm{h.c.} \ . \tag{2.26}$$

Similarly, orthogonal and normalised linear combinations,

$$\begin{array}{rcl} A_\mu & = & \cos\theta_{\mathrm{W}} B_\mu + \sin\theta_{\mathrm{W}} W^3_\mu \ , \\ Z_\mu & = & -\sin\theta_{\mathrm{W}} B_\mu + \cos\theta_{\mathrm{W}} W^3_\mu \ , \end{array} \tag{2.27}$$

of B_μ and W^3_μ may be used to derive the neutral current coupling $V_{\bar{\psi}\psi W}$ and the electric charge e. Using these relations and Equation 2.23, we may derive

$$\begin{array}{rcl} g\tau^3 W^3_\mu + \frac{1}{2} g' Y B_\mu & = & \left[g\tau^3 \sin\theta_{\mathrm{W}} + g'(Q - \tau^3)\cos\theta_{\mathrm{W}} \right] A_\mu \\ & & + \left[g\tau^3 \cos\theta_{\mathrm{W}} - g'(Q - \tau^3)\sin\theta_{\mathrm{W}} \right] Z_\mu \ , \end{array} \tag{2.28}$$

where θ_W is the weak mixing angle. From Equation 2.28, we may deduce the relationships $g \sin\theta_{\mathrm{W}} = g' \cos\theta_{\mathrm{W}} = e$ and $\tan\theta_{\mathrm{W}} = g'/g$. Subsequently, the neutral current coupling $V_{\bar{\psi}\psi W}$ may be derived as

$$V_{\bar{\psi}\psi Z} = \frac{g}{2\cos\theta_{\mathrm{W}}} \bar{\psi}\gamma_\mu \Big[\tau_{\mathrm{L}}^3(1-\gamma_5) + \tau_{\mathrm{R}}^3(1+\gamma_5) - 2Q\sin^2\theta_{\mathrm{W}}\Big]\psi Z^\mu \ . \tag{2.29}$$

Gauge boson self-interactions may be similarly derived from the $F_{\mu\nu}$ term in Equation 2.18 and Equation 2.25. It is to be noted that terms of the form $m^2 A^\mu A_\mu$, $m^2 W^\mu W_\mu$ and $m^2 Z^\mu Z_\mu$ are not gauge invariant and thus the gauge vector bosons are predicted to be massless in electroweak gauge theory.

2.1.3 Spontaneous Symmetry Breaking and the Higgs field

The Lagrangian density of a one-dimensional scalar field ϕ, given by

$$\mathcal{L} = \frac{1}{2}\left(\partial_\mu \phi\right)^2 - \left(\frac{1}{2}\mu^2\phi^2 + \frac{1}{4}\lambda\phi^4\right) \ , \tag{2.30}$$

may be used to demonstrate *spontaneous symmetry breaking* [20–25]. Derivatives of the field with respect to the spatial and temporal coordinates μ are contained in the kinetic term of the Lagrangian density. In the mass term $\frac{1}{2}\mu^2\phi^2$, μ represents the mass of the particle produced from the excitation of the field ϕ, and appears in the coefficient of the quadratic term. The quartic term $\frac{1}{4}\lambda\phi^4$ represents self-interactions of the field ϕ and contains the positive self-coupling constant λ.

In a situation where the mass μ is real and positive, the potential of the field $V(\phi)$ is parabolic with a minimum $V(\phi) = 0$ at $\phi = 0$. When the mass μ is imaginary, $\phi^2 > \phi^4$ for small ϕ while $\phi^2 < \phi^4$ for large ϕ, leading to $V(\phi)$ having the form shown on the left plot in Figure 2.1. The whole Lagrangian density exhibits symmetry about $\phi = 0$. At the minima of $V(\phi)$, the field ϕ has values $\pm\nu$ which represent a non-zero vacuum expectation value expressed as $\pm\sqrt{-\mu^2/\lambda}$. The fact that $V(\phi)$ exhibits a maximum at $\phi = 0$ is counter-intuitive and signifies an unstable situation. Mathematically, it is possible to redefine the field through a global transformation $\phi \to \eta$, where $\eta = \phi - \nu$. The potential of the field $V(\eta)$, after the global transformation, has the form shown on the right plot in Figure 2.1. The minimum of $V(\eta)$ lies at $\eta = 0$ and the theory for the field η now allows a real massive particle to be produced. However by insisting on a minimum potential at $\eta = 0$, the global transformation has led to spontaneous symmetry breaking, whereby the potential of the field is no longer symmetric about $\eta = 0$. The Lagrangian density of the field η may be expressed as

$$\mathcal{L}' = \frac{1}{2}(\partial\eta)^2 - \left(\lambda\nu^2\eta^2 + \lambda\nu\eta^3 + \frac{1}{4}\lambda\eta^4\right) + \text{const.} \ , \tag{2.31}$$

where the mass term $-\lambda\nu^2\eta^2$, when compared to the mass term in Equation 2.30, yields a real mass of $\sqrt{2\lambda\nu^2}$ for the particle produced from the field η.

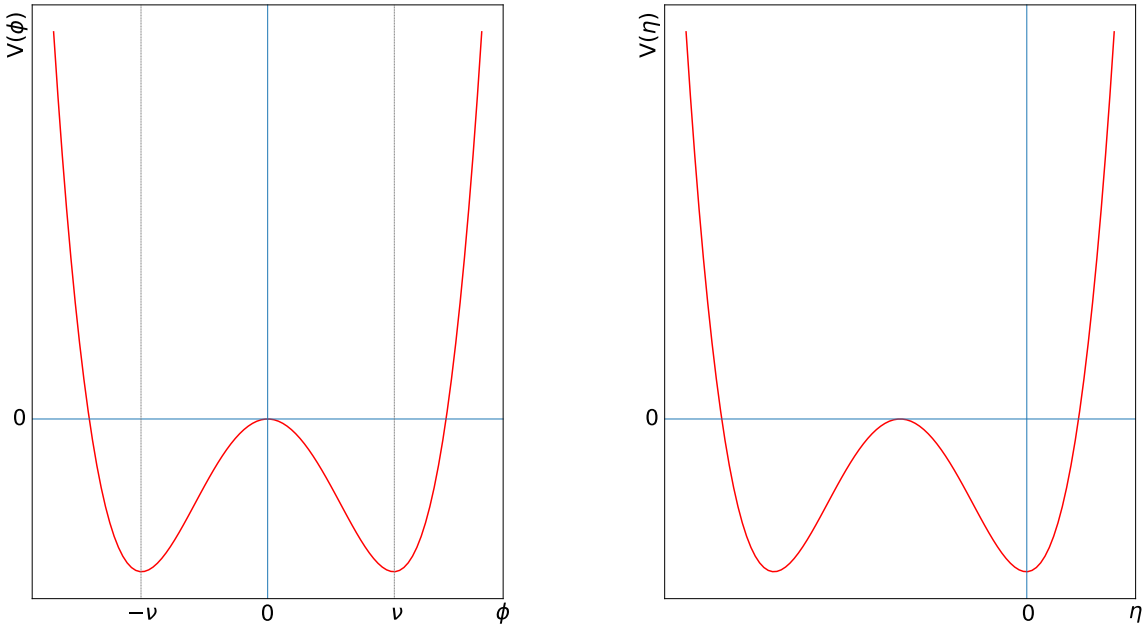

Figure 2.1: Shape of the potential $V(\phi)$ for imaginary values of the mass μ before (left) and after (right) a global transformation of ϕ.

Similar principles may be applied to a *complex* scalar field $\phi = \phi_1 + i\phi_2$ with Lagrangian density given by

$$\mathcal{L} = \frac{1}{2}(\partial_\mu \phi)(\partial_\mu \phi)^* - \left(\frac{1}{2}\mu^2\phi^*\phi + \frac{1}{4}\lambda(\phi^*\phi)^2\right) \ . \tag{2.32}$$

Given μ^2 is negative and λ is positive, the potential $V(\phi)$ has the form shown in Figure 2.2. The complex field is invariant under a phase transition which represents a *continuous* global symmetry, unlike the mirror symmetry displayed by the Lagrangian density of the real field in Equation 2.30.

In polar coordinates, the complex Lagrangian density may be written as

$$\mathcal{L} = \frac{1}{2}\partial\rho^2 + \frac{1}{2}\lambda^2\rho^2 + \frac{1}{2}\rho^2\partial\omega^2 - \frac{1}{4}\lambda\rho^4 \tag{2.33}$$

with $\phi = \rho e^{i\omega}$. The kinetic term containing $\partial\rho^2$ represents radial oscillations of the field which, given the shape of $V(\phi)$, result in changes in the potential, hence the mass term in ρ^2. The kinetic term in $\partial\omega^2$ represents angular fluctuations of the field. The latter do not involve changes in potential energy and thus there is no term in ω^2. The mass of the particles produced from oscillations of the field may be obtained by applying the global transformation $\rho \to h$, where $h = \rho - \nu$. Omitting self-interaction terms, the Lagrangian density of the complex scalar field after spontaneous symmetry breaking is

$$\mathcal{L}' = \frac{1}{2}\partial h^2 - \lambda\nu^2 h^2 + \frac{1}{2}\nu^2\partial\omega^2 \ . \tag{2.34}$$

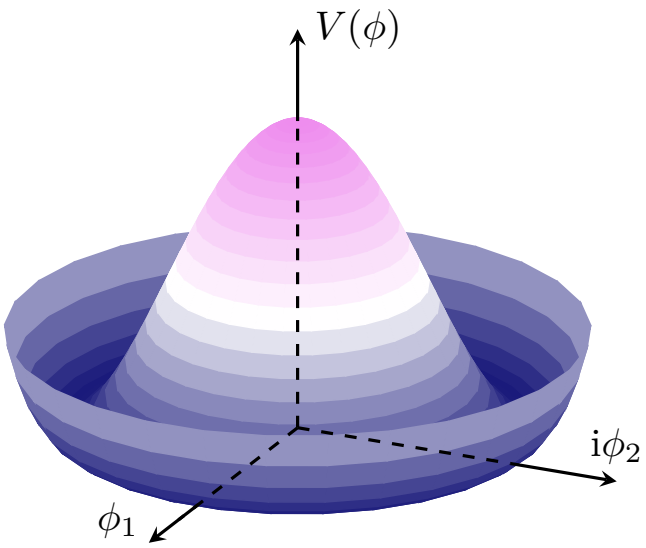

Figure 2.2: Potential $V(\phi)$ of a complex singlet scalar field.

It may be deduced that a massive scalar Higgs boson with mass $\sqrt{\lambda\nu^2}$ arises from radial oscillations of the field. Furthermore, as stated by the Goldstone theorem [66–68], the spontaneous breaking of a continuous symmetry of the Lagrangian generates a *massless* scalar, and hence an extra degree of freedom, for every *generator* of the broken symmetry.

The masses of the W and Z bosons are derived from the spontaneous symmetry breaking of the SM Lagrangian density. The term describing the scalar Higgs field is

$$\mathcal{L}_{Higgs} = (D^\mu\phi)^\dagger (D_\mu\phi) - V(\phi) \ , \tag{2.35}$$

where ϕ is a complex scalar doublet given by

$$\phi = \begin{pmatrix} \phi^+ \\ \phi^0 \end{pmatrix} \ . \tag{2.36}$$

The use of a covariant derivative $D_\mu\phi$ instead of a simple partial derivative makes the SM Lagrangian density gauge invariant. W^i_μ and B_μ are the $SU(2)$ and $U(1)$ gauge bosons described in Section 2.1.2 respectively. The definition of $D_\mu\phi$,

$$D_\mu\phi = \left(\partial_\mu + igT^iW^i_\mu + i\frac{1}{2}g'B_\mu\right)\phi \ , \tag{2.37}$$

demonstrates interactions between the gauge and scalar fields.

The SM Higgs potential $V(\phi)$ is given by

$$V(\phi) = -\mu^2\phi^\dagger\phi + \lambda\left(\phi^\dagger\phi\right)^2 \ , \tag{2.38}$$

and has an infinite degeneracy at the minimum with $\phi^\dagger\phi = \nu^2/2$. In order to maintain electric charge conservation, the vacuum expectation value is acquired by the neutral component of the field ϕ^0. The $SU(2)_L \times U(1)_Y$ symmetries are broken, leaving a linear combination of generators that span $U(1)_Q$ unbroken. Applying the gauge transformation $\phi^0 \to h$ as given

by

$$\phi = \frac{1}{\sqrt{2}} \begin{pmatrix} 0 \\ \nu + h \end{pmatrix} \ , \tag{2.39}$$

where $h = \phi^0 - (1/\sqrt{2})\nu$, therefore causes *electroweak* symmetry breaking ($SU(2)_L \times U(1)_Y \rightarrow U(1)_Q$), leaving one unbroken generator.

Expanding the kinetic term $(D^\mu\phi)^\dagger (D_\mu\phi)$, and omitting the h terms not involved in generating the gauge boson masses, gives the result

$$\begin{aligned} (D^\mu\phi)^\dagger (D_\mu\phi) &= \left| \left(\partial_\mu + igT^i W_\mu^i + \frac{i}{2} g' B_\mu \right) \frac{1}{\sqrt{2}} \begin{pmatrix} 0 \\ \nu \end{pmatrix} \right|^2 \\ &= \frac{\nu^2}{8} \left[g^2 \left(\left(W_\mu^1\right)^2 + \left(W_\mu^2\right)^2 \right) + \left(gW_\mu^3 - g'B_\mu \right)^2 \right] \ . \end{aligned} \tag{2.40}$$

In this *unitary* gauge, the three Goldstone boson kinetic terms arising from each of the three broken generators in $SU(2)_L \times U(1)_Y$ are *absorbed* by the kinetic terms in W_μ^i and B_μ to produce mass terms for the $W^\pm$ and Z bosons.

It is possible to define the mass states $W_\mu^\pm$, Z_μ, and A_μ as combinations of the gauge bosons W_μ^i and B_μ as given by

$$W_\mu^\pm \equiv \frac{1}{\sqrt{2}} \left(W_\mu^1 \mp i W_\mu^2 \right) \ , \tag{2.41}$$

$$Z_\mu \equiv \frac{1}{\sqrt{g^2 + g'^2}} \left(gW_\mu^3 - g'B_\mu \right) \ , \tag{2.42}$$

$$A_\mu \equiv \frac{1}{\sqrt{g^2 + g'^2}} \left(g'W_\mu^3 - gB_\mu \right) \ , \tag{2.43}$$

The coefficients of the $W_\mu^\dagger W^\mu$, $Z_\mu^\dagger Z^\mu$ and $A_\mu^\dagger A^\mu$ terms are used to deduce the masses $m_W = g\nu/2$, $m_Z = \nu\sqrt{g^2 + g'^2}/2$ and $m_A = 0$ of the $W^\pm$, Z and γ bosons respectively.

Yukawa couplings

The Dirac field ψ in Equation 2.5 may be described by a four-component function, called a Dirac spinor, given by

$$\psi = \begin{pmatrix} \psi_1 \\ \psi_2 \\ \psi_3 \\ \psi_4 \end{pmatrix} \ . \tag{2.44}$$

The ψ_1 and ψ_2 components represent positive and negative energy states for particles and anti-particles respectively. The ψ_3 and ψ_4 components represent spin $1/2$ and $-1/2$ states respectively.

Expanding the Dirac equation in Equation 2.6 for a left-handed fermion spinor ψ_L gives

$$i\gamma^0\partial_0\psi_L + i\gamma^1\partial_1\psi_L + i\gamma^2\partial_2\psi_L + i\gamma^3\partial_3\psi_L + i\gamma^4\partial_4\psi_L = m\psi_L \ , \tag{2.45}$$

$$i\partial_0\psi_L + i\gamma^0\gamma^1\partial_1\psi_L + i\gamma^0\gamma^2\partial_2\psi_L + i\gamma^0\gamma^3\partial_3\psi_L + i\gamma^0\gamma^3\partial_3\psi_L = m\gamma^0\psi_L = m\psi_R \ , \tag{2.46}$$

where a right-handed spinor arises from the action of γ^0 on ψ_L whereby the ψ_3 and ψ_4 components switch sign.

Given the weak force only couples to left-handed fermions, Equations 2.45 and 2.46 violate weak charge conservation. Therefore, fermions arising from a free field Lagrangian density are required to be massless. Similarly, gauge invariance of the Dirac Lagrangian density (Equation 2.5) does not allow for mass terms of the form $-m(\bar{\psi_R}\psi_L + \bar{\psi_L}\psi_R)$ since the ψ_L and ψ_R spinors do not transform in the same manner. Mass terms for the fermions are obtained from the Yukawa Lagrangian density [5] given by

$$\mathcal{L} = \frac{g_f}{\sqrt{2}}\bar{\psi_L}\phi\psi_R + h.c. \ , \tag{2.47}$$

for a single fermion field ψ. The coupling constant of the fermion to the Higgs field is g_f, and $h.c.$ represents the Hermitian conjugate. The presence of the Higgs field, represented by ϕ allows the Yukawa Lagrangian density to be gauge invariant.

Applying the gauge transformation $\phi \to h$ with $h = \phi - \nu$, and omitting terms in h, we have

$$\mathcal{L} = \frac{g_f\nu}{\sqrt{2}}(\bar{\psi_L}\psi_R + h.c.) \ , \tag{2.48}$$

from which the mass of the fermion may be deduced as $g_f\nu/\sqrt{2}$.

2.1.4 Standard Model Higgs boson predictions

Phenomenological predictions of the SM enable certain constraints to be placed on the properties of the Higgs boson. The only property of the Higgs boson that cannot be predicted by the SM is its mass (m_H) because, as described in Section 2.1.3, m_H is related to the vacuum expectation value of the Higgs field through the Higgs self-coupling parameter (λ) which is itself a free parameter in the SM.

Based on the theory described in Sections 2.1.2, 2.1.2 and 2.1.3, the Lagrangian density in the interacting Higgs sector of the SM may be written as

$$\begin{aligned}\mathcal{L}_{Higgs} = &\frac{1}{2}(\partial^\mu\phi)(\partial_\mu\phi) + \frac{m_H^2}{2}h^2 - \frac{m_H^2}{2\nu}h^3 - \frac{m_H^2}{8\nu^2}h^4 \\ &+ \left(m_W^2 W_\mu^+ W^{-\mu} + \frac{1}{2}m_Z^2 Z_\mu Z^\mu\right)\left(1 + \frac{\phi}{\nu}\right)^2 \\ &- \sum_f m_f\overline{\psi}\psi\left(1 + \frac{\phi}{\nu}\right)) \ .\end{aligned} \tag{2.49}$$

The couplings of all the fermions and the gauge bosons to the Higgs boson are, therefore, proportional to the mass of the said fermion or to the squared-mass of the said boson respectively. The vacuum expectation value ν can be defined from using a highly accurate measurement of the four-fermion interaction constant G_F as

$$\nu = \frac{1}{(\sqrt{2}G_F)^{1/2}} = 246.22 \text{ GeV} \ . \tag{2.50}$$

Feynman rules, SM self-consistency and SM unitarity requirements may be used to calculate

the Higgs boson decay widths and production cross-sections as a function of m_H, taking strong and electroweak radiative corrections into account.

2.2 Higgs boson phenomenology at the LHC

2.2.1 Production and decay channels

Since the couplings of the SM Higgs boson to elementary particles are related to the mass of the particle concerned, in a proton-proton (pp) collision, a Higgs boson will preferably be formed from couplings of heavy elementary particles such as the top quark and weak gauge bosons rather than from the relatively light up and down quarks that constitute the proton. As shown in Figure 2.3, the cross-section for the production of Higgs boson in pp collisions may still be predicted as a function of its mass, and decreases with increasing Higgs boson mass [40, 69–71]. The Feynman diagrams for the four main production modes, namely gluon-gluon fusion (ggH), vector boson fusion (VBF), Higgs-strahlung (VH) and production in association with top quarks (ttH), are given in Figure 2.5.

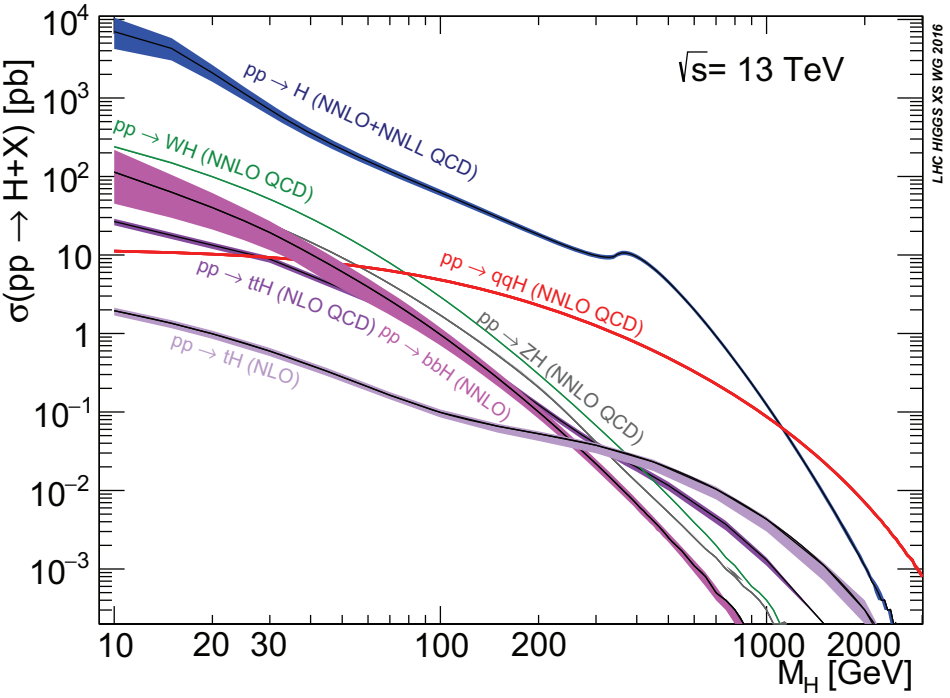

Figure 2.3: SM Higgs boson production cross-sections in pp collisions at a centre-of-mass energy of 14 TeV. [69]

Similarly, once produced, the SM Higgs boson will predominantly decay into the heaviest SM particles available (bottom quark, and W and Z bosons) [40, 69–71]. As described in Section 2.1.3, couplings of the Higgs boson to fermions are different from those to gauge bosons in the SM. Thus, decays into pairs of bosons ($\gamma\gamma$, ZZ, or WW) and decays into pairs of fermions (bb or $\tau\tau$) are purposefully targeted. The branching fractions in these decay

modes for different possible masses of a SM Higgs boson are shown in Figure 2.4. The mass the Higgs boson was experimentally inferred from measurements of the final states in each decay channel. Theoretical predictions for a Higgs boson of the observed mass can yield a corresponding cross-section for production, and branching fractions in the decay channels being considered. The Higgs mechanism was therefore confirmed when the experimentally observed particle was found to have the same quantum numbers and coupling constants with fermions and bosons as predicted for a SM Higgs boson of the observed mass [27, 28]. Clearly, the search sensitivity at a given luminosity essentially depends on the cross-section of the Higgs boson in its production modes, its branching fraction in the decay channels considered, and on the efficacy of the experiment to observe these processes.

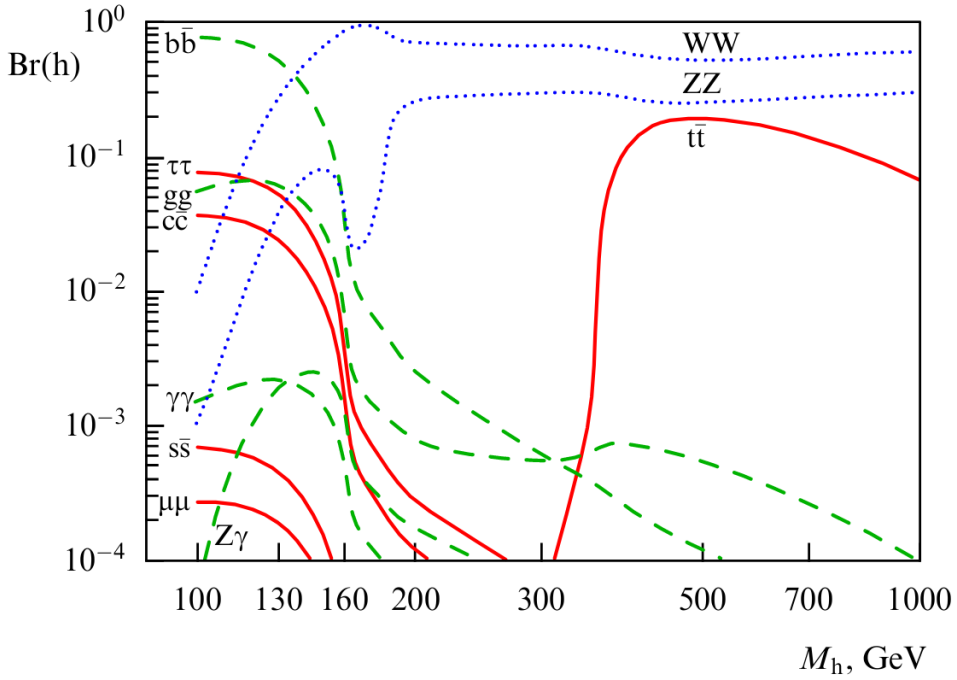

Figure 2.4: SM branching fractions of a SM Higgs boson as a function of the Higgs boson mass.[69]

The Large Hadron Collider (LHC), described in Section 3.2.1, and two dedicated detectors, namely ATLAS [72–74] and CMS [37, 38] (Section 3.3), were built to investigate the possible existence of the Higgs boson. Shortly after the Higgs particle was postulated, phenomenological research addressing possible Higgs boson production channels in e^+e^-, $p\bar{p}$ and pp collisions began in the 1970s. At a Higgs boson mass of around 125 GeV, the SM predicts the dominant production mechanism at the LHC (Table 2.1) to be gluon-gluon fusion (ggH) since, as shown in Figure 2.5 (a), it takes place through a quantum loop of virtual top quarks which, being heavy particles, readily couple to the Higgs boson. In vector boson fusion (VBF) and the associated production modes (VH and ttH), the decay products of distinctive particles produced in association with the Higgs boson enable higher signal-to-background ratios to be achieved than in the ggH process. However, as seen from Figure 2.3 and Table 2.1, these modes have relatively lower cross-sections. In the VBF process (Figure 2.5 (b)), a Higgs boson is produced from a pair of weak bosons, each emitted

from a quark of the two incoming protons. The final state quarks are distinctly identified in the forward region of the detector as two high-energy jets. Similarly, a Higgs boson produced in association with one W or Z (decaying leptonically or hadronically) or two to six jets (decays of t and $\bar{t}$) is indicative of associated VH and ttH production respectively as shown in Figure 2.5 (c) and (d). Aside from being easily tagged, VBF, VH and ttH production channels can shed light on the couplings of the Higgs boson to top quarks and vector bosons.

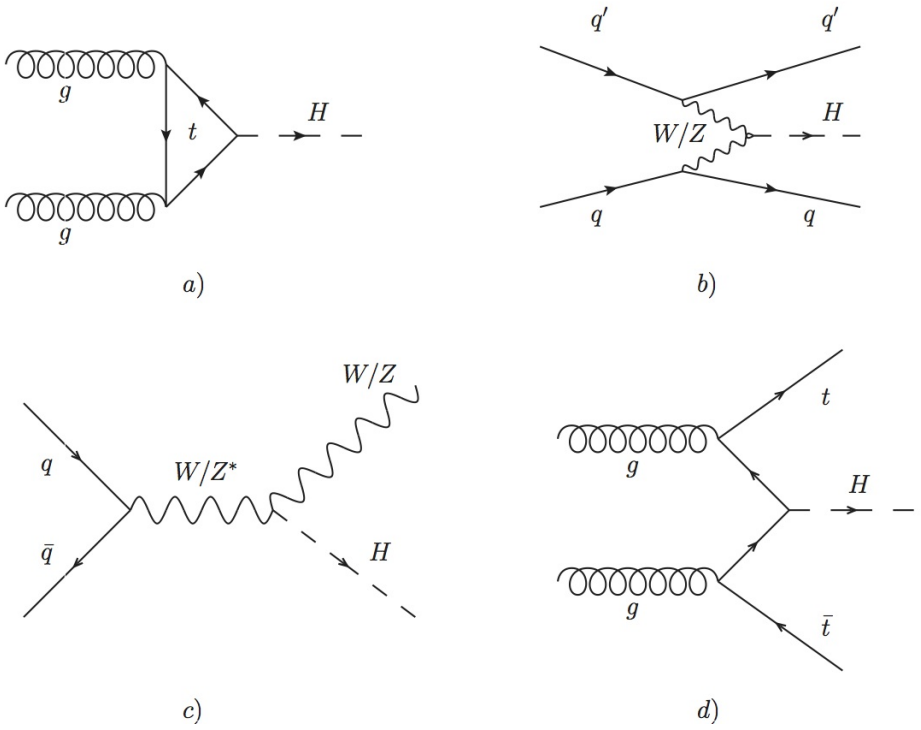

Figure 2.5: Feynman diagrams for the four main production modes of the Higgs boson at the LHC, namely ggH (a), VBF (b), VH (c) and ttH (d).

A salient property of the SM Higgs boson is its large Yukawa coupling to the top quark y_t^{SM}. The measurement of y_t is particularly important for understanding EWSB and allows for testing BSM theories. The magnitude and sign of y_t is indirectly tested by measurements of the associated production of Z and Higgs bosons via gluon-gluon fusion [75], which receives large contribution from loop diagrams involving the top quarks. In addition y_t is probed in H$\rightarrow \gamma\gamma$, as the decay width also involves loop diagrams with the top quark, providing sensitivity to the sign of y_t^{SM}. These measurements presently disfavour a negative value of the coupling [76, 77]. Although y_t can be directly measured in the ttH production, this mode is only sensitive to the magnitude of the coupling. In contrast, tH production proceeds via two types of Feynman diagrams [78–81], where the Higgs boson may couple to either the top quark or the W boson (Figure 2.6). In the SM the relative sign of the Higgs coupling to bosons and fermions is assumed to be negative. This leads to the destructive interference between the diagrams shown in Figure 2.6. The tH cross-section is therefore uniquely sensitive to the magnitude as well as the relative sign and phase of the couplings. A same-sign coupling would translate to a large enhancement in the tH cross-section relative to the cross-section of modes involving the coupling of the Higgs boson to bosons.

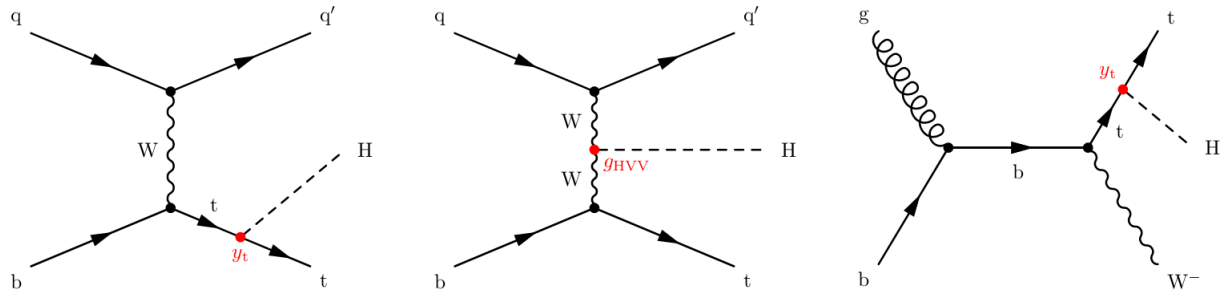

Figure 2.6: Leading order Feynman diagrams for the associated production of a single top quark and a Higgs boson in the t-channel, where the Higgs boson couples either to the top quark (left) or the W boson (centre), and one representative diagram of tHW production, where the Higgs boson couples to the top quark (right). [82]

Table 2.1: SM cross-section values for the main Higgs boson production processes at the LHC for $\sqrt{s} = 13\,\text{TeV}$ and $m_H = 125\,\text{GeV}$ [40].

Production mode	ggH	VBF	WH	ZH	$t\bar{t}H$	bbH	tH
cross-section (pb)	48.71	3.78	1.37	0.88	0.51	0.49	0.07

Measuring the branching fractions of an observed candidate state into the mentioned decay channels can enable the distinction of a SM Higgs boson from a new particle predicted in an extension of the SM or in an alternative BSM theory. The SM predictions for the branching fractions in the main Higgs bosson decay modes are given in Table 2.2. Despite their different branching fractions, all five decay channels are used to provide complementary information on the properties of the Higgs boson. The presence of a Higgs boson signal is indicated by an excess of events at approximately the same mass value in the reconstructed invariant mass spectrum of each channel. The narrower the range of mass over which the excess extends, the better is the mass resolution of the signal.

Table 2.2: SM branching fractions for the main Higgs boson decay modes. [40]

Decay mode	bb	WW	gg	$\tau\tau$	cc	ZZ	$\gamma\gamma$
Branching fraction (%)	58.2	21.4	8.2	6.3	2.8	2.6	0.23

Decay channels which yield a narrow mass peak over a continuous background are essential to precisely determine the mass of the SM Higgs boson, given its natural decay width of only a few MeV. The Higgs boson mass can be fully reconstructed with high resolution from the diphoton final state ($H \to \gamma\gamma$) and the Higgs boson decay into four charged leptons which may be electrons or muons ($H \to ZZ^* \to 4l$).

2.2.2 Theory and kinematics of the $H \to \gamma\gamma$ decay

Shortly after the Higgs boson was postulated, decay rates in the $H \to \gamma\gamma$ channel were precisely calculated [83, 84]. Since the Higgs boson has no tree-level couplings to the photon, the leading order Feynman diagrams for the $H \to \gamma\gamma$ decay are all loop-induced (Figure

2.7), with the $W^{\pm}$ loops and top quark loops interfering destructively. Although the W contribution leads to divergent integrals, the one-loop amplitude of the $H \to \gamma\gamma$ decay may be made finite through a gauge invariant regulator method such as dimensional regularisation. The $H \to \gamma\gamma$ width is given by

$$\Gamma_{H\to\gamma\gamma} = \frac{\alpha^2 g^2 m_H^3}{1024\pi^3 m_W^2} \left| \sum_i N_C e_i^2 F_i \right|^2 \quad , \tag{2.51}$$

with the summation being performed over all SM particles. The symbol, F_i, denotes a function of $(m_i/m_H)^2$ which vanishes for $m_i \ll m_H$, m_i being the mass of the particle in the loop. Notably, radiative corrections to the value of $\Gamma_{H\to\gamma\gamma}$ only significantly affect the top quark loop for which the QCD corrections are less than 3%. The $H \to \gamma\gamma$ channel, by virtue of its loop contributions, provides sensitivity to both SM masses and possible supersymmetric particle masses well above the mass of the Higgs boson itself. Most importantly, the very observation of the diphoton decay channel itself firmly establishes that the Higgs particle is a boson with a spin other than 1 (Landau-Yang theorem) [85, 86].

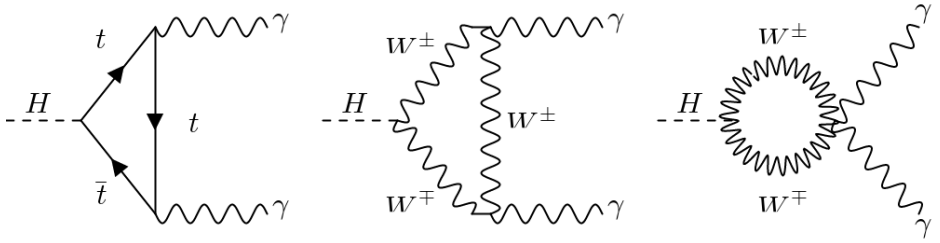

Figure 2.7: Feynman diagrams showing the decay of the SM Higgs boson to two photons via fermion (e.g top quark) and W loops [87].

The $H \to \gamma\gamma$ decay is coincidentally most significant in the region of the Higgs boson mass ($110 - 150\,\text{GeV}$) (Figure 2.4) and, compared to most of the other decay modes, can still give a signal of higher mass resolution and signal strength despite its low branching fraction ($\sim$0.23%). Indeed, at the time of discovery, the observed significance in the $H \to \gamma\gamma$ decay channel was the highest of all analysed decay modes [27, 28]. Kinematically, pairs of photons are produced almost isotropically, giving a clearly distinctive final state topology: two isolated photons with a diphoton invariant mass of $\sim 125\,\text{GeV}$. High resolution measurements of individual photon energy (E_γ) and azimuthal separation (θ) of pairs of photons are made possible by the ECAL (Section 3.3.4) of the CMS experiment which was purposely designed with excellent depth segmentation and around 1% energy resolution in the region relevant to the determination of the Lorentz-invariant diphoton mass ($m_{\gamma\gamma}$) [37, 38]. The latter variable may be calculated starting from the relativistic energy momentum equation,

$$m^2 = E^2 - |\,\vec{p}\,|^2 \quad . \tag{2.52}$$

For a two-particle decay such as $H \to \gamma\gamma$,

$$m^2 = (E_1 + E_2)^2 - |\,\vec{p_1} + \vec{p_2}\,|^2 = m_1^2 + m_2^2 + 2(E_1 E_2 - \vec{p_1} \cdot \vec{p_2}) \; . \tag{2.53}$$

Since photons are massless, we have

$$m_{\gamma\gamma}^2 = 2p_1p_2(1-\cos\theta) = 2E_\gamma^1 E_\gamma^2(1-\cos\theta)\ , \tag{2.54}$$

where θ represents the angles between the two photons in the frame of the laboratory.

The narrow mass peak from the $H \to \gamma\gamma$ process appears over a continuously falling background. The latter arises mostly from both prompt diphoton production in gg and $q\overline{q}$ annihilation. Additionally jets (in di-jet and $\gamma +$ jet events) may be misidentified as photons, when high-energy neutral mesons, such as neutral pions and η mesons, decay into a pair of photons. With an angular separation of the order of the ECAL granularity, these photons are measured as a single photon in the detector, fairly isolated from the remaining constituents of the jet. Such backgrounds can be reduced through strict photon identification criteria (Section 5.2.4). In an event reconstructed from two highest energy photons, the leading and subleading photons have the higher and lower momentum of the pair respectively.

2.3 Status of Higgs boson measurements

The LHC physics program announced the discovery of a 'Higgs boson-like' particle on the 4^{th} of July 2012, after nearly a five-decade search (Section 3.2.2) [27, 28]. With an aim to confirm whether the observed state was indeed the SM Higgs boson, the ATLAS and CMS experiments performed a series of subsequent measurements to evaluate its exact properties of decay width, spin-parity and couplings to other gauge bosons and fermions, requiring further analyses in more channels and at higher luminosities. It was only two years later, after its properties had been thoroughly studied, that the observed boson was confirmed to be the Higgs boson predicted by the SM. To this date, the existence of the majority of the main production and decay modes expected have been unambiguously confirmed. The ggH and VBF production modes were observed during Run I of the LHC [77, 88, 89] (Section 3.2.2), while the VH and ttH modes were observed during Run II [90–93]. As regards the decay channels, the $\gamma\gamma$, ZZ and WW modes were observed during Run I [77, 88, 89], while the bb and $\tau\tau$ channels were observed later during Run II [92–95]. In 2012, the CMS collaboration and the ATLAS collaboration respectively reported a mass of $125.3 \pm 0.4\,(\text{stat.}) \pm 0.5\,(\text{syst.})\,\text{GeV}$ and $126.0 \pm 0.4\,(\text{stat.}) \pm 0.4\,(\text{syst.})\,\text{GeV}$ for the observed boson [96]. With the availability of more data, CMS published the most precise measurement for the mass of the Higgs boson, $125.38 \pm 0.14\,\text{GeV}$, using data from the $H \to \gamma\gamma$ and $H \to ZZ^* \to 4l$ channels [97].

For a SM Higgs boson of mass around 125 GeV, a narrow decay width (Γ_H) of approximately 4 MeV is predicted [69]. Since the LHC detectors have energy resolutions of the order of GeV, any direct measurement of Γ_H from a peak in an invariant mass spectrum is presently unachievable. However, direct limits may be obtained by studying the relative rates of the off-shell $gg \to H^* \to ZZ$ to on-shell $gg \to H \to ZZ$ production of the particle in the gluon-gluon fusion mode. CMS analyses have yielded a 68% confidence level central values (with uncertainties) and a 95% confidence interval (in square brackets) of $3.2^{+2.8}_{-2.2}\,[0.08, 9.16]\,\text{MeV}$ for the observed Γ_H value [98].

In quantum mechanics, fermion fields follow Fermi-Dirac statistics [49, 99] while boson fields follow Bose-Einstein statistics [100]. As per the spin-statistics theorem, bosons possess integer spin and fermions possess half-integer spin. The spin quantum number of a particle may be further used to define a helicity whereby right-helicity particles have the same direction of spin and motion, while left-helicity particles have opposite directions of spin and motion. The parity quantum number of a particle relates to invariance under a parity (mirror) transformation of the corresponding particle field. The bosonic nature of the Higgs boson state was inferred from its peaks in the four-lepton and two-lepton invariant mass spectra and from its decay into two photons. According to the Landau-Yang theorem [85, 86], a spin-1 particle does not decay into a final state with two identical spin-1 particles such as the observed $\gamma\gamma$ state. Moreover, a half-integer spin particle cannot decay into a pair of bosons. These only suggest that the observed boson has an integer spin other than one; it is essential to know whether or not the observed boson is scalar, a feature characteristic of the SM Higgs boson. Angular correlations between decay products in spin-parity analyses in the $H \to ZZ \to 4l$ channel and in spin analyses in the $H \to \gamma\gamma$ and $H \to WW \to \mu\nu e\nu$ channels from both CMS and ATLAS supported the $J^P = 0^+$ state over the 0^- and 2^+ states at the 95% CL level [101–103]. However, the possibility of the Higgs boson being a mixture of scalar and pseudoscalar states is still being entertained.

Early after the discovery, the measured fermionic and bosonic couplings of the observed particle were found to agree within 10-20% with SM predictions [77, 88, 89]. Two parameterisation schemes, namely the signal strength modifier (μ) and the coupling modifier (κ), were considered [71]. In terms of the cross-section σ_j and the branching ratio (BR_j), μ_j for a process j is defined as

$$\mu = \frac{\sigma_j \times BR_j}{(\sigma_j \times BR_j)_{SM}} \ , \tag{2.55}$$

where the SM subscript denotes predicted values in the SM. In the κ framework, the coupling modifier for a particle or group of particles is derived from the width Γ_j or σ_j of the processes involving the particle(s) and the Higgs boson as

$$\kappa^2 = \frac{\Gamma_j}{\Gamma_j^{SM}} = \frac{\sigma_j}{\sigma_j^{SM}} \ . \tag{2.56}$$

Effective coupling modifiers are used for processes which involve loop corrections such as ggH and $H \to \gamma\gamma$. Ratios of κ_j multipliers do not require prior assumptions on Γ_H, κ_Z or κ_W, and therefore allow certain experimental and theoretical systematic uncertainties to be cancelled.

The inclusive Higgs boson signal strength is now measured to a precision of around 10% [104, 105]. Figure 2.8 shows the signal strength modifier measurements using the 2016 Run II dataset [106]. Examples of more recent CMS coupling measurements are detailed in Section 2.3.1.

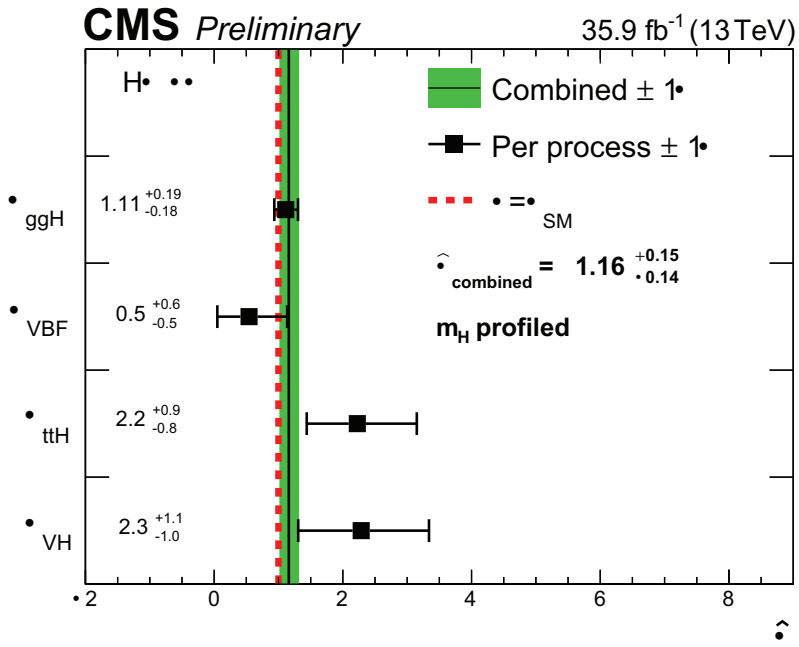

Figure 2.8: Signal strength modifier measurements in the $H \to \gamma\gamma$ decay channel. The modifiers for each process (black points) are shown, with the SM Higgs boson mass profiled, compared to the overall signal strength modifier (green band) and to the SM expectation (dashed red line). [106]

2.3.1 The simplified template cross-section framework

Building upon the signal strengths and coupling modifier frameworks described in Section 2.3 and used in the LHC Run I, Higgs coupling measurements are now presented in an improved framework, namely the simplified template cross-sections (STXS) framework [40]. Within a given SM production mode, kinematic thresholds are used to define regions of phase space, called *bins*, in which Higgs boson cross-section measurements are made. These may be subsequently used, together with ratios of bin decay widths, for interpreting signal strengths, coupling modifiers, effective field theory coefficients or BSM theories. These parameters may be further related to the interpretation of Lagrangian parameters of models not restricted to the SM. Further, the separation into production modes removes the dependence of measurements on the relative cross-sections in the SM.

The precision of measurements of a given process suffers from theoretical uncertainties in both the underlying model and the model predictions. Separating measurements into well-defined granular regions allows the theoretical uncertainties affecting individual sub-processes to be decoupled. For instance, BSM effects may be isolated by defining regions at large kinematic scales. Furthermore, as theoretical predictions for the individual bins are improved, STXS measurements made previously may be updated accordingly in the long term. It is thus important to quantify correlations between the STXS bins. In short, finely-grained measurements shift theory dependence from the measurement stage to the theoretical interpretation stage, whereby the precision of measurements is less affected by theoretical uncertainties. Residual theoretical uncertainties remain because of the exper-

imental acceptance of each STXS bin but these may be minimised by defining bins with minimal variation in experimental acceptance.

With a consistent STXS framework that encompasses all production modes, it is possible for STXS measurements from multiple decay channels to be globally combined across several analyses in a systematic manner in order to maximise the experimental sensitivity of the measurements. Multivariate analysis techniques as described in Section 5.4 may be used to target STXS bins during event categorisation.
The definition of the kinematic thresholds for the STXS regions should therefore allow for sufficient granularity to reduce theory dependence and maximise experimental sensitivity while simultaneously being broad enough to capture sufficient events at a given luminosity. The higher the integrated luminosity available, the lower are the uncertainties in the parameters measured from individual STXS regions. The STXS framework is therefore developed in stages of increasing granularity whereby more bins may be measured as more data is accumulated at the LHC.

Measurements of signal strenth modifiers from the CMS STXS ggH+VBF analysis with STXS Stage 1.0 in $H \to \gamma\gamma$ [3] are shown in Figure 2.9. The combination of coupling measurements across different decay channels may further increase precision.

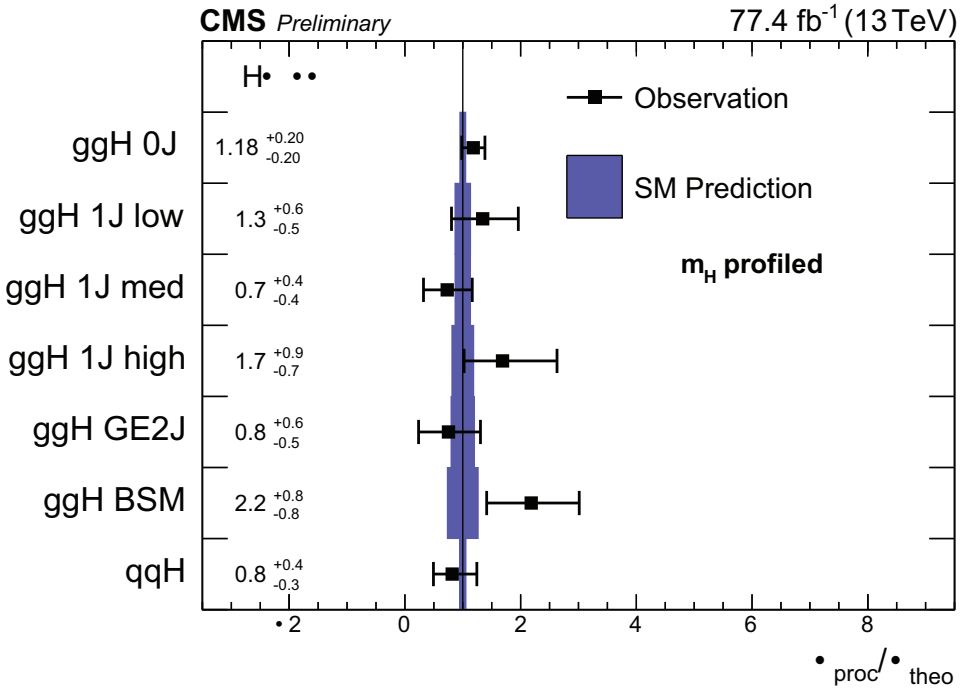

Figure 2.9: Normalised cross-sections measured for each Stage 1.0 bin (black points) in the STXS framework, with the SM Higgs boson mass profiled, compared to the SM expectations and their uncertainties (blue band). [3]

Presently, STXS measurements have been performed in all major Higgs boson decay channels, namely $H \to \gamma\gamma$, $H \to ZZ^* \to 4l$, $H \to WW^* \to 2l2\nu$, $H \to \tau\tau$, and $H \to b\bar{b}$, and from combinations of multiple decay modes [1, 107–112]. So far, all measurements have been

found to be consistent with the SM predictions. After the first STXS measurements, multiple refinements have been brought to the definitions of the kinematic STXS bins. Presently, the STXS Stage 1.2 serves as the baseline for the full LHC Run II dataset measurements. Details of the Stage 1.2 bins are given in Chapter 5. Cross-section measurements for STXS Stage 1.2 bins in the diphoton decay channel and using the full LHC Run II dataset are presented in Chapter 6 of this thesis [1]. Where necessary, intermediate stages to reach the full Stage 1.2 binning have been implemented by merging bins that cannot be split (Section 6.6.1).

2.3.2 Missing elements of Higgs boson measurements

As stated previously, the discovery of the Higgs boson was deemed a sufficient proof of the Higgs mechanism. However, several anomalies relating to the mechanism still remain unexplained. For instance, the Higgs field has an energy density 55 orders higher than the critical energy density of space as given by the cosmological constant [30]. In this context, the investigation of the self-coupling of the Higgs boson may verify the theoretical vacuum expectation value of the Higgs field, used to derive its energy density.

Among the other shortcomings of the SM is the absence of an explanation for dark matter and dark energy which account for 25% and 70% of the universe respectively [31]. In Higgs portal models [113], the Higgs boson mediates interactions between SM and dark matter. It is believed that the Higgs boson would have large couplings to dark matter candidates such as weakly-interacting massive particles [114] which might be detected through invisible decays of the Higgs boson. Limits derived on the branching ratio of $H \rightarrow invisible$ decays may thus be used to constrain dark matter models.

Owing to its multiple interactions with other SM particles, the SM Higgs boson is predicted to be much heavier than observed; a value of 125 GeV requires large loop corrections [29]. The leading BSM theory, supersymmetry (SUSY) [115] considers the possibility of a light Higgs boson by postulating partners to every SM particle which would counter the contributions of SM particles to the mass of the Higgs boson. In particular, possible heavy supersymmetric particles are expected to be observed through their decays into the Higgs boson. Previous experimental results [76, 77, 88–95, 116, 117] have severely constrained the possibility of additional Higgs bosons in the mass range of 65 -710 GeV, and these particles are now expected in the TeV range.

With the planned HL-LHC era (Section 3.2.2) higher achievable luminosity will enable precise Higgs boson coupling measurements and increase the sensitivity to rare SM and BSM decays and to new particles over a wider mass range.

With a view to deepening our present understanding of the Higgs boson from Runs I and II, the HL-LHC Higgs physics programme (Section 3.2.2) specifically aims at observing as many Higgs boson production modes as possible; making precise measurements of the Higgs boson width, charge-parity (CP) and couplings, especially in the newly accessible rare decay channels; testing SM unitarity via VBS; observing Higgs boson pair production, as well as subsequently measuring its self-coupling; and directly searching for BSM Higgs boson decays as well as heavier partners. [33–36]

2.4 Summary

Fundamental constituents of matter, quarks, and mediators of the forces of nature, bosons, may be described in a mathematical framework called the Standard Model. Properties of particle fields and their interactions may be deduced from their respective gauge field theories and the principle of gauge invariance. Interactions of the different gauge fields in the SM allow fermions and bosons to acquire mass through EWSB and Yukawa couplings, both of which involve the Higgs field. The Higgs mechanism in the SM led to the prediction of the Higgs boson, which was discovered in 2012 at the LHC. The Higgs boson may be detected and its properties measured through its production and decay channels. In this context, the STXS framework has been developed to perform granular measurements of the Higgs boson cross-sections and to enable wider interpretations of experimental measurements compared to the LHC Run 1 findings. Several physical phenomena relating to the Higgs boson still remain unexplained, and BSM theories are expected to be constrained or measured during the coming HL-LHC phase.

Chapter 3

The Compact Muon Solenoid detector

3.1 Introduction

The Large Hadron Collider (LHC) [26], the world's largest and most powerful particle accelerator, was designed and constructed by the *Centre Européen pour la Recherche Nucléaire* (CERN) between 1998 and 2008. The LHC lies on the border of France and Switzerland, near Geneva, and is installed in a 27 km tunnel, which previously housed the CERN Large Electron Positron (LEP) collider [118].

As mentioned in Chapter 2, the main scientific goals behind the construction of the LHC were to explore SM physics and EWSB, and discover or exclude the SM Higgs boson. The LHC was required to provide sufficient luminosity and centre-of-mass energy to allow the SM to be probed at an energy scale where new phenomena could be studied. In particular, the TeV energy scale allows the period between 10^{-32} s and 10^{-12} s after the Big Bang [119], termed the *electroweak epoch*, to be explored for evidence of the Higgs mechanism. Furthermore, several grand unification theories (GUTs) require modification of gravity at the TeV scale [120–123].

The LHC beam pipe (Figure 3.1), located $50 - 175$ m underground, forms eight arcs and eight straight sections, which are used to accelerate and collide two particle beams (protons or ionised nuclei). While the arcs contain magnets required to bend the beams, the straight sections house beam collimation systems at Points 3 and 7, radio frequency systems at Point 4, a beam dump system at Point 6 and and four interaction regions at Points 1, 5, 2, and 8. [26, 124]

Detectors are installed around the interaction points to observe the nature of the collisions and measure the properties of the particles created therein. The four main experiements at the LHC are Compact Muon Solenoid (CMS) [37, 38], A Toroidal LHC Apparatus (ATLAS)[72–74], LHC beauty (LHCb) [125] and A Large Ion Collider Experiment (ALICE) [126]. The CMS detector at Point 5, discussed in more detail in Section 3.3, and the ATLAS

detector at Point 1 are general-purpose high-luminosity experiments aimed at measuring proton-proton collisions at the peak LHC luminosity of $10^{34}\,\mathrm{cm}^{-2}\,\mathrm{s}^{-1}$. Since these two experiments have common physics goals but different designs, they can be used to provide independent measurements of the same phenomena, as was done in 2012 when the two experiments jointly claimed the discovery of the Higgs boson [27, 28]. The LHCb detector at Point 8, operating at a peak luminosity of $10^{32}\,\mathrm{cm}^{-2}\,\mathrm{s}^{-1}$, measures the properties of B hadrons, and the asymmetry between matter and antimatter in decays involving the beauty (b) quark. The ALICE detector at Point 2 is dedicated to measuring the properties of the quark-gluon plasma, created in lead-lead and other nuclei collisions at a peak luminosity of $10^{27}\,\mathrm{cm}^{-2}\,\mathrm{s}^{-1}$.

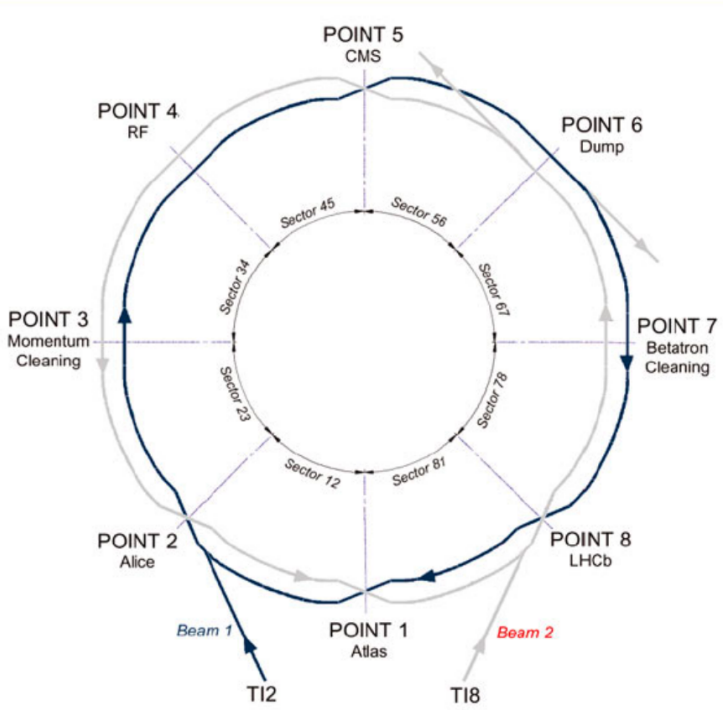

Figure 3.1: Plan of the LHC pipes with eight arcs and eight straight sections. Two counter-rotating particle beams interact at Points 1, 2, 5 and 8 in the ring. [127]

This chapter is dedicated to describing the CMS experiment at the LHC. The following sections describe the general functioning of the LHC facility, the requirements and design of the CMS detector, and the future of the LHC and the CMS experiment. Although the LHC is capable of producing lead-lead nuclei collisions, the focus of this chapter is solely on proton-proton collisions.

3.2 The Large Hadron Collider

3.2.1 Overview

The LHC is an approximately circular accelerator, also known as a *synchrotron*, designed to accelerate charged particles within beam pipes containing a vacuum [26, 124]. The LHC

synchrotron operates using two key forces, namely an accelerating force obtained from applying an electric field to the charged particles, and a Lorentz force for steering the beam, obtained using a magnetic field. The protons come from hydrogen atoms which are fed into the source chamber of a linear accelerator (LINAC 2), where an electric field is used to strip off the electrons, leaving hydrogen nuclei (protons). The protons then pass through a series of synchrotrons of increasing energy (Figure 3.2). The latter include multi-chamber resonant frequency (RF) cavities that apply an alternating electric field oscillating longitudinally at a specific frequency, thereby creating potential differences in the cavities. Therefore, in an isolated chamber in the cavity, a proton experiences an accelerating voltage which switches direction by the time the proton has travelled through the gap. The proton can subsequently be accelerated through the following gap in the cavity. The protons travel in the cavities in synchrony with the RF frequency, forming bunches.

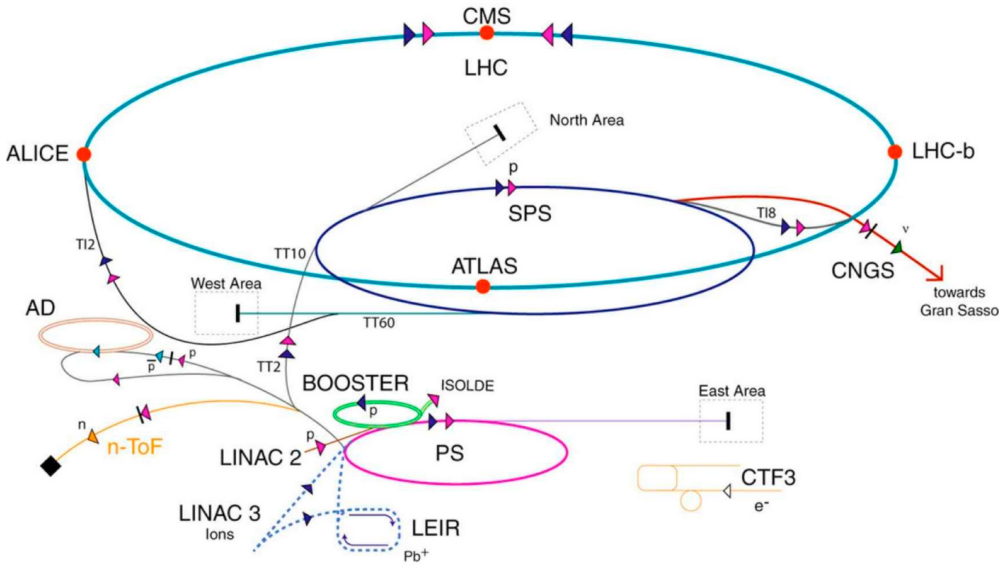

Figure 3.2: The CERN accelerator complex consists of several synchrotrons. Protons are accelerated by the LINAC 2 linear accelerator, the protron synchrotron booster (PSB), the proton synchrotron (PS), the super proton synchrotron (SPS) and the LHC main ring. [128]

As mentioned in Section 3.1, the LHC aims to collide protons with a centre-of-mass energy ($\sqrt{s}$) in the TeV range. The protons are therefore required to be accelerated to a speed close to the universal light speed limit. Precisely, the protons are eventually accelerated to only 3 m/s under the speed of light through a series of synchrotrons of increasing size. The proton synchrotron booster (PSB) of 157 m provides 1.4 GeV, the proton synchrotron (PS) of 628 m provides 25 GeV and the Super Proton Synchrotron (SPS) of 6.9 km then provides 450 GeV. The SPS injects 2808 proton bunches of 1.1×10^{11} protons each into the LHC as two counter-rotating proton beams. The protons eventually acquire a nominal energy of 7 TeV over about 28 minutes, leading to a design centre-of-mass energy of 14 TeV upon collision at one of the beam interaction points.

Owing to the large number of protons per bunch and a bunch collision rate of 40 MHz, it is possible to achieve approximately 20 effective inelastic collisions at every bunch crossing.

Collisions produce particle showers which result in the emission of electrons, muons, photons and jets (from quarks). These final states are measured in the LHC detectors and are used to infer the presence of heavier particles which might have briefly existed during the collision before decaying. The number of events N, given by

$$N = L\sigma \ , \tag{3.1}$$

generated by beam-beam collisions for a given process, is proportional to the cross-section for the process and the area density of beam particles per second per cm^2, known as the beam *luminosity* (L). The main cause of the luminosity decay during nominal LHC operation is the beam loss from collisions. Furthermore, bunches must have a crossing angle to prevent the particles in one beam from experiencing the global electromagnetic field of the other beam. This produces a geometrical luminosity reduction factor since a crossing angle results in smaller beam overlap. Protons that fail to collide are removed at a beam dumping section (Point 6) where they are absorbed by graphite.

While only 16 km of the LHC ring is dedicated to proton acceleration, the remaining sections consist of magnets which are used to bend and focus the proton beams. Of the ~9300 magnets at the LHC ring, 1232 of these are superconducting bending magnets which consist of a 15 m long main unit referred to as the dipole. The bending magnets operate at the nominal magnetic field of 8.3 T. The dipole tube contains two pipes that carry the proton beams, support structures, straps of electromagnets needed to deflect the beam, and space to allow the flow of liquid helium to cool the structure to 1.9 K. The field of 8.3 T in the magnet coils is achieved through the use of superconducting 6-7 μm-thick niobium titanium (Nb-Ti) filaments that carry a current of 11500 A. A cryogenic system bathes the superconducting wires in superfluid helium. The two pipe coils produce magnetic fields in opposing directions such that the resulting magnetic field produces a force towards the centre of the ring for protons in both of the pipes. Stainless steel yokes surround the pipes to resist the attractive force between the two pipe coils. In order to keep the radius of the circular motion constant as the velocity of the protons increases, the magnetic field needs to be increased and kept in synchrony with the proton momentum.

Since protons repel one another, they experience transverse oscillations in both the horizontal and vertical planes. Quadrupoles are used to prevent the protons from diverging by focusing the beam. Other magnetic multipoles correct effects on the beam size and position from other interactions.

3.2.2 Phases of operation

Proton beams were initially and successfully circulated in the main ring of the LHC in September 2008. After the suspension of operations following a major electrical fault, the proton beams were successfully circulated once more in November 2009 when the LHC first provided proton-proton collisions at $\sqrt{s} = 900\,\mathrm{GeV}$.

During Run I of the LHC, the accelerator operated at $\sqrt{s} = 7\,\mathrm{TeV}$ in 2010 and 2011, delivering an integrated luminosity of $\sim 6\,\mathrm{fb}^{-1}$, and setting a world record for the highest-energy man-made particle collisions and highest luminosity for an accelerator. The LHC operated

at $\sqrt{s} = 8\,\text{TeV}$ in 2012, delivering $\sim 23\,\text{fb}^{-1}$. The proton bunch spacing was 150 ns, 75 ns and 50 ns in 2010, 2011 and 2012 respectively. The excellent agreement between observed collisions and the theoretical modelling of proton-proton collisions at the LHC centre-of-mass energy allowed the knowledge of parton distribution functions (PDFs) to be refined.

Run I was marked by the discovery of the Higgs boson [27, 28]. The first indication of a possible Higgs boson particle came in 2011 in the low mass resolution $H \to WW$ channel. Excesses of events over the background with at significance of $2.1\,\sigma$ at a mass of 145 GeV and a significance of $2.3\,\sigma$ at a mass of 120 GeV were observed by the ATLAS and CMS experiments respectively [129, 130]. High mass-resolution decay processes had to be investigated to achieve a higher observed level of significance and confirm the genuineness of the signal. Indeed, later in 2011, both LHC experiments observed excesses of events at a significance slightly higher than $2\,\sigma$ in the 124-126 GeV mass region, compatible with a SM Higgs boson in this mass range [131–136]. An overall increase of 20% in the Higgs boson production cross-section and of 30% in search sensitivity was brought about by the rise in the centre-of-mass energy from 7 TeV to 8 TeV in 2012. On the 4^{th} of July 2012, both the CMS and ATLAS teams announced the discovery of a previously unknown scalar boson. Using a combined analysis across production and decay channels, the experiments, independently, achieved a local significance level of $5\,\sigma$ for the discovery. Results from the $H \to \gamma\gamma$, $H \to ZZ \to 4l$ and $H \to WW \to \mu\nu e\nu$ channels of the 8 TeV run were combined with the previous 7 TeV results in the $H \to WW$, $H \to \tau\tau$ and the $H \to bb$ channels, and with improved analyses of the 7 TeV results in the $H \to \gamma\gamma$ and $H \to ZZ \to 4l$ channels. The CMS collaboration and the ATLAS collaboration respectively reported a mass of $125.3 \pm 0.4\,(\text{stat.}) \pm 0.5\,(\text{syst.})$ GeV and $126.0 \pm 0.4\,(\text{stat.}) \pm 0.4\,(\text{syst.})$ GeV for the observed boson [96].

The LHC facility then underwent its first long shutdown, LS1, to enable an upgrade to the full design operation energy of 7 TeV per beam. Run II commenced in 2015, with the LHC operating at $\sqrt{s} = 13\,\text{TeV}$ and an instantaneous luminosity of $1.7 \times 10^{34}\,\text{cm}^{-1}\,\text{s}^{-1}$ which exceeded the design value. Further tests for the consistency of the observed boson with the SM Higgs boson were still required. Therefore, Run II was characterised by searches for the Higgs boson in all channels predicted by the SM, precise measurements of the mass and couplings of the Higgs boson [76, 116, 117], and BSM physics searches. Precision EW measurements and BSM searches set constraints on possible deviations of the Higgs properties from their SM expectations. Assuming new physics at an energy scale of λ affects the Higgs boson properties, one expects the Higgs boson branching ratios to vary at the level of $\delta \times (1\text{TeV}/\lambda)^2$, with δ of the order (1-10%). Therefore, a precision of a few percent on the measurements of the couplings of the Higgs boson would allow searches to be sensitive to new physics at the TeV scale.

Run II concluded at the end of 2018. At the LHC design luminosity, a 50% reduction in measured statistical errors would necessitate four times more data and hence a 10-year running period. For these reasons and the physics motivations outlined in Section 7.2, Run III will only start in 2021, after a three-year long *Phase I* upgrade (LS2) of the facility. By the end of 2024, the LHC will have accumulated $\sim 300\,\text{fb}^{-1}$ of integrated luminosity with collisions at $\sqrt{s} = 14\,\text{TeV}$ and a bunch spacing of 25 ns. Following a *Phase II* hardware installation and commissioning period (LS3), the *high-luminosity* LHC (HL-LHC) will begin Run IV by the end of 2027 [33, 34]. The instantaneous luminosity is planned to be levelled

at $5 \times 10^{34}\,\mathrm{cm}^{-1}\,\mathrm{s}^{-1}$ and, with an average of 140 effective collisions per bunch crossing, will lead to an integrated luminosity of $\sim 3000\,\mathrm{fb}^{-1}$ over 10-12 years. The LHC will even have the ability to deliver 50% higher instantaneous and integrated luminosities and ~ 200 collisions per bunch crossing. The mentioned upgrade phases are intended to address the issues of high occupancy and unsustainable radiation dose to detector components from the anticipated collision rate, and to increase the intrinsic detector efficiencies and measurement accuracy to maintain or improve current performance for increased data rates. Upgrades to the LHC include a new 160 MeV LINAC system, better beam collimation to boost the rate of collisions and stronger (11-12 T) dipole magnets with niobium tin filaments. Upgrades planned for the CMS detector are discussed in Section 3.4.

3.3 The CMS detector

3.3.1 Background

The CMS detector [37, 38] was designed to measure proton collisions at a centre-of-mass energy of $\sqrt{s} = 14\,\mathrm{TeV}$ at an instantaneous luminosity of $1.7 \times 10^{34}\,\mathrm{cm}^{-1}\,\mathrm{s}^{-1}$, the highest design luminosity of the LHC.

The physics motivations for building the CMS detector were mostly centred on the need to understand the origin of electroweak symmetry breaking (EWSB), described in Section 2.1.3. The goal was to allow the detection of a wide range of possible signatures from several EWSB mechanisms. This required the CMS detector to be able to probe the TeV energy scale where signals related to EWSB were expected to manifest as new particles, including possibly fundamental scalars, vectors or composite Higgs bosons, supersymmetric particles and technicolor states amongst others. The EWSB mechanism could also produce signals at the TeV scale that could restore unitarity in the scattering of longitudinally polarised intermediate vector bosons (IVBs), $W^{\pm}$ and Z^0. In particular, IVB processes as well as decays of the SM Higgs boson and SUSY particles could manifest themselves in the ZZ and WW states. Since the hadronic decay modes suffer from QCD backgrounds, it was preferable that the $W^{\pm}$ and Z^0 particles be detected through their charged leptonic decays despite the smaller branching fractions of the leptonic channels. These processes thus required a high luminosity to be measurable. Of particular interest was the ZZ decay since decays of the WW state are masked by top quark production and contain neutrinos. The CMS detector was designed to have excellent kinematic acceptance and momentum resolution for muons and electrons. The aim was for leptons to be detectable over a large pseudorapidity range ($|\eta| < 2.5$) and down to a transverse momentum of 5 GeV. A dilepton mass resolution that matches the width of the Z was also needed to reject non-resonant backgrounds. The dilepton mass resolution requirement was $\sim 1\%$ at 100 GeV. A magnetic field was needed to unambigously determine the charge of the particles.

The CMS detector was optimised for the search of the SM Higgs boson over a mass range from 90 GeV to 1 TeV. In the mass range between 90 GeV and 130 GeV, the $H \to \gamma\gamma$ decay was the preferred discovery channel. The Higgs boson natural width was expected to be very small and the width of the observed signal was expected to be entirely dominated by

instrumentation resolution. The CMS detector was designed to have excellent electromagnetic resolution so as to maximise sensitivity to the $\gamma\gamma$ mass peak. An exemplary inner tracking system was equally needed to calibrate the electromagnetic calorimeter to a high precision. A discovery in the $H \to \gamma\gamma$ channel also demanded a good measurement of the photon direction and neutral pion background rejection. In the mass range from 130 GeV up to 600 GeV, the $H \to ZZ \to 4l$ was the discovery channel of choice.

Other requirements included b-quark tagging and the ability to distinguish between tau decays and hadronic jets. Pile-up (PU) fluctuations dominate the mass resolution of hadronic jets and therefore the CMS hadronic calorimeter was not required to deliver the same level of energy resolution as the electromagnetic calorimeter. It was important, however, that the CMS detector be hermetic to contain all jets produced in the event and allow for missing transverse energy measurements. Furthermore, high-granularity components were needed to provide low occupancy since about 20 inelastic collisions per bunch crossing were expected to be superimposed on the event of interest (Section 3.2.1). The requirements of the hadronic calorimeter were, therefore, a large hermetic geometric coverage ($|\eta| < 5$) and a fine lateral segmentation ($\Delta\eta \times \Delta\phi < 0.1 \times 0.1$). An online selection system, or *trigger*, was further necessary to reduce the expected design maximum event rate of 40 MHz to approximately $100/s$. Lastly the CMS detector components, especially the inner tracking elements, were designed to operate in a high-radiation environment.

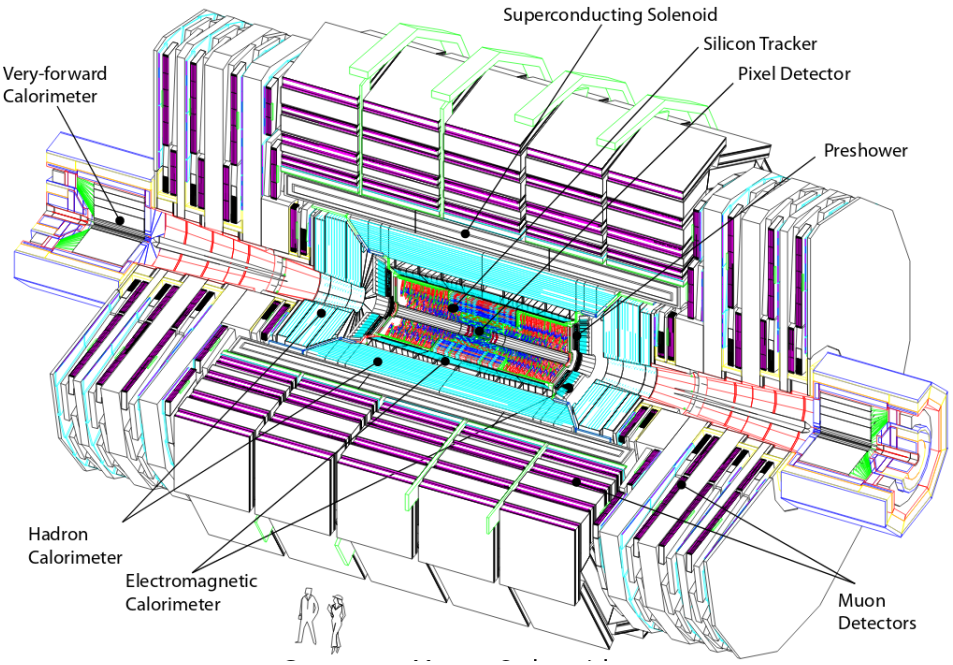

Figure 3.3: Exploded view of the CMS detector. [137]

Figure 3.3 shows the design of the CMS detector. The instrument weighs 14000 tons and has a length of 21.6 m and a diameter of 14.6 m. The CMS coordinate system has the origin centered at the nominal collision point inside the experiment, the y-axis pointing vertically upward, and the x-axis pointing radially inward toward the centre of the LHC. The pseudorapidity η is given by $-\ln[\tan(\theta/2)]$, where θ is the angle between the particle

three-momentum and the positive direction of the beam axis. At the core of the CMS detector lies a large superconducting solenoid generating a uniform magnetic field of 3.8 T, which allows a compact design for the muon spectrometer without compromising the momentum resolution. The inner tracking system consists of silicon pixels and strips which measure high momentum (p_T) charged tracks with a momentum precision of $\delta p_T \sim 0.1 p_T$ with p_T in TeV. A high resolution lead-tungstate crystal electromagnetic calorimeter is located inside the magnet coil where scintillation light is detected by silicon avalanche photodiodes (SPDs) and vacuum phototriodes (VPTs). A hermetic brass-scintillator sampling hadron calorimeter surrounds the ECAL. There, scintillation light is converted by wavelength-shifting (WLS) fibres and channeled to photodetectors. The steel return-yoke for the magnetic flux is instrumented with four stations of muon detectors. Forward sampling calorimeters extend the pseudorapidity coverage to high values ($|\eta| < 5$) assuring good hermeticity.

3.3.2 Solenoid

The CMS superconducting solenoid has a length of 13 m and an inner diameter of 6 m and is large enough to allow the tracker and calorimeters to be placed within the coil. Notably, in terms of bending power (12 Tm) and stored energy (2.6 GJ), the CMS magnet is the largest superconducting solenoid ever built for a physics experiment. When a charged particle is deflected from a straight trajectory in the magnetic field, the charge and momentum may be determined by the curvature of the track. With a bending power of 12 Tm and the inner tracker described in Section 3.3.3, a momentum resolution of $\sim$ 2-3% can be achieved in regions up to $\eta = 1.6$. The solenoid magnet consists of a cylindrical coil of superconducting niobuim titanium (NbTi) fibres which are cooled to a temperature of 4.6 K. The fibres are formed into a four-layer winding and carry a current of 18500 A to generate a magnetic field of approximately 3.8 T. A steel yoke surrounds the magnet coils and forms the bulk of the detector mass. The return yoke acts as an absorber to guide and confine the magnetic flux to the detector volume and houses the four muon stations (Section 3.3.6). The magnet coils and the return yoke weigh 12500 tons and provide most of the structural support for the experiment.

3.3.3 Tracking system

The tracking volume consists of a cylinder of 5.8 m in length and 2.6 m in diameter [37, 138]. The primary design goal of the tracking system is to be able to precisely measure charged particle trajectories and reconstruct secondary vertices. The position of charged particles is measured at a number of key points to a precision of up to 10 μm. All high p_T ($p_T > 2$ GeV) muons and isolated electrons produced in the central rapidity region can be reconstructed to a momentum precision of $\sim$ 2-3%. This allows lepton charge to be successfully measured up to p_T values of 2 TeV and masses of 4 TeV. As described in Section 3.3.2, the momentum resolution is also a direct consequence of the magnetic field. Given PU vertices are distributed along the beam direction with an r.m.s of approximately 5 cm, the precise tracking system can ensure that all interesting high p_T tracks in an event are consistent with a common vertex. Precise measurements of charged particle trajectories also allow every cell in the electromagnetic calorimeter to be precisely calibrated in-situ using electrons from W and Z decays measured in the tracker.

The tracking system is the innermost detector component and therefore receives the highest radiation dose. Silicon detector technology provides the radiation hardness, granularity and speed necessary for precision tracking in the conditions of the CMS detector. The inner tracking system covers the pseudorapidity range $|\eta| < 2.5$ and extends 54 cm lengthwise and 110 cm radially. With about 200 m^2 of active silicon area comprising 66 million silicon pixel sensors and 9.6 million silicon strip sensors, the CMS tracker is the largest silicon tracker ever built.

In order to keep the occupancy at or below 1% pixel detectors [139] are used at radii below 10 cm where the particle flux is the highest. In this region, $\approx 100 \times 150\,\mu m^2$ pixel sizes are used, covering a total area of $\approx 1\,m^2$, and giving an occupancy of approximately 10^{-4} per pixel per bunch crossing . The pixel detector consists of three 53 cm-long cylindrical barrel layers at radii of 4.4 cm, 7.3 cm and 10.2 cm around the interaction point. Two endcap disks, extending from 6 to 15 cm in radius, are placed on each side of the barrel at $|z| = 34.5$ and 46.5 cm. The pixel detector is essential for the reconstruction of secondary vertices from b and τ decays, and for forming seed tracks for the outer track reconstruction and high level triggering (Section 3.3.7).

At radii between 20 cm and 110 cm, the particle flux is low enough for larger cells to be appropriate. Silicon microstrip layers are used in the barrel part, while the forward region has 9 microstrip layers on each of the two endcaps. The silicon strip detectors cover a total area of $\approx 200\,m^2$. Given the large area that has to be instrumented in this region, the strip length has to be increased in order to limit the number of read-out channels. At radii of 20 cm to 55 cm, 10 cm $\times$ 80 μm microstrip cells are used with an occupancy of $\approx 2-3\%$ per bunch crossing. The modules in this region are called Tracker Inner Barrel and Disks (TIB/TID) in Figure 3.4. At radii beyond 55 cm, the strip cell size can be further increased to 25 cm $\times$ 180 μm whilst keeping an occupancy of $\approx 1\%$. The modules in this region are known as Tracker Outer Barrel (TOB) and Tracker End Caps (TEC).

Analogue signals and corresponding pixel addresses are stored in a data buffer while waiting for the Level-1 trigger decision (Section 3.3.7). In order to reduce the event rate from the LHC bunch crossing rate of 40 MHz, tracking information is further heavily used in the high-level trigger of CMS.

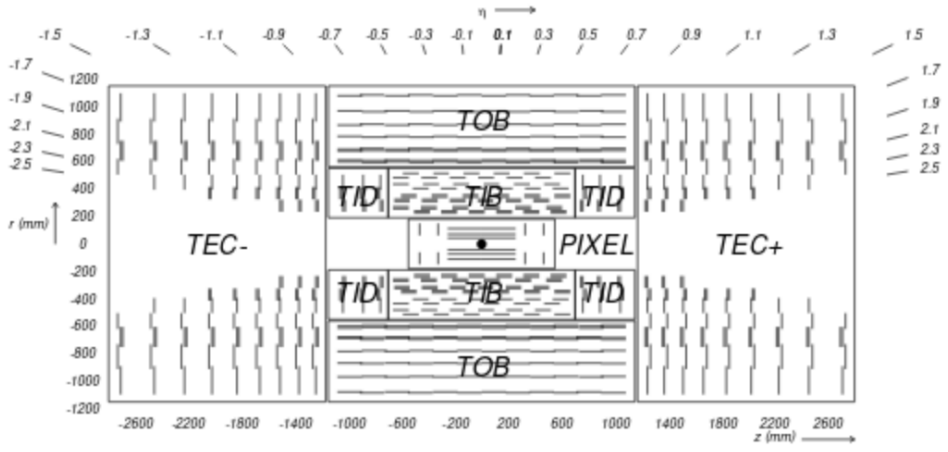

Figure 3.4: Schematic cross-section through the CMS tracker. [37]

3.3.4 Electromagnetic calorimeter

The CMS ECAL [37, 39] is a high-granularity, hermetic and homogeneous calorimeter with coverage in pseudorapidity up to $|\eta| < 3.0$. As discussed in Section 3.3.1, the ECAL is designed to provide an excellent energy resolution to increase sensitivity to the $H \to \gamma\gamma$ decay. The distinctive experimental signature of this decay is a narrow peak in the invariant mass distribution from two isolated photons of high transverse momentum. The energy (E) resolution (σ) is given by

$$\left(\frac{\sigma}{E}\right)^2 = \left(\frac{S}{\sqrt{E}}\right)^2 + \left(\frac{N}{E}\right)^2 + C^2 \,, \tag{3.2}$$

where S is the stochastic term, N is the noise term and C is the constant term [37]. These terms, which influence the energy resolution, need to be small, especially at photon energies corresponding to half of the Higgs boson mass. The stochastic term is influenced by event-to-event fluctuations in lateral shower containment and fluctuations in the energy deposited in various parts of the ECAL. The most important contributions to the constant term are the non-uniformity in the longitudinal light collection, inter-callibration errors and leakage of energy from the back of the ECAL crystals. Electronic noise, digitisation noise and PU noise all contribute to the noise term. Besides the energy, the direction of photons has to be precisely measured so as not to degrade the effective mass resolution.

The ECAL uses 61200 lead tungstate ($PbWO_4$) crystals in the central barrel region, and 7324 crystals in each of the two endcaps. The short radiation length (0.89 cm) and small Molière radius (2.19 cm) of lead tungstate results in a fine-granularity and compact calorimeter. Moreover, lead tungstate is radiation tolerant up to 10 Mrad. When electrons and photons with a given energy are absorbed, the crystals emit a proportional amount of blue-green scintillation light with a broad maximum at 420–430 nm. A fast detector response is possible since 99% of the light is collected within 100 ns.

As shown in Figure 3.5, the crystals in the central barrel section (EB) cover the pseudorapidity range $|\eta| < 1.479$. They have a length of 23 cm or 25.8 radiation lengths and a front-face cross-section of $2.2 \times 2.2\,\text{cm}^2$. The barrel crystal granularity is 360-fold in ϕ and 2×85-fold in η. The two endcaps (EE) extend the pseudorapidity coverage up to 3.0. The endcaps consist of identically-shaped 5×5 crystal units, called *supercrystals*, consisting of a carbon-fibre alveola structure. The endcap crystals have a length of 22 cm or 24.7 radiation lengths and a front-face cross-section of $2.86 \times 2.86\,\text{cm}^2$. Since the transverse size of the crystals in the ECAL is comparable to the typical shower size in lead tungstate, shower shape criteria may be used for photon identification.

Since, lead tungstate has a relatively low light yield (30 photons/MeV) the scintillation light signal needs to be amplified once it is detected. In this context, silicon avalanche photodiodes (APD) with an amplification factor of 50 and vacuum phototriodes (VPT) with an amplification factor of 10 are used in the EB and EE area respectively. The photodetectors are temperature-sensitive and operate at 0.1 °C. The amplified signal is digitised at a frequency of 40 MHz by analogue-to-digital converters (ADC), giving a set of amplitude measurements which are stored in a buffer until the Level-1 trigger decision is received

(Section 3.3.7).

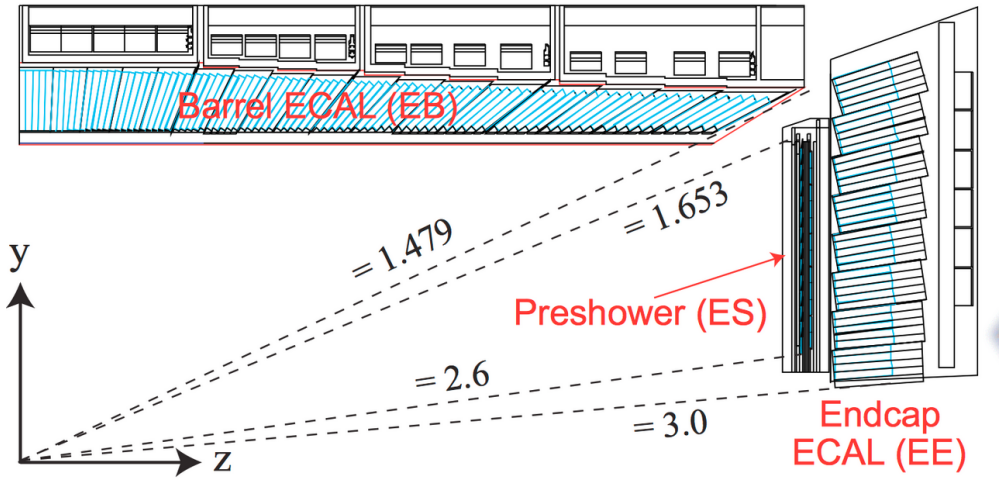

Figure 3.5: A quarter-section of the CMS ECAL. [39]

A preshower system (ES) is installed in front of the ECAL endcaps to identify neutral pions within a fiducial region of $1.653 < |\eta| < 2.600$. The ES consists of two layers of lead absorber, two and one radiation lengths in length, which initiate electromagnetic showers from incoming photons and electrons. Silicon strip sensors are placed after each radiator layer to measure the energy deposited, giving transverse shower profiles which can be used in π^0/γ separation.

3.3.5 Hadronic calorimeter

The hadronic calorimeter (HCAL) [37, 140] is a sampling calorimeter with a coverage up to a pseudorapidity of 3.0, and is made of repeating layers of dense brass absorber and tiles of plastic scintillator. Having a reasonably short interaction length and being malleable and non-magnetic, brass is an excellent choice of material for the absorber. When a hadronic particle hits an absorber layer, a cascade of shower particles is produced and as the shower develops, the particles travel through the active scintillation material where blue-violet light is emitted. The light is shifted to the green region of the light spectrum by optical wavelength-shifting (WLS) fibres, less than 1 mm in diameter, which are embedded in the scintillator tiles. Clear optic fibres then channel the green light to hybrid photodiodes (HPD) that amplify the signal by a factor of ~2000. The choice of thin tile and fibre technology for the active medium enables the amount of absorber to be maximised, leading to a compact detector.

The HCAL is particularly important for the direct measurement of hadronic jets. Furthermore, the indirect measurement of non-interacting, uncharged particles such as neutrinos is done by measuring momentum imbalance in the transverse direction relative to the beam line. For this reason, the overall assembly of the HCAL allows no uninstrumented cracks or uncovered areas in ϕ, providing excellent hermeticity, thereby ensuring a good missing transverse energy measurement. Such an assembly is possible because the HCAL is divided into barrel, endcap and forward sections which are built in a staggered fashion (Figure 3.6)

so that there are no gaps, in direct lines from the interaction region, through which a particle might escape. The hadronic barrel covers the pseudorapidity range $|\eta| < 1.3$. In addition to 36 HB wedges inside the magnet coil, a few additional layers are placed outside the coil in the outer hadronic barrel (HO) to measure late-starting showers and ensure that there are no undetected energy leaks through the back of the HB. Together, the HB and HO tail-catcher allow hadronic showers to be sampled with nearly 11 hadronic interaction lengths. The hadronic endcaps (HE) are similarly instrumented with 36 detector wedges which cover the pseudorapidity region $1.3 < |\eta| < 3.0$ and capture approximately 34% of final-state particles. Two hadronic forward (HF) calorimeters are positioned at either end of the CMS detector at 11.2 m from the interaction point. Since they extend the pseudorapidity coverage to 5.2, the HF sections capture particles travelling at small angles relative to the beam axis and are required to be more resistant to radiation than other HCAL parts. The signal originates from Cherenkov light emitted in quartz fibres which also carry the signal to photomultipliers. As in the ECAL, the signals from all HPDs in the HCAL are digitised and held in a buffer until the Level-1 trigger decision is received (Section 3.3.7).

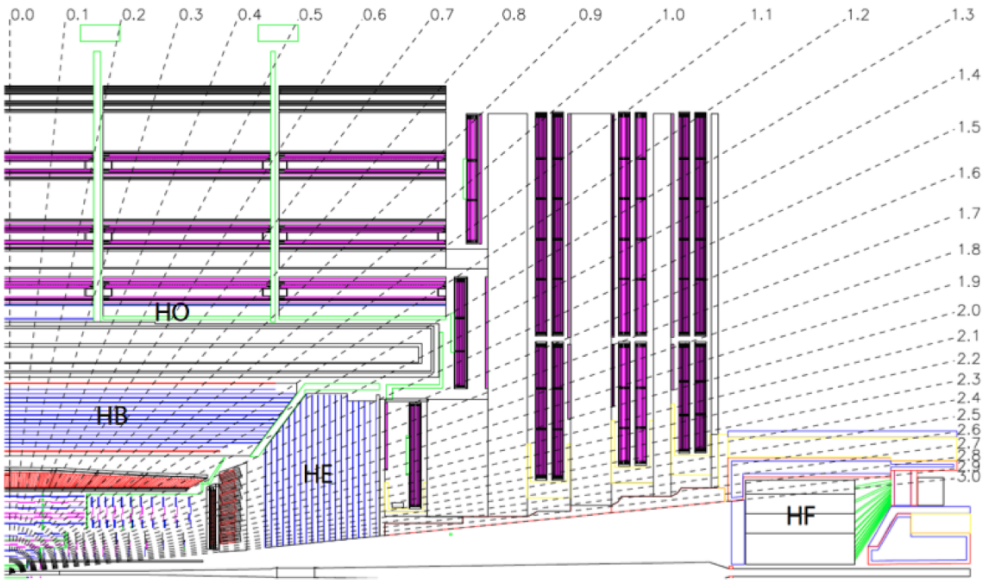

Figure 3.6: A quarter-section of the CMS HCAL. A quarter-section of the CMS muon system (unlabelled sections) is also visible in this figure. [37]

3.3.6 Muon system

As described in Section 3.3.1, the muon detectors play an important role in measuring the $H \to ZZ$ decay, especially in the case of the 4μ final state. Muons can penetrate several metres of iron without interacting and are not stopped by the ECAL and HCAL. The muon detector system [37, 141] is therefore placed behind the calorimeters and the magnet coil. The three principal functions of the muon system are muon identification, muon momentum measurement and triggering. Three independent measurements of the muon momentum, namely in the inner tracking volume, after the magnet coil and in the flux return yoke, make the performance of the muon system very robust.

Four identical muon stations (MS1 to MS4) are located in the iron return yoke. Gaseous chambers in different stations are staggered so that a high-p_T muon produced near a sector boundary crosses at least 3 out of the four stations where gas ionisation results in an electron avalanche. A precise position measurement is made by determining the centre of gravity of the charge distribution. Measurement of the muon momentum using only the muon system is determined by the muon bending angle at the exit of the magnet coil, taking the interaction point, known to $\sim 20\,\mu$m in the transverse direction, as the origin of the muon track. The resolution of this measurement is dominated by multiple scattering in the material before the first muon station up to p_T values of 200 GeV, after which the chamber spatial resolution dominates. Hence, for low momentum muons, the best momentum resolution, by an order of magnitude, is given by the resolution obtained in the silicon tracker.

In the barrel region, where the muon rate and neutron-induced background is low and the magnetic field is uniform, drift tube (DT) chambers with rectangular drift cells are interspersed among the layers of the flux return plates (Figures 3.6 and 3.7). The latter cover the pseudorapidity region $|\eta| < 1.2$ and are designed to give a muon vector with 100 μm precision in position and better than 1 mrad in direction. In the endcap region, where the muon rate and neutron-induced background is high and the magnetic field is large and non-uniform, the muon system uses cathode strip chambers (CSC) which cover the pseudorapidity region $0.9 < |\eta| < 2.4$. The CSCs provide fine segmentation, radiation resistance and a fast response time. Each endcap is instrumented with four CSC chambers which provide a spatial resolution of 200 μm and an angular resolution of 10 mrad in ϕ.

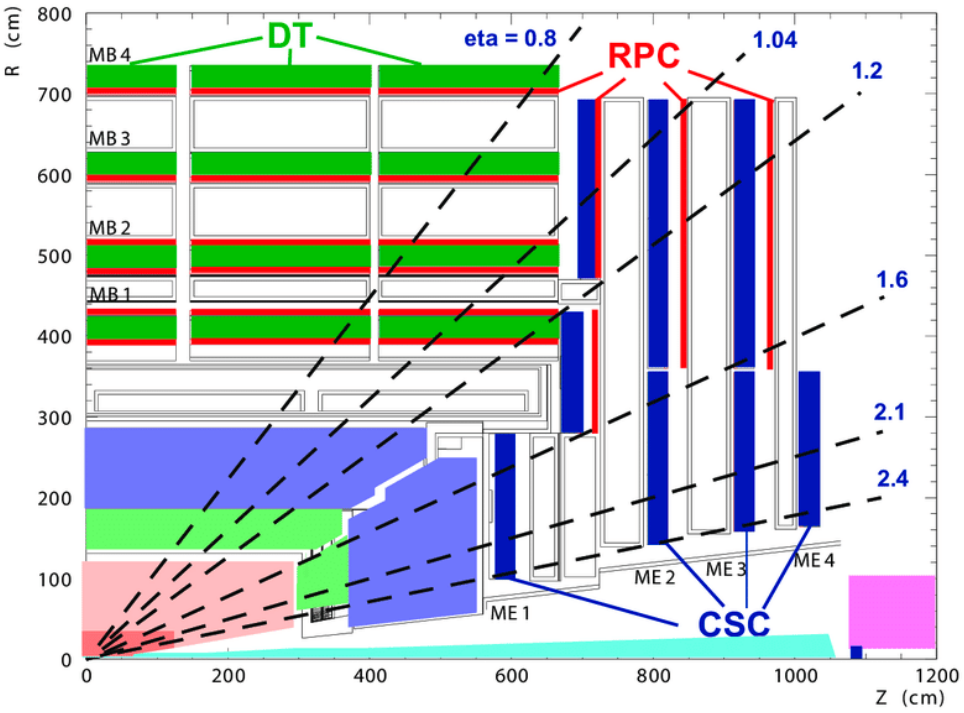

Figure 3.7: A quarter-section of the CMS muon system. [37]

In order to measure the muon time for independent bunch-crossing identification, the DTs

and CSCs in the barrel and endcap regions are complemented by resistive plate chambers (RPC) which form a dedicated trigger system. The RPCs cover a large portion of the $|\eta| < 1.6$ pseudorapidity range and provide a fast response with good timing resolution, albeit a poorer position resolution than the DTs and CSCs. A high-p_T muon crosses up to 6 RPCs and 4 DT chambers, giving up to 44 measured points from which a muon track candidate can be built. The DTs, CSCs and the RPCSs operate within the Level-1 trigger system (Section 3.3.7).

3.3.7 Trigger and Data Acquisition system

The LHC bunch crossing rate (or event rate) of 40 MHz leads to $\sim 10^9$ inelastic interactions per second at the design luminosity of $10^{34}\,\mathrm{cm^2\,s^{-1}}$. Given the Higgs boson is expected to be produced at a rate of $\sim 10^{-2}$ under the same conditions, the lower bound on the selectivity required is 1 in 10^{-11}. The upper selectivity limit is dictated by the data storage capacity, which only allows information from $\sim 10^2$ events to be stored per second. The CMS Trigger and Data Acquisition System (TriDAS) [37, 142], tasked to start the event-selection process, is therefore required to achieve a rejection factor of $\sim 10^5$ events every second.

The TriDAS is designed to perform parallel computations by exploiting detector symmetry. The full selection task is split into two steps. Firstly, a Level-1 (L1) Trigger, based on custom electronics, uses local, regional and global components to perform a primary event selection. This decision is based on coarsely segmented data. The Trigger Primitive Generators (TPG) form 'trigger primitive' objects such as photons, electrons, muons, jets above set energy and momentum thresholds in the calorimeters and muon chambers. Regional triggers combine TPG information and perform pattern recognition to rank trigger objects by energy, momentum and quality in individual detector regions. Global Calorimeter and Muon Triggers further rank the objects across the entire experiment before feeding the information to the Global Trigger. This way, the L1 trigger is able to reduce the rate of events to under 100 kHz within 3.2 μs, out of which less than 1 μs is allocated to calculations. The L1 decision is communicated to the sub-detectors through the Timing, Trigger and Control system. The second step in the trigger selection involves a High-Level Trigger (HLT) which reduces the L1 acceptance rate to 100 Hz by using a software system implemented on a filter farm of about a thousand commercial processors. The HLT has access to the complete read-out data and can therefore perform preliminary reconstruction of entire events for event selection. The data is then placed in memory in front-end read-out buffers to be accessed by the DAQ system.

3.3.8 LHC computing grid

On a yearly basis, the LHC gathers ~ 15 petabytes of data. Data from the DAQ system is accepted by the Worldwide LHC Computing Grid (WLCG) [143]. The grid consists of a three-tier network of computers, based on Grid Middleware software, that provides unprecedented parallel computing capabilities to perform a wide variety of simulation, data processing and analysis tasks. The Tier-0 computing centre at CERN is supplemented by Tier-1 physics computers connected by dedicated optical fibre networks. The Tier-1 sites are

located in Europe, North America and Asia, from where LHC data is distributed to over 140 Tier-2 centres around the world.

3.4 Upgrades of the CMS detector

3.4.1 Overview

As motivated in Section 3.2.2, the HL-LHC will begin Run IV by the end of 2027. Details regarding the scope for Higgs boson physics in the high-luminosity phase of the LHC are given in Section 7.2.

In addition to causing significant radiation damage to detector electronics, the surge in the PU level from ∼60 before 2023 to ∼140-200 at the HL-LHC luminosity will result in increased hits in the tracking system and energy deposits in the calorimeters other than from hard collisions of interest. High particle multiplicity and misidentification rates, together with the volume of data to be read out per bunch-crossing, pose significant challenges to setting trigger thresholds and executing timely offline combinatorial track reconstruction. *Forward jet tagging*, *central jet vetoing* and *charged hadron subtraction*, extensively used in identifying the vector boson fusion (VBF) production mode of the Higgs boson, become less effective, as does the selection of isolated leptons from purely electroweak processes. The precise measurement of systems in the 100 GeV range require that the current performance levels in jet energy-momentum resolution, primary-vertex reconstruction and b-tagging be upheld. Chief upgrade requirements are therefore the development of a more selective trigger system; radiation-hard detectors with enhanced granularity for accurate measurement of jet substructure; the apt use of calorimeter timing information to mitigate the mismatch between energy deposits and bunch crossings (out-of-time PU); and an efficient data transfer scheme. [33–36]

Corollaries of increased PU and radiation fluence are primarily manifested in the inner and forward detector regions. Therefore, the replacement of the entire tracking system with radiation-tolerant silicon trackers, featuring smaller pixel detectors in proximity to the beamline and strip detectors at larger radii, will bring about a fourfold increase in granularity of the outer tracker and pixel detectors. This upgrade is aimed at reducing occupancy and enhancing primary-vertex allocation, impact parameter resolution, track-separation and b-tagging efficiency for improved particle-flow reconstruction. An extension of the tracking coverage to a pseudorapidity range of $|\eta| = 4$ will maximise the solid angle of acceptance to VBF and vector boson scattering (VBS) processes where the oppositely-directed vector boson tagging jets are radiated from quarks into the forward/backward detector regions. [35, 139, 144, 145]

High radiation levels and requirements for improved forward VBF and VBS jet resolution similarly motivate the replacement of the endcap calorimeters by a high-granularity sampling calorimeter (HGCAL) [41–43] with electromagnetic and hadronic sections made of hexagonal silicon sensors and plastic scintillator tiles as the active elements. The HGCAL is described in detail in Section 3.4.2. The increased transverse and longitudinal segmentation

specifically improves efficiency in the $H \to ZZ^* \to 4l$ and $H \to WW^* \to l\nu l\nu$ channels where ~40% and ~15% of the decays respectively result in at least one lepton being emitted in the $|\eta| > 2.4$ region. The HGCAL transverse and longitudinal granularity facilitate particle-flow calorimetry (Section 5.2.1), triggering, PU rejection and particle identification. Furthermore, three-dimensional images of showers can provide separation of electromagnetic, charged hadronic and neutral hadronic components, facilitating more precise energy measurements, particularly of jets. The HGCAL segmentation also enhances the angular resolution and pointing capabilities of electromagnetic showers which may further help in detecting displaced vertices. The HGCAL will use time-of-arrival (ToA) measurements from upgraded calorimeter front-end electronics for tracking shower development and timing shower energy deposits [146–148]. High temporal resolution information will thereby enable PU mitigation and neutral energy removal during clustering [149]. Moreover, timed cluster density data will allow the discrimination of electromagnetic showers from less compact hadronic ones which can be further separated into gluon jets and denser quark jets [150]. The addition of a timing detector to improve the selection of minimum ionising particles (MIPs) from the primary vertex has also been approved [145].

PU rejection at high luminosity through the global increase of trigger thresholds would result in reduced detector acceptance for Higgs boson decay final states with low energy or transverse momentum (p_{T}). Excellent p_{T} resolution is therefore essential to achieve a sufficient reduction in the trigger rate while still maintaining low p_{T} thresholds. To this end, a *silicon self-seeded* approach will be deployed, involving the use of tracking information in the first level trigger (L1) so that high-momentum tracks or stubs may be selected locally [151]. Calorimeter cluster information and muon isolation criteria will be further implemented in hardware track reconstruction, requiring an increase in latency of the L1 trigger (by $\sim 9\,\mu$s) and a forward extension of the muon system for appropriate trigger performance on multi-muon final states, namely $H \to \mu\mu$. The latter will be achieved via the addition of Resistive Plate Chambers (RPCs) and Gas Electron Multipliers (GEMs) to muon detector regions that lack redundant coverage. Nonetheless, an upgraded data acquisition system with increased bandwidth will be required as trigger acceptance rates will still be raised (from $\sim 100\,$kHz to $\sim 750\,$kHz) in cases where track triggering is not as efficient, namely for hadrons and photons. [35, 36, 144, 145]

3.4.2 The High Granularity Calorimeter

As described in Section 3.4, the HL-LHC will pose significant challenges for radiation tolerance and event PU in the forward detector regions. The existing forward calorimeters, namely the lead-tungstate electromagnetic endcap calorimeter and the plastic scintillator hadronic endcap and forward calorimeters were designed for an integrated luminosity of $500\,\mathrm{fb}^{-1}$. To maintain good physics performance up to an integrated luminosity of $3000\,\mathrm{fb}^{-1}$, a new generation of calorimeters, with radiation-resistant technologies, will be installed.

An important element of the HL-LHC calorimeter upgrade program is the high-granularity calorimeter (HGCAL) [41–43], a forward sampling calorimeter based on the CALICE concept [152]. According to preliminary simulations, it is expected that the HGCAL will be required to withstand up to 2 MGy of total radiation dose, together with a maximum fluence of

around 1×10^{16} n_{eq}/cm^2. It has been shown that silicon sensors retain adequate charge collection even after having been exposed to fluences up to 1.5×10^{16} n_{eq}/cm^2. In small sizes $O(0.5 - 1cm^2)$, they also provide an adequate signal-to-noise ratio to allow inter-cell calibration with minimum ionising particles (MIPs) to an accuracy of a $\sim 3\%$ percent. Furthermore, the intrinsic high-resolution timing capabilities of the silicon sensors (< 100 ps for signals above 12 fC) will be used as an extra dimension in PU rejection and the identification of the vertex of the triggering interaction.

Hexagonal silicon sensors with cell sizes of $O(0.5 - 1cm^2)$ have been chosen as the most appropriate active material for the majority of the calorimeter while lower radiation dose (< 3 kGy) and fluence ($< 8 \times 10^{13}$ n_{eq}/cm^2) regions will instead be made of cheaper plastic scintillator tiles with a silicon photomultiplier (SiPMs) readout. Although larger scintillator cells help to reduce the channel count, they are still required to be small enough (~4-30 cm^2) to maintain a high light collection efficiency and signal-to-noise ratio by minimising the inclusion of energy from particles originating in PU interactions. In order to keep the radiation-induced leakage current noise sufficiently low, the calorimeter will operate in a thermally shielded volume that will be cooled by a two-phase CO_2 system and maintained at $-30\,^{o}$C. Layers of the active material are interleaved with absorber layers made of materials (tungsten, lead, copper, stainless steel) that provide a small Molière radius to allow for compact showers.

The HGCAL design (Figure 3.8) covers the pseudorapidity range $1.4 < \eta < 3.0$ and consists of one Endcap Electromagnetic section (CE-E), a Forward Hadronic (FH) section and a Back Hadronic (BH) section, together forming the CE-H. The CE-E is made of 28 sampling layers, extending from $|z| = 3.19$ to 3.53 m and covering a depth of approximately $26X_0$ and 1.7λ. Three different thicknesses (120, 200 and 300 μm) of hexagonal silicon sensors are used, with thickness decreasing as a function of fluence. A granularity of 0.5 cm^2 for the 120 μm and 1 cm^2 for the 200 and 300 μm thick sensors is used. The cell size is driven by physics performance requirements such as the lateral spread of electromagnetic showers, and by the need to keep the cell capacitance within a manageable range. The intrinsic energy resolution of the CE-E section for incident electrons is expected to have a stochastic term below $25\%/\sqrt{\text{GeV}}$ and a constant term below 1%. The silicon sensors are composed of a wafer which is sandwiched between a copper-tungsten baseplate and a printed circuit board that carries the front-end electronics . The hexagonal shape of the sensors makes efficient use of the available area of the circular wafers. Silicon modules are tiled on either side of a copper cooling plate, which together with the two copper-tungstate baseplates form one absorber layer. The alternate absorber layer consists of two lead planes, with stainless steel sheet cladding, that are placed on either side of the module-cooling plate sandwich. The assemblies of the absorber layer, detector modules and the copper cooling plate are called *cassettes* which cover 60^o sectors on the CE-E layers.

The hadronic section extends from $|z| = 3.53$ to 5.14 m and provides an additional depth of 9.0λ. Twelve layers with 35 mm stainless steel absorber form the FH section and another twelve layers, where the absorber thickness is 68 mm form the BH section. In the hadronic section, the first 8 layers are instrumented with silicon detector modules similar to those in the CE-E. In the remaining layers, silicon sensors are used closer to the beam line while scintillator tiles with SiPMs are used further away. The silicon modules and scintillator tileboards are found between the absorber plates but only on one side of the cooling plate.

Additionally, the baseplates are made of copper and the absorbers are made of carbon fibre and steel. The cassette modules with scintillator tiles each cover 30^o sectors on the wafers. The total calorimeter thickness, perpendicular to the layers, is 10.7λ, including the C-EE and a neutron moderator layer in front of the calorimeter which is used to reduce the neutron flux in the tracker.

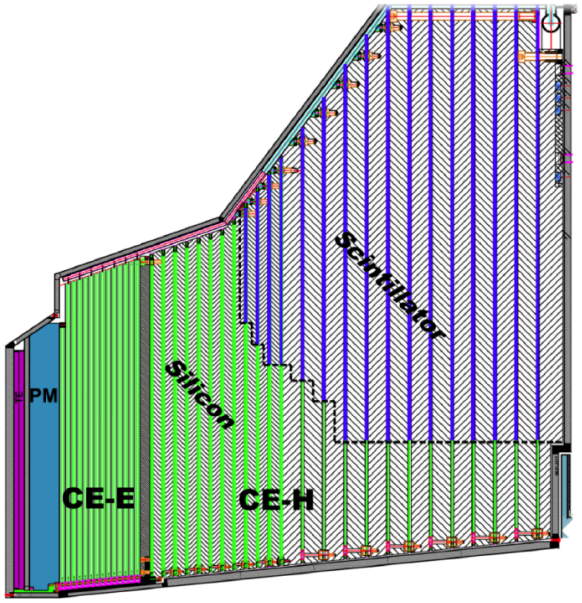

Figure 3.8: Schematic of the HGCAL longitudinal design. [44]

The front-end electronics, operating at 40 MHz, measure and digitise the charge deposits in the silicon sensors and the SiPMs, and provide a high precision measurement of the time of arrival (ToA) of the pulses. Precision timing in the HGCAL is further discussed in Chapter 4. Information in alternate layers in the C-EE and all layers in the FH & BH are used for making L1-trigger primitive objects.

3.5 Summary

The LHC is the largest and most powerful particle accelerator in the world, designed to fulfill CERN's primary mission of furthering our knowledge of fundamental physics. The LHC and its detectors present numerous innovations in superconductors, vacuum technologies, computing, electronics and industrial processes which push accelerator science to extreme limits. The CMS detector, operating in the LHC ring, measures particles produced in proton-proton collisions and was purposefully designed to discover the Higgs boson. The distinguishing features of the CMS detector include a powerful superconducting solenoid, a precise silicon tracking system, an electromagnetic calorimeter with excellent energy resolution, a fully hermetic hadron calorimeter, a robust muon detection system and a fast-reponse trigger. CMS was one of two general purpose experiments to jointly claim the discovery of the Higgs boson in proton-proton collisions in 2012. Since that time, the LHC experiments have been focusing on conducting precise measurements in the Higgs sector.

The need to increase the LHC physics performance and to acquire more data has driven a luminosity upgrade of the present LHC ring and detectors which will be realised through the HL-LHC project. To address the issues that arise from the high-luminosity environment, the CMS detector will be equipped with radiation-tolerant high granularity trackers with an increased coverage, and fine-grained endcap calorimeters (HGCAL). The HGCAL is expected to provide unprecedented granularity and timing capabilities in the forward dectector regions.

The LHC and its associated detector collaborations represent an ongoing global scientific effort to provide essential tests of the Standard Model and extend the present discovery reach for new physics.

Chapter 4

Timing in the High Granularity Calorimeter

4.1 Introduction

Since the publication of the HGCAL Technical Design Report (TDR) [44], the HGCAL reconstruction framework has undergone important developments. This chapter reports on the progress since made in the study and applications of precision timing in the HGCAL reconstruction chain. Building on the generator-level studies presented in the TDR, the performance of the timing analysis is now quantified using reconstruction-based detector objects which realistically reflect the detector and reconstruction effects associated with the newest version of the HGCAL geometry. The HGCAL geometry discussed in Section 3.4.2 is used in all sections of this chapter. The timing of reconstructed hits, 2D clusters, 3D clusters and complete showers is studied in detail. In particular, the timing performance of these reconstructed objects is presented in this order to quantify the timing performance for objects along the reconstruction chain. The aim of this chapter is to outline the current status and the prospective use of precision timing at the various stages of the HGCAL reconstruction of a complete shower. Details on how timing information could assist in local object reconstruction with the HGCAL iterative clustering framework (TICL) [153], and in global shower reconstruction are further discussed. In this context, the timing performance of objects reconstructed with TICL selections is compared to a baseline selection. The studies on the application of precision timing are only preliminary and serve to briefly outline the potential future use of timing information in the HGCAL reconstruction. In the absence of PU, the time of showers, within the achievable timing resolutions, does not bring as much information as topographical selections in the reconstruction. The aim is therefore to use timing information in PU to clean events of PU contributions (hits or 2D clusters in the reconstruction) which distort the shower energy resolution. The results of this chapter are documented in Ref. [2].

4.2 Precision timing of the HGCAL detector

This chapter presents studies involving HGCAL silicon sensors only. It is expected that future iterations of this study will also account for timing information from scintillators. As described in Ref. [44], the front-end ASIC (HGCROC) of the HGCAL silicon sensors provides time-of-arrival (ToA) information for energy deposits above a given threshold. In the presence of pileup, the energy deposited in a cell is likely to originate from showers of particles coming from several interactions, rather than from a single event. The ToA records the time at which the deposit of energy exceeded the threshold set in the HGCAL silicon sensors.

Figure 4.1 shows the expected resolution on the ToA measurements for a single cell in a silicon sensor. In particular the charge signals are digitised with a time-to-digital converter (TDC) which uses 10 bits to measure the time between every bunch crossing and the next (25 ns). The TDC is reset after every bunch crossing and thus measures the time relative to the most recent bunch crossing. The least significant bit on the TDC is therefore about 25 ps. This digitisation binning causes some calibration offsets as discussed in Section 4.3.2. It can be seen that the timing resolution obtained with silicon sensors does not vary significantly with sensor thickness when the resolution is measured as a function of S/N. Results from beam test further show that the timing resolution does not vary with irradiation up to fluences of at least 3000 fb^{-1} [44].

The timing resolution σ_t can be expressed as

$$\sigma_t = \sigma_{jitter} \bigoplus \sigma_{floor} \tag{4.1}$$

$$\sigma_{jitter} = \frac{A}{(S/N)} \tag{4.2}$$

where S/N is the signal-to-noise ratio, σ_{floor} is a constant term (a precision floor), and the symbol $\bigoplus$ denotes quadratic summation. The constant A, which determines the dependence on S/N, is fixed by the response time and noise characteristics of the sensor and preamplifier. A= 5 ns and C or $\sigma_{floor} = 20$ ps represents the achievable resolution on the ToA measurement expected from the specification of the sensors, the front-end electronics, and the clock distribution.

The ToA charge threshold of 12 fC corresponds to about 3 MIP in the 300 μm silicon cells, and to about 5 MIP and 10 MIP in the 200 μm and 120 μm cells respectively. ToA information is only available for cells with an energy deposit in excess of this threshold. For signals above the energy threshold, the single cell resolution ranges between 150 ps and 20 ps as a function of the cell signal-to-noise ratio (S/N).

It is important to note that the charge threshold at 12 fC produces the trend in the timing resolution in Figure 4.1. For signals with a large charge deposition, the signal shape is almost vertical, triggers the TDC and then falls. However, for signals with small charge deposition, the signal shape shows a slower rising slope. The TDC is therefore much more sensitive to the time the signal crosses the threshold, resulting in a poorer timing resolution for small signals. For similar reasons, the TDC also measures different times for small and large signals which occur at the same time at truth level; bigger charge depositions are assigned an earlier time measurement. This effect is known as *time-walk* and is not modelled or corrected for in the simulation samples used in this chapter.

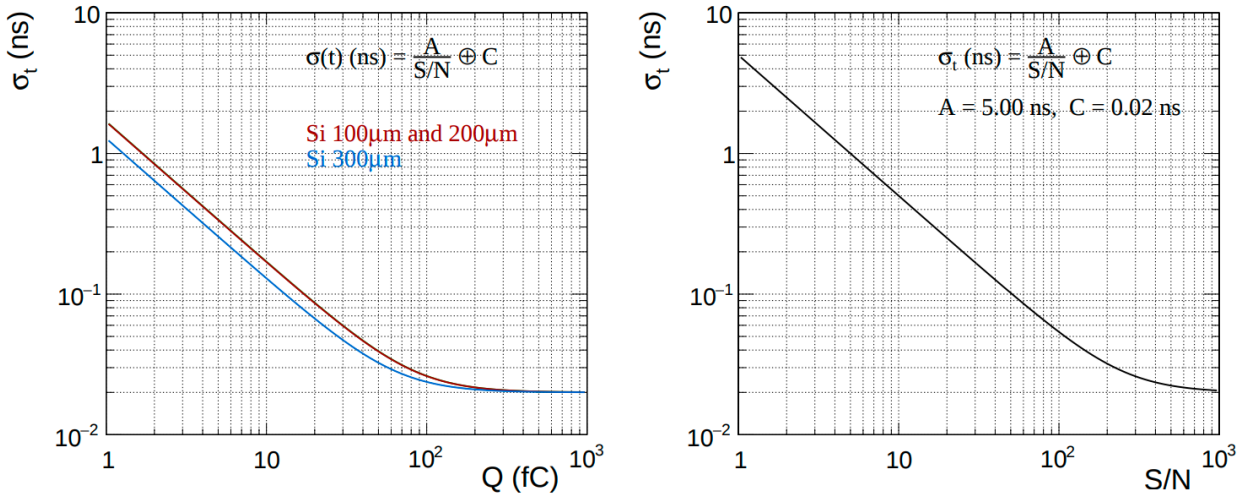

Figure 4.1: Timing resolution of single-cell rechits in silicon sensors, as a function of the charge deposited in the cell (left), and the cell signal-to-noise ratio (right). The threshold on the ToA is 12 fC. [44]

In the HGCAL, silicon sensors provide the ability to measure, with high precision, the time of electromagnetic and hadronic showers. A requirement on the compatibility of the measured time of the showers can help to assist in pileup rejection, and in the identification of the primary vertex of the interaction of interest. Given that a full reconstruction chain was not yet finalised, the preliminary studies and results presented in Ref. [44] were based on the collection of reconstructed hits (rechits) belonging to each shower. rechits were identified as hits falling in a cylinder of radius $\rho = 2$ cm around the shower axis, the latter being identified by the direction of particles at generator level. Optimised selections and tuned algorithms were studied to combine the time measurements from multiple cells and provide an estimate for the time of the full shower. The combination of measurements from multiple cells allows reduction of the uncertainty on the timing estimate. To make a time measurement, at least three cells within the selected radius from the shower axis are required, each with an energy deposit of at least 12 fC needed to fire the ToA. Showers that fail this requirement obtain no time measurement, resulting in a measurement inefficiency. Since the distribution in time of the hits collected for a shower has tails, in Ref. [44], simple algorithms were used to truncate the tails before taking the mean time of the remaining hits to obtain the time of a shower. The algorithm used is robust against pileup, ageing conditions and the position of the vertex.

In this chapter, timing measurements are not only made for rechits but also for every object in the chain used to reconstruct the full shower; these objects include rechits, two-dimensional clusters (2D clusters) and three-dimensional clusters (3D clusters), described further in this chapter.

4.3 The building blocks of the HGCAL reconstruction

As described in Section 3.4.2, the HGCAL offers a very high level of information to measure the development of showers, owing to its high granularity, fine longitudinal readout segmentation and precision timing. The HGCAL reconstruction is being designed to fully exploit these features of the detector, and is targeting a particle-flow-based approach [154]; the high

granularity allows the separation between the energy deposits that are clustered in local units and these are further connected, relying on compatibility criteria, to build full objects in the detector. The information from different subdetectors (tracker and calorimeters in primis) are then combined to identify reconstructed particles and provide precise energy estimates. (Section 5.2.1).

The HGCAL provides a 5D (position, energy, time) image of the shower with high granularity. The building blocks of the HGCAL local reconstruction are the rechits, clustered in each two-dimensional (2D) layer independently, where the cell ranking and the threshold for seeding a layer cluster is based on the energy density, rather than individual cell energy. This method is appropriate for clustering cells that are small compared to the shower size; it gives a better indication of the importance of the cell and is more sensitive to a multicell common deposit of energy than just a single cell local maximum. More precisely, electromagnetic showers in the HGCAL are reconstructed by clustering hits in each 2D layer independently. This is done starting from an energy density map of all hits above a threshold E_c. The threshold value is defined as a function of the noise resolution σ_{noise}, which depends on the cell type. The density is defined as the energy sum of all hits within a critical distance δ_c, the value of which is chosen to be similar to the Molière radius. For each hit, the distance to the nearest hit with higher density is evaluated. Hits with both density and distance parameters greater than threshold values are labelled cluster centres. The 2D clusters are formed by assigning each hit to the same cluster as the nearest hit with higher density. Subsequently, compatible layer clusters are connected over layers to build 3D clusters: this is done in TICL, where each iteration produces a collection of 2D clusters aligned as a track (trackster). Before the studies presented in this chapter were performed, the TICL reconstruction framework did not use the time of 2D clusters; this possibility is explored in this chapter and the results presented in Section 4.4.2 have now been implemented in the reconstruction. Where mentioned in this chapter, the TICL reconstruction is the version which does not yet use the time of 2D clusters.

As mentioned, the use of timing information in a 5D reconstruction has great potential for pileup mitigation and particle identification. It is expected that the precise timing information will ultimately be used in the last steps of the reconstruction in CMS, when dealing with the most complete and precise measurements for each reconstructed object. In this context, the time compatibility between the measurements provided by the different timing detectors in the CMS MTD and the ECAL barrel could be maximally exploited. Timing information can also be used in the intermediate steps of the local reconstruction, to help in pileup removal during the clustering of compatible energy deposits. For this purpose, the timing information, available as measurements for single rechits, needs to be propagated through the reconstruction chain, to provide a time measurement for each reconstructed object (2D and 3D clusters). In this chapter, these developments are reported and the characterisation of the timing performance at different stages of the local reconstruction are presented.

4.3.1 Characteristics of EM and hadronic showers in the HGCAL

In this section, the key features of electromagnetic and hadronic showers, illustrated by photons and pions (π^+) respectively, are discussed. Hadronic showers, produced in a calorimeter after a deep inelastic interaction of an incident hadron with a nucleus, are

characterised by a relatively narrow core from the electromagnetic component surrounded by an extended halo. The core is usually formed by electromagnetic cascades initiated by (π^+) decays, while charged mesons and baryons dominate in the radial halo and longitudinal tail of the shower. By using the TICL reconstruction framework, it is possible to reconstruct and study electromagnetic (EM) and hadronic (HAD) showers separately, as shown later in this chapter. In the studies in this chapter, some cleaning of events was performed to remove particles that interact in the detector before reaching the HGCAL. These percentages are typically 70 (15) % of particles interacting before reaching the HGCAL (or in the tracker) for photons (π^+), so typically only 30 (85) % of non-interacting photon (π^+) particles from the available samples are used. This impacts the resolution measurements minimally, and is expected to mainly affect the efficiency of finding a 2D cluster with a time measurement in the search region.

Since the energy sampled by Si sensors is very small when compared to the energy lost in the absorbers between them, dE/dx weights are applied to account for the energy not sampled by the Si sensors. dE/dx weights, different for each layer, also serve to recalibrate the energy deposited in the absorbers since the thicker the absorber, the more is the energy deposited in the shower process. This energy may be accounted for by averaging the number of MIPs (minimum ionising particles) in adjacent Si sensors and multiplying the number by the energy lost per unit distance per MIP in the absorber, and by the thickness of the absorber. Si cells are normally calibrated with MIP particles and, therefore, the use of MIP units in energy profiles leads to smoother transitions between detector regions of different absorber thickness. A cut was applied on the energy of the recorded hits at $3\,\sigma$, where σ is the width of the noise distribution. This is the typical noise threshold value used in the TDR. Even if the true energy in a cell is zero, there may still be fluctuations (noise) that would cause energy to be recorded, so energy profiles generated with no minimum selection may be misleading, especially if the shower process produces many hits with low energy. By applying a $3\,\sigma$ noise cut, we reject hits that are compatible with a fluctuation of the noise within 3 sigma of its central value.

In general, photons have a well-contained energy profile. The energy profile of a single photon event is a good approximation to the energy profile averaged over several events. A dip in the energy profile occurs after the CE-E section because photons normally deposit almost all of their energy after approximately 28 radiation lengths (which is about the length of the CE-E section). Photon showers peak around layer 12. π^+ particles have a greater contribution than photons in the CE-H section. There is still a significant amount of energy in the CE-E section, coming from π^+ interactions which lead to EM showers. The energy profiles from individual π^+ events is not usually representative of the profile averaged over several events. Absorber transitions CE-E→FH and FH→BH produce changes in the profile after layer 28 and 40 respectively.

It is useful to study how the shower energy profiles vary with different p_T values and this effect is shown in Figure 4.2. With photons, the lower the p_T, the earlier is the shower maximum and the lower is that maximum. It is interesting to note that the shower peaks of approximately 150, 300, and 900 MIP for p_T 5, 10 and 30 GeV samples respectively and thus the shower peak scales with p_T. This occurs because energy is proportional to p_T ($E = p_T \cosh \eta$) for a massless particle. In the hadronic section, the energy deposited is negligible, showing that the interesting physics processes occur in the CE-E section. With π^+ particles, the lower the p_T, the smaller is the shower maximum (around layer 30). The shape

of the shower in the CE-E section, when compared to corresponding profiles for photons, which peak around layer 12, show no clear peak or trend, especially at low p_T. Note that GeV units have been used for π^+ plots since most energy deposition occurs in the BH section which is mostly made of absorber. For photons, the shower mainly happens in the CE-E section where the weights are almost equal. For π^+ particles, the peaks at 1.2, 2.4 and 6 GeV do not obey the $E = p_T \cosh \eta$ equation exactly. However, the equation is still a good approximation at these p_T values.

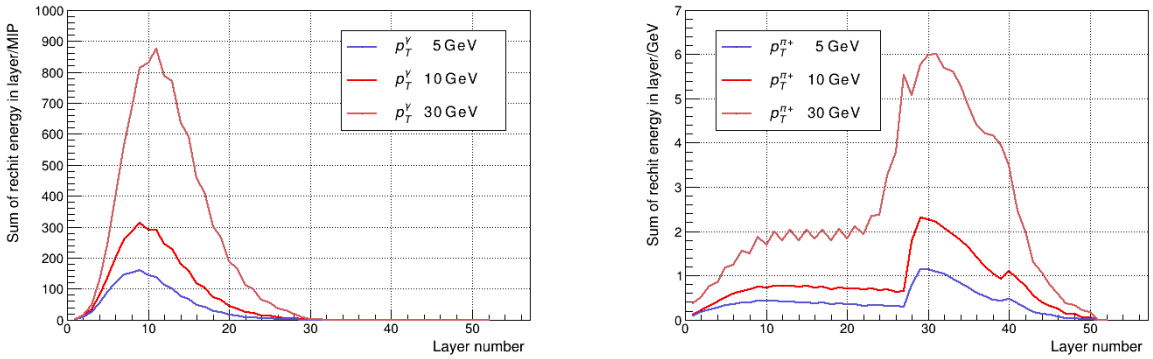

Figure 4.2: Energy profiles of photon (left) and π^+ particles (right) in the HGCAL layers. The energy profiles for p_T values of 5, 10 and 30 GeV are shown.

Energy deposition occurs in different layers in the HGCAL and at different rates for electromagnetic and hadronic showers. As seen from Figure 4.3, almost 60% of the photon shower energy (at p_T 10 GeV) is contained in the first 12 layers, and approximately 100% in the first 28 layers. As said previously, this supports the fact that photons deposit most of their energy in the CE-E section within 28 radiation lengths. This figure dictates the design geometry of the HGCAL. For pions, around 45% of the total shower energy is deposited by layer 28 and about 90% by layer 40. At least 50 layers are required to contain the π^+ shower. As said previously, most of the energy is deposited in the FH and BH sections. For a typical hadron shower, we normally expect 30% of energy deposition in the CE-E section [44]. The fraction here for π^+ particles particles is slightly higher. It is also useful to notice the change in the slope after layer 28 (the CE-E section); energy deposition for π^+ in the FH and BH sections is more rapid compared to photons where we observe a steep slope corresponding to rapid energy deposition in the CE-E section for the first 15 layers.

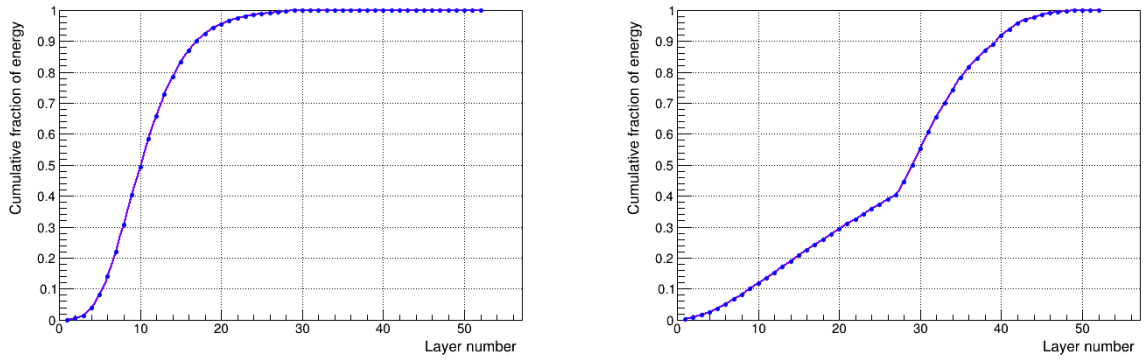

Figure 4.3: The cumulative fraction of energy of the whole photon (left) and pion (right) shower (averaged over several events) contained by each layer of the HGCAL.

It is also useful to study the spread of the energy profile about the average (Figure 4.4) when interpreting the average energy profile over several events. There is a tail in the photon spectrum at almost 0 GeV in the BH section and thus negligible. Comparing the photon energy spread over several events to the π^+ spread (Figure 4.4), we see a larger spread about the average energy for π^+ particles than for photons.

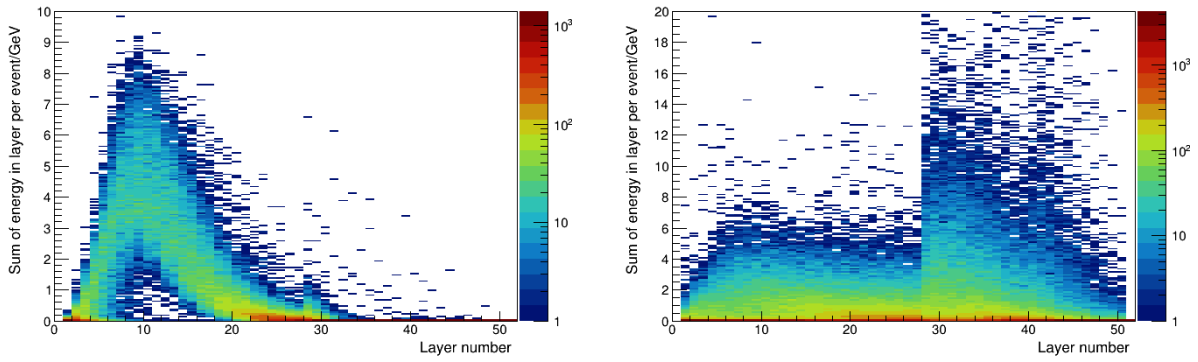

Figure 4.4: Two dimensional histogram for the sum of energy in the layer as a function of the HGCAL layer for photon showers (left) and π^+ showers (right).

It is further important to distinguish between *few hits of high energy* and *many hits of low energy*, both of which may produce regions with a high sum of energy. This may be investigated through distributions of hit occupancy and compared to the average energy profiles. Looking at the hit occupancy (Figure 4.5) plot for photons, most hits are between layers 8 and 20 and this is where the energy maximum is obtained. For π^+ particles, there are differences. There are many hits in the CE-E section, however, in the average energy profile, these do not contribute as much; these are many hits of low energy. Fewer hits appear to be in the FH and BH sections but this is where most of the energy is deposited; these hits have more energy than the hits in the CE-E section. The π^+ hit occupancy histogram also shows many more hits in the FH and BH sections than for photons. It is important to note that the number of hits also depends on the granularity. In the CE-E and FH sections, cells have a smaller area than in the BH section (Figure 3.8). Therefore, it is important to unfold the effects of granularity when comparing the number of hits in different sections.

The shower of a photon typically has many cells with significant energy deposits. For illustration the shower of a $p_T = 2\,\text{GeV}$ and $\eta = 1.7$ photon has an average of more than 20 cells above the 12 fC threshold, and the corresponding number for a photon with $p_T = 60\,\text{GeV}$ is more than 100. Hadronic showers usually have a prompt core and later-developing components that propagate laterally with respect to the shower axis, and the number of cells above a 12 fC threshold has large event-to-event fluctuations. The time distribution of the energy deposited has long tails of later time measurements. Hadron showers have a greater contribution than photons in the FH and BH sections, with still a significant energy deposit in the CE-E section, coming from hadron decays which lead to EM showers. Further details about the time of propagation and timing efficiency of electromagnetic and hadronic showers are covered in the next sections.

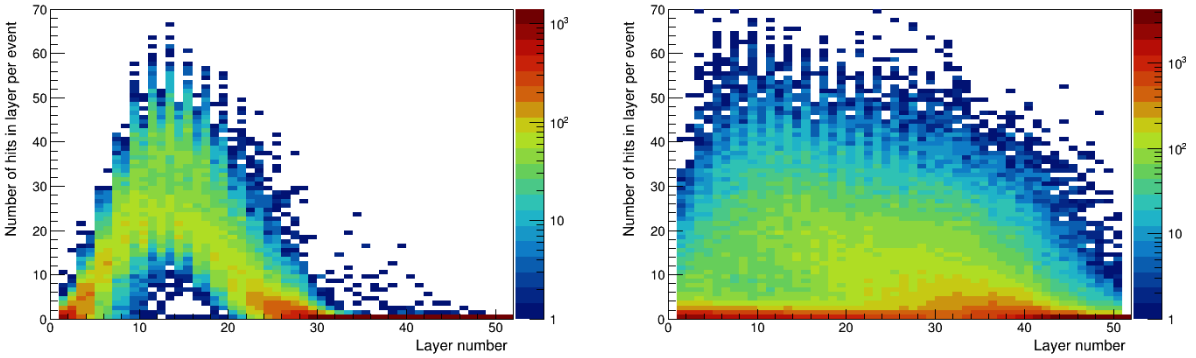

Figure 4.5: Two dimensional histogram of the hit occupancy as a function of the HGCAL layer for p_T 10 GeV photons (left) and π^+ particles (right).

4.3.2 Timing of reconstructed hits

In the simulated samples used in the studies in this section, the time resolution of hits is smeared depending on the signal-to-noise ratio in the given cell. rechits with less than a 12 fC charge deposition are not assigned a time measurement. The time of a rechit is corrected by the ToF (time of flight) from the primary vertex (the point at which a pp interaction occurred). This correction is illustrated in Figure 4.6, where the time of a hit is defined by the time recorded minus the time for a particle with the speed of light, c, to travel from the primary vertex to the position of the hit (along the dashed line).

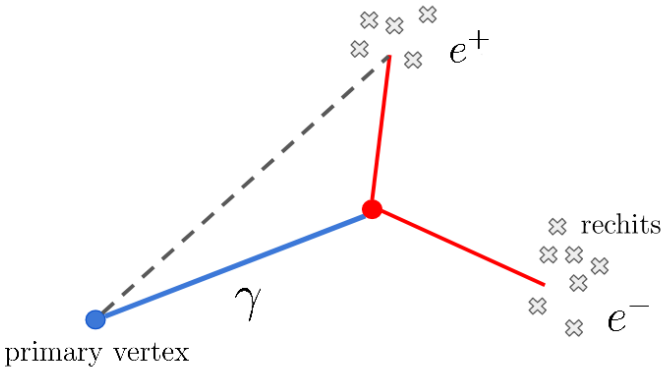

Figure 4.6: Schematic illustrating rechit ToF correction. The time of a hit is defined by the time recorded minus the time for a particle with the speed of light, c, to travel from the primary vertex to the position of the hit (along the dashed line).

In the samples used, the primary vertex is smeared in space and time to mimic realistic HL-LHC vertex conditions. The expected time resolution is 25 ps for an energy deposit equivalent to 50 fC [44], as compared to the spread of time of collisions in a single bunch crossing of a couple of hundred ps. Indeed, at the HL-LHC, the spread of the collision vertices in a single bunch crossing is expected to be around 4.5 cm along the beam direction and about 180-200 ps in time. It is thus essential to design algorithms that correct for

the vertex position and time while measuring the time of a shower. While analysing these samples a vertex correction is applied to recover the true vertex. Here, this is done using the generator-level values of v_t, v_x, v_y and vz (temporal and spatial vertex smearings). Ideally, this will be done using reconstruction-level vertex information from a 4D reconstructed vertex using the MIP-timing detector (Section 3.3.6).

Rechit timing vs distance from shower axis

The main cause of any timing resolution differences is due to the fact that the energy of rechits depends on their distance from the shower core. The mean time of rechits as a function of the distance from the shower axis gives insight into the time of propagation of the shower. For π^+ particles, the shower axis position is obtained by track propagation using the Lorentz force. The starting point of the track is v_x, v_y, v_z (position of primary vertex). The change in the z position is taken to be the z position of the rechit minus v_z.

A two-dimensinal histogram of the rechit time vs distance from shower axis for a photon p_T 10 GeV sample in 0 PU is shown in Figure 4.7.

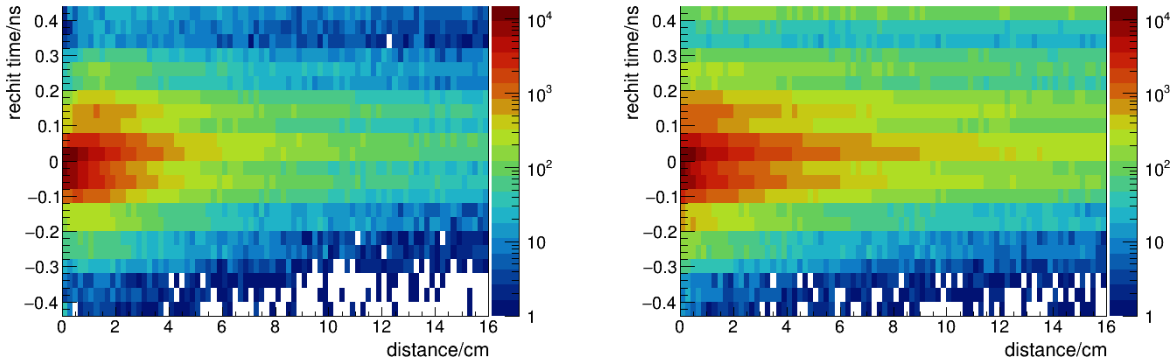

Figure 4.7: Two-dimensional histogram of the rechit time from photon (left) and π^+ (right) p_T 10 GeV particles as a function of the distance of the rechit from the shower axis.

The plot shows that most hits for a photon occur within 2 cm of the shower axis; photon showers have a lateral spread of about 2 cm. For this reason, the studies in the remaining sections of this chapter are done by placing a 2 cm cut on the distance from the shower axis while selecting photon rechits and 2D clusters. This provides a strong selection against PU as will be shown in Section 4.4.1. Figure 4.7 also shows a similar two-dimensional histogram for a π^+ p_T 10 GeV sample. The π^+ rechits extend laterally further from the shower axis. Since most rechits are contained within 5 cm of the shower axis, this is the selection threshold used later for π^+ rechits. Note that these thresholds have only been chosen roughly for these initial studies, while a precise reconstruction using the TICL framework is also studied in this chapter. The two-dimensional histograms are sliced vertically and a Gaussian function is fitted to the resulting rechit time distribution in each slice. The means of the fitted Gaussians are used to estimate the rechit mean time as a function of the distance from the shower axis.

The mean rechit time as a function of the distance of the rechit from the shower axis is shown in Figure 4.8 for photons and π^+ particles at p_T points of 5, 10 and 30 GeV and

in 0 PU. As expected, energy deposition at a given distance from the shower axis occurs faster at higher p_T. There is a clear increase in the hit mean time with distance from the shower axis. It takes on average 15 ps for energy from a 10 GeV photon rechit to be deposited laterally at 2 cm from the shower axis (after ToF subtraction). This gives an indication of the lateral time of propagation of the shower, and this happens, on average, within 15 ps for photons.

For π^+ particles, the shower takes more time than photons to propagate laterally. This is expected since, for pions, the showering process is different as described in Section 4.3.1. For a direct comparison, π^+ p_T 10 GeV rechit takes about 20 ps to travel laterally to 2 cm (after the ToF correction), and 40 ps to travel to 5 cm. The difference in the times of propagation at different p_T values does not scale as clearly with p_T as they did with photons, with π^+ p_T 10 GeV and 30 GeV rechits taking almost the same times to propagate laterally.

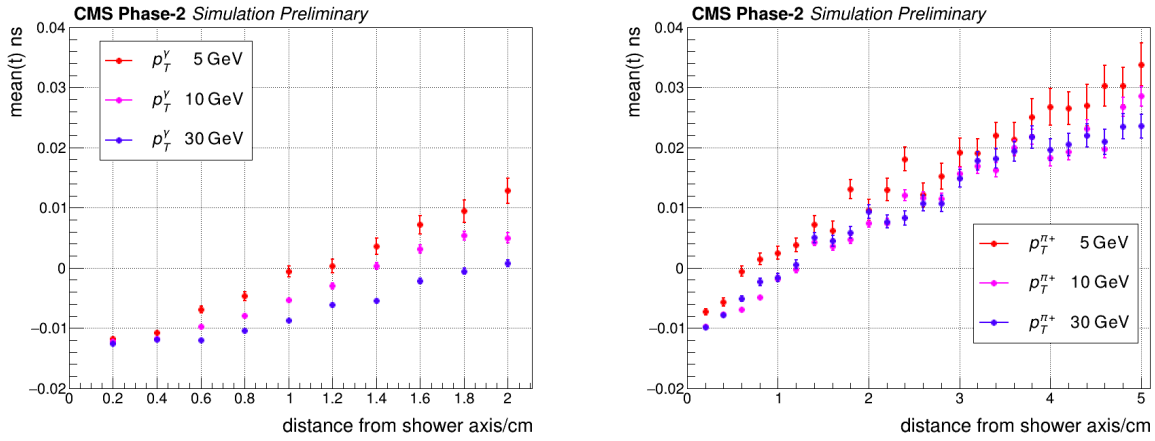

Figure 4.8: The mean rechit time of photon (left) and π^+ (right) rechits as a function of the distance of the rechit from the shower axis. Three p_T values, namely 5, 10 and 30 GeV, are considered.

It is useful to note from Figure 4.8 that the mean time of some rechits is negative. This is because of an effect of the digitisation after rechit time smearing in the simulation samples used. The important high weight, high energy hits in the shower core have times much less than 25 ps (but never negative). The time of these hits are smeared by small amounts in the simulation because they are high energy hits. The resulting smeared hit times may go below zero (roughly half of the time). Once these times are digitised in the 25 ps TDC least significant bits, hit times below zero are set to -25 ps and hit times slightly above zero are assigned to 0 ps. This effectively leads to an average of -12.5 ps (i.e due to the rounding to the centre of the TDC bin). This offset has not been accounted for in the studies in this chapter, and is not currently corrected in the HGCAL simulation framework.

Rechit timing vs rechit signal-to-noise ratio

It is useful to study the rechit timing as a function of the signal-to-noise ratio and observe if the reconstruction and selections degrades the rechit resolution smeared at generator level (Figure 4.1). This further helps to quantify the achievable rechit timing resolution for studies of the 2D cluster timing in the next sections.

The results for the mean time and timing resolution (from the width of the fitted Gaussians) are shown in Figure 4.9 for photon and pion rechits. Note that the noise threshold at $3\,\sigma$ has been omitted in these distributions and the effect of *time-walk* as described in Section 4.2 is not modelled.

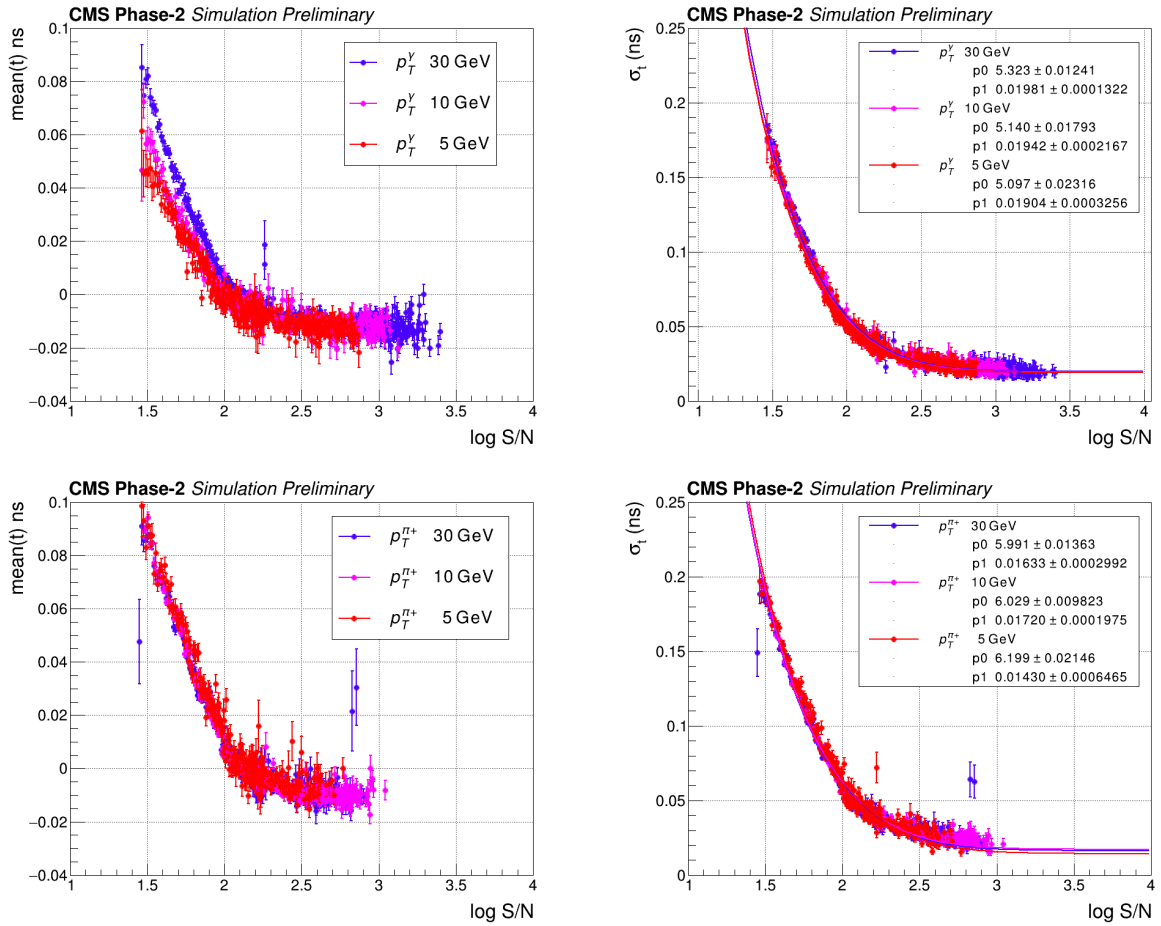

Figure 4.9: The mean time (left) and the timing resolution (right) of photon (top) and pion (bottom) rechits as a function of the cell signal-to-noise ratio for particle p_T values of 5, 10 and 30 GeV. The variables $p0$ and $p1$ are the fitted values of A and the floor C which are 5 ns and 0.02 ns respectively in the generator-level smearing for rechits.

The higher the signal-to-noise ratio, the earlier is the energy deposit. At higher photon p_T values, there are also more hits with high signal-to-noise ratio as indicated by the longer tails in the distributions at higher p_T points. From the fit to the rechit timing resolution it can be seen that the A value of 5 ns and the floor C of 0.02 ns injected in the generator-level smearing is not affected by the reconstruction (2 cm cylinder selection) for all three photon p_T points. At a signal-to-noise ratio of 1000, a 20 ps resolution on the photon rechit timing is attainable. The maximum mean photon rechit time is around 100 ps and this corresponds to a distance of approximately 3 cm covered at the speed of light. This is consistent with the expected size of the photon shower as described in Section 4.3.2.

Compared to photons, the hits from π^+ particles tend to have lower signal-to-noise ratio for corresponding p_T values, suggesting that hits from π^+ are of lower energy and this further

translates into a lower rechit timing efficiency [44]. Again, for the same signal to noise ratio, π^+ rechits have a higher mean time than photons, further confirming that π^+ showers take more time to propagate. The reconstructed rechit timing resolution fit deviates further than photons from the smearing function, as indicated by the fit values on the plot. The photon rechit timing resolution is less degraded by the reconstruction than the π^+ rechit timing resolution. At a signal-to-noise ratio of 1000, the pion rechit timing resolution is still around 20 ps as with photons. These values are in line (within errors) with the values reported in the HGCAL TDR with an older version of the geometry.

For both photons and π^+ particles, the mean times have negative values beyond a $\log \mathrm{S/N}$ value of about 2. This is because of the digitisation offset in the TDC as described in the previous section.

recHit Timing using TICL selection criteria

In this section, the rechit timing resolution of rechits from TICL 3D clusters are studied. As explained previously, TICL 3D clusters are formed by linking 2D clusters along the depth of the HGCAL using topographical selections only (i.e timing information is not used). In TICL, EM and HAD multiclusters correspond to different 2D cluster-linking iterations produced with tighter or looser compatibility parameters when targeting electromagnetic or hadronic showers respectively. Thus, in this chapter, EM TICL 3D clusters are studied for photons while HAD TICL 3D clusters are studied for π^+ particles. In this section, the rechits contained in the corresponding TICL 3D clusters are studied. The samples studied have a p_T value of 10 GeV and thus the results from using the TICL selection can be directly compared to the baseline selection of 2 cm (5 cm) on the distance from the shower axis of photon (π^+) rechits.

The mean time and timing resolution obtained from photon EM rechits and π^+ HAD rechits as a function of the signal-to-noise ratio are shown in Figure 4.10.

The photon rechit resolutions obtained using the TICL reconstruction are very similar to the resolutions obtained in Figure 4.9 with the simple 2 cm selection. This shows that the TICL reconstruction does not affect the baseline rechit timing resolution. Comparing the mean time of rechits in 3D clusters from TICL to the mean times obtained from the 2 cm cylinder selection, there is less spread in mean time, especially at low S/N. This shows a marked improvement in approximating the time of photon rechits using the TICL reconstruction. This is because the TICL reconstruction uses more elaborate topographical selections to iteratively link 2D clusters along the depth of the HGCAL, and thus selects the most energetic rechits [153]. These more energetic rechits are expected to have better timing resolution. The approximate spread in time is 60 ps, which corresponds to the time taken for light to travel 2 cm. This is also consistent with the lateral spread of photon showers observed previously.

For π^+ rechits, the timing resolution using the TICL reconstruction is better at low signal-to-noise ratio than with the 5 cm selection. Compared to photons, there is a much more marked improvement in the estimation of the mean times of π^+ rechits from using the TICL reconstruction. At a $\log \mathrm{S/N}$ value of 1.5, the mean time of π^+ rechits is about 60 ps less than that obtained from using the 5 cm selection. This is because the spread in mean times for π^+ was more pronounced to start with.

In the next section, the rechit mean times and rechit timing resolutions derived are

used to approximate the time of 2D clusters which represents the next step of the shower reconstruction after rechits.

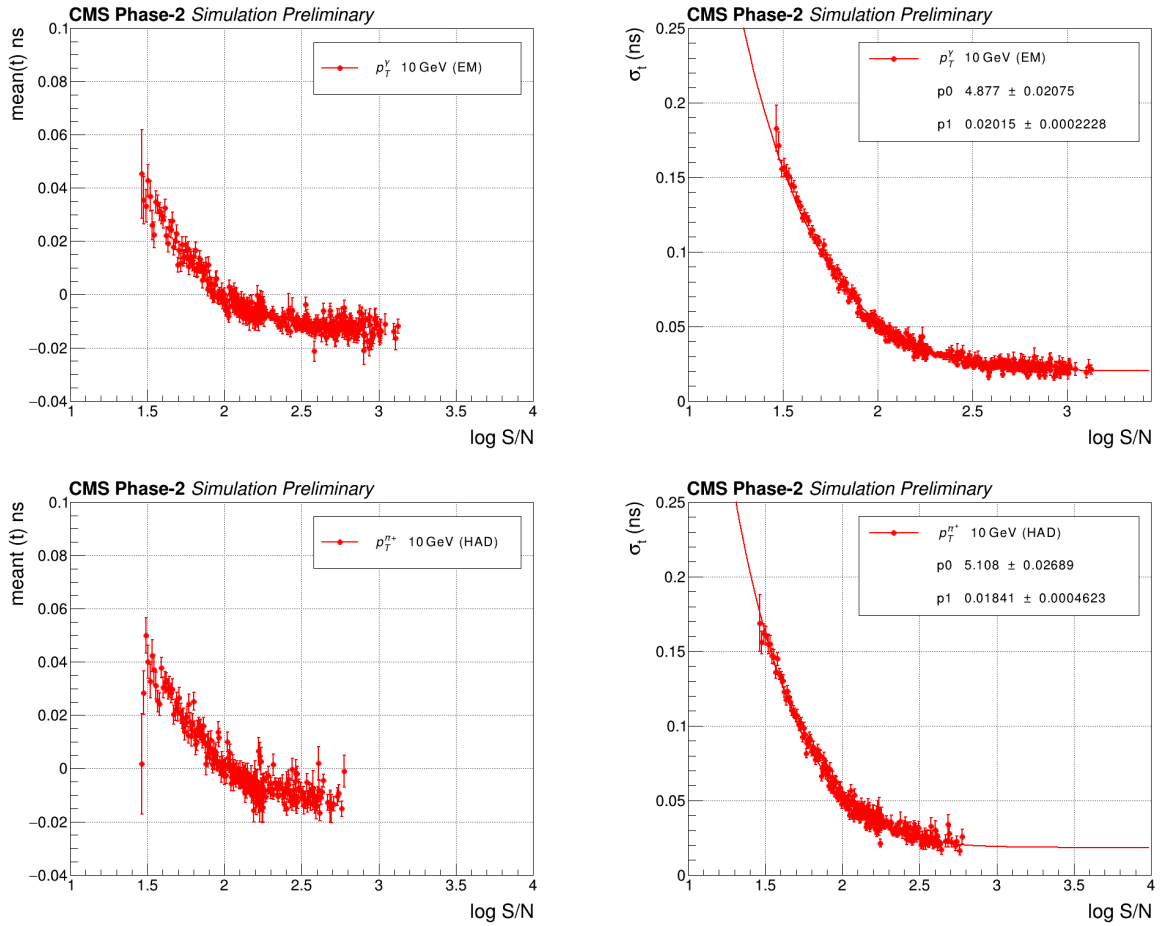

Figure 4.10: Distributions of the mean time (left) and timing resolution (right) of photon EM rechits (top) and π^+ HAD rechits (bottom) from the TICL reconstruction as a function of the cell signal-to-noise ratio. The variables $p0$ and $p1$ are the fitted values of A and the floor C which are 5 ns and 0.02 ns respectively in the generator-level smearing for rechits.

4.3.3 Timing of two-dimensional energy clusters

The study of the time of 2D clusters provides further information about the time of propagation of the shower. This can be used as an additional tool in 2D cluster pattern recognition when linking 2D clusters along the depth of the HGCAL to form 3D clusters in TICL (Section 4.4.2). For this purpose, the time compatibility between a 2D cluster already *clustered* and another 2D cluster candidate along the particle path can be used. If the timing resolution of the 2D clusters is good enough, the mean time of a 2D cluster can be used in the reconstruction.

A truncation is applied to the time distribution of the hits from the 2D cluster and the time of the 2D cluster is taken from the mean of the resulting distribution. The truncation window is 210 ps centered on the highest density bin of the distribution and is expected to get rid of PU hits with times that do not correlate well with other hit times and degrade

the timing resolution. The choice of this window is based on the spreads in mean time of rechits in the previous section. The truncation window is chosen so as not to lose too many rechits in 0 PU. Figure 4.11 shows the distribution of rechit times for an example p_T 10 GeV photon and π^+ 2D cluster (selected using the cylindrical selection). The rechits removed by the truncation function are highlighted in red.

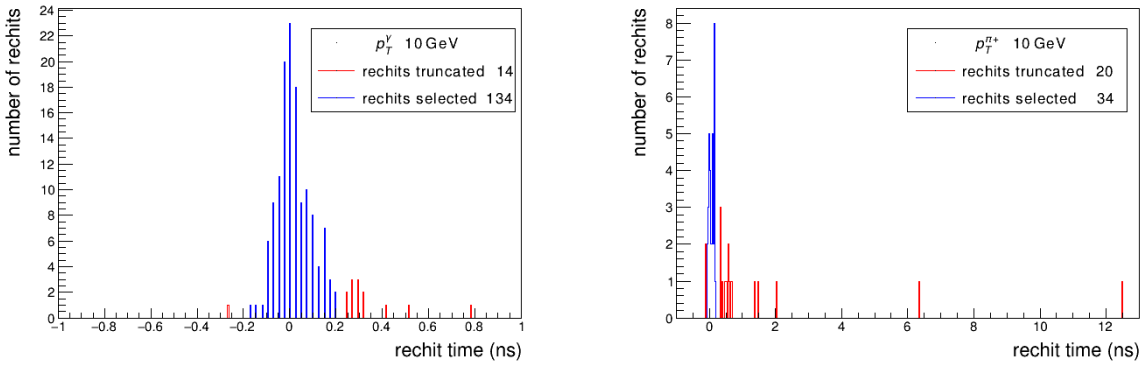

Figure 4.11: Distributions of rechit times for an example p_T 10 GeV photon (left) and π^+ (right) 2D cluster. The rechits removed by the truncation function are highlighted in red.

For a photon 2D cluster, since the shower is well contained and has a small lateral spread, most hits have a recorded time very close to zero. This is illustrated in Figure 4.11 where the tails in time of an example single photon 2D cluster extend only up to 0.8 ns. It can be seen that only 14 rechits are removed out of 134, allowing the time of the 2D cluster to be better approximated, and less skewed by late rechits. For a π^+ 2D cluster, there is a much greater spread in rechit times which extend up to 12 ns away from the central distribution. This is because, as shown in Section 4.3.1, π^+ showers are less contained both longitudinally and laterally and there is non-negligible time for shower propagation. However, rechits with times of several ns are unlikely to be from the shower, and are not addressed in this study. The truncation function thus removes more π^+ rechits to approximate the time of the 2D cluster. As observed in Section 4.3.2, mean times beyond 40 ps occur at low signal-to-noise ratio and are therefore low energy deposits.

2D cluster timing as a function of energy

As with rechits, it is useful to quantify the 2D cluster timing resolution as a function of energy so that the fitted trends may be used in approximating the time of 3D clusters and full showers in the next sections. The fitted trends versus energy also provide a direct comparison to the rechit timing trends versus the signal-to-noise ratio. The timing resolution and mean time as a function of the 2D cluster energy obtained after the truncation procedure is shown in Figure 4.12 for photon and π^+ 2D clusters. It was found that high energy clusters include many low energy hits with late times. Using a simple average of the rechit times after the truncation procedure is not optimal for approximating the time of 2D clusters and leads to a slight increase in the 2D cluster time at high energy (Figure 4.12).

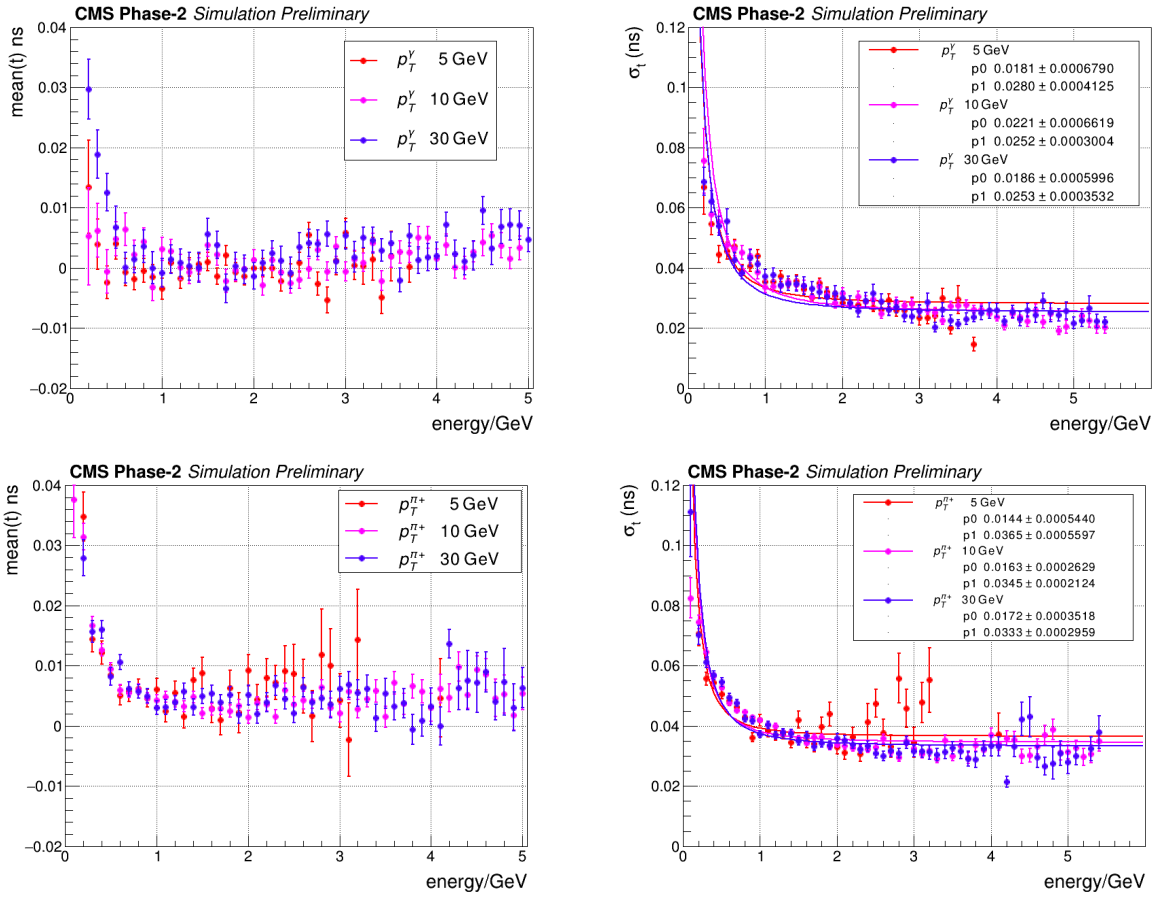

Figure 4.12: Distributions of the mean time (left) and the timing resolution (right) of photon (top) and π^+ (bottom) 2D clusters within 2 cm (photons) and 5 cm (pions) of the shower axis, with the time of 2D clusters computed from rechit times with no weighting procedure applied. The variables $p0$ and $p1$ are the fitted values of A and the floor C respectively.

Therefore, after the truncation on the rechit time distribution, the time of the 2D cluster is obtained by a weighted average of the time of the rechits. Several weighting schemes are considered:

1. **simple mean**: average of the time (corrected w.r.t the vertex) of rechits within 2cm (5cm) of the shower axis for photon (pion) rechits.
2. **weighted average** (E): the times of the rechits from the truncated rechit time distribution are weighted by the energy of the respective rechits before taking an average.
3. **weighted average** (E^2): the times of the rechits from the truncated rechit time distribution are weighted by the squared-energy of the respective rechits before taking an average.
4. **weighted average** $(1/\sigma)$: the times of the rechits from the truncated rechit time distribution are weighted by the inverse-resolution of the respective rechits before taking an average.
5. **weighted average** $(1/\sigma^2)$: the times of the rechits from the truncated rechit time distribution are weighted by the inverse-squared-resolution of the respective rechits before taking an average.

Note that for the schemes where a resolution weighting is used, the resolution of individual rechits is obtained from a fit function to the relevant rechit resolution versus the signal-to-noise distribution illustrated in Section 4.3.2.

Higher p_T photon 2D clusters have better resolutions for all methods. The best 2D timing resolution (floor value) for photons p_T 10 GeV 2D clusters is 25 ps, 14 ps, 15 ps, 16 ps, and 15 ps for the *simple mean*, *E weighting*, E^2 *weighting*, $1/\sigma$ *weighting* and $1/\sigma^2$ *weighting* procedures respectively. The fitted timing resolution floor ($p1$) from all weighting methods are very close within errors. The weighting by $1/\sigma^2$ gives the best results for the timing resolution. The timing resolution and mean time as a function of the 2D cluster energy when using the weighting by $1/\sigma^2$ is illustrated in Figures 4.13 for photon 2D clusters and π^+ 2D clusters. For reference, the same plots with the remaining weighting methods are included in Appendix A.

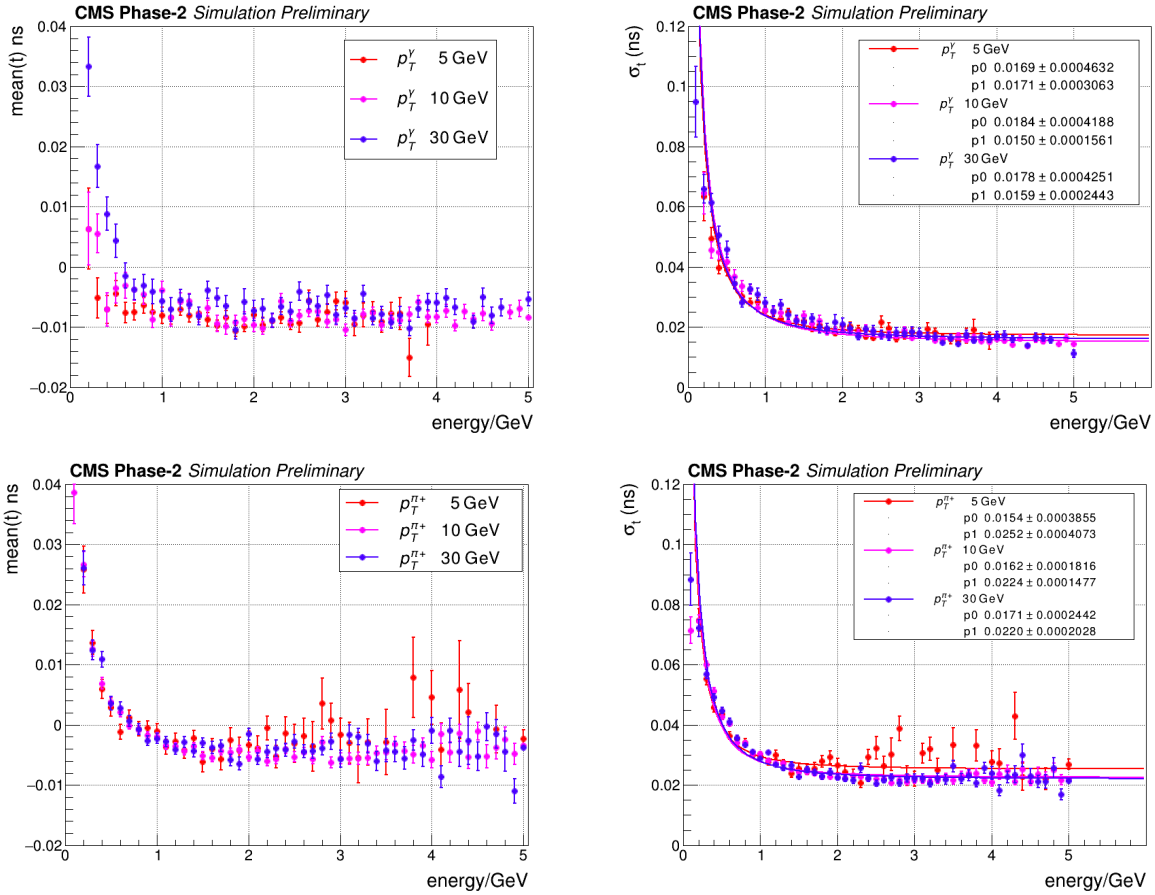

Figure 4.13: Distributions of the mean time (left) and the timing resolution of photon (top) and pion (bottom) 2D clusters within 2 cm (photons) and 5 cm (pions) of the shower axis, with the time of 2D clusters computed from rechit times with inverse-resolution-squared weighting procedure applied. The variables $p0$ and $p1$ are the fitted values of A and the floor C respectively.

Compared to the photon rechit timing resolutions versus $\log$ S/N where the resolution timing floor was around 20 ps, 2D clustering does bring a significant improvement in the achievable timing resolution, especially with the weighting procedures applied. All weighting methods bring the mean 2D cluster times to negative values (approximately -10 ps). This is

because of the digitisation issue discussed in Section 4.3.2. The $1/\sigma^2$ *weighting* gives the most central distribution in mean time over most of the energy range considered.

With π^+ 2D clusters, the best 2D cluster timing resolutions are approximately 35 ps, 22 ps, 22 ps, 23 ps, 22 ps with the *simple mean*, E *weighting*, E^2 *weighting*, $1/\sigma$ *weighting* and $1/\sigma^2$ *weighting* procedures respectively. As seen with rechits, there seems to be a minimum achievable 2D cluster timing resolution with increasing p_T. The importance of a weighting procedure is clear here and the $1/\sigma^2$ *weighting* is one of the best methods again. The π^+ 2D cluster resolutions seem to benefit more from increases in p_T than the photon 2D cluster resolutions. Compared to the rechit timing resolution values of about 15 ps (Figure 4.9), π^+ timing does not benefit as much from 2D clustering as photon timing. This is because of the poor 2D cluster timing efficiency for π^+ 2D clusters, illustrated in Figure 4.14 which shows 2D cluster timing efficiency as a function of 2D cluster energy. Here, the timing efficiency is the fraction of 2D clusters which have timing information (i.e 2D clusters with at least three rechits with energy depositions above 12 fC each).

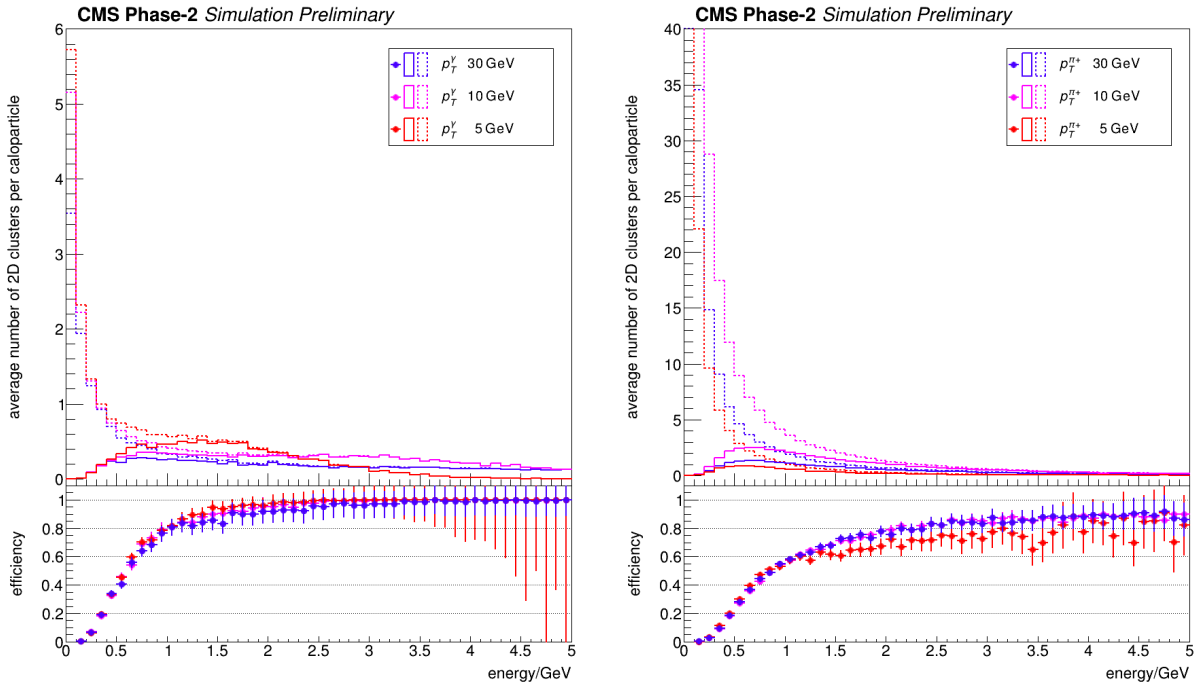

Figure 4.14: Distributions of photon (left) and π^+(right) 2D cluster timing efficiencies as a function of the 2D cluster energy. The dashed lines in the figure denote the distributions for all 2D clusters while the solid lines represent the distributions for 2D clusters which have time measurements.

The π^+ 2D cluster timing efficiency is only around 50% at 1 GeV. From Figure 4.4, most rechits have an energy well below 1 GeV for pion p_T 10 GeV, so most 2D clusters lie in the 0-1 GeV range. For photons, the 2D timing efficiency at 1 GeV is already 80%. These results also show that the criteria to assign a timing measurement to a 2D cluster should be optimised in the future, especially for π^+ showers, in order to increase the 2D cluster timing efficiency.

2D cluster timing as a function of energy using TICL selection criteria

The timing characteristics of 2D clusters selected by the TICL reconstruction framework is studied as a function of the energy of the 2D clusters. Using the TICL reconstruction allows for a more elaborate selection and further enables the behaviour of electromagnetic (EM) and hadronic (HAD) 2D clusters to be disentangled. As in Section 4.3.2, the 0 PU samples have a p_T value of 10 GeV and are directly comparable to the samples used in the selection of 2 cm (5 cm) on the distance from the shower axis of photon (π^+) 2D clusters. The performance of the weighting methods is further studied in this section under effect of PU. The p_T range in 200 PU is 8-150 GeV for photons and 0.7-10 GeV for π^+ particles. It is to be noted that the 0 PU and 200 PU samples are not directly comparable because of the different p_T ranges.

The mean time of EM photon 2D clusters from TICL 3D clusters are shown in Figure 4.15. The timing resolution of EM photon 2D clusters from TICL 3D clusters in 0 PU is shown in Figure 4.16. For 200 PU 2D clusters, the timing resolution is not useful since the ToF correction cannot be applied properly because the primary vertex of PU interactions is different from the primary vertex of the main event.

For photon 2D clusters from TICL in 0 PU, the mean time beyond a 2D cluster energy of 1 GeV is similar to the mean times obtained from the 2 cm selection. In the region below 1 GeV, EM 2D clusters have a mean time of about -8 ps. As a function of energy, the $1/\sigma^2$ *weighting* gives the least variation in the mean time and the most consistent distribution. Beyond 1 GeV, the timing resolution is best approximated using the $1/\sigma^2$ *weighting* method (as with the 2 cm selection) and lies at around 15 ps which is very similar to the resolutions observed from using the 2 cm selection (Figure 4.13). In 200 PU, the mean time of EM 2D clusters is now between -10 and 40 ps, compared to a range of -10 to 10 ps in 0 PU. There is a PU-like contribution at low energy (<2 GeV) with mean times between 0 and 30 ps. These likely represent low energy PU 2D clusters, although it is important to note that the 0 PU and 200 PU samples are not exactly comparable. Given the spread in the beam spot, a variation of up to 200 ps is expected in the time of rechits, and hence of 2D clusters in 200 PU. In the energy range 2-4 GeV, the mean time is not significantly different than the 0 PU case. The methods using a resolution weighting now consistently approximate higher mean times for the 2D clusters, which suggests that the resolution weighting methods are not as robust against low-energy PU 2D clusters as energy weighting methods.

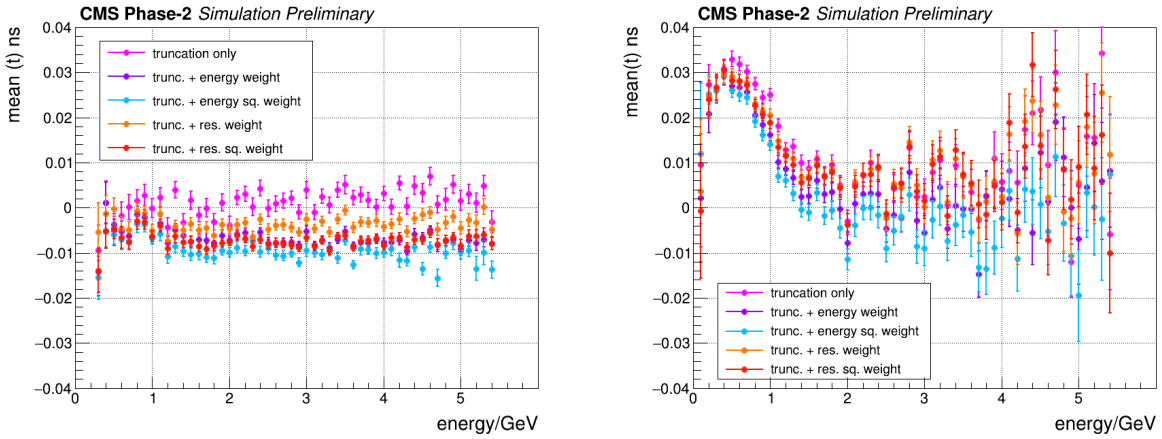

Figure 4.15: Distributions of the mean time of photon EM 2D clusters from the TICL reconstruction as a function of the 2D cluster energy in 0 PU (left) and 200 PU (right).

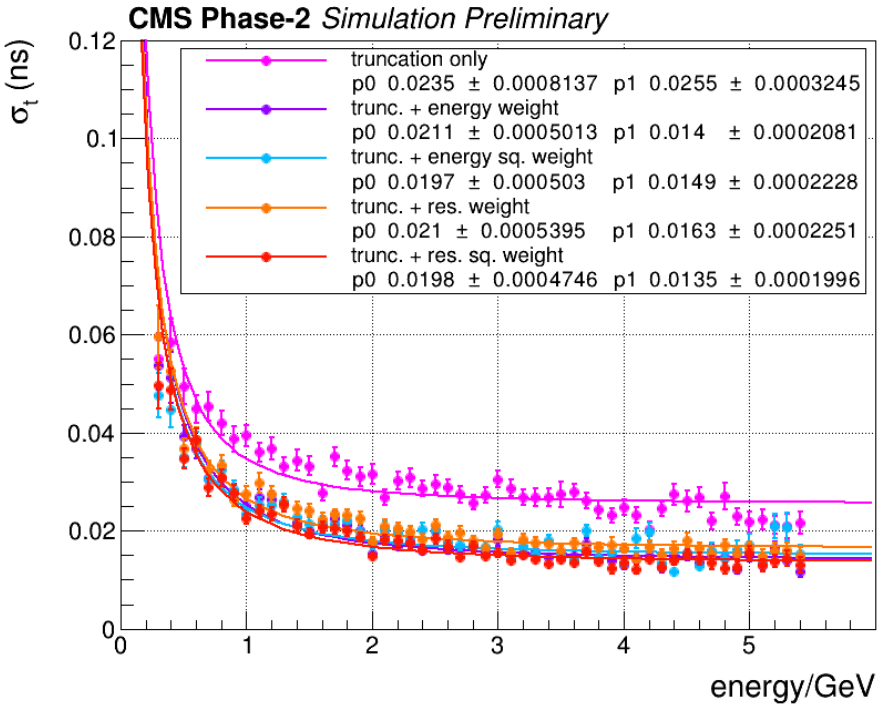

Figure 4.16: Distributions of the timing resolution of photon EM 2D clusters from the TICL reconstruction as a function of the 2D cluster energy in 0 PU. The variables $p0$ and $p1$ are the fitted values of A and the floor C respectively.

The mean time of HAD π^+ 2D clusters from TICL 3D clusters is shown in Figure 4.17. The timing resolution of HAD π^+ 2D clusters from TICL 3D clusters in 0 PU is shown in Figure 4.18.

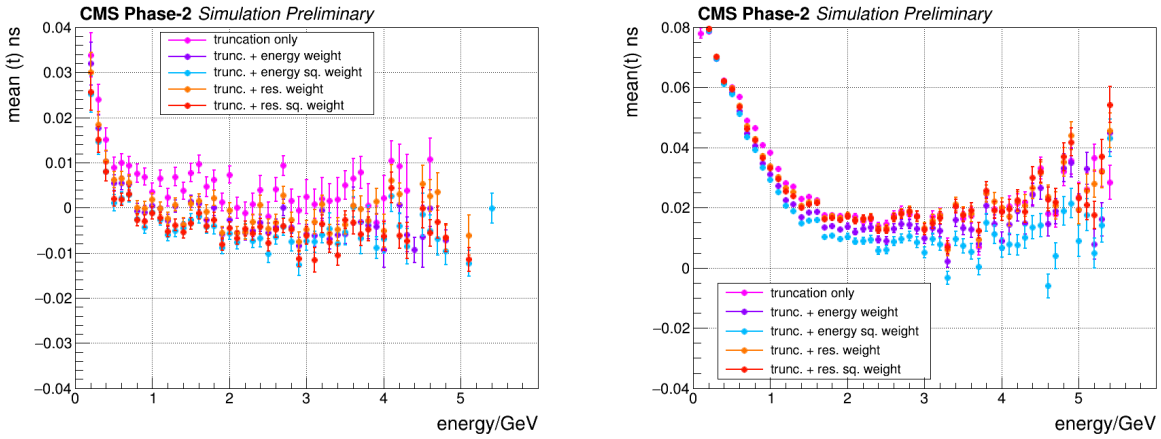

Figure 4.17: Distributions of the mean time of π^+ HAD 2D clusters from the TICL reconstruction as a function of the 2D cluster energy in 0 PU (left) and 200 PU (right)

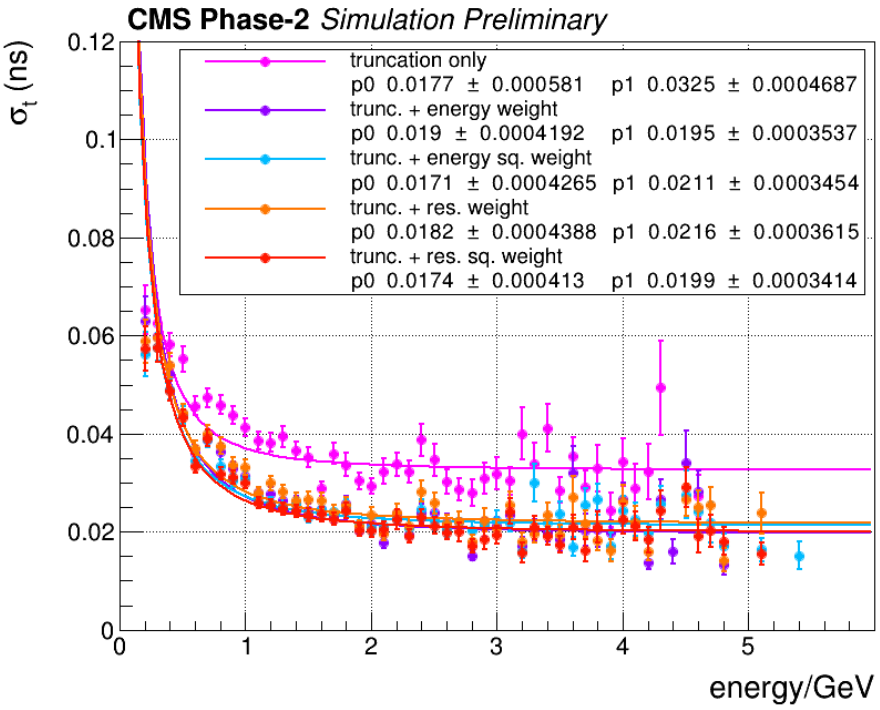

Figure 4.18: Distributions of the timing resolution of π^+ HAD 2D clusters from the TICL reconstruction as a function of the 2D cluster energy in 0 PU. The variables $p0$ and $p1$ are the fitted values of A and the floor C respectively.

For π^+ HAD 2D clusters in 0 PU, the mean time is -10 to 40 ps. This suggests that the slow component of π^+ showers is due to a slow component with low energy deposits and a wider (about 50 ps) spread in time. This is in line with the trend in the mean time below 1 GeV in the corresponding plot using the 5 cm selection (Figure 4.13). Beyond 2 GeV, the timing resolution of π^+ HAD 2D clusters is around 20 ps (5 ps worse than with photons) and is slightly better (by about 3 ps) than that obtained with the 5 cm selection (Figure 4.13).

Below 2 GeV, the timing resolution ranges from 20 to 80 ps. In 200 PU the mean time of π^+ 2D clusters distributions show a low energy PU contribution with later times below 2 GeV. This contribution has mean times between 10 and 80 ps.

2D cluster timing resolution of layers

A two-dimensional histogram of the 2D cluster time versus the layer (one entry per layer cluster) is used. Figure 4.19 shows examples of the two-dimensional histograms obtained with p_T 10 GeV photons and π^+ particles in 0 PU. The timing resolution for each layer is obtained by slicing the two dimensional histogram vertically and fitting a Gaussian function in every slice (the range of the fit is restricted to $-2 \times$ RMS to $2 \times$ RMS). 2D clusters within 2 cm (5 cm) of the shower axis are selected for photons (π^+ particles). From the two dimensional histograms, it is visible that photon 2D clusters have a spread in time of -0.2 ns to 0.2 ns. For π^+ 2D clusters, the spread extends well beyond 0.2 ns and thus 2D cluster timing for photons is expected give a better performance than for π^+ particles. This is because of the spread in time of π^+ 2D clusters and because of the smaller number of hits per layer since the hits for π^+ particles are spread across more layers, resulting in fewer 2D clusters with timing information per layer.

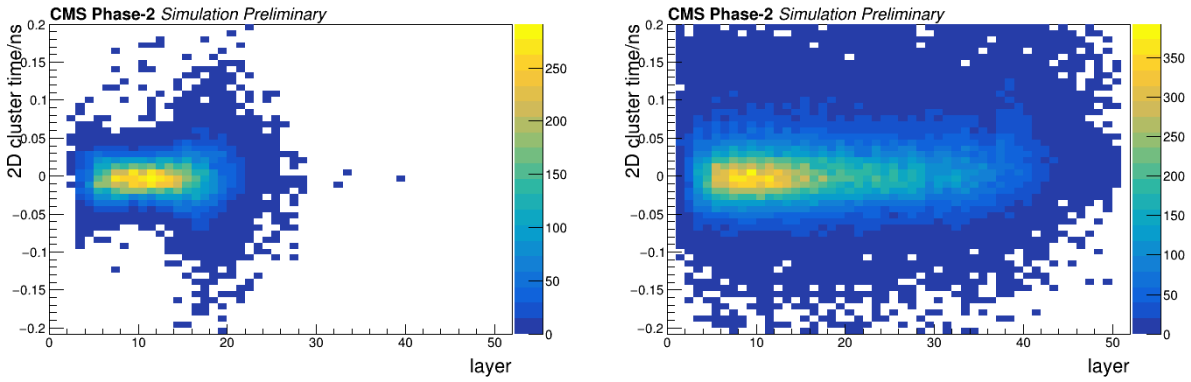

Figure 4.19: Two-dimensinal histogram of the 2D cluster time from photon (left) and π^+ (right) p_T 10 GeV particles as a function of the HGCAL layer.

The layer timing resolution and mean time obtained for photon 2D clusters is illustrated in Figure 4.20 for the $1/\sigma^2$ *weighting* procedure. For reference, similar distributions for the remaining methods are included in Appendix A. Generally for all weighting methods, the best resolution is at the shower maximum (layers 7-14); the resolution is poorer in the first and last layers because less energy is deposited. Measurements are dominated by noise and limited by statistics in the very first and last layers of the shower. As with rechits, the higher the p_T, the later is the shower maximum. Since the shower develops more rapidly and is better contained at higher p_T, 2D clusters are closer in time. This scaling is very clear for photons. Furthermore, at higher p_T, the signal-to-noise ratio is higher, hence a better timing resolution is achievable; there are also more hits with timing information.

Choosing photon p_T 10 GeV 2D clusters as example, the best resolutions are approximately 21 ps, 15 ps, 15 ps, 12 ps and 12 ps for the *simple mean*, *E weighting*, E^2 *weighting*, $1/\sigma$ *weighting* and $1/\sigma^2$ *weighting* procedures respectively at the shower maximum. Generally

the resolution weighting methods give a better resolution result than the energy weighting methods. Looking at all layers (not only the maximum), $1/\sigma^2$ and E^2 weightings give better results than $1/\sigma$ and E weightings. The $1/\sigma^2$ *weighting* method is therefore the best method and will be used in the next steps of the reconstruction.

The 2D cluster timing resolution range (12-20 ps at best for p_T 10 GeV photons) is thus better than those obtained with the previous geometry (20-30 ps for p_T 10 GeV photons [44]). The mean time of the 2D clusters is approximately zero within the timing resolutions stated above. However, the weighting methods bring the mean time of 2D clusters to negative values. This effect is explained in Section 4.3.3. The E *weighting*, E^2 *weighting*, $1/\sigma$ *weighting* and $1/\sigma^2$ *weighting* methods all reduce the spread in the mean time of the 2D clusters, giving a more central distribution. The resolution weighting methods give flatter distributions in the mean time of 2D clusters. The resulting spread in the mean time of about 10-15 ps is consistent with the time of propagation of the shower rechits obtained in Section 4.3.2.

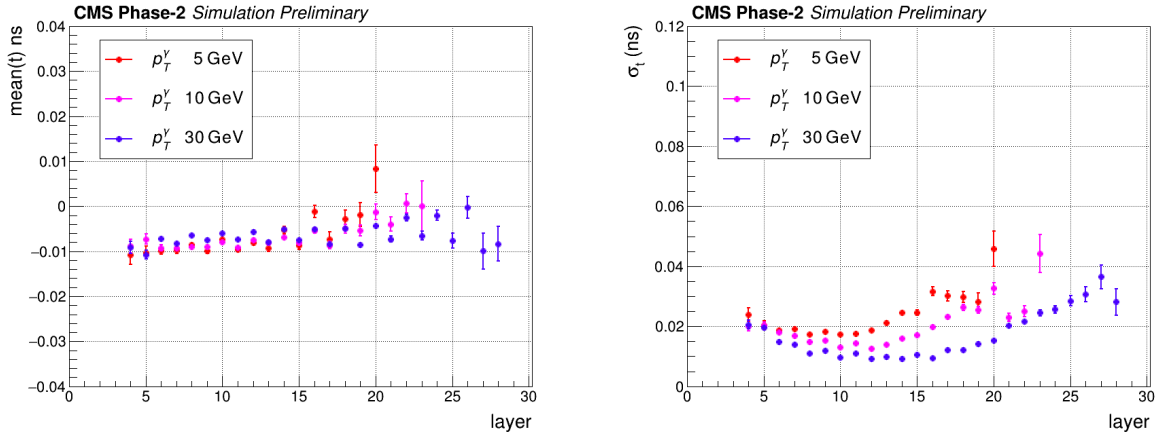

Figure 4.20: Distributions of the mean time (left) and the timing resolution (right) of photon 2D clusters within 2 cm of the shower axis, with the time of 2D clusters computed from rechit times with inverse-resolution-squared weighting procedure applied.

The layer timing resolution and mean time obtained for π^+ 2D clusters is illustrated in Figure 4.21 for the $1/\sigma^2$ *weighting* procedure. Similar distributions for the remaining weighting methods are included in Appendix A for reference.

For the π^+ 2D cluster time resolutions, the scaling of the trends with p_T is not as apparent as with photons; at p_T 10 GeV and p_T 30 GeV, the π^+ 2D cluster time resolution trends are very similar. This behaviour is similar to that observed with π^+ rechits. Since π^+ showers do not have a clearly defined shower maximum, the resolution distribution is fairly flat between layers 10 and 30, with a slight worsening in resolution after layer 30. This is most likely due to fewer hits in the deeper layers. The best resolutions for π^+ p_T 10 GeV 2D clusters is around 40 ps, 30 ps, 30 ps, 30 ps and 25 ps in the CE-E section for the *simple mean*, E *weighting*, E^2 *weighting*, $1/\sigma$ *weighting* and $1/\sigma^2$ *weighting* schemes respectively. For the FH and BH sections, although with large errors, the corresponding approximate numbers are 50 ps, 45 ps, 40 ps, 45 ps and 35 ps. As with photon 2D clusters, weighting the rechit times by $1/\sigma^2$ gives a better result for the timing resolution of the π^+ 2D clusters. These numbers are similar to the ones obtained in with the previous geometry (30-40 ps for p_T

10 GeV kaons [44]). Compared to photon 2D clusters, where the spread in mean time was around 15 ps, π^+ 2D clusters have a mean time which extends up to 40 ps in deeper layers. The mean times in the CE-E section have a spread of around 15 ps. This suggests that shower propagation for π^+ particles occurs as rapidly as for photons in the CE-E section, while shower propagation in the FH and BH takes up to 40 ps. This shows that hadronic showers have a fast electromagnetic core, followed by a slower hadronic component. Again, the $1/\sigma^2$ *weighting* scheme visibly produces the clearest and most consistent trend in the mean time of π^+ 2D clusters.

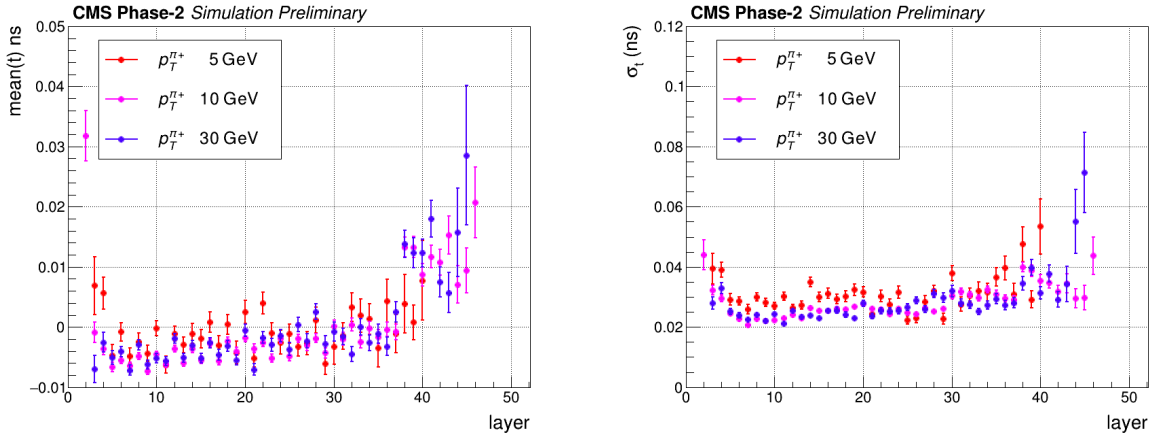

Figure 4.21: Distributions of the mean time (left) and the timing resolution (right) of π^+ 2D clusters within 5 cm of the shower axis, with the time of 2D clusters computed from rechit times with the inverse-resolution-squared weighting procedure applied.

The 2D cluster timing efficiency is shown in Figure 4.22. The dashed lines in the figure denote the distributions for all 2D clusters while the solid lines represent the distributions for 2D clusters with a time measurement.

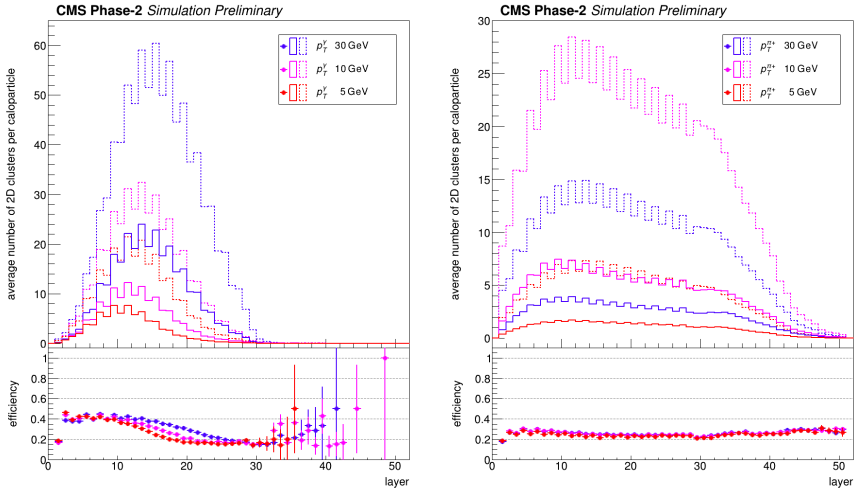

Figure 4.22: Distributions of photon (left) and π^+ (right) 2D cluster timing efficiencies as a function of the HGCAL layer. The dashed lines in the figure denote the distributions for all 2D clusters while the solid lines represent the distributions for 2D clusters with a time measurement.

The overall 2D cluster timing efficiency is 40% at the photon shower maximum. The further three top plots in Figure 4.23 show the timing efficiency when only 2D clusters at 2cm, 5 cm and 10 cm from the shower axis are chosen. When only 2D clusters at 2cm from the shower axis are selected for photons, a 100% 2D cluster timing efficiency is achievable. Considering 2D clusters beyond 2 cm degrades the 2D cluster timing efficiency as hits in 2D clusters further than 2 cm from the shower axis are likely to deposit less energy. As with the rechit timing efficiency in Section 4.3.2, the higher the p_T, the more the energy deposited by the hits, giving more 2D clusters with a time measurement. From Figure 4.22 and the bottom three plots in Figure 4.23, a similar trend is observed with π^+ 2D clusters; selecting hits further from the shower axis reduces the timing efficiency. The overall timing efficiency is only 30% for π^+ 2D clusters. Selecting 2D clusters only within 2 cm of the shower axis gives an efficiency of 40% at most and selecting 2D clusters within 5 cm gives a timing efficiency of 20% at most. This further suggests that π^+ showers are made of many hits of low energy.

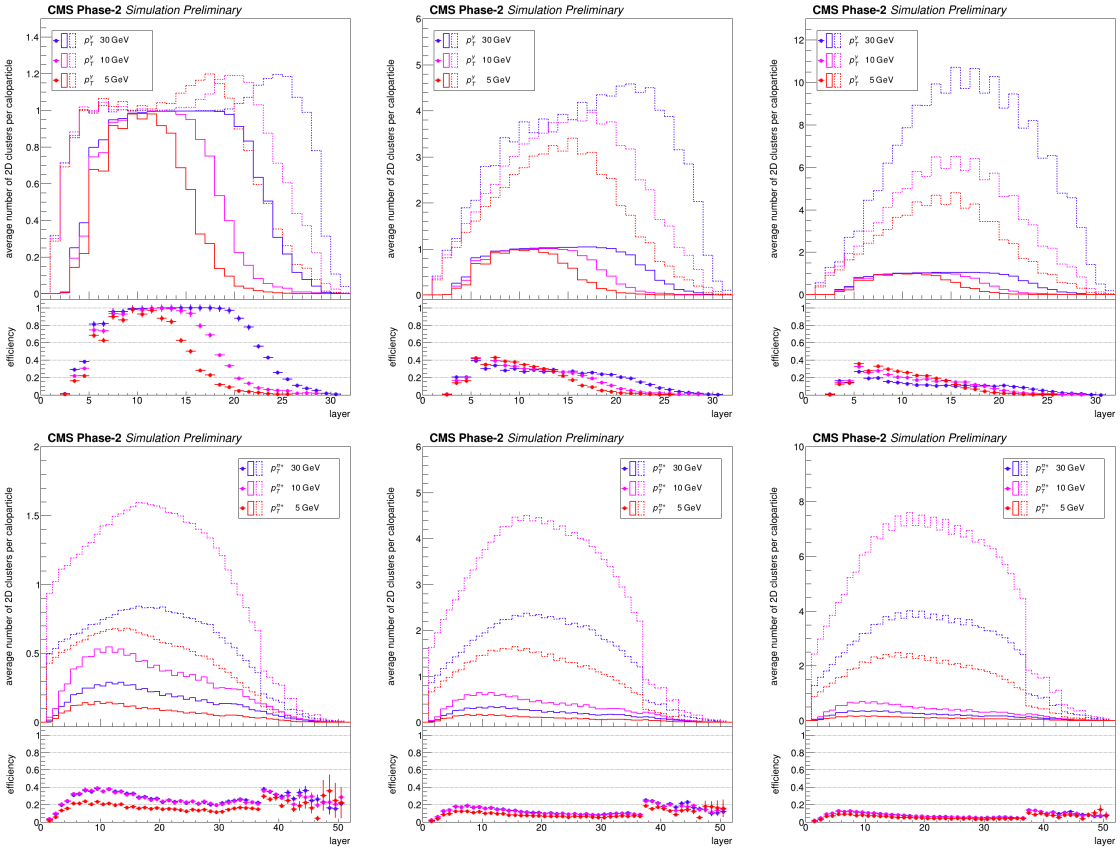

Figure 4.23: Distributions of photon (top) and π^+ (bottom) 2D cluster timing efficiencies within 2 cm (left), 5 cm (middle) and 10 cm (right) of the shower axis as a function of the HGCAL layer. The dashed lines in the figure denote the distributions for all 2D clusters while the solid lines represent the distributions for 2D clusters with a time measurement.

2D cluster timing resolution of layers with TICL selection criteria

The timing characteristics of 2D clusters selected by the TICL reconstruction framework is studied as a function of the HGCAL layers. As in Section 4.3.2, the 0 PU samples have a p_T

point of 10 GeV and are directly comparable to the numbers obtained with a selection of 2 cm (5 cm) on the distance from the shower axis of photon (π^+) 2D clusters. The p_T range in 200PU is 8-150 GeV for photons and 0.7-10 GeV for π^+ particles.

The mean time of EM photon 2D clusters from TICL 3D clusters are shown in Figure 4.24. The timing resolution of EM photon 2D clusters from TICL 3D clusters in 0 PU is shown in Figure 4.25. In 0 PU, the spread in the mean time of TICL photon 2D clusters of about 10 ps, 10 ps, 15 ps, 5 ps and 5 ps for or the *simple mean*, E *weighting*, E^2 *weighting*, $1/\sigma$ *weighting* and $1/\sigma^2$ *weighting* schemes respectively. These numbers are very similar to the results obtained without the TICL reconstruction. The least spread and most consistent trend in the mean times of photon 2D clusters is obtained from methods adopting a resolution-based weighting. From the distributions of the timing resolutions in 0 PU, it is clear that the method of weighting by $1/\sigma^2$ outperforms all other methods as seen in results without the TICL reconstruction. The truncation-only (simple mean) method gives resolutions 10-15 ps worse that any of the other weighting methods. In the layers 20-25, the timing resolution from the 2D clusters from TICL is approximately 5 ps better than in corresponding distributions using only the 2 cm selection.

Compared to the 0 PU case where the mean times of EM photon 2D clusters from TICL 3D clusters are within 10 ps of 0, in 200 PU, the mean time of photon EM 2D clusters ranges between -10 and 40 ps in the layers expected to contain the photon shower maximum. This is because the TICL reconstruction does not perfectly reject all PU 2D clusters. Any worsening of the performance in 200 PU is either from pure PU 2D clusters or PU contamination to signal clusters. In any case, for any PU deposit, the ToF correction applied is not correct and this degradation in the performace is expected. This is illustrated clearly by the mean time of 2D clusters in layers 28 onwards; these 2D clusters are expected to correspond to pure PU contributions and therefore, the mean time is up to 100 ps from zero (corresponding to a $\sim$4 cm spread in the beam spot position). Because of the spread in the position of the beam spot, a variation of up to 200 ps can be expected in the mean time of rechits, and hence 2D clusters in 200 PU. Furthermore, in the first layers, there are few hits with a time measurement and the mean time extends to 100 ps. This shows a non-negligible PU contribution in the first layers of the HGCAL.

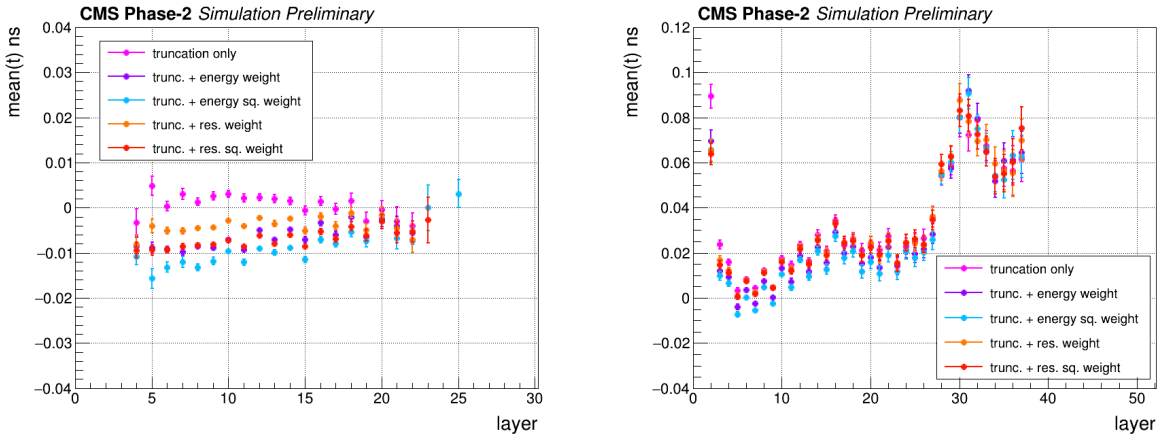

Figure 4.24: Distributions of the mean time of photon EM 2D clusters from the TICL reconstruction as a function of the HGCAL layer in 0 PU (left) and 200 PU (right).

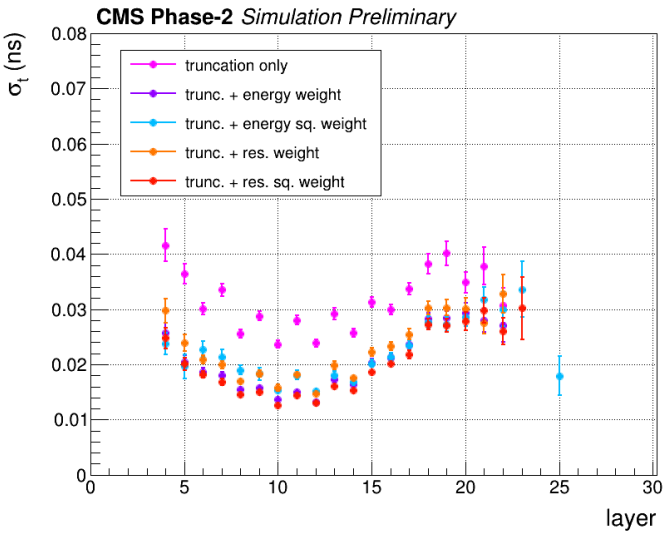

Figure 4.25: Distributions of the timing resolution of photon EM 2D clusters from the TICL reconstruction as a function of the HGCAL layer in 0 PU.

The mean time of HAD π^+ 2D clusters from TICL 3D clusters are shown in Figure 4.26.

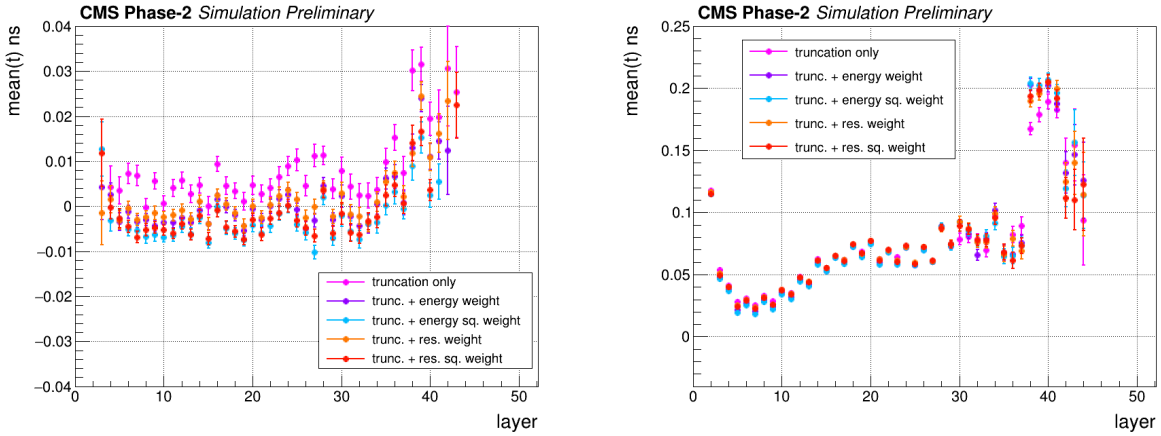

Figure 4.26: Distributions of the mean time of π^+ HAD 2D clusters from the TICL reconstruction as a function of the HGCAL layer in 0 PU (left) and 200 PU (right).

The timing resolution of of HAD π^+ 2D clusters from TICL 3D clusters are shown in Figure 4.27. In 0 PU, the mean time of EM π^+ 2D clusters in TICL ranges from around -5 ps in layers 10-20 to around 20 ps in layer 40, compared to a respective range of -5 ps to 30 ps when using the 5 cm selection (Figure 4.20). This shows that the TICL reconstruction achieves a more uniform distribution for approximating the time of π^+ 2D clusters. The $1/\sigma^2$ *weighting* method achieves the least spread in time and the clearest trend with the layer. As observed with photons, the best timing resolutions for π^+ 2D clusters in TICL is obtained from a $1/\sigma^2$ *weighting*. The truncation-only method consistently under performs across all layers when compared to all other weighting methods. As observed with photons, the π^+ 2D cluster timing resolution is poorer in layers 30-40. This shows that HAD π^+ 2D clusters are more spread in time and this is confirmed by the plots of the mean time.

In 200 PU, the mean time of π^+ EM 2D clusters ranges from -10 to 200 ps, compared to -10 to 20 ps in 0 PU. For the HAD 2D clusters, the range in 200 PU is 20 to 200 ps. There are clear PU contributions in layers 30 onwards which have mean times between 50 and 200 ps. As observed with photons in 200 PU, the methods using a resolution weighting give a higher approximated mean time and are therefore more affected by the PU contributions later in time.

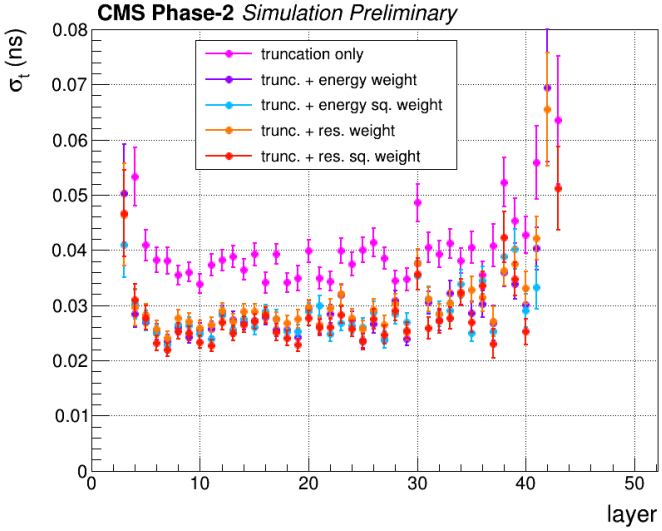

Figure 4.27: Distributions of the timing resolution of π^+ HAD 2D clusters from the TICL reconstruction as a function of the HGCAL layer in 0 PU.

Contribution from early showering

In this Section, the time of 2D clusters has been computed using the $1/\sigma^2$ *weighting* method. 2D clusters have been selected in a 2 cm cylinder around the shower axis unless stated otherwise. Time smearing has not been applied for rechits in this section so that the trend in the mean time as a function of layer is clearer.

Under the simulation and reconstruction conditions in the samples used in this study, the time of a photon shower is expected to be very close to 0. However, from the results shown in the previous section, there appears to be a trend in the mean time of 2D clusters as a function of the HGCAL layer. The mean time of layer 2D clusters appears always greater than zero and correlates with the pattern of energy deposition across layers. To investigate this behaviour, a dedicated photon sample was produced with the particle origin placed at the start of the HGCAL. These are compared to standard samples where the particle origin is at the centre of the detector. Results for this comparison are shown in Figure 4.28, where the trend in the mean time of 2D clusters is not visible for particles produced just in front of the HGCAL.

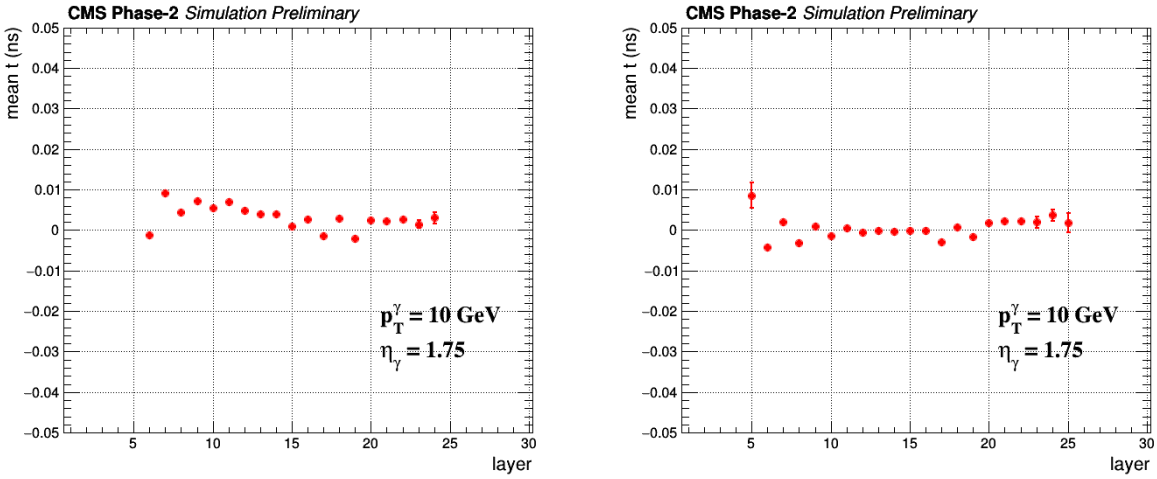

Figure 4.28: Comparison between the mean time of 2D clusters as a function of the HGCAL layer for p_T 10 GeV photon samples using the standard particle gun (left) and the particle gun at the start of the HGCAL (right).

Figures 4.29 and 4.30 show the average number of layer clusters as a function of the layer within 2 cm and 5 cm from the shower axis for both types of samples. It can be seen that when moving from 2 cm to 10 cm from the shower axis, there is no significant change in the number of layer clusters when particles are produced just in front of the HGCAL, as opposed to a noticeable increase in the number of layer clusters with the standard sample. The trend is believed to be due to early conversions of photons before the first sensitive layer of the HGCAL (e.g in the neutron moderator), leading to a pre-showering effect that results in clusters at large distances from the shower axis, for which the time is greater than zero.

Separation of e^+e^- pairs in the magnetic field leads to a wider shower with clusters away from the shower axis. The pre-showering effect can be further observed by studying the vertex spectrum of photon conversions in the standard sample (Figure 4.31). It can be seen that there are few conversions before the beginning of the HGCAL at approximately 300 cm. There is a flat and increased contribution in the region of the neutron moderator (300-320 cm).

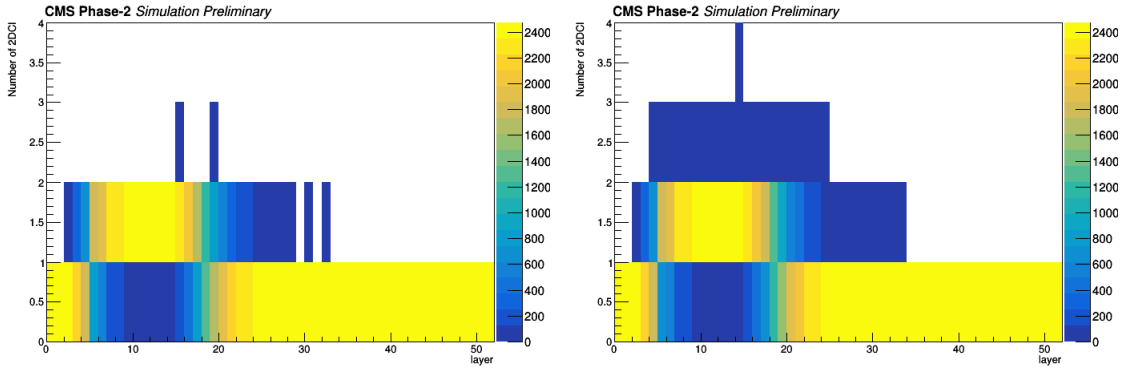

Figure 4.29: Number of 2D clusters versus layer for p_T 10 GeV photon samples using the standard particle gun and selecting 2D clusters within 2 cm (left) and 10 cm (right) of the shower axis.

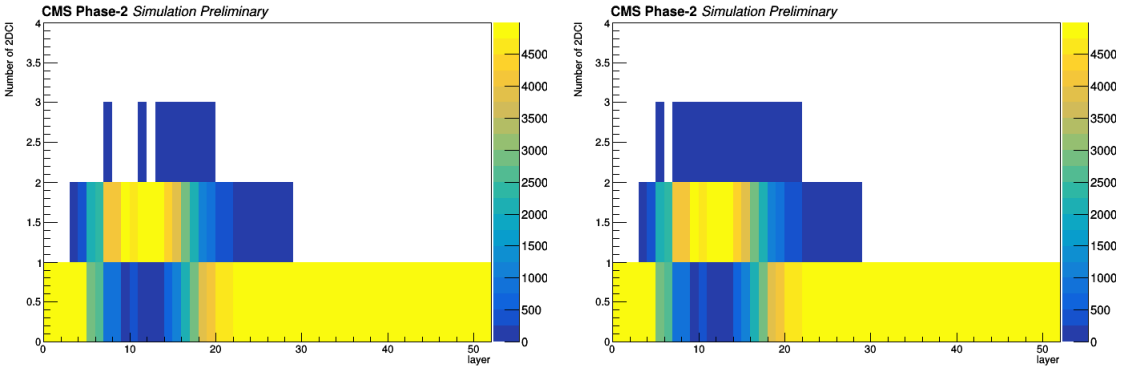

Figure 4.30: Number of 2D clusters versus layer for p_T 10 GeV photon samples using the particle gun at the start of the HGCAL and selecting 2D clusters within 2 cm (left) and 10 cm (right) of the shower axis.

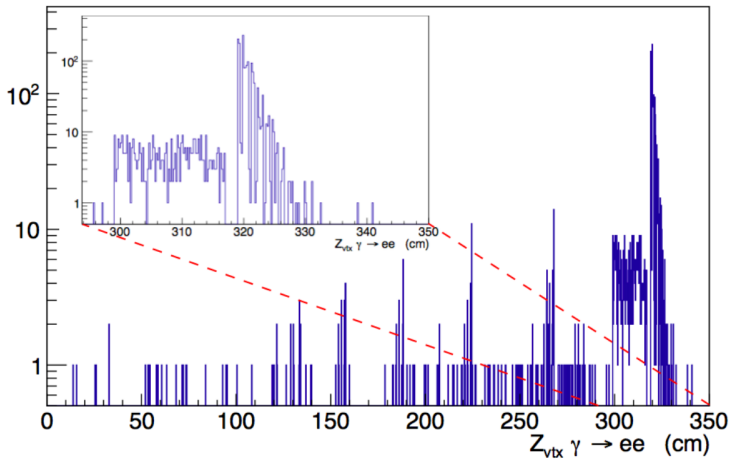

Figure 4.31: Distribution of the vertex of photon conversions in a p_T 10 GeV photon sample produced using the standard particle gun.

4.3.4 Timing of objects

Object timing methods

From Section 4.3.3, the mean time of 2D clusters and the achievable resolutions are known. The next step is to assign a time to the full shower to be used in particle ID and PU rejection. In this section, a few different methods to assign a time to a full shower (object) are studied, starting from 2D clusters obtained from the cylindrical selection. It is to be noted that these studies are not done with the samples using the particle gun at the beginning of the HGCAL; therefore the time of photon showers is not expected to be zero. In the samples in this section, the p_T range is 8-150 GeV for photons and 0.7-10 GeV for π^+ particles for both the 0 PU and the 200 PU samples. All 2D cluster times have been computed using the $1/\sigma^2$ *weighting* method discussed in Section 4.3.3.

Different methods to compute the time of a full shower, starting from the time of 2D clusters, are compared:

1. **simple mean**: average of the time (corrected w.r.t the vertex) of 2D clusters within 2cm (5cm) of the shower axis for photon (pion) 2D clusters.

2. **truncation + simple mean**: a truncation is done (window = 210 ps) before making an average of the time (corrected w.r.t the vertex) of 2D clusters within 2cm (5cm) of the shower axis for photon (pion) 2D clusters.

3. **weighted average (E)**: the times of the 2D clusters from the 2D cluster time distribution are weighted by the energy of the respective 2D clusters before taking an average.

4. **truncation + weighted average (E)**: a truncation is done (window = 210 ps) + the times of the 2D clusters from the truncated 2D cluster time distribution are weighted by the energy of the respective 2D clusters before taking an average.

5. **weighted average (E^2)**: the times of the 2D clusters from the 2D cluster time distribution are weighted by the squared-energy of the respective 2D clusters before taking an average.

6. **truncation + weighted average (E^2)**: a truncation is done (window = 210 ps) + the times of the 2D clusters from the truncated 2D cluster time distribution are weighted by the squared-energy of the respective 2D clusters before taking an average.

7. **weighted average ($1/\sigma$)**: the times of the 2D clusters from the 2D cluster time distribution are weighted by the inverse-resolution of the respective 2D cluster times before taking an average.

8. **truncation + weighted average ($1/\sigma$)**: a truncation is done (window = 210 ps) + the times of the 2D clusters from the truncated 2D cluster time distribution are weighted by the inverse-resolution of the respective 2D cluster times before taking an average.

9. **weighted average ($1/\sigma^2$)**: the times of the 2D clusters from the 2D cluster time distribution are weighted by the inverse-squared-resolution of the respective 2D cluster times before taking an average.

10. **truncation + weighted average ($1/\sigma^2$)**: a truncation is done (window = 210 ps) + the times of the 2D clusters from the truncated 2D cluster time distribution are weighted by the inverse-squared-resolution of the respective 2D cluster times before taking an average.

11. **weighted average ($1/error$)**: the times of the 2D clusters from the 2D cluster time distribution are weighted by the inverse-error of the respective 2D cluster times before taking an average.

12. **truncation + weighted average ($1/error$)**: a truncation is done (window = 210 ps) + the times of the 2D clusters from the truncated 2D cluster time distribution are weighted by the inverse-error of the respective 2D cluster times before taking an average.

13. **weighted average ($1/error^2$)**: the times of the 2D clusters from the 2D cluster time distribution are weighted by the inverse-squared-error of the respective 2D cluster times before taking an average.

14. **truncation + weighted average** ($1/error^2$): a truncation is done (window = 210 ps) + the times of the 2D clusters from the truncated 2D cluster time distribution are weighted by the inverse-squared-error of the respective 2D cluster times before taking an average.

For the weighting schemes that involve the resolution of 2D clusters, the fit to the respective distribution of the 2D cluster resolution as a function of the 2D cluster energy is used. As mentioned before, the method of selecting 2D clusters within a cylinder centered on the shower axis is suboptimal to properly reconstruct a full shower. For the purpose of preliminary shower studies, the approximation suffices. The timing characteristics of 3D clusters reconstructed using TICL are studied later in this section.

Time of a shower

In the plots that follow, results from methods using a truncation are studied separately from methods not using a truncation for clarity. The distributions of the photon shower times from each weighting method are overlaid and shown in Figure 4.32 for methods with and without a truncation.

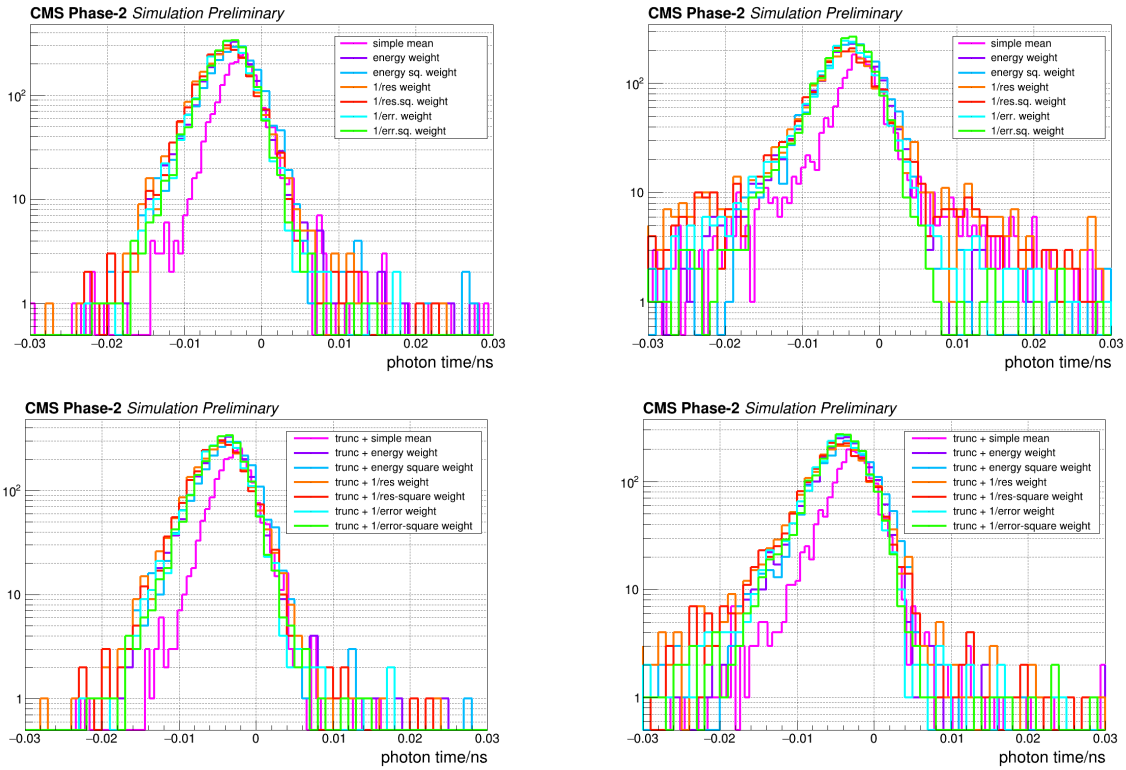

Figure 4.32: Distribution of the photon shower times computed from 2D cluster times using methods that do not adopt (top) and that adopt (bottom) a truncation. Distributions are shown for 0 PU (left) and 200 PU (right).

In 0 PU, the spread in time for the photon showers (including the very last tails) is approximately ± 30 ps and is consistent (within a few ps) for all methods. It is clear that the methods involving a truncation result in less tails for the timing distribution. It is also important to note that in 0 PU the truncation does not affect the central distribution, but

merely helps to remove tails which would otherwise skew the time approximation for the photon shower. Clearly, methods with no truncation are less central and give a poorer shower timing resolution. In 200 PU, the spread in the photon shower time extends well beyond ± 30 ps as shown in the distributions for methods not using a truncation. In 200 PU, a truncation helps to remove 2D clusters in the tails of the 2D cluster time distributions to recover a distribution more similar to that in 0 PU. This is because 2D clusters from PU are unlikely to have a distribution peaked at zero in time and are likely to have times which are not consistent with the times of 2D clusters from the main event.

The distributions of the π^+ shower times from each weighting method are overlaid and shown in Figure 4.33 for methods with and without a truncation.

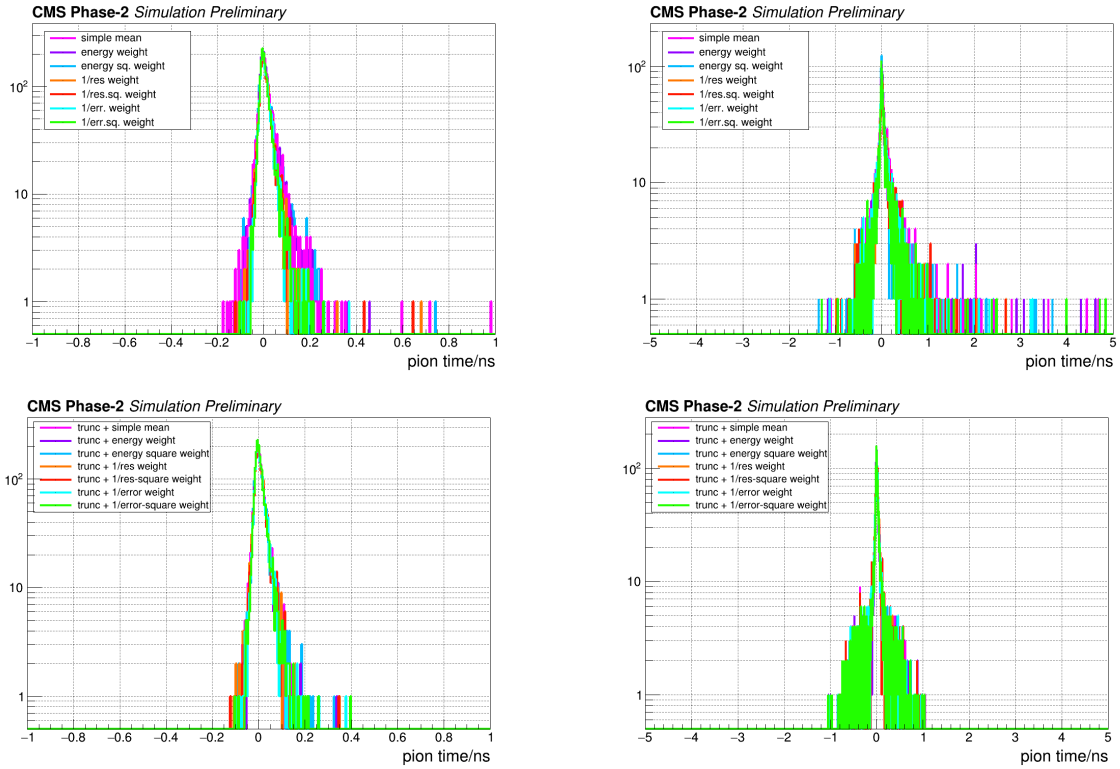

Figure 4.33: Distribution of the π^+ shower times computed from 2D cluster times using methods that do not adopt (top) and that adopt (bottom) a truncation. Distributions are shown in 0 PU (left) and 200 PU (right).

In 0 PU, the time for π^+ showers have very long tails, especially in the positive time direction. The spread is from -0.2 ns to 1 ns. This shows that π^+ showers take much more time to develop than photon showers. As with photon showers, the use of the truncation methods largely helps to reduce the spread in shower time to approximately -0.1 ns to 0.4 ns. This shows that in the case of π^+ particles, there can be many 2D clusters which are not in time with the shower, or with times much later away from the central shower time distribution. These skew the average time of the π^+ shower, causing the approximation to be up to 1 ns away from the expected value. Truncating the time distribution of the 2D clusters before approximating the time of the full shower is therefore very useful with π^+ showers. In 200 PU, the π^+ shower time ranges between -1.5 ns and 5 ns as observed in the distributions for methods not using a truncation. When compared to the plot in 0 PU,

it can be deduced that PU contributions mainly occur later (by up to 4 ns) than the π^+ showers. The effect of PU on the distribution of the π^+ shower time is significantly reduced (to a range of -1 to 1 ns) by using truncation methods; the long positive tail in the 200 PU distribution above 1 ns is completely removed.

The timing performance in terms of the mean and resolution of shower time given by the various timing approximation methods is studied as a function of the energy of the shower. The distributions of the mean photon shower times from each weighting method are shown in Figure 4.34 for methods with and without a truncation.

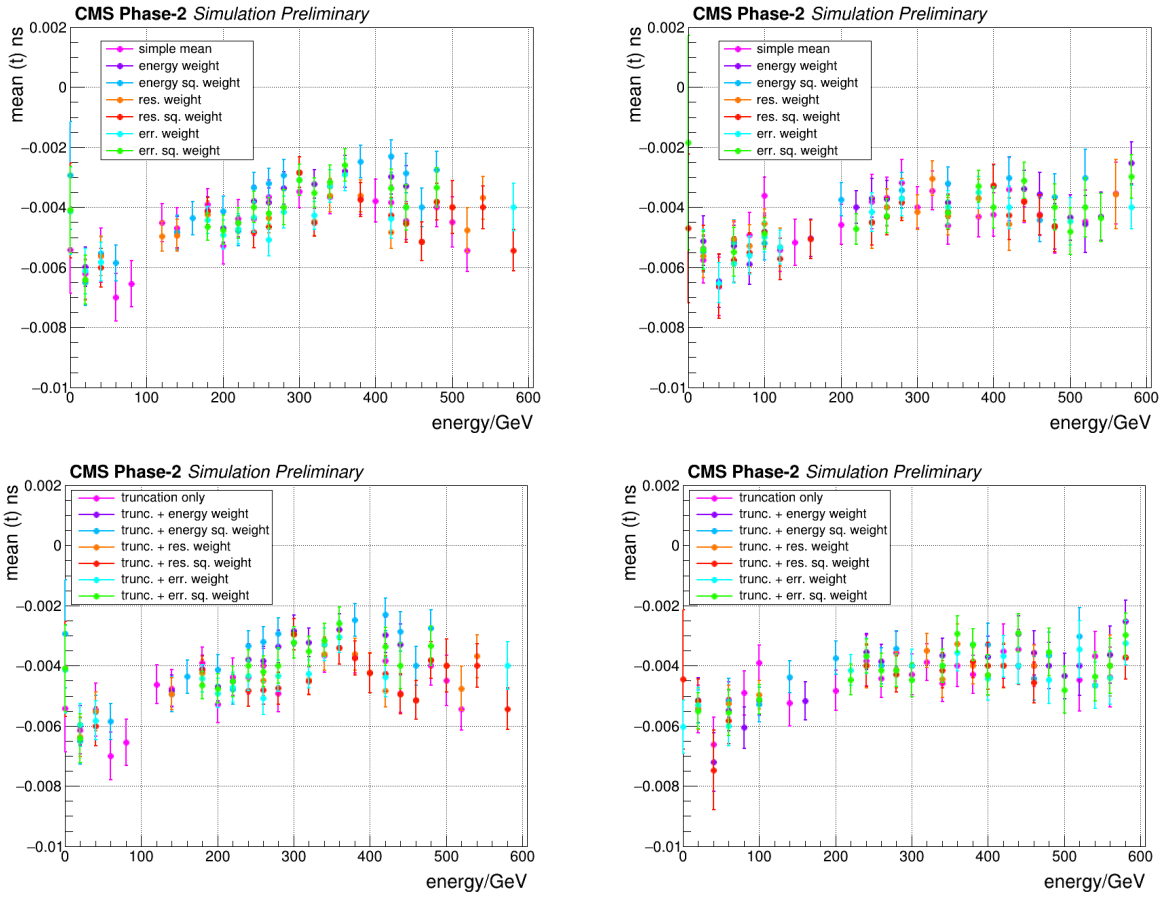

Figure 4.34: Distribution of the mean photon shower times, where the shower time is computed from the time of 2D cluster times using methods that do not adopt (top) and adopt (bottom) a truncation. Distributions are shown in 0 PU (left) and 200 PU (right).

In 0 PU, the mean time of the photon shower is approximated very closely by all methods, and is consistent within errors among all methods. The spread in the mean time of the shower over the energy range is approximately 10 ps. Note that since rechit times are being corrected to the vertex, the time of the photon is actually a measure the time of the vertex (to a resolution of approximately 10 ps). The similarity in the approximation between the truncation methods and the non-truncation methods further emphasises that the truncation does not affect the approximated time of the photon shower but only helps to remove the tails. The mean time seems to peak around 300-400 GeV. From Figure 4.32 , the bulk of the shower time distribution is between -0.015 ns and 0.01 ns, with a peak at about -0.005 ps; this translates to the 0-200 GeV range in the mean time plots, which is very consistent with

the nominal 8-150 photon p_T range of the samples. In 200 PU, the mean time of the photon showers increases with increasing energy and shows no clear peak. In the 0-200 GeV range, the mean times are around -0.005 ns as expected from the bulk distribution in the PU contributions in Figure 4.32. When compared to the 0 PU distributions, there is a noticeable rise in mean times in the 300-600 GeV range, where the mean times range from -4 to -2 ps. This is consistent with the long tails in distributions in Figure 4.32, especially on the negative end of the time axis. PU hits are more likely to have negative times, given the showering is more likely to start before the HGCAL. An interesting point in 200 PU is that the mean object time is very well approximated and stable even in the presence of PU 2D clusters with late times as shown in Figure 4.15.

The distributions of the timing resolution of photon shower times from each weighting method are shown in Figure 4.35 for methods with and without a truncation.

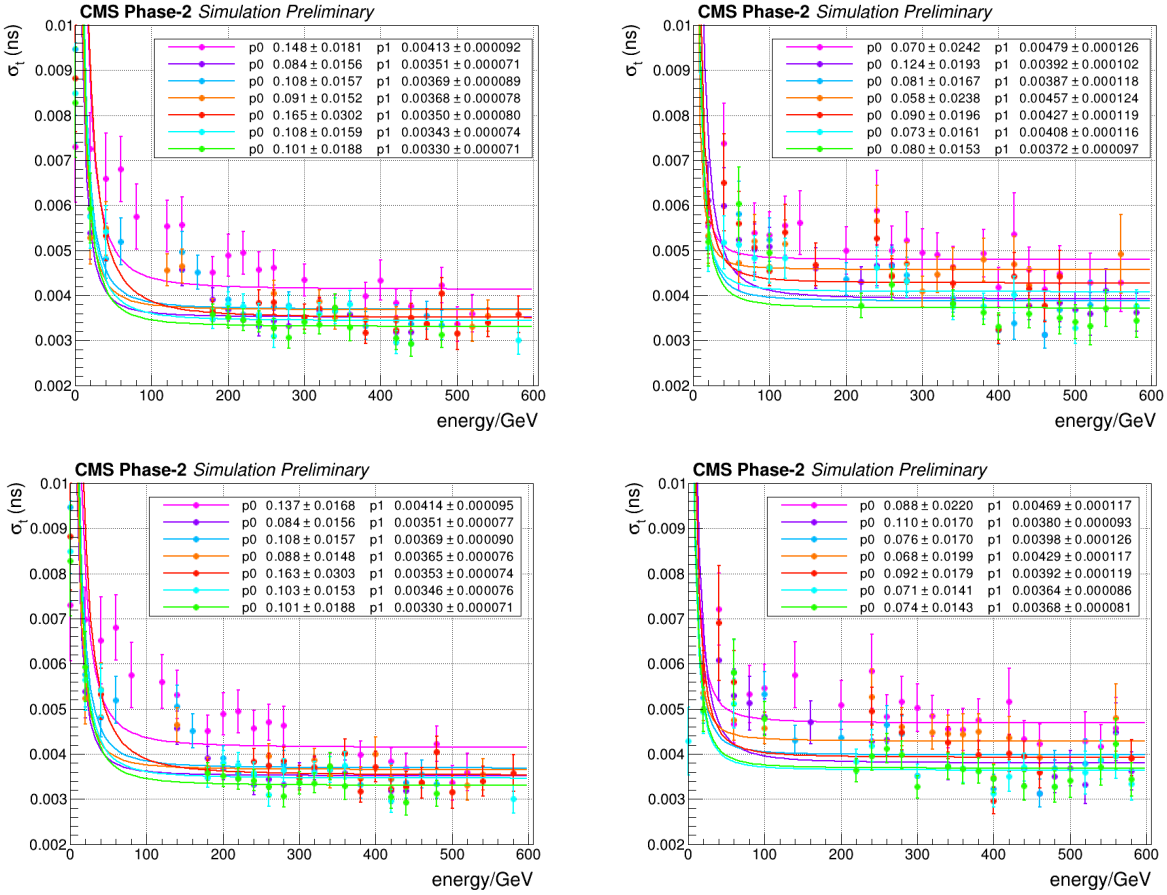

Figure 4.35: Distribution of the photon shower timimg resolution, where the shower time is computed from the time of 2D cluster times using methods that do not adopt (top) and that adopt (bottom) a truncation. Distributions are shown in 0 PU (left) and 200 PU (right). The variables $p0$ and $p1$ are the fitted values of A and the floor C respectively.

The generator-level rechit smearing function is used to fit the resolution distribution of the different methods vs energy. The photon shower resolutions do not follow the relationship as closely at energies below 200 GeV. The simple mean or truncation-only methods clearly give poorer resolutions compared to methods where a weighting procedure is used. In 0 PU, there is not much difference in the resolution distributions obtained from methods using

a truncation and methods not using one. This also shows that the truncation does not affect the resolution of the photon shower in 0 PU. The best resolution is obtained from the *truncation + weighted average* $(1/error^2)$ method. In 0 PU, the timing resolution of the photon showers is approximately 3-4 ps. When compared to the corresponding plots in 0 PU, there is a clear degradation in the achievable photon shower timing resolution for all methods in 200 PU. Generally, the degradation in resolution for non-truncation methods is by 2-9 ps with methods involving energy weightings, the *truncation + weighted average* $(1/error^2)$ method being the less affected in 200 PU. As described in Section 4.3.3, in 200 PU, the timing resolution on 2D clusters worsens, which would cause methods which use a resolution weighting to under-perform. The degradation in 200 PU (when compared to 0 PU timing resolution distributions) for methods that use a truncation is less pronounced and ranges from 1-6 ps. Again energy weighting and error weighting methods outperform methods using the resolution weighting because of the degradation in the timing resolution of 2D clusters in 200 PU. Thus considering performance in both 0 PU and 200 PU, the *truncation + weighted average* $(1/error^2)$ method remains the preferred method for approximating the time of photon showers. The distributions of the mean π^+ shower times from each weighting method are shown in Figure 4.36 for methods with and without a truncation

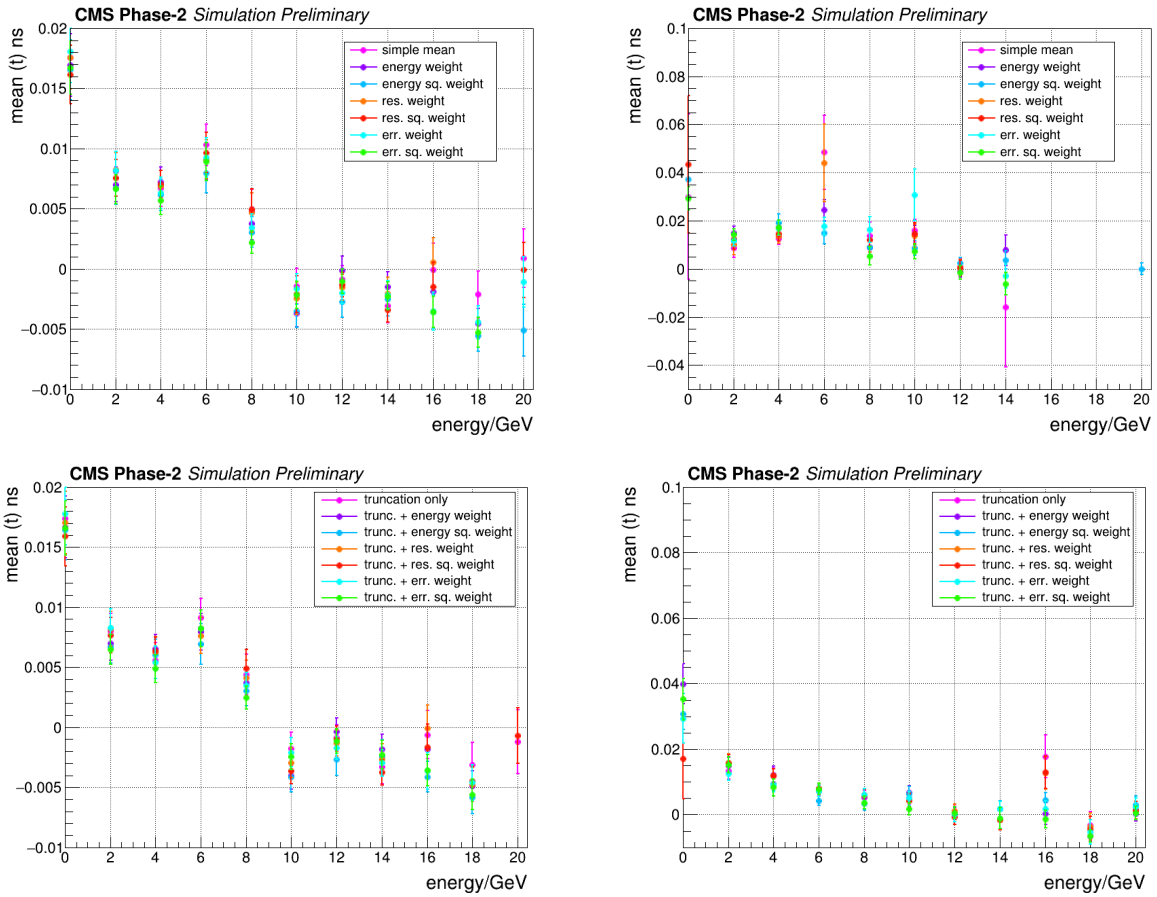

Figure 4.36: Distribution of the mean π^+ shower times, where the shower time is computed from the time of 2D cluster times using methods that do not adopt (top) and that adopt (bottom) a truncation. Distributions are shown in 0 PU (left) and 200 PU (right).

In 0 PU, as with photons, the truncation does not affect the central distribution and the mean time of π^+ showers is between -5 and 20 ps in this energy range. As expected, showers with higher energy deposits occur earlier. π^+ showers also have a mean time around 20 ps later than photon showers in 0 PU. In 200 PU, in the distributions for the non-truncation methods, the trend of the mean time versus energy is not clear. In the plot with the truncation methods, the trend versus energy is clearer and π^+ showers have a mean time between -10 ps and 40 ps in 200 PU. This is in line with the distributions shown in Figure 4.33. When compared to the 0 PU mean shower time distribution, it can be seen that even with the truncation, PU contributions have shifted the approximated time of the π^+ showers forward by approximately 20 ps. The different approximation methods give similar mean times for the π^+ shower. An interesting point in 200 PU is that the mean object time is very well approximated and stable even in the presence of PU 2D clusters with late times as shown in Figure 4.17.

The timing resolution of π^+ shower times from each weighting method are shown in Figure 4.37 for methods with and without a truncation.

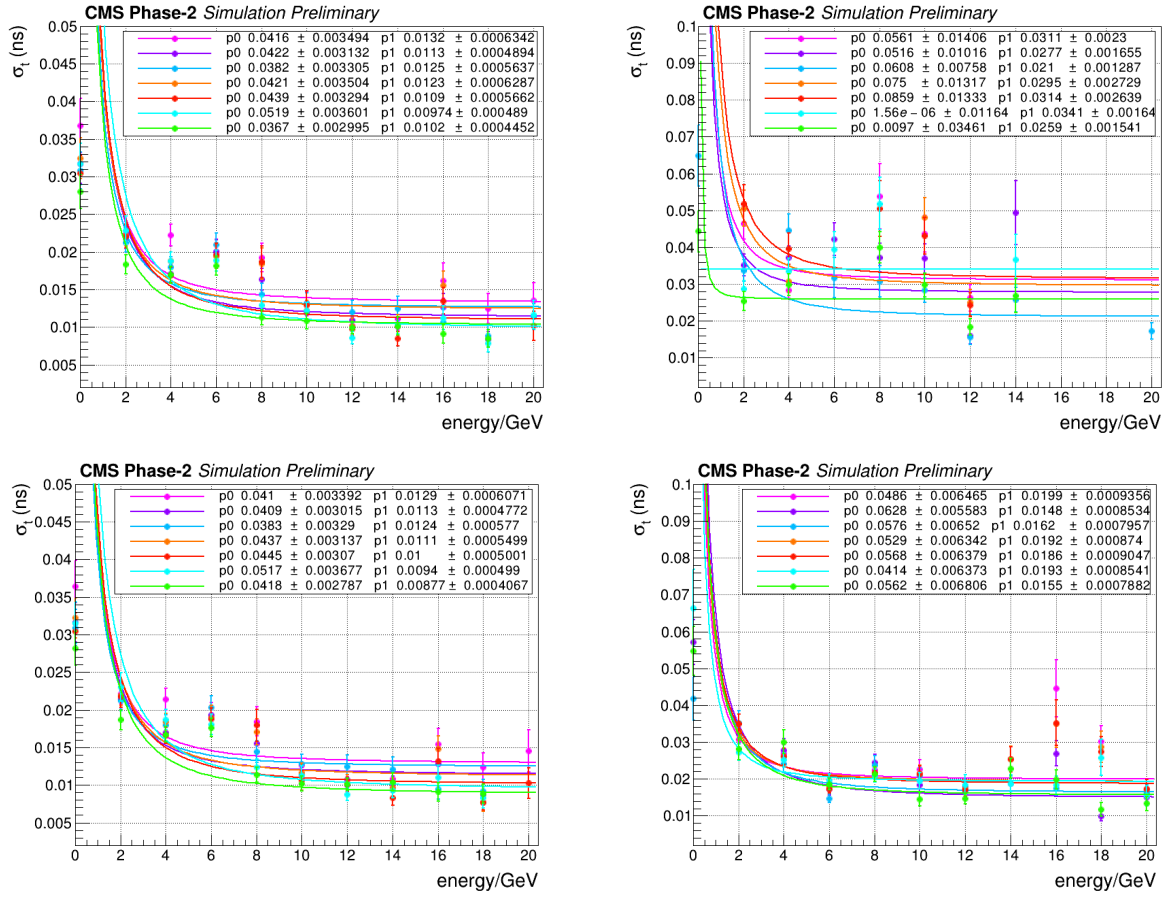

Figure 4.37: Distribution of the π^+ shower timimg resolution, where the shower time is computed from the time of 2D cluster times using methods that do not adopt (top plots) and that adopt (bottom plots) a truncation. Distributions are shown in 0 PU (left) and 200 PU (right). The variables $p0$ and $p1$ are the fitted values of A and the floor C respectively.

In 0 PU, it can be seen that all the shower time approximation methods give a π^+ shower

timing resolution between 9 and 15 ps above a shower energy of 6 GeV. As expected, the methods using a truncation give a better resolution and, as observed with photons, the best method for approximating π^+ shower times is the *truncation + weighted average* $(1/error^2)$ method. Compared to photon showers in 0 PU, the timing resolution of π^+ showers is up to 10 ps worse. As expected the timing resolution in 200 PU is better with truncation methods but only slightly (by about 1 ps). However, it is useful to note that in 200 PU, methods adopting a resolution weighting under-perform compared to methods adopting an energy weighting, due to the degradation in the timing resolution of 2D clusters in 200 PU.

4.3.5 Timing of TICL 3D clusters

The timing of the EM and HAD 3D clusters from the TICL reconstruction framework is studied. In this section, the 0 PU samples have a p_T point of 10 GeV. The p_T range in 200PU is 8-150 GeV for photons and 0.7-10 GeV for π^+ particles. Thus the 0 PU and 200 PU samples are not directly comparable. Because of the better results obtained with methods using a truncation in the previous section, only truncation methods are investigated in approximating the time of TICL 3D clusters.

The distributions of the EM photon and HAD π^+ 3D cluster times from each weighting method are overlaid and shown in Figure 4.38.

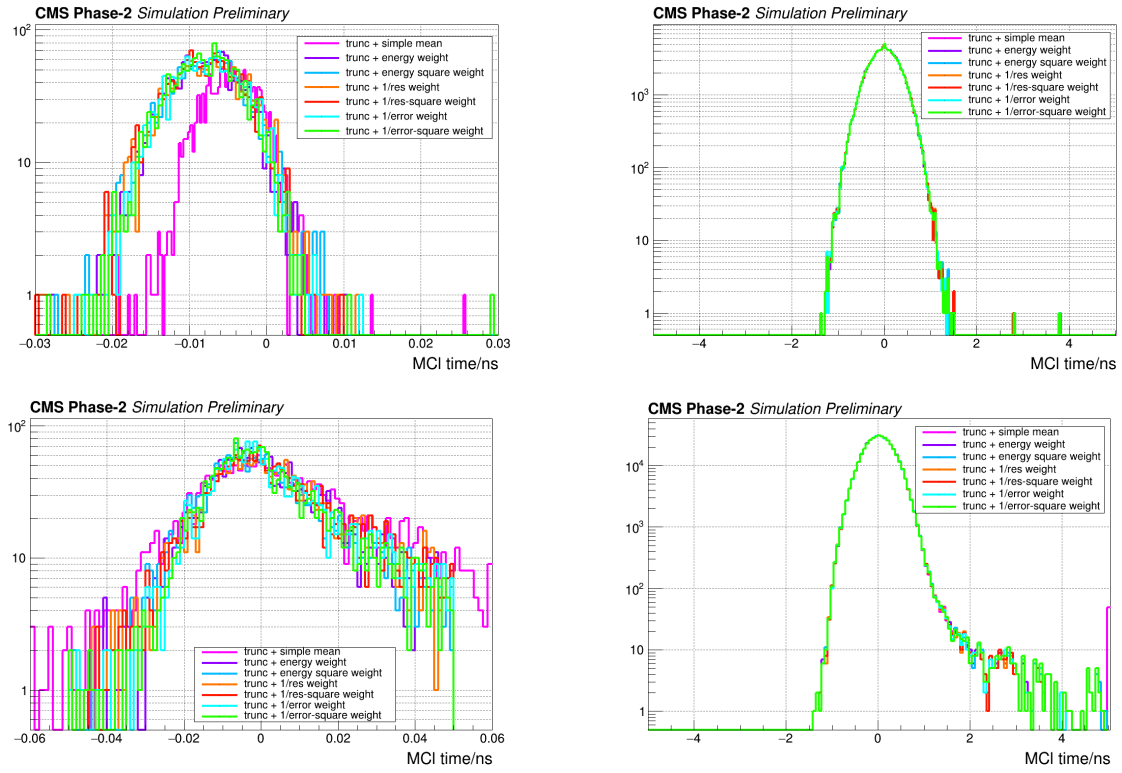

Figure 4.38: Distribution of the photon EM (top) and π^+ HAD (bottom) 3D cluster times computed from 2D cluster times using methods that adopt a truncation. Distributions are shown in 0 PU (left) and 200 PU (right).

In 0 PU, photon EM 3D clusters have a bulk time distribution between −20 and 20 ps (note that the time is slightly shifted because of early showering described in Section 4.3.3).

Very slight tails extend to −30 and 30 ps. It is clear that a truncation only results in a less central and sub-optimal distribution. Amongst the remaining methods, it is unclear which give the better performance by looking at the time distributions alone. In 200 PU, the time of EM 3D clusters lies between −1.5 and 1.5 ns with a very slight contribution above 2 ns.

Compared to photons, the spread in time for π^+ 3D clusters in 0 PU is much wider and the bulk distribution in 0 PU is between −60 and 60 ps (twice the range found for photon 3D clusters in 0 PU). This further supports the claim of slower shower propagation for π^+ particles. For π^+ HAD 3D cluster times, there is a clear positive tail extending beyond 40 ps for most methods. This represents the slow hadronic component in π^+ showers. As with photons, it is clear that using a truncation only, without any weighting, gives long tails in the distribution of the time of π^+ 3D clusters. In 200 PU, the π^+ 3D cluster distributions are very similar to the photon 200 PU distributions. These distributions can thus be assumed to be entirely dominated by PU contributions.

The distributions of the photon EM 3D cluster mean times and timing resolutions from each weighting method are shown in Figure 4.39.

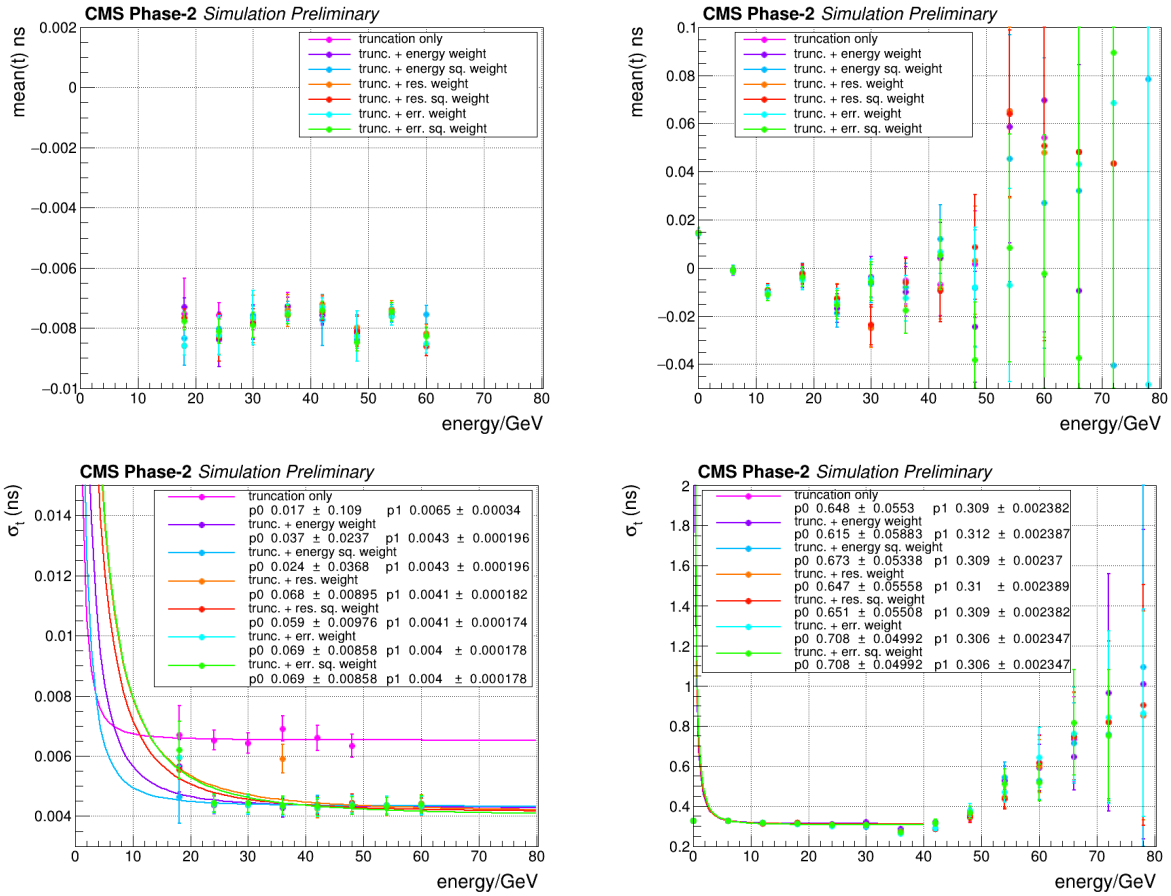

Figure 4.39: Distribution of the photon EM 3D cluster mean times (top) and timing resolutions (bottom), with 3D cluster times computed from 2D cluster times using methods that adopt a truncation. Distributions are shown as a function of the 3D cluster energy in 0 PU (left) and 200 PU (right). The variables $p0$ and $p1$ are the fitted values of A and the floor C respectively.

In 0 PU, all methods give very close results for the mean time and resolutions of photon EM 3D clusters. The mean time of photon 3D clusters is between −10 and −6 ps. The timing

resolution floor for photon 3D clusters is around 4-5 ps. This is a significant improvement compared to the timing resolution of 2D clusters. EM 3D clusters have better timing resolution at energies above 30 GeV than below. This shows that most of the EM 3D clusters have energies in the 30-60 GeV range. Although all weighting methods give similar 3D cluster resolutions, it is clear than a truncation-only method gives a resolution that is consistently worse than all the other methods by ~ 3 ps in 0 PU. In 200 PU the mean time of EM 3D clusters below 40 GeV is between -40 and 20 ps. Beyond 40 GeV, there are fewer EM 3D clusters (large error bars) and the spread in mean time is larger. This is reflected in the plot of the timing resolution of EM 3D clusters in 200 PU, where the resolution below 40 GeV is about 300 ps. Beyond 40 GeV, there are fewer contributions and the resolution degrades. Although all methods for finding the time of the 3D cluster give very similar results, the *truncation + weighted average* $(1/error^2)$ method marginally outperforms other methods by about 5 ps in the EM 3D cluster timing resolution. The resolution of photon EM 3D clusters degrades by up to 300 ps in 200 PU when compared to 0 PU.

The distributions of the mean π^+ HAD 3D cluster times and the corresponding timing resolutions from each weighting method are shown in Figure 4.40.

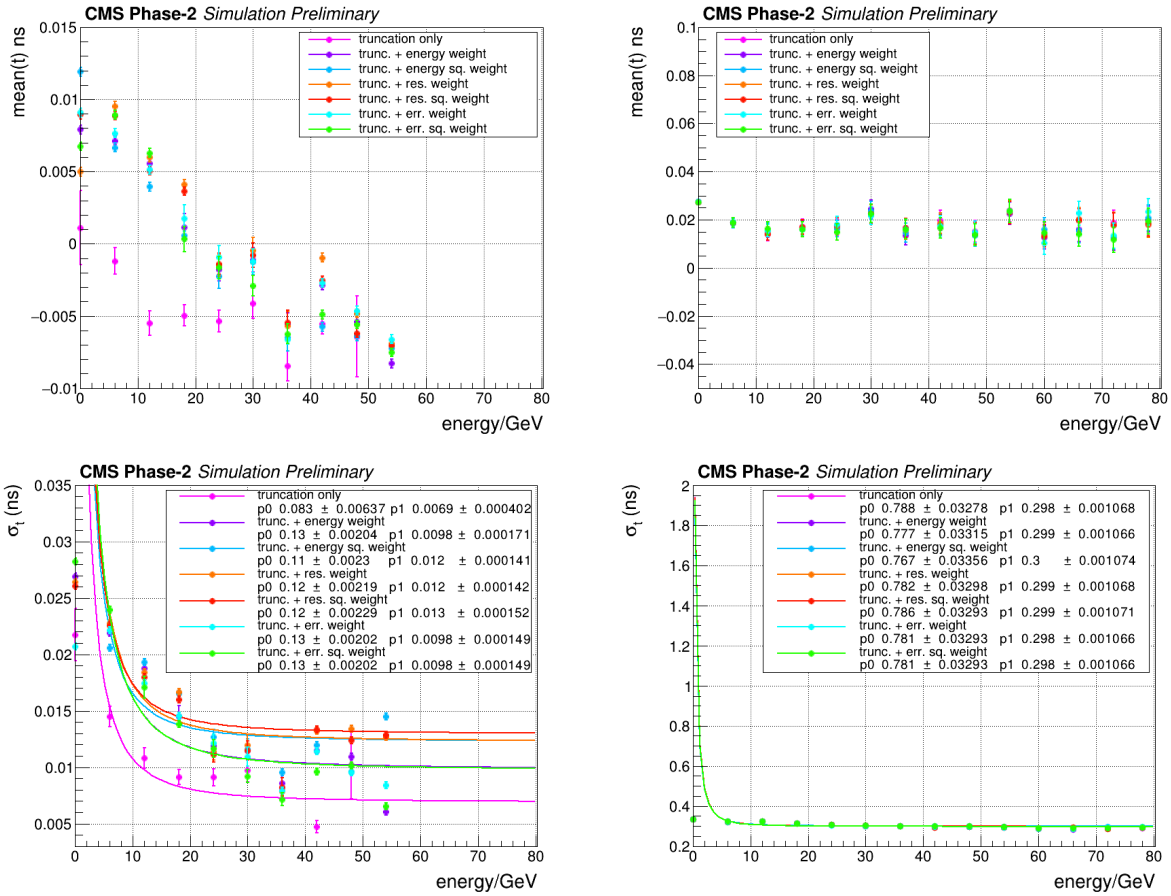

Figure 4.40: Distribution of the π^+ HAD 3D cluster mean times (top) and timing resolutions (bottom), with 3D cluster times computed from 2D cluster times using methods that adopt a truncation. Distributions are shown as a function of the 3D cluster energy in 0 PU (left) and 200 PU (right). The variables $p0$ and $p1$ are the fitted values of A and the floor C respectively.

In 0 PU, the spread in the mean time of π^+ EM 3D clusters is between -10 and 2 ps, with lower energy deposits occurring later in time. In 0 PU, the spread in the mean time of π^+ HAD 3D clusters ranges from -10 ps to 12 ps. In the plot for the mean time of π^+ HAD 3D clusters in particlular, it can be seen that the truncation method gives a very different distribution to all remaining methods; for reasons described previously, this method is likely sub-optimal. It is clear that the *truncation + weighted average* ($1/error^2$) method gives the best timing resolutions. This is particularly visible in the π^+ HAD 3D cluster resolution plot, where the difference in performance of the different 3D cluster time approximation methods is more visible. The timing resolution floor from the *truncation + weighted average* ($1/error^2$) method is around 10 ps. In 200 PU, the π^+ HAD 3D clusters show an approximate 20 ps offset in the mean time. This further confirms the non-negligible time of propagation of π^+ showers. The performance is more stable than with photon 3D clusters; this may be due to the looser selection criteria for HAD 3D clusters, resulting in more statistics for fitting the mean time and timing resolution.

4.4 Use of timing in the HGCAL reconstruction

This section explores two preliminary examples of the possible use of timing information in the reconstruction. The aim is to give a brief idea of the possible improvements achievable through the use of timing, and to provide a starting point for more detailed future studies.

4.4.1 Use of the time of a shower

In this section, 2D clusters which are not assigned a time measurement are not studied. A possible cut on the 2D cluster time using the full time of the shower (Section 4.3.4) is studied. The motivation is to be able remove 2D clusters that are not in time with the full shower. We would expect this cut to remove PU 2D clusters but keep the distributions similar in 0 PU. For this section, the *truncation + weighted average* ($1/error^2$) method is used. A cut of 90 (120) ps is chosen as a fairly loose cut for photon (π^+) 2D clusters. These cuts represent three times the timing resolution of the corresponding 2D clusters as obtained in Section 4.3.3. For this section, the same samples used in Section 4.3.4 are studied.

The total energy contained in the 2D clusters before and after the cut is shown in Figure 4.41 for photon and (π^+) showers. In 0 PU, for most photon showers, at least 99% of the energy is contained in 2D clusters that pass the cut. For π^+ showers in 0 PU, the fraction of energy after the cut is mostly above 80%. This shows that the cut on the shower time does not remove energetic clusters in 0 PU (as required). For photon showers in 200 PU, there is now a clear contribution in the 95% to 99% region. Although the 2D clusters have not been matched to generator-level simulated clusters, it is clear that this contribution is from PU since it was not present in the 0 PU plot. This shows that, in 200 PU, the cut on the 2D cluster time can help to remove up to 5% of the reconstructed shower energy which is likely to be from PU. For π^+ showers in 200 PU it can be deduced that contributions to the distribution below 60% are from PU (when compared to the 0 PU distributions). Thus for example, a contribution at 40% in 200 PU in Figure 4.41 is likely to mean that the cut has removed 60% of the energy reconstructed in the pion shower but that was very likely to be PU energy.

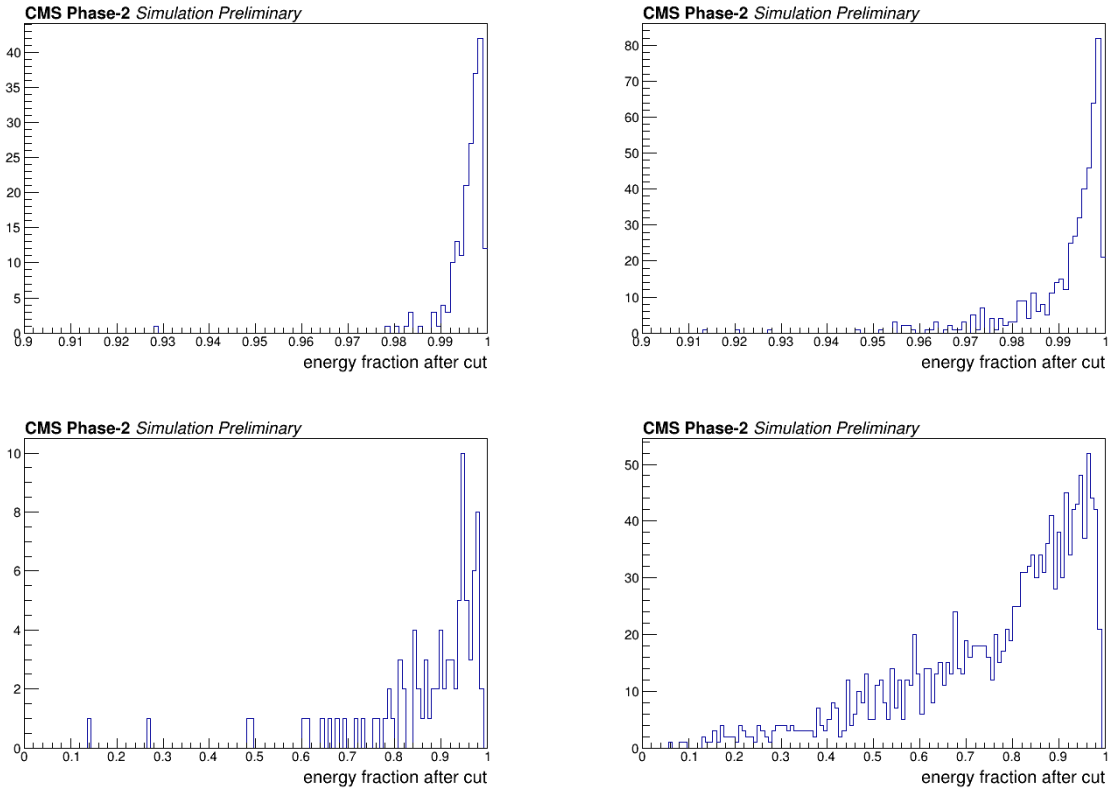

Figure 4.41: Distribution of the fraction of energy remaining in photon (left) and π^+ (right) showers after a 90 ps cut is applied on the time of the 2D clusters in the shower. Distributions are shown for 0 PU (left) and 200 PU (right).

The effect of the cut may be further explored by looking at the spatial distribution of the 2D clusters in $\eta - \phi$ space for a single event in 200 PU. This spatial distribution is shown in Figure 4.42 for a single photon event with and without the cut on the 2D cluster time. The position of the main event is marked in grey lines denoting the generator-level η and ϕ values for the event, extrapolated along the track direction. After the cut, a significant number of PU 2D clusters are cleared from the use of timing information alone. Although this plot is for a single shower, it can be deduced that the cut will have the potential to remove several PU showers when several events are overlaid. This may help significantly in missing E_T reconstruction, where topographical cuts are not that useful. Focussing on a 2 cm region around the shower axis for the same event (Figure 4.42), it can be seen that 2D clusters in the 2 cm selection region (and likely to be from the main event) remain unaffected by the cut. This also shows that the 2 cm spatial selection is already a robust selection for the photon shower in this case and the timing cut does not help to clean PU clusters within the 2 cm. However, it should be noted that pile-up increases with η and at higher η values, it is possible that the timing cut may help to remove 2D clusters within the 2 cm cylindrical selection region. A possible future development would be to study the efficiency of the cut as a function of the shower η.

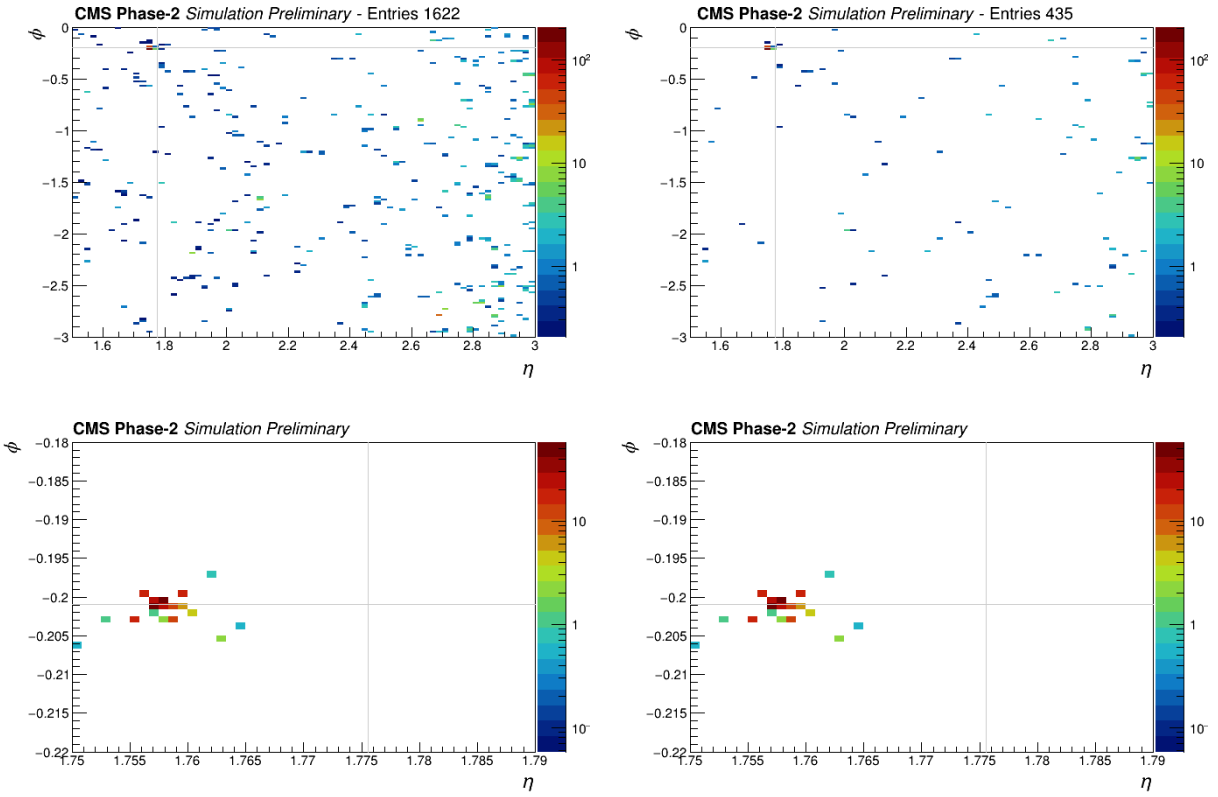

Figure 4.42: Distributions of 2D clusters (top) in $\eta-\phi$ space for a single photon event in 200 PU. For the same event, the region within 2cm of the shower axis in $\eta-\phi$ is also shown (bottom). All 2D clusters are included in the plots on the left while in the plots on the right, only 2D clusters within 90 ps of the calculated photon shower time are included. The grey lines represent the generator-level η and ϕ values for the event, extrapolated along the track direction.

A similar spatial distribution is shown in Figure 4.43 for a single π^+ event in 200 PU with and without the respective cut on the 2D cluster time. Here, a cut on the π^+ 2D cluster time removes 2D clusters. This is because, as seen in Section 4.3.3, PU 2D clusters in the energy range being used for π^+ are likely to have times away from the central π^+ shower time.

Focussing on a 5 cm region around the shower axis, it can be seen that the cut does remove 2D clusters in the 5 cm selection region and, although these 2D clusters have not been matched to generator-level simulated clusters, it is likely the 2D clusters removed are PU 2D clusters because the 120 ps cut for π^+ 2D clusters is very loose given the distributions in 2D cluster mean times observed in Section 4.3.3. Thus, in the case of π^+ 2D clusters, the timing information provides stronger discrimination against PU 2D clusters than the spatial selections for the particle energy range considered.

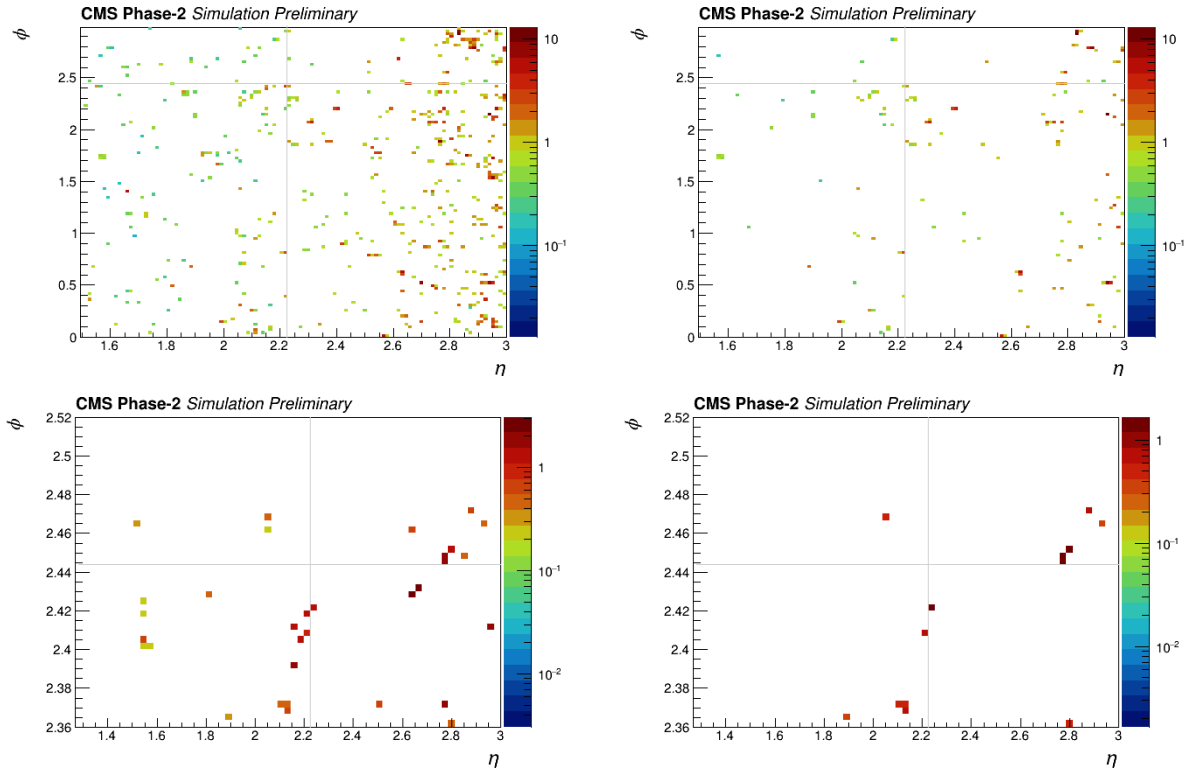

Figure 4.43: Distributions of 2D clusters (top) in $\eta-\phi$ space for a single π^+ event in 200 PU. For the same event, the region within 2cm of the shower axis in $\eta-\phi$ is also shown (bottom). All 2D clusters are included in the plots on the left while in the plots on the right, only 2D clusters within 120 ps of the photon shower time are included. The grey lines represent the generator-level η and ϕ values for the event, extrapolated along the track direction.

4.4.2 Use of precision timing in TICL doublet reconstruction

The study of the time of 2D clusters as a function of the layer and energy (Section 4.3.3), provides information about the time of propagation of the shower. This can be used as an additional tool in 2D cluster pattern recognition when linking 2D clusters along the depth of the HGCAL to form 3D clusters. For this purpose, the time compatibility between a 2D cluster already 'clustered' and another 2D cluster candidate along the particle path can be used. As mentioned in Section 4.3, 2D clusters are linked along the depth of the HGCAL to produce 3D clusters in the HGCAL iterative clustering framework (TICL). The full object (3D cluster or trackster) is built by linking individual 2D clusters, first into doublets, then into the full object. Presently, the compatibility criteria between the two 2D clusters forming a doublet is purely topographical. By requiring that the times of 2D clusters within a doublet agree within $3\,\sigma_t$, for instance, where σ_t is the time resolution of 2D clusters, PU 2D clusters can be rejected in the trackster-building process. The time of the full shower (full trackster) could also be used to clean the trackster object of PU 2D clusters. In this section, the difference in the time between 2D clusters (dT) in TICL doublets is studied in terms of σ_t and a $3\,\sigma_t$ cut on dT is explored. More precisely, dT is calculated by subtracting the time of the 2D cluster with the earlier time from the time of the 2D cluster with the later time in the doublet. For the studies in this section, both of the 2D clusters forming a doublet are rejected if they do not pass the $3\,\sigma_t$ cut. In the future, it is expected that topographical

information could be used together with timing in the 2D cluster linking process so that only the suspected PU 2D cluster is removed from the doublet. Thus in what follows, the term PU is being used to refer to a doublet where *one* of the 2D clusters is from PU, but where the whole doublet is rejected only for the purpose of this study. In this section, the 0 PU samples have a p_T point of 10 GeV. The p_T range in 200PU is 8-150 GeV for photons and 0.7-10 GeV for π^+ particles.

The distribution of dT (in units of σ_t) in 0 PU and 200 PU for photon EM 2D clusters and π^+ HAD 2D clusters is shown in Figure 4.44.

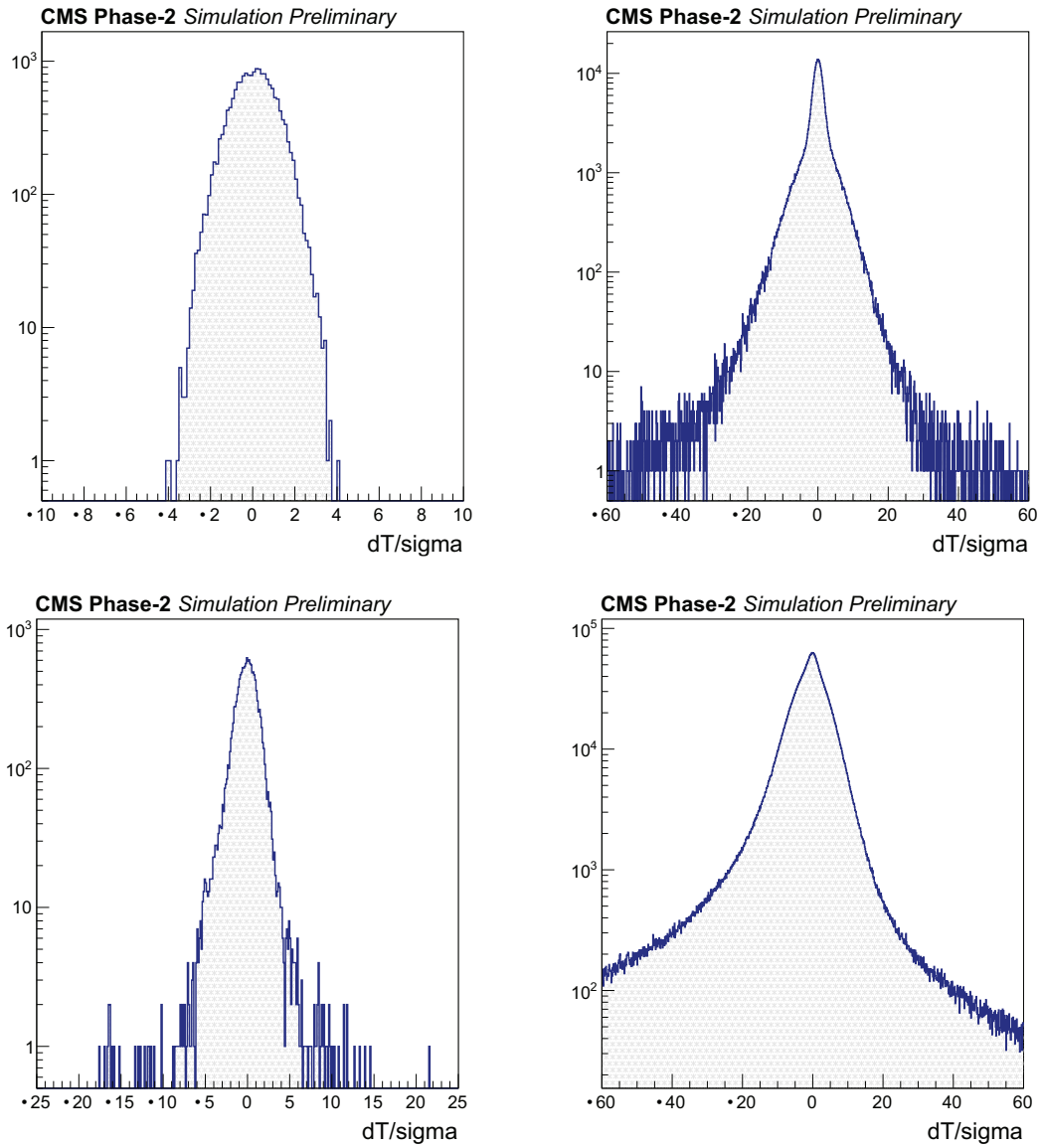

Figure 4.44: The distribution of the difference (dT) in the time between photon EM 2D clusters (top) and π^+ HAD 2D clusters (bottom) in TICL doublets in 0 PU (left) and 200 PU (right). The variable dT is measured in units of σ_t.

For photon 2D cluster doublets in 0 PU, the EM 2D cluster doublet members may be found up to $4\,\sigma_t$ away in time, although the bulk of the distribution lies between -3 and $3\,\sigma_t$. In 200 PU, there are long tails in the distributions for dT, showing that 2D clusters from PU, as expected, are not compatible in time. The bulk distribution for photon EM

2D cluster doublets in 200 PU lies between -20 and $20\,\sigma_t$. This suggests that a dT cut at $3\,\sigma_t$ (for example) will reduce PU contributions significantly. For π^+ 2D cluster doublets in 0 PU, the bulk distribution is found between -5 and $5\,\sigma_t$, with tails extending up to $20\,\sigma_t$. Compared to photons, the spread in dT is wider and this suggests that π^+ 2D cluster doublets might benefit from a looser dT cut. As with photons, the dT distributions for π^+ 2D cluster doublets in 200 PU have long tails.

The fractions of photon EM 2D clusters and π^+ 2D clusters that pass the dT cut as a function of the dT cut in 0 PU and 200 PU are shown in Figure 4.45.

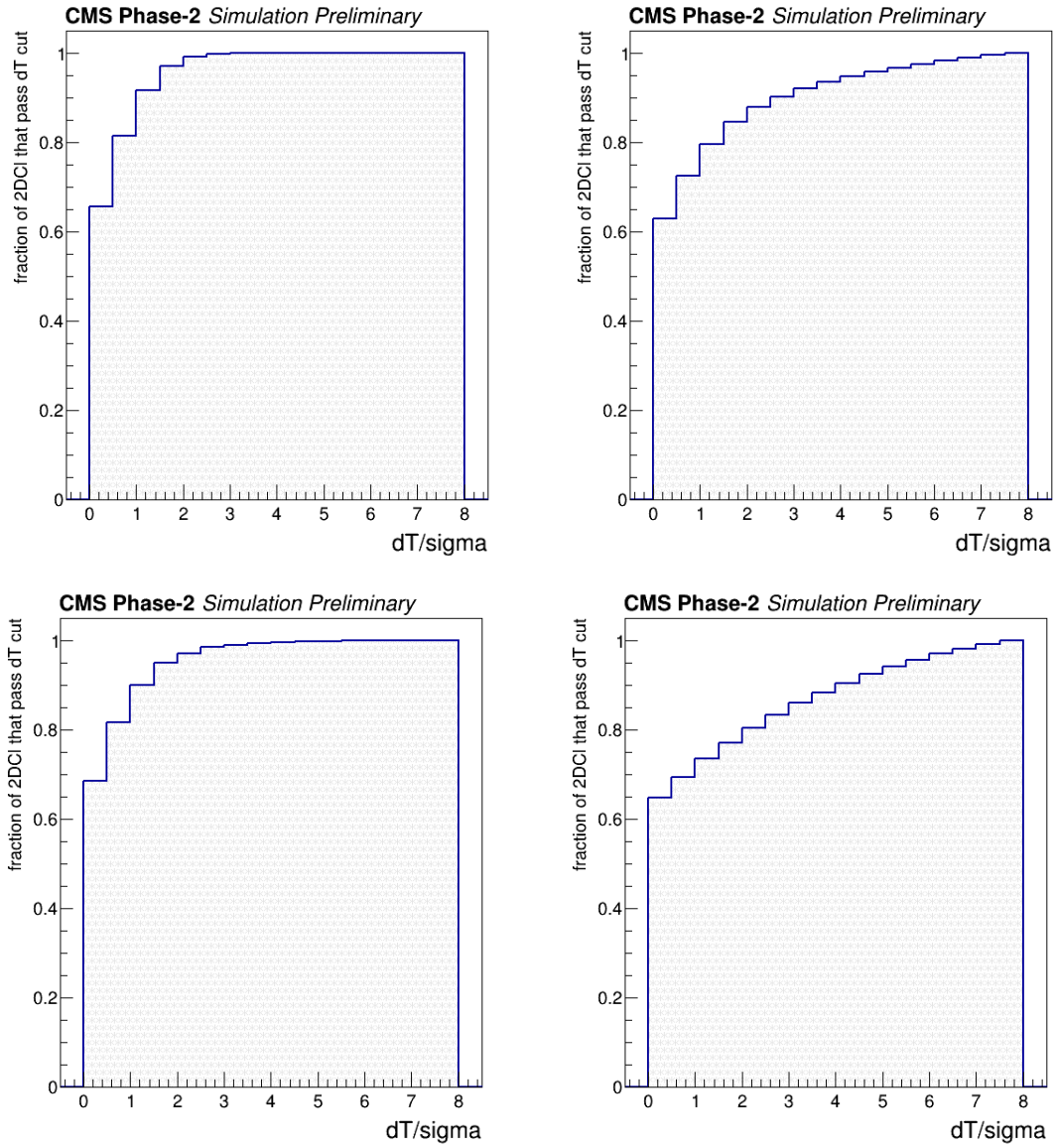

Figure 4.45: The fraction of photon EM 2D clusters (top) and π^+ HAD 2D clusters (bottom) that pass the dT cut as a function of the dT cut in 0 PU (left) and 200 PU (right).

In 0 PU, almost 100% of the 2D cluster doublets occur less than 3 σ_t apart in time. In 200 PU, these plots have a very different interpretation than in 0 PU. Within $3\,\sigma_t$, we find (90%) of all EM 2D clusters (including PU). Thus placing a cut at $3\,\sigma_t$, will allow to remove 10% of all 2D clusters in 200 PU. When comparing the 200 PU distribution to the 0 PU plot,

this 10% contribution is likely to come from PU anyway, although the caveat of the 0 PU and 200 PU samples having different p_T should be borne in mind. The $3\,\sigma_t$ cut in this section only serves as an example cut. Further dT cut optimisation and generator-level matching of 2D clusters in 200 PU could provide more optimal results. In 0 PU, almost 100% of pion 2D clusters pass the $3\,\sigma_t$ cut. In 200PU, 80% of the π^+ HAD 2D clusters pass the dT cut. This includes PU 2D clusters. The 20% contribution removed is likely to be from PU 2D clusters, although the caveat of the 0 PU and 200 PU samples having different p_T should be borne in mind.

The fraction of energy (of the total energy in the respective 2D clusters with a time measurement) contained in photon EM 2D clusters that pass the dT cut as a function of the dT cut in 0 PU and 200 PU is shown in Figure 4.46. In 0 PU, almost 100% of the total shower energy is contained in 2D cluster doublets compatible within $3\,\sigma_t$ in time. This shows that photon 2D doublets compatible in time also contain the most energetic deposits. As such, it makes sense to place a cut at $3\,\sigma_t$ and this can help to remove PU 2D clusters in 200 PU. In 200 PU, similar fractions to those in Figure 4.45 (the fraction of 2D clusters) are obtained with the energy fraction of 2D clusters. This suggests that the energy distribution in PU is relatively uniform across the 2D clusters.

The fraction of energy (of the total energy in the respective 2D clusters with a time measurement) contained in π^+ HAD 2D clusters that pass the dT cut as a function of the dT cut in 0 PU and 200 PU is also shown in Figure 4.46. As with photons, in 0 PU, almost 100% of the total shower energy is contained in π^+ 2D cluster doublets compatible within $3\,\sigma_t$ in time. Therefore, despite the tails in the dT distributions for π^+ 2D clusters (Figure 4.44), a $3\,\sigma_t$ cut is still reasonable since most energy is contained in π^+ 2D clusters that pass the $3\,\sigma_t$ cut. In 200 PU 80% of the total energy (including PU energy) is retained in HAD 2D clusters that pass the $3\,\sigma_t$ cut, the 20% of energy removed is likely to be from a uniform PU contribution.

The distribution of the energy contained in photon EM 2D clusters with a time measurement as a fraction of the total 3D cluster energy is shown in Figures 4.47. In 0 PU this represents the base energy-finding efficiency using 2D clusters with a time measurement. In 0 PU most energy (above 80%) for photon EM 3D clusters is contained in 2D clusters with a time measurement. This suggests that a cut on dT could be very powerful to reject PU as this criterium would be applied to 80% of the 2D clusters. In 0 PU, as expected, the $3\,\sigma_t$ cut does not affect the distributions significantly as most (almost 100%) photon 2D clusters pass the cut as seen in Figure 4.45.

The distribution of the energy contained in π^+ HAD 2D clusters with a time measurement as a fraction of the total 3D cluster energy is also shown in Figure 4.47. In 0 PU the spectrum is broader than with photons, especially for the π^+ HAD 2D clusters. This shows that the dT cut for π^+ 2D clusters will not be as powerful as with photons since not many π^+ 2D clusters have timing information and there is a non-negligible amount of energy in π^+ 2D clusters that are not assigned a time measurement. This is because the π^+ 2D clusters are lower in energy (compared to photons) and are less likely to be assigned a time as shown by the efficiency plots in Section 4.3.3. In 0 PU, the dT cut does not change this distribution significantly.

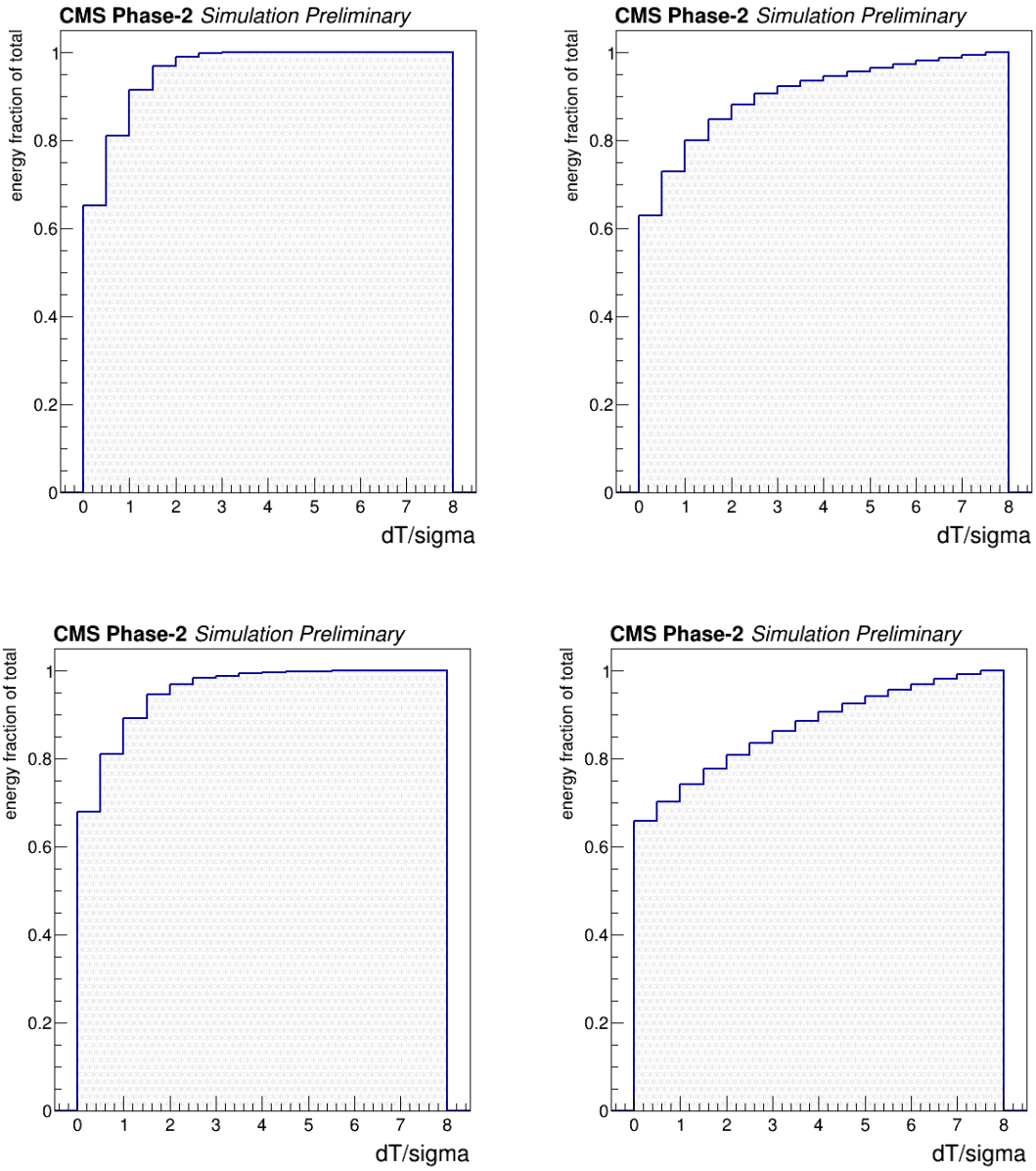

Figure 4.46: The fraction of energy (of the total energy in the 2D clusters with a time measurement) contained in 2D clusters that pass the dT cut as a function of the dT cut in 0 PU (left) and 200 PU (right). Plots are shown for photon EM 2D clusters (top) and π^+ HAD 2D clusters (bottom).

The effect of the dT cut may be observed spatially in η and ϕ by comparing the generator-level η and ϕ (extrapolated in the track direction) for the events with the reconstructed η and ϕ of the 2D clusters. On these plots, off-diagonal contributions are likely to be from PU 2D clusters. If the dT cut is able to remove 2D clusters on the diagonal as well, this implies that the dT cut is likely to be a more powerful criterion for selecting 2D clusters than topographical cuts.

For illustration, two-dimensional histograms of photon EM 2D cluster η versus the generator-level η of the respective events in 200 PU before and after the $3\,\sigma_t$ cut are shown in Figure 4.48. It can be seen that after the $3\,\sigma_t$ cut, the off-diagonal contributions are reduced. Two-dimensional histograms of the photon EM 2D cluster ϕ versus the generator-level ϕ of

the respective events in 200 PU before and after the $3\,\sigma_t$ cut are also shown in Figure 4.48. In ϕ, the effect of the dT cut is even more visible than in η and off-diagonal contributions are greatly reduced. The dT cut also visibly removes 2D clusters on the diagonal (PU 2D clusters very close to the main event) and this shows that the dT cut can be more effective than spatial topographical cuts in η and ϕ.

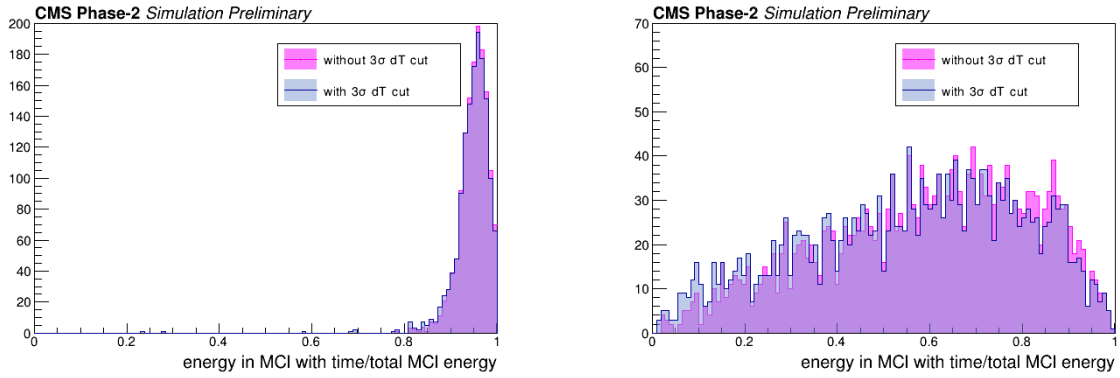

Figure 4.47: The distribution of the energy contained in 2D clusters with a time measurement as a fraction of the total 3D cluster (multicluster or MCl) energy in 0 PU. Plots are shown for photon EM 2D clusters (top) and π^+ HAD 2D clusters (bottom).

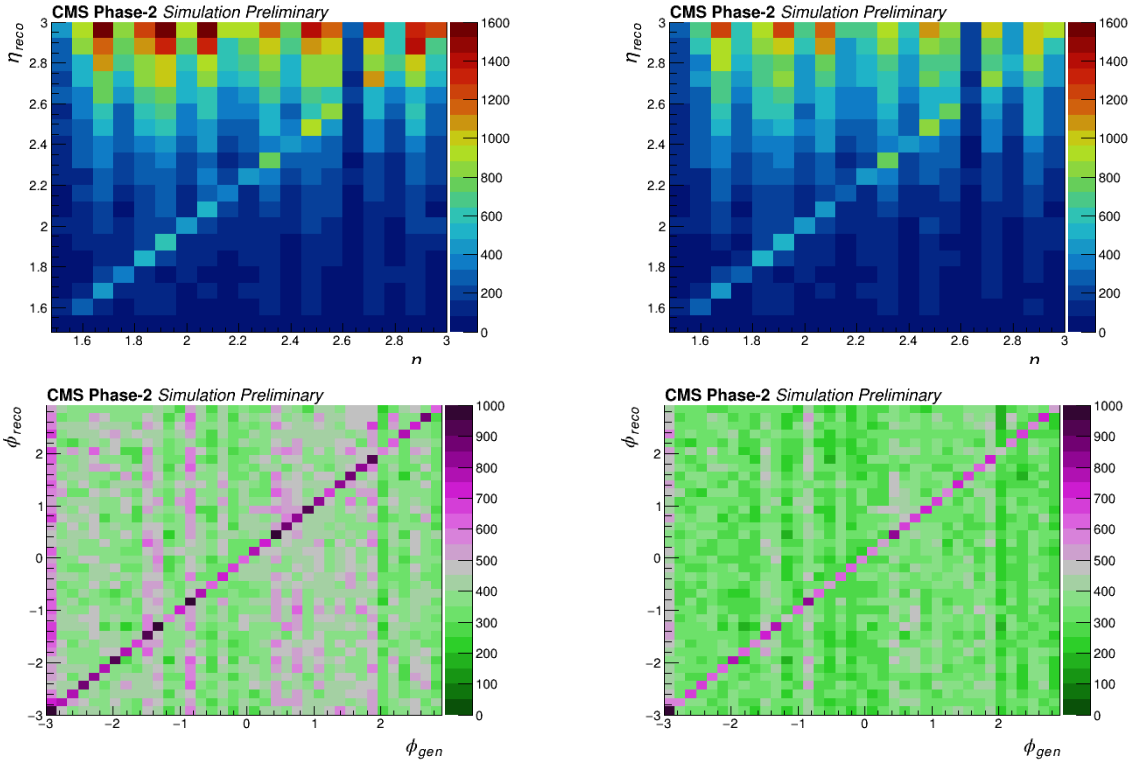

Figure 4.48: Two-dimensional histograms of the photon EM 2D cluster η (top) and ϕ (bottom) versus the generator-level η and ϕ. Events in 200 PU before (left) and after the $3\,\sigma_t$ cut (right) are shown.

4.5 Summary

The applications of precision timing, from silicon sensors in the HGCAL reconstruction chain, was studied using the latest version of the HGCAL geometry. In particular, the mean times and the timing resolution of rechits, 2D clusters, 3D clusters and full showers were analysed. The nature of the showers was used in the interpretation of the timing performance results. Notably, photon showers deposit more energy in the CE-E section while π^+ showers exhibit a main peak in the FH and BH sections with a smaller peak in the CE-E section arising from many hits with low energy. Photon showers are better contained laterally from the shower axis and along the HGCAL depth than π^+ showers. Two different selections were studied and compared, namely a simple rechit or 2D cluster selection within a cylinder around the shower axis, and TICL, the more elaborate HGCAL reconstruction framework. With TICL it is possible to apply different selections while reconstructing electromagnetic and hadronic showers.

Rechit timing was studied both as a function of the distance of the rechit from the shower axis and as a function of the rechit energy. Rechits further from the shower axis were found to have higher recorded times. Overall, mean rechit times showed that π^+ showers take more time to propagate both laterally from the shower axis and along the shower axis. Possible future timing developments could benefit from correcting for the time of propagation of showers laterally, especially for π^+ particles. Similarly, the measured time of propagation of the showers could be used in the reconstruction. Generally, the photon rechit timing performance was better than for π^+ rechits. The rechit timing resolutions follow the smearings applied at generator-level to within 5 ps. The TICL reconstruction was found to improve the π^+ rechit timing resolution by up to 30 ps and reduce the spread in mean time of π^+ rechits.

The 2D cluster timing performance was studied both as a function of the HGCAL layer and as a function of the 2D cluster energy. The aim of this study was to properly approximate the time of 2D clusters so as to be able to further propagate the 2D cluster timing in the reconstruction chain. This includes the possible use of 2D cluster timing in cluster pattern recognition. Simply computing the time of 2D clusters from a mean of rechit times contained in the cluster was found to be sub-optimal. Several methods were used to approximate the time of a 2D cluster from the time of its rechits. Of the methods studied, the best method for both photon and π^+ 2D clusters was to apply a truncation to the distribution of the rechit times before computing a weighted average, where the weight is the inverse-squared resolution of the individual rechits. This method gave the most optimal timing resolutions and the most consistent trends in the mean time of photon and π^+ 2D clusters. This weighting method has now been implemented in the HGCAL reconstruction chain. The 2D cluster timing efficiency at 2 (5) cm from the shower axis was found to be 100 (20)% for photon (π^+) 2D clusters. Thus future developments should aim to improve this efficiency, especially for pions. The use of TICL was found to improve 2D cluster timing resolutions by up to 5 ps compared to a cylindrical selection. In 200PU, there is a non-negligible PU contribution in the first layers of the HGCAL. PU 2D clusters were found to have low energies (< 2 GeV) and mean times of 50-200 ps.

It was investigated whether timing information is useful in assessing the compatibility between TICL 2D cluster doublets. A cut was placed on the allowable difference in time (dT) between 2D clusters forming a doublet. Photon (π^+) 2D clusters in 0 PU were found to be

up to 4 (20) σ_t away in time. Some photon and π^+ 2D cluster doublets in 200 PU were found to be over 60 σ_t away in time. In 0 PU, almost 100% of the 2D clusters were found to pass a 3 σ_t cut on dT and almost 100% of the shower energy was found to be contained in these 2D clusters passing the cut. In 200 PU, this cut was able to remove up to 20% of 2D clusters (believed to be from PU). This cut was also found to remove PU 2D clusters very close to the main events, providing a stronger selection than topographical cuts for selecting the 2D clusters. This cut is now implemented in the HGCAL reconstruction for EM 2D clusters. Possible future developments should consider the use of this cut for HAD 2D clusters as well. It is expected that further optimisation of the dT cut values and generator-level matching of 2D clusters to simulated clusters will yield better results for this study.

The time of a full shower was approximated from the time of 2D clusters using several methods. Of the methods studied, the best method was to truncate the distribution of 2D cluster times before computing a weighted average, where the weight is the inverse-squared error of the 2D clusters. This method gave the best timing resolutions and the most consistent trends in the mean time of the full shower. This method was also the most robust against PU. In 200 PU, the photon (π^+) shower time distributions have long positive tails. PU contributions occur up to 4 ns away from the mean time of the shower and shift the approximated shower time by up to 20 ps. The time of the reconstructed 2D clusters and of full showers are used to clean events of 2D clusters that are not compatible with the full shower time. At least 90 (80)% of the shower energy is contained in photon (π^+) 2D clusters that pass the tested cut. For π^+ showers, this timing cut is potentially more robust that topographical cuts for selecting the 2D clusters for a shower. The timing of TICL 3D clusters was studied and, as with the full shower timing, the best method to find the 3D cluster time was to truncate the distribution of 2D cluster times before computing a weighted average, where the weight is the inverse-squared error of the 2D clusters.

Chapter 5

Higgs boson measurements in the diphoton decay channel

5.1 Introduction

This chapter focuses on event categorisation in the $H \to \gamma\gamma$ channel using the STXS framework presented in Section 2.3.1. As stated previously, the STXS framework represents an improved method of conducting Higgs boson cross-section, signal-strength and coupling measurements whereby theoretical model and uncertainty dependence is reduced, and theoretical interpretations are made easier. Granular measurements made with the STXS framework can therefore be updated in the long term as theory predictions are improved. STXS measurements are made across all the major Higgs boson production modes, including ggH, VBF, VH, ttH and tH.

Measurements in the STXS *Stage 1.0* framework (Section 2.3.1) were first presented in Ref. [3] with data taken in the years 2016 and 2017. Since, the STXS framework has been updated to *Stage 1.2*, whereby additional STXS bins are defined in the categorisation process and improved techniques have been developed to target those regions. Measurements in the Stage 1.2 STXS framework are presented in Ref. [1] using data taken during the full LHC Run II, namely in the years 2016 to 2018. This chapter presents the improvements made in Ref. [1] (over Ref. [3]) in the categorisation of VBF events, including VH processes where the vector boson decays hadronically. In particular, principles used in deriving data-driven background models are outlined. The results of the new VBF and VH categorisation process were first presented in Ref. [1], and therefore the results of this thesis are expected to be close to those in Ref. [1]. However, in Ref. [1], the tHq process was only targeted through categories designed for cases where the W boson from the top quark decays leptonically. This chapter further presents techniques to implement a tHq *hadronic* categorisation tag. In this context, the methods adopted aim to specifically distinguish the tHq hadronic process from the ttH process as well as from backgrounds not involving the Higgs boson.

This chapter first presents a brief introduction to the reconstruction of $H \to \gamma\gamma$ events.

Emphasis is placed on the reconstruction of photons and jets that are essential to the categorisation of VBF, VH hadronic and tHq hadronic events into the STXS bins. The chapter then focusses on the categorisation techniques for each production process. All three processes discussed are targeted using boosted decision trees (BDT) which represent a family of machine learning techniques. The steps involved in the training, optimisation and validation of the BDT techniques are discussed in detail. For each process, the BDT results allow the definition of analysis categories enriched in events from the target kinematic regions and thus help to increase sensitivity to individual STXS bins. A summary of the other categories used in the full analysis is given at the end of the chapter.

The effect of the improved categorisation process and the increased precision from the full Run II dataset on the Higgs boson cross-section, signal strength and coupling measurements in the full STXS Stage 1.2 framework are then later presented in Chapter 6.

In the text that follows, the term *process* is used to refer to a production process and the term *tag* refers to a category defined in the categorisation procedure and which is used to targed a particular production process.

5.2 Event reconstruction and selection

5.2.1 Particle flow

The CMS particle flow (PF) [154] software is used in the global reconstruction of events produced in the CMS detector. The aim of the software is to identify and assign an energy measurement to all the particles in an event by combining information from the individual subdetectors discussed in Section 3.3. In particular, tracks from the tracker and muon system, and energy clusters from the ECAL and HCAL are used. The presence or absence of a track indicates whether a particle is charged while the pattern of energy deposition in the ECAL or both the ECAL and HCAL helps to distinguish photons and electrons from hadrons.

A particular advantage of using PF is that the energy measurement of objects is not solely driven by the calorimeter energy measurements but receives contributions from the track momentum measurements if a track exists. This is particularly beneficial for particles such as low energy charged hadrons, for which the energy deposition is often too small to be clustered in the calorimeters. The energy measurement in PF is thus driven by the subdetector with the best resolution. It is important, therefore, that charged-particle tracks be unambiguously matched to calorimeter deposits by the PF algorithm and this is possible in CMS because of high tracking precision described in Section 3.3.3. Furthermore, the calorimeter granularities and the high magnetic field strength allow excellent separation of energy deposits as described in Sections 3.3.2, 3.3.4 and 3.3.5.

PF uses a combinatorial track finder which is applied in several successive iterations. A track is first seeded using a hit in the tracker, which provides a coarse estimate of the track parameters and allows the prediction of paths compatible with the initial seed trajectory. For each candidate predicted path, hits are added to the tracks and the track parameters are iteratively adjusted. A selection is further applied to the candidate tracks based on quality criteria and compatibility with other event parameters. In the next iterations, with new seeds, the hits associated with the tracks already reconstructed are removed. This reduces the algorithm complexity and allows progressively more relaxed thresholds to be used which

in turn helps to increase the track-finding efficiency, particularly for low-p_T or more displaced tracks.

The energy clustering algorithm in PF uses the energy and position of hits (in the calorimeters) with an energy deposition above an energy threshold. The clustering algorithm first selects a seed which is defined as the most energetic hit in a region of 4-8 neighbouring hits. Neighbouring hits which possess a common side or common corner are used to create a topological cluster which may subsequently contain several seeds. If a hit is shared between two clusters, the hit contributes a fraction of its energy to each cluster depending on its distance from the seed of each cluster. The cluster energy, computed iteratively as hits are added, is assumed to be maximum in the core and decreases with the radius following a Gaussian function. The energy of the topological clusters are then calibrated for the energy lost in absorbers, and because of threshold conditions. A similar clustering algorithm is used for both the ECAL and HCAL calorimeters, however, with different thresholds and calibration parameters. PF uses tracks and energy clusters as input to form collections of candidates for five types of particles: muons, electrons, photons, neutral hadrons and charged hadrons. For muons, the path extrapolated from the tracker is required to be consistent with the track in the muon system. The muon track reconstruction is not specific to PF and was described briefly in Section 3.3.6. If the particle is charged, the track curvature and the calorimeter deposits are used to calculate the particle energy. For neutral particles, only the relevant calorimeter clusters are used. These identified objects may be used further to build jets and reconstruct missing transverse momentum. PF thus produces physics objects ready for use in analyses. While a brief overview of the object reconstruction and selection process is given in the next sections, further details may be found in Ref. [1].

5.2.2 Photon reconstruction

Photon EM showers are initiated by e^+e^- pair-production over a distance of ~ 1 radiation length, and the subsequent emission of additional photons from bremsstrahlung occurring from the electron pairs in the magnetic field of the detector solenoid. Eventually, photons and electrons, with energies below the bremsstrahlung and pair-production thresholds, are absorbed, causing an excitation of the ECAL crystals which, upon de-excitation, emit scintillation photons with a wavelength of approximately 420 mm [155]. The latter are collected by photo-diodes and photo-triodes, located behind the crystals in the calorimeter barrel and end-caps respectively. Analogue signals, created in the form of voltage pulses, are digitised and read out by a dedicated electronic system.

At the high-level trigger (HLT), clustering algorithms are deployed to identify candidate photons by scanning the ECAL crystals for seeds with local energy deposits above a threshold. The energies in adjacent seed crystals are summed to form clusters which, if found to match patterns consistent with photon or electron showers, form a supercluster. In the ECAL barrel, the latter are formed from strips of five crystals in the direction of η, and a variable length in ϕ, while in the end-caps, 5×5 crystal matrices with a narrow width in η are used. Where available ($| \eta | > 1.65$), the pre-shower energy is added for superclusters in the endcaps. To account for crystal imperfections and gaps, pile-up, and shower losses for photons that undergo pair-production in the tracker, a multivariate regression is performed to estimate the required correction to the energy of a photon, depending on the location of the associated supercluster in $\eta - \phi$ coordinate space. In particular, a R9 variable, defined as

the ratio of the sum of the energy within the centre 3×3 array of crystals in a supercluster to the energy of the entire supercluster, is used to identify pair-conversion occurring upstream of the ECAL. Supercluster energy is further scaled in data to match $Z \to e^+e^-$ events from simulation. As a result, approximately 95% of the energy of photons is recovered. Events passing the HLT are recorded and have at least one supercluster with an associated p_T over a threshold. Off-line analysis is performed with events triggered by two superclusters within the ECAL fiducial region defined by $\mid \eta \mid < 2.5$, and excluding the barrel-end-cap transition region given by $1.44 < \mid \eta \mid < 1.57$. Thus, superclusters with showers in both the barrel and end-caps are not included. Other selection criteria on photon p_T, shower width, R9, electron veto and the ratio of HCAL to ECAL supercluster energy are further applied.

5.2.3 Vertex identification

Since photons trajectories are not visible in the silicon tracker, identification of the primary diphoton vertex is not a trivial task. The latter is, however, essential to obtain the polar angles of the photons and subsequently derive the diphoton invariant mass (Section 2.2.2). If the chosen vertex is found within 1 cm of the correct one, the error in the angle between the photons is negligible and the reconstructed diphoton mass resolution is limited by the energy resolution of the ECAL. Remarkably, the latter scenario ends up being the case for approximately 80% of events. When the photons convert in the ECAL, kinematic variables related to the tracks produced and the transverse momentum of the diphoton system may be used for vertex identification. For photons which undergo pair-production before reaching the ECAL, electron trajectories in the tracker and impact points in the ECAL may be extrapolated back to the diphoton vertex. The vertex probability or vertex-finding efficiency is estimated on an event-by-event basis by a boosted decision tree trained on the kinematics of tracks recoiling from candidate vertices and is used in conjunction with the energy resolution of the event to estimate the corresponding event mass resolution. For the case of unconverted photons, $Z \to \mu\mu$ events, with muon tracks removed are fed to the vertex probability BDT. The output vertices are compared to the known $Z \to \mu\mu$ vertices from the muon tracks. This process helps to verify that the output of the vertex probability BDT, which has been trained on simulated events, is still sensible when applied to data. For photons which have converted, the validation is done with $\gamma + jet$ events by comparing the selected vertex to the vertex associated with the jet.

5.2.4 Photon identification

All superclusters reconstructed in the ECAL are not necessarily prompt photon-initiated; they may also originate from electrons or neutral pions. Although prompt diphoton production constitutes an irreducible background, misidentified jets may be discriminated from prompt photons. After pre-selection, photon shower shape variables and kinematics, including shower topology and isolation, η of the supercluster, and event density per unit area ρ, are used as inputs to a photon ID BDT. A score is assigned to every photon candidate and is a measure of how prompt or fake it appears to be. In particular, the energy sum of all charged and neutral particles around the photon considered is indicative of how isolated it is and may be used to reject showers from neutral pion decays. However, this sum also includes a contribution from other collisions in the same bunch crossing and is misleading if the wrong

primary vertex is chosen. In this context, ρ is used to account for the pile-up dependence in shower isolation variables while a selection requirement, dependent on the photon p_T, is applied to the isolation sum under the vertex hypothesis that maximises the sum. Depending on the η-R9 bin in which a photon is found, a different threshold is used to apply a cut on the photon ID, requiring the same signal purity in each bin. Good-quality photons are thereby selected while making the maximum use of the available resolution in different parts of the detector. Indeed, the different η bins exploit the superior sensitivity of the barrel over the endcaps while the R9 bins exploit the better energy resolution of photons that do not undergo pair-production. In addition, the change in crystal geometry and the detector material significantly impair the achievable resolution in the barrel-end-cap transition region. Since mismatch between data and simulation affects the BDT performance, shower shape and isolation corrections are derived and applied differentially in p_T, η, ϕ, and ρ using a method known as *chained quantile regression* whereby conditional shapes of the variable distributions in simulation are required to match those in data [1]. The photon ID BDT is validated by $Z \to ee$ events where the electrons are reconstructed as photons.

5.2.5 Jet reconstruction

As described in Section 2.1.2, because of colour confinement, quarks and gluons are not observed freely but occur as colour-neutral hadrons. One of the signatures of the hadronisation process is a collimated spray of particles, called a jet. PF flow brings multiple benefits to the reconstruction of jets since $\sim 90\%$ of the measured jet energy originates from charged hadrons (60%) and photons (30%), measured with the high-resolution CMS tracker and ECAL. However the remaining $\sim 10\%$ of the reconstructed energy originates from neutral hadrons in the HCAL which has a poorer resolution. PF therefore improves the jet energy resolution compared to methods using the calorimeter information only. Precise jet reconstruction is particularly important for the STXS analysis since jets are used to categorise events into the STXS bins and to distinguish between the Higgs boson production modes.

Jet reconstruction is done using the sequential clustering algorithm, anti-k_T. The algorithm takes as input particles for which charged hadron contributions not associated with the primary vertex are removed. The distance between every particle and the beamline is determined. The distance between all particles is also computed using a distance metric dependent on a distance parameter, D, set to 0.4 in CMS. Every particle is combined with the particle closest to it to form a new particle. Following this, all distances are recomputed and the jet clustering procedure is repeated iteratively for all particles until the smallest distance for a particle is the distance to the beamline. This process is repeated for all jets.

The jet energy corrections (JEC) serve to re-calibrate the energy of the reconstructed jet to obtain the particle-level energy, i.e to determine the real energy of the jet from the energy they deposit in the detector. As a first step the offset correction uses the area of the jet and the global average energy density to estimate and subtract the energy of the jet not associated with high p_T scattering (generally attributed to electronic noise and PU). The correction factors are determined as a function of η and p_T from two samples of simulated events with identical interactions, where one contains additional PU interactions. In the second step, JEC factors are obtained by comparing simulated events to the generator jets and are applied as a function of jet p_T and η. These JEC factors cover effects from calorimeter non-linearities, jet p_T thresholds and geometric effects. The absolute jet energy

scale (JES) in the central detector region ($\eta < 1.3$) is derived from events where the jet is balanced against a well-measured reference. For instance, Z + jet events where the Z boson decays to muons is used and the Z p_T is well measured from the muon p_T resolution of the CMS muon system. Similarly, γ + jet events may also be used for this purpose. The relative JES factors in the forward detector regions are obtained from QCD-dijet events, with one of the jets required to be central. The two jets are expected to be balanced and the JES is derived relative to the central jet. Any residual discrepancy between data and simulation in the JES is then calculated as a data-to-simulation ratio. PU collisions may also give rise to jets which tend to have low p_T but can overlap and mimic high p_T jets. A BDT is trained to learn jet shape variables and track variables from the interaction vertex of the jet to identify PU jets. The output score from the PU jet identification (PUJID) BDT is used to define thresholds in η and p_T to reject PU jets. Jets used in the analysis are required to pass the PUJID threshold and the thresholds $p_T > 25$ and $\eta < 4.7$. Depending on the analysis, stricter theresholds and conditions may be applied. Reconstruction tools also aim to distinguish between quark and gluon jets, the latter being made up of softer and less collimated particles. In particular, jets arising from the hadronisation of b quarks are specifically targeted by deep neural networks (DNN) trained to identify displaced vertices.

5.2.6 Additional objects

While the reconstruction of photons and jets has been described in detail as it is relevant to the specific production modes (VBF and tHq hadronic), studied in this chapter, other objects such as electrons, muons and missing transverse momentum are useful to target other production modes such as leptonic VH and ttH channels.

Electrons (muons) are required to pass a p_T threshold of 10 (5) GeV and an η threshold of 2.4, excluding the barrel-endcap transition area. Other requirements, including sufficient isolation from photons and jets, are imposed. Further details of the reconstruction of electrons and muons may be found in Ref. [156] and Ref. [141] respectively. In particular, muons are reconstructed using a mixture of tracks in the inner tracking system and in the muon system, which are required to be consistent. Electron reconstruction is very similar to the photon reconstruction process described in previous sections with the additional requirement of the presence of a track in the inner tracking system. The electron reconstruction also accounts for energy lost to bremsstrahlung.

The missing transverse momentum is measured by the imbalance in the sum of the transverse momentum of all reconstructed objects once all scale and resolution corrections have been applied. This allows the presence of neutrinos to be inferred and is possible because of the hermetic nature of the CMS detector as described in Chapter 3.

5.3 Samples

5.3.1 Data

The data used in this analysis is from LHC proton-proton collisions at $\sqrt{s} = 13\,\text{TeV}$ collected in the years 2016, 2017 and 2018 with integrated luminosities of 35.9, 41.5, and 59.4 fb^{-1} respectively. The full Run II dataset therefore contains data amounting to an integrated

luminosity of $137\,\text{fb}^{-1}$.

In the data, diphoton events are selected by the L1T and HLT (Section 3.3.7). Each HLT path is required to be seeded by at least one electromagnetic candidate at the L1T, i.e only one of the two photons is needed at the L1T. The individual photon candidates are selected based on shower shape and isolation criteria described in Section 5.2.2 and are required to pass p_T thresholds on the leading (subleading) photon p_T of 30 (30) GeV in 2016 data and of 22 (18) GeV in 2017 and 2018 data. The triggering efficiency is measured in $Z \to e^+e^-$ events in data using a "tag-and-probe" technique [157], whereby one electron (the tag) is required to pass strict identification criteria while only a loose requirement is placed on the second electron (the probe). The triggering efficiency measured this way is binned in p_T, η and $R9$ before being applied as weights to simulated events.

5.3.2 Simulation

Simulation samples are used in this analysis to train BDT classifiers described in Section 5.4, and to create a signal model as will be described in Section 6.3.1. Furthermore, these samples provide a baseline for the evaluation of the results expected from the analysis, such as the signal yields and significances in the STXS framework. The simulation software MADGRAPH5_aMC@NLO [158] is used to generate Monte Carlo (MC) simulation signal events at parton-level for each of the Higgs boson production modes. These samples are produced at three different mass points for m_H, namely 120, 125 and 130 GeV. The accuracy in perturbative QCD is at next-to-leading order (NLO). Additional signal samples are also generated at other mass points by the software POWHEG [159], also at NLO accuracy in QCD. Parton showering and hadronisation is simulated by the software PYTHIA8 and CUETP8M1 respectively which take as inputs the parton-level samples [160]. While the MADGRAPH samples (after the showering and hadronisation step) are used to compute the SM production cross-section prediction in each STXS bin, the POWHEG samples are used to train the BDT classifiers used in the categorisation process. It is important that the samples used to train the classifiers in the categorisation process be independent of those used to construct the final signal model (Section 6.3.1).

Simulated background samples are produced for the main backgrounds in the diphoton channel, namely $\gamma\gamma$, γ+jet and jet+jet events, where in the latter two cases, jets are misidentified as photons. The simulated background samples are merely used for training classifiers in the categorisation process while the final background model (Section 6.3.2) is derived from the diphoton mass distribution in data, with the Higgs boson mass window excluded. The dominant, irreducible background, SM $\gamma\gamma$ production, is simulated with the software SHERPA [161], while the remaining two reducible backgrounds, γ+jet and jet+jet, are modelled with PYTHIA8, where the samples are enriched with jets showing significant EM components. The Drell-Yan events used in the reconstruction corrections (Section 5.2) and the validation of the categorisation classifiers are simulated with MADGRAPH5_aMC@NLO.

The response of the CMS detector is simulated using the GEANT4 package [162] which accounts for PU vertices at the nominal bunch crossing (in-time PU) and PU vertices in previous and following bunch-crossings (out-of-time PU). Weights are then applied to the simulated events to reproduce the distribution of interaction vertices in data. The average number of interactions per bunch crossing in the 2016 (2017 and 2018) datasets is 23 (32).

5.4 Event categorisation

5.4.1 Categorisation strategy

The $H \to \gamma\gamma$ analysis aims to distinguish a narrow signal peak from the smoothly falling background in the diphoton mass distribution. The event selection and categorisation process increases the ratio of the number of signal events to the number of background events in the analysis regions considered. This enhances the sensitivity of the analysis to specific processes and reduces the expected uncertainties on the measured parameters. Furthermore, Higgs boson measurements aim to measure, amongst other parameters, the couplings of the Higgs boson to vector bosons and fermions. For this reason, the VH, VBF, ttH and tH production modes are of particular importance and are specifically targeted in the STXS analysis. The use of separate tags for these processes allows the specific Higgs boson couplings to be measured independently. The granular STXS categories still provide good sensitivity to more inclusive quantities, such as the overall or per-production mode cross-sections and signal strengths.

For each production mode, the event categorisation targets all of the STXS bins for which some sensitivity is achievable in the $H \to \gamma\gamma$ decay channel with the available data. The different particle-level bins defined in the STXS framework (Section 5.4.2) are first targeted through cuts on corresponding reconstructed event variables and multivariate techniques such as boosted decision trees. To increase the overall sensitivity of the analysis, events are subsequently separated into categories with different signal-to-background ratios. The category boundary values are chosen to maximise the significance of the Higgs boson peak. A brief description of the event categorisation in other production channels, not addressed explicitly in this chapter but used in the full analysis, is given in Section 5.7. The full list of all the categories measured in the STXS analysis is given in Table 5.11.

In order to enable the simultaneous measurement of different cross-sections, it is important that the contamination in each analysis category from processes in non-target STXS bins is kept to a minimum. Given that an event may satisfy the selection criteria for more than one analysis category, a priority sequence needs to be defined to assign these events to the analysis category with the highest priority. Generally, analysis categories with a lower expected signal yield are given a higher priority. This increases the sensitivity to low cross-section Higgs boson processes, giving analysis categories with a sufficiently high number of these rarer events. An adequate number of events is necessary to perform measurements of these low cross-section processes.

The main categorisation regions targeted in Ref. [1] are given in Figure 5.1 in order of the tag priority. In general, selection criteria get looser along the tag priority line. Leptonic regions are considered before the hadronic categorisation regions since single isolated leptons are more easily identified through strict criteria than quarks and gluons which appear as hadronised jets in the detector. Events first pass the tHq leptonic criteria, followed by the ttH leptonic, the VH leptonic and the VH MET tags. Events not selected for the leptonic categorisation regions are considered for ttH hadronic and VBF categories (which include the VH hadronic tag). Hadronic regions involving the t quark are considered first because of the dedicated b-tagging techniques available to identify the t quark decay. The ggH categories are populated by all remaining events (which do not pass the VH hadronic tag).

Figure 5.1: The order of event tagging priority for the categorisation regions considered in the $H \to \gamma\gamma$ STXS analysis described in Ref. [1].

In particular, the definition of the categories in the VBF and VH hadronic regions are detailed in this chapter. Additionally, the definition of a new tHq hadronic tag, not used in Ref. [1], is explored. The tHq hadronic tag is considered after the VH MET tag and before the ttH hadronic tag. The tHq hadronic tag is given priority over the ttH hadronic tag given the similarity in the decay products between the two processes and the smaller tHq hadronic cross-section; this order allows a relatively pure tHq hadronic tag to be constructed with minimal ttH hadronic contamination, although the correlation between these categories is expected to remain high.

Analysis categories are constructed by using the datasets from 2016 to 2018 grouped together. This provides a large training dataset for event classifiers, resulting in more optimal category definitions, especially for processes with low cross-sections and branching fractions. The process of grouping years together requires fewer categories to be defined and optimised but does result in the loss of year-dependent information such as variations in detector conditions and in the $m_{\gamma\gamma}$ resolution. However, the gain in sensitivity from the increased number of events in the grouped dataset is found to outweigh the effects of the loss in year-dependent information. Particularly, this is because variations in detector conditions are small, and not substantially greater than variations within a given year of data-taking. Nevertheless, variations in the detector and LHC beam parameters are accounted for by generating simulation events for each year separately, with the corresponding detector conditions, before they are merged together. Furthermore, corrections to the photon energy scale and other elements of the event reconstruction are performed for each year individually. Thus, simulated and data events from different years are only processed together at the stage of the event categorisation and final result extraction. Once the selection criteria for each analysis category are defined, results are obtained by performing a simultaneous fit to the resulting $m_{\gamma\gamma}$ distributions in all analysis categories. These results are presented in Chapter 6.

5.4.2 The STXS Stage 1.2 framework

The STXS Stage 1.2 framework is illustrated in Figure 5.2. STXS bins are bins of phase space which are split by production mode and further by kinematic variables within each production mode.

The $gg \to H$ (ggH) region in blue is split into STXS bins using the Higgs boson transverse momentum (p_T^H) and the number of jets. Notably, the ggH region has a VBF-like region with high dijet invariant mass (m_{jj}) defined by ≥ 2 jets and $m_{jj} > 350\,\text{GeV}$. This VBF-like region is split into four STXS bins according to m_{jj}, and the transverse momentum of the Higgs boson and dijet system (p_T^{Hjj}). VBF-like ggH events falling in these regions may be targeted by the VBF categorisation process, described in Section 5.5. The $bb \to H$ (bbH) and $gg \to Z(q\bar{q})H$ (ggZH) production modes are grouped with the ggH production mode in the categorisation process. The VBF and hadronic VH (V(q$\bar{\text{q}}$)H) modes make up the

electroweak qqH production region (in orange). Here the STXS bins are defined using the number of jets, p_T^H, m_{jj} and (p_T^{Hjj}). The four STXS bins which make up the "qqH rest" region (in white) are not explicitly targeted in this study. The leptonic VH bins (in green) are split into three separate regions representing the WH, ZH, and ggZH production modes, which are further split according to the number of jets and the transverse momentum of the vector boson (p_T^V) that decays leptonically. The ttH production mode (in pink) is split by p_T^H. The tH STXS bin (yellow) includes contributions from both the tHq and tHW production modes.

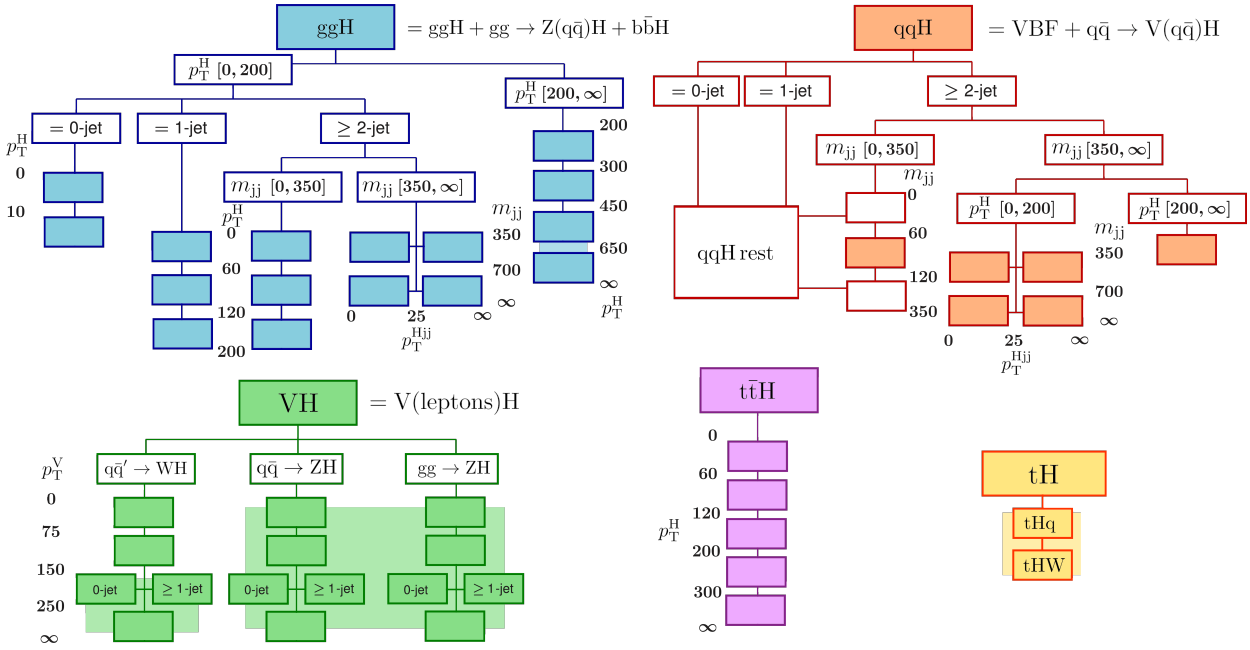

Figure 5.2: Diagram showing the full set of STXS Stage 1.2 bins [1], defined for events with a Higgs boson rapidity less than 2.5. The solid boxes represent each STXS Stage 1.2 bin. The units of p_T^H, m_{jj} , p_T^{Hjj}, and p_T^V are in GeV. The shaded regions indicate the STXS bins that are divided at Stage 1.2, but are not measured independently in this analysis.

After being classified into STXS bins, events are divided into analysis categories, referred to as *tags*. The tag names are given in decreasing order of the expected ratio of signal-to-background events (S/B). For example, the tag with the highest S/B targeting the ggH zero jet bin with $p_T < 10\,\text{GeV}$ is denoted 0J low $p_T^{\gamma\gamma}$ Tag 0.

Before events are categorised in the above-mentioned STXS bins, the event selection in all analysis categories requires the two leading preselected photon candidates to have $p_T^{\gamma 1} > m_{\gamma\gamma}/3$ and $p_T^{\gamma 2} > m_{\gamma\gamma}/4$, with an invariant mass in the range $100 < m_{\gamma\gamma} < 180\,\text{GeV}$. Both photons must also satisfy the pseudorapidity requirement $|\eta| < 2.5$ and must not be in the barrel-endcap transition region $1.44 < |\eta| < 1.57$. An additional requirement is placed on the Higgs boson rapidity $|y_H| < 2.5$. This removes the theoretical uncertainty which arises when measurements are extrapolated to the full phase space, a large part of which is not accessible experimentally. The experimental acceptance of $H \to \gamma\gamma$ events with $|y_H| > 2.5$, although negligible, is still taken into account [40]. Events are categorised using the detector-level equivalents of the particle-level quantities used to define the STXS bins. For instance, $p_T^{\gamma\gamma}$ is used to construct analysis categories targeting STXS bins defined by p_T^H

values. There is an additional selection applied to events when optimising the categorisation process; the region of the Higgs boson mass window (115-135 GeV) is kept blinded in data, so as not to introduce any bias in the categorisation definition.

As described previously, the STXS framework is developed in stages, namely Stage 0, Stage 1.1, Stage 1.2. Measurements of Stage 0 cross-sections in the $H \to \gamma\gamma$ decay channel were performed in a previous CMS $H \to \gamma\gamma$ analysis [106]. Results for ggH and VBF in the STXS Stage 1 framework are described in the previous version of this analysis, documented in Ref. [3]. In this chapter, the following improvements from Ref. [1] (over the Ref. [3] analysis) are described:

- The inclusion of 2018 data, which increases the total integrated luminosity from $77.4\,\text{fb}^{-1}$ to $137\,\text{fb}^{-1}$
- An extended and improved categorisation strategy for the VBF production mode. This includes the ability to constrain ggH production modes with a VBF-like final state topology
- The addition of analysis categories targeting associated production (VH) where the vector boson decays hadronically.
- A wider range of measurements and interpretations (discussed in Chapter 6). These include inclusive and per-production mode signal strengths, measurements of Higgs boson couplings using the κ-framework, and additional two-dimensional scans.

In addition to these improvements, already included in Ref. [1], the definition of a new tHq hadronic tag is explored.

5.4.3 Boosted decision trees

BDTs [163] are used for several purposes in CMS, including event reconstruction (Section 5.2) and, especially, event categorisation. The BDT provides an output score which indicates how signal-like an event is. Thresholds may be placed on this output score when selecting events or defining analysis categories.

In the case of event categorisation in the $H \to \gamma\gamma$ analysis, the algorithm is trained on simulated events for which the truth process is known. Characteristics of the simulated events are used as inputs or *predictors* to the machine learning algorithm. These predictors are reconstruction-level quantities and may be, for instance, the p_T and η of photons and jets, and are chosen so as to provide maximum discrimination between signal and background events.

The performance of the boosted decision tree depends on several hyperparameters including the learning rate, the allowable tree depth, the loss functions, the stopping criteria and the number of base learners (estimators) amongst others. These parameters are tuned to maximise the BDT performance while minimising overfitting. The performance and generalisability of the BDT may be evaluated on a test sample which consists of observations not used in the training.

Where BDTs are used in the $H \to \gamma\gamma$ analysis, two types of validations are performed. Firstly, the simulated background samples used to train the BDT are compared to the data.

This helps to ascertain that background processes used to train the BDT are accurately modelled. Since the simulated background samples are only used to train the BDTs, and not to produce the final results, it is not essential that the agreement in the background validation be perfect. The background model used in the extracting the final results (Chapter 6) is derived directly from data; poor agreement in background-like regions do not induce any biases in the results, but only result in sub-optimal performance of the BDT. In the second validation step, the classifier output scores in simulation and data are compared in a signal-like region. This second comparison is more important since it verifies that simulated Higgs boson signal events from the simulated Higgs boson signal model, used in the final measurement, is well-modelled. Therefore simulation and data should be expected to agree within statistical and systematic uncertainties in the signal validation. Furthermore, for all of the BDTs, the input variables are chosen such that $m_{\gamma\gamma}$ cannot be inferred. This prevents the BDT from being biased to the mass of the Higgs boson in the simulated samples used in signal modelling.

5.4.4 Diphoton BDT

A tighter selection is required to specifically target diphoton events from a $H \to \gamma\gamma$ decay, A diphoton BDT uses information from the photon ID BDT, the vertex identification BDT, the per-event mass resolutions under the right and wrong vertex hypotheses, together with kinematic variables of the diphoton system, to assign scores to diphoton events. In all BDTs used, the photon p_T variables are scaled by the diphoton invariant mass to ensure that the output is unbiased by the value of $m_{\gamma\gamma}$. Events with diphoton BDT scores below a threshold are not selected for further analysis.

5.5 Event categorisation in the qqH channel

5.5.1 VBF and VH hadronic kinematics

In proton-proton collisions at the LHC, production of the Higgs boson via VBF has the second highest cross-section after ggH (Section 7.2). Oppositely-directed vector bosons are radiated from quarks into the forward/backward detector regions (Figure 5.3) and appear as narrow cones due to hadronisation. The presence of two such jets with a high pseudo-rapidity separation has been shown to help in tagging the VBF production mode. Moreover, since the interacting quarks do not exchange colour, there is low hadronic activity in the central rapidity region, where the Higgs boson decay products are most likely to be produced. This allows better efficiency in the identification of decay final states and the vetoing of jet activity in the central region, especially for the rejection of background processes which proceed through t-channel colour exchange such as top pair production. In addition, the photon p_T from VBF $H \to \gamma\gamma$ events is generally higher than those from gluon-gluon fusion $H \to \gamma\gamma$ events; thus VBF events can also be targeted through tighter photon p_T cuts. A VBF-like ggH region is targeted as part of the VBF categorisation process.

From the decay products alone, it is not possible to distinguish hadronic VH production from VBF production. Thus these two processes are grouped together under electroweak qqH production in the STXS framework. Given that VBF events are expected to have two

high p_T jets, the m_{jj} distributions of VBF-like qqH events are expected to have much higher m_{jj} than VH-like qqH events. In the STXS framework, these two regions, namely VBF-like qqH and VH-like qqH are defined separately based on particle-level m_{jj} cuts.

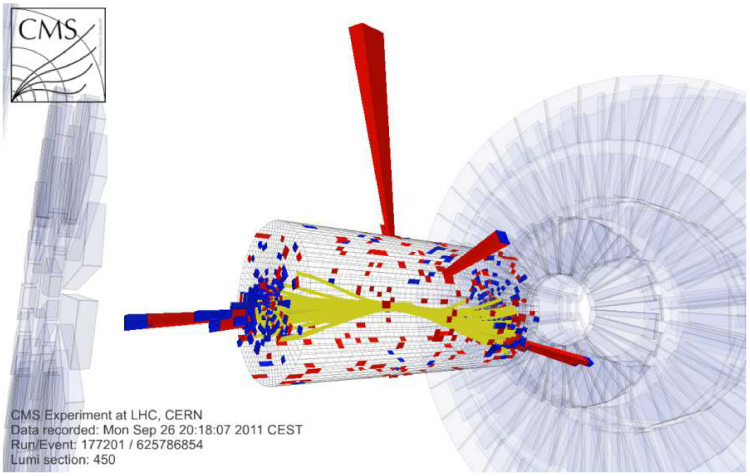

Figure 5.3: A diphoton plus dijet candidate event. This event contains two well-isolated central barrel photons. The tracks in yellow are part of two very high p_T jets which are well separated in η.

5.5.2 VBF and VH hadronic selection and STXS bin definitions

In the STXS framework, the qqH production mode includes both VBF events and VH events where the vector boson decays hadronically. Within qqH production, there are five STXS bins that correspond to typical VBF-like qqH events, with a single bin for VH-like qqH events. The definitions of the qqH STXS bins with SM cross-section predictions are given in Table 5.1. These correspond to the orange entries in Figure 5.4. The first VBF-like bin (qqH BSM) is defined as having a high p_T^H, with a threshold set at 200 GeV. The remaining four bins have $p_T^H < 200$ GeV. They are defined by boundaries on p_T^{Hjj} at 25 GeV and m_{jj} at 700 GeV. The p_T^{Hjj} threshold is chosen to separate events containing two jets from those containing three or more, which are referred to as two-jet-like ($p_T^{Hjj} < 25$) and three-jet-like ($p_T^{Hjj} > 25$) bins, respectively. The bin representing hadronic VH production is defined at the particle level by $60 < m_{jj} < 120$ GeV. The bins for events with fewer than two jets, and bins with two jet events with an $m_{jj} < 60$ GeV or $120 < m_{jj} < 350$ GeV are not considered as parameters of interest in the final result extraction and are assumed to have their respective SM cross-sections. The ggH STXS framework has a VBF-like region with high m_{jj} (Figure 5.2). This VBF-like ggH region is split into four STXS bins according to m_{jj}, and p_T^{Hjj}.

The analysis regions are defined using the reconstructed observables corresponding to each particle-level quantity; these are the $p_T^{\gamma\gamma}$, the reconstructed m_{jj}, and the reconstructed p_T^{Hjj}. Events are further divided into analysis categories using both the respective BDT output probabilities and the diphoton BDT score. Two analysis categories are constructed to target each STXS bin. In particular, two analysis categories targeting the set of four VBF-like ggH STXS bins together are constructed. VBF-like qqH and VBF-like ggH events have a dedicated categorisation scheme described in Section 5.5.4. VH-like qqH events are

categorised as described in Section 5.5.5. No analysis categories are constructed to target the zero or one jet qqH STXS bins, nor those with $m_{jj} < 60\,\text{GeV}$ or $120 < m_{jj} < 350\,\text{GeV}$.

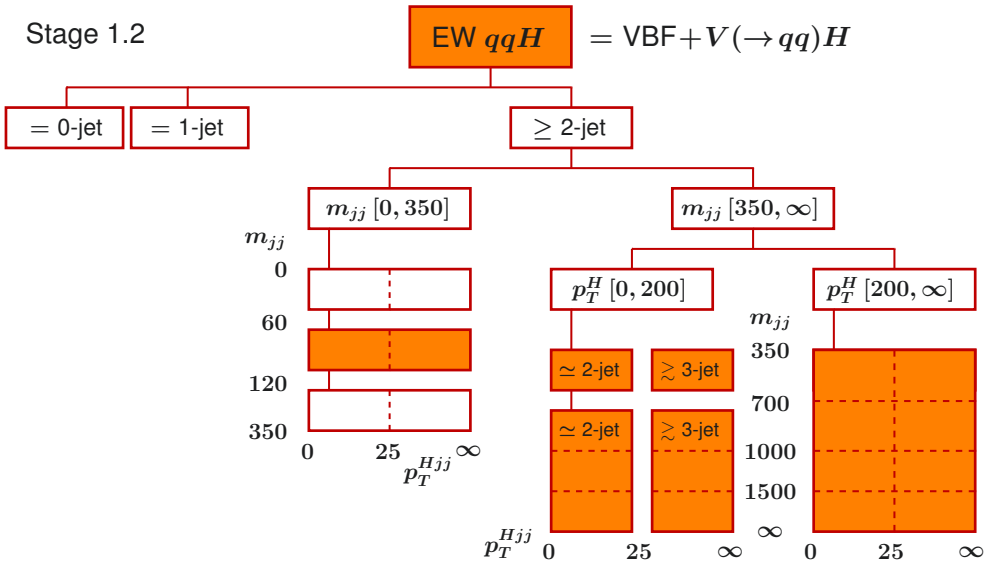

Figure 5.4: The STXS Stage 1.2 bins for EW qqH production.

Table 5.1: Definition of the qqH STXS bins. The product of the cross-section and branching fraction ($\mathcal{B}$), evaluated at $\sqrt{s} = 13\,\text{TeV}$ and $m_H = 125\,\text{GeV}$, is given for each bin in the last column. The fraction of the total production mode cross-section from each STXS bin is also shown. Unless stated otherwise, the STXS bins are defined for $|y_H| < 2.5$. Events with $|y_H| > 2.5$ are mostly outside of the experimental acceptance and therefore have a negligible contribution to all analysis categories.

STXS bin	Definition units of p_T^H, m_{jj} and p_T^{Hjj} in GeV	Fraction of cross-section VBF	$q\bar{q}' \to W(\bar{q}')H$	$q\bar{q} \to Z(q\bar{q})H$	$\sigma_{\text{SM}}\mathcal{B}$ (fb)
qqH forward	$\lvert y_H\rvert > 2.5$	6.69%	12.57%	9.84%	0.98
qqH 0J	Exactly 0 jets	6.95%	5.70%	3.73%	0.77
qqH 1J	Exactly 1 jet	32.83%	31.13%	25.03%	3.82
qqH $m_{jj} < 60$	At least 2 jets, $m_{jj} < 60$	1.36%	3.58%	2.72%	0.23
qqH VH-like	At least 2 jets, $60 < m_{jj} < 120$	2.40%	29.43%	28.94%	1.23
qqH $120 < m_{jj} < 350$	At least 2 jets, $120 < m_{jj} < 350$	12.34%	13.92%	12.59%	1.53
qqH VBF-like low m_{jj} low p_T^{Hjj}	At least 2 jets, $p_T^H < 200$, $350 < m_{jj} < 700$, $p_T^{Hjj} < 25$	10.26%	0.44%	0.35%	0.90
qqH VBF-like low m_{jj} high p_T^{Hjj}	At least 2 jets, $p_T^H < 200$, $350 < m_{jj} < 700$, $p_T^{Hjj} > 25$	3.85%	1.86%	1.74%	0.39
qqH VBF-like high m_{jj} low p_T^{Hjj}	At least 2 jets, $p_T^H < 200$, $m_{jj} > 700$, $p_T^{Hjj} < 25$	15.09%	0.09%	0.08%	1.30
qqH VBF-like high m_{jj} high p_T^{Hjj}	At least 2 jets, $p_T^H < 200$, $m_{jj} > 700$, $p_T^{Hjj} > 25$	4.25%	0.40%	0.39%	0.38
qqH BSM	At least 2 jets, $m_{jj} > 350$, $p_T^H > 200$	3.98%	0.88%	0.71%	0.37

When constructing the corresponding analysis categories at reconstruction level, a dijet preselection is applied. The VBF preselection requires two jets within $|\eta| < 4.7$, with $p_T > 40(30)\,\text{GeV}$ for the leading (subleading) jet, in addition to $m_{jj} > 350\,\text{GeV}$. The hadronic VH preselection requires two jets within $|\eta| < 2.4$ and with $p_T > 30\,\text{GeV}$, in addition to $60 < m_{jj} < 120\,\text{GeV}$. Jets are also required to pass a threshold on PUJID score (Section 5.2.5). Due to the use of the data control samples (Section 5.5.3) with photon ID BDT score below -0.5 in the qqH categorisation, an additional requirement that the two photons have a photon ID BDT score of larger than -0.2 is placed on events entering the qqH analysis. The pre-selections applied for the VBF-like and VH-like events are given in Table 5.2.

Table 5.2: The cuts applied on reconstruction-level event variables to select VBF and VH dijet events before the full categorisation process.

full VBF pre-selection	full VH pre-selection
$100 < m_{\gamma\gamma} < 180\,\text{GeV}$	$100 < m_{\gamma\gamma} < 180\,\text{GeV}$
$p_T^{\gamma_1}/m_{\gamma\gamma} > 1/3$	$p_T^{\gamma_1}/m_{\gamma\gamma} > 1/3$
$p_T^{\gamma_2}/m_{\gamma\gamma} > 1/4$	$p_T^{\gamma_1}/m_{\gamma\gamma} > 1/4$
$\eta_\gamma < 2.5$	$\eta_\gamma < 2.5$
$\eta_j < 4.7$	$\eta_j < 2.4$
$p_T^{j_1} > 40\,\text{GeV}$	$p_T^{j_1} > 30\,\text{GeV}$
$p_T^{j_2} > 30\,\text{GeV}$	$p_T^{j_2} > 30\,\text{GeV}$
$m_{jj} > 350\,\text{GeV}$	$60 < m_{jj} < 120\,\text{GeV}$
photon ID scores > -0.2	photon ID scores > -0.2

5.5.3 Data-driven background modelling

The dominant backgrounds in the VBF phase space are γ+jet events, made up of one prompt photon and a jet which is mis-identified as a photon. γ-jet and jet-jet events originate mainly from specific types of quark/gluon fragmentation processes which are not easily modelled and, therefore, simulated samples for these backgrounds are limited, especially when the event selections are applied, as shown in Figure 5.5. As a result, the weights, which serve to normalise the total number of simulated events to the appropriate number of expected events for a given integrated luminosity, tend to be high for events in these simulation samples. Training the VBF and VH BDTs on such events results in inefficient tagging, with qqH categories being contaminated by tH and ttH events. Such an effect was partially fixed in the previous versions of the analysis by reducing QCD weights during the BDT training, or by removing the fake-fake component. Such approaches impact the performance of the multi-class BDT for rejecting QCD background.

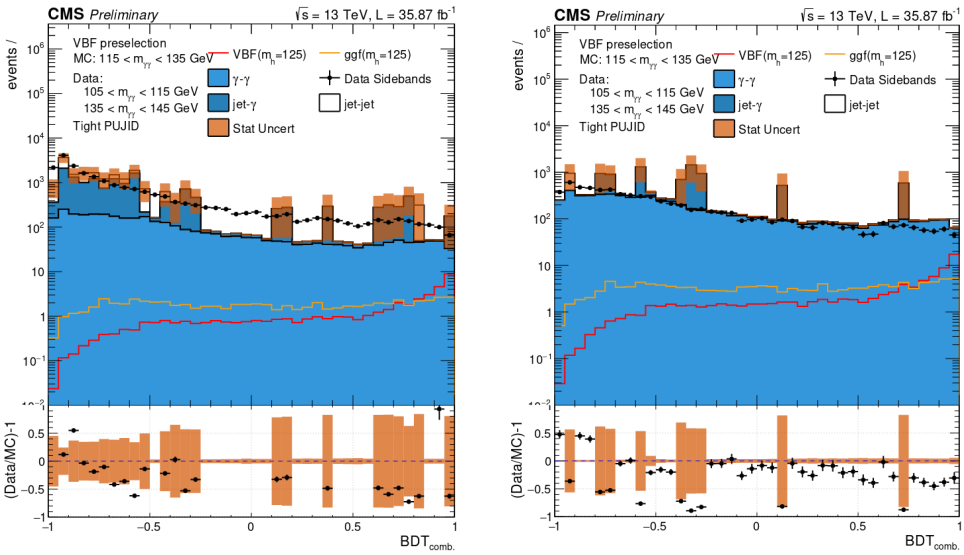

Figure 5.5: Distributions of the VBF BDT score in Ref. [106] without (left) and with (right) VBF selections. It can be seen that the jet-gamma line (dark blue) is very uneven, which a result of the low MC statistics. The resulting high weights in the sample can cause problems with the training of the BDT.

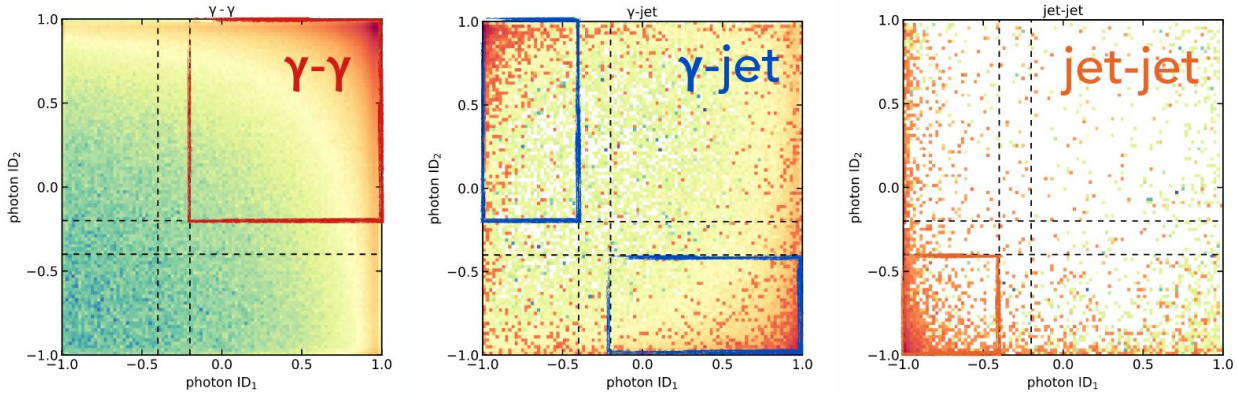

Figure 5.6: A schematic of the distribution of γ-jet and jet-jet events in photon ID coordinate space. The photon ID cuts are generally at -0.2.

An alternative solution is to re-use data from a control region to model the prompt-fake and fake-fake backgrounds by inverting the photon-ID requirement for the leading and sub-leading photons as shown in the schematic of Figure 5.6. These control regions benefit from a large number of QCD-like events from recorded data. Figure 5.6 illustrates how the photon ID$_1$-photon ID$_2$ space is populated by γ-jet and jet-jet events in simulation samples. As expected, by applying photon ID cuts (> -0.2) very few γ-jet and jet-jet backgrounds end up in the simulated signal region (where both photon ID values are > -0.2) and are inadequate for training the BDTs. Higher statistical samples for these processes in the signal region may be obtained by employing a data-driven method for generating background samples. Three control regions (CRs) are populated by events passing the standard selection and inverted photon ID cuts and are illustrated in Figure 5.6 by two (prompt-fake and fake-prompt) regions outlined in blue for γ-jet events and one (fake-fake) region outlined in orange for jet-jet events.

In the data-driven method, higher statistics for γ-jet and jet-jet in the signal region are obtained using data events in the control regions to generate a combined data-driven background sample, labelled *QCD*. Simulation samples for the diphoton, ggH, VH and VBF process are used in training BDTs without any such modification. Simulation samples do contain sufficient $\gamma - \gamma$ background events since these are made up of two prompt photons which will generally pass the photon ID cuts. The simulated γ-jet and jet-jet samples are used to extract factors to link the prompt-fake (or fake-prompt) region to the prompt-prompt region in simulation. Reconstruction-level (reco) regions are defined using cuts on the photon ID score as shown below. Note that, given these regions are defined at reconstruction level, truth prompt-prompt events may land in a different reco region (not reco prompt-prompt).

- **Reco prompt-prompt region**: both photons have an ID MVA score > -0.2
- **Reco prompt-fake region**: lead photon has an IDMVA score > -0.2, sublead photon has a photon IDMVA score of < -0.4
- **Reco fake-prompt region**: sublead photon has an IDMVA score > -0.2, lead photon has a photon IDMVA score of < -0.4
- **Reco fake-fake region**: both photons have an ID MVA score < -0.4

For the backgrounds in the VBF-like categorisation, the data-driven factors are extracted after a *relaxed* preselection is applied to the simulation samples, instead of the full VBF preselection (Table 5.3).

The relaxed VBF selection has looser requirements on $p_T/m_{\gamma\gamma}$, m_{jj} and jet p_T because of the already low statistics of the γ-jet and jet-jet events in the signal region. Once the factors are extracted from simulation samples and applied to data control regions to obtain the *QCD* data-driven sample, the full VBF preselection is applied before the BDT training procedure. For the backgrounds in the VH-like categorisation, the data-driven procedure was found to work well even without a relaxed preselection.

Table 5.3: List of relaxed (full) VBF preselection cuts used before (after) extracting the data-driven factors.

full VBF preselection	relaxed VBF preselection
$100 < m_{\gamma\gamma} < 180$ GeV	$100 < m_{\gamma\gamma} < 180$ GeV
$p_T^{\gamma_1}/m_{\gamma\gamma} > 1/3$	$p_T^{\gamma_1}/m_{\gamma\gamma} > 1/4$
$p_T^{\gamma_2}/m_{\gamma\gamma} > 1/4$	$p_T^{\gamma_1}/m_{\gamma\gamma} > 1/5$
$\eta_\gamma < 2.5$	$\eta_\gamma < 2.5$
$p_T^{j_1} > 40\,\text{GeV}$	$p_T^{j_1} > 30\,\text{GeV}$
$p_T^{j_2} > 30\,\text{GeV}$	$p_T^{j_2} > 20\,\text{GeV}$
$m_{jj} > 250\,\text{GeV}$	$m_{jj} > 120\,\text{GeV}$

The fake factors are derived on a per-photon basis; there is a fake factor for the lead photon $f(\gamma_1)$, one for the sublead photon $f(\gamma_2)$. Both factors are derived as the ratio of the number of simulated events in the reco signal region (N^{SR}) to the number of simulated events falling in the reco control regions (N^{CR}) as

$$f(\gamma_i) = f(\eta(\gamma_i), p_T(\gamma_i)) = \left(\frac{N^{SR}(\eta(\gamma_i), p_T(\gamma_i))}{N^{CR}(\eta(\gamma_i), p_T(\gamma_i))} \right)_{MC} \quad i = 1, 2 \ . \tag{5.1}$$

For $f(\gamma_1)$, the fake factor is binned in the $\eta(\gamma_1)$ (EE, EB) and $p_T(\gamma_1)$ (0-30, 30-50, 50-70, >70 GeV) of the lead photon. For $f(\gamma_2)$, the fake factor is binned in the $\eta(\gamma_2)$ and $p_T(\gamma_2)$ of the sublead photon. The events in this control sample can potentially have both a different normalisation and different kinematic properties from those in the signal region. The binning in η and p_T ensures that these two key variables are well-modelled. The distribution of the remaining variables is assumed to be the same between objects passing and failing the photon ID cuts. This assumption is found to work well when the distributions from the data-driven method are compared to data in the validation of the data-driven procedure, illustrated later in this section.

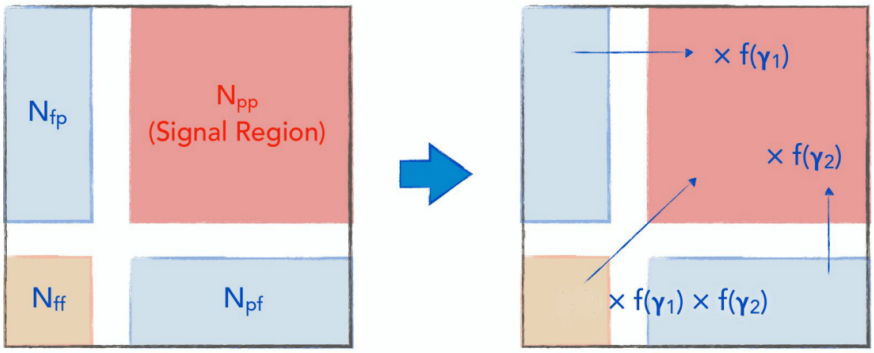

Figure 5.7: A schematic of how fake factors can provide a link between the number of γ-jet and jet-jet events in the control and signal regions.

The fake factors are applied to the weights of the events in the control regions in data (Figure 5.7) as follows:

- if the data event falls in the **reco fake-prompt region** in data, the $f(\gamma_1)$ factor (derived from MC γ-jet events) is applied.
- if the data event falls in the **reco prompt-fake region** in data, the $f(\gamma_2)$ factor (derived from MC γ-jet events) is applied.
- if the data event falls in the **reco fake-fake region** in data, a $f(\gamma_1) \times f(\gamma_2)$ factor (derived from MC jet-jet events) is applied. The two factors are assumed not to be correlated for the purpose of this method so the product is used. The data-driven validation procedure shows that this method works well.

For illustration the fake factors are shown for simulation samples for the year 2018 for the VBF backgrounds (Figure 5.8) and VH backgrounds (Figure 5.9). The fake factors derived for the years 2017 and 2016 may be found in Appendix B (C) for VBF (VH) selections. Although, some of the errors on the fake factors are large, varying the fake factors within the errors was not found to affect the agreement with data as later shown in the validation of the data-driven method.

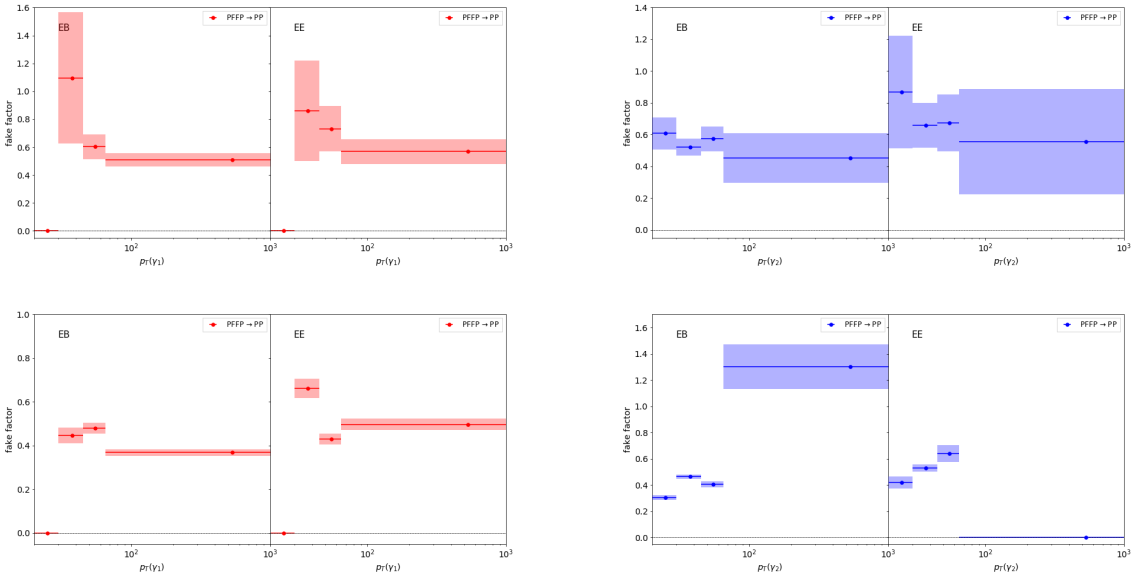

Figure 5.8: VBF $f(\gamma_1)$ factors (left) and $f(\gamma_2)$ factors (right) derived from γ-jet (top) and jet-jet (bottom) simulation samples for the year 2018. The $f(\gamma_1)$ and $f(\gamma_2)$ factors are binned in the η and p_T of the lead and sublead photon respectively.

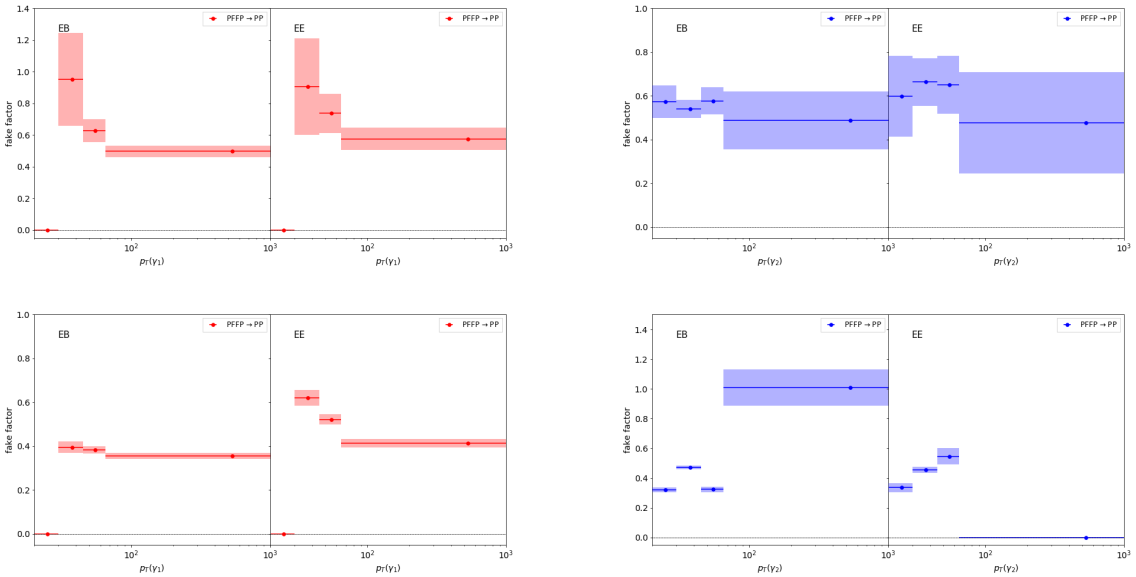

Figure 5.9: VH $f(\gamma_1)$ factors (left) and $f(\gamma_2)$ factors (right) derived from γ-jet (top two) and jet-jet (bottom two) simulation samples for the year 2018. The $f(\gamma_1)$ and $f(\gamma_2)$ factors are binned in the η and p_T of the lead and sublead photon respectively.

QCD purity fractions are also derived from simulation samples. The reason that number is needed is because when the fake factors are applied to the control regions in data, only the γ-jet and jet-jet samples need to be replaced. However, control regions data samples also contain real $\gamma\gamma$ events. The QCD fractions are derived on a per-photon basis; there is a fraction for the lead photon $p(\gamma_1)$ and one for the sublead photon $p(\gamma_2)$. Both fractions are defined as

$$p(\gamma_i) = p(\eta(\gamma_i), p_T(\gamma_i)) = \left(\frac{N_{j\gamma}^{CR} + N_{jj}^{CR}}{N_{\gamma\gamma}^{CR} + N_{j\gamma}^{CR} + N_{jj}^{CR}} \right)_{MC} \quad i = 1, 2 \ . \tag{5.2}$$

For $p(\gamma_1)$, the fraction is binned in the η and p_T of the lead photon. For $p(\gamma_2)$, the fraction is binned in the η and p_T of the sublead photon. The factors are applied to the weights of the events in the control regions in data as follows:

- if the data event falls in the **reco fake-prompt region** in data, the $p(\gamma_1)$ factor is applied.
- if the data event falls in the **reco prompt-fake region** in data, the $p(\gamma_2)$ factor is applied.
- if the data event falls in the **reco fake-fake region** in data, a $p(\gamma_1) \times p(\gamma_2)$ factor is applied.

For illustration the QCD fractions are shown for simulation samples for the year 2018 for the VBF backgrounds (Figure 5.10) and VH backgrounds (Figure 5.11). The QCD fractions derived for the years 2017 and 2016 may be found in Appendix B (C) for VBF (VH) selections. Although, some of the errors on the fake factors are large, varying the fake factors within the errors was not found to affect the agreement with data as later shown in the validation of the data-driven method.

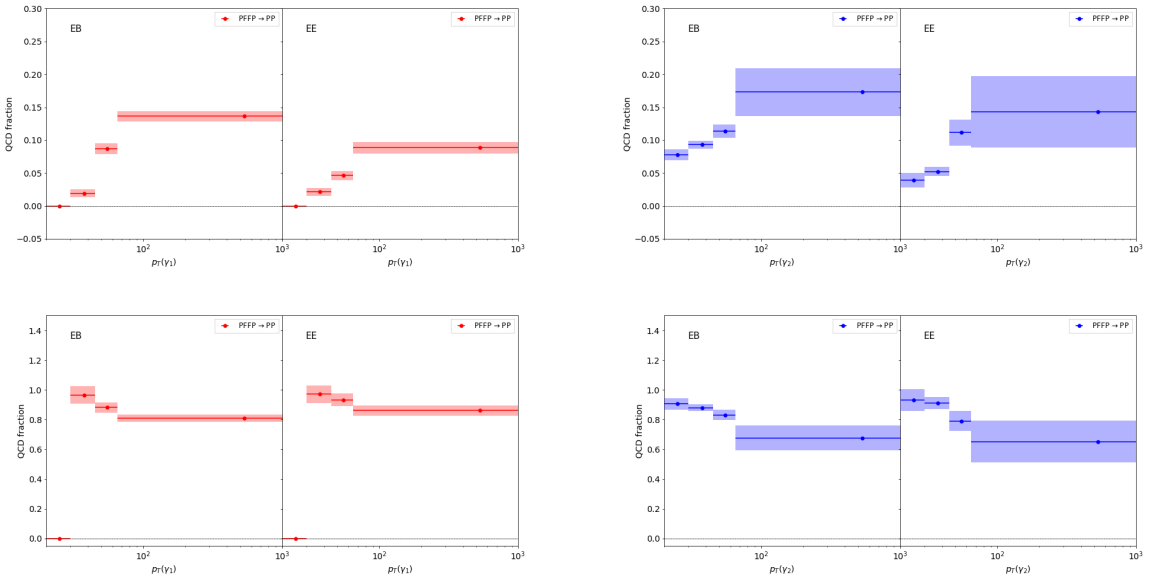

Figure 5.10: VBF $p(\gamma_1)$ factors (left) and $p(\gamma_2)$ factors (right) from γ-jet (top two) and jet-jet (bottom two) simulation samples for the year 2018. The $p(\gamma_1)$ factors and $p(\gamma_2)$ factors are binned in the η and p_T of the lead and sublead photon respectively.

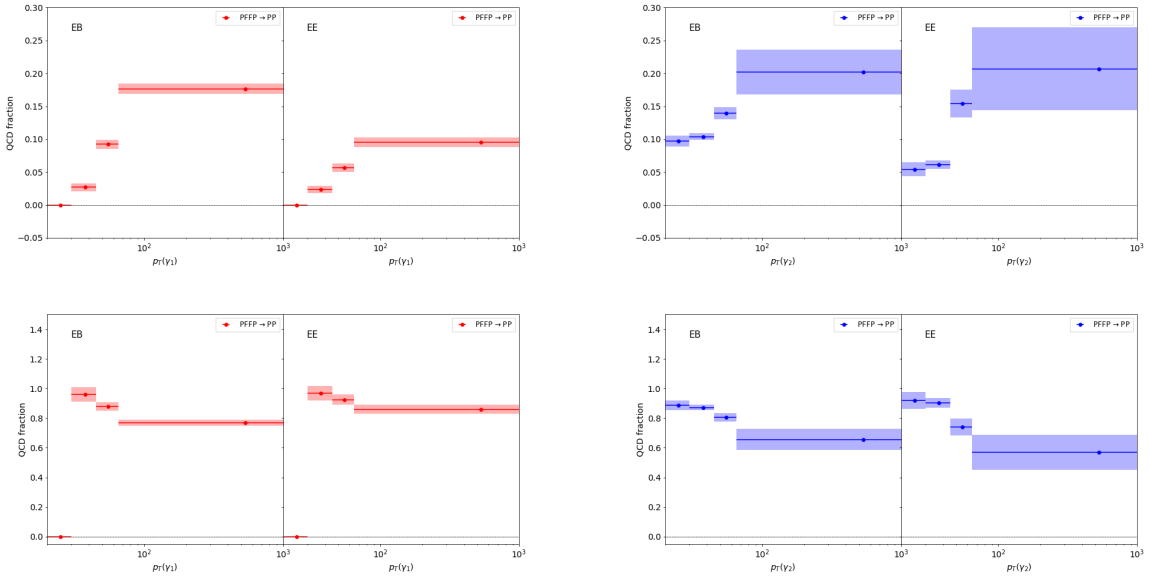

Figure 5.11: VH $p(\gamma_1)$ factors (left) and $p(\gamma_2)$ factors (right) from γ-jet (top two) and jet-jet (bottom two) simulation samples for the year 2018. The $p(\gamma_1)$ factors and $p(\gamma_2)$ factors are binned in the η and p_T of the lead amd sublead photon respectively.

The fake factors and QCD fractions, once extracted from simulated events, are applied to the control regions in data as event weights w_{event}. The fake factors are applied as events weights as a function of the leading and the sub-leading photons kinematics and are given by

$$w_{event} = \begin{cases} p(\eta(\gamma_1), p_T(\gamma_1)) \times f(\eta(\gamma_1), p_T(\gamma_1)), & \in \text{FP} \\ p(\eta(\gamma_2), p_T(\gamma_2)) \times f(\eta(\gamma_2), p_T(\gamma_2)), & \in \text{PF} \\ p(\eta(\gamma_1), p_T(\gamma_1)) \times f(\eta(\gamma_1), p_T(\gamma_1)) \times p(\eta(\gamma_2), p_T(\gamma_2)) \times f(\eta(\gamma_2), p_T(\gamma_2)), & \in \text{FF} \end{cases} \tag{5.3}$$

These reweighted events are subsequently used to train the respective BDTs. A schematic illustrating the application of the data-driven procedure is shown in Figure 5.12 to summarise the steps.

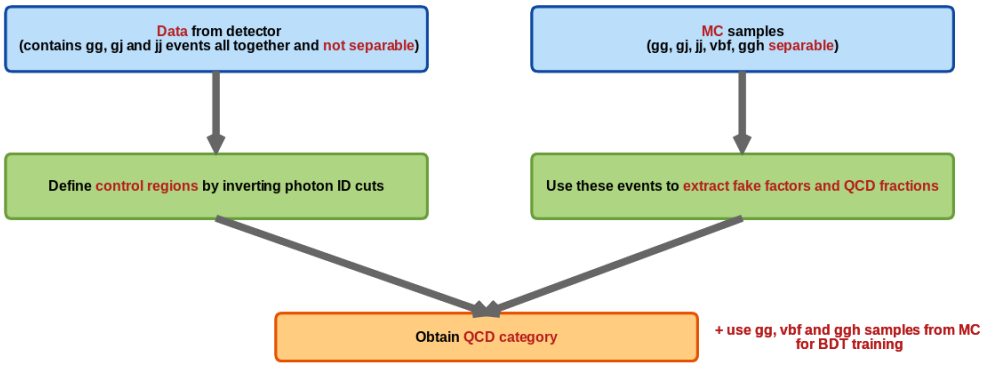

Figure 5.12: A schematic illustrating the application of the data-driven procedure to derive a *QCD* sample with sufficient observations to train BDTs used in the categorisation.

Once the factors have been applied, it is verified that the input variables of interest (used in BDTs) are better modelled with the data-driven procedure than with using simulation

samples only. This validation procedure helps to also verify the assumptions made during the derivation of the fake factors and the QCD fractions. For illustration, validation plots for the year 2018 for variables used in training BDTs and for some additional diphoton variables are shown in Figure 5.12 for VBF and in Figure 5.12 for VH hadronic selections. The corresponding 2016 and 2017 validations are included in Appendix B (C) for VBF (VH hadronic) selections.

It can be seen that variable distributions are better modelled with the "data-driven + Monte Carlo" (DD+MC) method (ratio plot with black dots) than with MC only (ratio plot with blue dots); a better agreement between data and background is obtained when the data-driven method is used. Note that the overall normalisation is of no importance in these plots since class weights are normalised before BDT training as discussed later in this chapter; only the shapes of the distributions matter. Allowing the fake factors and QCD purity fractions to vary within their errors was found not to change these distributions significantly. Within these variations, the DD+MC method still consistently outperforms the MC-only method. Note that the blue shaded error bars are the errors are from the simulated diphoton, γ-jet and jet-jet samples. When there are only a few γ-jet and jet-jet events, the diphoton error dominates. Since there are enough diphoton events in simulation, the weights are low and the error is tiny. When there are many γ-jet and jet-jet events, the γ-jet and jet-jet weights dominate; these are high and result in large errors.

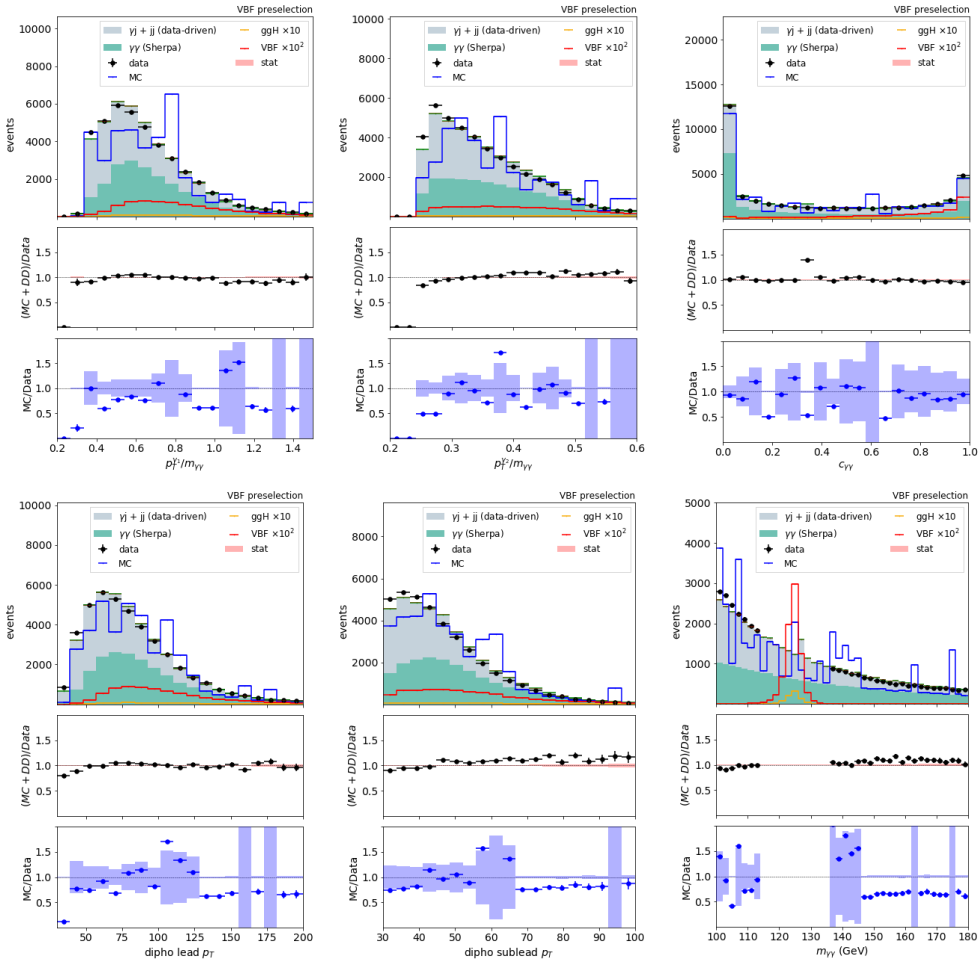

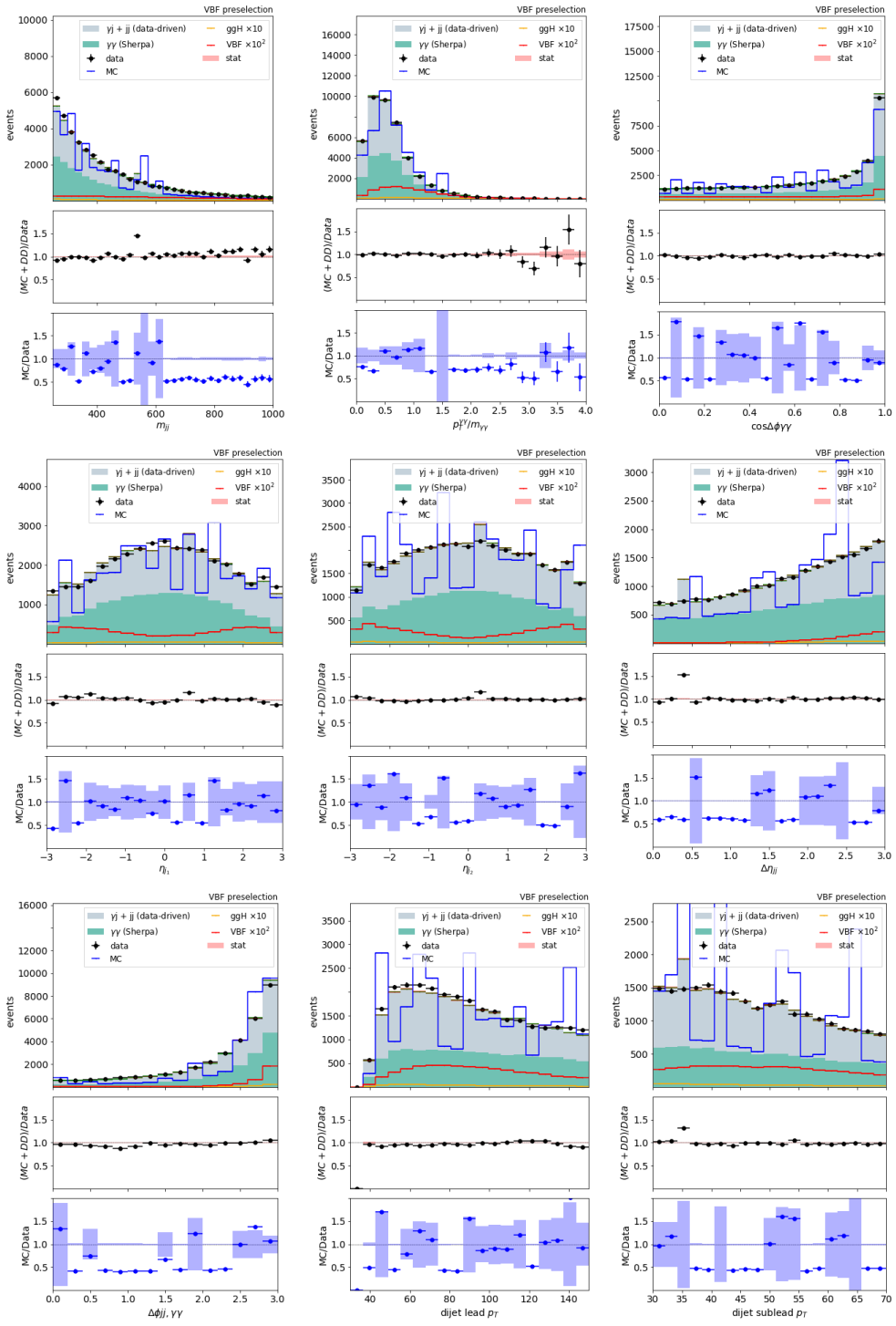

Figure 5.12: 2018 validation of the data-driven method on various kinematics variables relevant to the VBF BDT. The data points represent data outside the Higgs boson mass window (115-125 GeV) and satisfying the VBF preselection criteria. The DD+MC method is compared to data in the ratio plot with black dots while the MC-only method is compared to data in the ratio plot with blue dots.

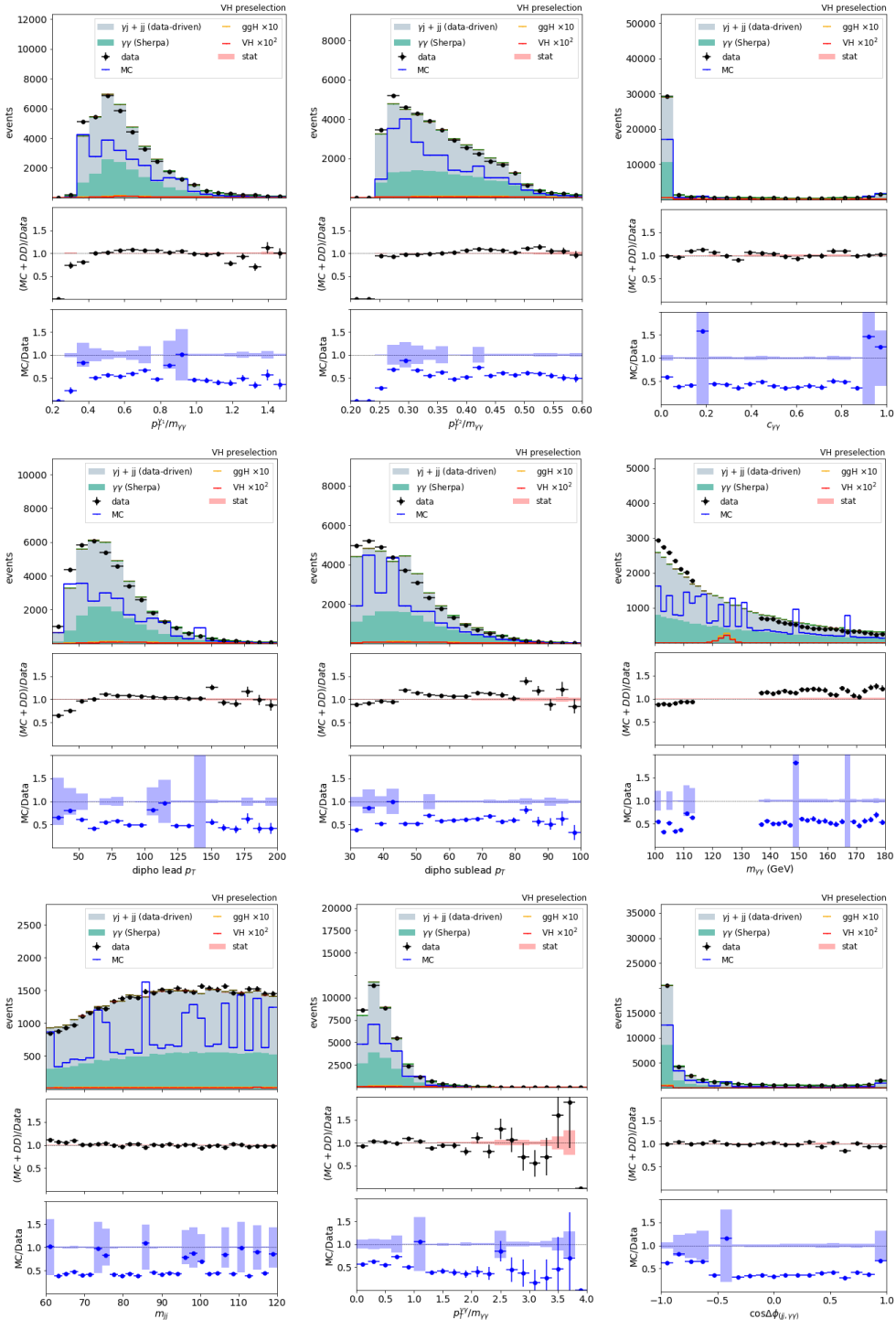
VH preselection
γj + jj (data-driven)
γγ (Sherpa)
data
MC
ggH ×10
VH ×10²
stat
events
(MC + DD)/Data
MC/Data
$p_T^{\gamma\gamma}/m_{\gamma\gamma}$
$c_{\gamma\gamma}$
dipho lead p_T
dipho sublead p_T
$m_{\gamma\gamma}$ (GeV)
m_{jj}
$p_T^{\gamma\gamma}/m_{\gamma\gamma}$
$\cos\Delta\phi_{(jj,\gamma\gamma)}$

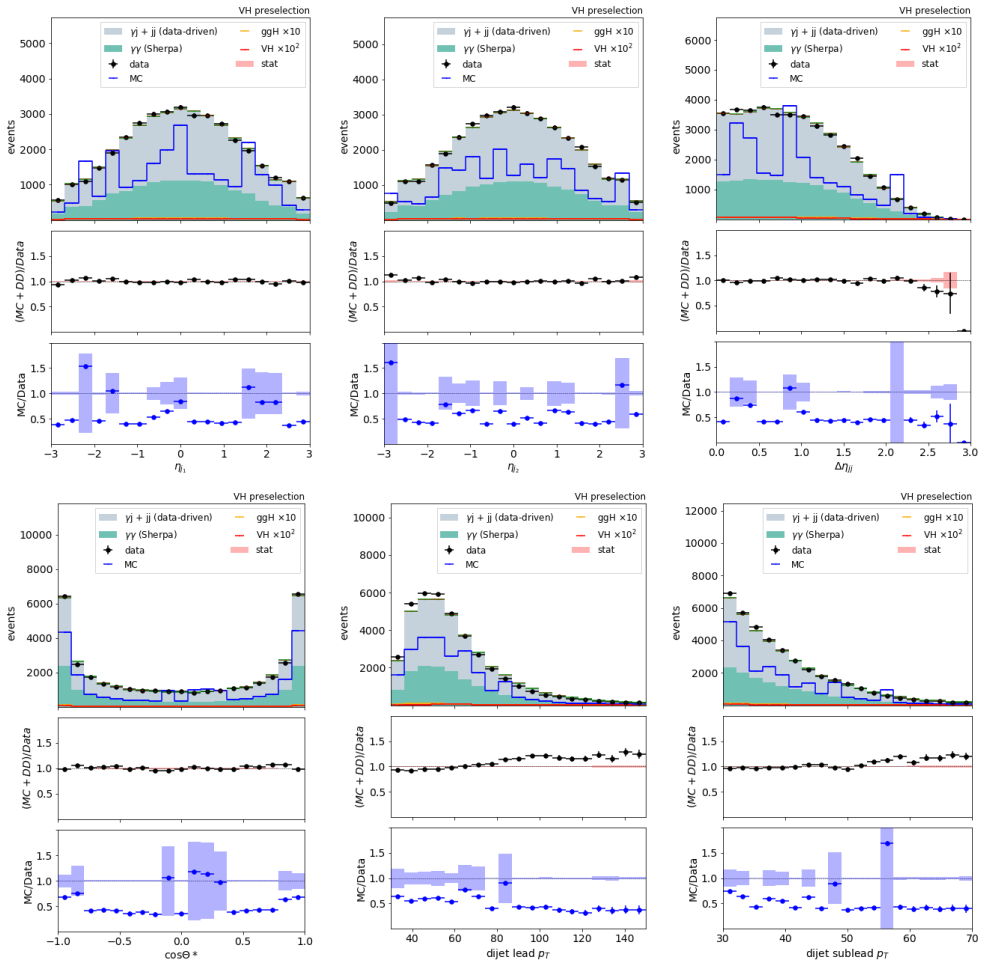

Figure 5.12: 2018 validation of the data-driven method on various kinematics variables relevant to the VH BDT. The data points represent data outside the Higgs boson mass window (115-125 GeV) and satisfying the VH preselection criteria. The DD+MC method is compared to data in the ratio plot with black dots while the MC-only method is compared to data in the ratio plot with blue dots.

5.5.4 VBF categorisation

In this analysis, a similar approach to previous analyses [3, 106] is used for VBF categorisation; a dedicated BDT is constructed to separate VBF from ggH and non-Higgs backgrounds. However, in this analysis, the BDT implemented comprises of three classes compared to the binary BDT used in the previous analyses. To train this *multi-class* BDT, simulation events passing the full VBF preselection are divided into three classes, namely VBF signal, ggH background, and non-Higgs backgrounds, each treated separately. The simulated non-Higgs backgrounds where at least one photon is not prompt are replaced using the data-driven method described in the previous section.

The inputs to the BDT include various jet kinematic and angular variables, as well as the $p_T/m_{\gamma\gamma}$ of each photon and angular variables involving both jets and photons. These input variable distributions for ggH are significantly different to those from non-Higgs backgrounds.

Thus it would be sub-optimal to leave ggH events out of the BDT training process or to consider them together with non-Higgs backgrounds. In previous analyses, various attempts have been made to optimally separate the VBF signal from these two distinct sources of background. In the 2016 analysis [106], a BDT with VBF trained against both ggH and non-Higgs background was trained first. Subsequently, a combined BDT was trained using the output of the dijet BDT together with the diphoton BDT, but omitting ggH from the training. However, in the 2016+2017 analysis [3], this approach was found not to perform as well as simply placing thresholds on the VBF and diphoton BDTs directly.

The use of a multi-class BDT, as described in this section, enables the construction of a dedicated category targeting VBF-like ggH production for the first time in the STXS analysis. The multi-class VBF BDT is trained to estimate the probability that an event passing the VBF preselection originated from VBF, ggH, or non-Higgs boson backgrounds. Categories are constructed using cuts on the BDT output probabilities, together with cuts on the diphoton BDT. The final categorisation therefore uses cuts on three outputs: the VBF probability, the ggH probability, and the diphoton BDT score. The non-Higgs background score is not used since it is determined once the VBF and ggH probabilities are specified. For categories targeting VBF production, the event is required to have a VBF score greater than a threshold, and a ggH score below a threshold. For the categories targeting VBF-like ggH processes, the opposite is true. Optimisation of these thresholds are also discussed in this section.

The parameters of the multi-class VBF BDT, trained on simulation events, are propagated to the main CMS analysis software, to be used on real data during the categorisation process.

Input variables to the VBF BDT

The inputs to the VBF BDT are chosen to maximise the discrimination of the VBF signal. These include various jet kinematic and angular variables, as well as the $p_T/m_{\gamma\gamma}$ of each photon, and angular variables involving both jets and photons. Additionally, a centrality variable $c_{\gamma\gamma}$, dependent on the pseudo-rapidities of the jets (η_1, η_2) and the diphoton system $(\eta_{\gamma\gamma})$, is used to introduce an idea of the compatibility between the di-jet and diphoton systems. The dijet centrality variable is defined as:

$$c_{\gamma\gamma} = exp\left(-\frac{4}{(\eta_1 - \eta_2)^2}\left(\eta_{\gamma\gamma} - \frac{\eta_1 + \eta_2}{2}\right)^2\right) \tag{5.4}$$

The list of input variables to the VBF BDT is given below:

- the transverse momentum of the lead photon divided by the diphoton invariant mass $(p_T^{\gamma_1}/m_{\gamma\gamma})$
- the transverse momentum of the sublead photon divided by the diphoton invariant mass $(p_T^{\gamma_2}/m_{\gamma\gamma})$
- the transverse momentum of the lead jet $(p_T^{j_1})$
- the transverse momentum of the sublead jet $(p_T^{j_2})$
- the dijet invariant mass (m_{jj})

- the difference in pseudorapidity of the leading and subleading jets ($\Delta\eta_{jj}$)
- the minimum distance between the leading (or subleading) jet and lead (or sublead) photon ($\Delta R_{min}(\gamma, j)$), this is to veto photons reconstructed as jets
- the difference in ϕ between the lead and sublead jets ($\Delta\phi_{jj}$)
- the difference in ϕ between di-jet and diphoton systems ($\Delta\phi_{jj,\gamma\gamma}$)
- the dijet centrality variable ($c_{\gamma\gamma}$)

The full set of normalised distributions for the input variables of the three class VBF BDT are shown in Figure 5.12. The plots highlight the differences between the VBF, ggH and non-Higgs background processes; this motivates the separation of these three classes in the classifier. The non-Higgs background processes considered here include γ-jet, jet-jet and γ-γ events. All events are required to pass the full VBF preselection and the PUJID cuts. These normalised distributions are representative of the direct BDT inputs since the three class weights are equalised during the BDT training. During the training, the region $115 < m_{\gamma\gamma} < 135$ GeV was removed.

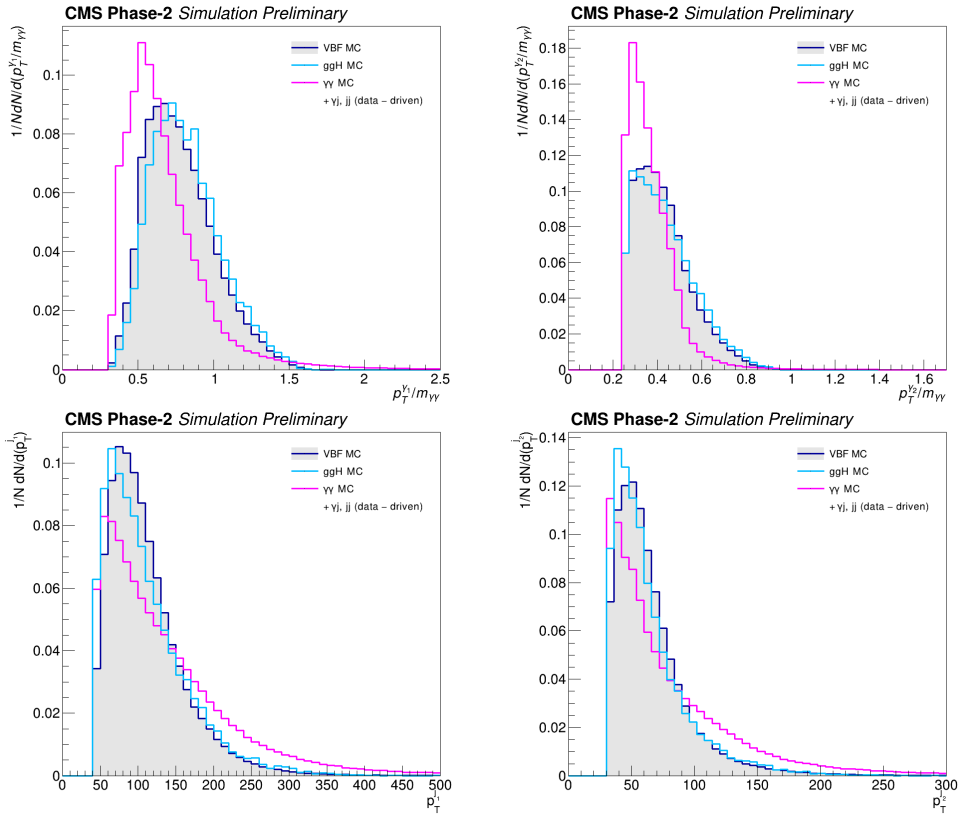

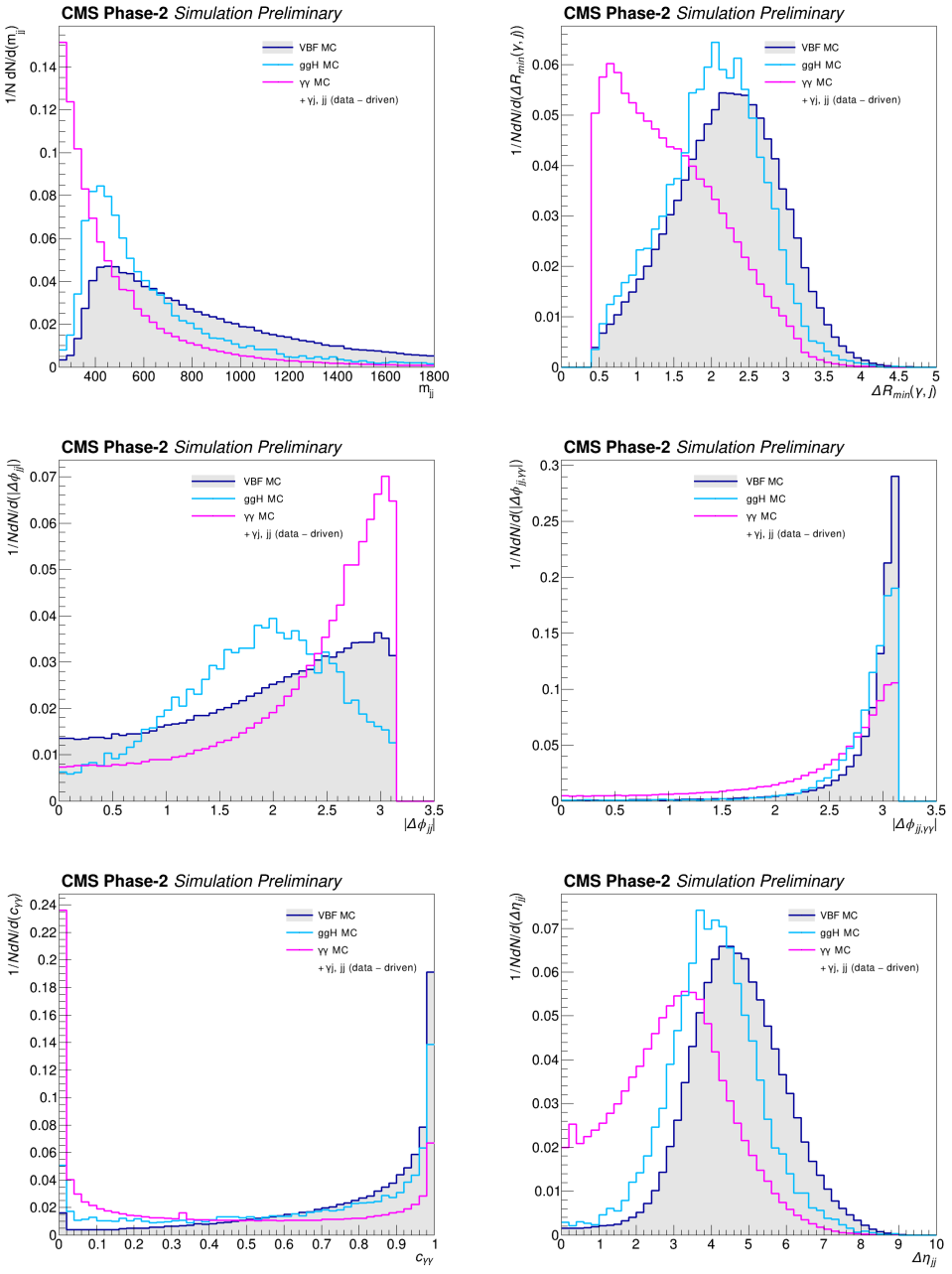

Figure 5.12: Distributions of the input variables to the VBF BDT for the combination of the 2016, 2017, and 2018 datasets.

Training and validation of the VBF BDT

The VBF BDT is trained to discriminate between three classes, namely VBF, ggH and non-Higgs backgrounds. The latter are is a mixture of diphoton, γ-jet and jet-jet processes, where the data-driven background sample is used for γ-jet and jet-jet events, The weights of all three classes are equalised in training the BDT so that there is no bias towards the statistically dominant process. The BDT is implemented as a Gradient-Boosted Classifier (GBC) in *XGBoost* [164]. A range of hyper-parameters of the BDT are studied in order to maximise the performance. The effect of changing the input variables or the BDT hyperparameters may be gauged by monitoring the loss function or the receiver operating characteristic (ROC) curves, discussed later in this section. Of the set of hyper-parameters studied, a train/test split of 90%/10%, a learning rate of 0.2, and a maximum tree depth 6, with all other parameters set to default were found to give optimal performance [1]. The loss function that quantifies model performance is the multi-class logarithmic loss function, otherwise known as the cross-entropy. The cross-entropy increases as the predicted probability diverges from the true class label, resulting in more penalisation for models that predict class probabilities far from the true values.

BDT score distributions for the three classes are shown in Figures 5.13, 5.14 and 5.15. The figures also compare the results of training the VBF BDT on MC-only backgrounds, without the data-driven procedure applied. As expected, the truth VBF, ggH and non-Higgs background processes receive the highest VBF, ggH and background scores respectively. With the data-driven process included in the training inputs, it can be seen that the total simulated background agrees well with the data. This serves as a validation that the simulated background processes used to train the BDT are well modelled.

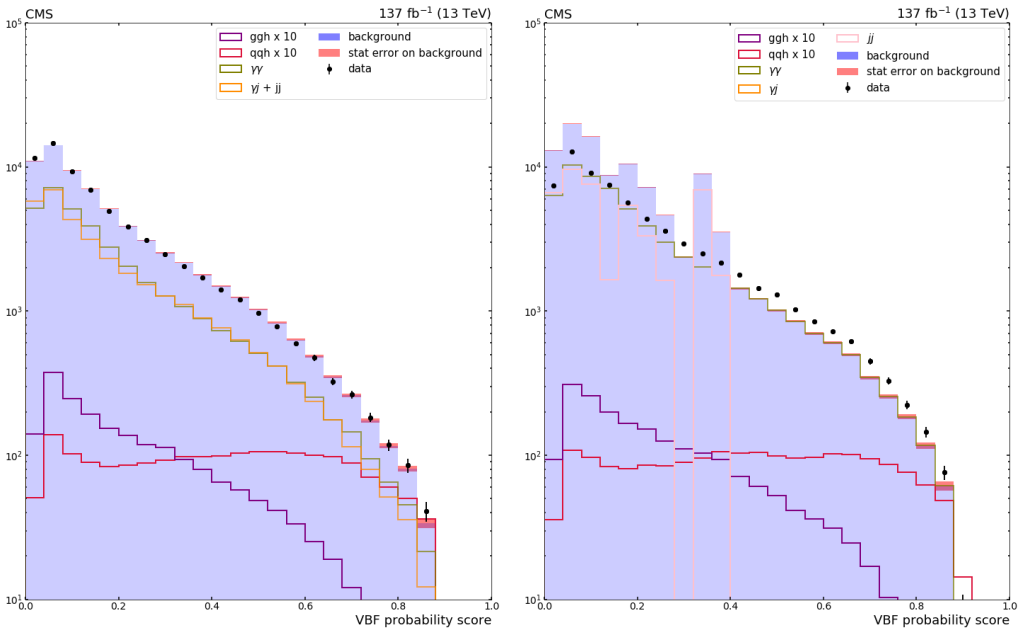

Figure 5.13: VBF BDT VBF score distribution for data events passing the VBF preselection (black points), and for simulated background events (blue filled histogram). In the left (right) plot, the data-driven background modelling is (not) used. Here, "ggh" denotes the ggH process and "qqh" denotes VBF events and VH events which fall in the VBF STXS regions.

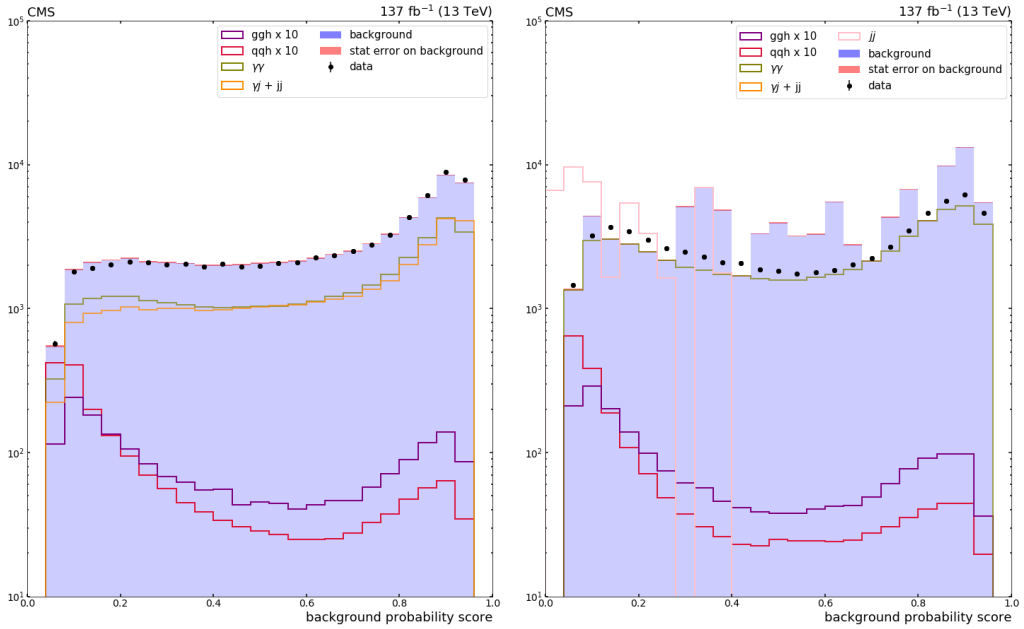

Figure 5.14: VBF BDT background score distribution for data events passing the VBF preselection (black points), and for simulated background events (blue filled histogram). In the left (right) plot, the data-driven background modelling is (not) used. Here, "ggh" denotes the ggH process and "qqh" denotes VBF events and VH events which fall in the VBF STXS regions.

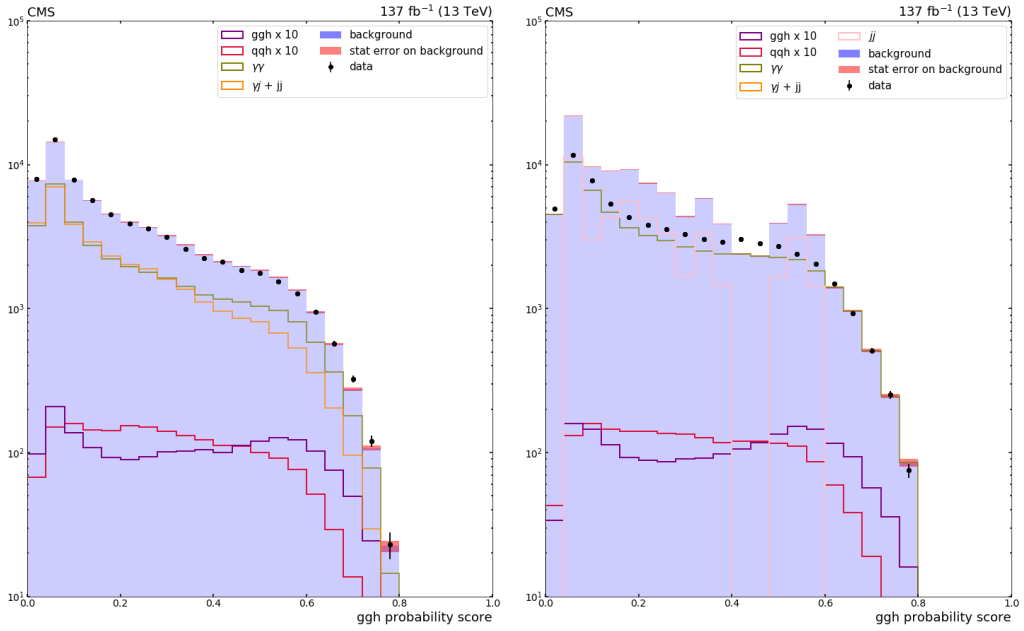

Figure 5.15: VBF BDT ggH score distribution for data events passing the VBF preselection (black points), and for simulated background events (blue filled histogram). In the left (right) plot, the data-driven background modelling is (not) used. Here, "ggh" denotes the ggH process and "qqh" denotes VBF events and VH events which fall in the VBF STXS regions.

A set of simulated events, generated in the same way as training events, are not used in the training but are used as an independent check of the generalisation ability of the trained VBF BDT. The result of the check is shown in Figures 5.16, 5.17 and 5.18, where it can be seen that the test samples have been scored in a similar way to training samples, confirming

that there has no over-training when the data-driven background modelling is used. These figures further illustrate the poor quality of training and lack of generalisation ability when the VBF BDT is trained on simulated samples only, without any data-driven background modelling.

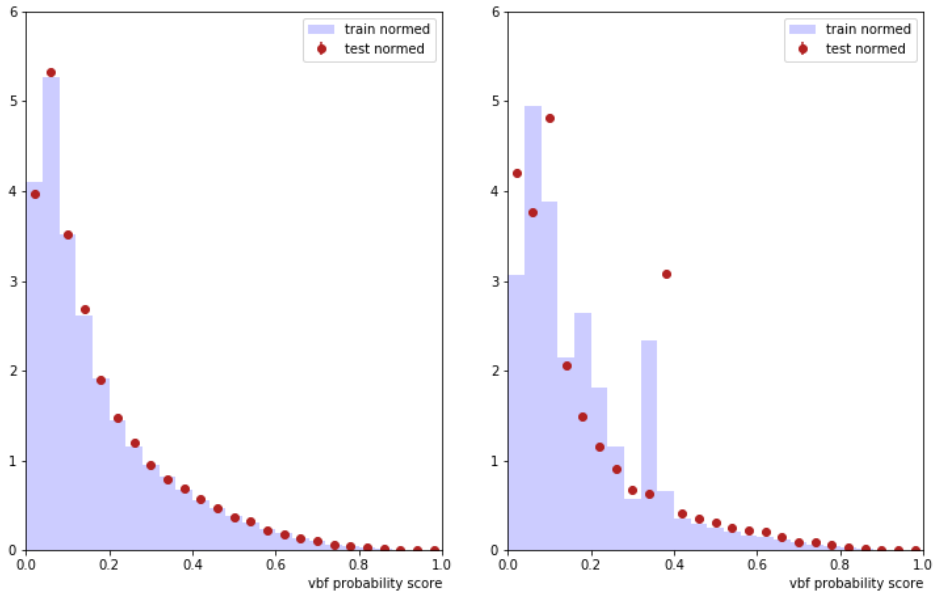

Figure 5.16: A comparison of the VBF BDT output VBF scores between the training sample (blue filled histogram) and the testing sample (red points) with (left) and without (right) the data-driven background modelling implemented.

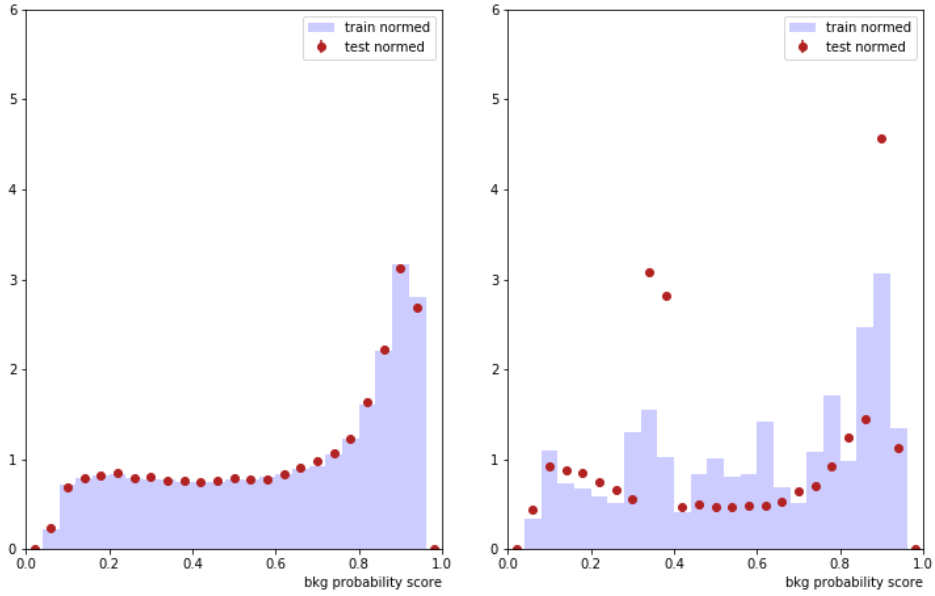

Figure 5.17: A comparison of the VBF BDT output background scores between the training sample (blue filled histogram) and the testing sample (red points) with (left) and without (right) the data-driven background modelling implemented.

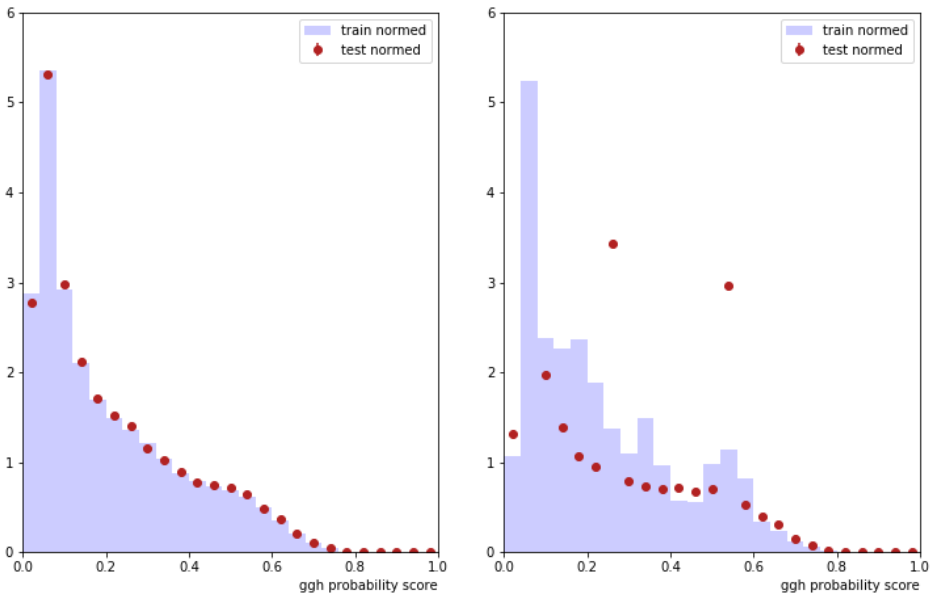

Figure 5.18: A comparison of the VBF BDT output ggH scores between the training sample (blue filled histogram) and the testing sample (red points) with (left) and without (right) the data-driven background modelling implemented.

The diagnostic decision-making capability of the VBF BDT may be investigated through receiver operating characteristic (ROC) curves. The probability that a true VBF event will be assigned to the VBF class (true positive rate) is plotted against the probability that an event from a different process (background or ggH) will be classified as VBF (false positive rate) for different decision thresholds. These rates are representative of the network sensitivity and 1-specificity respectively. A classifier with a perfect discrimination capability would produce a ROC curve with 100% sensitivity and 100% specificity that passes through the upper left corner of the ROC plot. The area under a ROC curve, referred to as AUC, corresponds to the average value of sensitivity over all specificity values or the average specificity over all sensitivity values. Hence when the classifier is unable to distinguish between two classes, the AUC is equal to 0.5 and the ROC curve coincides with the diagonal. However, for perfect classification, the AUC is equal to 1 [165, 166]. ROC performances are evaluated both on the testing and training samples and, if there is no overtraining, the two curves should be similar. The ROC curves for the individual VBF, ggH and background classes are shown in Figures 5.19, 5.20 and 5.21. These figures also include comparisons to the case where the data-driven background modelling is not implemented.

It is clear that the use of the data-driven samples results in better discrimination and less overtraining. The ROC curves give an idea of the sensitivity and specificity achievable at different cuts on the output probabilities. This helps in understanding the cuts later defined to construct the VBF categories

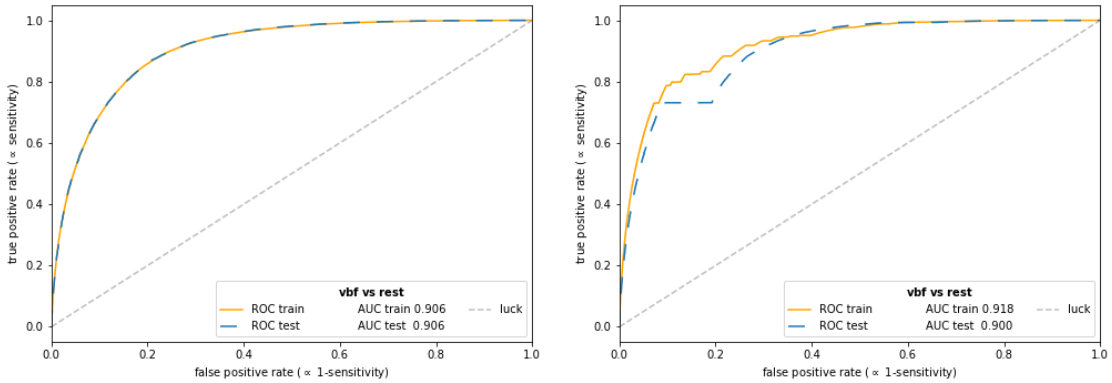

Figure 5.19: ROC curves for the VBF class versus the ggH and background classes with the training (solid yellow line) and testing (dashed blue line) datasets with (left) and without (right) the data-driven background modelling implemented.

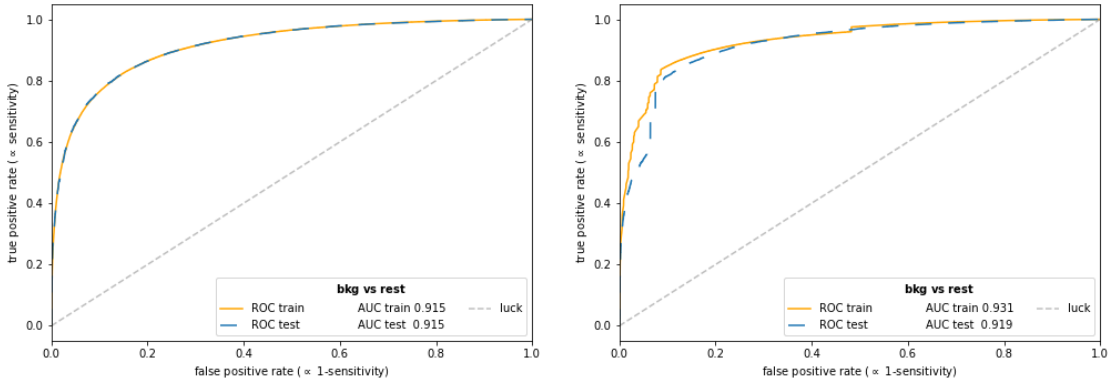

Figure 5.20: ROC curves for the background class versus the ggH and VBF classes with the training (solid yellow line) and testing (dashed blue line) datasets with (left) and without (right) the data-driven background modelling implemented.

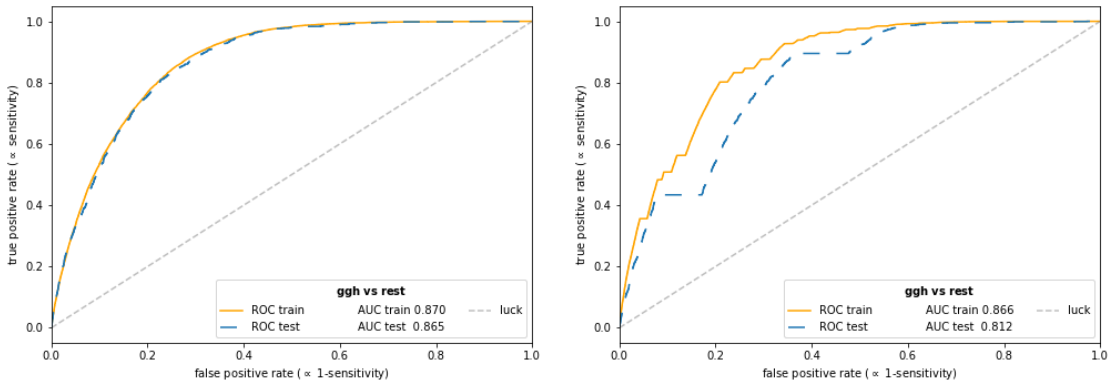

Figure 5.21: ROC curves for the ggH class versus the VBF and background classes with the training (solid yellow line) and testing (dashed blue line) datasets with (left) and without (right) the data-driven background modelling implemented.

.

In this analysis the signal model is taken from simulation. Therefore it is necessary to ensure that there is reasonable agreement between data and simulation for signal-like objects, for both the inputs to the diphoton BDT and the output score itself. Drell-Yan $Z \to ee$ events, where the electrons are reconstructed as photons, are used to verify that the input signal is properly simulated. The $Z \to ee$ events are selected through an inverted electron veto while the trajectories from the electrons in the tracker are not considered in the reconstruction. The invariant mass of the electron pair is required to lie within the Z boson mass window (80-100 GeV). Drell-Yan processes are chosen for this validation since electron and photon showers are similar and the $Z \to ee$ decay is relatively free from backgrounds. All shower shape and photon isolation corrections discussed in the reconstruction (Section 5.2) are applied. A minimal re-weighting of simulated samples to match data, in bins of $p_{T,\mathrm{ee}}$ is applied, such that the simulated sample agrees with data by construction for this variable. This is designed to correct for known p_T mis-modelling in simulation, and improves agreement in BDT inputs correlated with $p_{T,\mathrm{ee}}$. The VBF preselection criteria required to enter the VBF-like analysis categories are also applied to the $Z \to ee$ events. Key systematics affecting the input variables are included in the systematic band. These are the uncertainties on the photon IDMVA, the σ_E/E shift (where σ_E is the photon energy resolution and E is the photon energy), and on the jet energy scale and resolution corrections (JES and JER respectively).

The output score distribution for the BDT signal validation is shown in Figure 5.22 for each of the three classes for the combinatation of data taken in 2016, 2017, and 2018. Reasonable agreement between data and MC is observed, and discrepancies are mostly covered by the systematic uncertainties. Similar plots for all the VBF BDT input variables can be found in Appendix B. The principal sources of di-jet systematic uncertainties are jet reconstruction and pile-up jet identification efficiency. The latter is largely affected by uncertainties on parton distribution functions and the QCD scale factor. Both the jet energy scale (JES) and the jet energy resolution (JER) contribute to the jet reconstruction efficiency. The jet energy scale may be shifted by $\pm 1\sigma$ to estimate JES systematics, while JER systematics are evaluated by comparing the average width of the jet p_T distributions at generator and reconstruction level ($p_{T_{true}} - p_{T_{reco}}$) for jets in simulation. The migration of events in and out of di-jet categories as a result of the mentioned jet reconstruction systematics are also separately considered. The differences between data and simulation in the p_T and η distributions for $Z + 1$ jet events are further used to find the shift required in order to cover the data/simulation disagreement and estimate pile-up jet identification systematics. Additional studies have shown that without PUJID, low p_T jets and high η jets enter the analysis, such that the resulting JEC are larger. Large JECs in the plots have been shown to come from cases where at least one of the jets is at $\mid \eta \mid > 2.5$.

Boundary optimisation for VBF categories

Each of five STXS VBF bins are targeted individually while the four STXS VBF-like ggH bins are targeted as a group. For each of the target regions, two categories (tags) are defined by simultaneously optimising cuts on the BDT VBF and ggH output probabilities and the diphoton BDT score. The VBF score is maximised when targeting VBF-like VBF bins and minimised when targeting the VBF-like ggH bins. The ggH score is minimised when targeting VBF-like VBF bins and maximised when targeting the VBF-like ggH bins. Boundary values

in a three-dimensional volume, where each dimension corresponds to a choice of boundary, are evaluated. The point giving the highest overall significance (Equation 5.5) in the target region is chosen. The parameter b_{reg} is set to 3.

$$Z_0 = \sqrt{2\left((s+b+b_{reg})\ln\left(1+\frac{s}{b+b_{reg}}\right)-s\right)} \tag{5.5}$$

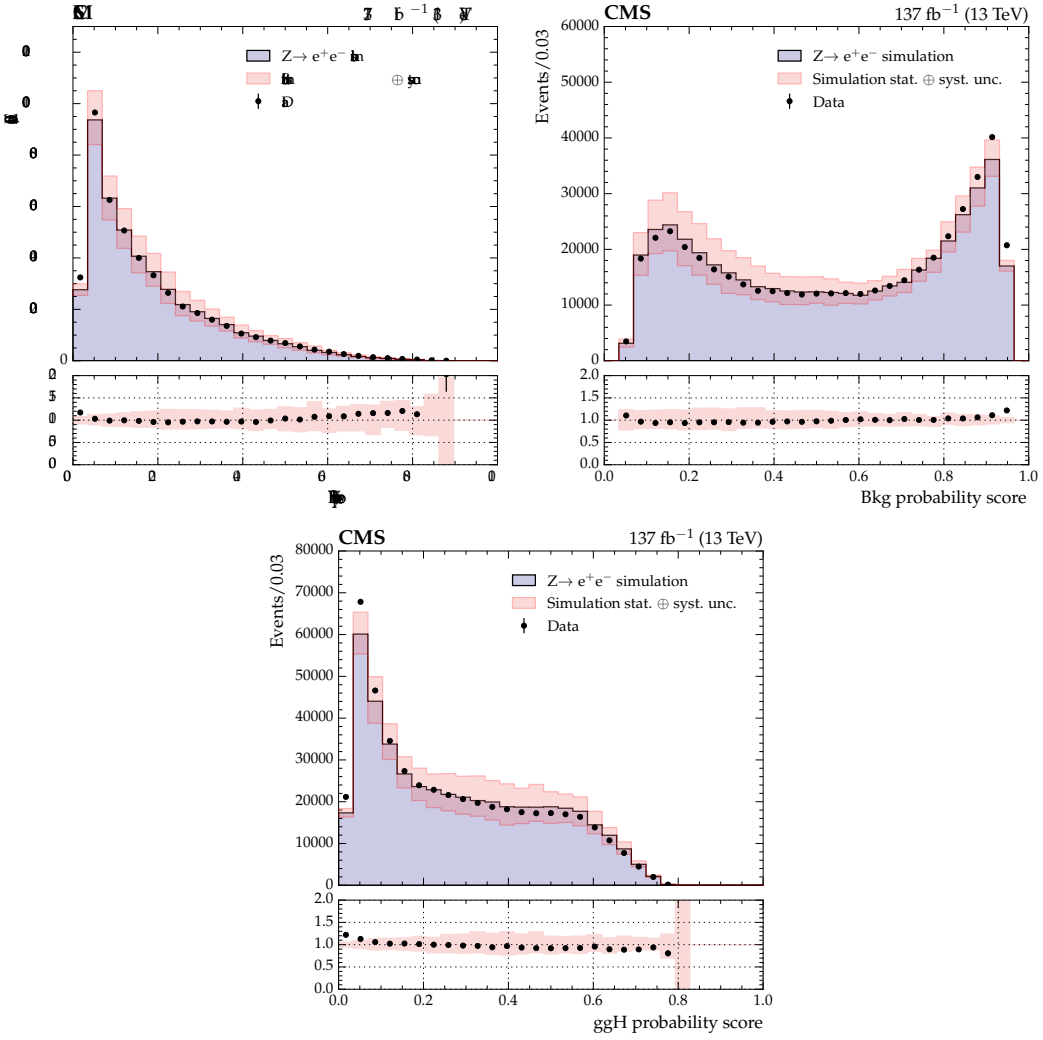

Figure 5.22: The score distributions for the VBF, ggH, and background classes, from the VBF BDT classifier in the $Z \to ee$ control region. The DY simulation (grey histogram) is compared to data taken in 2016, 2017, and 2018 (black points) for each output score.

The optimised cuts defining each of the VBF-like categories is shown in Table 5.4 (with data-driven background modelling) and in Table 5.5 (without data-driven background modelling), together with the expected composition and significances. The signal yields shown in the table are extracted by fitting a simulated signal model to simulation signal events and integrating in a window of $125 \pm \sigma_{eff}$. The background yield is derived by fitting a smoothly falling function to data and and integrating in a window of $125 \pm \sigma_{eff}$, where the σ_{eff} is defined as the smallest interval containing 68.3% of the $m_{\gamma\gamma}$ distribution. The expected VBF significance, obtained from summing individual VBF STXS bin significances

in quadrature, is 5.8 (4.7) σ with (without) the data-driven modelling procedure applied. Thus, the data-driven modelling brings a substantial improvement (23% increase) in the inclusive VBF significance.

Table 5.4: The expected number of signal and background events, and the expected significance of each category in the VBF phase space for all years, resulting from cuts on the diphoton BDT, VBF probability, and ggH probability. The table also includes the VBF-like ggH process. The data-driven background modelling procedure has been applied.

Bin	Category	Diphoton BDT	VBF BDT		S	B	Significace	
			VBF probability	ggH probability				
low, low	Tag 0 Tag 1	0.800, 0.779	0.379, 0.279	0.565, 0.726	9.3 4.4	22.5 27.1	1.6 0.7	1.8
high, low	Tag 0 Tag 1	0.790, 0.606	0.410, 0.260	0.583, 0.919	5.5 5.4	42.5 372.4	0.7 0.2	0.8
low, high	Tag 0 Tag 1	0.826, 0.650	0.302, 0.137	0.928, 0.876	19.8 1.0	15.2 10.2	3.7 0.2	3.8
high, high	Tag 0 Tag 1	0.800, 0.774	0.611, 0.218	0.362, 0.742	9.3 10.1	16.3 65.6	1.8 1.1	2.2
VBF BSM	Tag 0 Tag 1	0.918, 0.509	0.268, 0.051	0.756, 0.965	10.8 3.3	7.5 13.1	2.9 0.8	3.0
VBF-like ggH	Tag 0 Tag 1	0.829, 0.720	0.599, 0.478	0.482, 0.319	14.0 17.5	154.1 1176.8	1.0 0.5	1.2

Table 5.5: The expected number of signal and background events, and the expected significance of each category in the VBF phase space for all years, resulting from cuts on the diphoton BDT, VBF probability, and ggH probability. The table also includes the VBF-like ggH process. The data-driven background modelling procedure has not been applied.

Bin	Category	Diphoton BDT	VBF BDT		S	B	Significance	
			VBF probability	ggH probability				
low, low	Tag 0 Tag1	0.827, 0.604	0.435, 0.370	0.657, 0.573	5.5 4.3	9.5 19.4	1.3 0.9	1.6
high, low	Tag 0 Tag 1	0.649, 0.636	0.460, 0.398	0.407, 0.698	2.3 1.7	21.4 21.7	0.4 0.3	0.5
low, high	Tag 0 Tag1	0.780, 0.595	0.752, 0.407	0.659, 0.539	4.5 18.4	4.4 31.2	1.4 2.8	3.1
high, high	Tag 0 Tag 1	0.783, 0.602	0.552, 0.390	0.413, 0.614	10.9 6.8	21.8 52.7	1.9 0.9	2.1
VBF BSM	Tag 0 Tag 1	0.795, 0.651	0.437, 0.356	0.661, 0.439	6.6 1.1	6.3 2.9	2.0 0.4	2.0
VBF-like ggH	Tag 0 Tag 1	0.835, 0.552	0.456, 0.510	0.663, 0.312	2.6 15.6	20.4 172.2	0.5 1.1	1.2

5.5.5 VH categorisation in the hadronic channel

Categories targeting the VH hadronic STXS Stage 1.2 bin are constructed using an additional dedicated BDT. This is trained with the VH hadronic simulated process as signal, and all other Higgs and non-Higgs processes treated trogether as background. As described in Section 5.5.3, the γ-jet and the jet-jet samples are replaced by a data-driven background sample. The diphoton BDT score and the score from the VH hadronic BDT are simultaneously optimised

to define the final analysis categories. The use of a BDT to target the VH hadronic STXS bin was not used in previous analyses. In particular, in Ref. [106], the bin was targeted through a simple cut-based selection on the jets from the hadronic decays of the vector bosons. These included cuts on the jet p_T, m_{jj} and a veto for electrons/photons reconstructed as jets. One of the important variables identified in Ref. [106] for the discrimination of VH hadronic from ggH was $\cos\theta^*$, the angle that the diphoton system makes, in the diphoton-dijet centre-of-mass frame, with respect to the direction of motion of the diphoton-dijet system in the lab frame. The distribution of this variable is rather uniform for VH events, while it is strongly peaked at 1 for background and events from ggH production (Figure 5.22).

Input variables to the VH hadronic BDT

The input variables for the VH hadronic BDT are very similar to those used in the VBF BDT. Variables that aid in identifying events consistent with the vector boson decay are added, including $\cos\theta^*$. The full list of input variables to the VH hadronic BDT are given below. These input distributions are shown for VH and background processes (including ggH) in Figure 5.22, for the combination of the 2016, 2017, and 2018 simulated samples. Good separation between classes is seen in inputs such as p_T and $\cos\theta^*$.

- the transverse momentum of the lead photon divided by the diphoton invariant mass ($p_T^{\gamma_1}/m_{\gamma\gamma}$)
- the transverse momentum of the subleading photon divided by the diphoton invariant mass ($p_T^{\gamma_2}/m_{\gamma\gamma}$)
- the transverse momenta of the two leading jets ($p_T^{j_1}$,$p_T^{j_2}$)
- the pseudorapidities of the two leading jets (η_{j_1},η_{j_2})
- the difference in pseudorapidity of the two leading jets ($\Delta\eta_{jj}$)
- the dijet invariant mass, m_{jj}
- $\cos\theta^*$, where θ is the angle that the diphoton system makes, in the diphoton-dijet centre-of-mass frame, with respect to the direction of motion of the diphoton-dijet system in the lab frame.

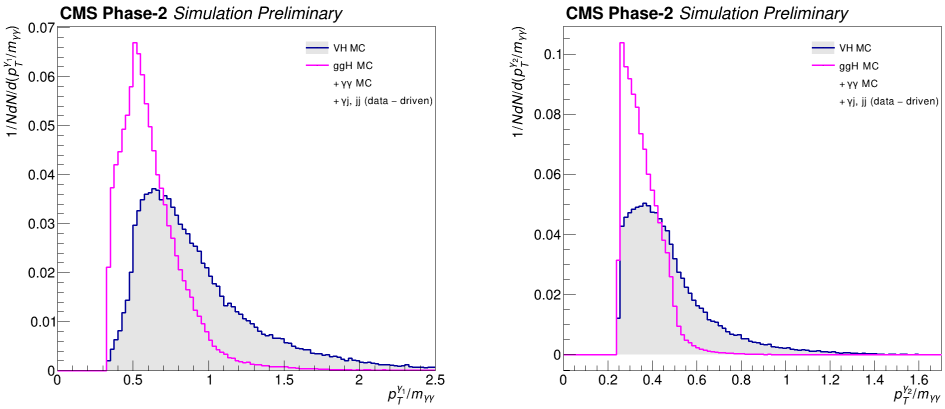

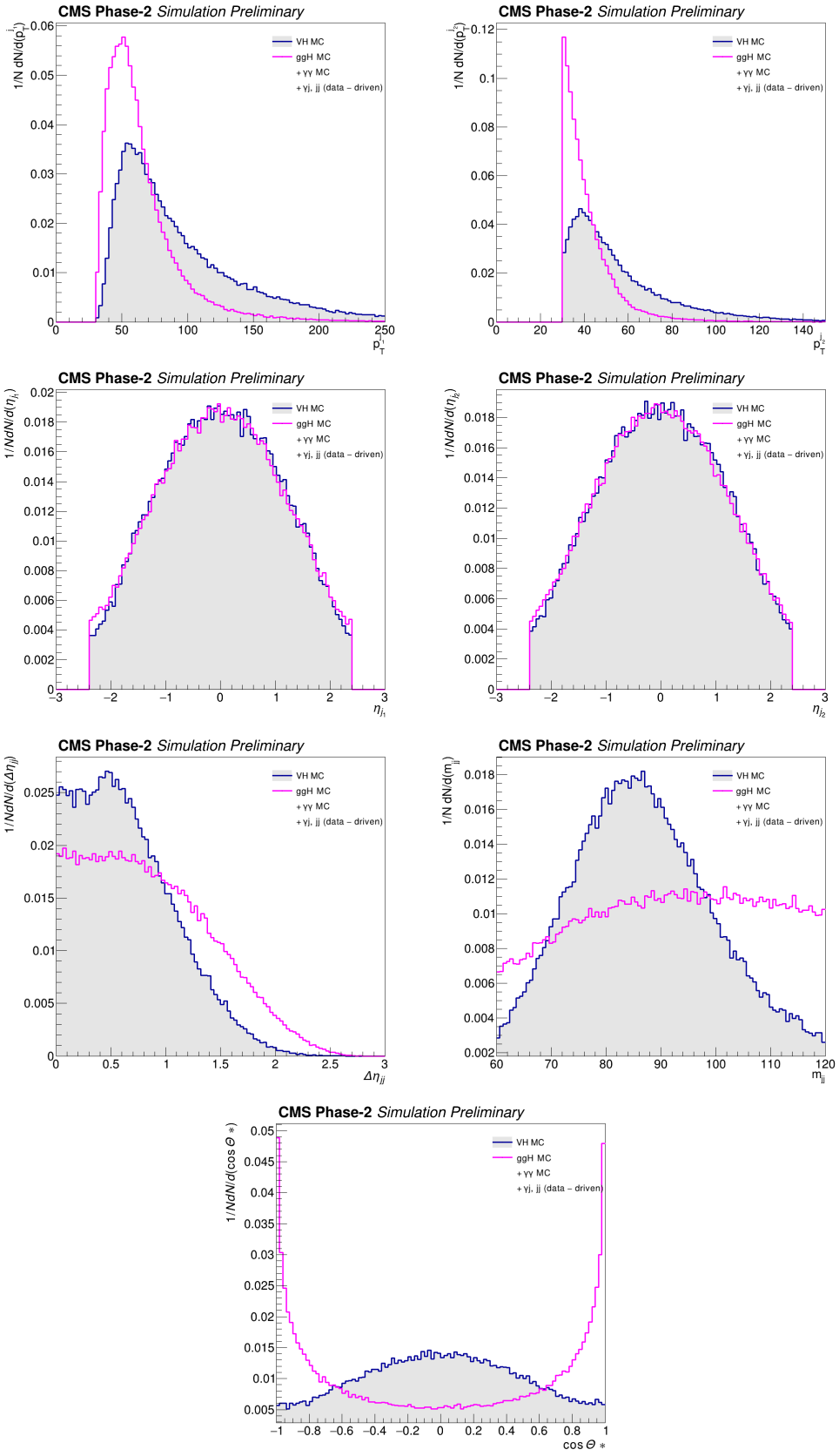

Figure 5.22: Distribution of the input variables to the VH BDT. Events in the distributions are required to pass the full VH preselection.

Training and validation of the VH hadronic BDT

The VH BDT is trained to discriminate between two classes, namely VH hadronic and all backgrounds (non-Higgs backgrounds and ggH). The data-driven background sample is used for γ-jet and jet-jet events. The sum of weights of the signal and background processes are equalised to reduce bias in the training. Given there are two classes, the loss function is a binary logistic one. Of the set of hyper-parameters studied, a train/test split of 90%/10%, a learning rate of 0.4, and a maximum tree depth 6, with all other parameters set to default were found to give optimal performance [1].

The BDT score distribution is shown in Figure 5.23. The figure also compares the result of training the VH hadronic BDT on MC-only backgrounds, without the data-driven procedure applied.

As expected, the truth VH hadronic events receive the highest VH hadronic BDT score. With the data-driven process included in the training inputs, it can be seen that the total simulated background agrees well with the data.

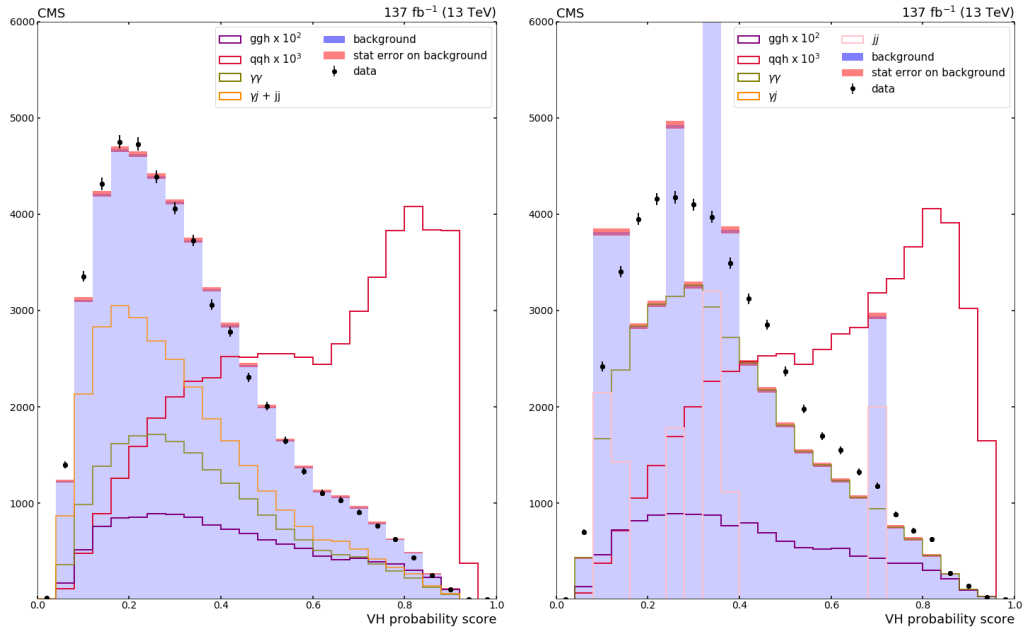

Figure 5.23: VH BDT score distribution for data events passing the VH preselection (black points), and for simulated background events (blue filled histogram). In the left (right) plot, the data-driven background modelling is (not) used.

As done with the VBF BDT, a set of events, generated in the same way as training events, are not used in the training but are used as an independent check of the generalisation ability of the trained VH hadronic BDT. The result of the check is shown in Figure 5.24, where it can be seen that the test samples have been scored in a similar way to training samples, confirming that there has no over-training when the data-driven background modelling is used. These figures further illustrate the poor quality of training and lack of generalisation ability when the VH hadronic BDT is trained on simulated samples only, without any data-driven background modelling.

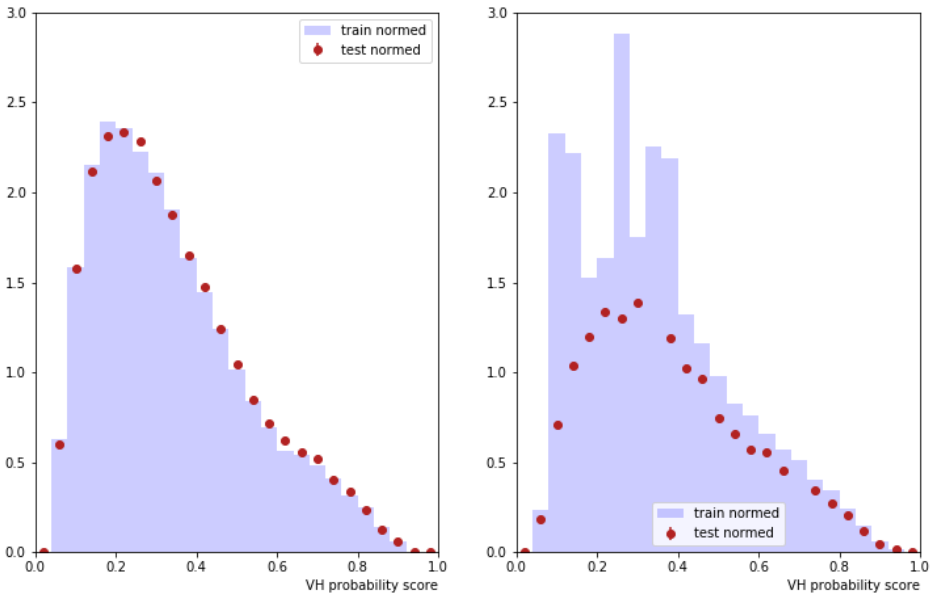

Figure 5.24: A comparison of the VH hadronuc BDT output background scores between the training sample (blue filled histogram) and the testing sample (red points) with (left) and without (right) the data-driven background modelling implemented.

The ROC curves for the binary classifier are shown in Figure 5.25. This figure also includes a comparison to the case where the data-driven background modelling is not implemented. It is clear that the use of the data-driven samples results in better discrimination and less overtraining.

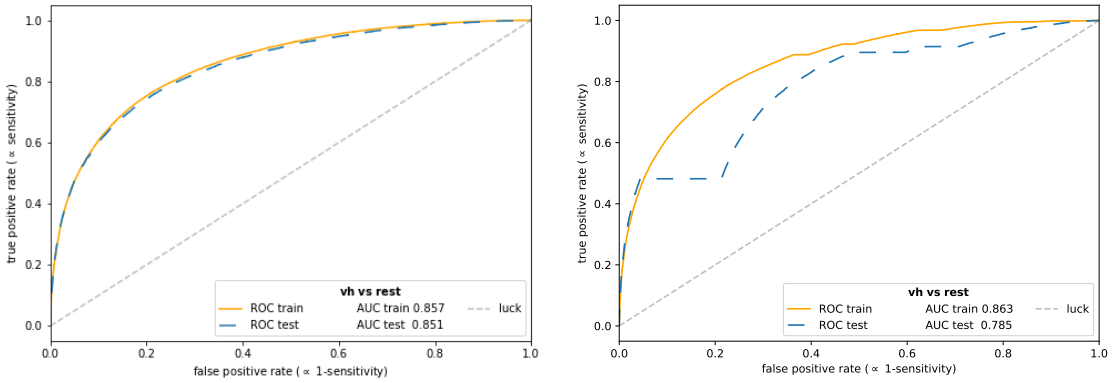

Figure 5.25: ROC curves for the VH hadronic class versus all backgrounds with the training (solid yellow line) and testing (dashed blue line) datasets with (left) and without (right) the data-driven background modelling implemented.

Drell-Yan $Z \to ee$ events, where the electrons are reconstructed as photons, are used to verify that the input variables are properly simulated, as done with the VBF BDT. A VH hadronic pre-selection is applied whereby the p_T of both the leading and sub-leading jets are required to be greater than 30 GeV, and the dijet mass is required to be between 60-120 GeV.

The signal validation for the VH hadronic BDT output score is shown in Figure 5.26. Reasonable agreement between data and MC is observed, and discrepancies are mostly within

the systematic uncertainties. For reference, similar validations for the input variables to the VH hadronic BDT with data from all three years, and simulation, are given in Appendix C.

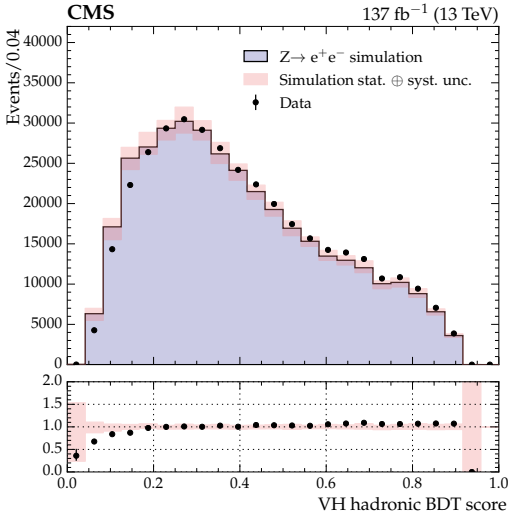

Figure 5.26: The score distributions from the VH hadronic BDT classifier in the $Z \to ee$ control region. The DY simulation (grey histogram) is compared to the combination of data taken in 2016, 2017, and 2018 (black points)

Boundary optimisation

The final categories are defined by placing thresholds on the VH BDT output score and the diphoton BDT. It is found that two categories are required to reach the optimal sensitivity. Further increasing the number of categories results in less than 1% increase in significance. The resulting categories are summarised in Table 5.7 with the optimised boundaries. The improvement in significance over a cut-based analysis, as was performed for the previous version of the analysis with a VH hadronic tag included [106], is slightly more than 20%. The signal yields shown in the table are extracted by fitting a simulated signal model to simulation signal events and integrating in a window of $125 \pm \sigma_{eff}$. The background yield is derived by fitting a smoothly falling function to data and and integrating in a window of $125 \pm \sigma_{eff}$. The expected VH significance is 1.47 (1.34) σ with (without) the data-driven modelling procedure applied.

Table 5.6: This table shows the expected number of signal and background events, and the expected significance of categories targeting the VH hadronic process. The data-driven background modelling procedure has been applied.

Category	VH BDT score	Diphoton BDT score	S	B	Significance	
VH hadronic Tag 0	>0.842	>0.832	5.8	12.7	1.25	1.47
VH hadronic Tag 1	0.613 - 0.842	>0.745	11.1	168	0.79	

Table 5.7: This table shows the expected number of signal and background events, and the expected significance of categories targeting the VH hadronic process. The data-driven background modelling procedure has not been applied.

Category	VH BDT score	Diphoton BDT score	S	B	Significance	
VH hadronic Tag 0	>0.703	>0.805	13.4	103.2	1.28	1.34
VH hadronic Tag 1	0.288-0.703	>0.834	7.3	307.3	0.41	

5.6 Event categorisation in the tHq hadronic channel

The STXS analysis in Ref. [1] only targets leptonic tHq production. In this section, the construction of a category, specifically targeting hadronic tHq production, is described. Due to the similarities between the final state topologies, there is a significant overlap in the signal regions for ttH and tHq events. In the full Run II ttH STXS analysis [167], it was found that the level of contamination from tHq is between 6-9% in each ttH analysis category. Since in the $H \to \gamma\gamma$ analysis framework, the analysis categories implemented by defining a priority for each tag, the yields in the ttH and tHq categories will therefore depend on the ordering, with the higher priority tag being assigned the events which could have potentially entered either category. Thus, the tHq hadronic tag is given priority over the ttH hadronic tag given the similarity in the decay products between the two processes and the smaller tHq hadronic cross-section; this order allows a relatively pure tHq hadronic tag to be constructed with minimal ttH hadronic contamination, although the correlation between these categories is expected to remain high.

In this section, two BDTs are used. One BDT is used to reject possible ttH events from entering the tHq hadronic tags. This ensures the minimum possible contamination, and therefore reduces the anti-correlation between the two in the final result extraction. The second BDT is used to discriminate between tHq hadronic events and non-Higgs boson backgrounds.

5.6.1 tHq kinematics

As decribed in Section 2.2, the final state of the tHq production process consists of a Higgs boson, a top quark and a quark. The top quark decays to a bottom quark and a W boson; the W boson may decay hadronically or leptonically. Since the Higgs boson is being radiated from the one of the heavier legs of a t-channel process, the light quark is expected to have high rapidity and this can be seen from the forward jet η distribution. Therefore, these special features, namely the forward jet η and the angular separation of the forward jet with different final state objects, are considered in the categorisation to select tHq events.

Note that the middle diagram in Figure 2.6 is actually a VBF process. Normally we would want to target this process in the VBF categorisation but, since at reconstruction-level, only the final objects are visible, the process is considered in the tHq categories. Correlations with the VBF categories are quantified in Chapter 6. The definitions of the ttH and tHq STXS bins with SM cross-section predictions are given in Table 5.8. These correspond to the purple and yellow entries in Figure 5.2.

The hadronic tHW process, which has similar final states (one additional final state quark) to the hadronic tHq final state, is also considered in this section. The SM predicts

production cross-sections of about 71, 16, and 2.9 fb for the t-channel process, the tHW process, and the s-channel process respectively, at a centre-of-mass energy of $\sqrt{s} = 13$ [40]. The full Run II dataset is not expected to be sensitive to the tHW process individually.

Table 5.8: Definition of the ttH and tH STXS bins. The product of the cross-section and branching fraction ($\mathcal{B}$), evaluated at $\sqrt{s} = 13\,\text{TeV}$ and $m_H = 125\,\text{GeV}$, is given for each bin in the last column. The fraction of the total production mode cross-section from each STXS bin is also shown. Unless stated otherwise, the STXS bins are defined for $y_H < 2.5$. Events with $y_H > 2.5$ are mostly outside of the experimental acceptance and therefore have a negligible contribution to all analysis categories.

STXS bin	Definition units of p_T^H in GeV	Fraction of cross-section ttH	tHq	tHW	$\sigma_{\text{SM}}\mathcal{B}$ (fb)
ttH forward		1.35%	-	-	0.016
tH forward	$y_H > 2.5$	-	2.79%	1.06%	0.005
ttH $p_T^H < 60$	No jet requirements, $p_T^H < 60$	22.42%	-	-	0.259
ttH $60 < p_T^H < 120$	No jet requirements, $60 < p_T^H < 120$	34.61%	-	-	0.400
ttH $120 < p_T^H < 200$	No jet requirements, $120 < p_T^H < 200$	25.60%	-	-	0.296
ttH $200 < p_T^H < 300$	No jet requirements, $200 < p_T^H < 300$	10.72%	-	-	0.124
ttH $p_T^H > 300$	No jet requirements, $p_T^H > 300$	5.31%	-	-	0.061
tH	No additional requirements	-	97.21%	98.94%	0.204

5.6.2 tHq hadronic selection

The cuts applied in the tHq hadronic preselection are outlined in Table 5.9. Although the hadronic tHq process has four jets in the final stage, only three jets or more are required in the preselection to allow for jet merging and other inefficiencies in the reconstruction. It was also found better not to place a cut on the number of b-jets before training the BDT.

Table 5.9: The cuts applied on reconstruction-level event variables to select tHq hadronic events before the full categorisation process.

tHq preselection
$100 < m_{\gamma\gamma} < 180\,\text{GeV}$
$p_T^{\gamma_1}/m_{\gamma\gamma} > 1/3$
$p_T^{\gamma_2}/m_{\gamma\gamma} > 1/4$
photon ID scores > -0.7
number of jets > 2
$p_T^{j_1}, p_T^{j_2}, p_T^{j_3} > 25\,\text{GeV}$
$\Delta R_{j_1\gamma_1}, \Delta R_{j_1\gamma_2}, \Delta R_{j_2\gamma_1}, \Delta R_{j_2\gamma_2}, \Delta R_{j_3,\gamma_1}, \Delta R_{j_3,\gamma_2} > 0.4$

5.6.3 Discrimination vs ttH

A BDT is trained to discriminate between hadronic tHq events and ttH events. Hadronic tHW processes which pass the tHq hadronic preselection are considered together with tHq hadronic in the signal class when training the BDT. This method gives better discrimination against ttH than when the tHW process is considered as part of the background class.

Input variables to tHq hadronic BDT vs ttH

The input variables to the tHq hadronic BDT vs ttH, listed below and shown in Figures 5.27-5.30, are chosen to maximise the discrimination of tHq hadronic events from the ttH processes. The output of a b quark tagging algorithm is also used [167].

- the transverse momentum of the leading and subleading photons divided by the diphoton invariant mass ($p_T^{\gamma_1}/m_{\gamma\gamma}$, $p_T^{\gamma_2}/m_{\gamma\gamma}$)
- the transverse momentum of the diphoton system divided by the diphoton invariant mass ($p_T^{\gamma\gamma}/m_{\gamma\gamma}$)
- the difference in distance, in η-ϕ coordinate space, between the lead and sublead photons ($\Delta R_{\gamma\gamma}$)
- the cosine of the angle in ϕ between the lead and sublead photons ($\cos\phi_{\gamma\gamma}$)
- the pseudorapidity of the lead and sublead photons (η_{γ_1}, η_{γ_2})
- the ϕ value of the lead and sublead photons (ϕ_{γ_1}, ϕ_{γ_2})
- electron veto values for the lead and sublead photons (*leadPixelSeed, subleadPixelSeed*)
- the minimum photon ID score out of the lead/sublead photons (*min photon IDMVA*)
- the maximum photon ID score out of the lead/sublead photons (*max photon ID MVA*)
- the number of jets, the number of b jets, the number of central jets
- the transverse momentum and pseudorapidity of the most forward jet (p_T *and* η *of most forward jet*)
- b-tagging scores of the two jets receiving the highest b-tagging scores (*highest and second highest b-scores*)
- the transverse momentum of the jet receiving the highest b-tagging score (*b-jet 1* p_T)
- the b-tagging scores of the three most forward jets (*jet 1 b-score, jet 2 b-score, jet 3 b-score*)
- the transverse momentum of the three most forward jets (*jet 1* p_T*, jet 2* p_T*, jet 3* p_T)
- the pseudorapidity of the three most forward jets (*jet 1* η*, jet 2* η*, jet 3* η)
- the difference in distance, in η-ϕ coordinate space, between the lead photon and the most forward jet ($\Delta R_{\gamma_1 j_1}$)
- the difference in distance, in η-ϕ coordinate space, between the sublead photon and the most forward jet ($\Delta R_{\gamma_2 j_1}$)
- the difference in distance, in η-ϕ coordinate space, between the jet receiving the highest b-tagging score and the most forward jet ($\Delta R_{b_1 j_1}$)
- the rapidity of the diphoton system (*diphoton rapidity*)

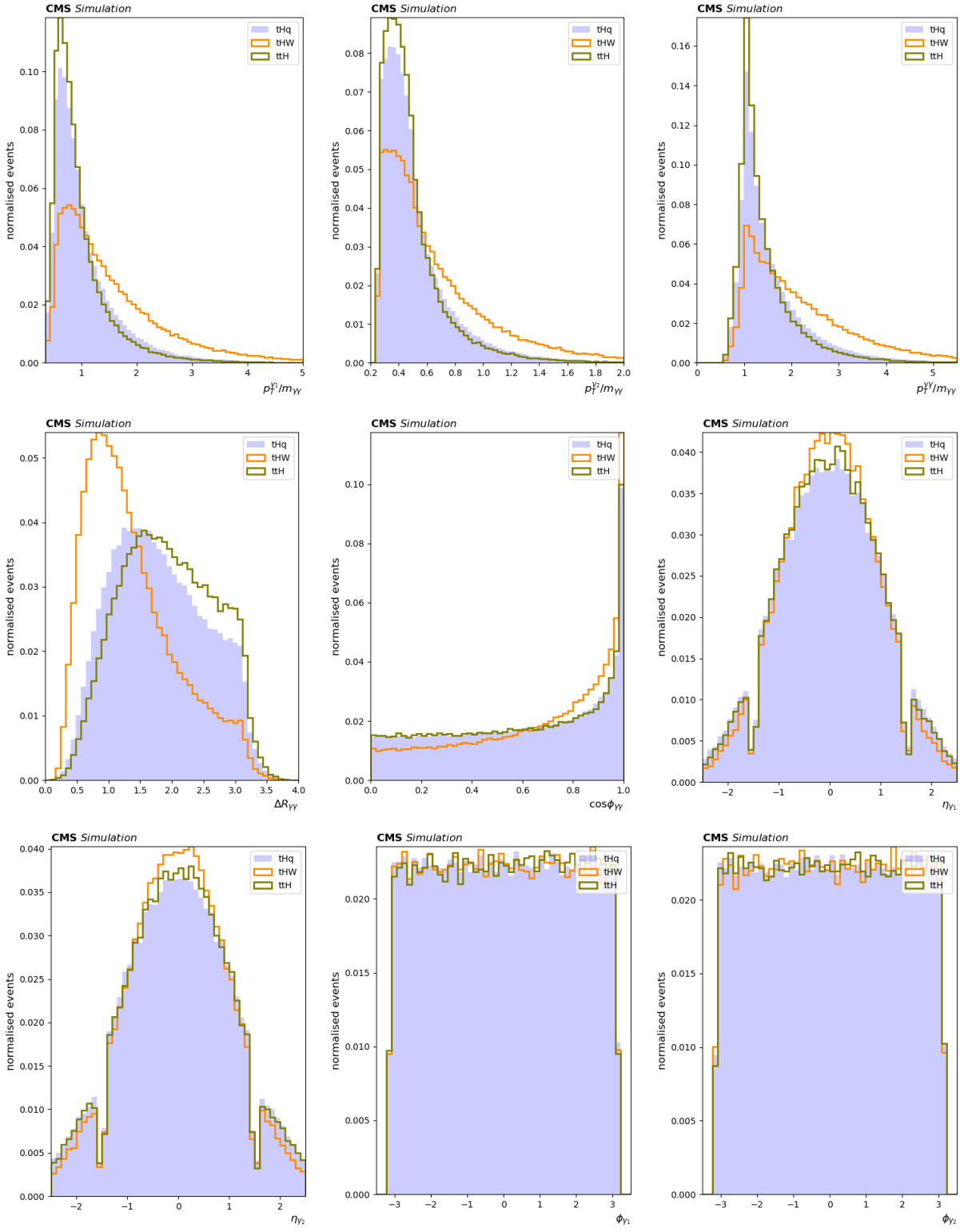

Figure 5.27: Distribution of the input variables to the tHq hadronic BDT vs ttH for the combination of the 2016, 2017, and 2018 datasets. Events in the distributions are required to pass the full tHq hadronic preselection.

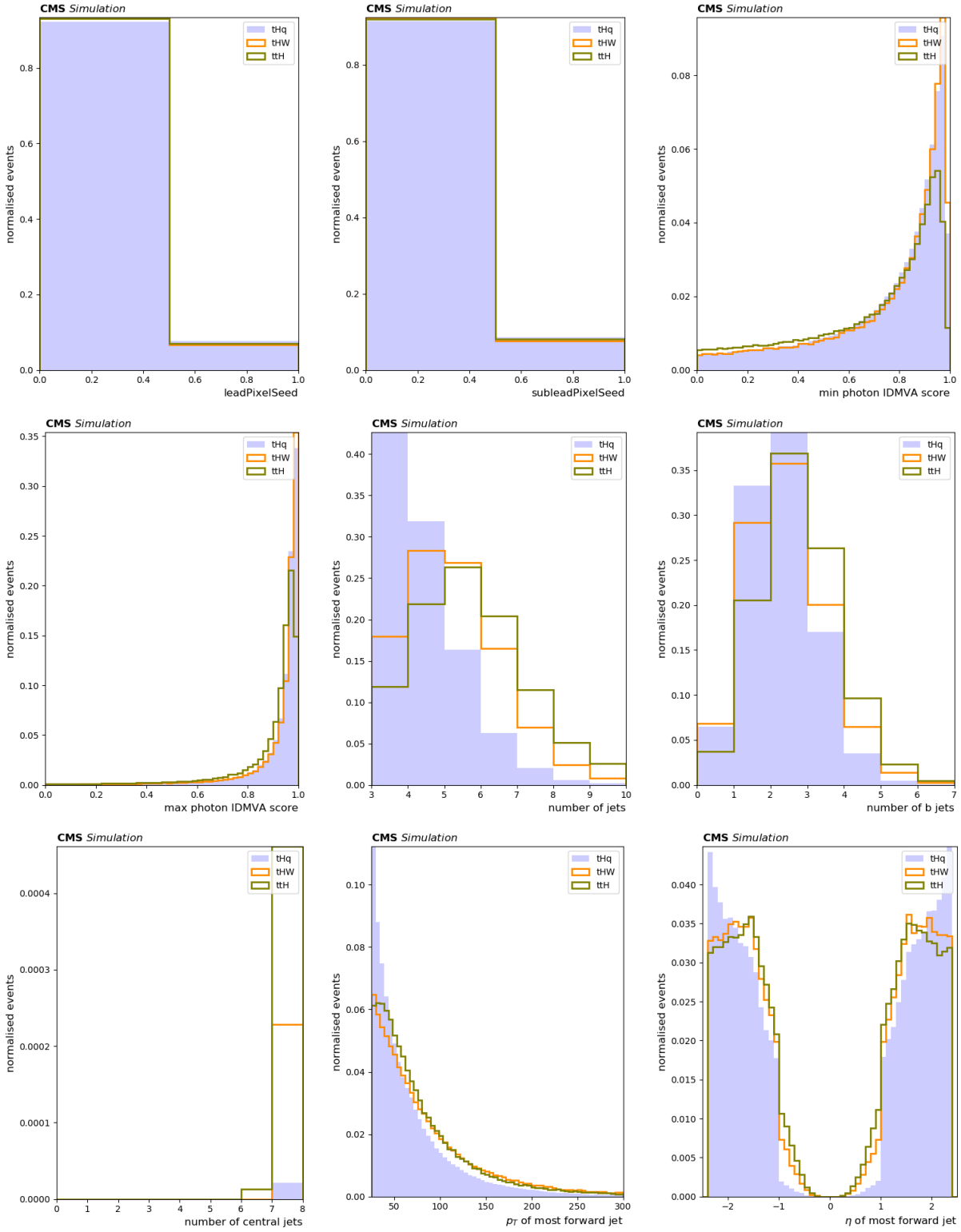

Figure 5.28: Distribution of the input variables to the tHq hadronic BDT vs ttH for the combination of the 2016, 2017, and 2018 datasets. Events in the distributions are required to pass the full tHq hadronic preselection.

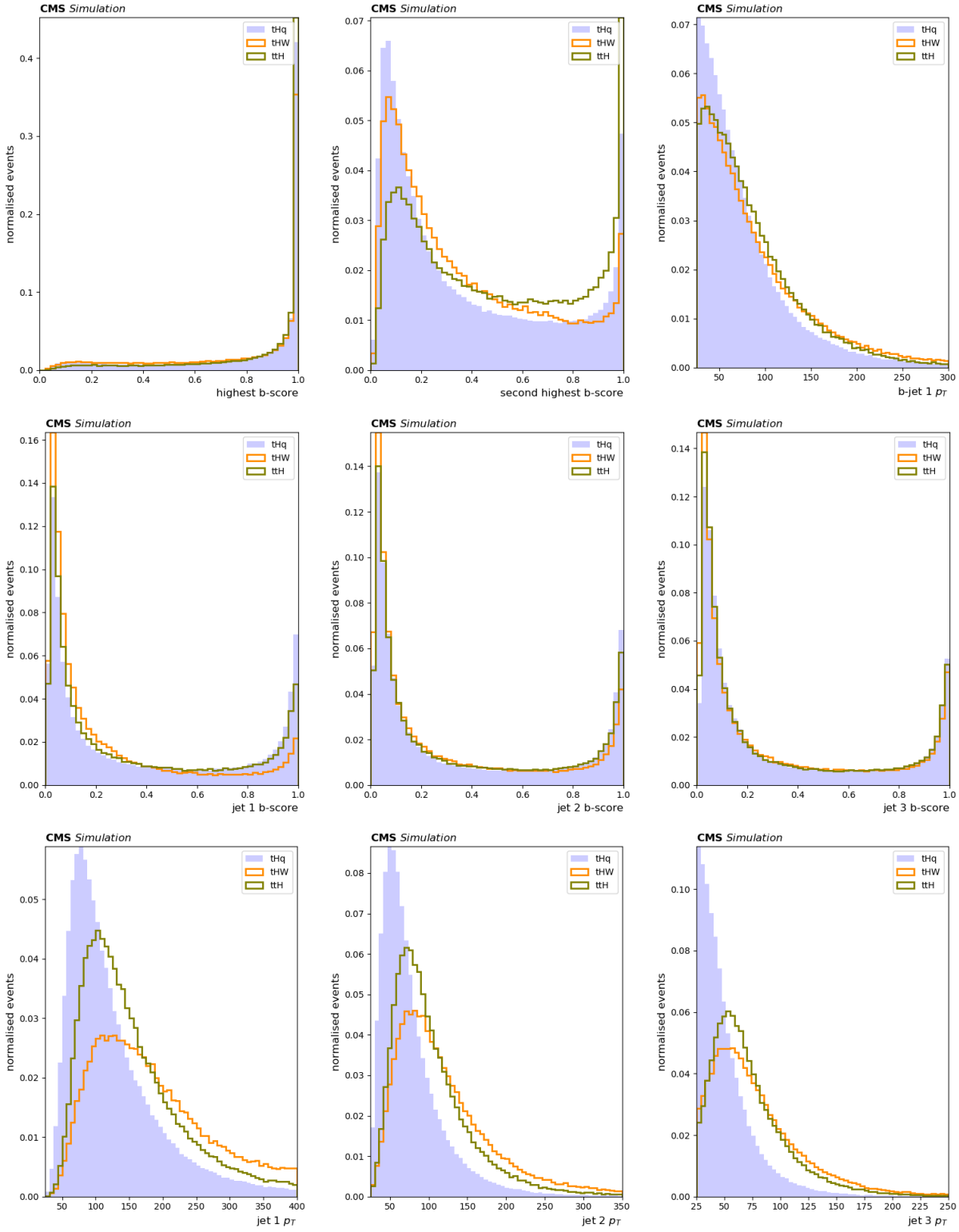

Figure 5.29: Distribution of the input variables to the tHq hadronic BDT vs ttH for the combination of the 2016, 2017, and 2018 datasets. Events in the distributions are required to pass the full tHq hadronic preselection.

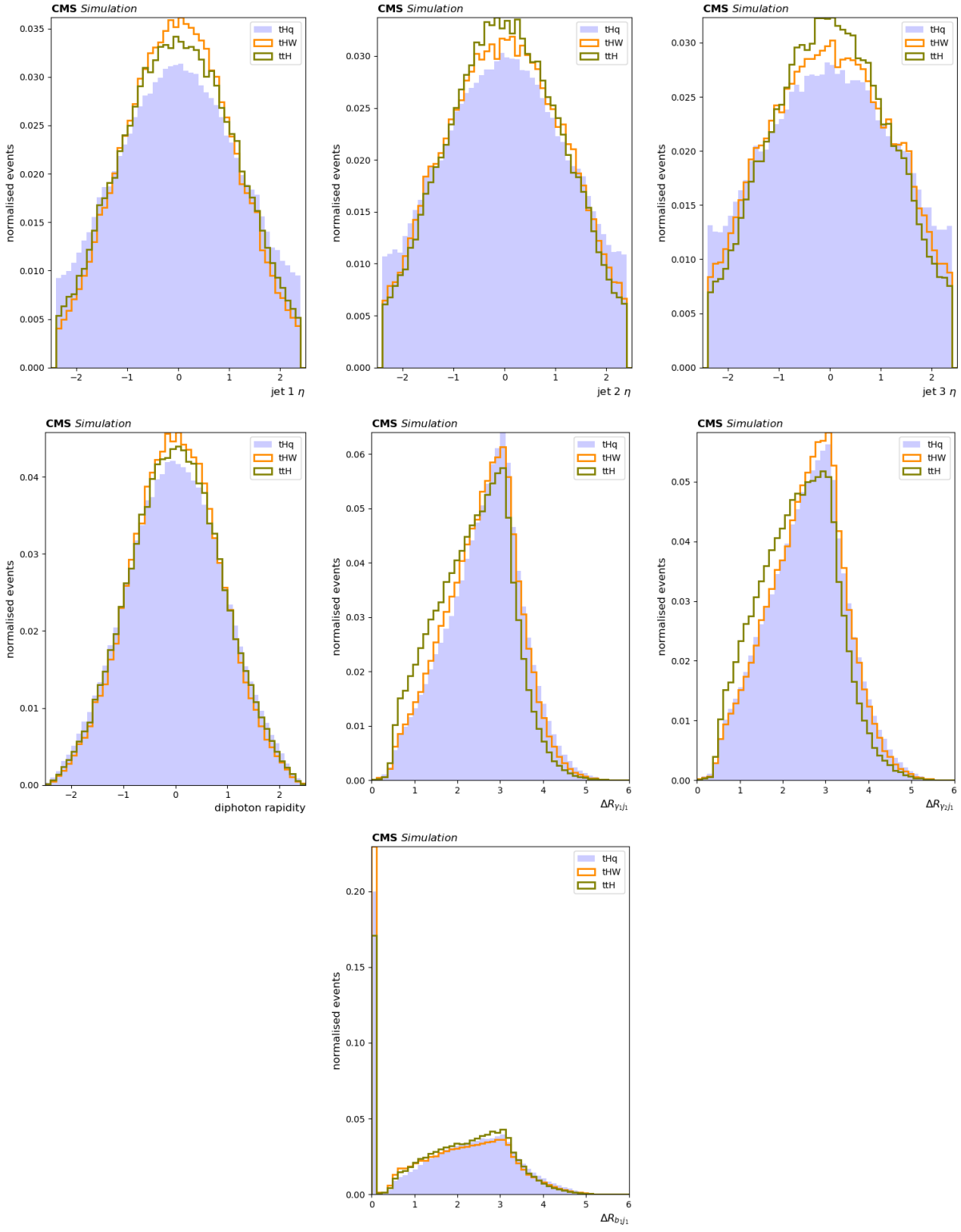

Figure 5.30: Distribution of the input variables to the tHq hadronic BDT vs ttH for the combination of the 2016, 2017, and 2018 datasets. Events in the distributions are required to pass the full tHq hadronic preselection.

Training and validation of the tHq hadronic BDT vs ttH

The tHq hadronic BDT vs ttH is trained to discriminate between two classes, namely tHq (with tHW included) and ttH. The sum of weights of the signal and background processes are equalised to reduce bias in the training. Of the set of hyper-parameters studied, a train/test split of 90%/10%, a learning rate of 0.4, and a maximum tree depth 6, with all other parameters set to default were found to give optimal performance.

The BDT score distribution is shown in Figure 5.31. The figure shows both distributions normalised by the process and the distributions normalised to the full Run II luminosity with the data included. As expected, the truth tHq hadronic events receive the highest tHq hadronic BDT score. Given that the data is expected to be more background-like (non-Higgs boson backgrounds) than signal like, these distributions are not expected to match between simulation and data.

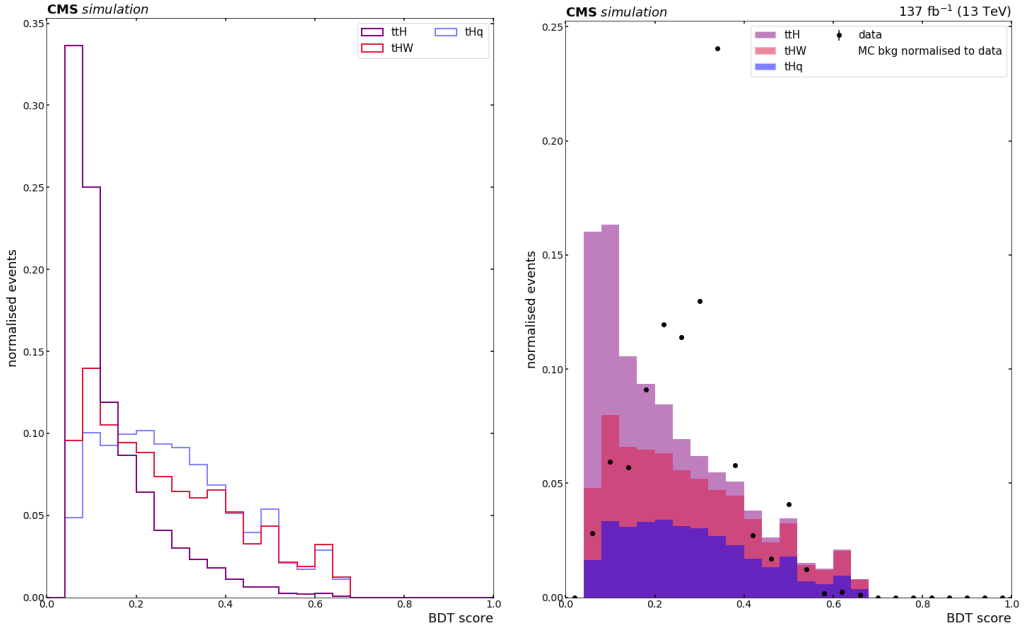

Figure 5.31: tHq hadronic BDT vs ttH score distribution for data events passing the tHq preselection (black points), and for simulated signal and background events (coloured histograms. The left plot shows a distributions normalised by process and the right plot shows distributions normalised to the full Run II luminosity, with the different process histograms stacked.

As done with the qqH BDTs, a set of events, generated in the same way as training events, are not used in the training but are used as an independent check of the generalisation ability of the trained tHq hadronic BDT vs ttH. The result of the check is shown in Figure 5.32, where it can be seen that the test samples have been scored in a similar way to training samples, confirming that there has no overtraining.

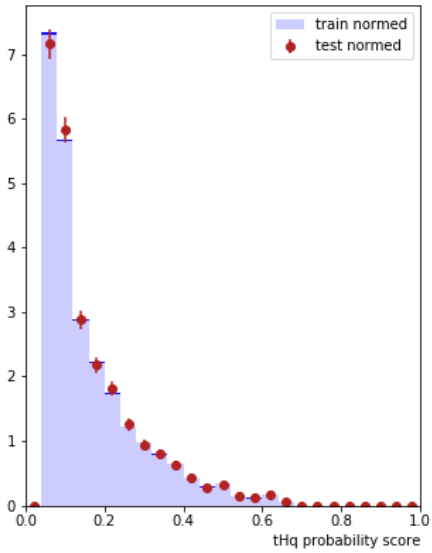

Figure 5.32: A comparison of the tHq hadronic BDT vs ttH output scores between the training sample (blue filled histogram) and the testing sample (red points).

The diagnostic decision-making capability of the tHq hadronic BDT vs ttH is investigated through ROC curves. The probability that a true tHq hadronic event will be will be assigned to the tHq hadronic class (true positive rate) is plotted against the probability that an event from ttH will be classified as tHq hadronic (false positive rate) for different decision thresholds. The ROC curves for the binary classifier are shown in Figure 5.33.

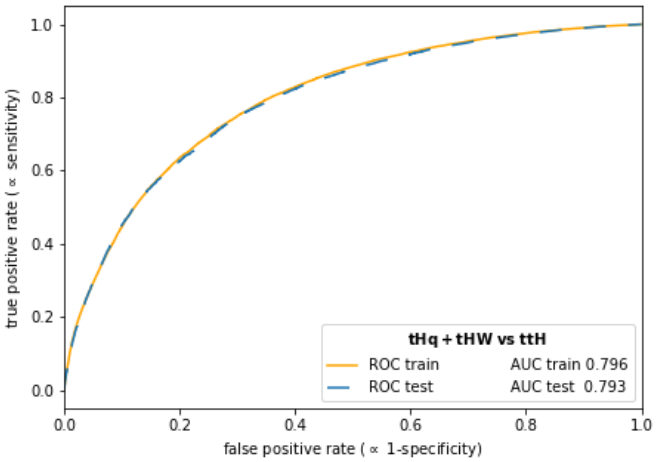

Figure 5.33: ROC curves for the tHq hadronic class versus ttH with the training (solid yellow line) and testing (dashed blue line) datasets.

The BDT trained to separate tHq from the ttH background is validated with the dedicated ttZ and tZq control region events. The tZq and ttZ modes have very similar kinematics to tHq and ttH processes respectively, which gives a test of the data and simulation agreement

in the MVA distributions. The invariant mass of the electron pair is required to lie within the Z boson mass window (80-100 GeV). All the tHq hadronic selections in Table 5.9, except the cut on the diphoton invariant mass, are also applied.

The signal validation for the tHq hadronic BDT vs ttH output score is shown in Figure 5.34. Several other backgrounds are also included in this validation, namely jet-jet, γ-jet and Drell-Yan events. Reasonable agreement between data and simulation is observed, and discrepancies are mostly covered by the statistical uncertainties. It is to be noted here that the tZq yield is very small and the test is not perfect for this reason.

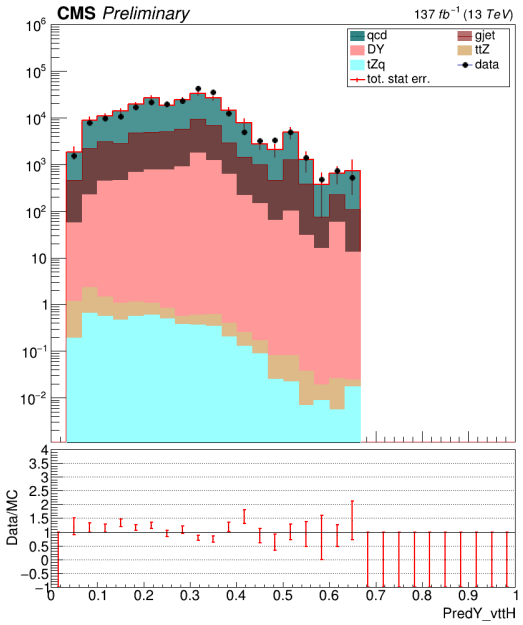

Figure 5.34: The BDT score (denoted here by *PredY_vttH*) distributions from the tHq hadronic BDT vs ttH classifier in the $Z \rightarrow ee$ control region. The simulation (stacked coloured histograms) is compared to the combination of data taken in 2016, 2017, and 2018 (black points).

5.6.4 Discrimination vs non-H backgrounds

The second BDT used in the tHq hadronic categorisation is a classifier used to discriminate tHq hadronic events from non-Higgs boson backgrounds. The simulated backgrounds used while training the BDT include $\gamma\gamma$, γ+jet, tt+$\gamma\gamma$, tt+γ+jet, t+γ+jet, tt+jets, jet-jet events.

Input variables

The input variables to the tHq hadronic BDT vs non-H backgrounds are chosen to maximise the discrimination of the tHq hadronic events from the non-H backgrounds. The output of a b quark tagging algorithm is also used. The list of chosen input variables is given below, with plots of the normalised input variable distributions given in Figures 5.37-5.40. In the variable distributions, it can be seen that diphoton, jet-jet, and γ-jet backgrounds dominate the tHq preselection region.

- the transverse momentum of the lead and sublead photons divided by the diphoton invariant mass ($p_T^{\gamma_1}/m_{\gamma\gamma}$, $p_T^{\gamma_2}/m_{\gamma\gamma}$)
- the transverse momentum of the diphoton system divided by the diphoton invariant mass ($p_T^{\gamma\gamma}/m_{\gamma\gamma}$)
- the difference in distance, in η-ϕ coordinate space, between the lead and sublead photons ($\Delta R_{\gamma\gamma}$)
- the rapidity of the diphoton system (*diphoton rapidity)*
- the cosine of the helicity angle of the diphoton system ($\cos(helicity\,angle(\theta))$)
- electron veto values for the lead and sublead photons (*leadPixelSeed, subleadPixelSeed*)
- the minimum of the photon ID scores of the lead/sublead photons (*min photon IDMVA score)*
- the maximum of the photon ID scores of the lead/sublead photons (*max photon IDMVA score*)
- the number of jets
- the number of b jets
- the number of central jets
- b-tagging scores of the three jets receiving the highest b-tagging scores (*highest, second highest and third highest b-score*)
- the transverse momentum of the three jets receiving the highest b-tagging scores (*b-jet 1* p_T*, b-jet 2* p_T*, b-jet 3* p_T)
- the pseudorapidity of the three jets receiving the highest b-tagging scores (*b-jet 1* η*, b-jet 2* η*, b-jet 3* η)
- the b-tagging scores of the three most forward jets (*jet 1 b-score, jet 2 b-score, jet 3 b-score*)
- the transverse momentum of the three most forward jets (*jet 1* p_T*, jet 2* p_T*, jet 3* p_T)
- the pseudorapidity of the three most forward jets (*jet 1* η*, jet 2* η*, jet 3* η)
- the difference in distance, in η-ϕ coordinate space, between the lead photon and the most forward jet ($\Delta R_{\gamma_1 j_1}$)
- the difference in distance, in η-ϕ coordinate space, between the sublead photon and the most forward jet ($\Delta R_{\gamma_2 j_1}$)
- the difference in distance, in η-ϕ coordinate space, between the jet receiving the highest b-tagging score and the most forward jet ($\Delta R_{b_1 j_1}$)

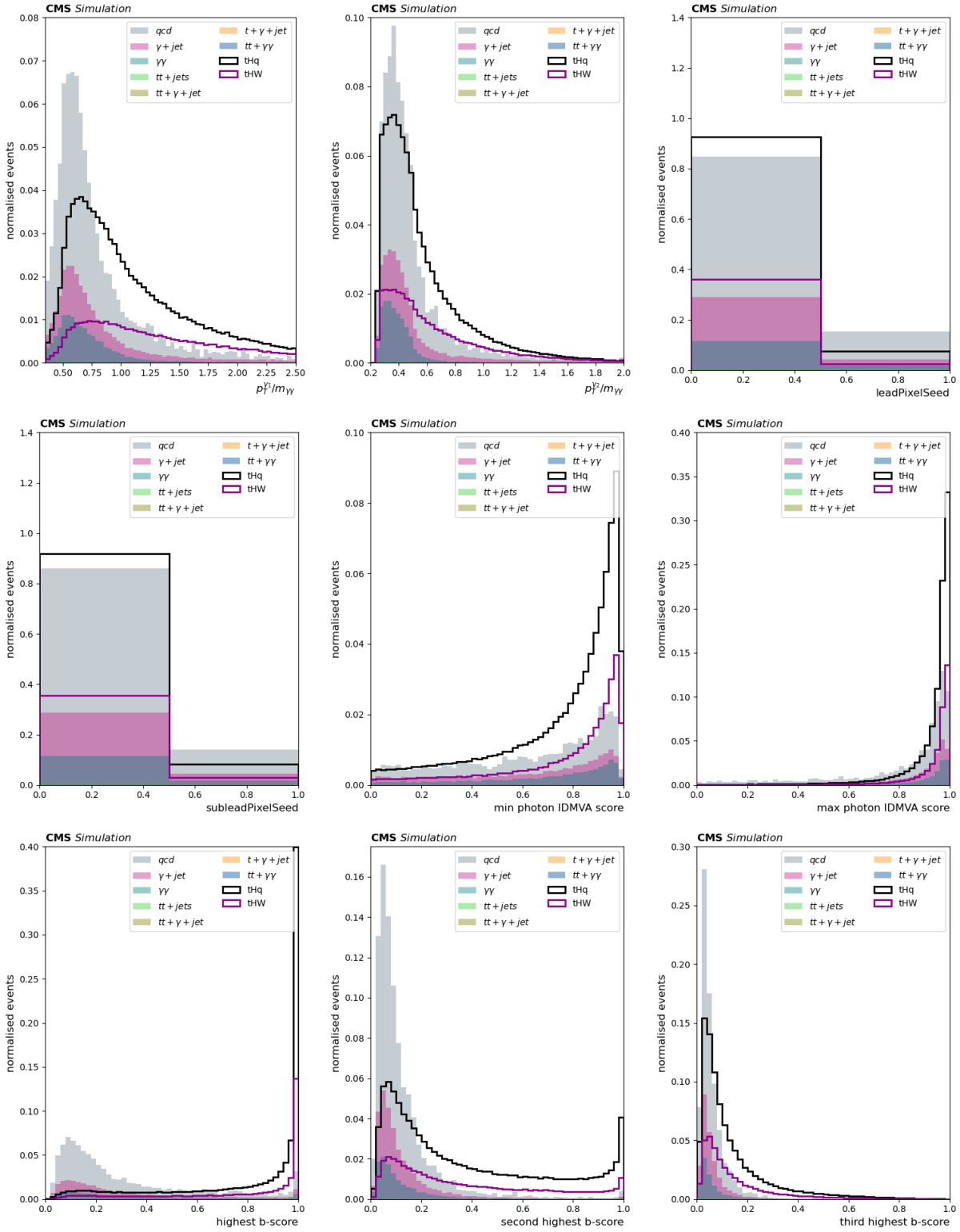

Figure 5.35: Distribution of the input variables to the tHq hadronic BDT vs non-H backgrounds for the combination of the 2016, 2017, and 2018 datasets. Events in the distributions are required to pass the full tHq hadronic preselection.

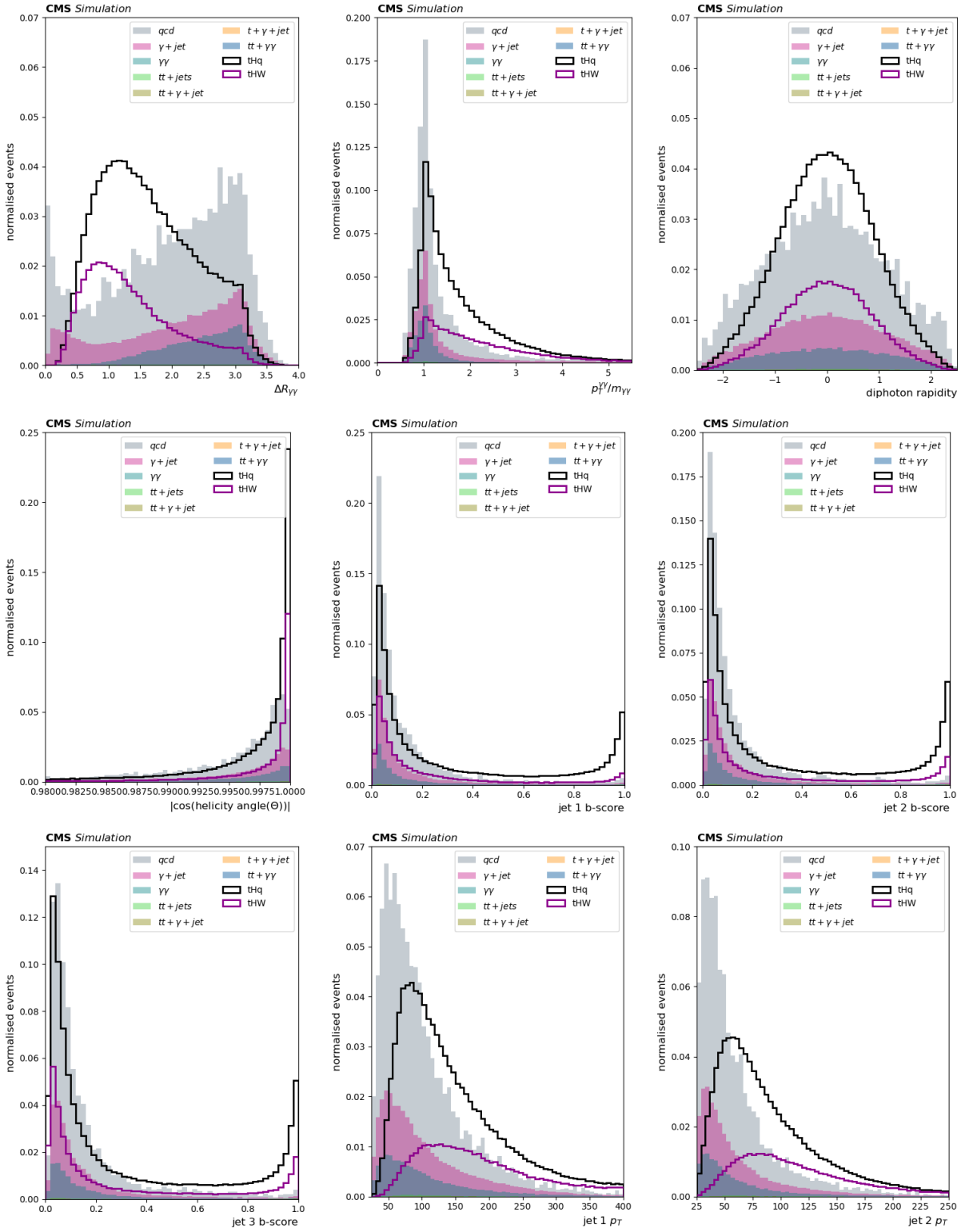

Figure 5.36: Distribution of the input variables to the tHq hadronic BDT vs non-H backgrounds for the combination of the 2016, 2017, and 2018 datasets. Events in the distributions are required to pass the full tHq hadronic preselection.

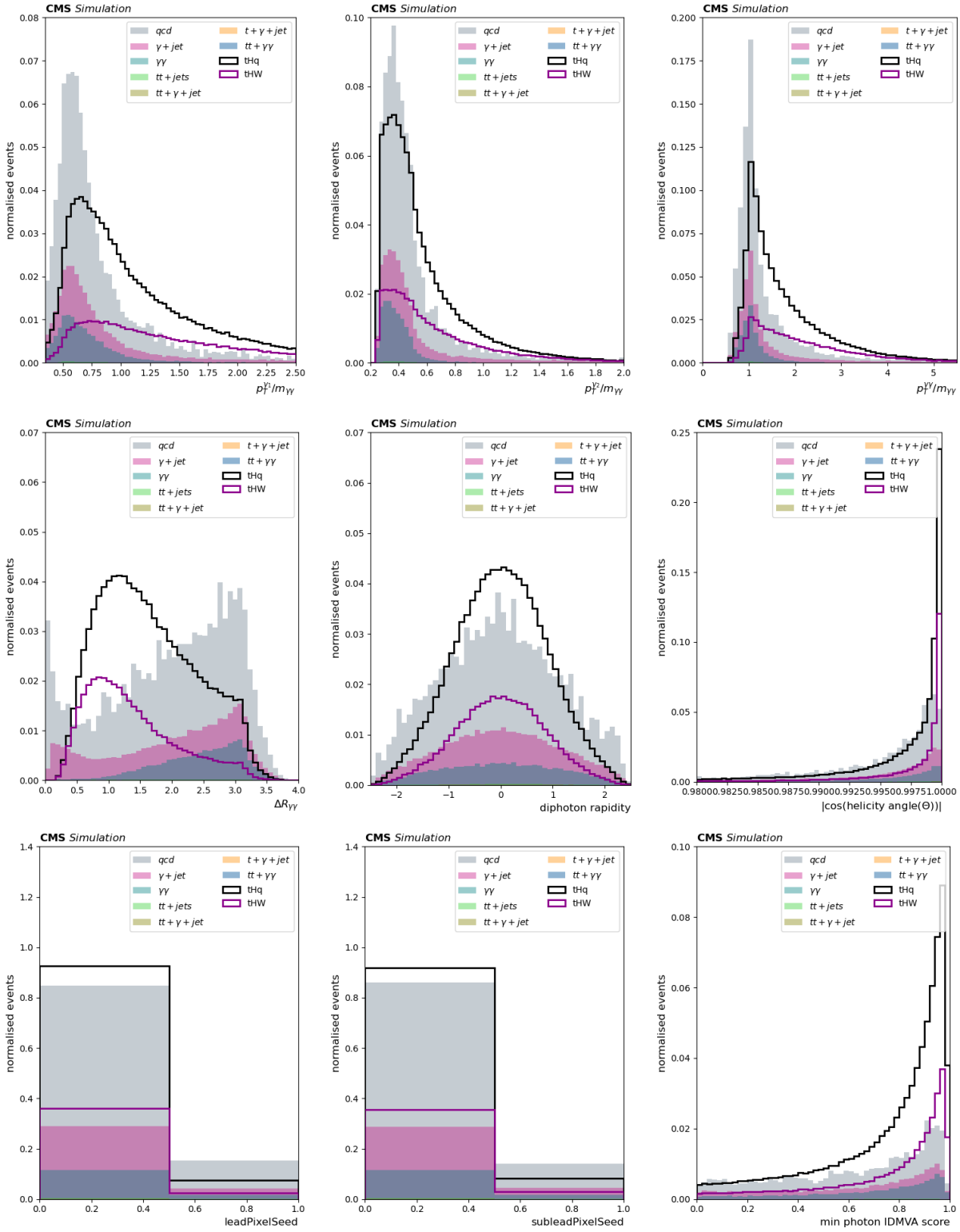

Figure 5.37: Distribution of the input variables to the tHq hadronic BDT vs non-H backgrounds for the combination of the 2016, 2017, and 2018 datasets. Events in the distributions are required to pass the full tHq hadronic preselection.

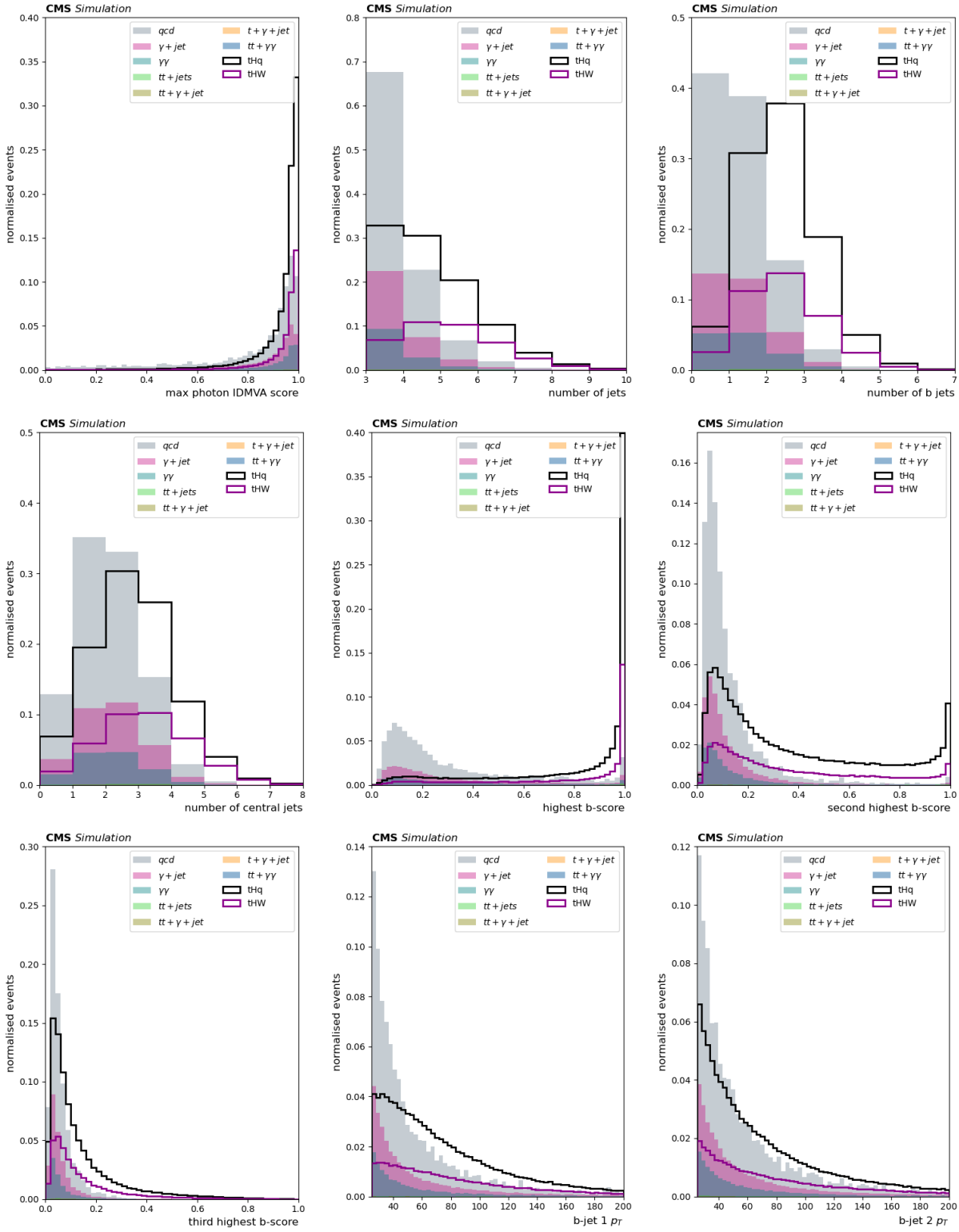

Figure 5.38: Distribution of the input variables to the tHq hadronic BDT vs non-H backgrounds for the combination of the 2016, 2017, and 2018 datasets. Events in the distributions are required to pass the full tHq hadronic preselection.

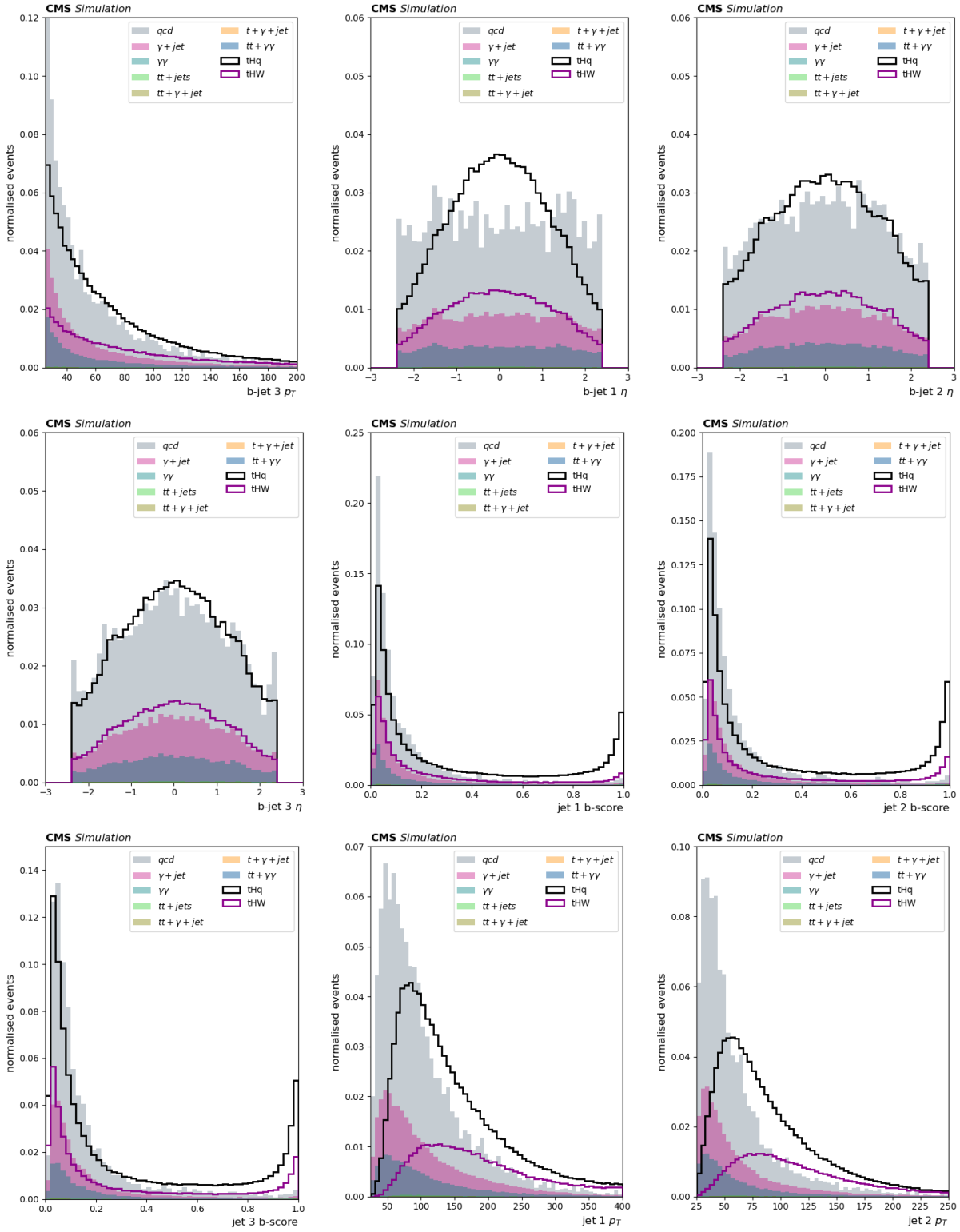

Figure 5.39: Distribution of the input variables to the tHq hadronic BDT vs non-H backgrounds for the combination of the 2016, 2017, and 2018 datasets. Events in the distributions are required to pass the full tHq hadronic preselection.

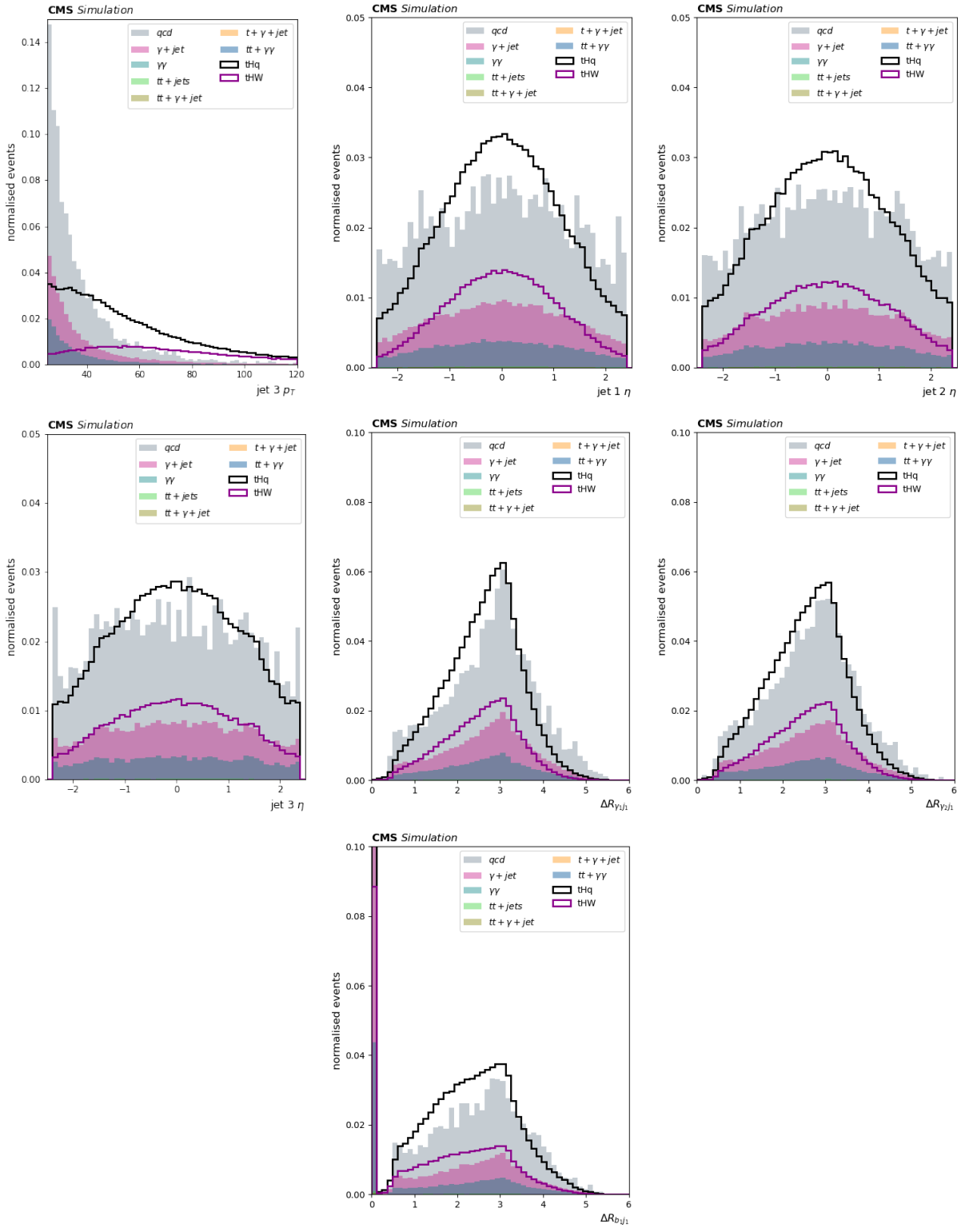

Figure 5.40: Distribution of the input variables to the tHq hadronic BDT vs non-H backgrounds for the combination of the 2016, 2017, and 2018 datasets. Events in the distributions are required to pass the full tHq hadronic preselection.

Training and validation of the tHq hadronic BDT vs non-H backgrounds

The tHq hadronic BDT vs non-H backgrounds is trained to discriminate between two classes, namely tHq (with tHW included) and non-H backgrounds grouped together. Of the set of hyper-parameters studied, a train/test split of 80%/20%, a learning rate of 0.3, and a maximum tree depth of 4, with all other parameters set to default were found to give optimal performance.

The BDT score distribution is shown in Figure 5.41. The figure shows both distributions normalised by the class and the distributions normalised to the full Run II luminosity (using SM branching fractions) with the data included. As expected, the truth tHq hadronic events receive the highest tHq hadronic BDT score. It can be seen that the total simulated background agrees well with the data. This serves as a validation that the simulated background processes used to train the BDT are well modelled.

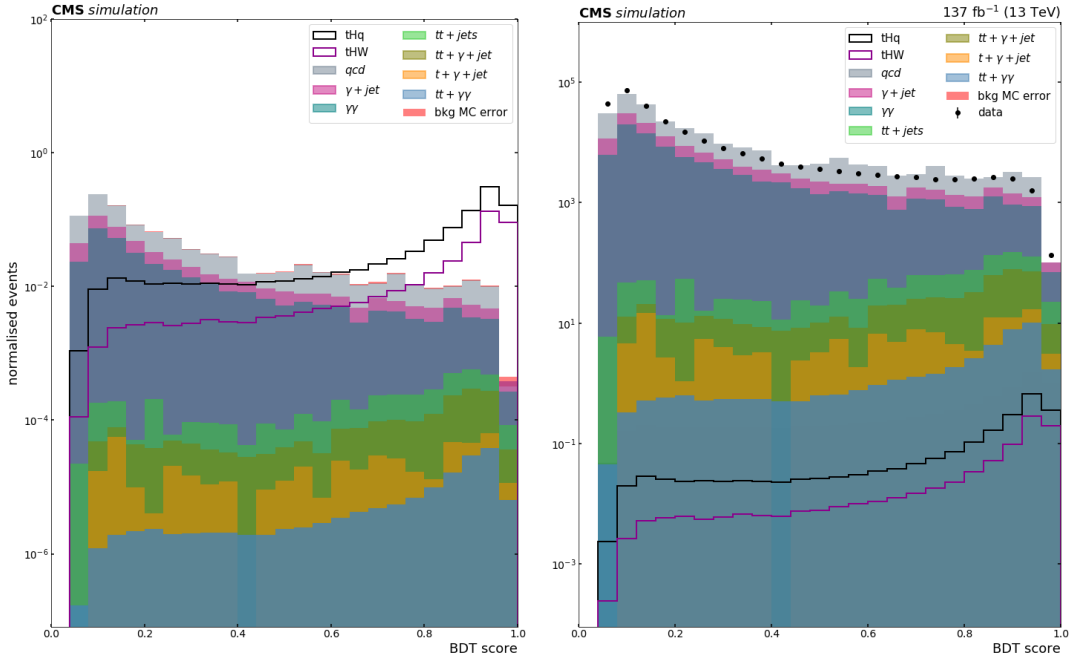

Figure 5.41: tHq hadronic BDT vs non-H backgrounds score distribution for data events passing the tHq preselection (black points), and for simulated signal and background events (coloured histograms). The left plot shows a distributions normalised by process and the right plot shows distributions normalised to the full Run II luminosity.

As done with previous BDTs, a set of events, generated in the same way as training events, are not used in the training but are used as an independent check of the generalisation ability of the trained tHq hadronic BDT vs non-H backgrounds. The result of the check is shown in Figure 5.42, where it can be seen that the test samples have been scored in a similar way to training samples, confirming that there has no overtraining.

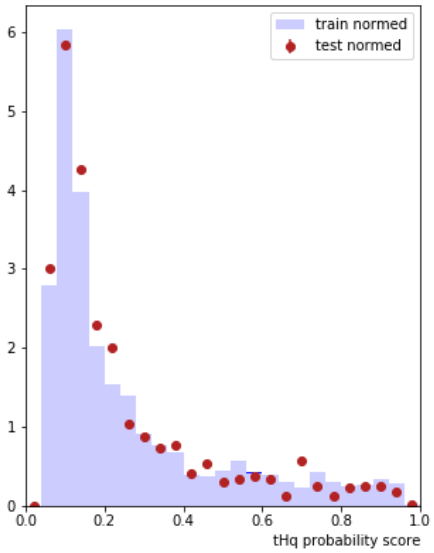

Figure 5.42: A comparison of the tHq hadronic BDT vs non-H backgrounds output scores between the training sample (blue filled histogram) and the testing sample (red points).

The diagnostic decision-making capability of the tHq hadronic BDT vs non-H backgrounds is investigated through ROC curves. The probability that a true tHq hadronic event will be assigned to the tHq hadronic class (true positive rate) is plotted against the probability that an event from the non-H backgrounds will be classified as tHq hadronic (false positive rate) for different decision thresholds. The ROC curves for the binary classifier are shown in Figure 5.43.

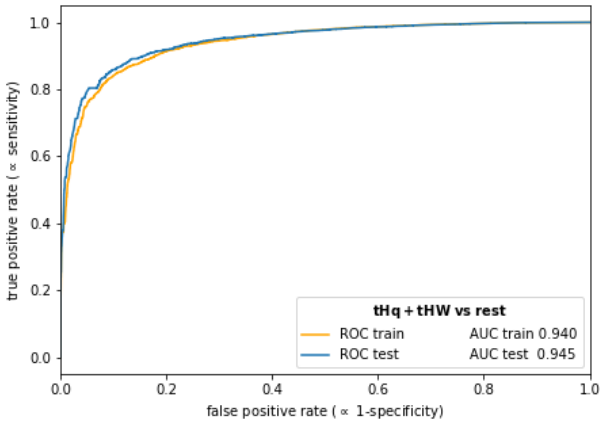

Figure 5.43: ROC curves for the tHq hadronic class versus non-H backgrounds with the training (solid yellow line) and testing (dashed blue line) datasets.

The BDT trained to separate tHq from non-H backgrounds is validated with the dedicated ttZ and tZq control region events. The invariant mass of the electron pair is required to lie within the Z boson mass window (80-100 GeV). All the tHq hadronic selections in Table 5.9, except the cut on the diphoton invariant mass, are also applied. The signal validation for the

tHq hadronic BDT vs non-H backgrounds output score is shown in Figure 5.44. Reasonable agreement between data and simulation is observed, and discrepancies are mostly covered by the statistical uncertainties.

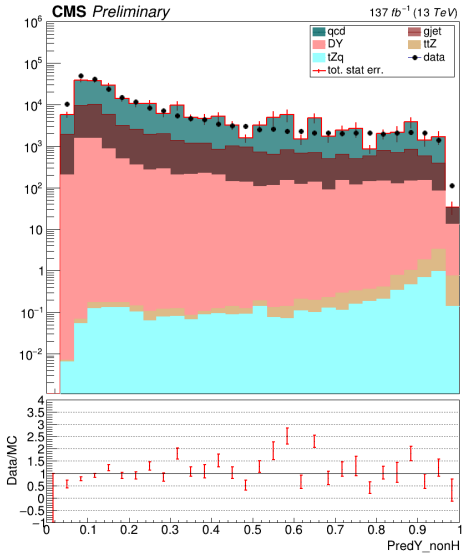

Figure 5.44: The score (denoted by *PredY_nonH*) distribution from the tHq hadronic BDT vs non-H backgrounds classifier in the $Z \rightarrow ee$ control region. The simulation (stacked coloured histograms) is compared to the combination of data taken in 2016, 2017, and 2018 (black points).

5.6.5 Category optimisation

The final categories are defined by placing thresholds on the tHq hadronic BDT vs ttH output score and the tHq hadronic BDT vs non-H backgrounds output score. It is found that one category is sufficient to reach the optimal sensitivity. The resulting categories are summarised in Table 5.10 with the optimised boundaries. The signal yields shown in the table are extracted by fitting a simulated signal model to simulation signal events and integrating in a window of $125 \pm \sigma_{eff}$. The background yield is derived by fitting a smoothly falling function to data and and integrating in a window of $125 \pm \sigma_{eff}$. Note that the fact that there is contamination from ttH processes, and the fact that ttH measurements have some uncertainty, affects the measurement of the tHq hadronic production and the correlations are studied in Chapter 6.

Table 5.10: The expected number of signal and background events, and the expected significance of categories targeting the tHq hadronic process.

No.cat.	Cat.	BDT vs ttH score	BDT vs non-H score	signal tHq + tHW	data	ttH	data + ttH	Sig.	Total sig.
1	Tag 0	>0.11	>0.943	0.819	8.169	2.001	10.17	0.223	0.223
2	Tag 0	>0.11	>0.946	0	9999	0	9999	0	
	Tag 1	0.062 - 0.11	0.628 - 0.946	0.813	8.164	1.979	10.143	0.222	0.222

5.7 Event categorisation in other production channels

This section briefly describes the categorisation process for the remaining production modes (other than qqH and hadronic tHq) measured in the STXS Stage 1.2 framework. These categorisation techniques are not part of the work of this thesis but are used in the full Stage 1.2 categorisation process, and hence in the final measurements in Chapter 6. The full details of these studies may be found in Ref. [1].

The ggH BDT is used to target the ggH STXS bins; the BDT targets the eight bins defined by zero, one and two jets with $p_T^H < 200\,\text{GeV}$ and $m_{jj} < 350\,\text{GeV}$. All events in the four ggH STXS bins with $p_T^H > 200\,\text{GeV}$ are grouped together and form the ninth bin targeted by the ggH BDT. The diphoton BDT is used, after events are classified by the ggH BDT, to define analysis categories within each of the nine bins.

The leptonic VH categorisation process targets events in which the Higgs boson is produced in association with a W or Z vector boson that subsequently decays leptonically. A dedicated BDT is used in each of the three leptonic VH channels where the final states include zero, one, or two charged leptons. The ZH leptonic BDT targets the Z(ll)H production mode, with events with two same-flavour reconstructed leptons with a dilepton invariant mass consistent with the Z boson decay ($60 < m_{ll} < 120\,\text{GeV}$). The Run II dataset is not sensitive to the individual leptonic ZH STXS bins, and thus the leptonic ZH mode is targeted inclusively. Boundaries on the ZH leptonic BDT score are used to define ZH leptonic categories. The WH leptonic BDT targets the W($l\nu$)H production mode, with events with one reconstructed lepton, and additional cuts on the photon ID BDT. The Run II dataset is sensitive to a reduced set of leptonic WH STXS bins, defined by $p_T^{\gamma\gamma} < 75\,\text{GeV}$, $75 < p_T^{\gamma\gamma} < 150\,\text{GeV}$, and $p_T^{\gamma} > 150\,\text{GeV}$. The VH MET BDT is used to target the Z($\nu\nu$)H production mode, with events with no reconstructed leptons and a missing transverse momentum of $p_T^{miss} > 50\,\text{GeV}$. These categories also receive contributions from W($l\nu$)H processes.

The ttH categorisation process targets leptonic and hadronic decays of the top quarks separately. Additionally the leptonic tHq mode is also targeted as part of the ttH categorisation. A deep neural network, called the top DNN, is used to distinguish between leptonic tHq events and ttH events (leptonic and hadronic). In each of the three resulting bins (leptonic tHq, leptonic ttH, hadronic ttH), a dedicated BDT is used to reduce non-Higgs boson backgrounds. These BDTs are called tHq BDT-bkg, ttH leptonic BDT-bkg and ttH hadronic BDT-bkg respectively. The final tHq leptonic analysis category is defined by a cut on both the top DNN and the tHq BDT-bkg. The ttH hadronic channel is defined by zero isolated leptons, while the leptonic channel requires one or more isolated leptons. The inputs to the ttH leptonic and ttH hadronic BDTs are photon, lepton and jet kinematics, but also scores from a top quark tagger and background-specific DNNs. The events are then split into the specific STXS bins using the reconstructed $p_T^{\gamma\gamma}$ values.

5.8 Summary

The CMS detector uses information from all of its subdetectors in order to reconstruct different types of particles, using a technique known as particle flow. Photon candidates reconstructed by the particle flow algorithm are subjected to a set of selection requirements before entering the $H \to \gamma\gamma$ analysis. In particular, a diphoton BDT uses information from

the photon ID BDT, the vertex identification BDT, the per-event mass resolutions together with kinematic variables of the diphoton system, to assign scores to diphoton events.

Candidate events from the reconstruction are categorised using reconstruction-level event variables to target the particle-level bins of the STXS Stage 1.2 framework. The framework allows events to be separated into the different production modes and into different kinematic regions within the production modes. The qqH region of the STXS Stage 1.2 framework consists of five VBF-like bins and one VH-like bin which are targeted in the categorisation, while the remaining bins are constrained to their SM expectations. Events from the reconstruction are required to pass preselection criteria before being categorised. Two BDTs, namely a VBF BDT and a VH hadronic BDT are trained to categorise events into the target STXS bins. Notably, the VBF BDT provides sensitivity to four VBF-like ggH bins in the ggH region of the STXS framework. The BDTs are trained on simulated events and for simulated backgrounds involving jet-jet and γ-jet processes, a data-driven background modelling procedure is adopted to improve the BDT performance. The use of the data-driven background modelling was found to increase the expected observation significance in each of the qqH STXS bins targeted by approximately 4-50%, the inclusive VBF significance by $\sim$20%, and the inclusive VH significance by $\sim$10%. The hyperparameters of the BDTs are optimised to maximise discrimination in simulation, while preserving the generalisability of the algorithms. The simulated background samples used in the training are validated by comparisons to data while the simulated signal models are validated using Drell-Yan events where the electrons are reconstructed as photons. The output scores from the BDTs indicate how signal- or background-like an event is and may be used to set thresholds or boundaries to define categories within the target STXS bins. These boundaries are defined by optimising cuts on the VBF (or VH) BDT output scores and the diphoton BDT output score simultaneously. The weights of the trained BDTs are stored and are applied to data events during the categorisation process.

An additional tHq hadronic tag is defined to target tHq processes where the vector boson, from the top quark decay, decays hadronically. Two BDTs are trained to target this process; one BDT is trained to provide discrimination against ttH processes while a second BDT prvides discrimination against non-Higgs boson background processes. Boundaries on the scores from these two BDTs are optimised simultaneously to define the tHq hadronic tag.

A summary of the different regions of the analysis and the targeted STXS stage 1.2 bins is shown in Table 5.11.

Table 5.11: Description of the different STXS categorisation regions, listed in descending order of priority in the first column. The priority is used to perform the category assignment for events which pass the requirements for more than one analysis category. The second column shows each targeted STXS bin, or merged group of bins, together with the number of associated analysis categories. The last row contains the bins for which no analysis categories are constructed.

Categorisation region	Particle level STXS bin, (units in GeV)	Number of categories
tHq leptonic	tHq	1
ttH leptonic	ttH $p_T^H < 60$	3
	ttH $60 < p_T^H < 120$	3
	ttH $120 < p_T^H < 200$	2
	ttH $200 < p_T^H < 400$	1
	ttH $p_T^H > 300$	1
ZH leptonic	all ZH lep and ggZH lep bins (10 bins total)	2
WH leptonic	WH lep $p_T^V < 75$	2
	all WH lep $75 < p_T^V < 150$ (3 bins total)	2
	WH lep $p_T^V > 150$	1
VH MET	all VH leptonic bins (15 bins total)	3
tHq hadronic	tHq	1
ttH hadronic	ttH $p_T^H < 60$	3
	ttH $60 < p_T^H < 120$	3
	ttH $120 < p_T^H < 200$	4
	ttH $200 < p_T^H < 400$	3
	ttH $p_T^H > 300$	2
VBF	qqH VBF-like low m_{jj} low p_T^{Hjj}	2
	qqH VBF-like low m_{jj} high p_T^{Hjj}	2
	qqH VBF-like high m_{jj} low p_T^{Hjj}	2
	qqH VBF-like high m_{jj} high p_T^{Hjj}	2
	qqH BSM	2
	all ggH VBF-like (4 bins total)	2
VH hadronic	qqH VH-like	2
ggH	ggH 0J low p_T^H	3
	ggH 0J high p_T^H	3
	ggH 1J low p_T^H	3
	ggH 1J med p_T^H	3
	ggH 1J high p_T^H	3
	ggH $\geq$2J low p_T^H	3
	ggH $\geq$2J med p_T^H	3
	ggH $\geq$2J high p_T^H	3
	ggH $200 < p_T^H < 300$	2
	ggH $300 < p_T^H < 450$	2
	ggH $450 < p_T^H < 650$	1
	ggH $p_T^H > 650$	1
No categories	qqH 0J, 1J, $m_{jj} < 60, 120 < m_{jj} < 350$, bbH, tHW, (6 bins total)	0

Chapter 6

Higgs boson measurement results and uncertainties

6.1 Introduction

The categories defined in Chapter 5 are used as regions within which maximum likelihood fits of the signal and background models to the observed $m_{\gamma\gamma}$ distributions in data are performed. Event yields from these fits are in turn used to measure Higgs boson properties.

The elements of the fitting process are presented in this chapter and include signal and background models for the $m_{\gamma\gamma}$ distributions in each analysis category. The signal models are derived from simulation while the data-driven background models use a combination of different functions to describe the smoothly falling $m_{\gamma\gamma}$ background spectrum with the discrete profiling method [168]. The statistical procedure is identical to that used in previous CMS $H \to \gamma\gamma$ analyses [1, 3, 106].

This chapter further describes the treatment of uncertainties, both statistical and systematic, which affect the fits and the measurements made. The systematic uncertainties include both theoretical and experimental uncertainties. Every uncertainty is accounted for in the fitting procedure in the form of a nuisance parameter, which is any parameter of the signal and background model for which an uncertainty interval is not constructed. The values of nuisance parameters are allowed to vary in the fits; the nuisance parameters are said to be *profiled*.

The expected event yields in the various categorisation regions defined in Chapter 5 are presented and these shed light on the sensitivity to various processes in the analysis and on the levels of contamination from non-target processes within categories.

The values of the parameters of interest are estimated using the profile likelihood test statistic, whereby twice the negative log-likelihood (2NLL) is minimised simultaneously in all analysis categories. The best-fit value of a parameter and its uncertainty may be extracted from the resulting 2NLL curve. The process of profiling nuisance parameters widens the 2NLL curve and increases the uncertainty in the measured parameter. In this analysis,

the measurements made include those of signal strength modifiers, cross-sections in two bin-merging scenarios of the STXS framework, and coupling modifiers. Additionally, the correlations between the various parameters measured are also presented.

Most of the elements of this analysis were first presented in Ref. [1], where the results after including the VBF BDT and the VH hadronic BDT (Chapter 5) were reported. Thus the results in this chapter are expected to be very close to the results presented in Ref. [1], the only difference being the effects arising from the addition of the new tHq hadronic category described in Chapter 5.

6.2 Systematic uncertainties

The systematic uncertainties considered in this chapter are mostly unchanged from those used in previous STXS analyses [1, 3].

The systematic uncertainty associated with the data-driven background estimation is treated using the discrete profiling method, as described in Section 6.3.2. The systematic uncertainties which affect the signal model are handled in one of two ways. Uncertainties which modify the shape of the $m_{\gamma\gamma}$ distribution are included in the signal modelling process as nuisance parameters. These uncertainties are generally experimental uncertainties relating to the energy of the individual photons. Uncertainties which do not change the shape of the $m_{\gamma\gamma}$ distribution are treated as a log-normal variation in the event yield. These uncertainties include theoretical uncertainties, and experimental uncertainties such as those relating to the BDTs used in the event categorisation process. The magnitude of the impact of each uncertainty on the measured quantities is determined individually in each signal bin in each analysis category.

6.2.1 Theoretical uncertainties

Theoretical uncertainties in the overall cross-sections are considered as uncertainties in the SM predictions and are not included in the cross-section measurement uncertainty in each STXS bin. Uncertainties relating to the event kinematics which affect the distributions of variables used in the event selection and categorisation processes are included in the cross-section measurement uncertainty in each STXS bin. Both types of uncertainties, i.e cross-section and event kinematics uncertainties, are included in the measurement of signal strengths and coupling modifiers. When deriving the effect on the kinematic distributions, the impact on the STXS bin cross-section normalisation is factored out to avoid double counting.

The sources of theoretical uncertainty considered in this analysis are outlined below:

- *QCD scale uncertainties*: these uncertainties arise from variations of the renormalisation and factorisation scales used when computing the expected SM cross-section and event kinematic variables. These account for the missing higher-order terms in QCD perturbative calculations and are treated as per the recommendations provided in Ref. [40]. The uncertainty in the overall normalisation is estimated using three sources: varying the renormalisation by a factor of two, varying the factorisation scale by a factor of two, and varying both in the same direction simultaneously. The size of the uncertainty in the overall normalisation varies from around 0.5% for VBF production

to 15% for tHq production. To estimate the uncertainty in the event kinematics, the distribution of events falling into each analysis category is re-evaluated after varying both the renormalisation and factorisation scales by a factor of two in the same direction simultaneously. In this process, the overall cross-section for a given STXS bin is kept constant. The 22 bin-to-bin event migration uncertainties are around 1%.

- *Uncertainties in the ggH STXS fractions*: uncertainties in the modelling of the p_T^H distributions, the number of jets in the event, and the ggH contamination in the VBF categories, are additionally considered for ggH production. The migration of events around the p_T^H bin boundaries at 60 and 120 GeV are estimated by two sources respectively, each depending on the number of jets and the p_T^H. An additional uncertainty in p_T^H arises from the assumption of an infinite top quark mass in the ggH loop and is determined by comparing the p_T^H distribution to the predictions from finite-mass calculations. Two further sources account for the migration of events between the 0J, 1J and $\geq$ 2J bins. The uncertainty in the ggH production of events with a VBF-like dijet system is covered by two sources corresponding to the prediction in the 2J-like and 3J-like bins. The total magnitude of these uncertainties varies from around 5% to 30%, with events that have one or more jets and high values of p_T^H typically having the greatest associated uncertainty.
- *Uncertainties in the qqH STXS fractions*: for qqH production, additional sources are introduced to account for the uncertainty in the modelling of the p_T^H, m_{jj} and p_T^{Hjj} distributions, and the number of jets in the event. Six sources are defined to reflect migrations of events across m_{jj} boundaries at 60, 120, 350, 700, 1000 and 1500 GeV. Two additional nuisance parameters account for migrations across the p_T^H bin boundary of 200 GeV and the p_T^{Hjj} bin boundary of 25 GeV. A single source is defined to account for a migration between the 0J, 1J, and $\geq$ 2J bins. In each case, the uncertainty is computed by varying the QCD scales and recalculating the fractional breakdown of qqH STXS Stage 1.2 cross-sections. The total magnitude varies between bins but is at most 8%.
- *Uncertainties in the ttH STXS fractions*: for ttH production, four nuisance parameters are used to account for the uncertainty in the p_T^H distributions. Each nuisance parameter represents the migration across one of the boundaries at the p_T^H values of 60, 120, 200, and 300 GeV that define the ttH STXS bins. The magnitudes of these uncertainties are derived by varying the renormalisation and factorisation scales, and have values of up to 9%.
- *Uncertainties in the VH leptonic STXS fractions*: for leptonic VH production, additional sources are introduced to account for the uncertainty in the modelling of the p_T^V distributions, and the number of jets in the event. Four independent sources are defined to reflect the migrations of events across the p_T^V boundaries at 75, 150, and 250 GeV, in addition to the migration between the 0J and $\geq$ 1J bins for events with a p_T^V of 150-250 GeV. These sources are defined separately for the WH leptonic, ZH leptonic, and ggZH leptonic production modes. In each case, the uncertainty is computed by varying the renormalisation and factorisation scales and recalculating the fractional breakdown of VH leptonic STXS Stage 1.2 cross-sections. The total magnitude varies between bins but is at most 5% for the dominant WH and ZH leptonic production modes.

- *Uncertainty in the ggH contamination of the top quark associated categories*: the theoretical predictions for ggH are less reliable in a regime where the Higgs boson is produced in association with a large number of jets. Three different contributions are considered. The uncertainty from the parton shower modelling is estimated by taking the observed difference in the jet multiplicity between MADGRAPH predictions and data in tt+jets events. The uncertainty in the gluon splitting modelling is estimated by scaling the fraction of events from ggH with real b quark jets in simulation by the measured difference between data and simulation of $\sigma(\mathrm{t\bar{t}b\bar{b}})/\sigma(\mathrm{t\bar{t}jj})$ and the uncertainty due to the limited size of the simulated samples. The combined impact of these uncertainties in the top quark associated signal strength is about 2%.
- *PDF (parton density functions) uncertainties*: these account for the uncertainty due to imperfect knowledge of the composition of the proton, which affects which partons are most likely to initiate high energy events. The overall normalisation uncertainties are computed following the PDF4LHC prescription [71, 169], while the uncertainties in the event kinematics are calculated from the NNPDF3.0 [170] PDF set using the MC2HESSIAN procedure [171]. The overall normalisation uncertainties are between 1-5%, with the migrations significantly smaller, usually less than 1%.
- *Uncertainty in the strong force coupling constant*: the uncertainty in the value of the strong force coupling constant α_s is included in the treatment of the PDF uncertainties, following the PDF4LHC prescription. An additional source is included to account for changes in the event kinematics due to the uncertainty in α_s. This is calculated using a similar procedure to the QCD scale migration uncertainties but by varying the value of α_s instead.
- *Uncertainty in the $H \to \gamma\gamma$ branching fraction*: the probability of the Higgs boson decaying to two photons is required to calculate the SM expected cross-section, but this branching fraction is not known exactly. The uncertainty is currently estimated to be 2% [40].
- *Underlying event and parton shower uncertainties*: these uncertainties are obtained using dedicated simulated samples where the choice and specific tune of the event generator have been modified. The normalisation uncertainties are in general around 5%, but can be as large as 30% for bins corresponding to high p_T^H and high jet multiplicity. The impact of the migration uncertainties range from 1-16% depending on the process and analysis category. The impact is in general around 5%, but can be as large as 30% for bins corresponding to high p_T^H and high jet multiplicity.
- *Uncertainties in the composition of merged STXS bins*: as described in Section 6.6.1, it is necessary to merge certain STXS bins when measuring cross-sections to avoid large uncertainties or very high correlations between parameters. The act of merging bins across a boundary means the cross-section measurement is sensitive to the relative fraction of the two bins. As a result, the uncertainty sources accounting for migrations across the merged boundaries are included in the relevant cross-section measurements.

6.2.2 Experimental uncertainties

The uncertainties which affect the shape of the signal $m_{\gamma\gamma}$ distribution are:

- *Photon energy scale and resolution*: the uncertainties associated with the corrections applied to the photon energy scale in data and the resolution in simulation are evaluated using $Z \to e^+e^-$ events. The estimate is computed by varying the regression training

scheme, the distribution of the R_9 variable, and the electron selection criteria. For most photons, the energy scale uncertainty lies in the range 0.05-0.15%, with very high p_T photons having an energy scale uncertainty in the range 0.5-3.0%.

- *Non-linearity of the photon energy scale*: a further source of uncertainty covers possible remaining differences in the linearity of the photon energy scale between data and simulation. The uncertainty is estimated using boosted $Z \to e^+e^-$ events. In this analysis, an uncertainty of 0.2% on the photon energy scale is assigned, which accounts for the non-linearity across the full range of photon p_T values.
- *Shower shape corrections*: an uncertainty in the shower shape corrections accounts for the imperfect modelling of shower shapes in simulation. The impact is estimated by comparing the energy scale before and after the corrections to shower shape variables (used to improve the agreement between data and simulation) are applied. The magnitude of this uncertainty lies in the range of 0.01-0.15% depending on photon η and R_9 values.
- *Longitudinal non-uniformity of light collection*: an uncertainty is associated with the modelling of the light collection as a function of emission depth within a given ECAL crystal. The calculation of this uncertainty is described in detail in Ref. [97]. The uncertainty is between 0.16-0.25% for photons with $R_9 > 0.96$; the magnitude for low R_9 photons is below 0.07%.
- *Modelling of material in front of the ECAL*: the amount of material through which objects pass before reaching the ECAL affects the behaviour of the electromagnetic showers, and may not be perfectly modelled in simulation. Dedicated samples with variations in the amount of upstream material are used to estimate the impact on the photon energy scale. The magnitude of the resulting uncertainty ranges from 0.02-0.05% for the most central photons, increasing to up to 0.24% for those in the endcap.
- *Vertex assignment*: the largest contribution to the uncertainty in the fraction of right and wrong vertices comes from the modelling of the underlying event and the uncertainty in the ratio of data and simulation obtained using $Z \to \mu\mu$ events. A nuisance parameter is included in the signal model that allows the fraction of events in each vertex scenario to vary by $\pm 2\%$.

The uncertainties that only modify the event yield have an effect of around 4% on the inclusive Higgs boson signal strength modifier measurement and include the set of sources below:

- *Integrated luminosity uncertainties*: these are estimated to be 2.5%, 2.3% and 2.5% for the 2016, 2017 and 2018 data sets respectively [172–174].
- *Photon identification BDT score*: the uncertainty arising from the photon identification BDT score is estimated by requiring the systematic variation to account for the residual discrepancies between data and simulation. The uncertainty in the signal yields is estimated by propagating this uncertainty through the full category selection procedure. The impact in the most sensitive analysis categories is around 3%.

- *Jet energy scale and smearing corrections*: the energy scale of jets is measured using the p_T balance of jets with Z bosons and photons in $Z \to e^+e^-$, $Z \to \mu\mu$ and γ+jets events, as well as the p_T balance between jets in dijet and multijet events [175]. The uncertainty in the jet energy scale is a few percent and depends on p_T and η. The impact of jet energy scale uncertainties on event yields is evaluated by varying the jet energy corrections within their uncertainties and propagating the effect to the final result. Correlations between years are introduced for the different jet energy scale uncertainty sources, ranging between 0 and 100%. The impact on the analysis category yields is largest for those targeting VBF, hadronic VH and top-associated production and can be as high as 22% for the scale uncertainties, but is less than around 8% for the resolution.
- *Per-photon energy resolution estimate*: the uncertainty in the per-photon resolution is parametrised as a rescaling of the resolution by $\pm 5\%$ about its nominal value. This is designed to cover all differences between data and simulation in the distribution, which is an output of the energy regression. The maximum yield variation in an analysis category is around 5%. However, for most categories, the impact is at the sub-percent level.
- *Trigger efficiency*: the efficiency of the trigger selection is measured with $Z \to e^+e^-$ events using the tag-and-probe technique. The size of its uncertainty is less than 1%. An additional uncertainty is introduced to account for a gradual shift in the timing of the inputs of the ECAL L1 trigger in the region $|\eta| > 2.0$, which caused a specific trigger inefficiency during 2016 and 2017 data taking [1]. Both photons, and to a greater extent jets, can be affected by this inefficiency. The resulting uncertainty is largest for the categories targeting VBF production, with a maximum impact on the yield of 1.4%.
- *Photon preselection*: the uncertainty in the preselection efficiency is computed as the ratio between the efficiency measured in data and in simulation. Its magnitude is less than 1%.
- *Missing transverse momentum*: this uncertainty is computed by shifting the reconstructed p_T of the particle candidates entering the missing transverse momentum computation, within the momentum scale and resolution uncertainties appropriate to each type of reconstructed object, as described in Ref. [175]. In this analysis, the impact on the analysis category yields is never larger than 5%, even for analysis categories which explicitly use the missing transverse momentum in their definition.
- *Pileup jet identification*: the uncertainty in the pileup jet classification output score is estimated by comparing the score of jets in events with a Z boson and one balanced jet in data and simulation. The magnitude is of the order 1%.
- *Lepton isolation and identification*: this uncertainty, affecting electrons and muons, is computed by varying the ratio of the efficiency in simulation to the efficiency in data and using the tag-and-probe technique in $Z \to e^+e^-$ events. The resulting impact on the categories selecting leptons is up to around 1%.
- *Uncertainties in b-tagging*: uncertainties in the b-tagging efficiency are evaluated by comparing data and simulated distributions for the b-tag discriminator. The

uncertainties include the statistical component on the estimate of the fraction of heavy and light flavour jets in data and simulation. Its magnitude is around 2% for the analysis categories targeting top associated production, which make use of the b-tagging discriminant.

6.2.3 Uncertainty correlations

Since the analysis inputs and the analysis category definitions are constructed by merging the 2016, 2017 and 2018 datasets, the theoretical and experimental uncertainties can be chosen to be correlated or uncorrelated across years. If an uncertainty is taken to be correlated between years, only one nuisance parameter is used to represent this uncertainty in the final fits. Conversely, if an uncertainty is uncorrelated between years, three independent nuisance parameters are introduced in the final fits.

In this analysis, all the sources of theory systematic uncertainties are taken to be correlated between years. This is done because the underlying theoretical predictions are the same for each year and independent of the data-taking conditions. For the experimental uncertainties, most uncertainties are left uncorrelated since both the data-taking conditions and the reconstruction procedures vary between years. Exceptions include the uncertainty on the photon identification BDT output, which is kept correlated because the uncertainty prescription is identical across years, and the partially correlated integrated luminosity and jet energy correction uncertainties. This is expected, since the predominant source of uncertainty in all the STXS measurements is statistical in origin. A cross-check of the final results with all uncertainties taken to be correlated confirmed that the difference between the two correlation treatment schemes is minimal.

6.3 Statistical procedure

The statistical procedure used in this analysis is identical to that described in Ref. [89], as developed by the ATLAS and CMS Collaborations.

In each analysis category, a fit of the analytic signal and background models to the observed $m_{\gamma\gamma}$ distribution in data is performed.

The type of fit performed is a binned maximum likelihood fit in the range $100 < m_{\gamma\gamma} < 180\,\text{GeV}$. The bin size (250 MeV) is chosen to be sufficiently small so as not to affect the diphoton mass resolution. In this analysis, the m_H is fixed to its most precisely known value of 125.38 GeV [97]. This choice is made to ensure that all measurements are consistent with the best available knowledge of m_H.

For each analysis category, the likelihood function ($\mathcal{L}_c$) may be defined as

$$\mathcal{L}_c(\text{data}|\vec{\sigma},\vec{\theta}) = \prod_{i=1}^{N_b} \text{Poisson}\left(d_i|s_i(\vec{\sigma},\vec{\theta}) + b_i(\vec{\theta})\right) \times C(\vec{\theta}), \tag{6.1}$$

where $\vec{\sigma}$ represents the set of parameters of interest (POIs). In this analysis, the POIs can be signal strengths, cross-sections or coupling modifiers, depending on the fit being performed. Here, $\vec{\theta}$ is the set of nuisance parameters (defined previously); N_b is the number of bins used for the binned maximum likelihood fit in the analysis category; *Poisson* indicates a

Poisson function evaluated with the observed number of events in the i$^{\text{th}}$ bin d_i, and the expected number of events from the sum of the signal expectation s_i and the background expectation b_i; $C(\vec{\theta})$ penalises deviations of signal nuisance parameters from expected values. The expected number of signal events in each bin depends on the POIs, and the nuisance parameters, whilst the expected number of background events depends only on unconstrained nuisance parameters.

The product of likelihoods over all categories gives the total likelihood function ($\mathcal{L}$), defined as

$$\mathcal{L}(\text{data}|\vec{\sigma},\vec{\theta}) = \prod_{c=1}^{N_c} \mathcal{L}_c(\text{data}|\vec{\sigma},\vec{\theta}), \tag{6.2}$$

where N_c is the number of analysis categories.

The fit is performed by minimising the value of the negative log-likelihood (2NLL) which is defined as

$$2\text{NLL} = -2\ln\mathcal{L}(\text{data}|\vec{\sigma},\vec{\theta}) \tag{6.3}$$

Thus the POIs and the background nuisance parameters are the only free parameters in the fit; the signal nuisance parameters may vary within the constraints of the $C(\vec{\theta})$ term.

The statistical data analysis package, RooFit [176], is used to numerically minimise the value of the 2NLL and extract the corresponding best-fit values of the POIs.

The uncertainty on each POI is extracted using the distribution of the likelihood ratio test statistic, 2ΔNLL or q, given by

$$2\Delta\text{NLL} = -2\ln\frac{\mathcal{L}(\text{data}|\vec{\sigma},\vec{\hat{\theta}})}{\mathcal{L}(\text{data}|\vec{\hat{\sigma}},\vec{\hat{\theta}})}, \tag{6.4}$$

where $\vec{\hat{\theta}}$ is the set of conditional best-fit nuisance parameters at the POIs values of $\vec{\sigma}$, while $\vec{\hat{\sigma}}$ and $\vec{\hat{\theta}}$ are the global (unconditional) best-fit values of the POIs and the nuisance parameters respectively.

The distribution of the likelihood ratio test statistic is used to derive the uncertainties on the measured POIs. Over a sufficient number of events, the likelihood ratio test statistic can be approximated from a χ^2 distribution with a number of degrees of freedom equal to the number of POIs [177]. Thus confidence intervals for the values of the POIs may be extracted approximately from the corresponding χ^2 distributions. For example, the 68% confidence interval may be interpreted as the interval containing the true POIs value in 68% of cases. For a single POI, the parameter values corresponding to ±0.99 (3.84) for the 2ΔNLL can be used as the boundaries of the 68% (95%) confidence interval. In the case where there are multiple parameters of interest in the fit, the intervals are determined treating the other parameters as nuisance parameters. For two-dimensional measurements, such as those performed to coupling modifiers in the κ-framework, the 68 and 95% confidence regions are defined by the set of parameter values corresponding to the range between 2ΔNLL values of ±2.30 and ±5.99 respectively.

After the cross-section in each STXS analysis category has been measured as a POI, the value is divided by the SM prediction. It is to be noted that the cross-section measurement is independent of the SM prediction and the related theoretical uncertainties. In signal

strength modifier measurements, however, the SM prediction uncertainties are included in the fit since the definition of the signal strength modifier includes the SM prediction in the denominator.

The signal and background models are described in detail in the remainder of this section.

6.3.1 Signal modelling

An analytic signal model, derived from simulation, is constructed for each particle level STXS bin in each reconstructed analysis category. Both the shape and normalisation of the model are parametrised as functions of m_H. Moreover, since the shape of the $m_{\gamma\gamma}$ distribution is dependent on whether the right vertex (RV) or wrong vertex (WV) was chosen, the signal modelling is performed separately for each of these cases. The correct vertex is defined as being within 1 cm of the true vertex position.

Each signal model is constructed using a sum of up to five Gaussian functions. The shape of the $m_{\gamma\gamma}$ distribution and the number of available simulated events dictates the number of Gaussian functions required. The number of Gaussian functions is determined using an $\mathcal{F}$-test [178]. For categories where there is an insufficient number of simulated events to produce a signal model, the shape from the STXS bin with the highest expected yield in the analysis category being considered is used as a replacement. This procedure is justified since events ending in the same analysis category tend to have similar diphoton mass resolutions.

Simulated signal samples with different nominal m_H values are used. A simultaneous fit to all the different m_H samples is performed, where the individual parameters of the Gaussian functional form are themselves polynomials of m_H. The floating parameters in the fit are the coefficients of these polynomials. This method guarantees a sensible parametric model with the shape and normalisation varying smoothly as a function of m_H.

Systematic uncertainties corresponding to the smearing and scale of the individual photon energies, the fraction of events where the RV was correctly identified, and the material corrections and ECAL crystal light yields are incorporated into the signal model as nuisance parameters.

The final fit function for each analysis category is obtained by summing the individual functions for all STXS bins in both vertex scenarios. The relative size of the RV and WV shapes in the summed fit is given by the vertex selection efficiency determined in the simulation as a linear function of m_H. For categories with few simulated events, where a replacement model was needed, the RV fraction is set to 1. The contribution from each STXS Stage 1.2 bin in a given analysis category is estimated using inclusive SM cross-sections and $H \to \gamma\gamma$ branching fractions taken from Ref. [40]. The fraction for the cross-sections of each individual STXS bin are taken directly from the simulation. The product of the detector efficiency and analysis acceptance is also taken into account and is modelled as a linear function of m_H. This is calculated as the fraction of events entering a given analysis category for each signal bin, taking into account the events which are not selected to enter any analysis category.

The signal models for the VBF 2J-like Tag 0, VBF-like ggH Tag 0, qqH VH-like Tag 0 and tHq hadronic analysis categories are shown in Figure 6.1. The plots show the shape and normalisation of the model for each year individually, as well as the summed model for all years together. The full set of the signal models for each analysis category is shown in Appendix E.

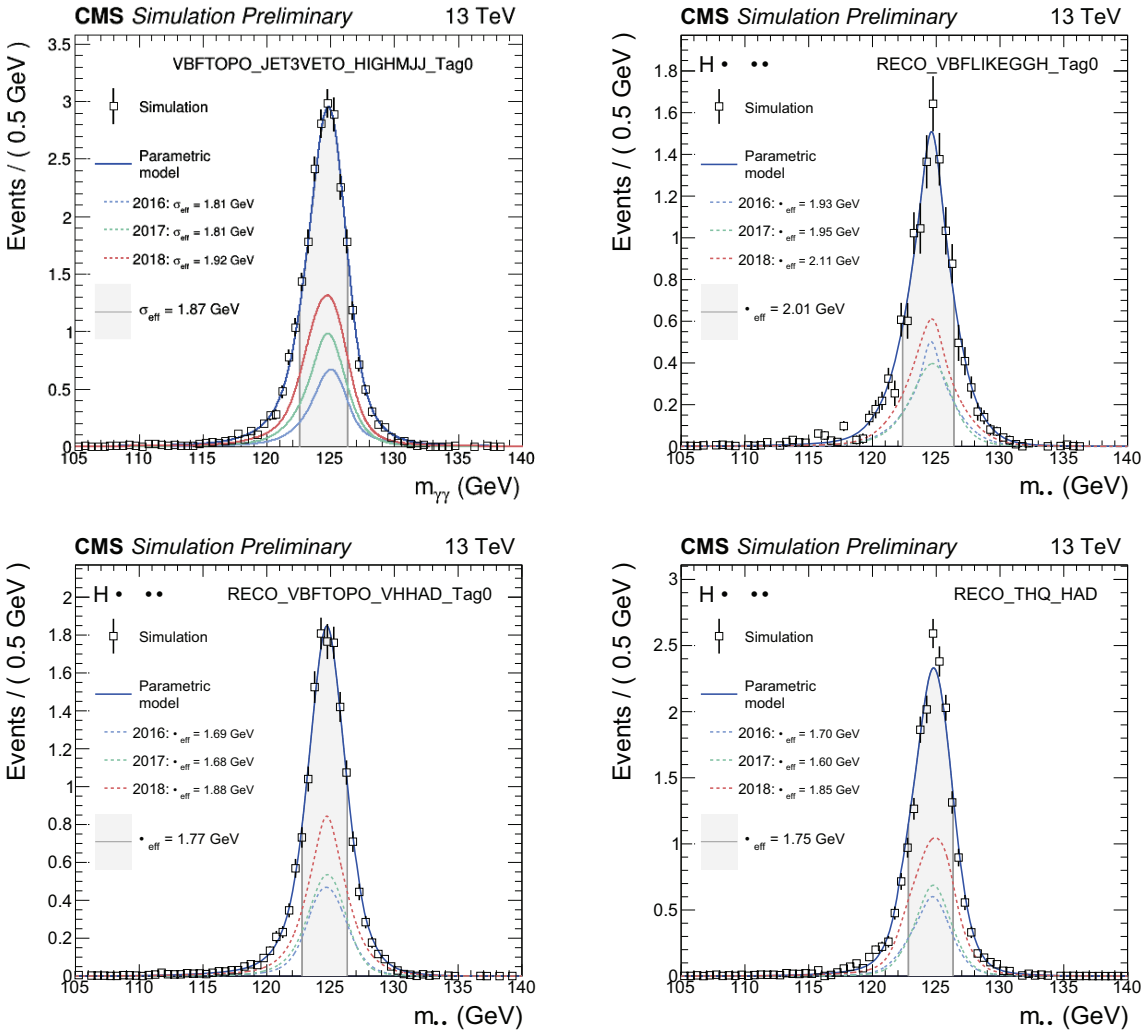

Figure 6.1: Signal models for the VBF 2J-like Tag 0 (top left), VBF-like ggH Tag 0 (top right), qqH VH-like Tag 0 (bottom left) and tHq hadronic (bottom right) analysis categories. Models are shown for each year separately (dotted lines) and all years summed together. The open squares represent weighted simulation events and the blue line shows the corresponding model. Also shown in the grey shaded area is the σ_{eff} value (half the width of the narrowest interval containing 68.3% of the invariant mass distribution).

6.3.2 Background modelling

The background model is determined directly from data and serves to model the smoothly falling spectrum of the $m_{\gamma\gamma}$ distribution resulting from non-Higgs boson production processes. The analytic background model for each analysis category can take one out of a range of different functional forms. The choice of this function affects the signal yields and the uncertainty associated with this choice should be accounted for in the final results.

Figure 6.2 shows the functions chosen in the background modelling for the same analysis categories as shown in Figure 6.1. It is clear from these plots that different choices of functions lead to a different number of events integrated under the signal peak. Equivalent plots for the remaining categories are included in Appendix F.

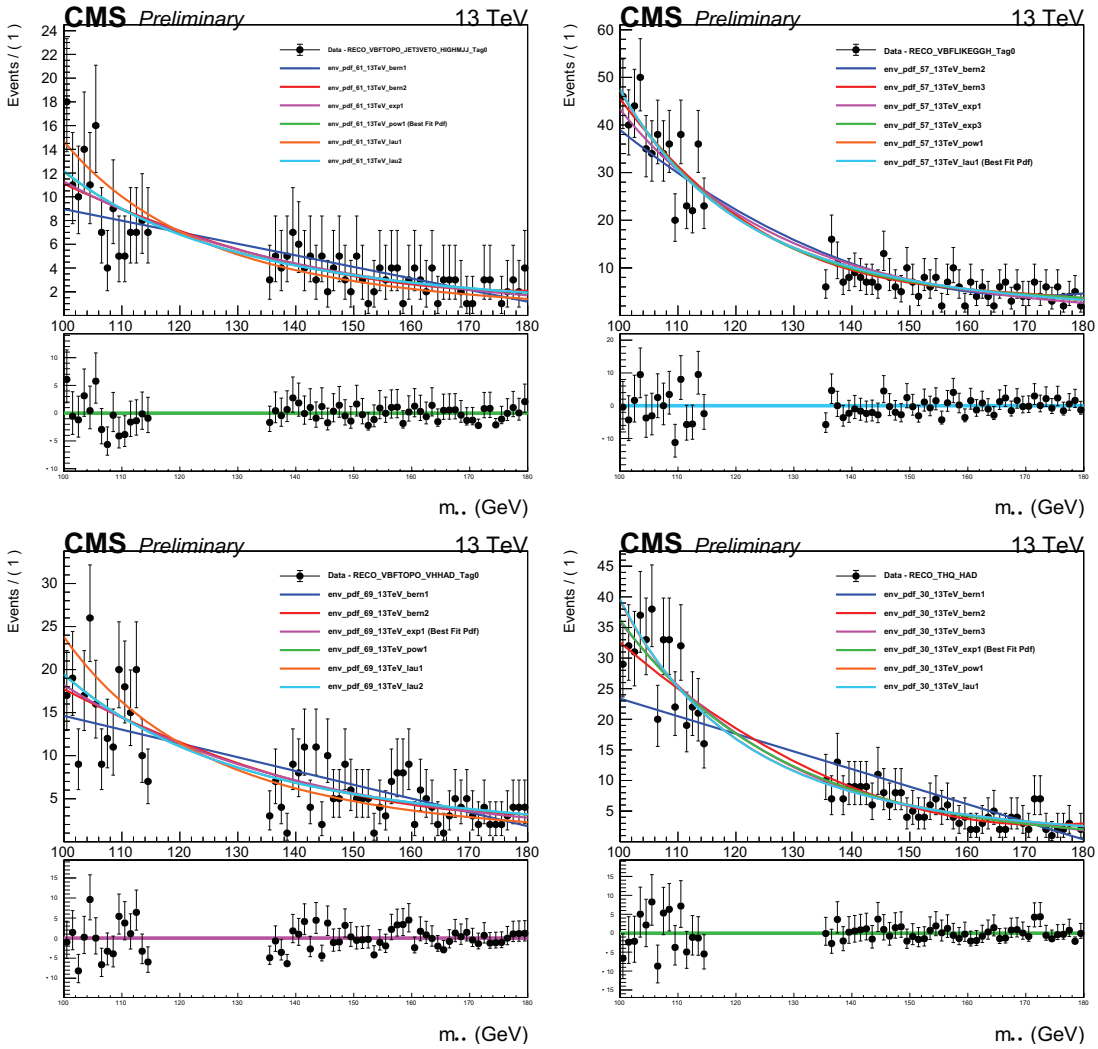

Figure 6.2: Functions chosen to fit the background using the discrete profiling method. Background models for the VBF 2J-like Tag 0 (top left), VBF-like ggH Tag 0 (top right), qqH VH-like Tag 0 (bottom left) and tHq hadronic (bottom right) categories are shown.

In this analysis, the discrete profiling (or envelope) method is used to model the diphoton mass $m_{\gamma\gamma}$ distribution between 100 and 180 GeV in each analysis category. The method is described in detail in Ref. [168], and has been used in many past $H \to \gamma\gamma$ analyses. Only a brief description is given in this section. Following this method, the systematic uncertainty associated with choosing a particular analytic function to fit the background $m_{\gamma\gamma}$ distribution is treated as a discrete nuisance parameter in the likelihood fit to the data. This treatment of the background uncertainty is similar to the treatment of other nuisance parameters, the only difference being that the choice of background function is discrete rather than continuous. A different 2NLL curve is generated by each choice of background function, and the final 2NLL curve represents the *envelope* of each of these individual curves. Since the resulting envelope is necessarily wider than any of the individual curves corresponding to individual functions, the final 2NLL curve returns a greater uncertainty. Thus the discrete profiling method accounts for the uncertainty in the background function.

For each analysis category, a range of analytical functions are used as candidates to the discrete profiling method. A large set of candidate function families is considered, including

exponential functions, Bernstein polynomials, Laurent series, and power law functions. To maintain computational efficiency, an $\mathcal{F}$-Test is performed to determine the maximum order of parameters needed for each family of functions. This test measures the increase in the goodness-of-fit with each increase in function complexity. To prevent functions of arbitrarily high order from being selected, a penalty equal to the number of parameters in the function is applied to the value of the 2NLL. The minimum order is obtained by placing a requirement on the goodness-of-fit to the data.

Figure 6.3 shows the result of the signal-plus-background model fit in the same categories as shown in Figures 6.1 and 6.2.

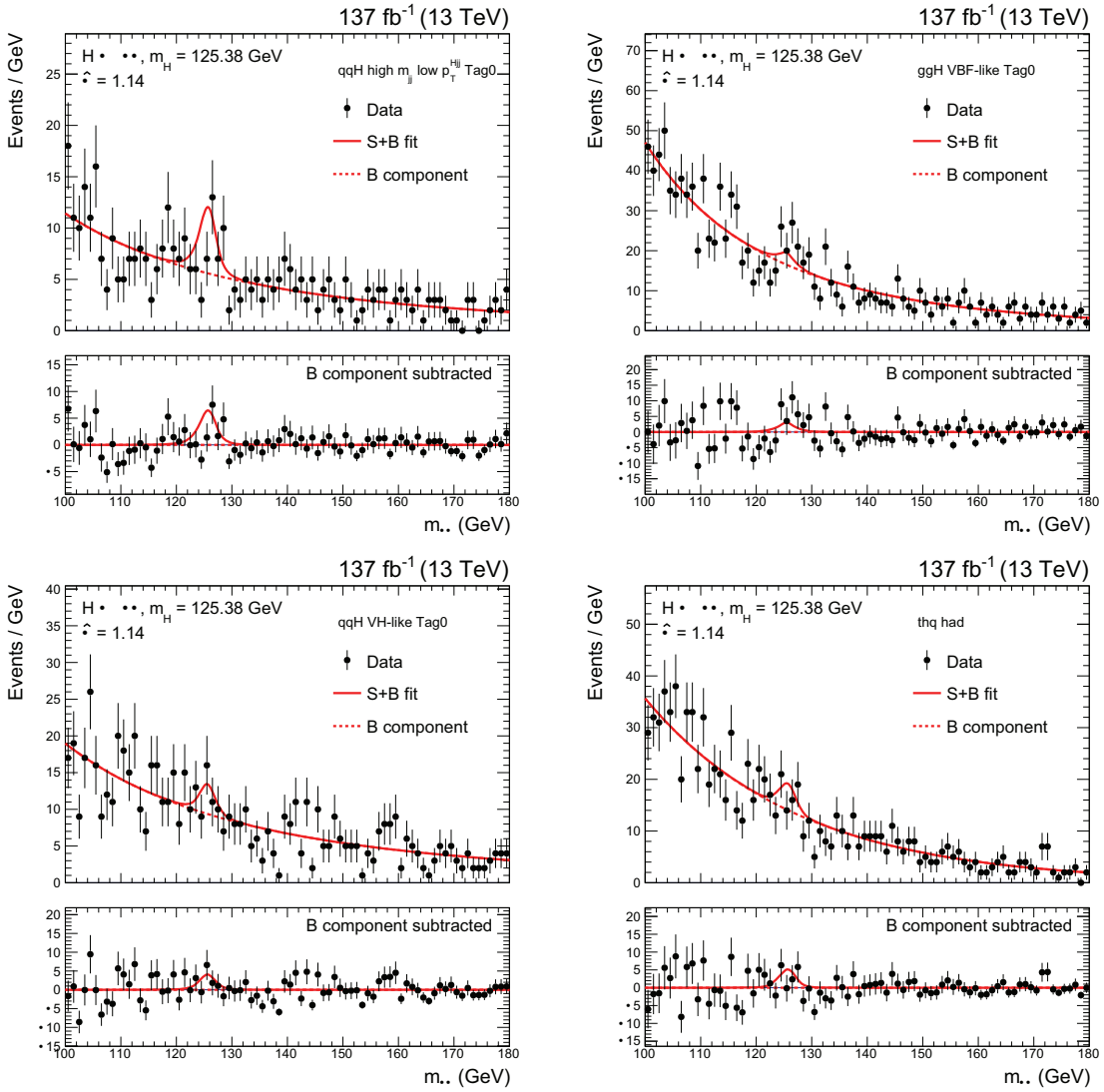

Figure 6.3: Data points (black) and signal-plus-background model fit to the mass sidebands in the VBF 2J-like Tag 0 (top left), VBF-like ggH Tag 0 (top right), qqH VH-like Tag 0 (bottom left) and tHq hadronic (bottom right) analysis categories. The solid red line shows the contribution from the total signal, plus the background contribution. The dashed red line shows the contribution from the background component of the fit. The bottom plot shows the residuals after subtraction of this background component. The parameter $\hat{\mu}$ shows the observed inclusive signal strength over all categories.

Each of the background functions selected as described in the previous section is considered in the final signal-plus-background (S+B) fit to the data, where the one resulting in the overall best fit is chosen for each value of the POIs. In the fit, the normalisation and shape parameters for the background functions are also free to float. The per-production-mode signal strengths μ_i are allowed to float and m_H is fixed to 125.38 GeV. In the plots, the signal model for the respective analysis category is shown to illustrate the signal-to-background ratio. Equivalent plots for the all analysis categories are provided in Appendix G.

The signal-plus-background model fit, performed simultaneously to all analysis categories, is shown with data in Figure 6.4. In the plot, the contribution from each analysis category is weighted by the ratio of signal events to background events, such that the absolute signal yield is kept constant. The signal peak due to Higgs boson production can be clearly seen.

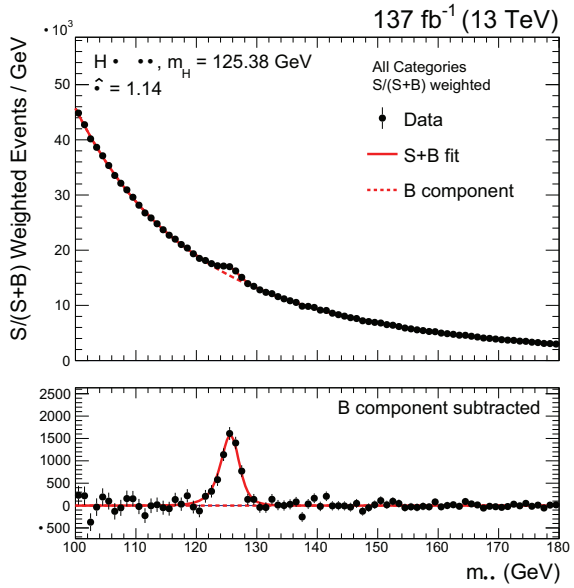

Figure 6.4: Data points (black) and signal-plus-background model fit for the sum of all categories is shown. The solid red line shows the total signal-plus-background contribution, whereas the dashed red line shows the background component only. The bottom panel shows the residuals after subtraction of this background component. In the plot each analysis category is weighted by S/(S+B), where S and B are the numbers of expected signal and background events, respectively, in a $\pm 1\sigma_{eff}$ mass window centered on m_H. The parameter $\hat{\mu}$ shows the observed inclusive signal strength over all categories.

6.4 Event yields and analysis category compositions

Simultaneous fits to all the categories are performed under different scenarios to extract best-fit values and uncertainties of Higgs boson properties. All analysis categories suffer from varying levels of contamination from non-Higgs boson background events as well as from Higgs boson processes other than those being targeted. The extent of contamination affects the sensitivity of the analysis category during the fitting procedure.

The expected number of signal events for a Higgs boson mass of 125 GeV is shown for each analysis category in Tables 6.1 to 6.4. For expected results, an Asimov dataset (a dataset in which all observed quantities are set equal to their expected values) is generated with a

signal rate set to the SM prediction and the background obtained from the best-fit candidate function. The percentage contributions to the total signal yield from each production mode is also shown. Additionally, the percentage of signal events originating from the targeted STXS stage 1.2 processes is given. The σ_{eff} are listed and serve as a measure of the $m_{\gamma\gamma}$ resolution in each analysis category. The expected ratio of signal to signal-plus-background, S/(S+B), quantifies the purity of each analysis category. Here, the S and B are the expected signal and background yields in a $\pm 1\,\sigma_{\text{eff}}$ mass window around 125 GeV. The S/(S+B) ratio is highest in the *Tag 0* categories and decreases as the tag number increases.

Table 6.1: The expected number of signal events for a Higgs boson mass of 125 GeV in categories targeting ggH production. The yield in each analysis category is broken down into percentage contributions from each production mode, and also the percentage of events originating from the targeted STXS Stage 1.2 bins. The σ_{eff}, defined as the smallest interval containing 68.3% of the invariant mass distribution is listed as a measure of the resolution in each analysis category. The final column shows the expected ratio of signal to signal-plus-background, S/(S+B), where S and B are the numbers of expected signal and background events in a $\pm 1\sigma_{\text{eff}}$ window centred on m_H.

Analysis categories	SM 125 GeV Higgs boson expected signal								
	Total	Target STXS bin(s)	Production Mode Fractions					σ_{eff} (GeV)	S/S+B
			ggH	bbH	qqH	VH lep	top		
0J low $p_T^{\gamma\gamma}$ Tag0	295.4	87.1%	98.6%	1.3%	0.2%	-	-	1.93	0.06
0J low $p_T^{\gamma\gamma}$ Tag1	337.7	89.1%	98.7%	1.2%	0.1%	-	-	2.35	0.03
0J low $p_T^{\gamma\gamma}$ Tag2	277.8	90.0%	98.9%	1.1%	-	-	-	2.60	0.01
0J high $p_T^{\gamma\gamma}$ Tag0	618.2	84.0%	97.0%	1.5%	1.5%	-	-	1.68	0.09
0J high $p_T^{\gamma\gamma}$ Tag1	1123.4	81.7%	96.9%	1.5%	1.6%	-	-	2.22	0.04
0J high $p_T^{\gamma\gamma}$ Tag2	1173.4	80.5%	96.6%	1.6%	1.5%	0.3%	-	2.58	0.02
1J low $p_T^{\gamma\gamma}$ Tag0	126.5	66.4%	89.5%	0.9%	8.8%	0.7%	-	1.61	0.10
1J low $p_T^{\gamma\gamma}$ Tag1	328.5	66.6%	89.3%	0.9%	8.9%	0.9%	-	2.01	0.05
1J low $p_T^{\gamma\gamma}$ Tag2	250.2	66.6%	88.9%	1.0%	9.1%	1.0%	-	2.47	0.02
1J med $p_T^{\gamma\gamma}$ Tag0	174.9	66.0%	82.3%	0.5%	15.8%	1.4%	-	1.73	0.13
1J med $p_T^{\gamma\gamma}$ Tag1	295.3	67.0%	84.5%	0.5%	13.4%	1.6%	-	1.96	0.07
1J med $p_T^{\gamma\gamma}$ Tag2	277.0	66.2%	84.8%	0.6%	12.7%	1.9%	-	2.17	0.03
1J high $p_T^{\gamma\gamma}$ Tag0	34.1	62.3%	76.8%	-	22.9%	0.3%	-	1.63	0.26
1J high $p_T^{\gamma\gamma}$ Tag1	29.0	62.0%	75.9%	0.3%	23.4%	0.4%	-	1.89	0.13
1J high $p_T^{\gamma\gamma}$ Tag2	75.0	63.3%	77.9%	-	21.4%	0.8%	-	2.05	0.06
$\geq$2J low $p_T^{\gamma\gamma}$ Tag0	17.1	53.8%	78.0%	0.7%	18.1%	1.1%	2.2%	1.66	0.06
$\geq$2J low $p_T^{\gamma\gamma}$ Tag1	55.4	55.1%	75.5%	0.7%	19.7%	1.4%	2.7%	1.97	0.03
$\geq$2J low $p_T^{\gamma\gamma}$ Tag2	42.1	51.5%	73.8%	0.7%	20.3%	1.4%	3.9%	2.60	0.01
$\geq$2J med $p_T^{\gamma\gamma}$ Tag0	20.3	65.6%	81.9%	0.3%	15.7%	0.4%	1.7%	1.56	0.14
$\geq$2J med $p_T^{\gamma\gamma}$ Tag1	66.6	63.2%	79.5%	0.3%	17.4%	0.6%	2.3%	1.93	0.06
$\geq$2J med $p_T^{\gamma\gamma}$ Tag2	128.9	59.0%	75.9%	0.4%	19.4%	0.9%	3.4%	2.17	0.02
$\geq$2J high $p_T^{\gamma\gamma}$ Tag0	26.9	67.9%	80.2%	-	18.0%	0.3%	1.5%	1.58	0.20
$\geq$2J high $p_T^{\gamma\gamma}$ Tag1	48.8	65.2%	78.4%	-	18.8%	0.8%	2.1%	1.88	0.09
$\geq$2J high $p_T^{\gamma\gamma}$ Tag2	43.2	60.8%	76.1%	-	19.9%	0.9%	3.1%	2.04	0.05
BSM low $p_T^{\gamma\gamma}$ Tag0	27.6	78.2%	80.0%	-	19.0%	-	1.0%	1.47	0.35
BSM low $p_T^{\gamma\gamma}$ Tag1	36.1	73.0%	76.8%	-	20.6%	0.6%	2.0%	2.02	0.09
BSM med-low $p_T^{\gamma\gamma}$ Tag0	13.8	76.5%	78.0%	-	20.3%	0.4%	1.3%	1.64	0.30
BSM med-low $p_T^{\gamma\gamma}$ Tag1	2.3	67.5%	69.3%	-	22.6%	2.6%	5.6%	1.96	0.06
BSM med-high $p_T^{\gamma\gamma}$	2.8	60.2%	63.4%	-	31.1%	1.5%	4.0%	1.61	0.18
BSM high $p_T^{\gamma\gamma}$	0.5	52.5%	52.5%	-	37.1%	5.1%	5.4%	1.44	0.20

Table 6.2: The expected number of signal events for a Higgs boson mass of 125 GeV in categories targeting EW qqH production. The yield in each analysis category is broken down into percentage contributions from each production mode, and also the percentage of events originating from the targeted STXS Stage 1.2 bins. The σ_{eff}, defined as the smallest interval containing 68.3% of the invariant mass distribution is listed as a measure of the resolution in each analysis category. The final column shows the expected ratio of signal to signal-plus-background, S/(S+B), where S and B are the numbers of expected signal and background events in a $\pm 1\sigma_{\text{eff}}$ window centred on m_H.

Analysis categories	SM 125 GeV Higgs boson expected signal								
	Total	Target STXS bin(s)	Production Mode Fractions					σ_{eff}(GeV)	S/S+B
			ggH	VBF	VH_had	VH lep	top		
ggH VBF-like Tag0	13.0	39.2%	68.7%	27.1%	2.7%	-	1.5%	2.01	0.11
ggH VBF-like Tag1	29.7	31.5%	63.2%	30.9%	3.0%	0.1%	2.9%	1.98	0.08
qqH low m_{jj} low p_T^{Hjj} Tag0	16.4	52.7%	34.7%	65.3%	-	-	-	2.01	0.17
qqH low m_{jj} low p_T^{Hjj} Tag1	13.1	51.7%	35.2%	64.7%	0.1%	-	-	1.83	0.17
qqH high m_{jj} low p_T^{Hjj} Tag0	25.5	70.1%	16.9%	83.1%	-	-	-	1.87	0.44
qqH high m_{jj} low p_T^{Hjj} Tag1	12.3	57.4%	20.6%	79.4%	-	-	-	2.09	0.22
qqH low m_{jj} high p_T^{Hjj} Tag0	9.8	12.4%	57.7%	40.9%	0.7%	-	0.6%	2.22	0.10
qqH low m_{jj} high p_T^{Hjj} Tag1	18.5	14.2%	61.2%	35.3%	1.7%	-	1.7%	1.96	0.06
qqH high m_{jj} high p_T^{Hjj} Tag0	17.8	29.7%	28.0%	72.0%	-	-	-	1.99	0.26
qqH high m_{jj} high p_T^{Hjj} Tag1	17.3	28.0%	38.6%	60.2%	0.2%	-	1.1%	2.18	0.11
qqH BSM Tag0	10.1	73.4%	23.5%	76.5%	-	-	-	1.70	0.50
qqH BSM Tag1	6.3	57.5%	37.9%	60.5%	0.6%	-	1.1%	1.72	0.36
qqH VH-like Tag0	15.2	58.9%	36.5%	2.0%	58.1%	0.4%	3.1%	1.77	0.22
qqH VH-like Tag1	44.5	28.4%	65.9%	3.2%	28.7%	0.3%	2.0%	1.77	0.11

Table 6.3: The expected number of signal events for a Higgs boson mass of 125 GeV in categories targeting VH leptonic production. The yield in each analysis category is broken down into percentage contributions from each production mode, and also the percentage of events originating from the targeted STXS Stage 1.2 bins. The σ_{eff}, defined as the smallest interval containing 68.3% of the invariant mass distribution is listed as a measure of the resolution in each analysis category. The final column shows the expected ratio of signal to signal-plus-background, S/(S+B), where S and B are the numbers of expected signal and background events in a $\pm 1\sigma_{\text{eff}}$ window centred on m_H.

Analysis categories	SM 125 GeV Higgs boson expected signal									
	Total	Target STXS bin(s)	Production Mode Fractions						σ_{eff} (GeV)	S/S+B
			ggH	qqH	WH lep	ZH lep	ggZH lep	top		
ZH lep Tag0	2.4	99.9%	-	-	-	93.9%	6.0%	0.1%	1.79	0.52
ZH lep Tag1	0.9	98.0%	-	-	-	92.2%	5.8%	2.0%	2.54	0.23
WH lep $p_T^V < 75$ Tag0	2.1	81.4%	0.3%	-	95.7%	3.3%	-	0.7%	1.96	0.43
WH lep $p_T^V < 75$ Tag1	4.9	77.1%	2.2%	-	88.7%	7.2%	-	1.9%	1.98	0.18
WH lep $75 < p_T^V < 150$ Tag0	3.2	78.4%	1.0%	-	94.6%	3.1%	-	1.4%	2.02	0.52
WH lep $75 < p_T^V < 150$ Tag1	3.4	62.7%	1.6%	0.5%	85.8%	8.1%	0.4%	3.6%	2.14	0.31
WH lep $p_T^V > 150$ Tag0	3.7	81.7%	0.3%	-	93.8%	3.6%	-	2.3%	1.81	0.78
VH MET Tag0	2.3	98.4%	0.9%	0.4%	24.5%	59.1%	14.8%	0.4%	2.05	0.47
VH MET Tag1	3.7	92.5%	4.5%	2.3%	29.9%	49.5%	13.0%	0.7%	2.15	0.34
VH MET Tag2	6.6	75.8%	14.6%	7.8%	29.6%	37.3%	9.0%	1.8%	2.17	0.17

Table 6.4: The expected number of signal events for a Higgs boson mass of 125 GeV in categories targeting top associated production. The yield in each analysis category is broken down into percentage contributions from each production mode, and also the percentage of events originating from the targeted STXS Stage 1.2 bins. The σ_{eff}, defined as the smallest interval containing 68.3% of the invariant mass distribution is listed as a measure of the resolution in each analysis category. The final column shows the expected ratio of signal to signal-plus-background, S/(S+B), where S and B are the numbers of expected signal and background events in a $\pm 1\sigma_{\text{eff}}$ window centred on m_H.

Analysis categories	SM 125 GeV Higgs boson expected signal									
	Total	Target STXS bin(s)	Production Mode Fractions							S/S+B
			ggH	qqH	VH lep	ttH	tHq	tHW	σ_{eff} (GeV)	
tHq had	19.5	8.8%	48.1%	19.7%	0.7%	22.6%	6.8%	2.0%	1.75	0.21
tHq lep	1.7	32.0%	5.0%	2.4%	34.3%	26.3%	25.6%	6.4%	1.72	0.43
ttH lep $p_T^{\gamma\gamma} < 60$ Tag0	0.7	93.5%	-	-	0.8%	97.8%	0.8%	0.5%	1.90	0.54
ttH lep $p_T^{\gamma\gamma} < 60$ Tag1	0.9	91.7%	0.3%	-	1.7%	95.6%	1.7%	0.8%	1.82	0.45
ttH lep $p_T^{\gamma\gamma} < 60$ Tag2	1.6	87.1%	0.3%	0.1%	5.6%	89.5%	3.4%	1.2%	2.08	0.15
ttH lep $60 < p_T^{\gamma\gamma} < 120$ Tag0	1.3	94.6%	-	-	1.0%	97.0%	1.1%	0.9%	1.65	0.58
ttH lep 60 $p_T^{\gamma\gamma} < 120$ Tag1	0.6	89.6%	-	0.8%	1.6%	94.4%	1.9%	1.3%	1.76	0.44
ttH lep 60 $p_T^{\gamma\gamma} < 120$ Tag2	1.9	89.0%	-	0.2%	3.6%	92.0%	2.7%	1.5%	2.03	0.34
ttH lep $120 < p_T^{\gamma\gamma} < 200$ Tag0	3.2	90.1%	0.1%	-	2.2%	92.9%	2.4%	2.4%	1.80	0.63
ttH lep $120 < p_T^{\gamma\gamma} < 200$ Tag1	0.8	78.0%	2.1%	0.7%	10.5%	80.3%	3.6%	2.9%	1.87	0.37
ttH lep $200 < p_T^{\gamma\gamma} < 300$ Tag0	2.3	84.5%	-	-	4.3%	86.6%	3.6%	5.5%	1.69	0.61
ttH lep $p_T^{\gamma\gamma} > 300$ Tag0	1.9	59.7%	1.2%	0.3%	18.1%	66.7%	3.6%	10.0%	1.68	0.57
ttH had $p_T^{\gamma\gamma} < 60$ Tag0	1.1	93.1%	2.4%	0.4%	-	95.5%	1.1%	0.4%	1.97	0.42
ttH had $p_T^{\gamma\gamma} < 60$ Tag1	0.3	92.1%	-	1.3%	-	95.9%	2.1%	0.6%	1.91	0.31
ttH had $p_T^{\gamma\gamma} < 60$ Tag2	2.7	90.0%	1.7%	1.0%	0.2%	92.8%	3.5%	0.8%	2.08	0.12
ttH had $60 < p_T^{\gamma\gamma} < 120$ Tag0	1.6	92.7%	0.6%	0.1%	0.1%	97.2%	1.3%	0.6%	1.74	0 .69
ttH had 60 $p_T^{\gamma\gamma} < 120$ Tag1	0.4	88.5%	4.7%	1.3%	-	90.7%	2.3%	0.9%	1.87	0.28
ttH had 60 $p_T^{\gamma\gamma} < 120$ Tag2	4.7	88.2%	2.0%	1.7%	-	91.1%	4.1%	1.1%	2.00	0.19
ttH had $120 < p_T^{\gamma\gamma} < 200$ Tag0	2.8	91.8%	1.5%	0.2%	-	94.4%	2.5%	1.4%	1.68	0.55
ttH had $120 < p_T^{\gamma\gamma} < 200$ Tag1	1.7	83.6%	4.6%	2.1%	0.2%	86.7%	4.4%	1.9%	1.93	0.32
ttH had $120 < p_T^{\gamma\gamma} < 200$ Tag2	1.3	75.8%	9.0%	4.3%	0.4%	77.7%	6.4%	2.2%	1.89	0.21
ttH had $120 < p_T^{\gamma\gamma} < 200$ Tag3	2.1	62.1%	13.8%	9.7%	1.2%	64.7%	8.5%	2.2%	1.91	0.11
ttH had $200 < p_T^{\gamma\gamma} < 300$ Tag0	1.3	89.8%	0.9%	0.7%	0.5%	91.2%	3.7%	3.0%	1.65	0.60
ttH had $200 < p_T^{\gamma\gamma} < 300$ Tag1	1.0	74.3%	9.6%	3.5%	1.0%	76.4%	5.9%	3.7%	1.52	0.52
ttH had $200 < p_T^{\gamma\gamma} < 300$ Tag2	1.1	56.7%	18.0%	8.8%	0.9%	58.6%	9.4%	4.3%	1.62	0.26
ttH had $p_T^{\gamma\gamma} > 300$ Tag0	0.7	67.8%	9.2%	3.4%	0.8%	69.0%	8.2%	9.4%	1.86	0.53
ttH had $p_T^{\gamma\gamma} > 300$ Tag1	0.8	43.6%	25.3%	9.0%	1.8%	44.7%	10.9%	8.2%	1.94	0.43

As described in Chapter 5, all categories are merged across years. This benefits categories with low statistics since more data is available for constraining the parameters of the background model and for training the BDT classifiers. As described in Section 6.3.1, the signal models are constructed separately for each year to maintain mass resolution information and to keep track of year-dependent systematic uncertainties. The gain in sensitivity from splitting the high statistics categories by year and using the year-dependent resolution information was found to be negligible.

Figure 6.5 shows the expected signal compositions of the year-merged analysis categories in terms of a reduced (merged) set of the STXS Stage 1.2 bins. The contribution of each Stage 1.2 bin to the total number of expected signal events in an analysis category is displayed, meaning the values in each row sum to 100%. In the plot, signal compositions of the individual analysis categories are weighted according to the ratio S/(S+B). The fractional contribution of the total signal yield in a given analysis category group arising from each process is shown. The migration matrix in Figure 6.6 shows the percentage of each signal process falling into the analysis categories (normalised by column) for the same set of

reduced STXS Stage 1.2 bins. The overall efficiency × acceptance is consistent with the value observed in Ref. [106], which was around 40%. In general, the migration between categories due to $p_T^{\gamma\gamma}$ is very low, while significantly higher migrations arise from jet miscounting.

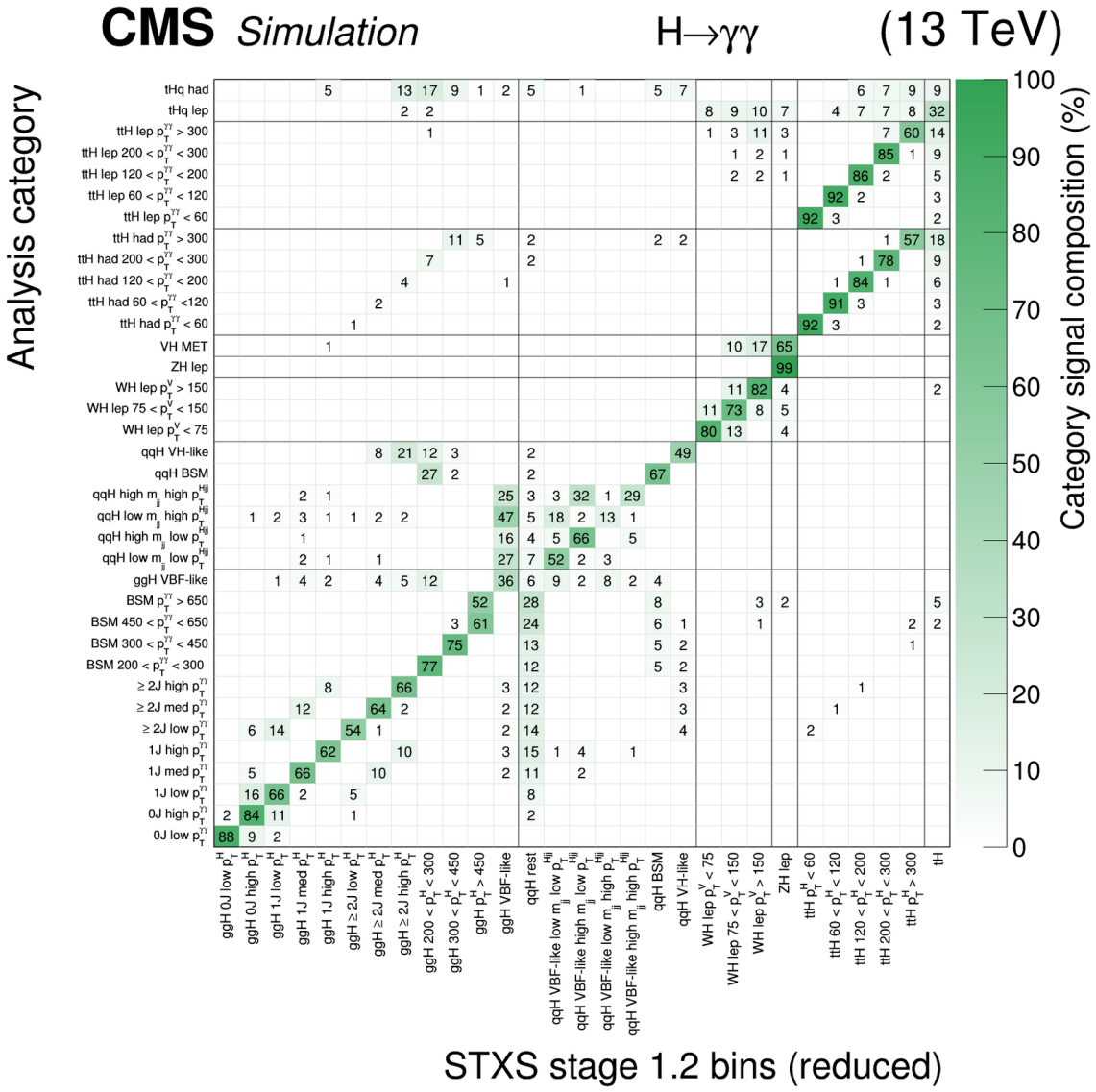

Figure 6.5: The signal composition of each year-merged analysis category in terms of the signal processes defined in a reduced set of STXS bins. Analysis categories targeting a common STXS region are summed, where the signal compositions of the individual categories are weighted in the sum by the expected ratio of signal to signal-plus-background events. The colour scale indicates the fractions of each STXS process (column) in a given analysis category (row). Each row therefore sums to 100%. Entries with values less than 0.5% are not shown. Simulated events for each year in the period 2016 to 2018 are combined with appropriate weights corresponding to their relative integrated luminosity in data. The column labelled as *qqH rest* includes contributions from the qqH 0J, qqH 1J, qqH $m_{jj} < 60\,\text{GeV}$ and qqH $120 < m_{\gamma\gamma} < 350\,\text{GeV}$ STXS bins.

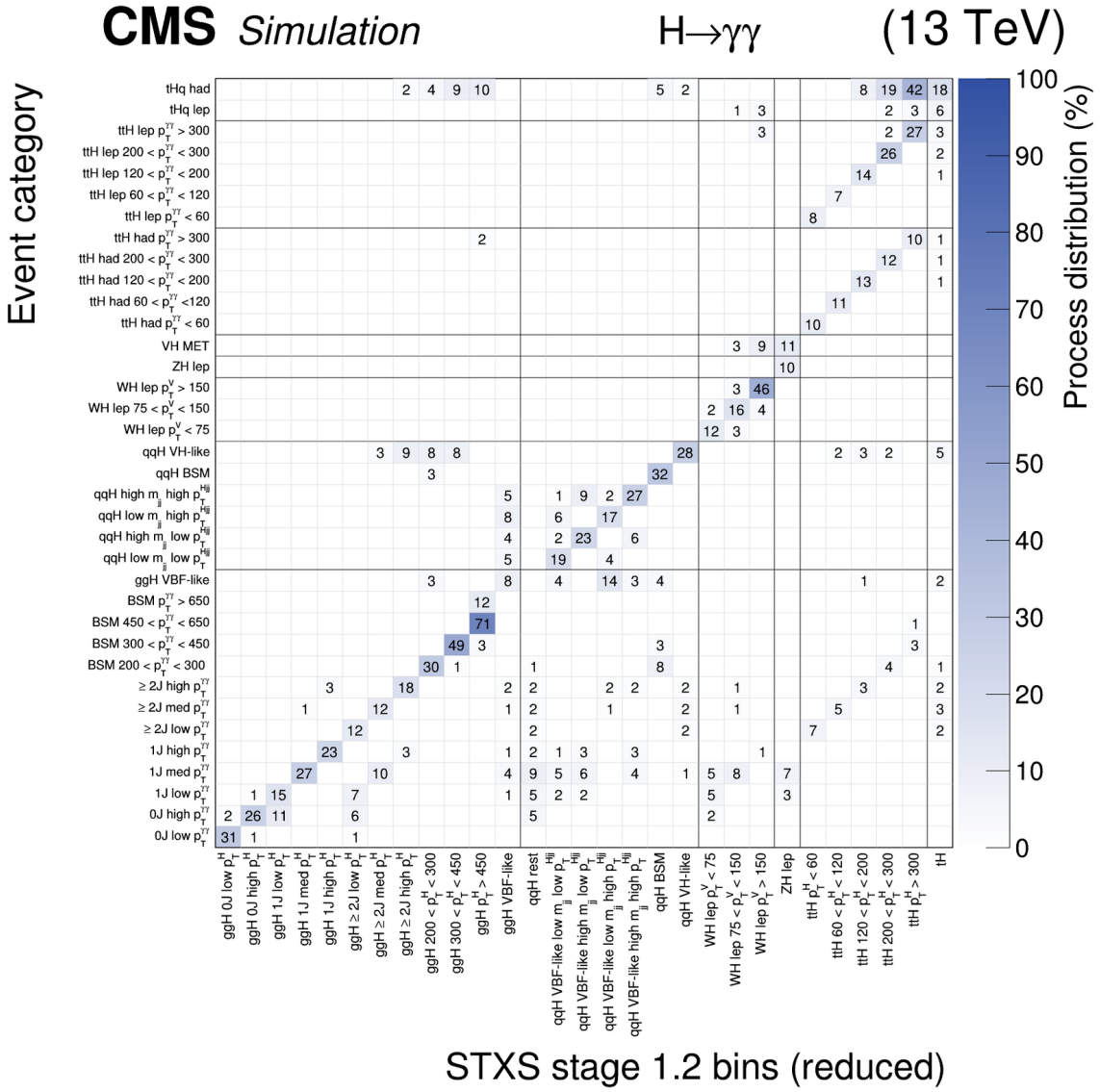

Figure 6.6: Migration matrix showing the percentage of each signal process falling into the analysis categories. The signal processes correspond to those defined in a reduced set of STXS bins. The colour scale indicates the fractions of a given process (column) in each analysis category (row). Each column therefore sums to 100%. Entries with values less than 0.5% are not shown. Simulated events for each year in the period 2016 to 2018 are combined with appropriate weights corresponding to their relative integrated luminosity in data. The column labelled as *qqH rest* includes contributions from the qqH 0J, qqH 1J, qqH $m_{jj} < 60\,\text{GeV}$ and qqH $120 < m_{\gamma\gamma} < 350\,\text{GeV}$ STXS bins.

6.5 Results for signal strength modifiers

A common signal strength modifier, μ, is defined as the ratio of the observed product of the Higgs boson cross-section and diphoton branching fraction to the SM expectation. The

inclusive signal strength, μ has an expected value of

$$\mu = 1.00^{+0.10}_{-0.10} = 1.00^{+0.07}_{-0.06}(\text{Th.})^{+0.03}_{-0.03}(\text{Exp.})^{+0.07}_{-0.07}(\text{Stat.}).$$

The observed value is

$$\mu = 1.14^{+0.11}_{-0.10} = 1.14^{+0.08}_{-0.07}(\text{Th.})^{+0.03}_{-0.03}(\text{Exp.})^{+0.07}_{-0.07}(\text{Stat.}).$$

The uncertainty is decomposed into theoretical systematic, experimental systematic, and statistical components. The statistical component includes the uncertainty in the background modelling. The systematic component of the uncertainty on the POI is determined by subtracting the statistical component from the total uncertainty. The compatibility of the observed fit with respect to the SM prediction, expressed as a p-value, is approximately 16%.

The expected likelihood scan for the inclusive signal strength is shown in Fig. 6.7, with the observed scan shown in Fig. 6.8. As stated previously, in this fit (and in all subsequent fits), m_H is fixed to its most precisely measured value of 125.38 GeV [97]. The precise determination of m_H and the systematic uncertainties that enter its measurement are not in the scope of this analysis. It was checked that profiling m_H without constraint, rather than fixing it to 125.38 GeV, has a small impact on the measured results; the best fit signal strength values change by 0.7–1.8%, and in each case, the change is less than 10% of the measured signal strength uncertainty.

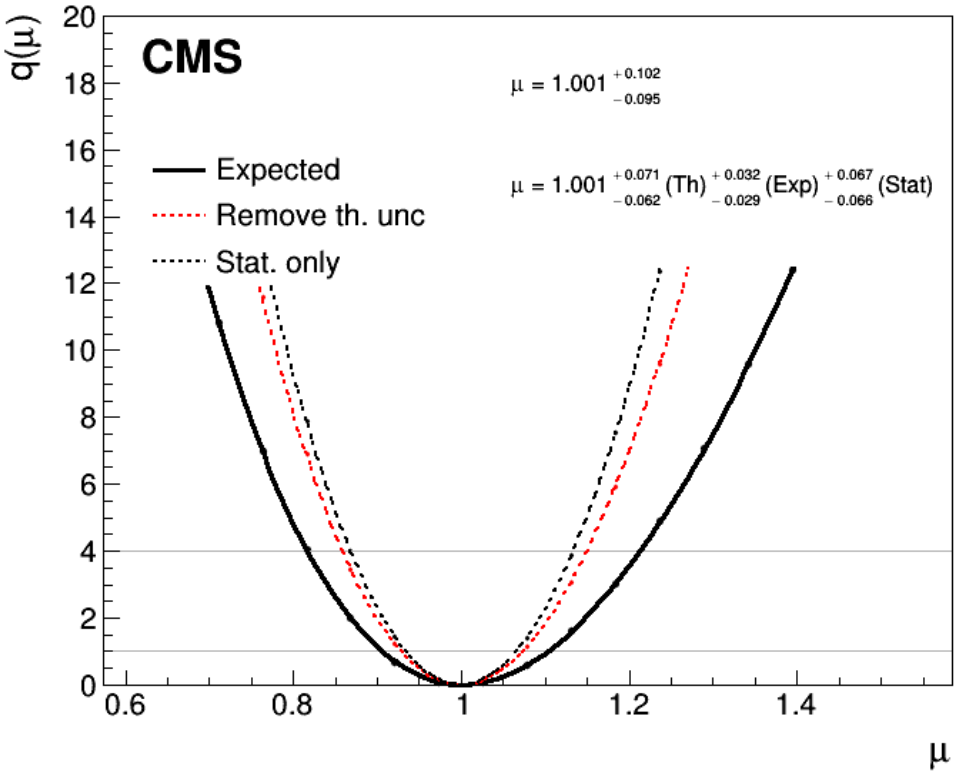

Figure 6.7: Expected likelihood scan where are all signal processes are made to scale according to a common signal strength, μ. Three scans are shown: one corresponding to the full fit, one corresponding to the fit without theoretical uncertainties, and one corresponding to the fit without any systematic uncertainties.

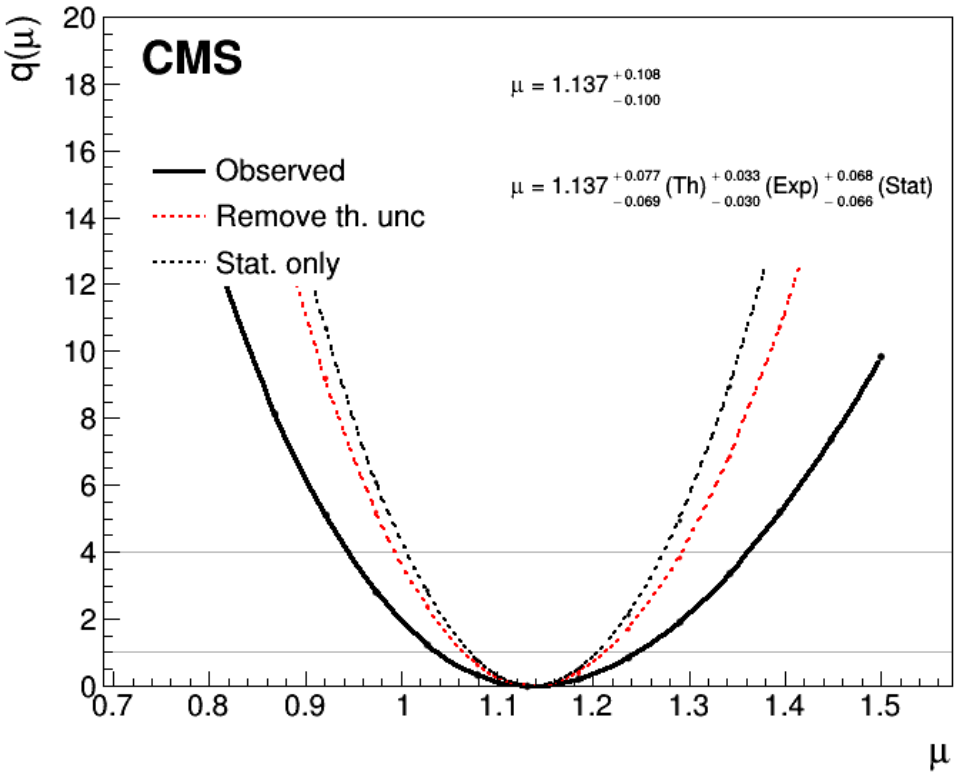

Figure 6.8: Observed likelihood scan where are all signal processes are made to scale according to a common signal strength, μ. Three scans are shown: one corresponding to the full fit, one corresponding to the fit without theoretical uncertainties, and one corresponding to the fit without any systematic uncertainties.

Signal strength modifiers for each Higgs boson production mode are also measured. A fit is performed with four signal strengths which scale the four production modes independently: μ_{ggH}, μ_{VBF}, μ_{VH} and μ_{top}. Unlike the subsequent STXS fits described in Section 6.6, the VH hadronic and VH leptonic processes are grouped to scale according to μ_{VH}, whereas the VBF production mode scales with μ_{VBF}. The parameter μ_{top} scales the ttH, tHq and tHW production modes equally and μ_{ggH} scales both ggH and bbH production. The expected results are extracted using an Asimov dataset with all $\mu_i = 1$ (SM) and are summarised in Figure 6.9. The observed results are shown in Figure 6.10. The full set of likelihood scans for the fits are included in Appendix H. The precision of these measurements is significantly improved from previous analyses performed by the CMS Collaboration in the $H \to \gamma\gamma$ decay channel. In particular, the measurement of the μ_{VH} signal strength modifier has improved substantially from that shown in Ref. [106], beyond what would be expected from the increase in the size of the dataset alone. The p-value of the production mode signal strength modifier fit with respect to the SM prediction is approximately 52%.

The observed (expected) significances for the individual production modes are:

- ggH: $12.3\,\sigma$ $(11.4\,\sigma)$
- VBF: $3.6\,\sigma$ $(3.6\,\sigma)$
- VH: $4.7\,\sigma$ $(3.6\,\sigma)$
- Top = ttH + tH: $6.9\,\sigma$ $(3.8\,\sigma)$

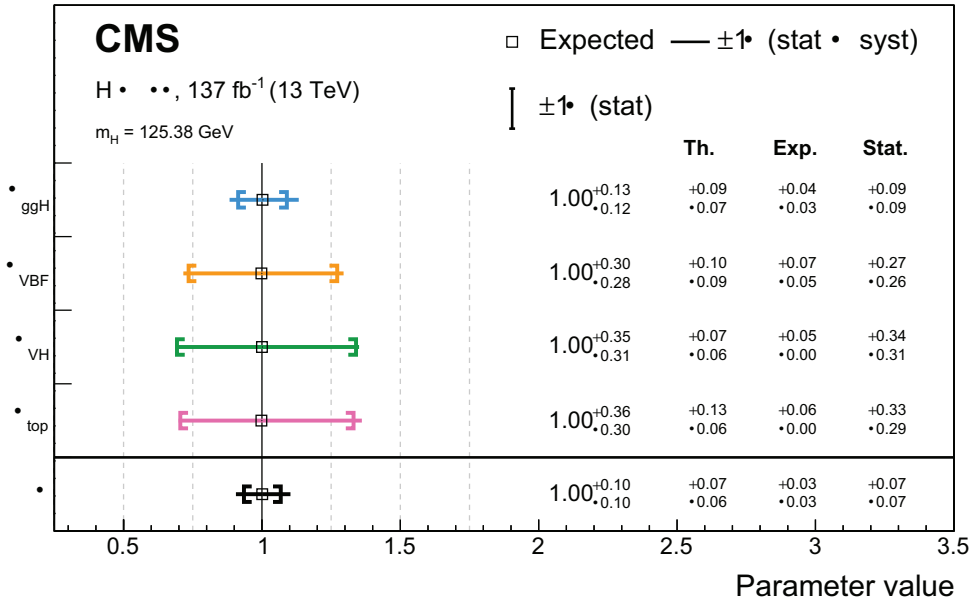

Figure 6.9: Expected results of the per-production-mode signal strengths fit. The contributions to the total uncertainty in each parameter from the theoretical systematic, experimental systematic, and statistical components are shown. The colour scheme is chosen to match the diagram presented in Figure 5.2.

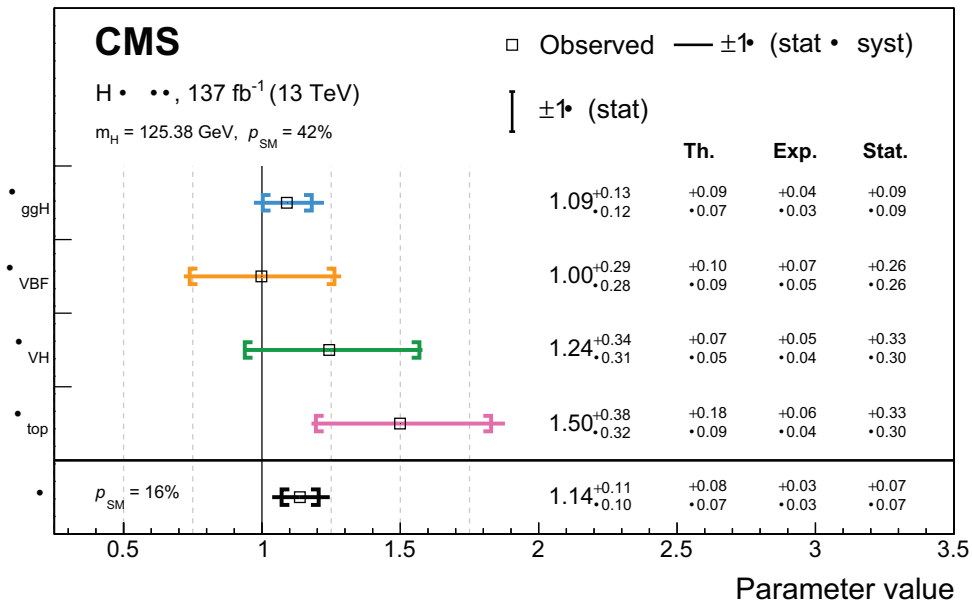

Figure 6.10: Observed results of the per-production-mode signal strengths fit. The contributions to the total uncertainty in each parameter from the theoretical systematic, experimental systematic, and statistical components are shown. The colour scheme is chosen to match the diagram presented in Figure 5.2. The compatibility of this fit with respect to the SM prediction, expressed as a p-value, is approximately 42%. Also shown in black is the result of the fit to the inclusive signal strength modifier, which has a p-value of 16%.

The expected and observed correlation between the signal strengths are shown in Figures 6.11 and 6.12 respectively. The highest correlation is between the VBF and ggH production modes.

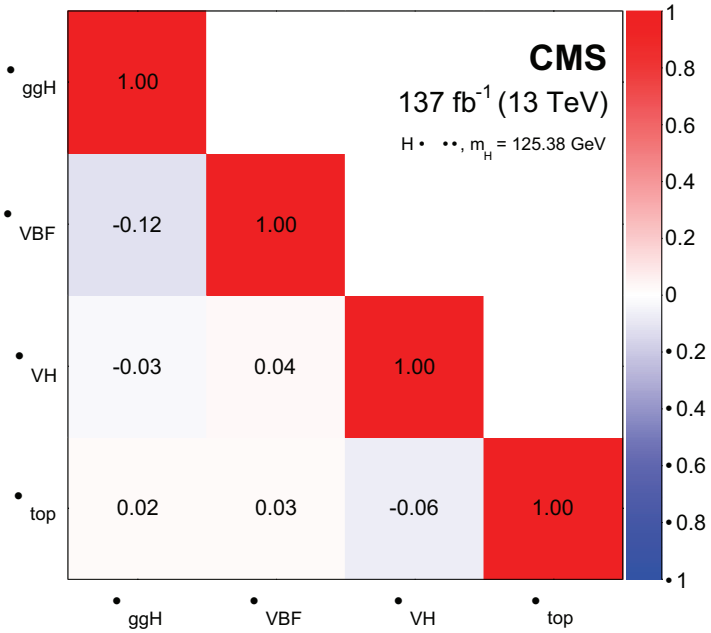

Figure 6.11: Expected correlations between the parameters in the per-production-mode signal strengths fit.

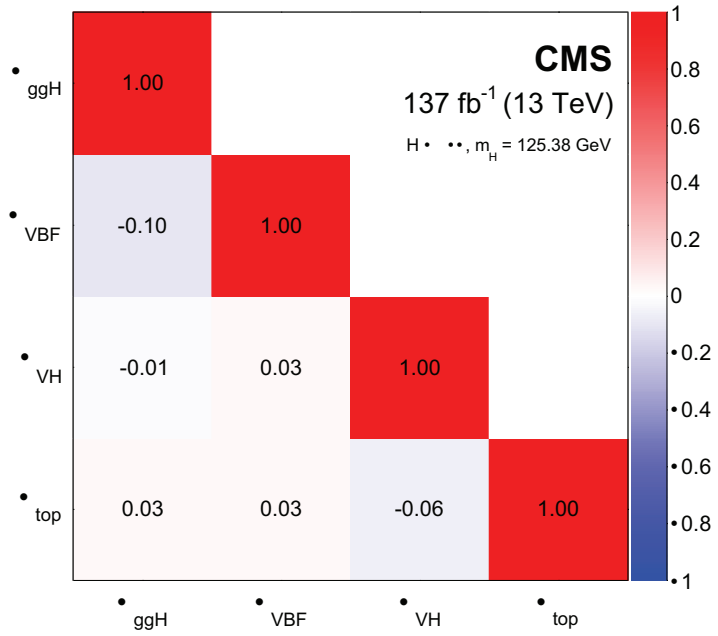

Figure 6.12: Observed correlations between the parameters in the per-production-mode signal strengths fit.

The signal-plus-background fits to data under this parameter scheme are shown in Figure 6.13. Here, the analysis categories are divided into groups for those targeting the ggH, VBF, VH and top production modes. In each group, the individual categories are again summed after weighting by the ratio of the number of signal to signal-plus-background events, where signal corresponds to all Higgs boson events regardless of production mode.

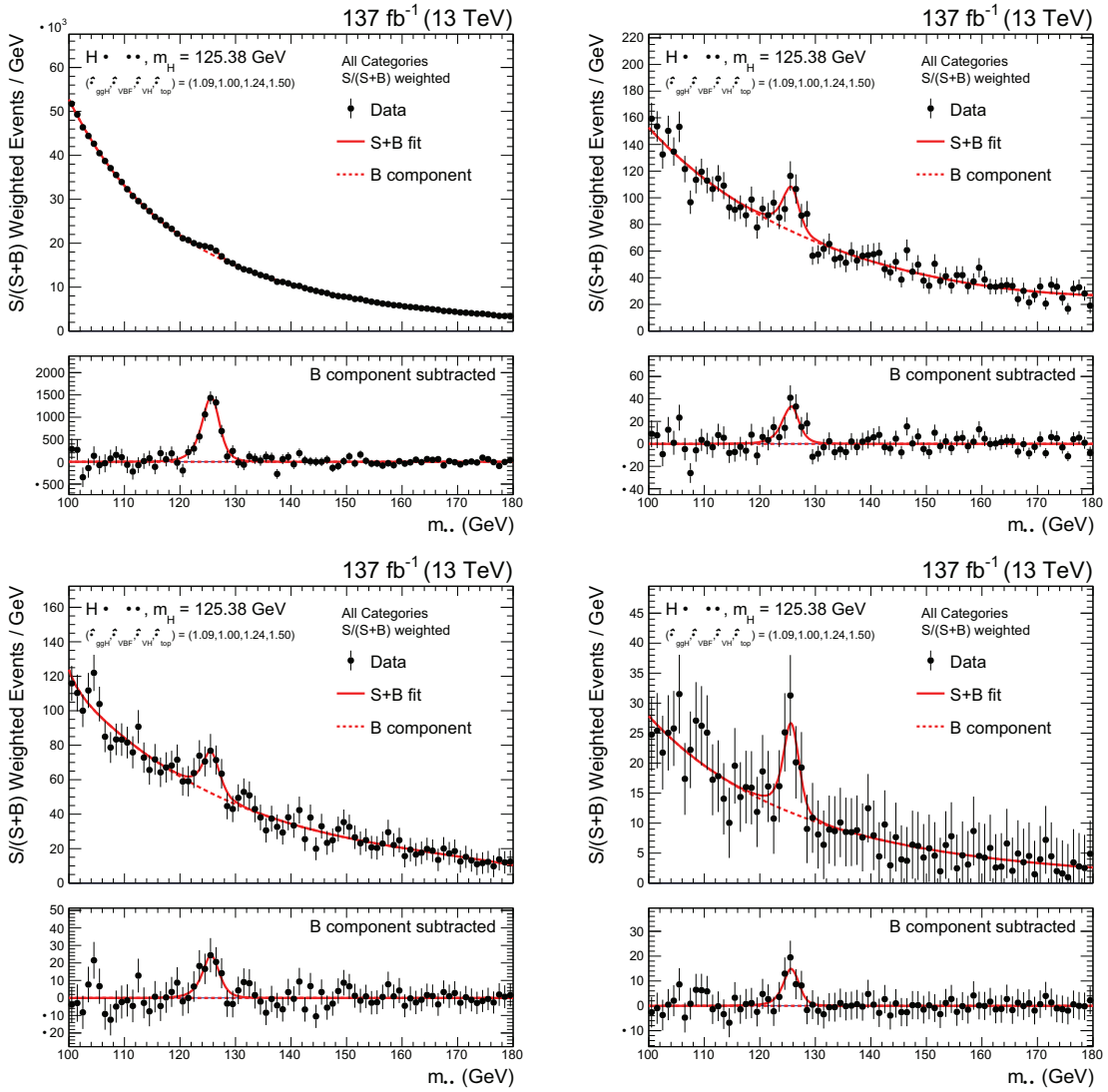

Figure 6.13: The best-fit signal-plus-background model with data points (black) in the per-production mode signal strength fit. The model is shown separately for groups of categories targeting the ggH (top left), VBF (top right), VH (bottom left) and top (bottom right) production modes. Here, the categories in each group are summed after weighting by S/(S+B), where S and B are the numbers of expected signal and background events in a $\pm 1\sigma_{eff}$ $m_{\gamma\gamma}$ window centered on m_H. The solid red line shows the total signal-plus-background contribution, whereas the dashed red line represents the background component only. The bottom panel in each plot shows the residuals after subtraction of this background component.

Impacts

The observed and expected main sources of systematic uncertainty affecting the signal strength modifier in each each production mode are summarised in Figure 6.14. The dominant contributions to the measurement systematic uncertainty in the μ_{ggH}, μ_{VH} and μ_{top} signal strength modifiers come from the corresponding renormalisation and factorisation scale uncertainties, whereas the underlying event and parton shower uncertainties are the dominant sources of uncertainty in the μ_{VBF} measurement. The largest experimental uncertainties originate from the integrated luminosity, the photon identification, and the photon energy measurement for the μ_{ggH} and μ_{VH} signal strength modifiers. The uncertainties in the jet energy scale and resolution have a larger impact on μ_{VBF} and μ_{top}, where μ_{top} has an additional large contribution from the uncertainty in the b-tagging. Further details may be found in Appendix I.

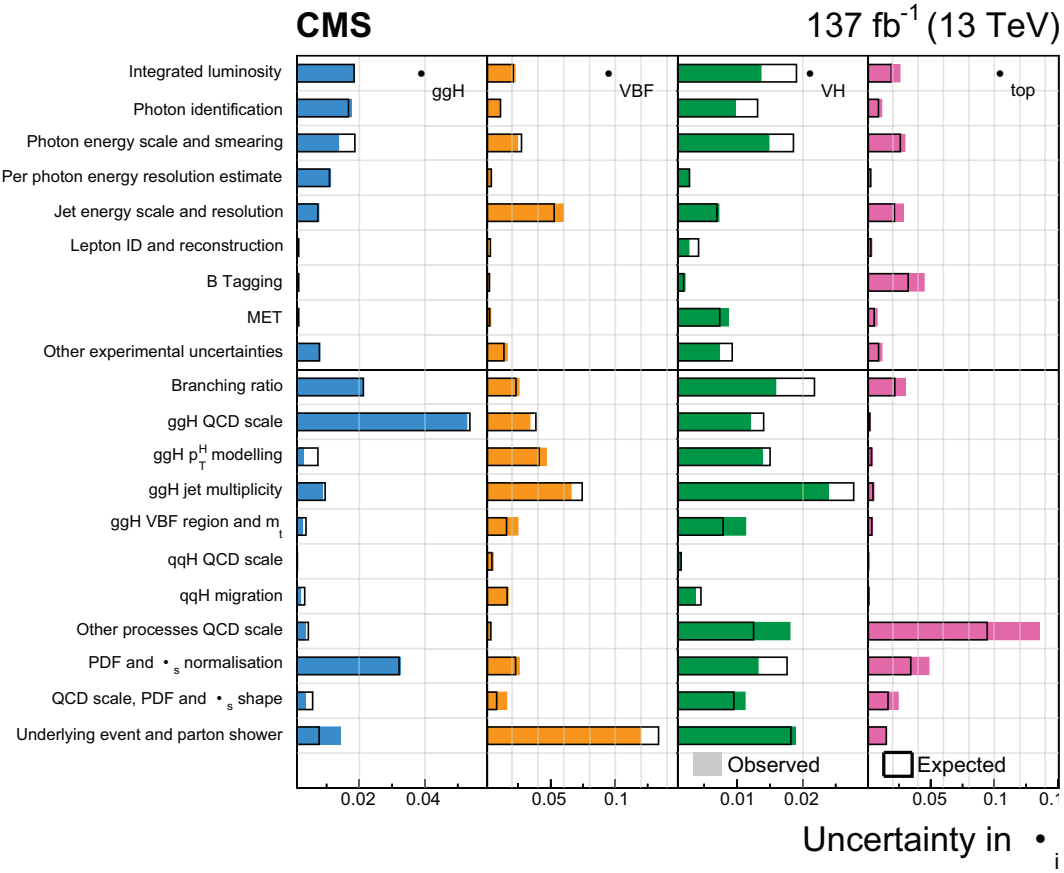

Figure 6.14: A summary of the impact of the main sources of systematic uncertainty in the fit to signal strength modifiers of the four principal production modes. The observed (expected) impacts are shown by the solid (empty) bars. The background modelling uncertainty is defined as a statistical uncertainty. The colour scheme is chosen to match the diagram presented in Figure 5.2.

6.6 Results in the STXS framework

6.6.1 Parameter merging scenarios

The data available is insufficient to constrain all STXS Stage 1.2 bins simultaneously. Certain bins, if kept separate, would induce very large uncertainties on some parameters or very high correlations between parameters. Therefore, these bins are merged in the fit to form a single bin defined by a common POI.

Two different parameterisations are considered, with varying levels of granularity defined by the merging of certain bins. The parameter merging scenarios are shown by the schematics in Figures 6.15 and 6.16. The solid black boxes indicate the parameters of interest in the fit, such that the merged bins are covered in a single box. The hatched boxes show the regions of phase space which are fixed to the SM prediction.

Merging fewer bins keeps the model-dependence of the results as low as possible, as no additional assumptions are made about the relative contributions of different STXS bins to the merged bin. The results with reduced model-dependence, however, have larger uncertainties in the measured cross-section parameters. The first merging scenario is referred to as the *maximal* merging scenario, where STXS bins are merged until their expected uncertainty is less than 150% of the SM prediction. The second scenario, referred to as the *minimal* merging scenario, instead involves the merging of as few bins as possible whilst ensuring that parameter anti-correlations stay below around 90%.

Maximal bin merging scenario

The maximal merging scheme defines 17 parameters of interest and is summarised in Table 6.5. The VBF-like regions ($\geq$ 2-jets, $m_{jj} > 350$ GeV) in the ggH and qqH schemes are merged to define the ggH VBF-like and qqH VBF-like parameters respectively. The four bins with $p_T^H > 200$ GeV in the ggH scheme are merged into a single bin, labelled as ggH BSM. Additionally, the WH leptonic, ZH leptonic and ttH bins are each fully merged into single parameters. The ZH leptonic parameter groups both ZH and ggZH production.

Minimal bin merging scenario

The minimal merging scheme defines a more granular fit than the maximal merging scheme, with 27 parameters of interest and is also summarised in Table 6.5. The qqH VBF-like region is fully split into the four STXS Stage 1.2 bins defined by the boundaries at $m_{jj} = 700\,\text{GeV}$ and $p_T^{Hjj} = 25\,\text{GeV}$. To avoid large correlations between the fitted parameters, the four ggH VBF-like bins are merged with the corresponding bins in the qqH scheme. Additional splittings are included in the ggH scheme at $p_T^H = 300\,\text{GeV}$ and $p_T^H = 450\,\text{GeV}$, and in the WH leptonic scheme at $p_T^V = 75\,\text{GeV}$ and $p_T^V = 150\,\text{GeV}$. Furthermore, the ttH region is split into five parameters according to the boundaries at $p_T^H = 60$, 120, 200, and 300 GeV.

Table 6.5 summarises the maximal and minimal merging schemes by listing the STXS bins that contribute to each parameter of interest. The STXS bins that are constrained to their respective SM predictions in both fits are also listed.

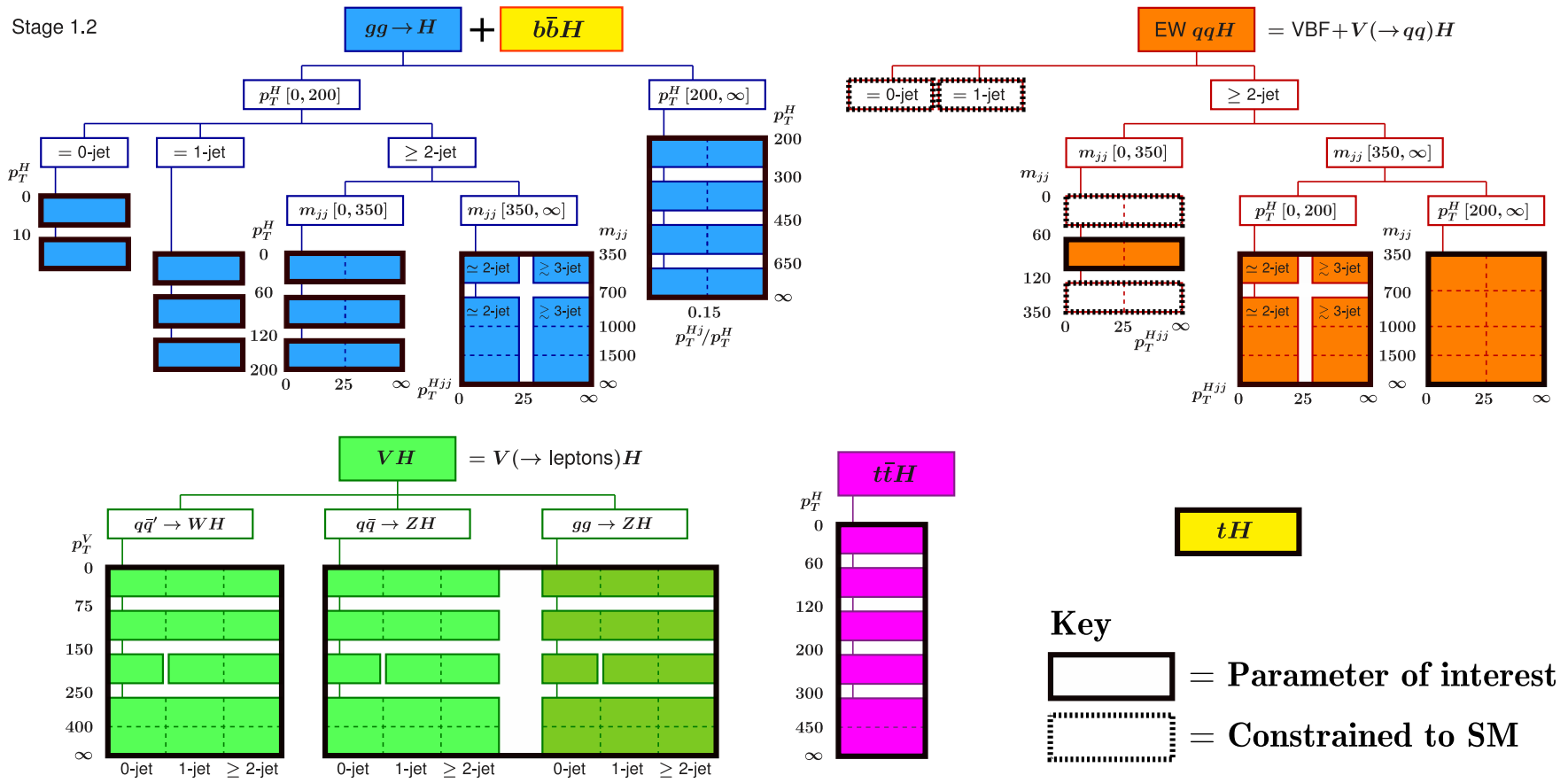

Figure 6.15: Schematic to show the maximal parameter merging scenario. The parameters of interest are defined by the solid black boxes, which span over multiple bins for the cases in which bins are merged. The hatched boxes demonstrate the regions of phase space which are fixed to the SM prediction in the fit.

,

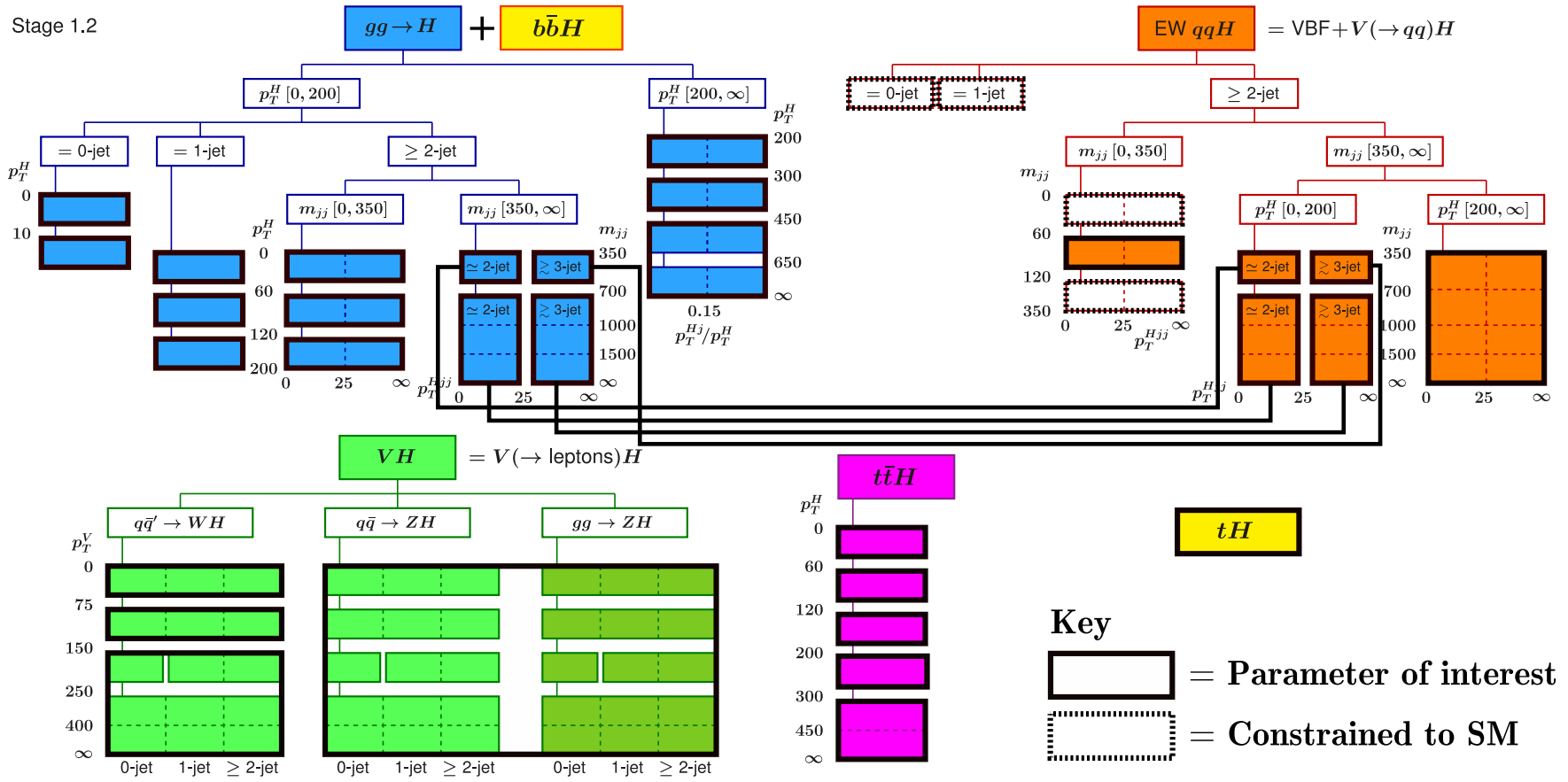

Figure 6.16: Schematic to show the minimal parameter merging scenario. The parameters of interest are defined by the solid black boxes, which span over multiple bins for the cases in which bins are merged. The hatched boxes demonstrate the regions of phase space which are fixed to the SM prediction in the fit.

Table 6.5: A summary of the maximal and minimal parameter merging scenarios. The STXS bins that contribute to each parameter are listed. Furthermore, the bins that are constrained to their respective SM predictions in the fits are listed in the final row.

Scheme	Parameters	STXS stage 1.2 bins (total number of bins)
Maximal (17 parameters)	ggH 0J low p_T^H	ggH 0J low p_T^H (1)
	ggH 0J high p_T^H	ggH 0J high p_T^H, bbH (2)
	ggH 1J low p_T^H	ggH 1J low p_T^H (1)
	ggH 1J med p_T^H	ggH 1J med p_T^H (1)
	ggH 1J high p_T^H	ggH 1J high p_T^H (1)
	ggH $\geq$ 2J low p_T^H	ggH $\geq$2J low p_T^H (1)
	ggH $\geq$ 2J med p_T^H	ggH $\geq$2J med p_T^H (1)
	ggH $\geq$ 2J high p_T^H	ggH $\geq$2J high p_T^H (1)
	ggH BSM	$\left\{\begin{array}{l}\text{ggH BSM } 200 < p_T^H < 300\text{, ggH BSM } 300 < p_T^H < 450 \\ \text{ggH BSM } 450 < p_T^H < 650\text{, ggH BSM } p_T^H > 650\end{array}\right\}$ (4)
	ggH VBF-like	$\left\{\begin{array}{l}\text{ggH VBF-like low } m_{jj} \text{ low } p_T^{Hjj}\text{, ggH VBF-like low } m_{jj} \text{ high } p_T^{Hjj} \\ \text{ggH VBF-like high } m_{jj} \text{ low } p_T^{Hjj}\text{, ggH VBF-like high } m_{jj} \text{ high } p_T^{Hjj}\end{array}\right\}$ (4)
	qqH VBF-like	$\left\{\begin{array}{l}\text{qqH VBF-like low } m_{jj} \text{ low } p_T^{Hjj}\text{, qqH VBF-like low } m_{jj} \text{ high } p_T^{Hjj} \\ \text{qqH VBF-like high } m_{jj} \text{ low } p_T^{Hjj}\text{, qqH VBF-like high } m_{jj} \text{ high } p_T^{Hjj}\end{array}\right\}$ (4)
	qqH VH-like	qqH VH-like (1)
	qqH BSM	qqH BSM (1)
	WH lep	All WH lep (5)
	ZH lep	All ZH lep and ggZH lep (10)
	ttH	All ttH (5)
	tH	tH = tHq + tHW (1)
Minimal (27 parameters)	ggH 0J low p_T^H	ggH 0J low p_T^H (1)
	ggH 0J high p_T^H	ggH 0J high p_T^H, bbH (2)
	ggH 1J low p_T^H	ggH 1J low p_T^H (1)
	ggH 1J med p_T^H	ggH 1J med p_T^H (1)
	ggH 1J high p_T^H	ggH 1J high p_T^H (1)
	ggH $\geq$ 2J low p_T^H	ggH $\geq$2J low p_T^H (1)
	ggH $\geq$ 2J med p_T^H	ggH $\geq$2J med p_T^H (1)
	ggH $\geq$ 2J high p_T^H	ggH $\geq$2J high p_T^H (1)
	ggH BSM $200 < p_T^H < 300$	ggH BSM $200 < p_T^H < 300$ (1)
	ggH BSM $300 < p_T^H < 450$	ggH BSM $300 < p_T^H < 450$ (1)
	ggH BSM $p_T^H > 450$	ggH BSM $450 < p_T^H < 650$, ggH BSM $p_T^H > 650$ (2)
	VBF-like low m_{jj} low p_T^{Hjj}	ggH + qqH VBF-like low m_{jj} low p_T^{Hjj} (2)
	VBF-like low m_{jj} high p_T^{Hjj}	ggH + qqH VBF-like low m_{jj} high p_T^{Hjj} (2)
	VBF-like high m_{jj} low p_T^{Hjj}	ggH + qqH VBF-like high m_{jj} low p_T^{Hjj} (2)
	VBF-like high m_{jj} high p_T^{Hjj}	ggH + qqH VBF-like high m_{jj} high p_T^{Hjj} (2)
	qqH VH-like	qqH VH-like (1)
	qqH BSM	qqH BSM (1)
	WH lep $p_T^V < 75$	WH lep $p_T^V < 75$ (1)
	WH lep $75 < p_T^V < 150$	WH lep $75 < p_T^V < 150$ (1)
	WH lep $p_T^V > 150$	$\left\{\begin{array}{l}\text{WH lep 0J } 150 < p_T^V < 250\text{, WH lep } \geq\text{1J } 150 < p_T^V < 250 \\ \text{WH lep } p_T^V > 250\end{array}\right\}$ (3)
	ZH lep	All ZH lep and lep (10)
	ttH $p_T^H < 60$	ttH $p_T^H < 60$ (1)
	ttH $60 < p_T^H < 120$	ttH $60 < p_T^H < 120$ (1)
	ttH $120 < p_T^H < 200$	ttH $120 < p_T^H < 200$ (1)
	ttH $200 < p_T^H < 300$	ttH $200 < p_T^H < 300$ (1)
	ttH $p_T^H > 300$	ttH $p_T^H > 300$ (1)
	tH	tH = tHq + tHW (1)
Constrained to SM prediction		qqH 0J, qqH 1J, qqH $m_{jj} < 60$, qqH $120 < m_{jj} < 350$ (4)

6.6.2 Cross-sections

This section details the fits performed to extract cross-sections within the STXS framework and their respective 68% confidence level (CL) intervals. The theoretical uncertainties in the normalisation of the signal parameters are not included in the cross-section measurements. In each fit, ggZH events in which the Z boson decays hadronically are grouped with the corresponding ggH STXS bin. All bbH events are treated as part of the ggH 0J high p_T^H bin. The hadronic VH processes are grouped with VBF production to form the qqH parameters. Parameters which are not measured are constrained to their SM prediction, within theoretical uncertainties. These are the 0J, 1J, $m_{jj} < 60\,\text{GeV}$, and $120 < m_{jj} < 350\,\text{GeV}$ bins in the qqH binning scheme. Two fits are performed with varying levels of granularity. The two STXS Stage 1.2 fits correspond to the parameter merging scenarios described in Section 6.6.1: the maximal merging fit (17 parameters) and the minimal merging fit (27 parameters). These merging scenarios are effectively a reduced set of the STXS Stage 1.2 bins. The expected and observed results of the fits are shown in the summary plots in Figures 6.17 and 6.18. The parameters are colour-coded according the colours used in the STXS framework (Figure 5.2). The full set of likelihood scans for the fits are included in Appendix H.

The values for the best-fit cross-sections and 68% intervals for the two merging schemes are given in Tables 6.6 and 6.7. All of the cross-section measurements are statistically limited. Overall, the results from both merging scenario fits are in agreement with SM predictions; the observed p-values with respect to the SM predictions are 61% and 87% for the maximal and minimal merging scenarios respectively. In the maximal merging scenario, the product of the tH production cross-section times the $H \to \gamma\gamma$ branching fraction is measured to be $0.4^{+0.7}_{-0.4}\,\text{fb}$, corresponding to an excess of $1.9^{+3.3}_{-1.9}$ times the SM expectation. This represents a more SM-like measurement than that in Ref. [1], where the value reported was $6.3^{+3.4}_{-3.7}$.. The minimal merging scenario fit represents the current most granular cross-section measurement performed in a single Higgs boson decay channel, with good sensitivity to many different regions of Higgs boson production phase space. In the minimal merging scenario, the product of the tH production cross-section times the $H \to \gamma\gamma$ branching fraction is measured to be $0.6^{+0.6}_{-0.6}\,\text{fb}$, corresponding to an excess of $2.8^{+3.0}_{-2.8}$ times the SM expectation. This still represents a more SM-like measurement than that in Ref. [1], where the value reported was $8.4^{+3.5}_{-4.6}$. The observed (expected) upper limit on the tH cross-section as a fraction of the SM expectation is 9.47 (7.89) and 9.47 (9.47) for the maximal and minimal merging scenarios respectively. This represents an improvement to the limits in Ref. [1].

The correlations (expected and observed) between the fitted parameters are shown for each fit in Figures 6.19 to 6.22. The correlations for the ggH parameters are observed to be small between adjacent p_T^H bins and larger between adjacent number of jet bins. This results from the fact that $p_T^{\gamma\gamma}$ is a well-measured quantity, whereas reconstructing the number of jets in an event is more arbitrary. The application of the ggH BDT in the event categorisation helps to minimise these correlations. The largest correlations in the maximal merging scheme exist between the ggH VBF-like and qqH VBF-like cross-sections and the ttH and tH cross-sections, with expected values of -0.76 and -0.58 respectively. In particular, the expected correlation between the ttH and tH cross-sections (-0.58) is smaller than the value (-0.63) expected in the Ref. [1] analysis. This reflects the effect of introducing a new tHq hadronic category. The difficulty in distinguishing ggH 2J production from VBF is illustrated in the high anti-correlation between the ggH 2J and qqH parameters.

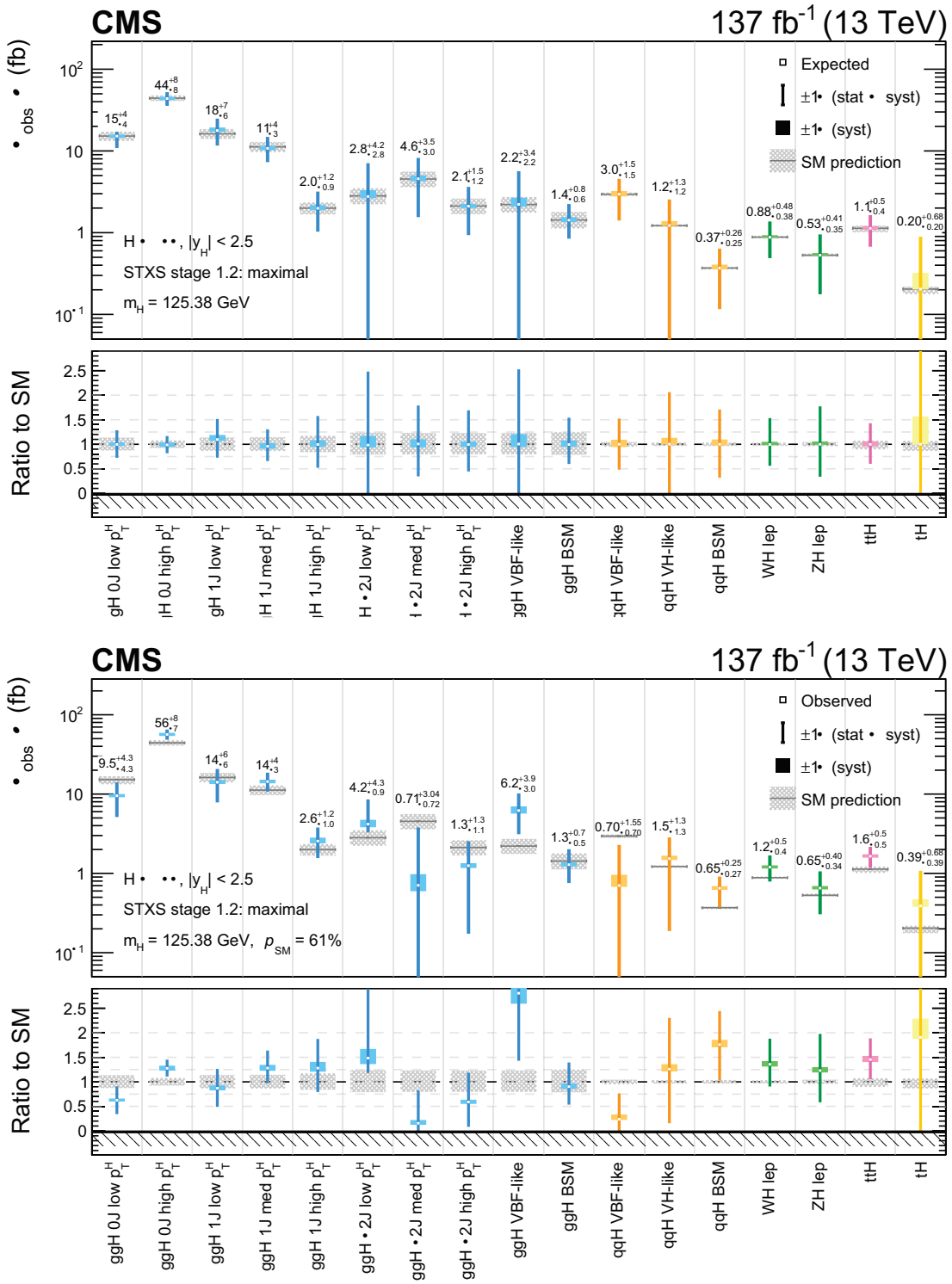

Figure 6.17: Expected (top) and observed (bottom) results of the STXS Stage 1.2 fit in the maximal parameter merging scenario. The best-fit cross-sections are plotted with the respective 68% CL intervals. The systematic uncertainty in each parameter (coloured boxes) and the theoretical uncertainties in the SM predictions (hatched grey boxes) are shown. The lower panel shows the ratio of the fitted values to the SM predictions. The cross-sections are constrained to be non-negative (hashed pattern below zero). The colour scheme matches that in Figure 5.2. The observed fit has a p-value of approximately 61%.

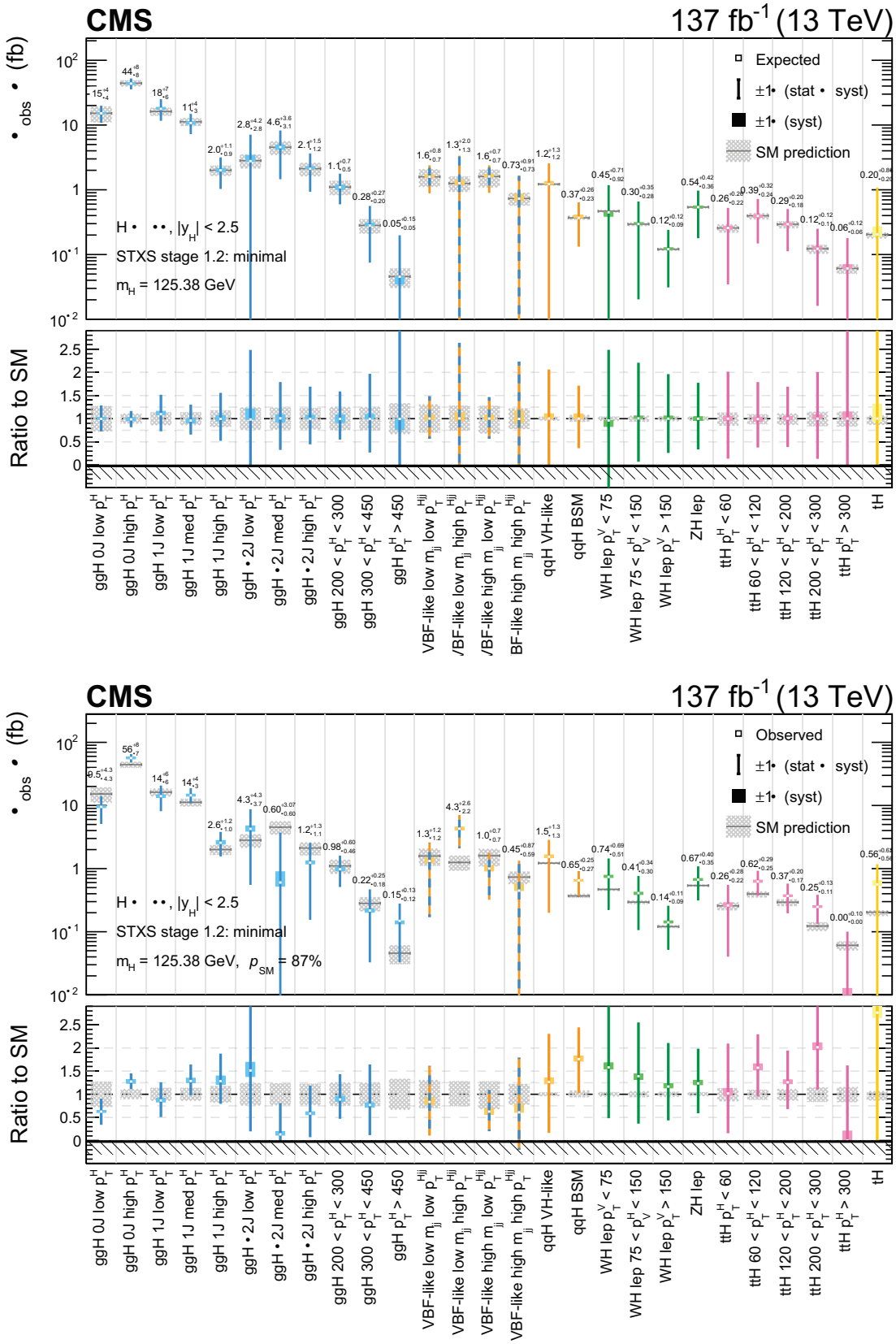

Figure 6.18: Expected (top) and observed (bottom) results of the STXS Stage 1.2 fit in the minimal parameter merging scenario. The parameters corresponding to merged ggH and qqH bins are shown by orange and blue dashed lines. The remaining elements of the plots are similar to those in Figure 6.17. The observed fit has a p-value of approximately 87%.

Table 6.6: The best-fit cross-sections with 68% confidence intervals for the maximal merging scenario. The uncertainty is decomposed into the systematic and statistical components. The expected uncertainties on the fitted parameters, computed assuming the SM predicted cross-section values, are given in brackets. Also listed are the SM predictions for the cross-sections and the theoretical uncertainty in these predictions.

STXS stage 1.2: maximal merging scheme						
Parameters	$\sigma\mathcal{B}$ [fb]					$\sigma\mathcal{B}/(\sigma\mathcal{B})_{\text{SM}}$
	SM prediction	Observed (Expected)				Observed (Expected)
	(m_H = 125.38 GeV)	Best fit		Stat unc.	Syst unc.	Best fit
ggH 0J low p_T^H	$15.21\ ^{+2.05}_{-1.87}$	$9.52\ ^{+4.29}_{-4.32}\ \left(^{+4.40}_{-4.14}\right)$		$^{+3.88}_{-4.30}\ \left(^{+4.21}_{-4.08}\right)$	$^{+0.38}_{-0.29}\ \left(^{+0.50}_{-0.33}\right)$	$0.63\ ^{+0.28}_{-0.28}\ \left(^{+0.29}_{-0.27}\right)$
ggH 0J high p_T^H	$44.25\ ^{+3.36}_{-3.24}$	$56.46\ ^{+7.79}_{-7.43}\ \left(^{+7.97}_{-7.57}\right)$		$^{+6.86}_{-6.59}\ \left(^{+7.17}_{-7.17}\right)$	$^{+1.99}_{-1.77}\ \left(^{+1.77}_{-1.33}\right)$	$1.28\ ^{+0.18}_{-0.17}\ \left(^{+0.18}_{-0.17}\right)$
ggH 1J low p_T^H	$16.20\ ^{+2.22}_{-2.09}$	$14.11\ ^{+6.37}_{-6.16}\ \left(^{+6.79}_{-5.99}\right)$		$^{+5.75}_{-5.67}\ \left(^{+6.20}_{-5.73}\right)$	$^{+0.78}_{-0.55}\ \left(^{+1.36}_{-0.32}\right)$	$0.87\ ^{+0.39}_{-0.38}\ \left(^{+0.42}_{-0.37}\right)$
ggH 1J med p_T^H	$11.22\ ^{+1.58}_{-1.49}$	$14.37\ ^{+4.01}_{-3.48}\ \left(^{+3.88}_{-3.38}\right)$		$^{+3.10}_{-3.11}\ \left(^{+3.29}_{-3.22}\right)$	$^{+0.64}_{-0.53}\ \left(^{+0.59}_{-0.44}\right)$	$1.28\ ^{+0.36}_{-0.31}\ \left(^{+0.35}_{-0.30}\right)$
ggH 1J high p_T^H	$2.00\ ^{+0.34}_{-0.31}$	$2.55\ ^{+1.19}_{-0.97}\ \left(^{+1.16}_{-0.95}\right)$		$^{+0.99}_{-0.97}\ \left(^{+0.95}_{-0.96}\right)$	$^{+0.24}_{-0.13}\ \left(^{+0.16}_{-0.08}\right)$	$1.28\ ^{+0.59}_{-0.49}\ \left(^{+0.58}_{-0.47}\right)$
ggH $\geq$ 2J low p_T^H	$2.82\ ^{+0.66}_{-0.58}$	$4.18\ ^{+4.27}_{-0.85}\ \left(^{+4.23}_{-2.77}\right)$		$^{+3.79}_{-3.65}\ \left(^{+3.92}_{-5.58}\right)$	$^{+0.50}_{-0.32}\ \left(^{+0.50}_{-0.10}\right)$	$1.48\ ^{+1.51}_{-0.91}\ \left(^{+1.50}_{-0.98}\right)$
ggH $\geq$ 2J med p_T^H	$4.53\ ^{+1.04}_{-0.91}$	$0.71\ ^{+3.04}_{-0.72}\ \left(^{+3.55}_{-3.00}\right)$		$^{+2.89}_{-0.71}\ \left(^{+3.12}_{-2.96}\right)$	$^{+0.26}_{-0.10}\ \left(^{+0.39}_{-0.27}\right)$	$0.16\ ^{+0.66}_{-0.56}\ \left(^{+0.78}_{-0.66}\right)$
ggH $\geq$ 2J high p_T^H	$2.12\ ^{+0.48}_{-0.43}$	$1.25\ ^{+1.26}_{-1.07}\ \left(^{+1.48}_{-1.16}\right)$		$^{+1.09}_{-1.07}\ \left(^{+1.17}_{-1.14}\right)$	$^{+0.08}_{-0.07}\ \left(^{+0.11}_{-0.08}\right)$	$0.59\ ^{+0.60}_{-0.51}\ \left(^{+0.70}_{-0.55}\right)$
ggH VBF-like	$2.21\ ^{+0.51}_{-0.44}$	$6.20\ ^{+3.85}_{-3.04}\ \left(^{+3.36}_{-2.22}\right)$		$^{+2.78}_{-2.88}\ \left(^{+3.05}_{-2.21}\right)$	$^{+0.68}_{-0.46}\ \left(^{+0.42}_{-0.11}\right)$	$2.81\ ^{+1.75}_{-1.38}\ \left(^{+1.52}_{-1.01}\right)$
ggH BSM	$1.43\ ^{+0.35}_{-0.30}$	$1.29\ ^{+0.70}_{-0.52}\ \left(^{+0.78}_{-0.57}\right)$		$^{+0.50}_{-0.48}\ \left(^{+0.54}_{-0.55}\right)$	$^{+0.08}_{-0.05}\ \left(^{+0.10}_{-0.05}\right)$	$0.90\ ^{+0.49}_{-0.37}\ \left(^{+0.55}_{-0.40}\right)$
qqH VBF-like	$2.95\ ^{+0.13}_{-0.14}$	$0.70\ ^{+1.55}_{-0.70}\ \left(^{+1.54}_{-1.53}\right)$		$^{+1.52}_{-0.70}\ \left(^{+1.52}_{-1.47}\right)$	$^{+0.25}_{-0.02}\ \left(^{+0.24}_{-0.14}\right)$	$0.24\ ^{+0.53}_{-0.24}\ \left(^{+0.52}_{-0.52}\right)$
qqH VH-like	$1.22\ ^{+0.04}_{-0.04}$	$1.54\ ^{+1.27}_{-1.35}\ \left(^{+1.29}_{-1.22}\right)$		$^{+1.26}_{-1.35}\ \left(^{+1.28}_{-1.22}\right)$	$^{+0.11}_{-0.04}\ \left(^{+0.15}_{-0.00}\right)$	$1.26\ ^{+1.04}_{-1.10}\ \left(^{+1.06}_{-1.00}\right)$
qqH BSM	$0.37\ ^{+0.01}_{-0.01}$	$0.65\ ^{+0.25}_{-0.27}\ \left(^{+0.26}_{-0.25}\right)$		$^{+0.25}_{-0.27}\ \left(^{+0.26}_{-0.23}\right)$	$^{+0.03}_{-0.02}\ \left(^{+0.03}_{-0.01}\right)$	$1.76\ ^{+0.68}_{-0.73}\ \left(^{+0.71}_{-0.68}\right)$
WH lep	$0.88\ ^{+0.03}_{-0.03}$	$1.20\ ^{+0.46}_{-0.40}\ \left(^{+0.48}_{-0.38}\right)$		$^{+0.46}_{-0.40}\ \left(^{+0.47}_{-0.38}\right)$	$^{+0.05}_{-0.03}\ \left(^{+0.04}_{-0.00}\right)$	$1.36\ ^{+0.52}_{-0.45}\ \left(^{+0.54}_{-0.43}\right)$
ZH lep	$0.53\ ^{+0.02}_{-0.02}$	$0.65\ ^{+0.40}_{-0.34}\ \left(^{+0.41}_{-0.35}\right)$		$^{+0.39}_{-0.34}\ \left(^{+0.41}_{-0.35}\right)$	$^{+0.03}_{-0.02}\ \left(^{+0.03}_{-0.00}\right)$	$1.23\ ^{+0.75}_{-0.65}\ \left(^{+0.77}_{-0.66}\right)$
ttH	$1.13\ ^{+0.08}_{-0.11}$	$1.65\ ^{+0.49}_{-0.45}\ \left(^{+0.49}_{-0.45}\right)$		$^{+0.48}_{-0.45}\ \left(^{+0.48}_{-0.45}\right)$	$^{+0.07}_{-0.05}\ \left(^{+0.06}_{-0.03}\right)$	$1.46\ ^{+0.43}_{-0.40}\ \left(^{+0.43}_{-0.40}\right)$
tH	$0.20\ ^{+0.01}_{-0.03}$	$0.39\ ^{+0.68}_{-0.39}\ \left(^{+0.68}_{-0.20}\right)$		$^{+0.67}_{-0.39}\ \left(^{+0.67}_{-0.21}\right)$	$^{+0.08}_{-0.00}\ \left(^{+0.11}_{-0.00}\right)$	$1.91\ ^{+3.31}_{-1.91}\ \left(^{+3.31}_{-1.00}\right)$

Table 6.7: The best-fit cross-sections with 68% confidence intervals for the minimal merging scenario. The uncertainty is decomposed into the systematic and statistical components. The expected uncertainties on the fitted parameters, computed assuming the SM predicted cross-section values, are given in brackets. Also listed are the SM predictions for the cross-sections and the theoretical uncertainty in these predictions.

STXS stage 1.2: extended merging scheme						
Parameters	$\sigma\mathcal{B}$ [fb]					$\sigma\mathcal{B}/(\sigma\mathcal{B})_{\text{SM}}$
	SM prediction	Observed (Expected)				Observed (Expected)
	(m_H = 125.38 GeV)	Best fit	Stat unc.		Syst unc.	Best fit
ggH 0J low p_T^H	$15.21\ ^{+4.14}_{-4.18}$	$9.51\ ^{+4.27}_{-4.32}\ \left(^{+4.40}_{-4.14}\right)$	$^{+3.88}_{-4.29}$	$\left(^{+4.21}_{-4.38}\right)$	$^{+0.40}_{-0.29}\ \left(^{+0.52}_{-0.23}\right)$	$0.62\ ^{+0.28}_{-0.28}\ \left(^{+0.29}_{-0.27}\right)$
ggH 0J high p_T^H	$44.25\ ^{+4.84}_{-4.61}$	$56.42\ ^{+7.79}_{-7.39}\ \left(^{+7.92}_{-7.57}\right)$	$^{+6.81}_{-6.59}$	$\left(^{+7.17}_{-7.17}\right)$	$^{+1.95}_{-1.77}\ \left(^{+1.77}_{-1.33}\right)$	$1.27\ ^{+0.18}_{-0.17}\ \left(^{+0.18}_{-0.17}\right)$
ggH 1J low p_T^H	$16.20\ ^{+2.25}_{-2.27}$	$14.05\ ^{+6.35}_{-5.82}\ \left(^{+6.77}_{-5.99}\right)$	$^{+5.75}_{-5.65}$	$\left(^{+6.24}_{-5.75}\right)$	$^{+0.78}_{-0.57}\ \left(^{+1.02}_{-0.15}\right)$	$0.87\ ^{+0.39}_{-0.36}\ \left(^{+0.42}_{-0.37}\right)$
ggH 1J med p_T^H	$11.23\ ^{+1.56}_{-1.55}$	$14.44\ ^{+4.00}_{-3.48}\ \left(^{+3.87}_{-3.38}\right)$	$^{+3.04}_{-3.12}$	$\left(^{+3.29}_{-3.23}\right)$	$^{+0.71}_{-0.43}\ \left(^{+0.55}_{-0.51}\right)$	$1.29\ ^{+0.36}_{-0.31}\ \left(^{+0.34}_{-0.30}\right)$
ggH 1J high p_T^H	$2.00\ ^{+0.36}_{-0.36}$	$2.57\ ^{+1.19}_{-0.98}\ \left(^{+1.12}_{-0.95}\right)$	$^{+0.99}_{-0.94}$	$\left(^{+0.95}_{-0.93}\right)$	$^{+0.23}_{-0.13}\ \left(^{+0.15}_{-0.09}\right)$	$1.28\ ^{+0.59}_{-0.49}\ \left(^{+0.56}_{-0.47}\right)$
ggH $\geq$ 2J low p_T^H	$2.82\ ^{+0.68}_{-0.68}$	$4.26\ ^{+4.33}_{-3.70}\ \left(^{+4.23}_{-2.77}\right)$	$^{+3.81}_{-3.70}$	$\left(^{+3.84}_{-2.78}\right)$	$^{+0.50}_{-0.37}\ \left(^{+0.64}_{-0.00}\right)$	$1.51\ ^{+1.54}_{-1.31}\ \left(^{+1.50}_{-0.98}\right)$
ggH $\geq$ 2J med p_T^H	$4.53\ ^{+1.07}_{-1.07}$	$0.60\ ^{+3.07}_{-0.60}\ \left(^{+3.55}_{-3.09}\right)$	$^{+2.92}_{-0.60}$	$\left(^{+3.12}_{-2.96}\right)$	$^{+0.29}_{-0.08}\ \left(^{+0.36}_{-0.39}\right)$	$0.13\ ^{+0.68}_{-0.13}\ \left(^{+0.78}_{-0.68}\right)$
ggH $\geq$ 2J high p_T^H	$2.12\ ^{+0.49}_{-0.50}$	$1.24\ ^{+1.28}_{-1.08}\ \left(^{+1.48}_{-1.16}\right)$	$^{+1.10}_{-1.08}$	$\left(^{+1.16}_{-1.14}\right)$	$^{+0.08}_{-0.06}\ \left(^{+0.18}_{-0.00}\right)$	$0.59\ ^{+0.60}_{-0.51}\ \left(^{+0.70}_{-0.55}\right)$
ggH $200 < p_T^H < 300$	$1.10\ ^{+0.28}_{-0.27}$	$0.98\ ^{+0.60}_{-0.46}\ \left(^{+0.65}_{-0.49}\right)$	$^{+0.46}_{-0.44}$	$\left(^{+0.50}_{-0.46}\right)$	$^{+0.08}_{-0.05}\ \left(^{+0.09}_{-0.09}\right)$	$0.89\ ^{+0.55}_{-0.42}\ \left(^{+0.59}_{-0.45}\right)$
ggH $300 < p_T^H < 450$	$0.28\ ^{+0.07}_{-0.07}$	$0.22\ ^{+0.25}_{-0.18}\ \left(^{+0.27}_{-0.20}\right)$	$^{+0.20}_{-0.18}$	$\left(^{+0.22}_{-0.20}\right)$	$^{+0.01}_{-0.01}\ \left(^{+0.03}_{-0.00}\right)$	$0.77\ ^{+0.87}_{-0.65}\ \left(^{+0.97}_{-0.72}\right)$
ggH $p_T^H > 450$	$0.05\ ^{+0.02}_{-0.02}$	$0.15\ ^{+0.13}_{-0.12}\ \left(^{+0.15}_{-0.05}\right)$	$^{+0.13}_{-0.11}$	$\left(^{+0.13}_{-0.04}\right)$	$^{+0.00}_{-0.02}\ \left(^{+0.00}_{-0.01}\right)$	$3.25\ ^{+2.75}_{-2.52}\ \left(^{+3.28}_{-0.99}\right)$
VBF-like low m_{jj} low p_T^{Hjj}	$1.59\ ^{+0.49}_{-0.48}$	$1.32\ ^{+1.23}_{-1.15}\ \left(^{+0.76}_{-0.69}\right)$	$^{+1.22}_{-1.14}$	$\left(^{+0.72}_{-0.69}\right)$	$^{+0.15}_{-0.09}\ \left(^{+0.12}_{-0.05}\right)$	$0.83\ ^{+0.78}_{-0.73}\ \left(^{+0.48}_{-0.44}\right)$
VBF-like low m_{jj} high p_T^{Hjj}	$1.25\ ^{+0.35}_{-0.32}$	$4.29\ ^{+2.64}_{-2.17}\ \left(^{+2.05}_{-1.26}\right)$	$^{+2.31}_{-0.81}$	$\left(^{+1.90}_{-1.26}\right)$	$^{+0.29}_{-0.21}\ \left(^{+0.16}_{-0.07}\right)$	$3.42\ ^{+2.11}_{-1.74}\ \left(^{+1.63}_{-1.00}\right)$
VBF-like high m_{jj} low p_T^{Hjj}	$1.60\ ^{+0.45}_{-0.51}$	$1.00\ ^{+0.75}_{-0.68}\ \left(^{+0.74}_{-0.70}\right)$	$^{+0.74}_{-0.67}$	$\left(^{+0.73}_{-0.70}\right)$	$^{+0.12}_{-0.09}\ \left(^{+0.12}_{-0.05}\right)$	$0.63\ ^{+0.47}_{-0.42}\ \left(^{+0.46}_{-0.44}\right)$
VBF-like high m_{jj} high p_T^{Hjj}	$0.73\ ^{+0.16}_{-0.16}$	$0.45\ ^{+0.87}_{-0.59}\ \left(^{+0.91}_{-0.73}\right)$	$^{+0.85}_{-0.59}$	$\left(^{+0.89}_{-0.73}\right)$	$^{+0.13}_{-0.00}\ \left(^{+0.13}_{-0.07}\right)$	$0.61\ ^{+1.18}_{-0.81}\ \left(^{+1.24}_{-1.00}\right)$
qqH VH-like	$1.22\ ^{+0.05}_{-0.05}$	$1.54\ ^{+1.27}_{-1.34}\ \left(^{+1.29}_{-1.22}\right)$	$^{+1.26}_{-1.34}$	$\left(^{+1.29}_{-1.22}\right)$	$^{+0.11}_{-0.05}\ \left(^{+0.13}_{-0.00}\right)$	$1.26\ ^{+1.04}_{-1.10}\ \left(^{+1.06}_{-1.00}\right)$
qqH BSM	$0.37\ ^{+0.03}_{-0.02}$	$0.65\ ^{+0.25}_{-0.27}\ \left(^{+0.26}_{-0.23}\right)$	$^{+0.25}_{-0.27}$	$\left(^{+0.26}_{-0.24}\right)$	$^{+0.03}_{-0.02}\ \left(^{+0.04}_{-0.00}\right)$	$1.76\ ^{+0.69}_{-0.74}\ \left(^{+0.71}_{-0.64}\right)$
WH lep $p_T^V < 75$	$0.47\ ^{+0.02}_{-0.02}$	$0.74\ ^{+0.69}_{-0.51}\ \left(^{+0.71}_{-0.92}\right)$	$^{+0.68}_{-0.51}$	$\left(^{+0.72}_{-0.45}\right)$	$^{+0.05}_{-0.02}\ \left(^{+0.00}_{-0.06}\right)$	$1.58\ ^{+1.47}_{-1.10}\ \left(^{+1.53}_{-1.96}\right)$
WH lep $75 < p_V^H < 150$	$0.29\ ^{+0.02}_{-0.02}$	$0.41\ ^{+0.34}_{-0.30}\ \left(^{+0.35}_{-0.28}\right)$	$^{+0.34}_{-0.30}$	$\left(^{+0.35}_{-0.28}\right)$	$^{+0.01}_{-0.02}\ \left(^{+0.02}_{-0.00}\right)$	$1.39\ ^{+1.16}_{-1.02}\ \left(^{+1.20}_{-0.94}\right)$
WH lep $p_T^V > 150$	$0.12\ ^{+0.01}_{-0.01}$	$0.14\ ^{+0.11}_{-0.09}\ \left(^{+0.12}_{-0.09}\right)$	$^{+0.11}_{-0.09}$	$\left(^{+0.12}_{-0.09}\right)$	$^{+0.01}_{-0.00}\ \left(^{+0.01}_{-0.00}\right)$	$1.17\ ^{+0.94}_{-0.73}\ \left(^{+0.96}_{-0.74}\right)$
ZH lep	$0.54\ ^{+0.03}_{-0.02}$	$0.67\ ^{+0.40}_{-0.35}\ \left(^{+0.42}_{-0.36}\right)$	$^{+0.40}_{-0.35}$	$\left(^{+0.42}_{-0.36}\right)$	$^{+0.03}_{-0.02}\ \left(^{+0.02}_{-0.02}\right)$	$1.24\ ^{+0.75}_{-0.65}\ \left(^{+0.78}_{-0.66}\right)$
ttH $p_T^H < 60$	$0.26\ ^{+0.03}_{-0.04}$	$0.26\ ^{+0.28}_{-0.22}\ \left(^{+0.26}_{-0.22}\right)$	$^{+0.28}_{-0.22}$	$\left(^{+0.26}_{-0.22}\right)$	$^{+0.03}_{-0.01}\ \left(^{+0.01}_{-0.01}\right)$	$1.02\ ^{+1.08}_{-0.86}\ \left(^{+1.01}_{-0.86}\right)$
ttH $60 < p_T^H < 120$	$0.40\ ^{+0.04}_{-0.05}$	$0.62\ ^{+0.29}_{-0.25}\ \left(^{+0.32}_{-0.24}\right)$	$^{+0.28}_{-0.24}$	$\left(^{+0.32}_{-0.24}\right)$	$^{+0.03}_{-0.02}\ \left(^{+0.02}_{-0.02}\right)$	$1.57\ ^{+0.72}_{-0.62}\ \left(^{+0.80}_{-0.61}\right)$
ttH $120 < p_T^H < 200$	$0.29\ ^{+0.03}_{-0.04}$	$0.37\ ^{+0.20}_{-0.17}\ \left(^{+0.20}_{-0.18}\right)$	$^{+0.20}_{-0.17}$	$\left(^{+0.20}_{-0.18}\right)$	$^{+0.02}_{-0.01}\ \left(^{+0.01}_{-0.01}\right)$	$1.26\ ^{+0.69}_{-0.58}\ \left(^{+0.69}_{-0.61}\right)$
ttH $200 < p_T^H < 300$	$0.12\ ^{+0.02}_{-0.02}$	$0.25\ ^{+0.13}_{-0.11}\ \left(^{+0.12}_{-0.11}\right)$	$^{+0.13}_{-0.11}$	$\left(^{+0.12}_{-0.11}\right)$	$^{+0.01}_{-0.01}\ \left(^{+0.01}_{-0.00}\right)$	$2.01\ ^{+1.07}_{-0.91}\ \left(^{+1.01}_{-0.87}\right)$
ttH $p_T^H > 300$	$0.06\ ^{+0.01}_{-0.01}$	$0.00\ ^{+0.10}_{-0.00}\ \left(^{+0.12}_{-0.06}\right)$	$^{+0.10}_{-0.00}$	$\left(^{+0.11}_{-0.06}\right)$	$^{+0.01}_{-0.00}\ \left(^{+0.01}_{-0.00}\right)$	$0.00\ ^{+1.62}_{-0.00}\ \left(^{+1.90}_{-1.00}\right)$
tH	$0.20\ ^{+0.01}_{-0.03}$	$0.56\ ^{+0.62}_{-0.56}\ \left(^{+0.86}_{-0.20}\right)$	$^{+0.61}_{-0.56}$	$\left(^{+0.86}_{-0.20}\right)$	$^{+0.08}_{-0.02}\ \left(^{+0.06}_{-0.01}\right)$	$2.76\ ^{+3.03}_{-2.76}\ \left(^{+4.23}_{-1.00}\right)$

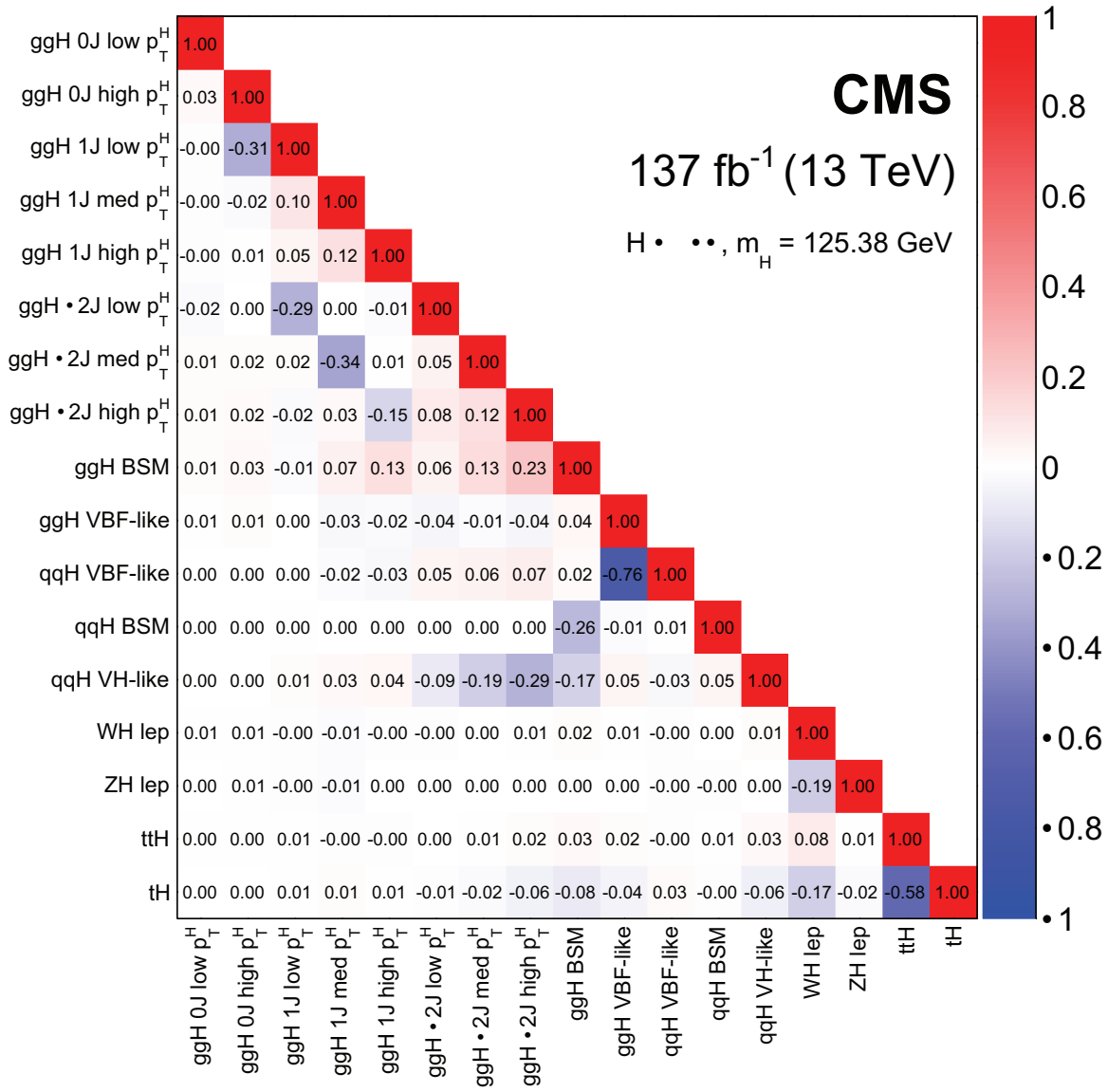

Figure 6.19: Expected correlations between the 17 parameters considered in the STXS Stage 1.2 maximal merging fit. The size of the correlations is indicated by the colour scale.

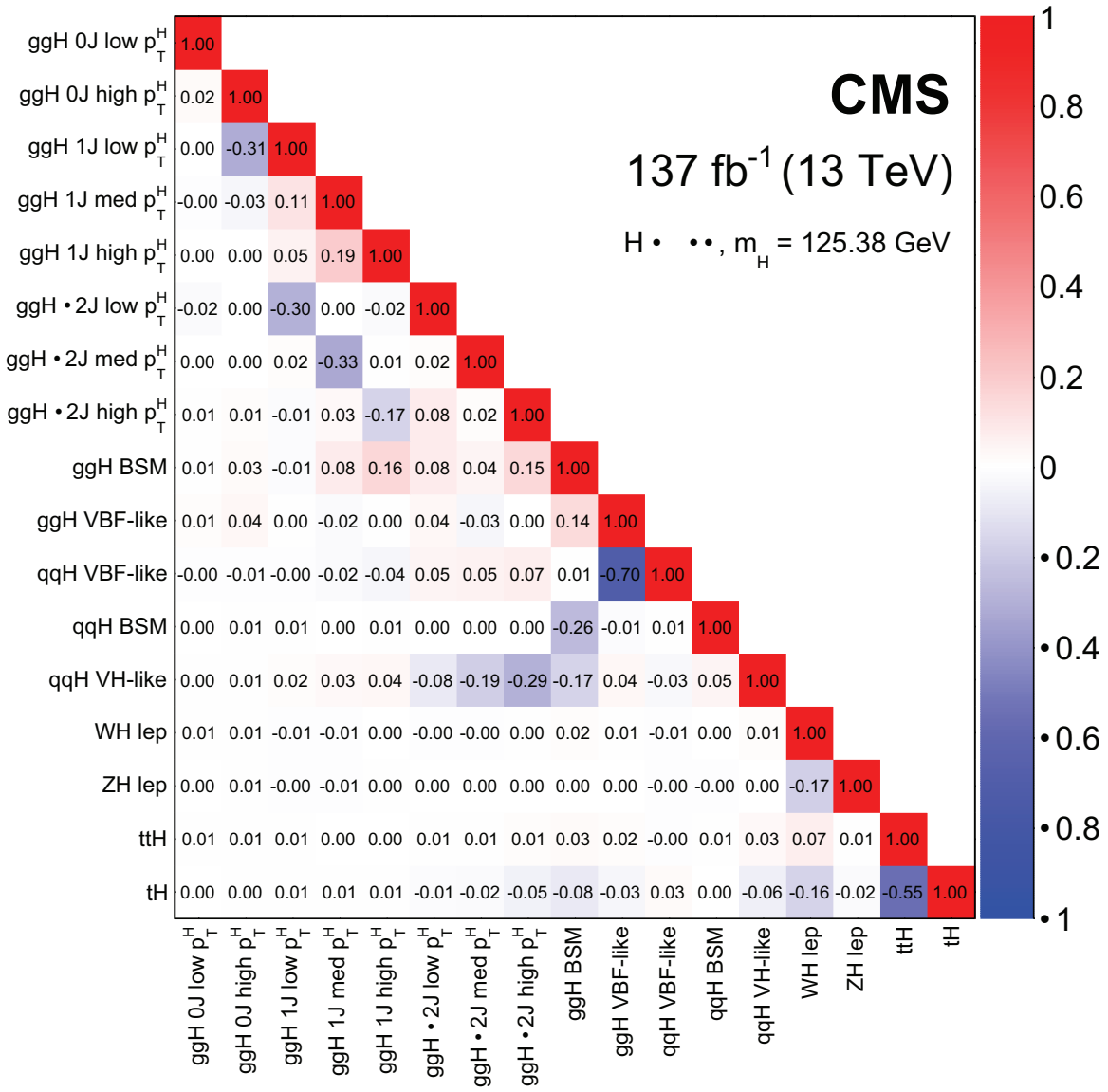

Figure 6.20: Observed correlations between the 17 parameters considered in the STXS Stage 1.2 maximal merging fit. The size of the correlations is indicated by the colour scale.

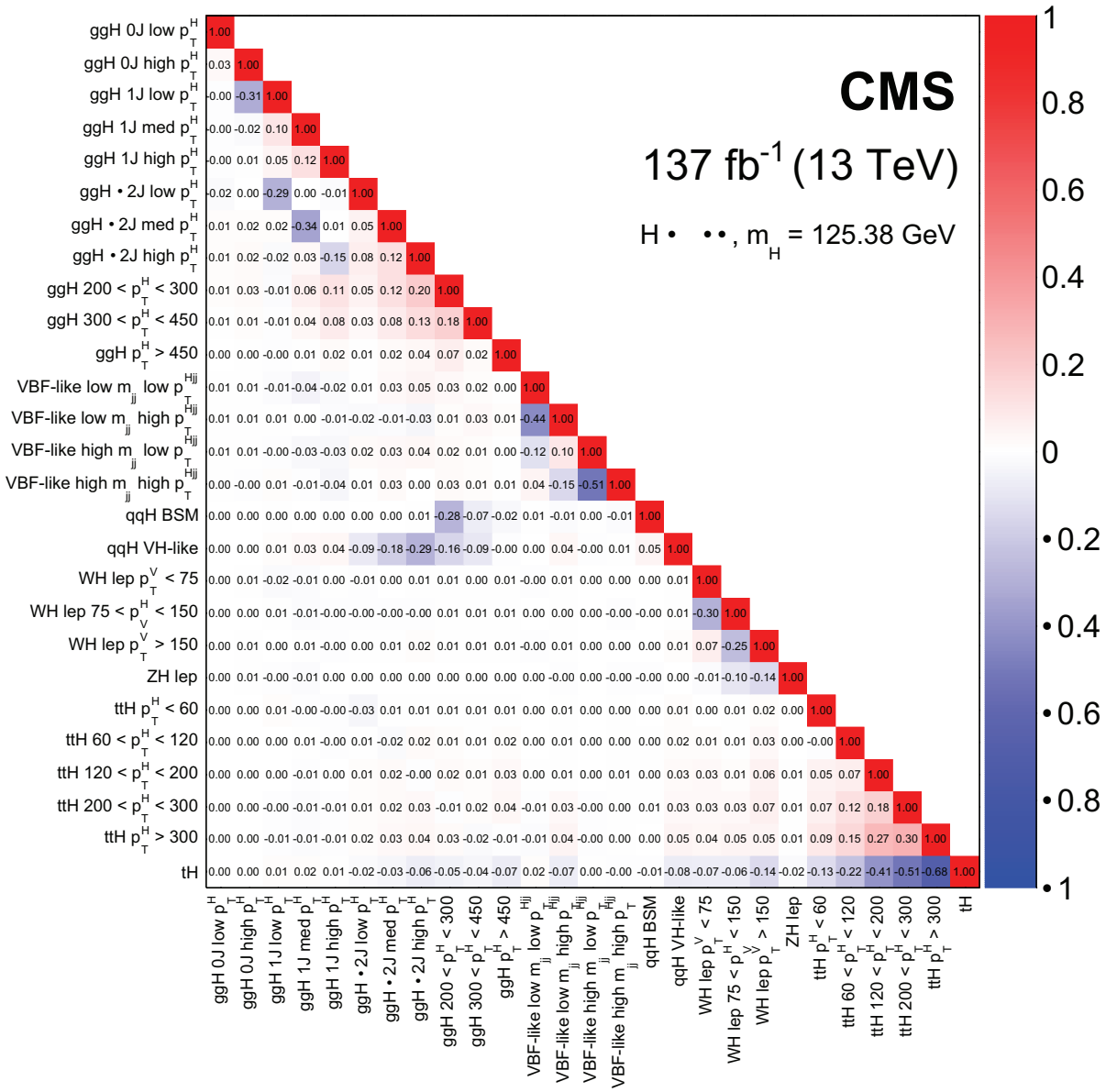

Figure 6.21: Expected correlations between the 27 parameters considered in the STXS Stage 1.2 minimal merging fit. The size of the correlations is indicated by the colour scale.

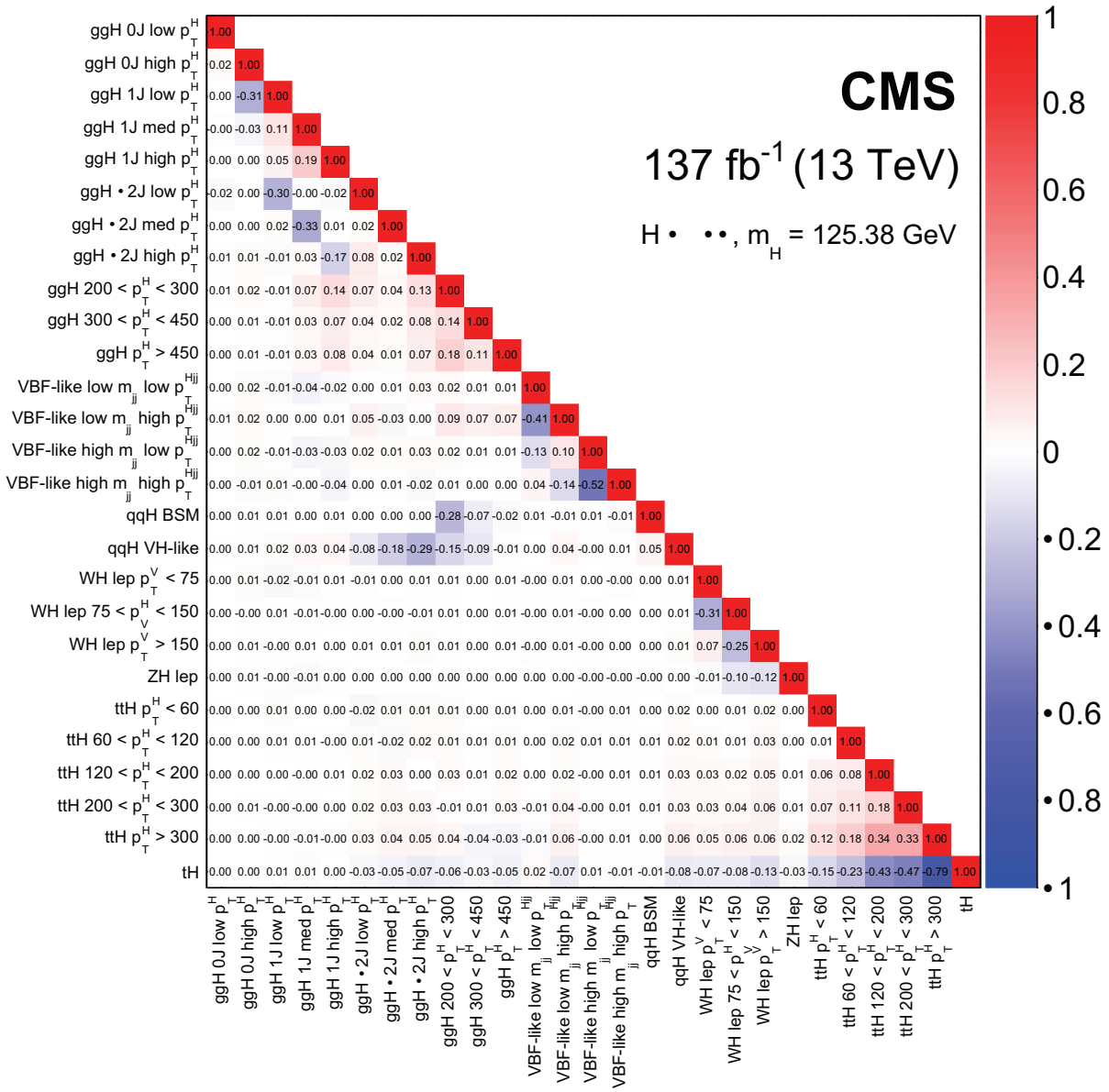

Figure 6.22: Observed correlations between the 27 parameters considered in the STXS Stage 1.2 minimal merging fit. The size of the correlations is indicated by the colour scale.

6.7 Results for coupling modifiers

The κ-framework defines coupling modifiers as parameters which directly parametrise deviations from the SM expectation in the couplings of the Higgs boson to other particles [71].

Two different likelihood scans, each with two dimensions, are performed. Full details of each parameterisation are given in Ref. [105].

In the first fit, the resolved κ model is used. This means that the scaling factors of loops are resolved into their SM components, in terms of the other κ parameters. The most important of these are in the ggH production and $H \to \gamma\gamma$ decay loops, but others, such as the loop in ggZH production, are also resolved. The expected and observed results of a two-dimensional scan in κ_V and κ_F, scaling the Higgs boson coupling to vector bosons and to fermions, respectively, are shown in Figure 6.23. The best fit point is consistent with the SM expectation at approximately the 68% CL. The $H \to \gamma\gamma$ decay rate contains an interference term proportional to $\kappa_V\kappa_F$. This means that the rate of ggH and ttH production ($\propto \kappa_F^2$), relative to the rate of VBF and VH production ($\propto \kappa_V^2$), can be used to gain sensitivity to the relative sign of the tt-H and VV-H couplings. In addition, the tHq and tHW production modes also include a term proportional to $\kappa_V\kappa_F$. This analysis explicitly targets tHq production via the tHq leptonic and tHq hadronic analysis categories, the inclusion of which helps to further reduce the degeneracy between positive and negative κ_F values. The region with negative values of κ_F is observed (expected) to be excluded with a significance of 3.0 (2.4) standard deviations.

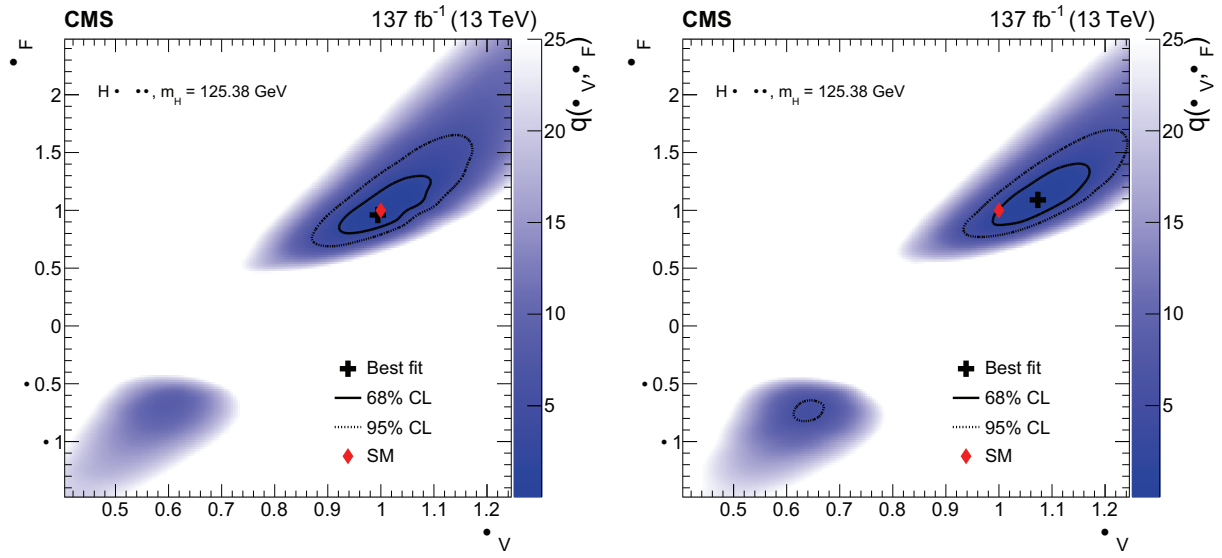

Figure 6.23: Expected (left) and observed (right) two dimensional likelihood scan of κ_V-vs-κ_F in the resolved κ model. The expected 68% and 95% confidence regions are given by the solid and dashed contours respectively. The SM point is shown by the red diamond. The colour scale indicates the value of the test statistic.

A second fit is performed using the unresolved κ model, where the ggH and $H \to \gamma\gamma$ loops are given their own effective scaling factors denoted by κ_g and κ_γ respectively. These parameters are particularly sensitive to possible BSM states, that contribute to the rate of Higgs boson production and decay via loop processes. The expected and observed results of a two-dimensional scan in these two parameters is shown in Figure 6.24. In the scan, the other κ parameters in the unresolved model are fixed to unity. The observed scan shows no evidence for BSM physics.

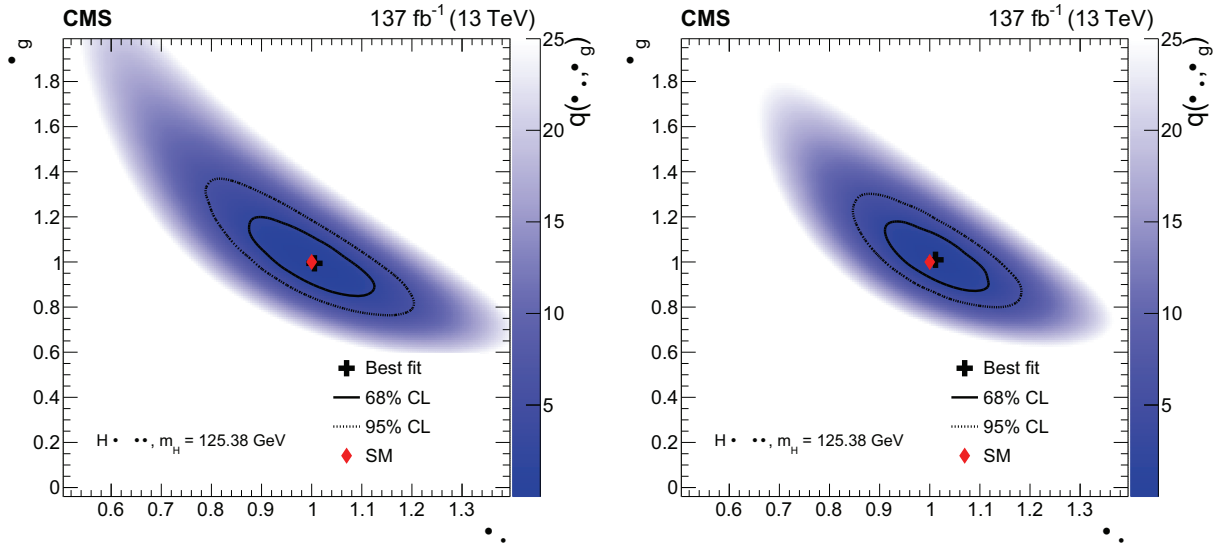

Figure 6.24: Expected (left) and observed (right) two dimensional likelihood scan of κ_g-vs-κ_γ in the unresolved κ model. The expected 68% and 95% confidence regions are given by the solid and dashed contours respectively. The SM point is shown by the red diamond. The colour scale indicates the value of the test statistic.

6.8 Summary

Several Higgs boson properties have been measured by performing fits to the $m_{\gamma\gamma}$ distribution in the $H \to \gamma\gamma$ decay channel using the full LHC Run II dataset. Signal and background models are fitted in categories targeting the kinematic regions defined by the STXS Stage 1.2 framework. The signal models are constructed from simulated events while background models are constructed from data. The parameters of interest are obtained by performing a simultaneous maximum likelihood fit in all the categories considered. The theoretical and experimental uncertainties which affect the measurements have been quantified, together with the statistical uncertainties. Furthermore, studies of the contamination of categories from non-target Higgs boson processes have been presented.

The amount of data available does not allow all STXS Stage 1.2 bins to be measured individually. The parameters of interest principally include Higgs boson cross-sections measured in two STXS Stage 1.2 bin merging schemes: a maximal merging scheme with 17 POIs and a minimal merging scheme with 27 POIs. The expected and observed best-fit values for these cross-sections have been presented, together with their 68% CL intervals. The corresponding p-values with respect to the SM are 61% and 87% for the maximal and minimal merging scenarios respectively. For all of the cross-sections measured, the statistical uncertainty is the limiting factor.

In both merging schemes, the tH kinematic region is measured including a tHq hadronic category for the first time. In the maximal merging scenario, the product of the tH production cross-section times the $H \to \gamma\gamma$ branching fraction is measured to be $0.4^{+0.7}_{-0.4}$ fb, corresponding to an excess of $1.9^{+3.3}_{-1.9}$ times the SM expectation. In the minimal merging scenario, this value is measured to be $0.6^{+0.6}_{-0.6}$ fb, corresponding to an excess of $2.8^{+3.0}_{-2.8}$ times the SM expectation. Both of these measurements are more SM-like when compared to the value reported in

Ref. [1]. The observed (expected) upper limit on the tH cross-section as a fraction of the SM expectation is 9.47 (7.89) and 9.47 (9.47) for the maximal and minimal merging scenarios respectively. This represents an improvement to the limits in Ref. [1]. Correlations between the fitted parameters were also studied. The largest correlations in the maximal merging scheme exist between the ggH VBF-like and qqH VBF-like cross-sections and the ttH and tH cross-sections. In particular, the expected correlation between the ttH and tH cross-sections (-0.58) is smaller than the value expected in the Ref. [1] analysis. This reflects the effect of introducing a new tHq hadronic category.

Measurements outside of the STXS framework were also performed. These include signal strength modifier measurements. The total Higgs boson signal strength, relative to the SM prediction, is measured to be $1.14^{+0.11}_{-0.10}$. A simultaneous measurement of the signal strengths of the four principal Higgs boson production mechanisms was performed and found to be compatible with the SM prediction with a p-value of 42%. All other results, such as measurements of the Higgs boson couplings to vector bosons and to fermions, are also in agreement with the SM expectations.

Chapter 7

Conclusions and future prospects

7.1 Conclusions

Since the discovery of the Higgs boson, LHC experiments have been focusing on conducting precise measurements in the Higgs sector. In this context, the STXS framework has been developed to perform granular measurements of the Higgs boson cross-sections and to enable wider interpretations of experimental measurements as compared to the LHC Run 1 findings. In this thesis, measurements of the Higgs boson production cross-sections via the decay of the Higgs boson to two photons are reported. The measurements are made using data collected in the period 2016-2018 by the CMS detector at the LHC in proton-proton collisions at a centre-of-mass energy of 13 TeV, amounting to an integrated luminosity of $137\,\text{fb}^{-1}$.

Candidate events from the reconstruction are categorised using reconstruction-level event variables to target the particle-level bins of the STXS Stage 1.2 framework. The framework allows events to be separated into the different production modes and into different kinematic regions within the production modes. Key elements of the analysis in this thesis include two BDT classifiers, namely a VBF BDT and a VH hadronic BDT, which are trained to categorise events into the target qqH STXS bins. A data-driven background modelling procedure is adopted to improve the BDT performance. The use of the data-driven background modelling was found to increase the expected observation significance in each of the qqH STXS bins targeted by approximately 4-50%, the inclusive VBF significance by $\sim$20%, and the inclusive VH significance by $\sim$10%. The results of applying these two classifiers were first presented in Ref. [1]. This thesis also introduces a new tHq hadronic tag to target tHq processes where the vector boson, from the top quark decay, decays hadronically.

Several Higgs boson properties have been measured by performing fits to the $m_{\gamma\gamma}$ distribution in the categories targeting the kinematic regions defined by the STXS Stage 1.2 framework. The parameters of interest are obtained by performing a simultaneous maximum likelihood fit in all the categories considered. The parameters of interest principally include Higgs boson cross-sections measured in two STXS Stage 1.2 bin merging schemes. The expected and observed best-fit values for these cross-sections have been presented, together with their 68% CL intervals. All results were found to be in agreement with the SM. In both

merging schemes, the tH kinematic region is measured via a tHq hadronic category for the first time.

The theoretical and experimental uncertainties which affect the measurements have been quantified, together with the statistical uncertainties. For all of the cross-sections measured, the statistical uncertainty dominates, indicating that the systematic limit has not yet been been reached with the full LHC Run II dataset. This limit is expected to be reached in future runs of the LHC, and thus future analyses should also focus on understanding and minimising the impact of systematic uncertainties.

Measurements outside of the STXS framework were also performed. These include signal strength modifier measurements. The total Higgs boson signal strength, relative to the standard model (SM) prediction, is measured to be $1.14^{+0.11}_{-0.10}$. The observed upper limit on the tH cross-section as a fraction of the SM expectation is 9.47. This represents an improvement to the limits in Ref. [1]. All other results, such as measurements of the Higgs boson couplings to vector bosons and to fermions, are also in agreement with the SM expectations.

7.2 Future prospects

Despite excellent agreement of the measured quantities with the SM, many of the corresponding uncertainties are still relatively large. Notably, several BSM theories expect Higgs coupling parameters to deviate from the SM at the percent level [179]. In this context, the STXS framework is a useful tool to characterise any possible deviations from the SM, for example within effective field theories [180]. Although all the STXS measurements have been found to be statistically-limited, future LHC runs are expected ro reach the systematic limit for several measurements and thus further progress will require improvements in theoretical predictions, experimental data-collection and event reconstruction techniques.

The HL-LHC physics programme is expected to deepen our present understanding of the Higgs boson obtained from Runs I and II data and to increase both the statistical and experimental reach of the LHC experiments. To address the issues that arise from the high-luminosity environment, the CMS detector will be upgraded and one of the key upgrades, discussed in this thesis, is the implementation of fine-grained endcap calorimeters (HGCAL). The HGCAL is expected to provide unprecedented granularity and timing capabilities in the forward dectector regions. In particular, precision timing from silicon sensors in the HGCAL reconstruction chain was studied in this thesis, and possible improvements to the HGCAL reconstruction using the results of the timing studies were presented.

The HL-LHC will provide improved precision on existing measurements in the Higgs sector and will also enable entirely new measurements to be made. The key future prospects from the HL-LHC are outlined in the following paragraph. Any projections are taken from Ref. [181].

Uncertainties in signal strength in the 300 fb^{-1} dataset are expected to be roughly halved with 3000 fb^{-1} of data, achieving the precision required to test BSM models. A 2-10% precision is foreseen on the measurement of each of the Higgs boson couplings. Coupling predictions show a more pronounced improvement in measurements of fermionic couplings which are generally statistically limited, over the normally theoretically-limited measurements of bosonic couplings. Higgs boson couplings to gg, $\gamma\gamma$, and $Z\gamma$ proceed via W boson and top quark loops in the SM and are therefore sensitive to possible radiative corrections from BSM

particles. With 3000 fb^{-1} of integrated luminosity, CMS projects 20-24% uncertainty on the inclusive signal strength of the $H \to Z\gamma$ decay, and ∼10% precision on $\kappa_{Z\gamma}$. The HL-LHC will also provide increased accessibility to the rare $H \to J/\psi\gamma$ and $H \to ee\gamma$ decays which are sensitive to Higgs boson couplings to light quarks and leptons respectively. With the HL-LHC dataset, CP-odd Higgs boson contributions, which are required to vanish in the SM, are expected to be constrained to 2%. CP measurements of the Higgs boson may be extracted from the $H \to ZZ$ decay, the $H \to \tau\tau$ decay, and the VBF production mode. The limits on the Higgs boson invisible branching ratio, $BR \to invisible$, can be derived from the rates of measured decays by assuming SM Higgs boson couplings to visible particles. The current upper limit is $\sim$ 19% and is expected to reach $\sim$ 6% with the 3000 fb^{-1} dataset. While complementing non-collider direct dark matter searches in the lower mass range, the HL-LHC will further provide the opportunity to explore production mechanisms coupling dark matter to the Higgs boson namely, *mono-Higgs production* [182] whereby a single Higgs boson is produced together with invisible particles. An experimental test of the SM Higgs field potential may be made by measurement of the Higgs boson trilinear self-coupling λ_{HHH}, and its subsequent comparison to the SM value of $3m_H^2/\nu$. Pair production of the Higgs boson provides sensitivity to λ_{HHH} through a self-coupling diagram involving the off-shell $H^* \to HH$ process [183]. The value of σ_{HH} is predicted to be significantly enhanced in many BSM scenarios. With the HL-LHC datasets, $O(1)$ limits are expected to be set on the value of λ_{HHH}. Prospects for measuring λ_{HHH} from anomalous trilinear couplings in single-Higgs boson processes are also being considered [184]. Generic two-Higgs-doublet models (2-HDM) [185] involve an extension of the SM to accommodate a second Higgs doublet and are further parameterised by the ratio of the vacuum expectation values of the Higgs doublets, $\tan\beta$, and the mixing angle α between the two CP-even states. In restricted $\tan\beta$ parameter space, heavy flavour measurements have placed a lower limit of ∼1 TeV on the mass of additional Higgs bosons. Nonetheless, the HL-LHC aims at surveying the whole range of $\tan\beta$ up to Higgs boson masses of at least 500 GeV [186, 187].

7.3 Outlook

Measurements of Higgs boson cross-sections, signal strengths and couplings have all been consistent with SM predictions to date. More precise measurements are needed to test the SM as thoroughly as possible, to understand several physical phenomena relating to the Higgs boson which still remain unexplained, and to constrain BSM theories. It is expected that increased precision will be achieved through the HL-LHC phase through the availability of more data and the use of improved experimental techniques. Nonetheless, theoretical predictions still need to be improved so that uncertainties from SM predictions are maintained below the achievable experimental precision. Current projections for HL-LHC measurements show immense potential for further progress in Higgs boson measurements at the HL-LHC. In this context, the LHC and its associated detector collaborations represent an ongoing global scientific effort to improve our fundamental understanding of the universe and to extend the present discovery reach for new physics.

Bibliography

[1] CMS Collaboration, "Measurements of Higgs boson production cross sections and couplings in the diphoton decay channel at $\sqrt{s} = 13$ TeV," *J. High Energ. Phys.*, vol. 27, 2021. DOI: 10.1007/JHEP07(2021)027.

[2] S.Bonomally, A.Martelli, C.Seez, "Precision timing in the hgcal reconstruction," *CERN Document Server*, vol. DN-19-056, 2021, (unpublished).

[3] CMS Collaboration, "Measurements of Higgs boson production via gluon fusion and vector boson fusion in the diphoton decay channel at $\sqrt{s} = 13$ TeV," 2019. [Online]. Available: https://cds.cern.ch/record/2667225.

[4] S. L. Glashow, "Partial Symmetries of Weak Interactions," *Nuclear Physics*, vol. 22, pp. 579–588, 1961. DOI: 10.1016/0029-5582(61)90469-2.

[5] S. Weinberg, "A Model of Leptons," *Physical Review Letters*, vol. 19, no. 21, pp. 1264–1266, 1967. DOI: 10.1103/PhysRevLett.19.1264.

[6] A. Salam, "Weak and Electromagnetic Interactions," *8th Nobel Symposium, Sweden, Conf. Proc. C*, vol. 680519, pp. 367–377, 1968. DOI: 10.1142/9789812795915_0034.

[7] G. 't Hooft and M. Veltman, "Regularization and renormalization of gauge fields," *Nuclear Physics B*, vol. 44, no. 1, pp. 189–213, 1972. DOI: https://doi.org/10.1016/0550-3213(72)90279-9.

[8] M. Gell-Mann, "A Schematic Model of Baryons and Mesons," *Physics Letters*, vol. 8, pp. 214–215, 1964. DOI: 10.1016/S0031-9163(64)92001-3.

[9] G. Zweig, "An SU(3) model for strong interaction symmetry and its breaking," Feb. 1964. [Online]. Available: https://cds.cern.ch/record/570209.

[10] ALEPH Collaboration, "Precision electroweak measurements on the Z resonance," *Physics Reports*, vol. 427, pp. 257–454, 2006. DOI: 10.1016/j.physrep.2005.12.006. arXiv: hep-ex/0509008.

[11] M. L. Perl *et al.*, "Evidence for Anomalous Lepton Production in e^+-e^- Annihilation," *Physics Review Letters*, vol. 35, pp. 1489–1492, 1975. DOI: 10.1103/PhysRevLett.35.1489.

[12] UA1 Collaboration, "Experimental observation of isolated large transverse energy electrons with associated missing energy at $\sqrt{s}$= 540 gev," *Physics letters B*, vol. 122, no. 1, pp. 103–116, 1983. DOI: 10.5170/CERN-1983-004.123.

[13] UA2 collaboration *et al.*, "Observation of single isolated electrons of high transverse momentum in events with missing transverse energy at the cern $\bar{p}p$ collider," *Physics Letters B*, vol. 122, no. 476, p. 1, 1983. DOI: 10.1016/0370-2693(83)91605-2.

[14] UA2 collaboration *et al.*, "Evidence for $z^0 \to e^+e^-$ at the cern $\bar{p}p$ collider," *Physics Letters B*, vol. 129, pp. 130–140, 1983. DOI: 10.1016/0370-2693(83)90744-X.

[15] CDF collaboration *et al.*, "Observation of top quark production in $\bar{p}p$ collisions," *Physics Review Letters*, vol. 74, pp. 2626–2631, 1995. DOI: 10.1103/PhysRevLett.74.2626. arXiv: hep-ex/9503002.

[16] D0 Collaboration, "Observation of the top quark," *Physical Review Letters*, vol. 74, no. 14, p. 2632, 1995. DOI: 10.1103/PhysRevLett.74.2632.

[17] J. Augustin *et al.*, "Discovery of a narrow resonance in e^+-e^- annihilation," *Physical Review Letters*, vol. 33, no. 23, p. 1406, 1974. DOI: 10.1103/PhysRevLett.33.1406.

[18] E598 Collaboration, "Experimental Observation of a Heavy Particle J," *Physical Review Letters*, vol. 33, pp. 1404–1406, 1974. DOI: 10.1103/PhysRevLett.33.1404.

[19] Fermilab, "Observation of a Dimuon Resonance at 9.5 GeV in 400 GeV Proton-Nucleus Collisions," *Physics Review Letters*, vol. 39, pp. 252–255, 1977. DOI: 10.1103/PhysRevLett.39.252.

[20] F. Englert and R. Brout, "Broken Symmetry and the Mass of Gauge Vector Mesons," *Physical Review Letters*, vol. 13, J. C. Taylor, Ed., pp. 321–323, 1964. DOI: 10.1103/PhysRevLett.13.321.

[21] P. W. Higgs, "Broken symmetries, massless particles and gauge fields," *Physics Letters*, vol. 12, pp. 132–133, 1964. DOI: 10.1016/0031-9163(64)91136-9.

[22] P. W. Higgs, "Broken Symmetries and the Masses of Gauge Bosons," *Physical Review Letters*, vol. 13, J. C. Taylor, Ed., pp. 508–509, 1964. DOI: 10.1103/PhysRevLett.13.508.

[23] G. S. Guralnik, C. R. Hagen, and T. W. B. Kibble, "Global Conservation Laws and Massless Particles," *Physical Review Letters*, vol. 13, J. C. Taylor, Ed., pp. 585–587, 1964. DOI: 10.1103/PhysRevLett.13.585.

[24] P. W. Higgs, "Spontaneous Symmetry Breakdown without Massless Bosons," *Phys. Rev.*, vol. 145, pp. 1156–1163, 1966. DOI: 10.1103/PhysRev.145.1156.

[25] T. W. B. Kibble, "Symmetry breaking in non-Abelian gauge theories," *Physical Review*, vol. 155, J. C. Taylor, Ed., pp. 1554–1561, 1967. DOI: 10.1103/PhysRev.155.1554.

[26] L. Evans and P. Bryant, "LHC Machine," *JINST*, vol. 3, S08001, 2008. DOI: 10.1088/1748-0221/3/08/S08001.

[27] ATLAS Collaboration, "Observation of a new particle in the search for the Standard Model Higgs boson with the ATLAS detector at the LHC," *Physics Letters B*, vol. 716, pp. 1–29, 2012. DOI: 10.1016/j.physletb.2012.08.020. arXiv: 1207.7214 [hep-ex].

[28] CMS Collaboration, "Observation of a New Boson at a Mass of 125 GeV with the CMS Experiment at the LHC," *Physics Letters B*, vol. 716, pp. 30–61, 2012. DOI: 10.1016/j.physletb.2012.08.021. arXiv: 1207.7235 [hep-ex].

[29] G. 't Hooft, "Naturalness, chiral symmetry, and spontaneous chiral symmetry breaking," *NATO Sci. Ser. B*, vol. 59, pp. 135–157, 1980. DOI: 10.1007/978-1-4684-7571-5_9.

[30] Y. B. Zel'Dovich, "Cosmological Constant and Elementary Particles," *JETP Letters*, vol. 6, p. 316, 1967.

[31] Supernova Cosmology Project, "Improved Cosmological Constraints from New, Old and Combined Supernova Datasets," *Astrophys. J.*, vol. 686, pp. 749–778, 2008. DOI: 10.1086/589937. arXiv: 0804.4142 [astro-ph].

[32] Super-Kamiokande Collaboration, "Evidence for oscillation of atmospheric neutrinos," *Physical Review Letters*, vol. 81, pp. 1562–1567, 1998. DOI: 10.1103/PhysRevLett.81.1562. arXiv: hep-ex/9807003.

[33] L. Rossi, "LHC Upgrade Plans: Options and Strategy," *Conf. Proc. C*, vol. 110904, pp. 908–912, Dec. 2011. [Online]. Available: https://cds.cern.ch/record/1407911.

[34] G. Apollinari, O. Brüning, T. Nakamoto, and L. Rossi, "High luminosity large hadron collider hl-lhc," *CERN Yellow Report CERN-2015-005*, pp. 1–19, 2017. DOI: 10.5170/CERN-2015-005.1.

[35] F. Gianotti, M. L. Mangano, T. Virdee, *et al.*, "Physics potential and experimental challenges of the lhc luminosity upgrade," *Eur.Phys.J*, vol. 39, no. 3, pp. 293–333, 2005. DOI: 10.1140/epjc/s2004-02061-6.

[36] B. Schmidt, "The High-Luminosity upgrade of the LHC: Physics and Technology Challenges for the Accelerator and the Experiments," *J. Phys. Conf. Ser.*, vol. 706, no. 2, p. 022 002, 2016. DOI: 10.1088/1742-6596/706/2/022002.

[37] CMS Collaboration, "The CMS Experiment at the CERN LHC," *JINST*, vol. 3, S08004, 2008. DOI: 10.1088/1748-0221/3/08/S08004.

[38] CMS Collaboration, "CMS: letter of intent by the CMS Collaboration for a general purpose detector at LHC," CERN, Geneva, Tech. Rep., 1992, Open presentation to the LHCC 5 November 1992, M. Della Negra/CERN, CMS Spokesman. [Online]. Available: https://cds.cern.ch/record/290808.

[39] Benaglia, A. for the CMS Collaboration, "The CMS ECAL performance with examples," *JINST*, vol. 9, p. C02008, 2014. DOI: 10.1088/1748-0221/9/02/C02008.

[40] LHC Higgs Cross Section Working Group, "Handbook of LHC Higgs Cross Sections: 4. Deciphering the Nature of the Higgs Sector," CERN Yellow Reports: Monographs, Oct. 2016. DOI: 10.23731/CYRM-2017-002. [Online]. Available: https://cds.cern.ch/record/2227475.

[41] Magnan, A. M. for the CMS Collaboration, "HGCAL: a High-Granularity Calorimeter for the endcaps of CMS at HL-LHC," *JINST*, vol. 12, no. 01, p. C01042, 2017. DOI: 10.1088/1748-0221/12/01/C01042.

[42] Bilki, B. for the CMS Collaboration, "CMS Forward Calorimeters Phase II Upgrade," *J. Phys. Conf. Ser.*, vol. 587, no. 1, p. 012 014, 2015. DOI: 10.1088/1742-6596/587/1/012014.

[43] Pitters, F. for the CMS Collaboration, "The CMS High-Granularity Calorimeter for Operation at the High-Luminosity LHC," *Springer Proc. Phys.*, vol. 213, pp. 7–11, 2018. DOI: 10.1007/978-981-13-1316-5_2. arXiv: 1802.05987 [physics.ins-det].

[44] CMS Collaboration, "The Phase-2 Upgrade of the CMS Endcap Calorimeter," CERN, Geneva, Tech. Rep., Nov. 2017. [Online]. Available: http://cds.cern.ch/record/2293646.

[45] M. E. Peskin and D. V. Schroeder, *An Introduction to quantum field theory*. Reading, USA: Addison-Wesley, 1995, ISBN: 978-0-201-50397-5.

[46] W. Heisenberg, J. A. Wheeler, and W. H. Zurek, "Quantum theory and measurement," *Zeitschrift für Physik*, vol. 43, pp. 172–198, 1983.

[47] J. Lagrange, "Mécanique analytique, nouvelle édition," *Courcier, Paris*, 1811.

[48] P. A. M. Dirac, "The quantum theory of the electron," *Proc. Roy. Soc. Lond. A*, vol. 117, pp. 610–624, 1928. DOI: 10.1098/rspa.1928.0023.

[49] J. C. Maxwell, "Viii. a dynamical theory of the electromagnetic field," *Philosophical transactions of the Royal Society of London*, no. 155, pp. 459–512, 1865.

[50] H. Weyl, "Gruppentheorie und quantenmechanik (s. hirzel, leipzig)," *Theory of Groups and Quantum Mechanics, 2nd ed. (1931), transl.H. P. Robertson, Dover, N.Y. (1950), p.100-101*, pp. 87–88, 1928.

[51] H. Weyl, "Gravitation and the electron," *Proceedings of the National Academy of Sciences of the United States of America*, vol. 15, no. 4, p. 323, 1929.

[52] H. Weyl, "Electron and Gravitation. 1. (In German)," *Zeitschrift für Physik*, vol. 56, no. 5-6, pp. 330–352, 1929. DOI: 10.1007/BF01339504.

[53] E. Noether, "Invariant variation problems," *Transport Theory and Statistical Physics*, vol. 1, no. 3, pp. 186–207, Jan. 1918, ISSN: 1532-2424. DOI: 10.1080/00411457108231446.

[54] H. Fritzsch, M. Gell-Mann, and H. Leutwyler, "Advantages of the Color Octet Gluon Picture," *Physics Letters B*, vol. 47, pp. 365–368, 1973. DOI: 10.1016/0370-2693(73)90625-4.

[55] H. Fritzsch, M. Gell-Mann, and P. Minkowski, "Vector-Like Weak Currents and New Elementary Fermions," *Physics Letters B*, vol. 59, pp. 256–260, 1975. DOI: 10.1016/0370-2693(75)90040-4.

[56] D. J. Gross and F. Wilczek, "Ultraviolet behavior of non-abelian gauge theories," *Physical Review Letters*, vol. 30, no. 26, p. 1343, 1973. DOI: 10.1103/PhysRevLett.30.1343.

[57] H. D. Politzer, "Reliable perturbative results for strong interactions?" *Physical Review Letters*, vol. 30, no. 26, pp. 1346–1349, 1973. DOI: 10.1103/PhysRevLett.30.1346.

[58] R. P. Feynman, "The behavior of hadron collisions at extreme energies," in *Special Relativity and Quantum Theory*, Springer, 1988, pp. 289–304. DOI: 10.1007/978-94-009-3051-3_25.

[59] J. D. Bjorken and E. A. Paschos, "Inelastic electron-proton and γ-proton scattering and the structure of the nucleon," *Physical Review*, vol. 185, no. 5, p. 1975, 1969. DOI: 10.1103/PhysRev.185.1975.

[60] C. N. Yang and R. L. Mills, "Conservation of isotopic spin and isotopic gauge invariance," *Physical review*, vol. 96, no. 1, p. 191, 1954. DOI: 10.1103/PhysRev.96.191.

[61] W. Pauli Jr, "On the quantum mechanics of magnetic electrons," *Zeit. f. Phys*, vol. 43, pp. 601–623, 1927.

[62] C.-S. Wu, E. Ambler, R. W. Hayward, D. D. Hoppes, and R. P. Hudson, "Experimental test of parity conservation in beta decay," *Physical review*, vol. 105, no. 4, p. 1413, 1957. DOI: 10.1103/PhysRev.105.1413.

[63] R. P. Feynman and M. Gell-Mann, "Theory of the fermi interaction," *Phys. Rev.*, vol. 109, pp. 193–198, 1 1958. DOI: 10.1103/PhysRev.109.193.

[64] E. C. G. Sudarshan and R. e. Marshak, "Chirality invariance and the universal Fermi interaction," *Phys. Rev.*, vol. 109, pp. 1860–1860, 1958. DOI: 10.1103/PhysRev.109.1860.2.

[65] Y. Nambu, "Quasi-particles and gauge invariance in the theory of superconductivity," *Physical Review*, vol. 117, no. 3, p. 648, 1960.

[66] J. Goldstone, "Field theories with «superconductor» solutions," *Il Nuovo Cimento*, vol. 19, no. 1, pp. 154–164, 1961. DOI: 10.1007/BF02812722.

[67] J. Goldstone, A. Salam, and S. Weinberg, "Broken symmetries," *Physical Review*, vol. 127, no. 3, p. 965, 1962. DOI: 10.1103/PhysRev.127.965.

[68] LHC Higgs Cross Section Working Group, "Handbook of LHC Higgs Cross Sections: 1. Inclusive Observables," CERN Yellow Reports: Monographs, 2011. DOI: 10.5170/CERN-2011-002. [Online]. Available: http://cds.cern.ch/record/1318996.

[69] LHC Higgs Cross Section Working Group, "Handbook of LHC Higgs Cross Sections: 2. Differential Distributions," CERN Yellow Reports: Monographs, 2012. DOI: 10.5170/CERN-2012-002. [Online]. Available: https://cds.cern.ch/record/1416519.

[70] LHC Higgs Cross Section Working Group, "Handbook of LHC Higgs Cross Sections: 3. Higgs Properties: Report of the LHC Higgs Cross Section Working Group," CERN Yellow Reports: Monographs, Jul. 2013. DOI: 10.5170/CERN-2013-004. [Online]. Available: https://cds.cern.ch/record/1559921.

[71] ATLAS Collaboration, "ATLAS Letter of Intent for a General-Purpose pp experiment at the Large Hadron Collider at CERN," CERN/LHCC/92-4, Tech. Rep., 1992.

[72] ATLAS Collaboration, "ATLAS: Technical proposal for a general-purpose $p\bar{p}$ experiment at the Large Hadron Collider at CERN," Dec. 1994.

[73] ATLAS Collaboration, "The ATLAS Experiment at the CERN Large Hadron Collider," *JINST*, vol. 3, S08003, 2008. DOI: 10.1088/1748-0221/3/08/S08003.

[74] B. Hespel, F. Maltoni, and E. Vryonidou, "Higgs and Z boson associated production via gluon fusion in the SM and the 2HDM," *JHEP*, vol. 06, p. 065, 2015. DOI: 10.1007/JHEP06(2015)065.

[75] CMS Collaboration, "Precise determination of the mass of the higgs boson and tests of compatibility of its couplings with the standard model predictions using proton collisions at 7 and 8 tev," *Eur. Phys. J. C*, vol. 75, p. 212, 2015. DOI: 10.1140/epjc/s10052-015-3351-7.

[76] ATLAS and CMS Collaborations, "Measurements of the Higgs boson production and decay rates and constraints on its couplings from a combined ATLAS and CMS analysis of the LHC pp collision data at $\sqrt{s} = 7$ and 8 TeV," *JHEP*, vol. 08, p. 045, 2016. DOI: 10.1007/JHEP08(2016)045. arXiv: 1606.02266 [hep-ex].

[77] F. Maltoni, K. Paul, T. Stelzer, and S. Willenbrock, "Associated production of Higgs and single top at hadron colliders," *Phys. Rev. D*, vol. 64, p. 094 023, 2001. DOI: 10.1103/PhysRevD.64.094023.

[78] M. Farina, C. Grojean, F. Maltoni, E. Salvioni, and A. Thamm, "Lifting degeneracies in Higgs couplings using single top production in association with a Higgs boson," *JHEP*, vol. 05, p. 022, 2013. DOI: 10.1007/JHEP05(2013)022.

[79] P. Agrawal, S. Mitra, and A. Shivaji, "Effect of Anomalous Couplings on the Associated Production of a Single Top Quark and a Higgs Boson at the LHC," *JHEP*, vol. 12, p. 077, 2013. DOI: 10.1007/JHEP12(2013)077.

[80] F. Demartin, F. Maltoni, K. Mawatari, and M. Zaro, *Higgs production in association with a single top quark at the LHC*, 2015. arXiv: 1504.00611 [hep-ph].

[81] CMS Collaboration, "Search for associated production of a higgs boson and a single top quark in proton-proton collisions at $\sqrt{s}$= 13 tev," *Physical Review D*, vol. 99, no. 9, 2019. DOI: 10.1103/physrevd.99.092005.

[82] A. Djouadi, M. Spira, and P. M. Zerwas, "Two-photon decay widths of Higgs particles," *Physics Letters B*, vol. 311, no. 1-4, pp. 255–260, 1993. DOI: 10.1016/0370-2693(93)90564.

[83] J. Ellis, M. K. Gaillard, and D. V. Nanopoulos, "A phenomenological profile of the Higgs boson," in *Current Physics–Sources and Comments*, vol. 8, Elsevier, 1991, pp. 24–72. DOI: 10.1016/B978-0-444-88807-5.50066-2.

[84] L. D. Landau, "On the angular momentum of a system of two photons," *Dokl. Akad. Nauk SSSR*, vol. 60, p. 207, 1948. [Online]. Available: http://cds.cern.ch/record/436783.

[85] C.-N. Yang, "Selection rules for the dematerialisation of a particle into two photons," *Physical Review*, vol. 77, no. 2, p. 242, 1950.

[86] S. Bhattacharya and S. Jain, "A review of the discovery of SM-like Higgs boson in $H \to \gamma\gamma$ decay channel with the CMS detector at the LHC," *Pramana*, vol. 87, no. 3, pp. 1–30, 2016. DOI: 10.1007/s12043-016-1245-3.

[87] G. Aad *et al.*, "Measurements of Higgs boson production and couplings in diboson final states with the ATLAS detector at the LHC," *Physics Letters B*, vol. 726, pp. 88–119, 2013. DOI: 10.1016/j.physletb.2014.05.011. arXiv: 1307.1427 [hep-ex].

[88] CMS Collaboration, "Precise determination of the mass of the Higgs boson and tests of compatibility of its couplings with the standard model predictions using proton collisions at 7 and 8 TeV," *Eur. Phys. J. C*, vol. 75, no. 5, p. 212, 2015. DOI: 10.1140/epjc/s10052-015-3351-7. arXiv: 1412.8662 [hep-ex].

[89] ATLAS Collaboration, "Observation of Higgs boson production in association with a top quark pair at the LHC with the ATLAS detector," *Phys. Lett. B*, vol. 784, 173–191. 19 p, Jun. 2018. DOI: 10.1016/j.physletb.2018.07.035.

[90] CMS collaboration, "Observation of ttH production," *Phys. Rev. Lett.*, vol. 120, no. 23, p. 231 801, 2018. DOI: 10.1103/PhysRevLett.120.231801. arXiv: 1804.02610.

[91] ATLAS Collaboration, "Observation of $H \to b\bar{b}$ decays and VH production with the ATLAS detector," *Phys. Lett. B*, vol. 786, pp. 59–86, 2018. DOI: 10.1016/j.physletb.2018.09.013. arXiv: 1808.08238 [hep-ex].

[92] CMS Collaboration, "Observation of Higgs boson decay to bottom quarks," *Phys. Rev. Lett.*, vol. 121, no. 12, p. 121 801, 2018. DOI: 10.1103/PhysRevLett.121.121801. arXiv: 1808.08242 [hep-ex].

[93] ATLAS Collaboration, "Cross-section measurements of the Higgs boson decaying into a pair of τ-leptons in proton-proton collisions at $\sqrt{s} = 13$ TeV with the ATLAS detector," *Physical Review D*, vol. 99, no. 7, 2019. DOI: 10.1103/physrevd.99.072001.

[94] CMS Collaboration, "Observation of the Higgs boson decay to a pair of τ leptons with the CMS detector," *Phys. Lett. B*, vol. 779, pp. 283–316, 2018. DOI: 10.1016/j.physletb.2018.02.004. arXiv: 1708.00373 [hep-ex].

[95] ATLAS and CMS Collaborations, "Combined measurement of the Higgs Boson mass in pp Collisions at $\sqrt{s} = 7$ and 8 TeV with the ATLAS and CMS experiments," *Physical Review Letters*, vol. 114, p. 191 803, 2015. DOI: 10.1103/PhysRevLett.114.191803.

[96] CMS Collaboration, "A measurement of the Higgs boson mass in the diphoton decay channel," *Phys. Lett. B*, vol. 805, p. 135 425, 2020. DOI: 10.1016/j.physletb.2020.135425. arXiv: 2002.06398 [hep-ex].

[97] CMS Collaboration, "Measurements of the Higgs boson width and anomalous HVV couplings from on-shell and off-shell production in the four-lepton final state," *Phys. Rev. D*, vol. 99, no. 11, p. 112 003, 2019. DOI: 10.1103/PhysRevD.99.112003. arXiv: 1901.00174 [hep-ex].

[98] E. Fermi, "Sulla quantizzazione del gas perfetto monoatomico," *Rendiconti Lincei*, vol. 145, 1926.

[99] S. N. Bose, "Plancks gesetz und lichtquantenhypothese," *Z. Physik*, vol. 36, pp. 178–181, 1924. DOI: 10.1007/BF01327326.

[100] CMS Collaboration, "Study of the Mass and Spin-Parity of the Higgs Boson Candidate Via Its Decays to Z Boson Pairs," *Phys. Rev. Lett.*, vol. 110, no. 8, p. 081 803, 2013. DOI: 10.1103/PhysRevLett.110.081803. arXiv: 1212.6639 [hep-ex].

[101] ATLAS Collaboration, "Evidence for the spin-0 nature of the Higgs boson using ATLAS data," *Physics Letters B*, vol. 726, pp. 120–144, 2013. DOI: 10.1016/j.physletb.2013.08.026.

[102] CMS Collaboration, "Measurement of the Properties of a Higgs Boson in the Four-Lepton Final State," *Phys. Rev. D*, vol. 89, no. 9, p. 092 007, 2014. DOI: 10.1103/PhysRevD.89.092007. arXiv: 1312.5353 [hep-ex].

[103] ATLAS Collaboration, "Combined measurements of Higgs boson production and decay using up to 80 fb^{-1} of proton–proton collision data at $\sqrt{s} = 13$ TeV collected with the ATLAS experiment," CERN, Tech. Rep., 2019. [Online]. Available: https://cds.cern.ch/record/2668375.

[104] CMS Collaboration, "Combined measurements of Higgs boson couplings in proton-proton collisions at $\sqrt{s} = 13$ TeV," *Eur. Phys. J. C*, vol. 79, 421. 67 p, 2018. DOI: 10.1140/epjc/s10052-019-6909-y.

[105] CMS Collaboration, "Measurements of Higgs boson properties in the diphoton decay channel in proton-proton collisions at $\sqrt{s} = 13$ TeV," *JHEP*, vol. 11, p. 185, 2018. DOI: 10.1007/JHEP11(2018)185. arXiv: 1804.02716 [hep-ex].

[106] ATLAS Collaboration, "Measurement of the properties of Higgs boson production at $\sqrt{s}$=13 TeV in the $H \to \gamma\gamma$ channel using 139 fb^1 of pp collision data with the ATLAS experiment," CERN, Tech. Rep., Aug. 2020. [Online]. Available: https://cds.cern.ch/record/2725727.

[107] ATLAS Collaboration, "Higgs boson production cross-section measurements and their EFT interpretation in the 4ℓ decay channel at $\sqrt{s}$ =13 TeV with the ATLAS detector," *Eur. Phys. J. C*, vol. 80, no. 10, p. 957, 2020. DOI: 10.1140/epjc/s10052-020-8227-9.

[108] CMS Collaboration, "Measurements of production cross sections of the Higgs boson in the four-lepton final state in proton–proton collisions at $\sqrt{s} = 13\,\text{TeV}$," *Eur. Phys. J. C*, vol. 81, no. 6, p. 488, 2021. DOI: 10.1140/epjc/s10052-021-09200-x. arXiv: 2103.04956 [hep-ex].

[109] ATLAS Collaboration, "Measurements of gluon fusion and vector-boson-fusion production of the Higgs boson in $H \to WW^* \to e\nu\mu\nu$ decays using pp collisions at $\sqrt{s} = 13$ TeV with the ATLAS detector," CERN, Tech. Rep., Mar. 2021. [Online]. Available: https://cds.cern.ch/record/2759651.

[110] CMS Collaboration, "Measurement of Higgs boson production in the decay channel with a pair of τ leptons," CERN, Tech. Rep., 2020. [Online]. Available: https://cds.cern.ch/record/2725590.

[111] ATLAS Collaboration, "Measurements of WH and ZH production in the $H \to b\bar{b}$ decay channel in pp collisions at 13 TeV with the ATLAS detector," *Eur. Phys. J. C*, vol. 81, no. 2, p. 178, 2021. DOI: 10.1140/epjc/s10052-020-08677-2. arXiv: 2007.02873 [hep-ex].

[112] A. Djouadi, O. Lebedev, Y. Mambrini, and J. Quevillon, "Implications of LHC searches for Higgs-portal dark matter," *Physics Letters B*, vol. 709, no. 1, pp. 65–69, 2012. DOI: https://doi.org/10.1016/j.physletb.2012.01.062.

[113] L. Roszkowski, E. M. Sessolo, and S. Trojanowski, "WIMP dark matter candidates and searches—current status and future prospects," *Reports on Progress in Physics*, vol. 81, no. 6, p. 066 201, May 2018. DOI: 10.1088/1361-6633/aab913.

[114] F. Iachello, "Dynamical supersymmetries in nuclei," *Physical Review Letters*, vol. 44, no. 12, pp. 772–775, 1980. DOI: 10.1103/PhysRevLett.44.772.

[115] ATLAS Collaboration, "Coupling properties of the new Higgs-like boson observed with the ATLAS detector at the LHC," CERN, Geneva, Tech. Rep., Sep. 2012. [Online]. Available: https://cds.cern.ch/record/1476765.

[116] J.Sanabria for the ATLAS and CMS Collaborations, "Higgs results from atlas and cms," *Nuclear and Particle Physics Proceedings*, vol. 267, pp. 25–34, 2015. DOI: 10.1016/j.nuclphysbps.2015.10.078.

[117] S. Myers and E. Picasso, "The LEP collider," *Scientific American*, vol. 263N1, pp. 54–61, 1990. DOI: 10.1038/scientificamerican0790-54.

[118] S. Weinberg, "Gravitation and cosmology," 1972.

[119] H. Georgi and S. L. Glashow, "Unity of All Elementary Particle Forces," *Phys. Rev. Lett.*, vol. 32, pp. 438–441, 1974. DOI: 10.1103/PhysRevLett.32.438.

[120] J. C. Pati and A. Salam, "Unified lepton-hadron symmetry and a gauge theory of the basic interactions," *Physical Review D*, vol. 8, no. 4, p. 1240, 1973. DOI: 10.1103/PhysRevD.8.1240.

[121] J. C. Pati and A. Salam, "Lepton Number as the Fourth Color," in, vol. 10, 1974, pp. 275–289. DOI: 10.1103/PhysRevD.10.275.

[122] A. J. Buras, J. R. Ellis, M. K. Gaillard, and D. V. Nanopoulos, "Aspects of the Grand Unification of Strong, Weak and Electromagnetic Interactions," *Nucl. Phys. B*, vol. 135, pp. 66–92, 1978. DOI: 10.1016/0550-3213(78)90214-6.

[123] C. Lefévre, "The CERN accelerator complex," Tech. Rep., 2008. [Online]. Available: https://cds.cern.ch/record/1260465.

[124] LHCb Collaboration, "The LHCb Detector at the LHC," *JINST*, vol. 3, S08005, 2008. DOI: 10.1088/1748-0221/3/08/S08005.

[125] ALICE Collaboration, "The ALICE experiment at the CERN LHC," *JINST*, vol. 3, S08002, 2008. DOI: 10.1088/1748-0221/3/08/S08002.

[126] *Cern*, Oct. 2013. [Online]. Available: http://www.lhc-closer.es/taking_a_closer_look_at_lhc/0.lhc_layout.

[127] *Cern*, Oct. 2013. [Online]. Available: http://cds.cern.ch/images/OPEN-PHO-ACCEL-2013-056-1.

[128] *Europhysics Conf. on High-Energy Physics (EPS-HEP-2011)*, vol. 031, Grenoble, Rhone-Alpes, France (SISSA, 2012), 2011. [Online]. Available: https://cds.cern.ch/record/1233501.

[129] A. Nisati for the ATLAS Collaboration, "Proc. of lepton–photon 2011," *PRAMANA79*, vol. 541, 2012.

[130] ATLAS Collaboration, "Search for the Standard Model Higgs boson in the diphoton decay channel with 4.9 fb^{-1} of pp collisions at $\sqrt{s} = 7$ TeV with ATLAS," *Physics Review Letters*, vol. 108, p. 111 803, 2012. DOI: 10.1103/PhysRevLett.108.111803.

[131] CMS Collaboration, "Search for the Standard Model Higgs boson decaying into two photons in pp collisions at $\sqrt{s} = 7$ TeV," *Phys. Lett. B*, vol. 710, pp. 403–425, 2012. DOI: 10.1016/j.physletb.2012.03.003.

[132] ATLAS Collaboration, "Search for the Standard Model Higgs boson in the decay channel $H \to ZZ^{(*)} \to 4\ell$ with 4.8 fb^{-1} of pp collision data at $\sqrt{s} = 7$ TeV with ATLAS," *Phys. Lett. B*, vol. 710, pp. 383–402, 2012. DOI: 10.1016/j.physletb.2012.03.005.

[133] CMS Collaboration, "Search for the standard model higgs boson in the decay channel $h \to zz \to 4l$ in pp collisions at $\sqrt{s}$= 7 TeV," *Phys. Rev. Lett.*, vol. 108, p. 111 804, 11 2012. DOI: 10.1103/PhysRevLett.108.111804.

[134] ATLAS Collaboration, "Combined search for the Standard Model Higgs boson using up to 4.9 fb^{-1} of pp collision data at $\sqrt{s} = 7$ TeV with the ATLAS detector at the LHC," *Phys. Lett. B*, vol. 710, pp. 49–66, 2012. DOI: 10.1016/j.physletb.2012.02.044.

[135] CMS Collaboration, "Combined results of searches for the Standard Model Higgs boson in pp collisions at $\sqrt{s} = 7$ TeV," *Phys. Lett. B*, vol. 710, pp. 26–48, 2012. DOI: 10.1016/j.physletb.2012.02.064.

[136] F. del Aguila *et al.*, "Collider aspects of flavour physics at high Q," *Eur. Phys. J. C*, vol. 57, pp. 183–308, 2008. DOI: 10.1140/epjc/s10052-008-0713-4.

[137] CMS collaboration, "Description and performance of track and primary-vertex reconstruction with the CMS tracker," *Journal of Instrumentation*, vol. 9, no. 10, P10009, 2014. DOI: 10.1088/1748-0221/9/10/P10009.

[138] CMS Collaboration, "CMS Technical Design Report for the Pixel Detector Upgrade," Tech. Rep., Sep. 2012. [Online]. Available: http://cds.cern.ch/record/1481838.

[139] CMS Collaboration, *The CMS hadron calorimeter project: Technical Design Report*, ser. Technical design report. CMS. Geneva: CERN, 1997. [Online]. Available: https://cds.cern.ch/record/357153.

[140] CMS Collaboration, "Performance of the CMS muon detector and muon reconstruction with proton-proton collisions at $\sqrt{s} = 13$ TeV," *JINST*, vol. 13, no. 06, P06015, 2018. DOI: 10.1088/1748-0221/13/06/P06015.

[141] CMS Collaboration, "The CMS trigger system," *JINST*, vol. 12, no. 01, P01020, 2017. DOI: 10.1088/1748-0221/12/01/P01020.

[142] I. Bird *et al.*, "Update of the Computing Models of the WLCG and the LHC Experiments," Tech. Rep., Apr. 2014. [Online]. Available: https://cds.cern.ch/record/1695401.

[143] D. Contardo, M. Klute, J. Mans, L. Silvestris, and J. Butler, "Technical Proposal for the Phase-II Upgrade of the CMS Detector," Jun. 2015. [Online]. Available: https://cds.cern.ch/record/2020886.

[144] J. Butler, D. Contardo, M. Klute, J. Mans, L. Silvestris, and on behalf of the CMS Collaboration, "CMS Phase II Upgrade Scope Document," Sep. 2015. [Online]. Available: https://cds.cern.ch/record/2055167.

[145] A. Apresyan, "Investigation of fast timing capabilities of silicon sensors for the CMS high granularity calorimeter at HL-LHC," in *2016 IEEE Nuclear Science Symposium and Medical Imaging Conference*, Oct. 2016. DOI: 10.1109/NSSMIC.2016.8069873.

[146] CMS Collaboration, "Electronics and Triggering Challenges for the CMS High Granularity Calorimeter for HL-LHC," Z.-A. Liu, Ed., vol. 212, 2018, pp. 149–153. DOI: 10.1007/978-981-13-1313-4_30.

[147] CMS Collaboration, "Challenges of front-end and triggering electronics for High Granularity Calorimetry," *PoS*, vol. EPS-HEP2017, p. 514, 2017. DOI: 10.22323/1.314.0514.

[148] CMS Collaboration, "Challenges of particle flow reconstruction in the CMS High-Granularity Calorimeter at the High-Luminosity LHC," 1, vol. 928, 2017, p. 012 027. DOI: 10.1088/1742-6596/928/1/012027.

[149] D. Krohn, M. D. Schwartz, M. Low, and L.-T. Wang, "Jet cleansing: Separating data from secondary collision induced radiation at high luminosity," *Physical Review D*, vol. 90, no. 6, p. 065 020, 2014. DOI: 10.1103/physrevd.90.065020.

[150] A. Tapper and D. Acosta, "CMS Technical Design Report for the Level-1 Trigger Upgrade," Tech. Rep., Jun. 2013. [Online]. Available: https://cds.cern.ch/record/1556311.

[151] CALICE Collaboration, "Construction and commissioning of the CALICE analog hadron calorimeter prototype," *Journal of Instrumentation*, vol. 5, no. 05, P05004, 2010. DOI: 10.1088/1748-0221/5/05/P05004.

[152] CMS Collaboration, "A novel reconstruction framework for an imaging calorimeter for HL-LHC," *Presented at the Connecting the Dots Workshop 2020 (CTD2020), Zenodo*, 2020. [Online]. Available: https://doi.org/10.5281/zenodo.4088464.

[153] CMS Collaboration, "Particle-flow reconstruction and global event description with the CMS detector," *JINST*, vol. 12, P10003, 2017. DOI: 10.1088/1748-0221/12/10/P10003. arXiv: 1706.04965 [physics.ins-det].

[154] R. Wigmans, *Calorimetry: Energy measurement in particle physics*. 2000, vol. 107. DOI: 10.1093/oso/9780198786351.001.0001.

[155] CMS Collaboration, "Performance of Electron Reconstruction and Selection with the CMS Detector in Proton-Proton Collisions at $\sqrt{s} = 8\,\text{TeV}$," *JINST*, vol. 10, no. 06, P06005, 2015. DOI: 10.1088/1748-0221/10/06/P06005.

[156] N. Adam, J. Berryhill, V. Halyo, A. Hunt, and K. Mishra, "Generic tag and probe tool for measuring efficiency at cms with early data," *CMS Analysis Note*, vol. CMS AN 2009/111, 2009.

[157] J. Alwall, R. Frederix, S. Frixione, V. Hirschi, F. Maltoni, O. Mattelaer, H.-S. Shao, T. Stelzer, P. Torrielli, and M. Zaro, "The automated computation of tree-level and next-to-leading order differential cross sections, and their matching to parton shower simulations," *Journal of High Energy Physics*, vol. 2014, no. 7, Jul. 2014. DOI: 10.1007/jhep07(2014)079.

[158] C. Oleari, "The POWHEG BOX," *Nuclear Physics B - Proceedings Supplements*, vol. 205-206, pp. 36–41, Aug. 2010. DOI: 10.1016/j.nuclphysbps.2010.08.016.

[159] T. Sjostrand, S. Mrenna, and P. Z. Skands, "A Brief Introduction to PYTHIA 8.1," *Comput. Phys. Commun.*, vol. 178, pp. 852–867, 2008. DOI: 10.1016/j.cpc.2008.01.036. arXiv: 0710.3820 [hep-ph].

[160] T. Gleisberg, S. Höche, F. Krauss, M. Schönherr, S. Schumann, F. Siegert, and J. Winter, "Event generation with SHERPA 1.1," *Journal of High Energy Physics*, vol. 2009, no. 02, pp. 007–007, Feb. 2009. DOI: 10.1088/1126-6708/2009/02/007.

[161] S. Agostinelli *et al.*, "GEANT4–a simulation toolkit," *Nucl. Instrum. Meth. A*, vol. 506, pp. 250–303, 2003. DOI: 10.1016/S0168-9002(03)01368-8.

[162] L. Breiman, J. H. Friedman, and R. A. Olshen, "Classification and regression trees," *Wadsworth*, 1984.

[163] T. Chen and C. Guestrin, "XGBoost," *Proceedings of the 22nd ACM SIGKDD International Conference on Knowledge Discovery and Data Mining*, Aug. 2016. DOI: 10.1145/2939672.2939785.

[164] M. B. Hanley JA, "The meaning and use of the area under a receiver operating characteristic (ROC) curve," *Radiology*, vol. 143, no. 1, pp. 29–36, 1982. DOI: 10.1148/radiology.143.1.7063747.

[165] M. CE, "Basic principles of ROC analysis," *Semin Nucl Med*, vol. 8, no. 4, pp. 283–298, 1978. DOI: 10.1016/s0001-2998(78)80014-2.

[166] CMS Collaboration, "Measurements of ttH Production and the CP Structure of the Yukawa Interaction between the Higgs Boson and Top Quark in the Diphoton Decay Channel," *Phys. Rev. Lett.*, vol. 125, no. 6, p. 061 801, 2020. DOI: 10.1103/PhysRevLett.125.061801.

[167] P. D. Dauncey, M. Kenzie, N. Wardle, and G. J. Davies, "Handling uncertainties in background shapes: the discrete profiling method," *JINST*, vol. 10, no. 04, P04015, 2015. DOI: 10.1088/1748-0221/10/04/P04015. arXiv: 1408.6865 [physics.data-an].

[168] J.Butterworth et al., "PDF4LHC recommendations for LHC Run II," *J.Phys*, vol. G43, p. 023 001, 2016. DOI: 10.1088/0954-3899/43/2/023001.

[169] R.Ball et al., "Parton distributions for the LHC Run II," *JHEP*, vol. 04, p. 040, 2015. DOI: 10.1007/JHEP04(2015)040.

[170] S.Carrazza et al., "An Unbiassed Hessian Representation for Monte Carlo PDFs," *Eur.Phys.J*, vol. C75.8, p. 369, 2015. DOI: 10.1140/epjc/s10052-015-3590-7.

[171] "CMS Luminosity Measurements for the 2016 Data Taking Period," CERN, Geneva, Tech. Rep., 2017. [Online]. Available: https://cds.cern.ch/record/2257069.

[172] "CMS luminosity measurement for the 2017 data-taking period at $\sqrt{s} = 13$ TeV," CERN, Geneva, Tech. Rep., 2018. [Online]. Available: https://cds.cern.ch/record/2621960.

[173] "CMS luminosity measurement for the 2018 data-taking period at $\sqrt{s} = 13$ TeV," CERN, Geneva, Tech. Rep., 2019. [Online]. Available: https://cds.cern.ch/record/2676164.

[174] "Jet algorithms performance in 13 TeV data," CERN, Geneva, Tech. Rep., 2017. [Online]. Available: https://cds.cern.ch/record/2256875.

[175] W. Verkerke and D. Kirkby, "The RooFit toolkit for data modeling," *eConf*, vol. C0303241, 2003.

[176] G. Cowan, K. Cranmer, E. Gross, and O. Vitells, "Asymptotic formulae for likelihood-based tests of new physics," *Eur. Phys. J. C*, vol. 71, p. 1554, 2011. DOI: 10.1140/epjc/s10052-011-1554-0. arXiv: 1007.1727 [physics.data-an].

[177] R. A. Fisher, "On the interpretation of χ^2 from contingency tables, and the calculation of p," *J. Royal Stat. Soc.*, vol. 85, p. 87, 1922. DOI: doi:10.2307/2340521.

[178] S. Dawson *et al.*, "Working Group Report: Higgs Boson," in *Community Summer Study 2013: Snowmass on the Mississippi*, Oct. 2013. arXiv: 1310.8361 [hep-ex].

[179] C. Hays, V. Sanz Gonzalez, and G. Zemaityte, "Constraining EFT parameters using simplified template cross sections," Oct. 2017. [Online]. Available: https://cds.cern.ch/record/2290628.

[180] "Updates on Projections of Physics Reach with the Upgraded CMS Detector for High Luminosity LHC," Oct. 2016. [Online]. Available: https://cds.cern.ch/record/2221747.

[181] A. Petrov and W. Shepherd, "Searching for dark matter at LHC with mono-Higgs production," *Physics Letters B*, vol. 730, pp. 178–183, Mar. 2014, ISSN: 0370-2693. DOI: 10.1016/j.physletb.2014.01.051. [Online]. Available: http://dx.doi.org/10.1016/j.physletb.2014.01.051.

[182] A. Djouadi, W. Kilian, M. Muhlleitner, and P. M. Zerwas, "Production of neutral Higgs boson pairs at LHC," *Eur. Phys. J. C*, vol. 10, pp. 45–49, 1999. DOI: 10.1007/s100529900083. arXiv: hep-ph/9904287.

[183] M. J. Dolan, C. Englert, and M. Spannowsky, "Higgs self-coupling measurements at the LHC," *JHEP*, vol. 10, p. 112, 2012. DOI: 10.1007/JHEP10(2012)112. arXiv: 1206.5001 [hep-ph].

[184] G. Branco, P. Ferreira, L. Lavoura, M. Rebelo, M. Sher, and J. P. Silva, "Theory and phenomenology of two-Higgs-doublet models," *Physics Reports*, vol. 516, no. 1-2, pp. 1–102, Jul. 2012. DOI: 10.1016/j.physrep.2012.02.002.

[185] V. Barger, L. L. Everett, H. E. Logan, and G. Shaughnessy, "Scrutinizing the 125 GeV Higgs boson in two Higgs doublet models at the LHC, ILC, and Muon Collider," *Physical Review D*, vol. 88, no. 11, Dec. 2013. DOI: 10.1103/physrevd.88.115003.

[186] K. Peters, "Prospects for beyond Standard Model Higgs boson searches at future LHC runs and other machines," *PoS*, vol. CHARGED2016, p. 028, 2017. DOI: 10.22323/1.286.0028. arXiv: 1701.05124 [hep-ex].

Appendix A

A.1 Photon 2D cluster timing as a function of energy

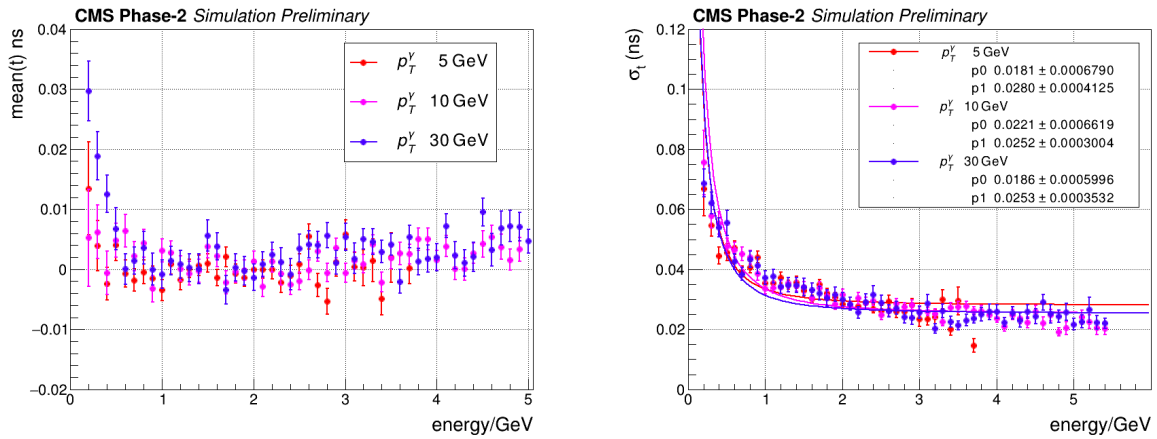

Figure A.1: Distributions of the mean time (left) and the timing resolution of photon 2D clusters within 2 cm of the shower axis, with the time of 2D clusters computed from rechit times with no weighting procedure applied.

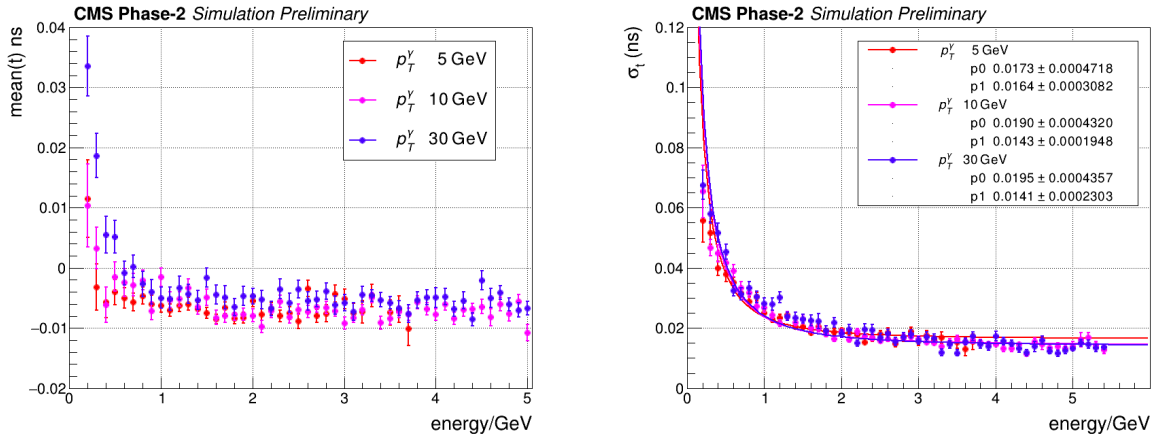

Figure A.2: Distributions of the mean time (left) and the timing resolution of photon 2D clusters within 2 cm of the shower axis, with the time of 2D clusters computed from rechit times with an energy weighting procedure applied.

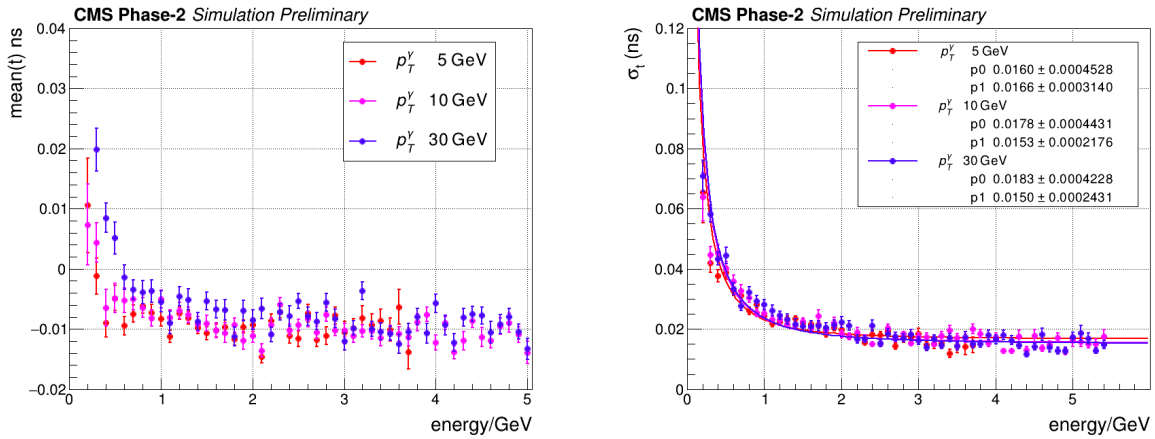

Figure A.3: Distributions of the mean time (left) and the timing resolution of photon 2D clusters within 2 cm of the shower axis, with the time of 2D clusters computed from rechit times with an energy-squared weighting procedure applied.

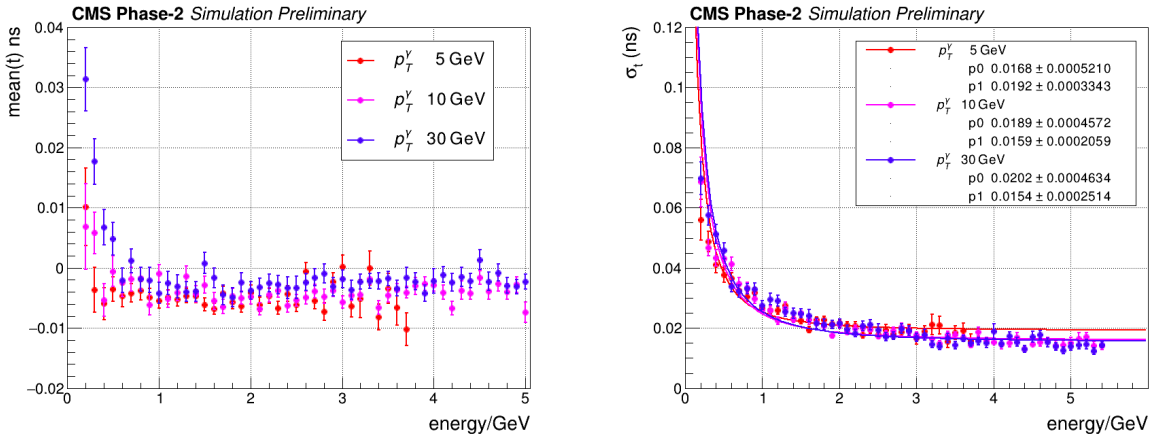

Figure A.4: Distributions of the mean time (left) and the timing resolution of photon 2D clusters within 2 cm of the shower axis, with the time of 2D clusters computed from rechit times with an inverse-resolution weighting procedure applied.

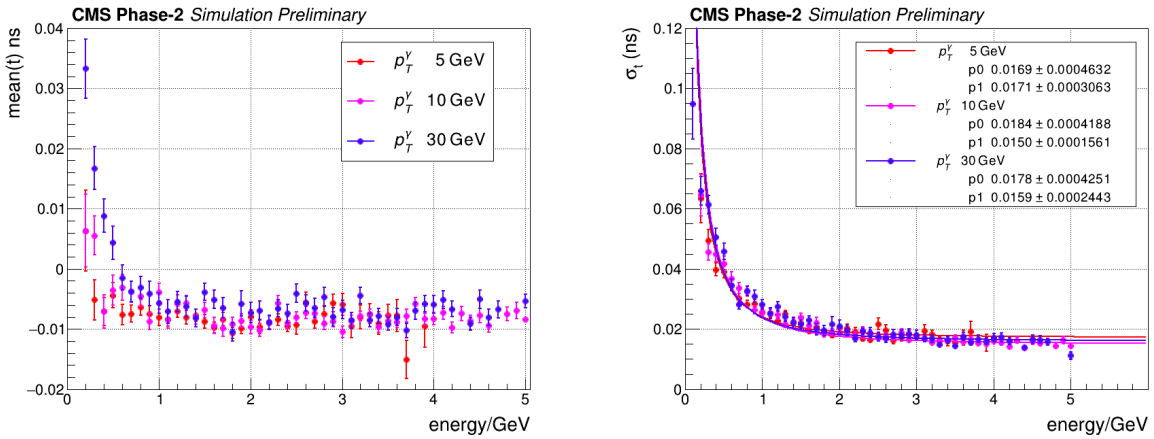

Figure A.5: Distributions of the mean time (left) and the timing resolution of photon 2D clusters within 2 cm of the shower axis, with the time of 2D clusters computed from rechit times with inverse-resolution-squared weighting procedure applied.

A.2 π^+ 2D cluster timing as a function of energy

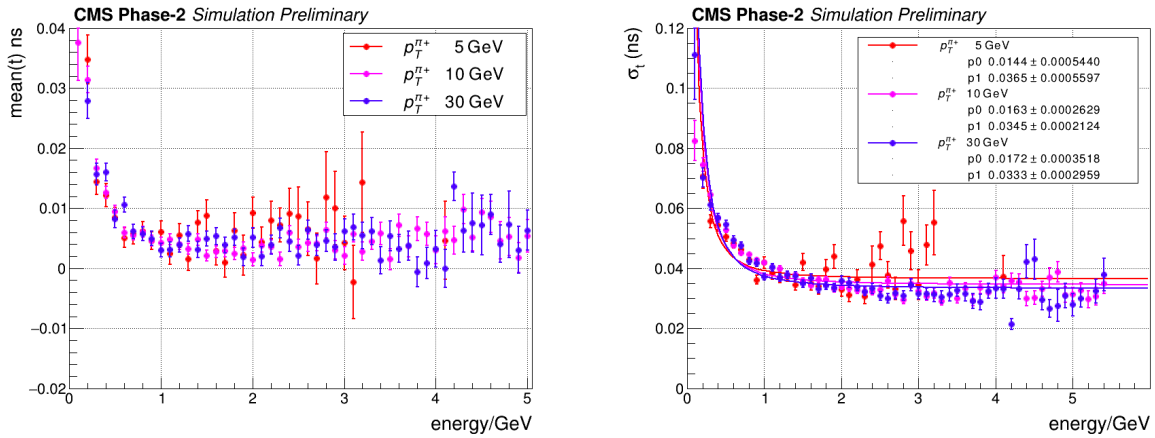

Figure A.6: Distributions of the mean time (left) and the timing resolution of π^+ 2D clusters within 2 cm of the shower axis, with the time of 2D clusters computed from rechit times with no weighting procedure applied.

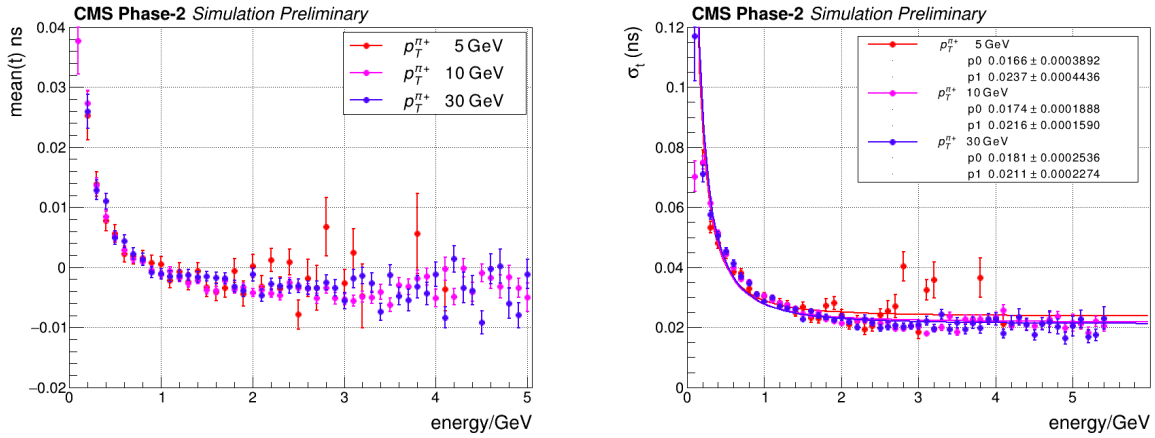

Figure A.7: Distributions of the mean time (left) and the timing resolution of π^+ 2D clusters within 2 cm of the shower axis, with the time of 2D clusters computed from rechit times with an energy weighting procedure applied.

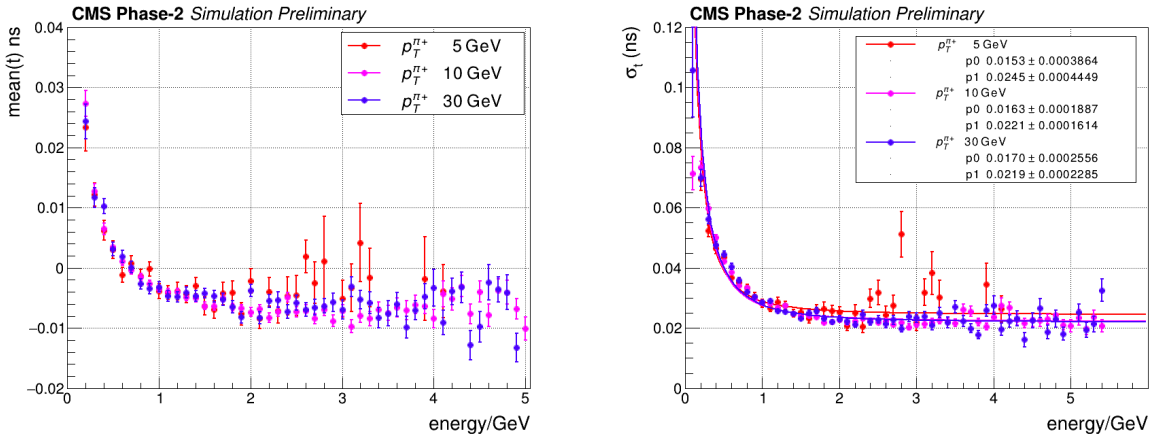

Figure A.8: Distributions of the mean time (left) and the timing resolution of π^+ 2D clusters within 2 cm of the shower axis, with the time of 2D clusters computed from rechit times with an energy-squared weighting procedure applied.

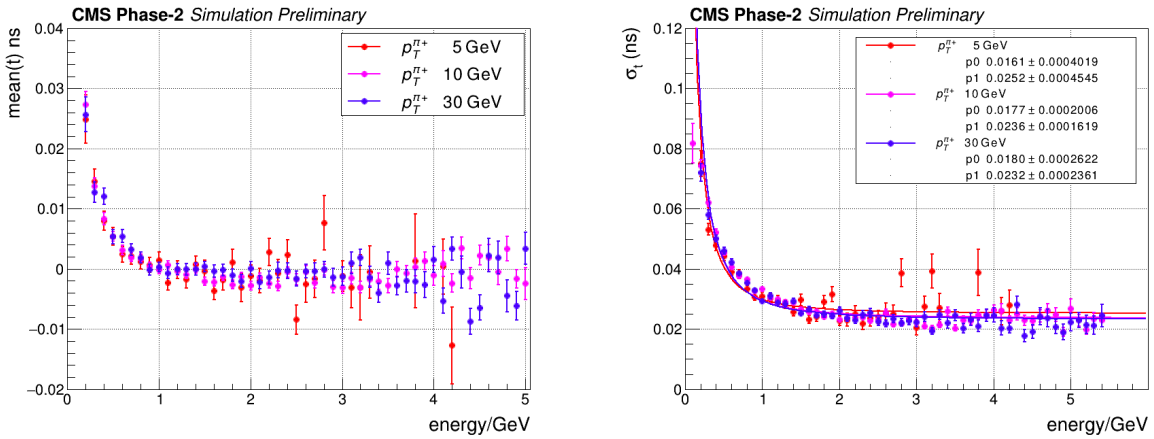

Figure A.9: Distributions of the mean time (left) and the timing resolution of π^+ 2D clusters within 2 cm of the shower axis, with the time of 2D clusters computed from rechit times with an inverse-resolution weighting procedure applied.

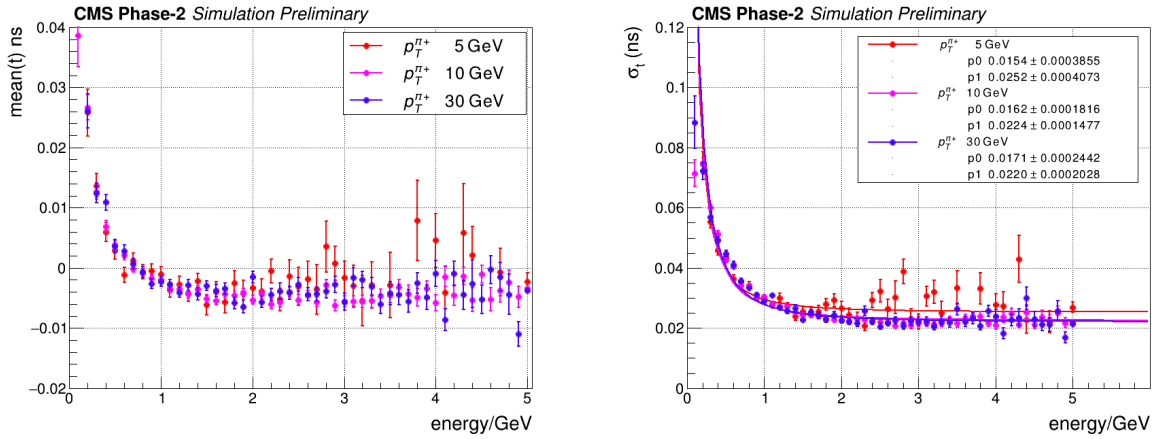

Figure A.10: Distributions of the mean time (left) and the timing resolution of π^+ 2D clusters within 2 cm of the shower axis, with the time of 2D clusters computed from rechit times with inverse-resolution-squared weighting procedure applied.

A.3 photon 2D cluster timing as a function of the HGCAL layer

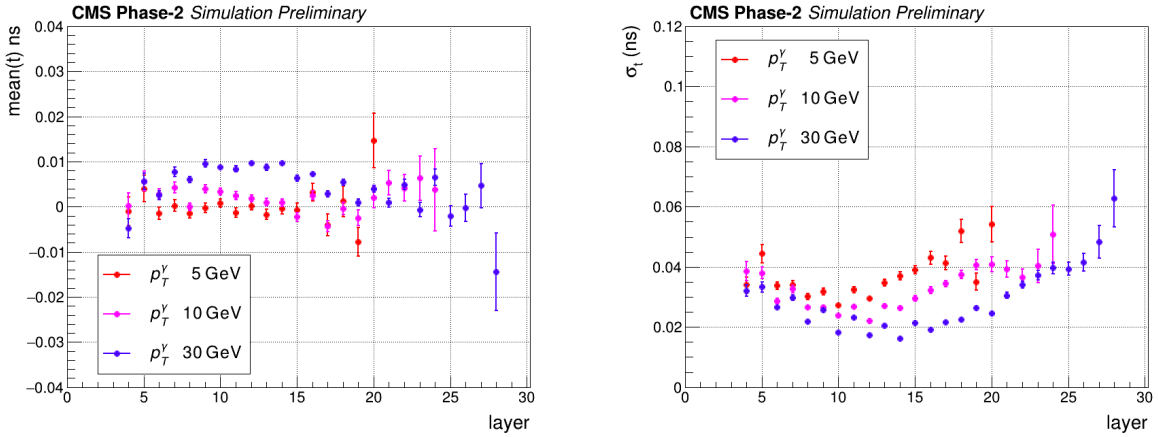

Figure A.11: Distributions of the mean time (left) and the timing resolution of photon 2D clusters within 2 cm of the shower axis, with the time of 2D clusters computed from rechit times with no weighting procedure applied.

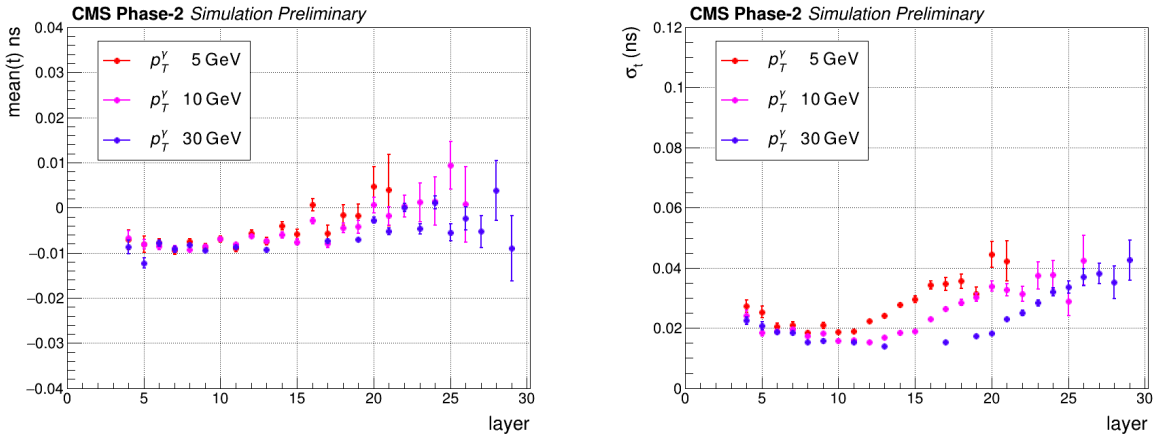

Figure A.12: Distributions of the mean time (left) and the timing resolution of photon 2D clusters within 2 cm of the shower axis, with the time of 2D clusters computed from rechit times with an energy weighting procedure applied.

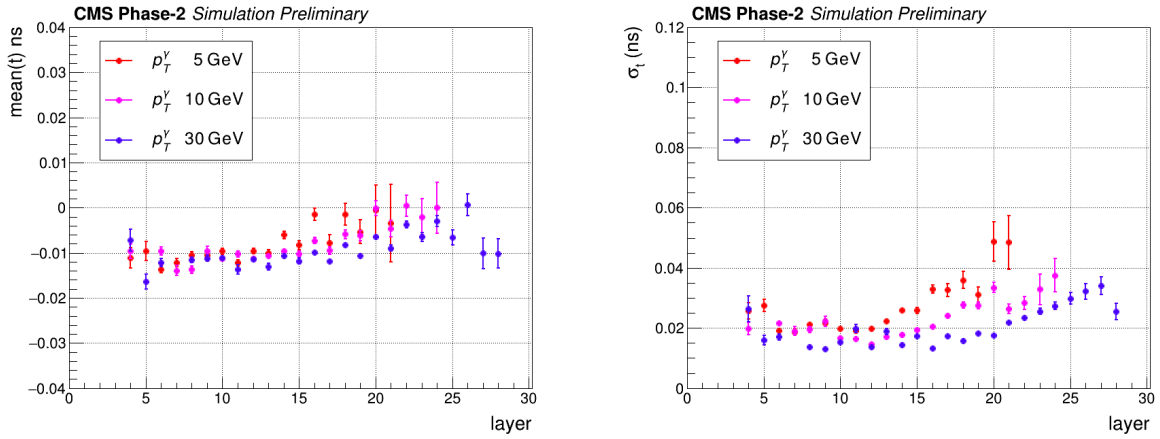

Figure A.13: Distributions of the mean time (left) and the timing resolution of photon 2D clusters within 2 cm of the shower axis, with the time of 2D clusters computed from rechit times with an energy-squared weighting procedure applied.

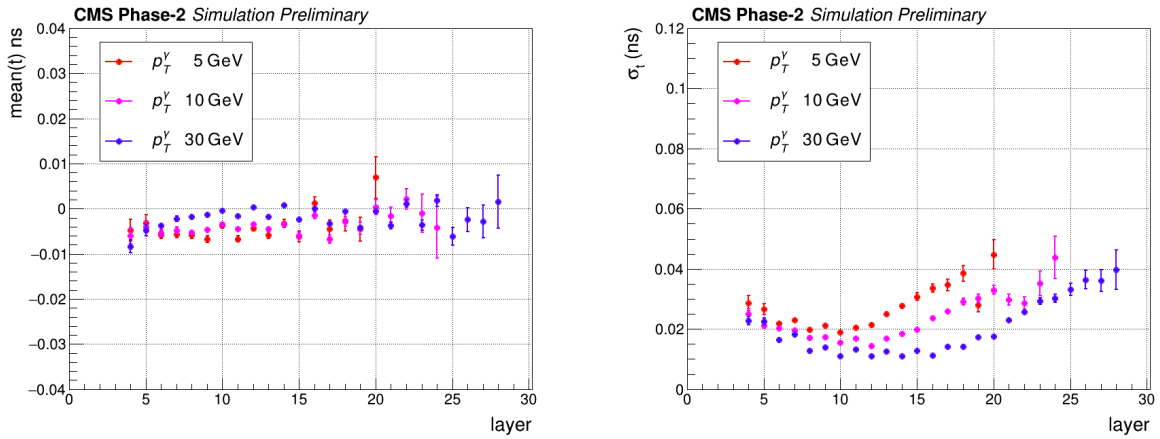

Figure A.14: Distributions of the mean time (left) and the timing resolution of photon 2D clusters within 2 cm of the shower axis, with the time of 2D clusters computed from rechit times with an inverse-resolution weighting procedure applied.

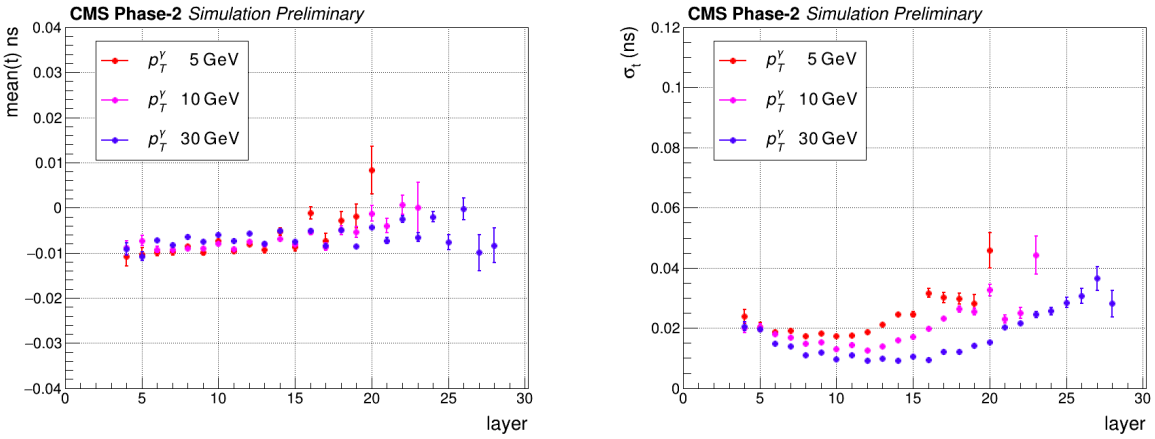

Figure A.15: Distributions of the mean time (left) and the timing resolution of photon 2D clusters within 2 cm of the shower axis, with the time of 2D clusters computed from rechit times with inverse-resolution-squared weighting procedure applied.

A.4 π^+ 2D cluster timing as a function of the HGCAL layer

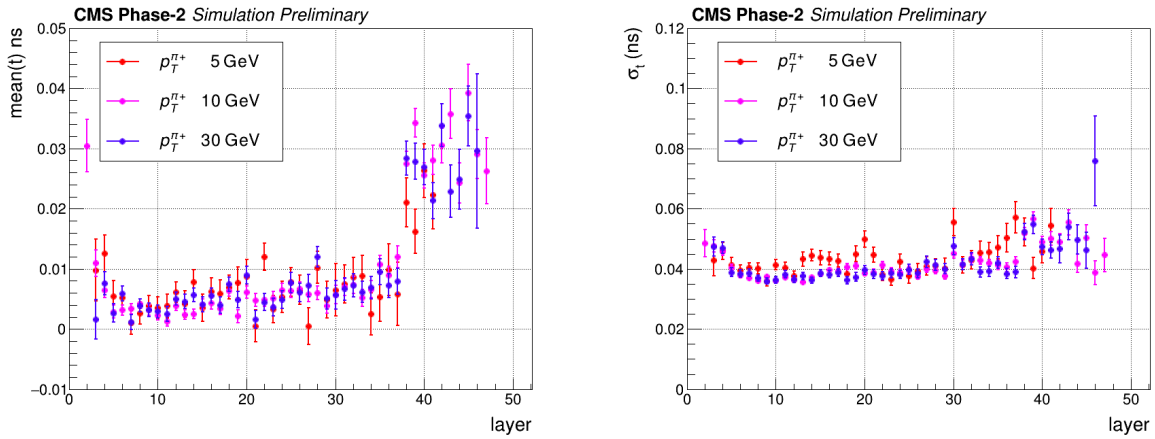

Figure A.16: Distributions of the mean time (left) and the timing resolution of π^+ 2D clusters within 5 cm of the shower axis, with the time of 2D clusters computed from rechit times with no weighting procedure applied.

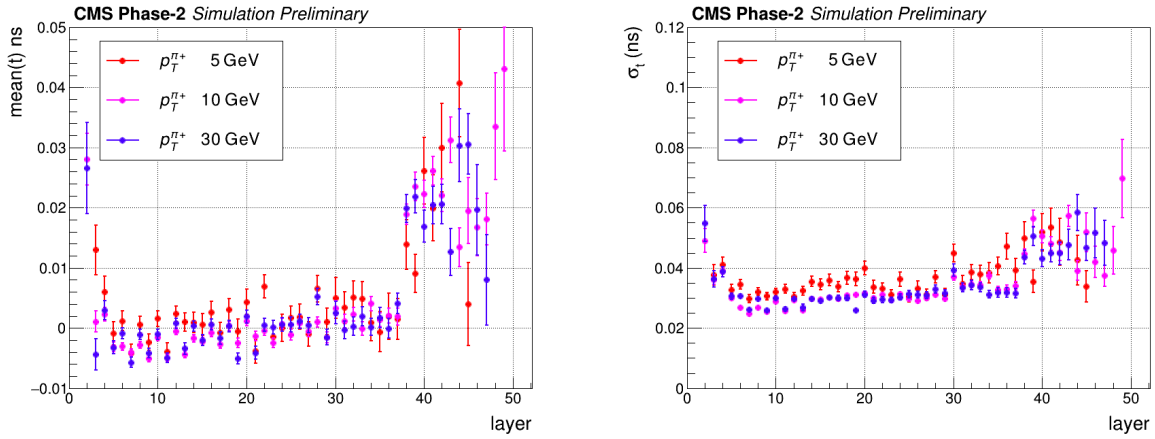

Figure A.17: Distributions of the mean time (left) and the timing resolution of π^+ 2D clusters within 5 cm of the shower axis, with the time of 2D clusters computed from rechit times with an energy weighting procedure applied.

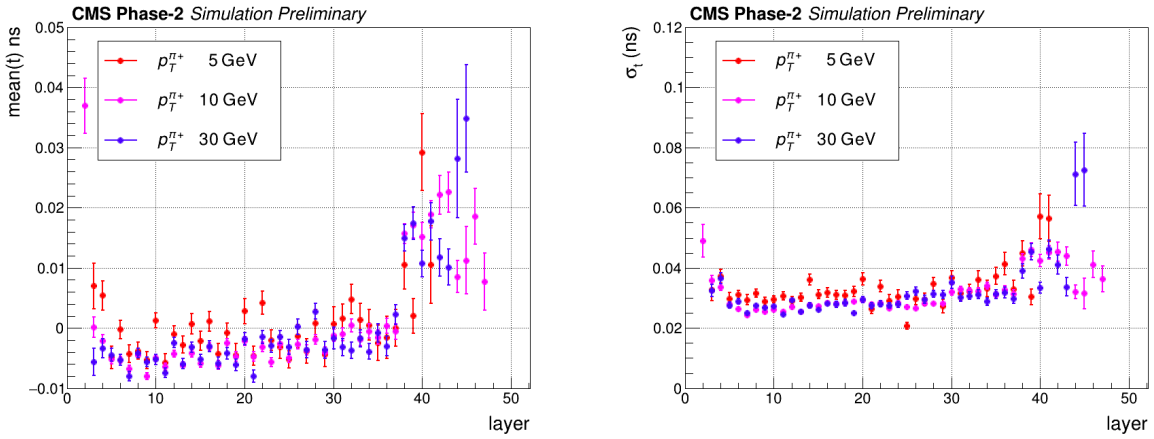

Figure A.18: Distributions of the mean time (left) and the timing resolution of π^+ 2D clusters within 5 cm of the shower axis, with the time of 2D clusters computed from rechit times with an energy-squared weighting procedure applied.

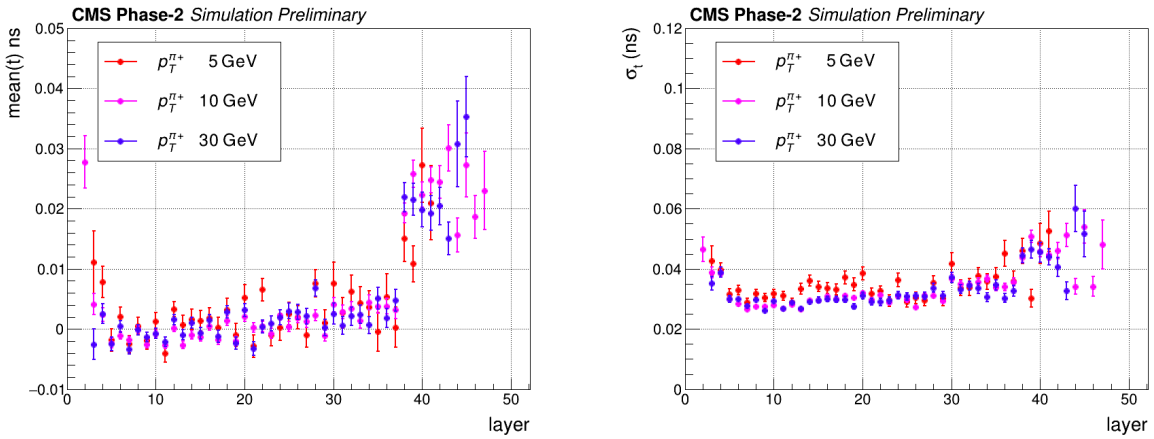

Figure A.19: Distributions of the mean time (left) and the timing resolution of π^+ 2D clusters within 5 cm of the shower axis, with the time of 2D clusters computed from rechit times with an inverse-resolution weighting procedure applied.

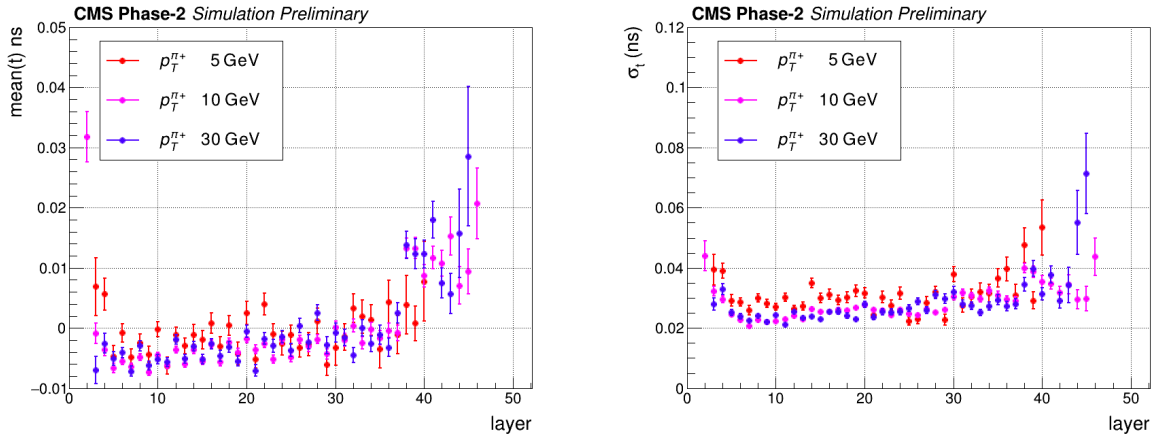

Figure A.20: Distributions of the mean time (left) and the timing resolution of π^+ 2D clusters within 5 cm of the shower axis, with the time of 2D clusters computed from rechit times with inverse-resolution-squared weighting procedure applied.

Appendix B

B.1 VBF fake factors for the years 2016 and 2017

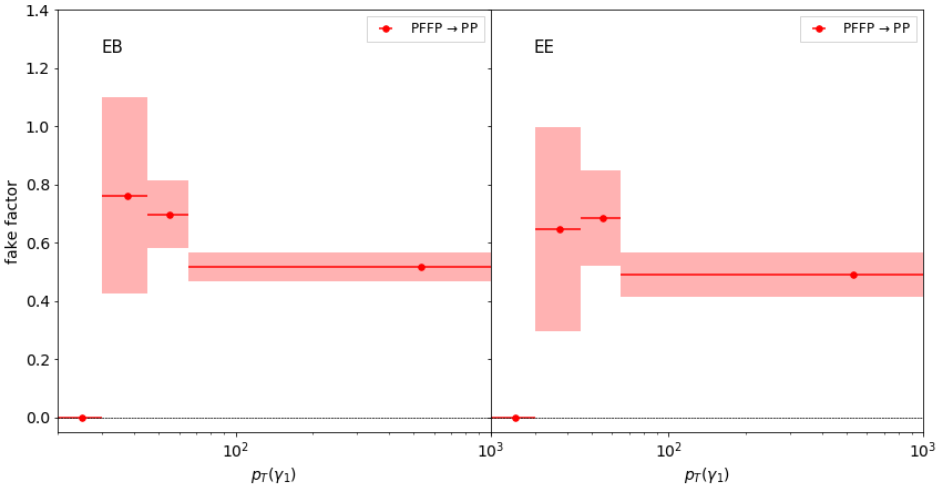

Figure B.1: VBF $f_{\gamma 1}$ factors derived from γ-jet simulation samples for the year 2016. The $f_{\gamma 1}$ factors are binned in the η and p_T of the lead photon.

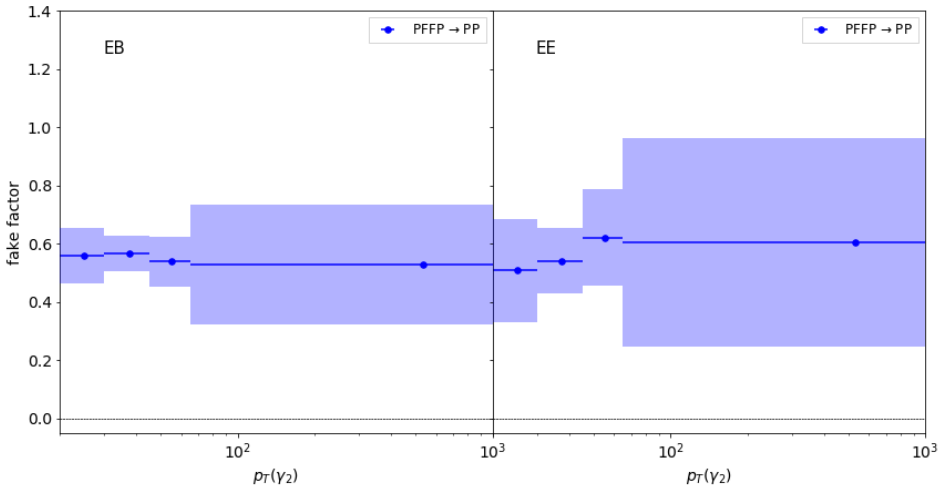

Figure B.2: VBF $f_{\gamma 2}$ factors derived from γ-jet simulation samples for the year 2016. The $f_{\gamma 2}$ factors are binned in the η and p_T of the sublead photon.

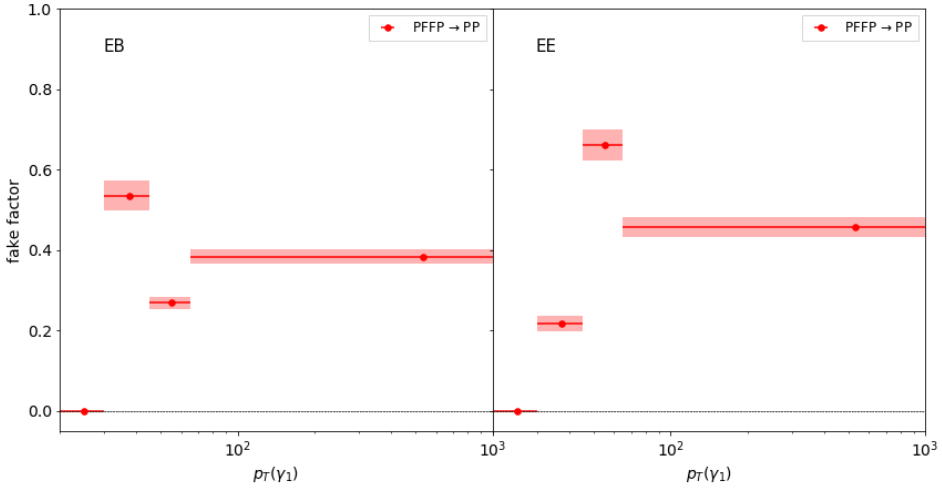

Figure B.3: VBF $f_{\gamma 1}$ factors derived from jet-jet simulation samples for the year 2016. The $f_{\gamma 1}$ factors are binned in the η and p_T of the lead photon.

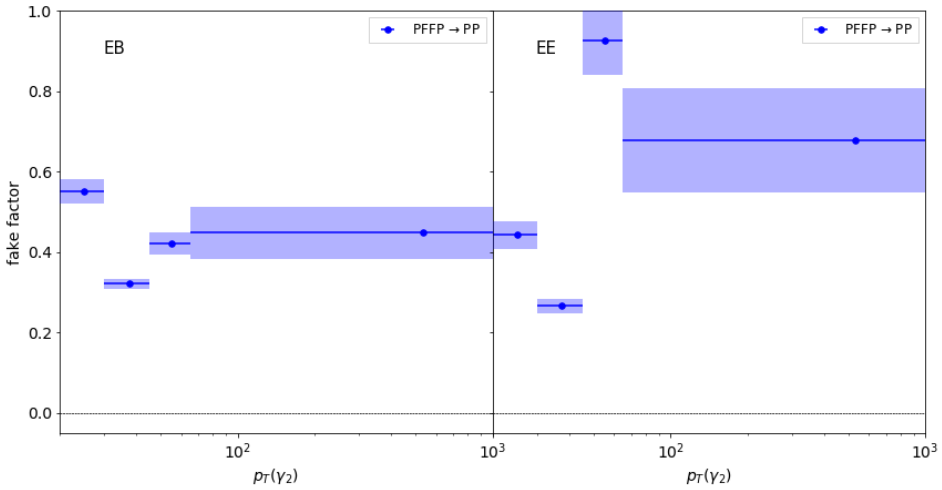

Figure B.4: VBF $f_{\gamma 2}$ factors derived from jet-jet simulation samples for the year 2016. The $f_{\gamma 2}$ factors are binned in the η and p_T of the sublead photon.

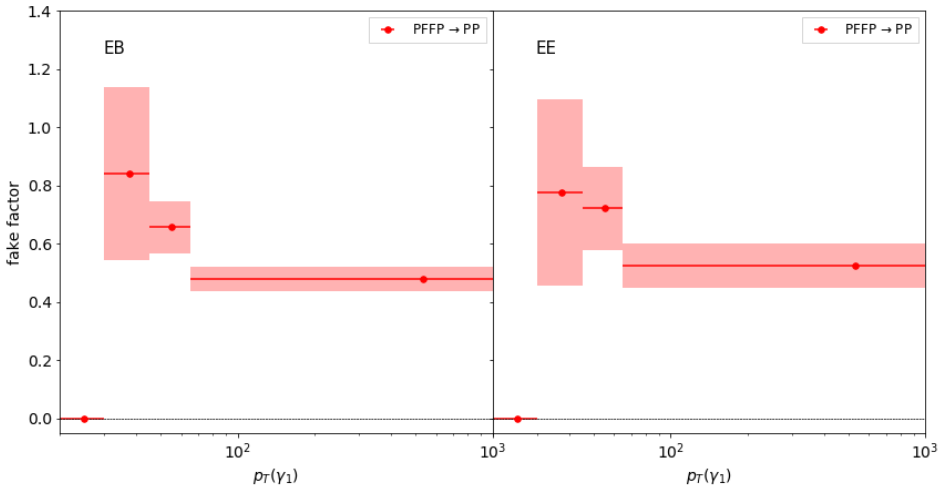

Figure B.5: VBF $f_{\gamma 1}$ factors derived from γ-jet simulation samples for the year 2017. The $f_{\gamma 1}$ factors are binned in the η and p_T of the lead photon.

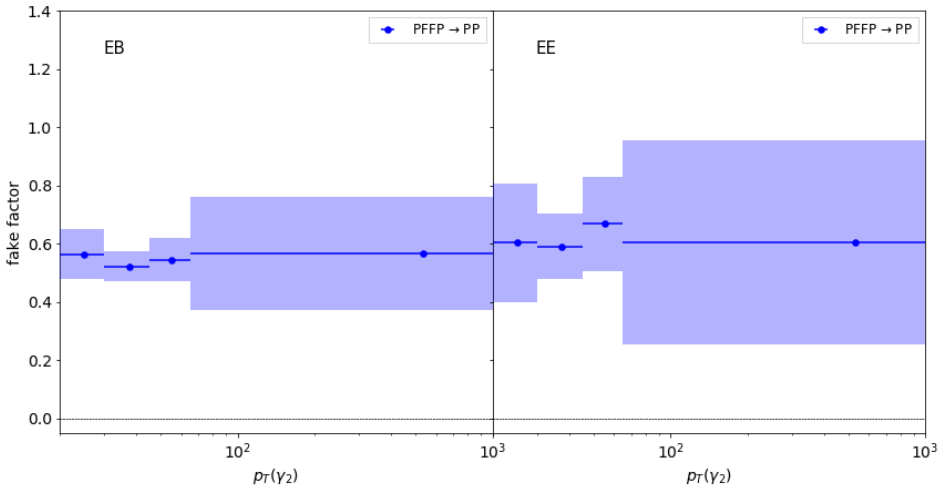

Figure B.6: VBF $f_{\gamma 2}$ factors derived from γ-jet simulation samples for the year 2017. The $f_{\gamma 2}$ factors are binned in the η and p_T of the sublead photon.

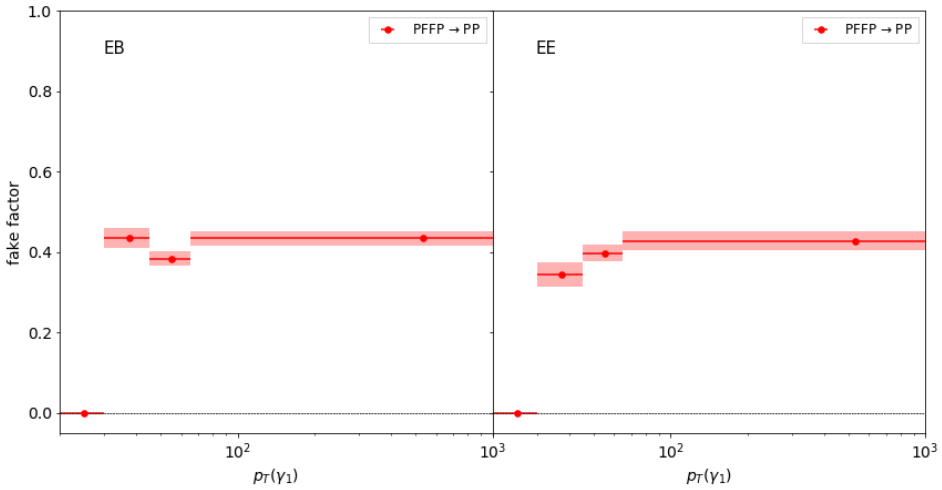

Figure B.7: VBF $f_{\gamma 1}$ factors derived from jet-jet simulation samples for the year 2017. The $f_{\gamma 1}$ factors are binned in the η and p_T of the lead photon.

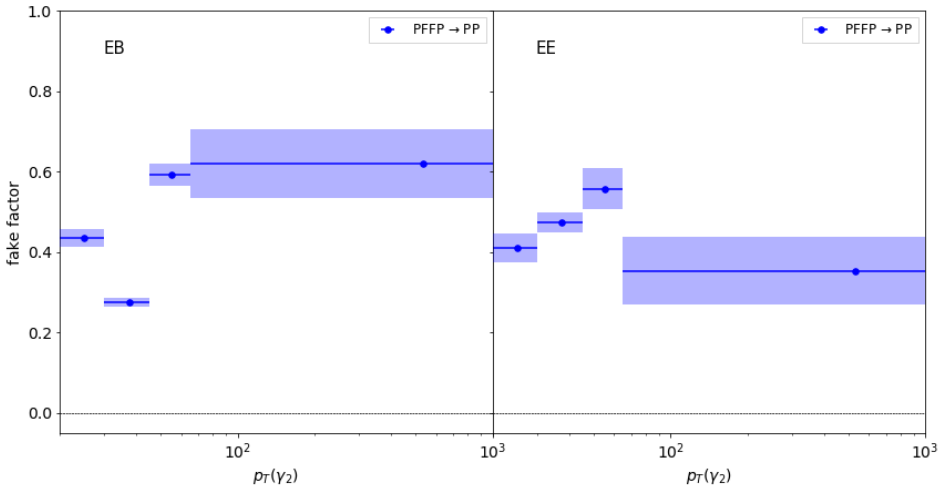

Figure B.8: VBF $f_{\gamma 2}$ factors derived from jet-jet simulation samples for the year 2017. The $f_{\gamma 2}$ factors are binned in the η and p_T of the sublead photon.

B.2 VBF QCD purity fractions for the years 2016 and 2017

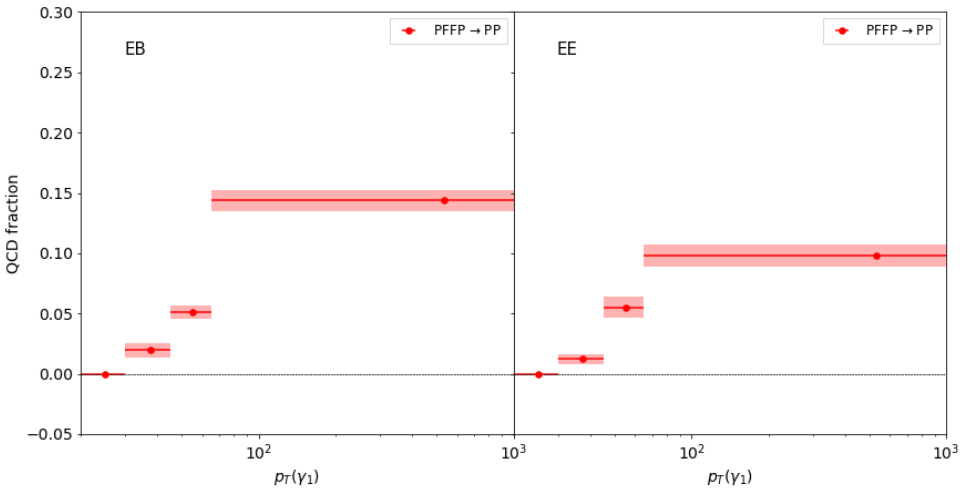

Figure B.9: VBF $p_{\gamma 1}$ factors derived from γ-jet simulation samples for the year 2016. The $p_{\gamma 1}$ factors are binned in the η and p_T of the lead photon.

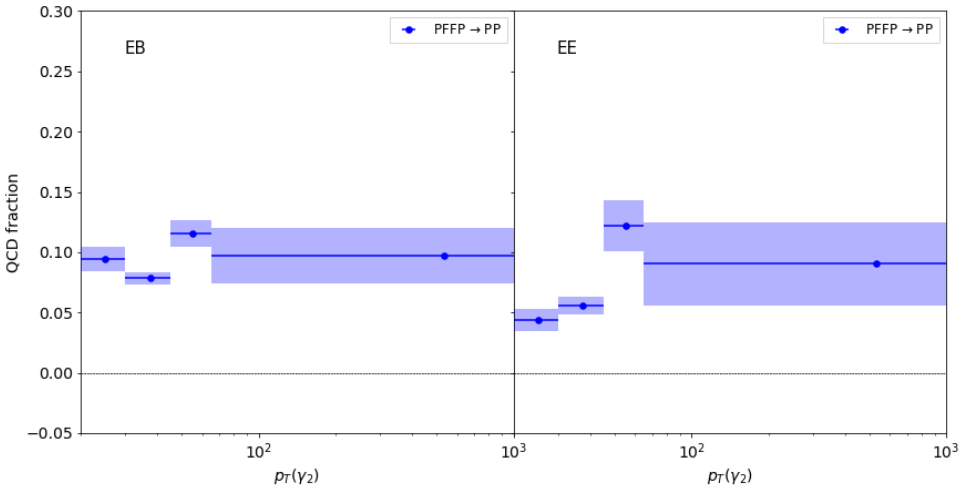

Figure B.10: VBF $p_{\gamma 2}$ factors derived from γ-jet simulation samples for the year 2016. The $p_{\gamma 2}$ factors are binned in the η and p_T of the sublead photon.

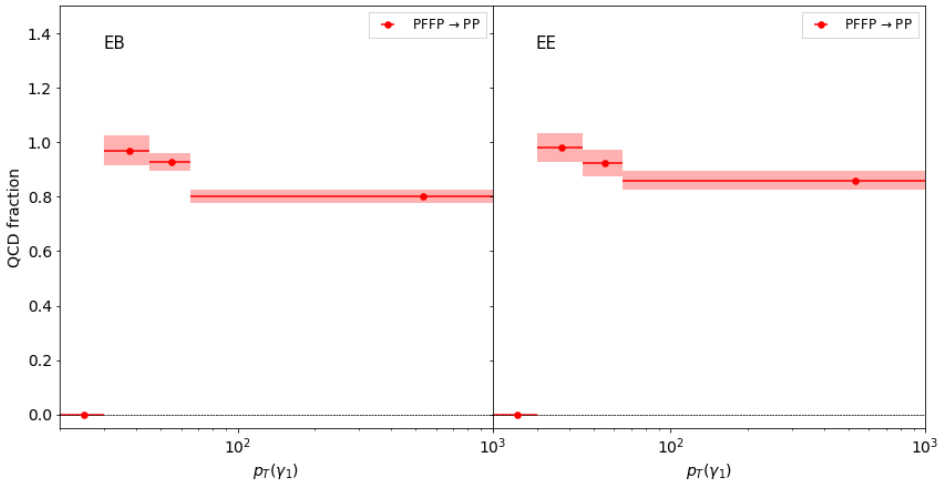

Figure B.11: VBF $p_{\gamma 1}$ factors derived from jet-jet simulation samples for the year 2016. The $p_{\gamma 1}$ factors are binned in the η and p_T of the lead photon.

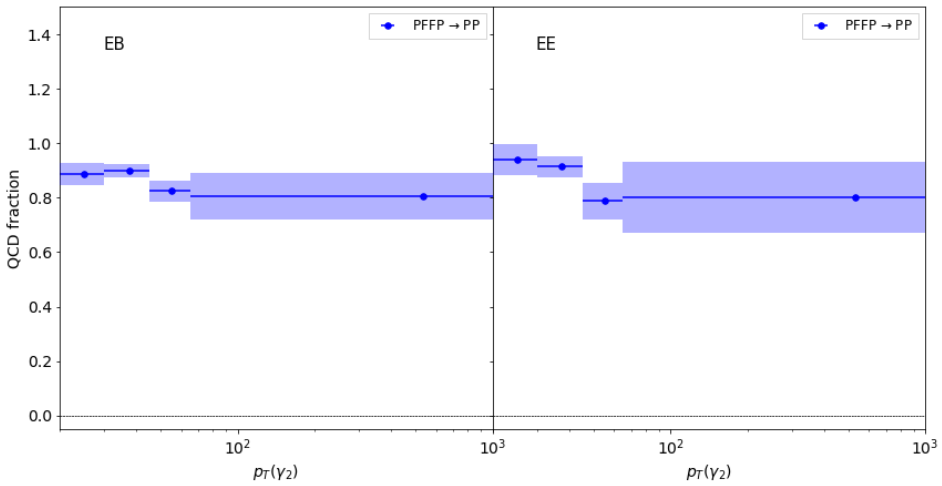

Figure B.12: VBF $p_{\gamma 2}$ factors derived from jet-jet simulation samples for the year 2016. The $p_{\gamma 2}$ factors are binned in the η and p_T of the sublead photon.

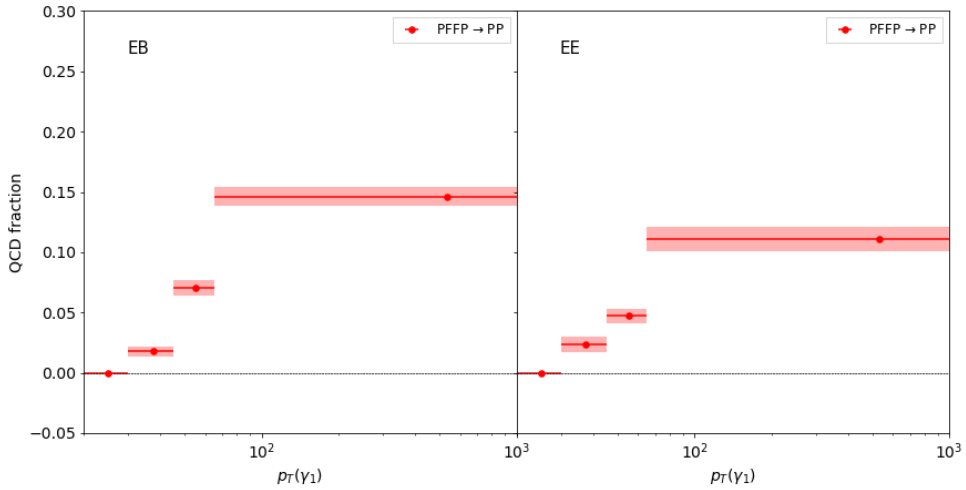

Figure B.13: VBF $p_{\gamma 1}$ factors derived from γ-jet simulation samples for the year 2017. The $p_{\gamma 1}$ factors are binned in the η and p_T of the lead photon.

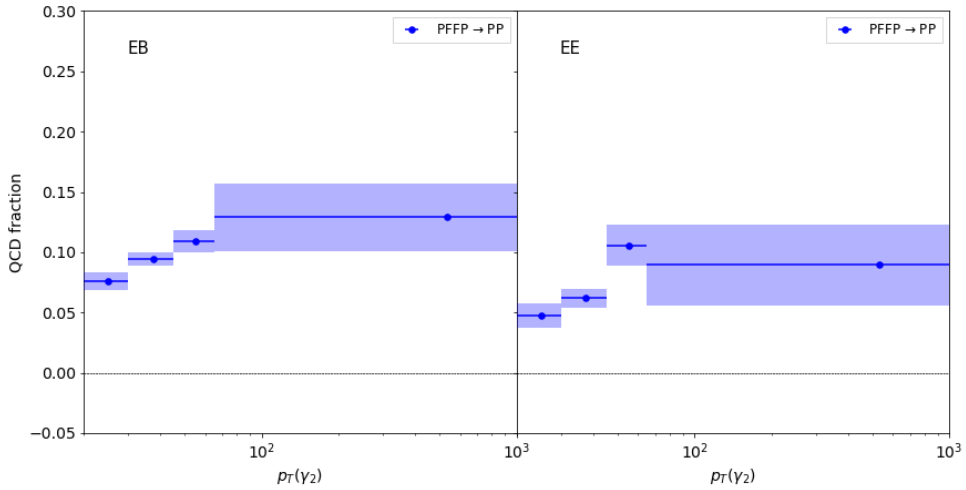

Figure B.14: VBF $p_{\gamma 2}$ factors derived from γ-jet simulation samples for the year 2017. The $p_{\gamma 2}$ factors are binned in the η and p_T of the sublead photon.

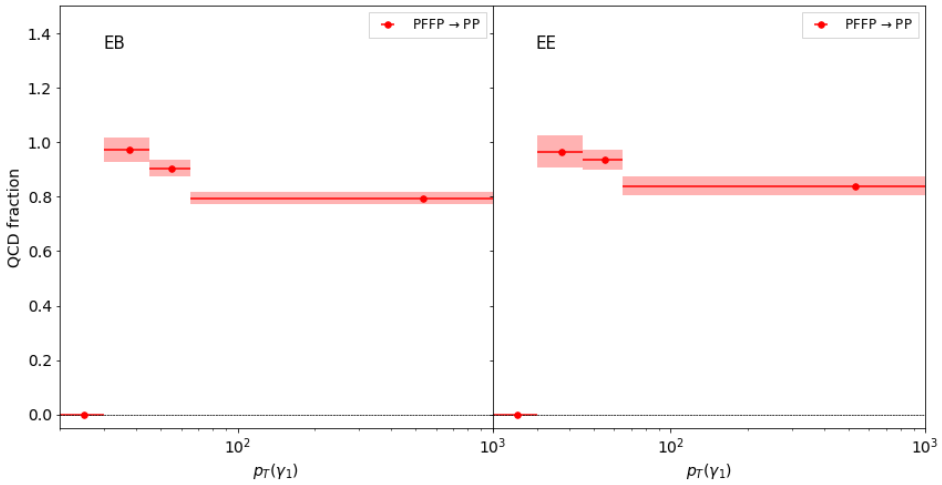

Figure B.15: VBF $p_{\gamma 1}$ factors derived from jet-jet simulation samples for the year 2017. The $p_{\gamma 1}$ factors are binned in the η and p_T of the lead photon.

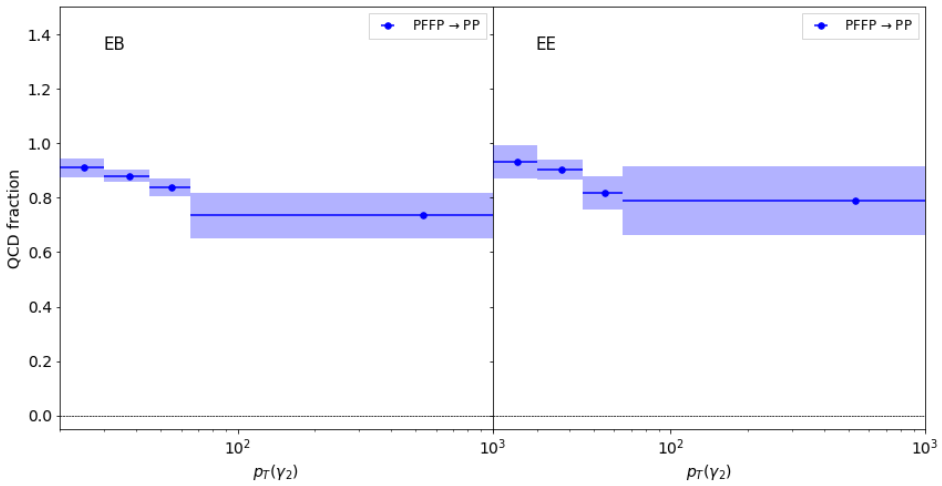

Figure B.16: VBF $p_{\gamma 2}$ factors derived from jet-jet simulation samples for the year 2017. The $p_{\gamma 2}$ factors are binned in the η and p_T of the sublead photon.

B.3 VBF data-driven background modelling validations

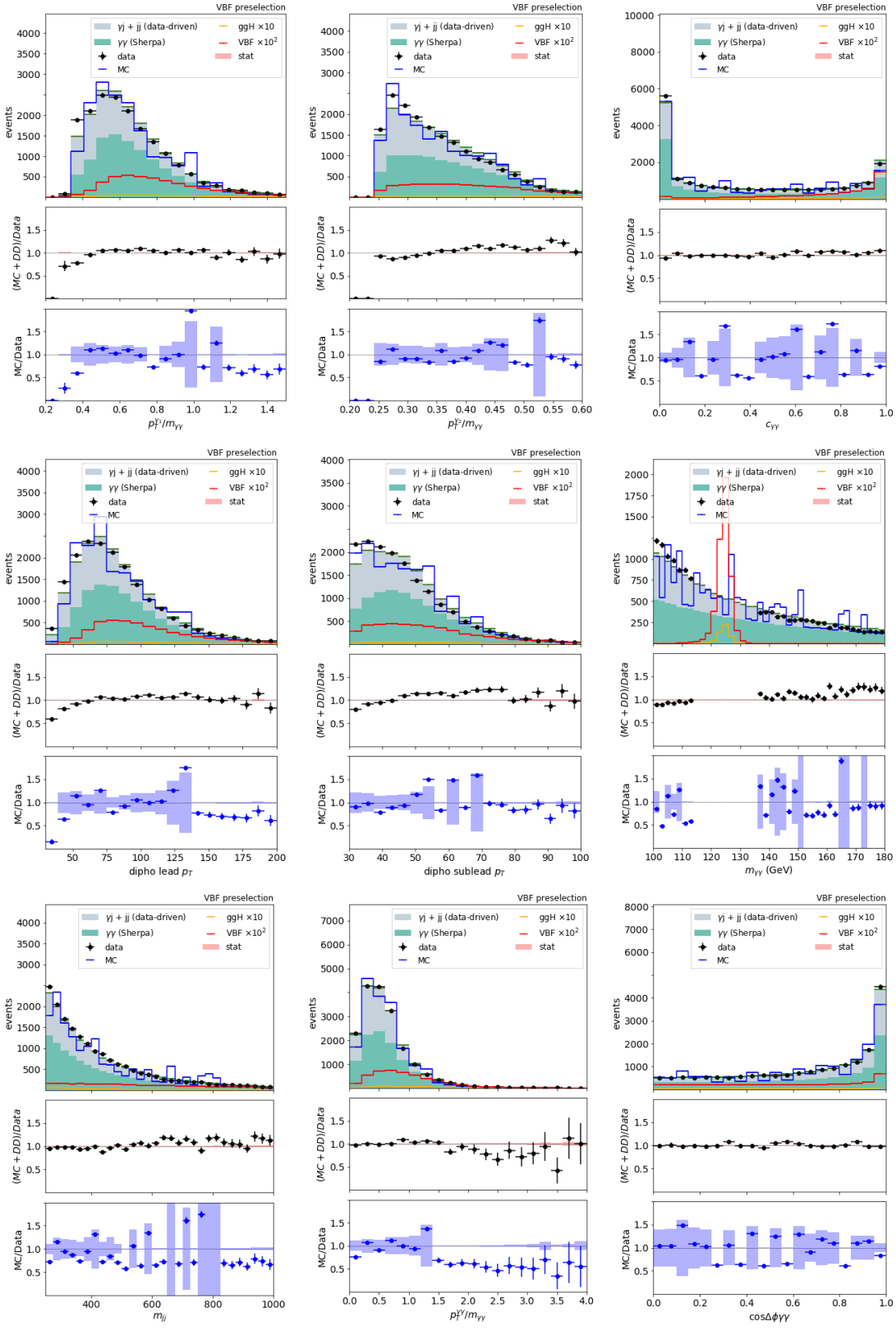

Figure B.17: 2016 validation of the data-driven method on various kinematics variables relevant to the VBF BDT.

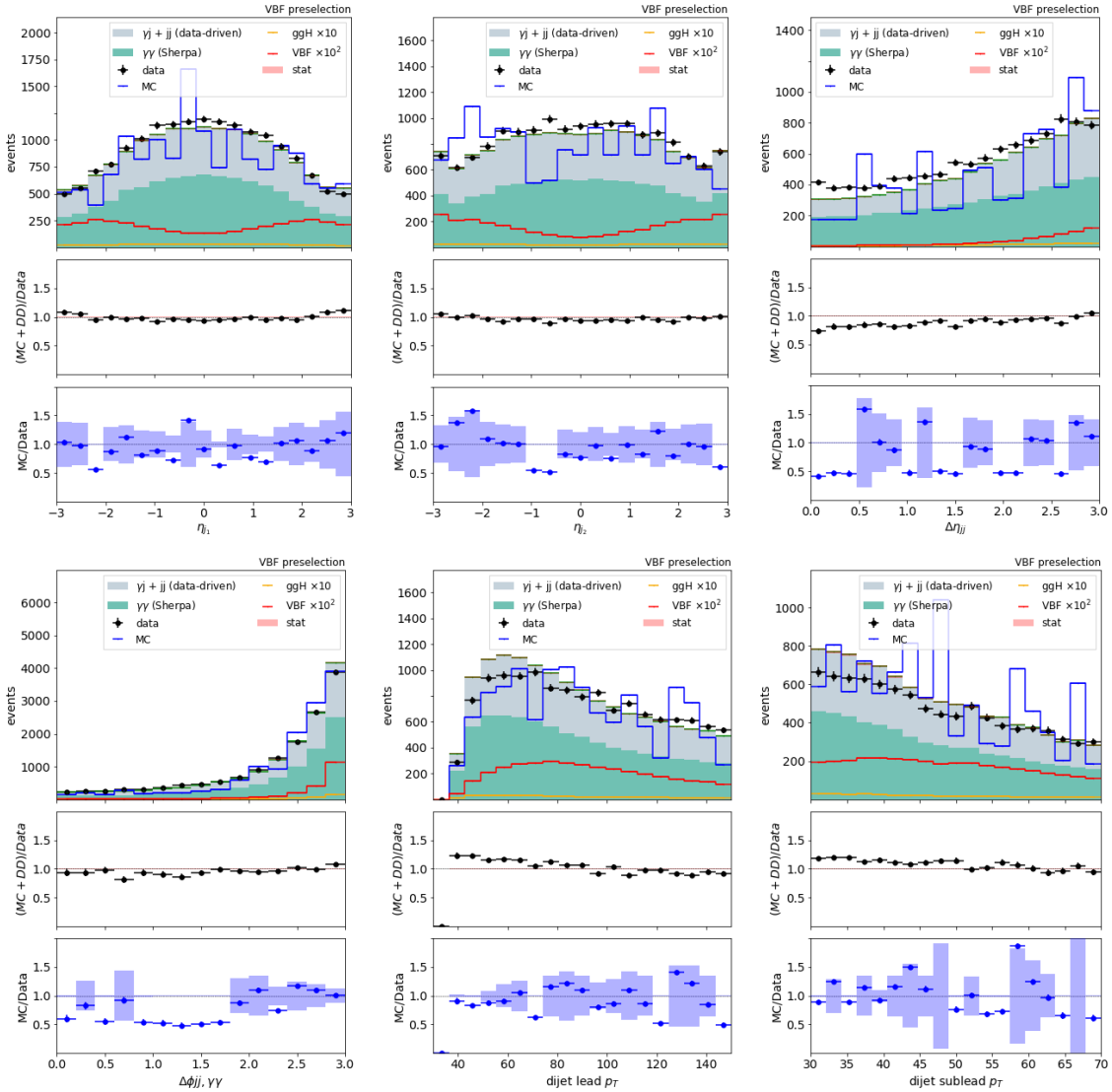

Figure B.18: 2016 validation of the data-driven method on various kinematics variables relevant to the VBF BDT.The data points represent data outside the Higgs boson mass window (115-125 GeV and satisfying the VBF preselection criteria. The DD+MC method is compared to data in the ratio plot with black dots while the MC-only method is compared to data in the ratio plot with blue dots.

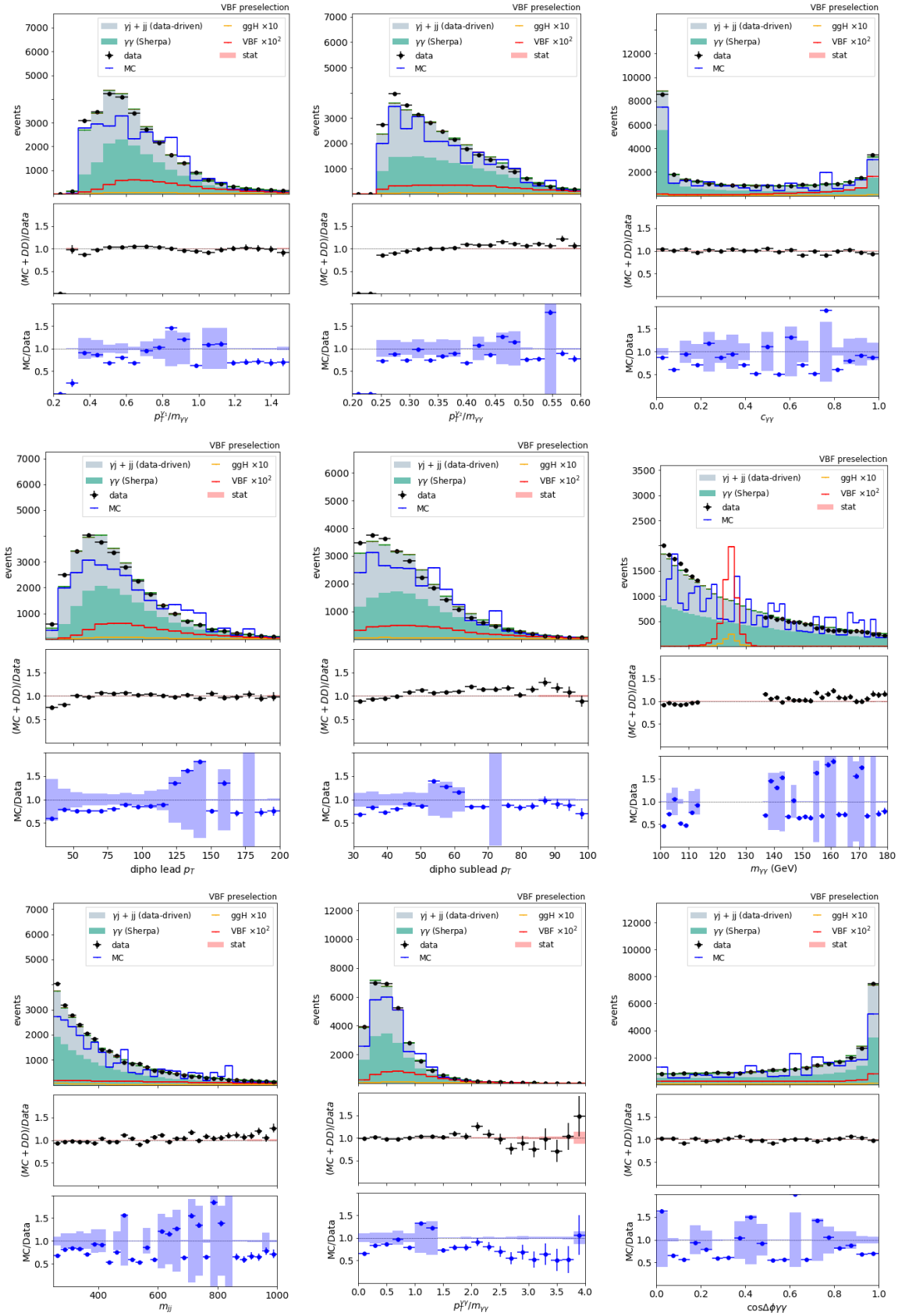

Figure B.19: 2017 validation of the data-driven method on various kinematics variables relevant to the VBF BDT.

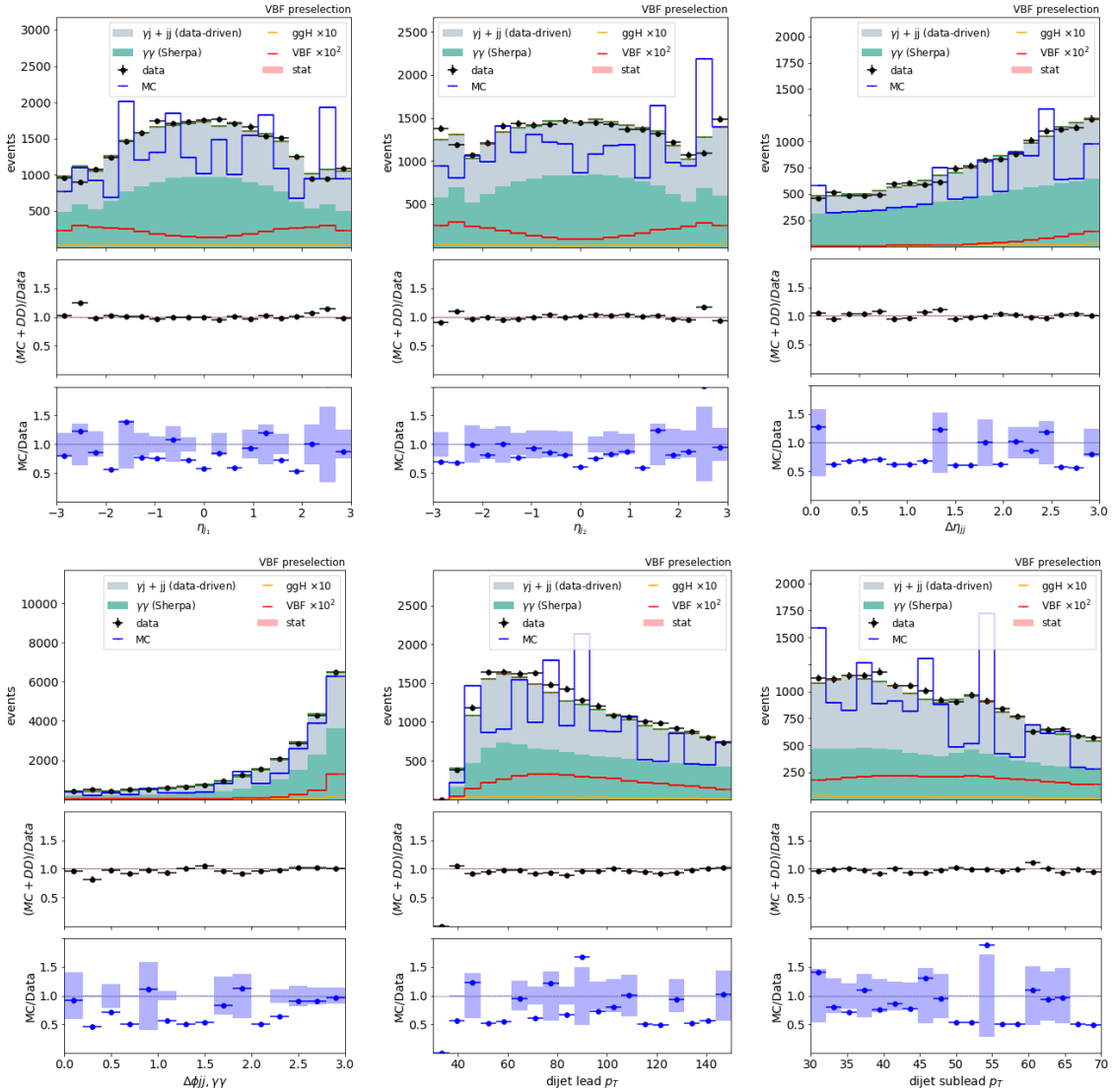

Figure B.20: 2017 validation of the data-driven method on various kinematics variables relevant to the VBF BDT. The data points represent data outside the Higgs boson mass window (115-125 GeV and satisfying the VBF preselection criteria. The DD+MC method is compared to data in the ratio plot with black dots while the MC-only method is compared to data in the ratio plot with blue dots.

B.4 VBF BDT signal validation

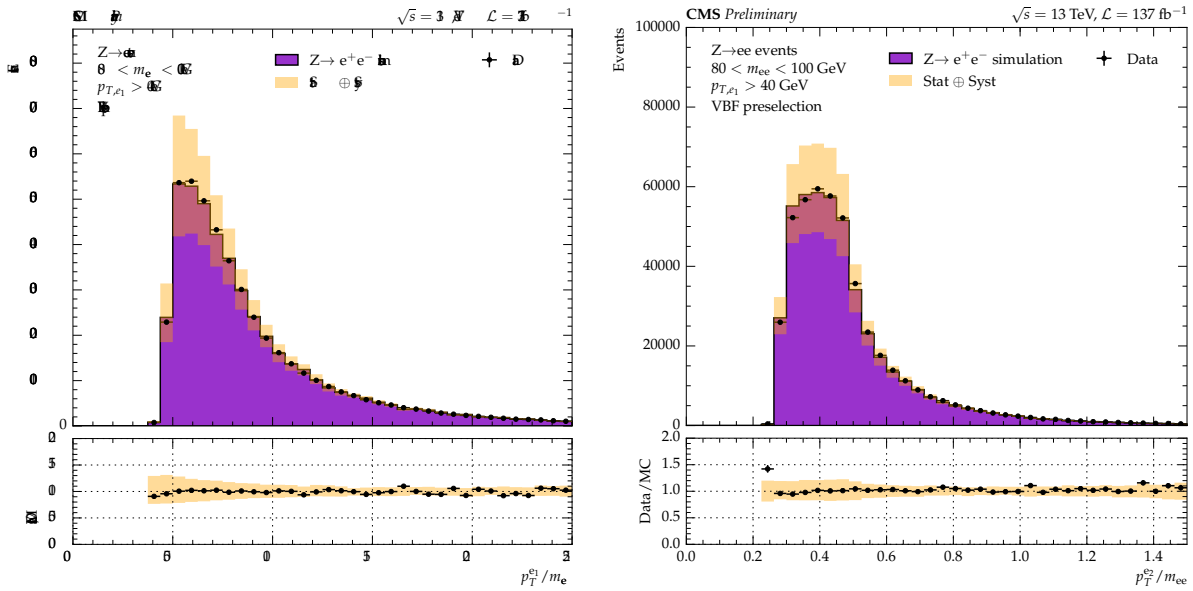

Figure B.21: VBF BDT signal validation in the $Z \to ee$ control region. The DY simulation is compared to data taken in 2016, 2017, and 2018 (black points) for each variable.

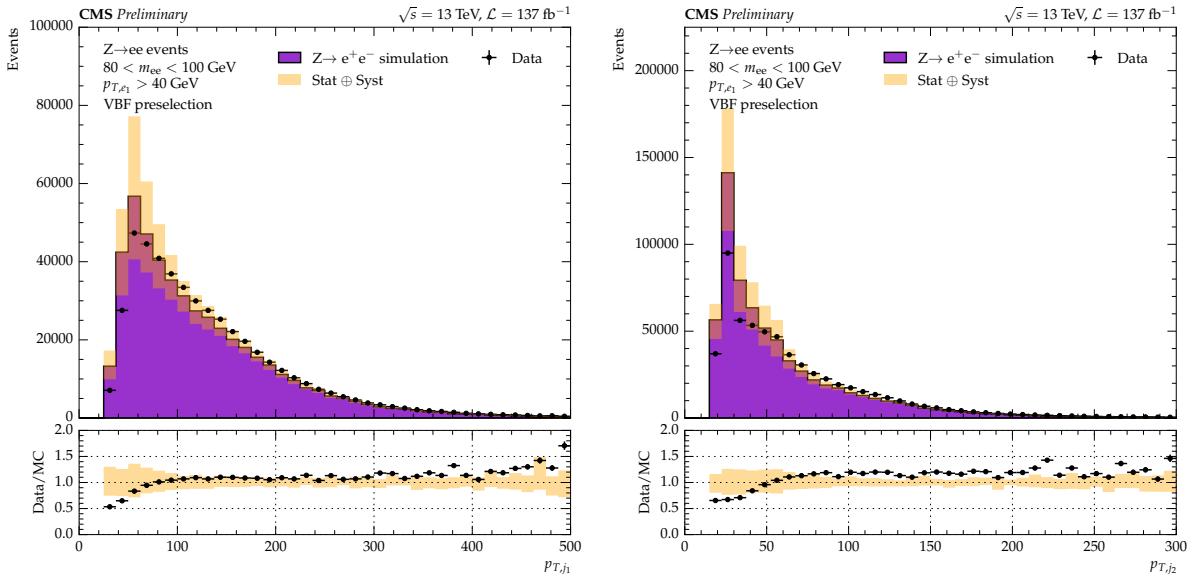

Figure B.22: VBF BDT signal validation in the $Z \to ee$ control region. The DY simulation is compared to data taken in 2016, 2017, and 2018 (black points) for each variable.

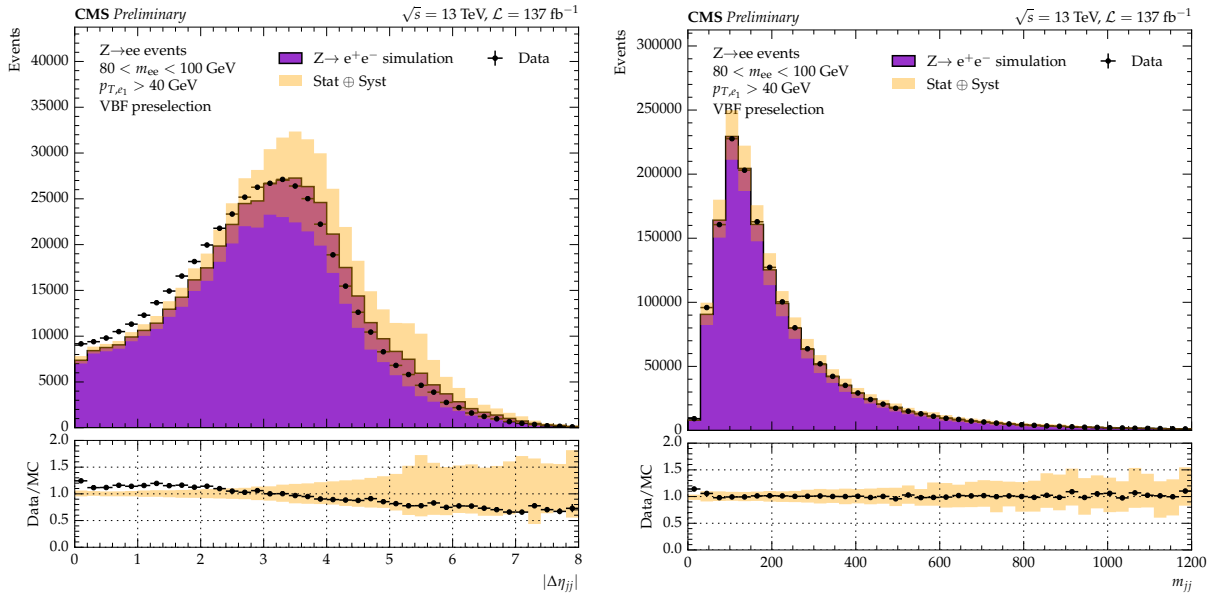

Figure B.23: VBF BDT signal validation in the $Z \to ee$ control region. The DY simulation is compared to data taken in 2016, 2017, and 2018 (black points) for each variable.

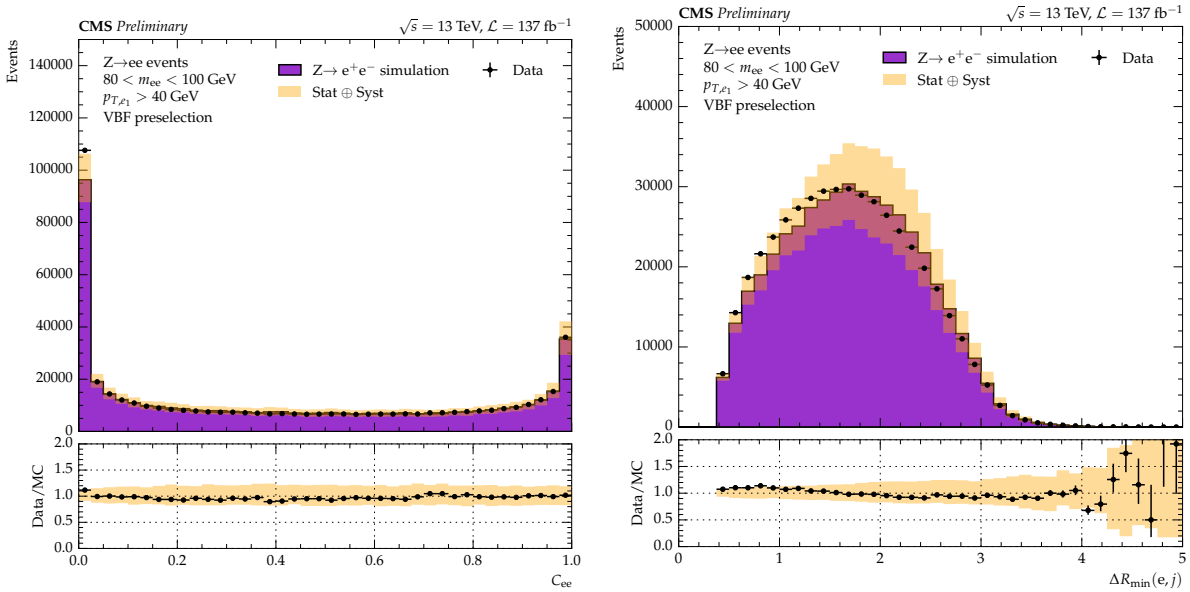

Figure B.24: VBF BDT signal validation in the $Z \to ee$ control region. The DY simulation is compared to data taken in 2016, 2017, and 2018 (black points) for each variable.

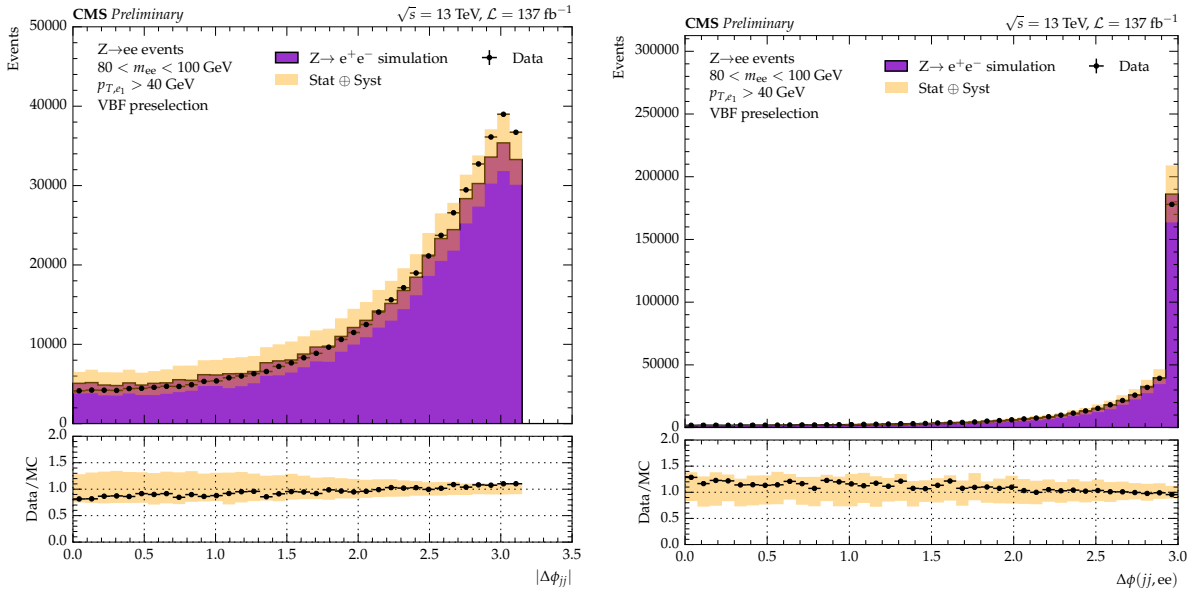

Figure B.25: VBF BDT signal validation in the $Z \to ee$ control region. The DY simulation is compared to data taken in 2016, 2017, and 2018 (black points) for each variable.

Appendix C

C.1 VH fake factors for the years 2016 and 2017

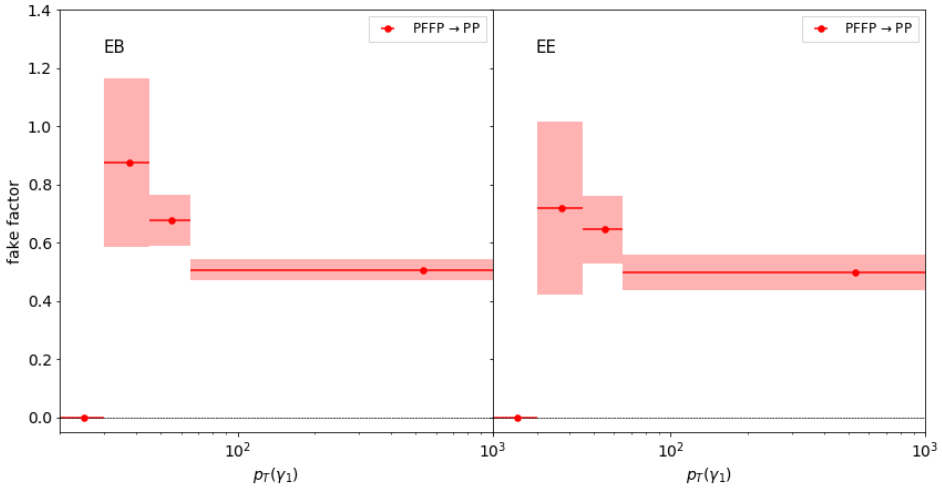

Figure C.1: VH $f_{\gamma 1}$ factors derived from γ-jet simulation samples for the year 2016. The $f_{\gamma 1}$ factors are binned in the η and p_T of the lead photon.

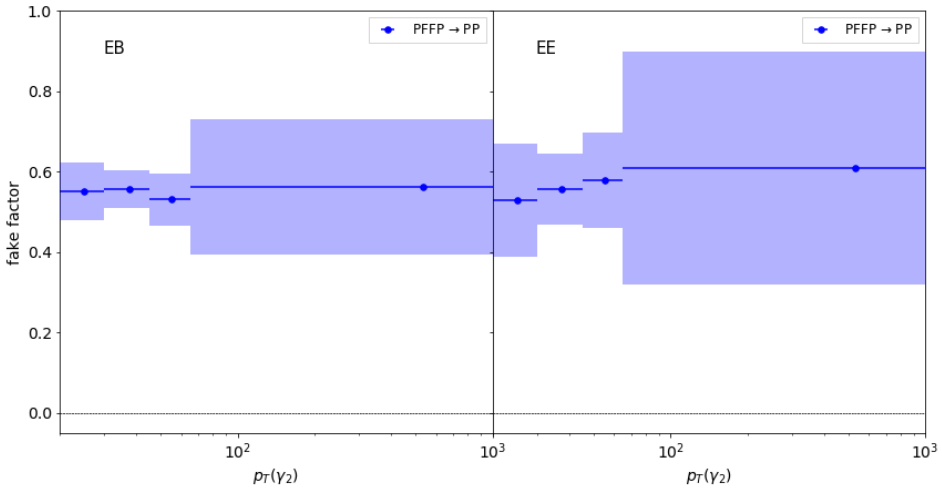

Figure C.2: VH $f_{\gamma 2}$ factors derived from γ-jet simulation samples for the year 2016. The $f_{\gamma 2}$ factors are binned in the η and p_T of the sublead photon.

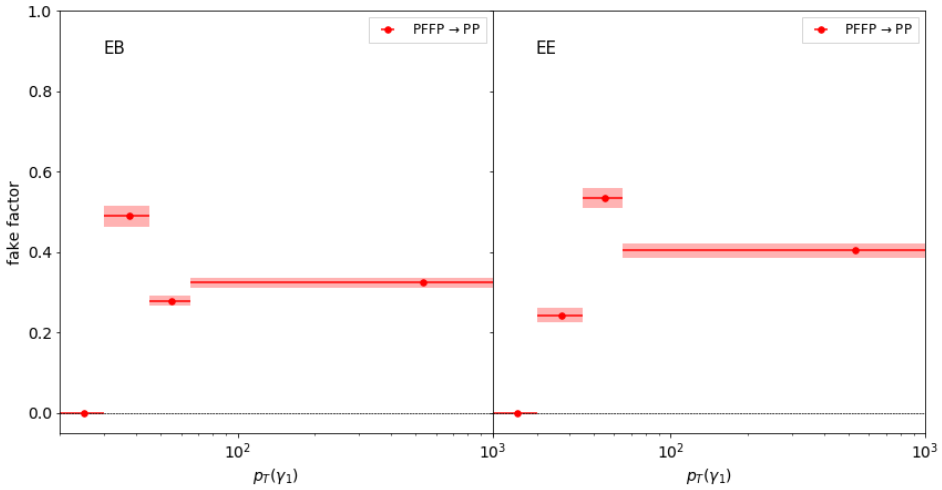

Figure C.3: VH $f_{\gamma 1}$ factors derived from jet-jet simulation samples for the year 2016. The $f_{\gamma 1}$ factors are binned in the η and p_T of the lead photon.

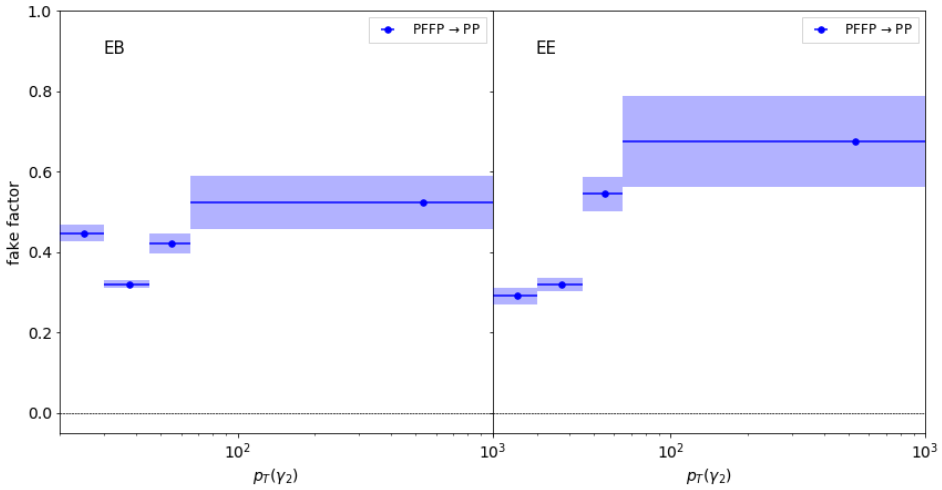

Figure C.4: VH $f_{\gamma 2}$ factors derived from jet-jet simulation samples for the year 2016. The $f_{\gamma 2}$ factors are binned in the η and p_T of the sublead photon

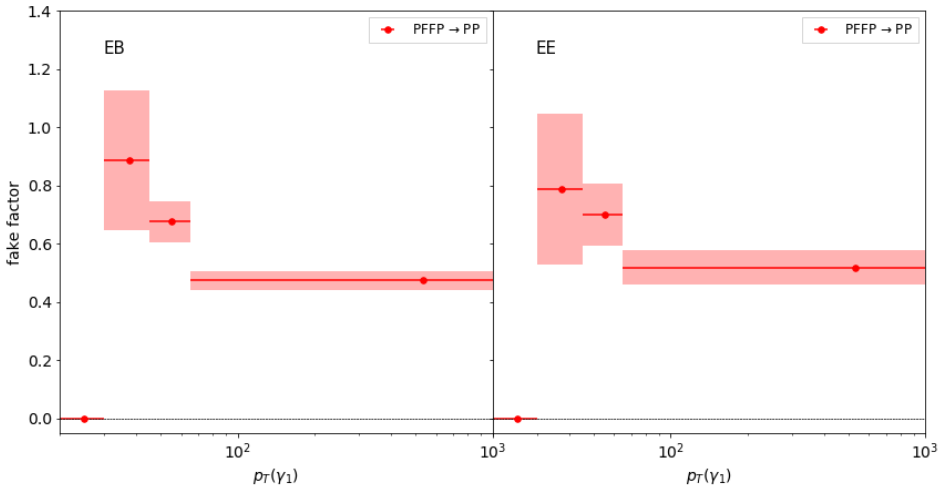

Figure C.5: VH $f_{\gamma 1}$ factors derived from γ-jet simulation samples for the year 2017. The $f_{\gamma 1}$ factors are binned in the η and p_T of the lead photon.

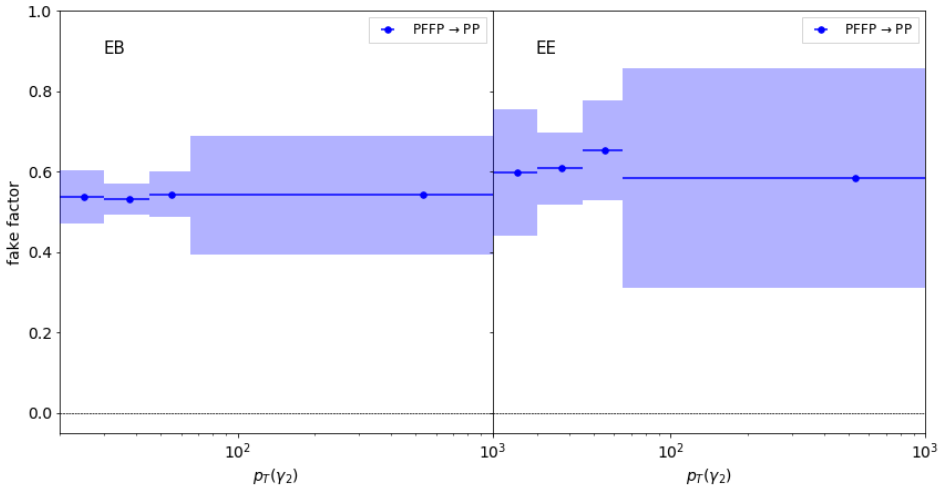

Figure C.6: VH $f_{\gamma 2}$ factors derived from γ-jet simulation samples for the year 2017. The $f_{\gamma 2}$ factors are binned in the η and p_T of the sublead photon.

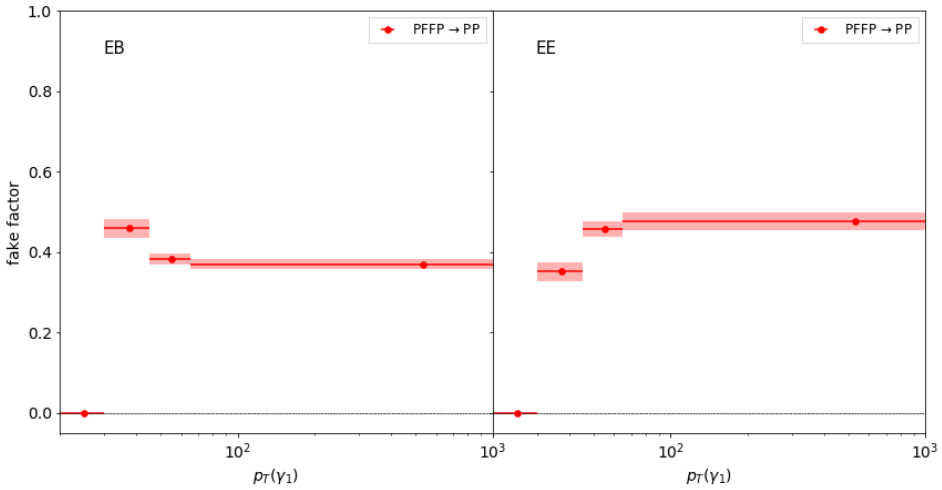

Figure C.7: VH $f_{\gamma 1}$ factors derived from jet-jet simulation samples for the year 2017. The $f_{\gamma 1}$ factors are binned in the η and p_T of the lead photon.

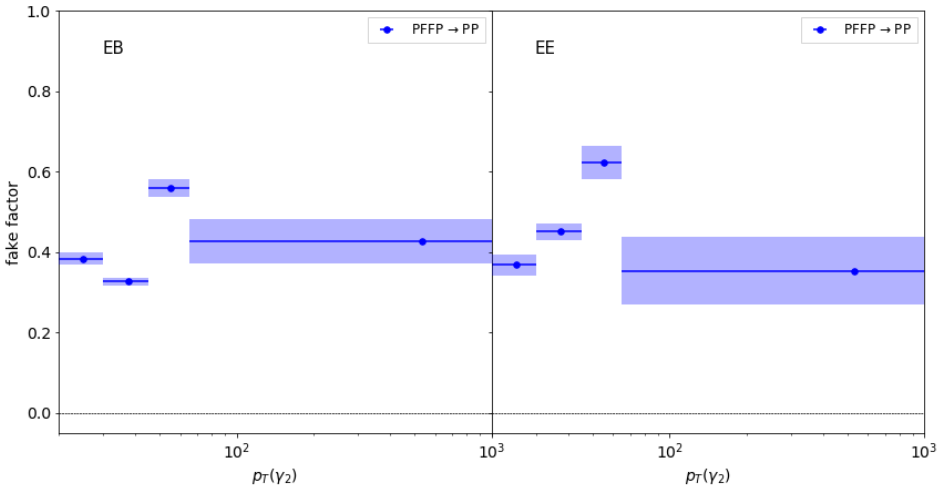

Figure C.8: VH $f_{\gamma 2}$ factors derived from jet-jet simulation samples for the year 2017. The $f_{\gamma 2}$ factors are binned in the η and p_T of the sublead photon.

C.2 VH QCD purity fractions for the years 2016 and 2017

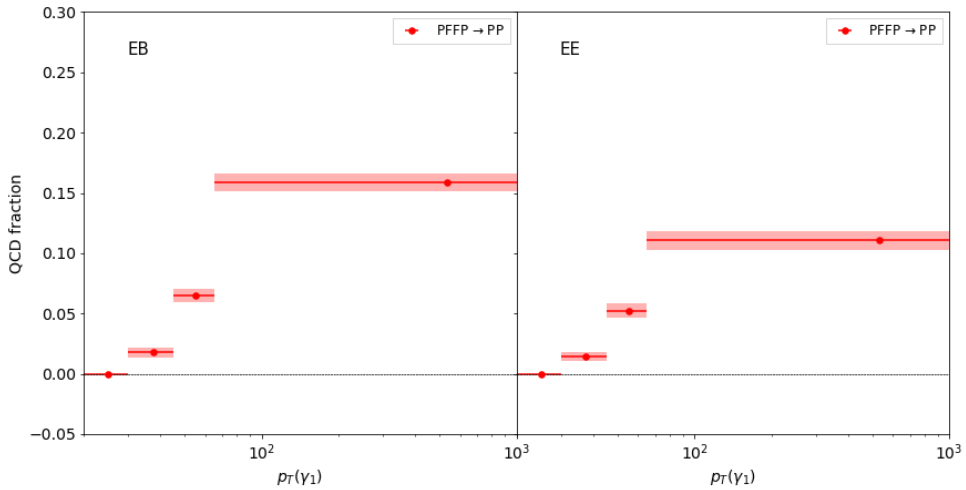

Figure C.9: VH $p_{\gamma 1}$ factors derived from γ-jet simulation samples for the year 2016. The $p_{\gamma 1}$ factors are binned in the η and p_T of the lead photon.

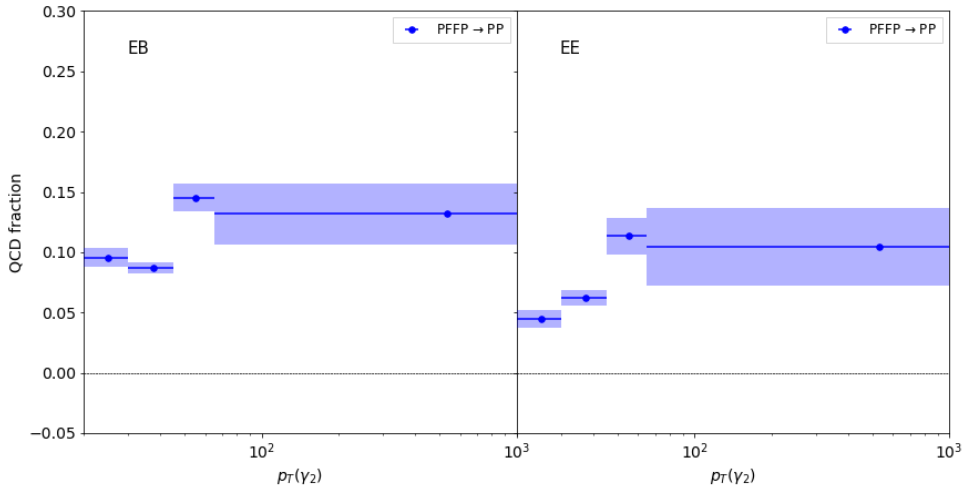

Figure C.10: VH $p_{\gamma 2}$ factors derived from γ-jet simulation samples for the year 2016. The $p_{\gamma 2}$ factors are binned in the η and p_T of the sublead photon.

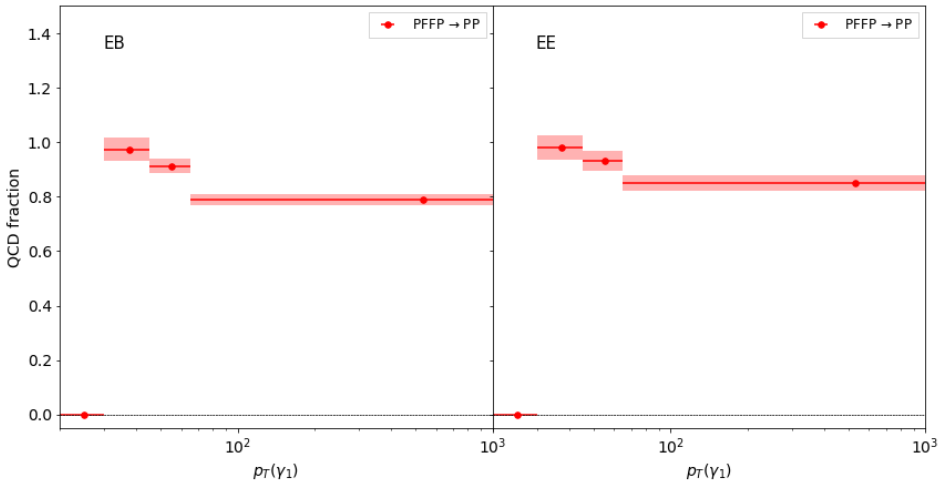

Figure C.11: VH $p_{\gamma 1}$ factors derived from jet-jet simulation samples for the year 2016. The $p_{\gamma 1}$ factors are binned in the η and p_T of the lead photon.

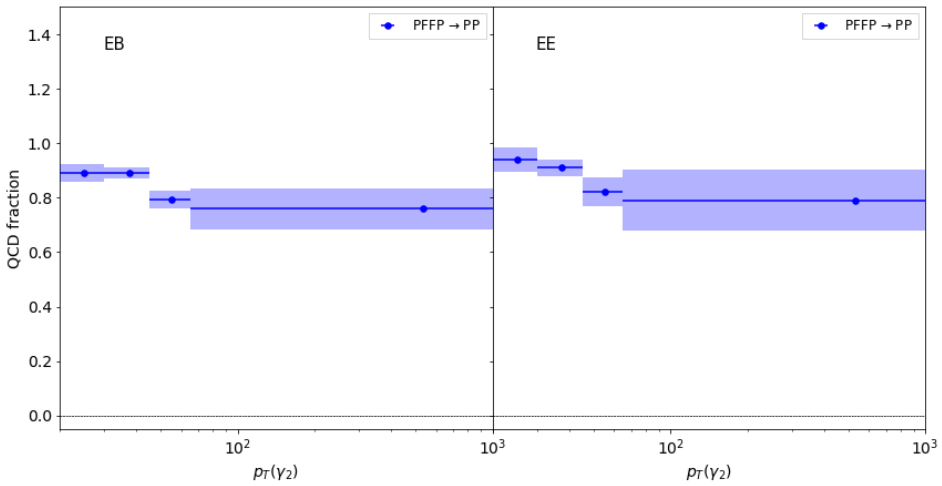

Figure C.12: VH $p_{\gamma 2}$ factors derived from jet-jet simulation samples for the year 2016. The $p_{\gamma 2}$ factors are binned in the η and p_T of the sublead photon.

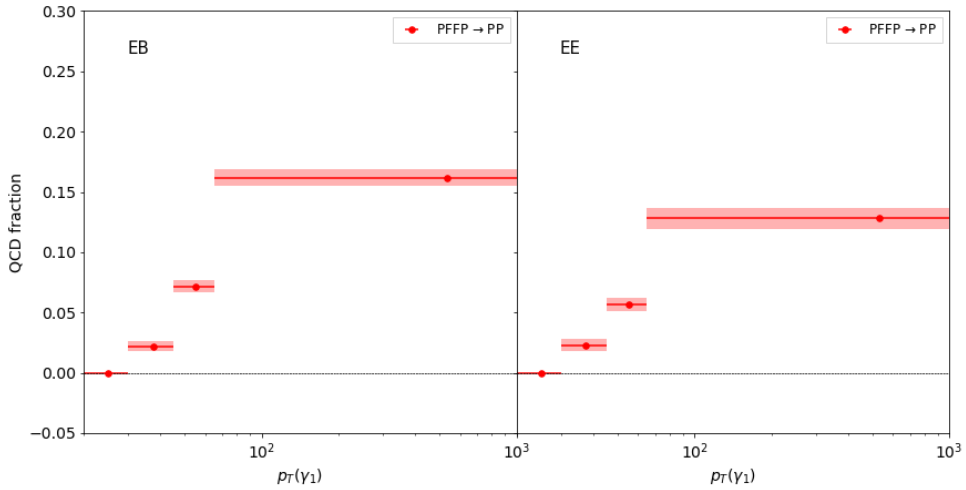

Figure C.13: VH $p_{\gamma 1}$ factors derived from γ-jet simulation samples for the year 2017. The $p_{\gamma 1}$ factors are binned in the η and p_T of the lead photon.

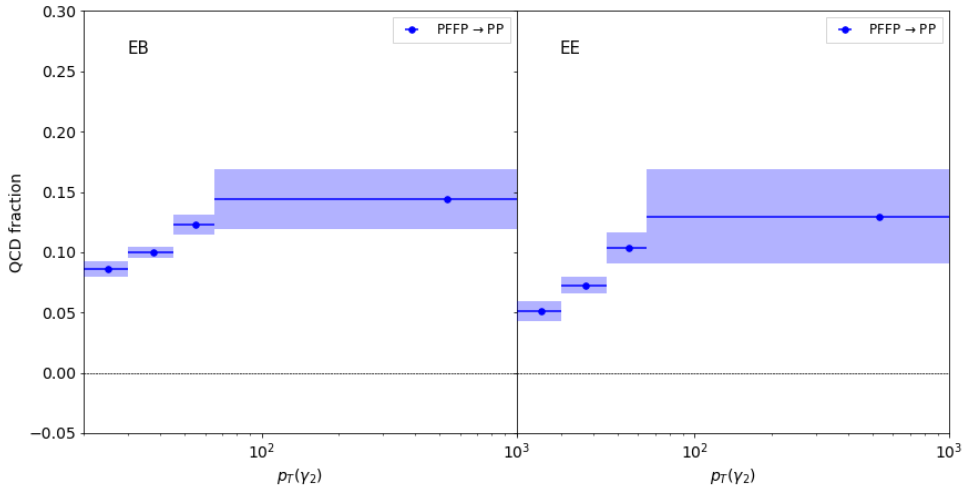

Figure C.14: VH $p_{\gamma 2}$ factors derived from γ-jet simulation samples for the year 2017. The $p_{\gamma 2}$ factors are binned in the η and p_T of the sublead photon.

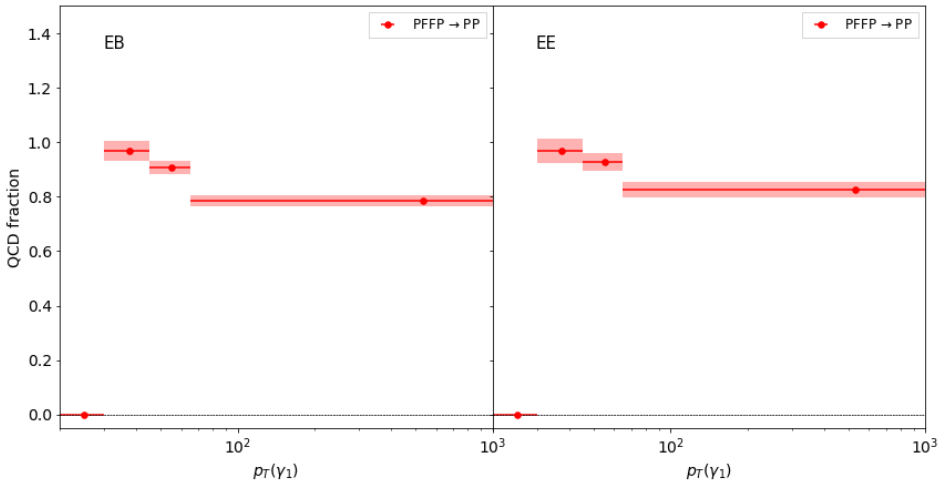

Figure C.15: VH $p_{\gamma 1}$ factors derived from jet-jet simulation samples for the year 2017. The $p_{\gamma 1}$ factors are binned in the η and p_T of the lead photon.

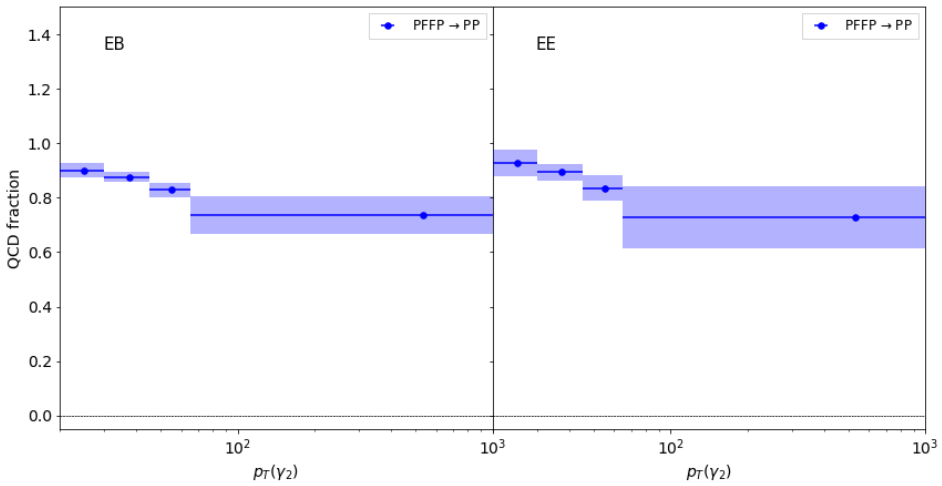

Figure C.16: VH $p_{\gamma 2}$ factors derived from jet-jet simulation samples for the year 2017. The $p_{\gamma 2}$ factors are binned in the η and p_T of the sublead photon.

C.3 VH data-driven background modelling validations

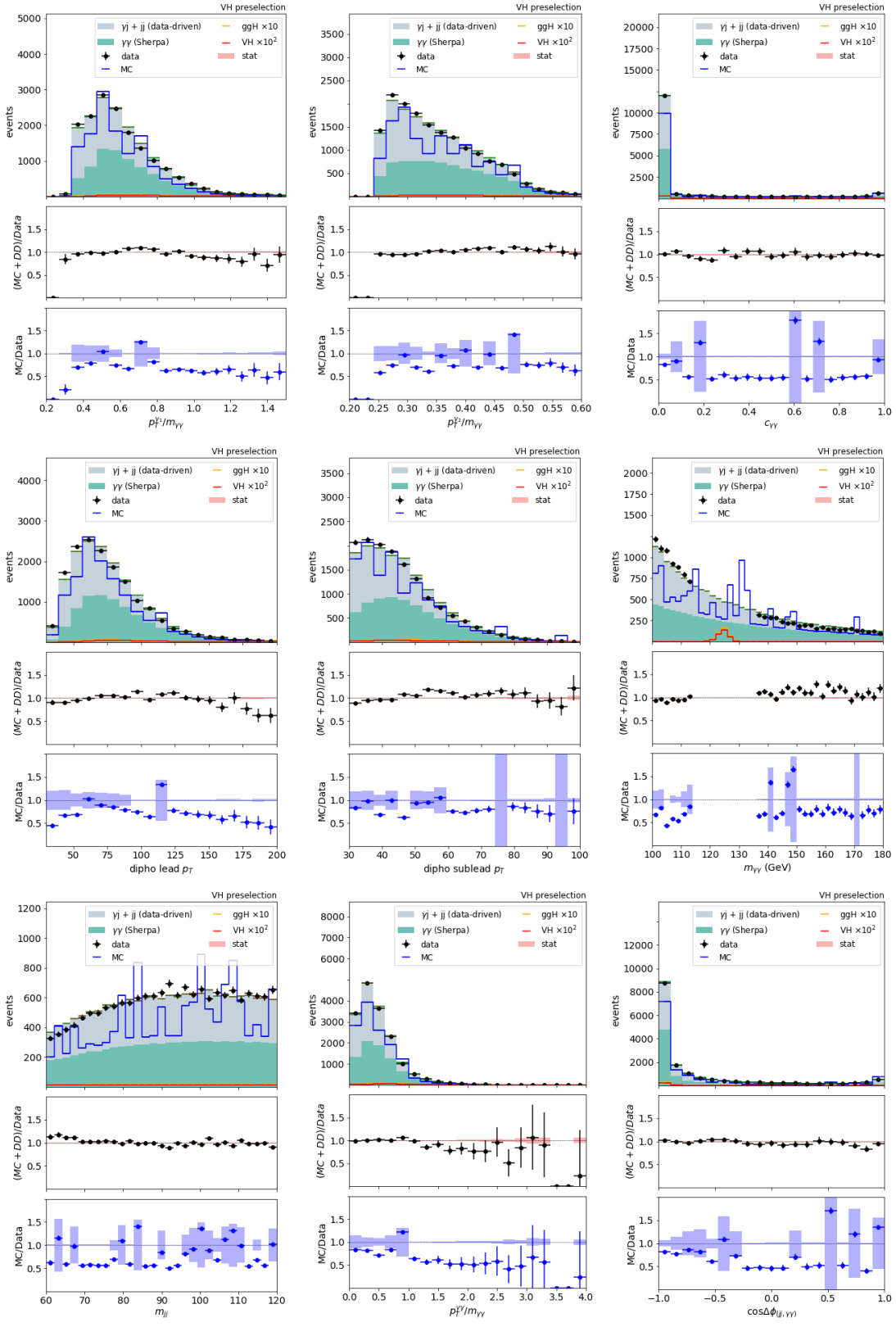

Figure C.17: 2016 validation of the data-driven method on various kinematics variables relevant to the VH BDT.

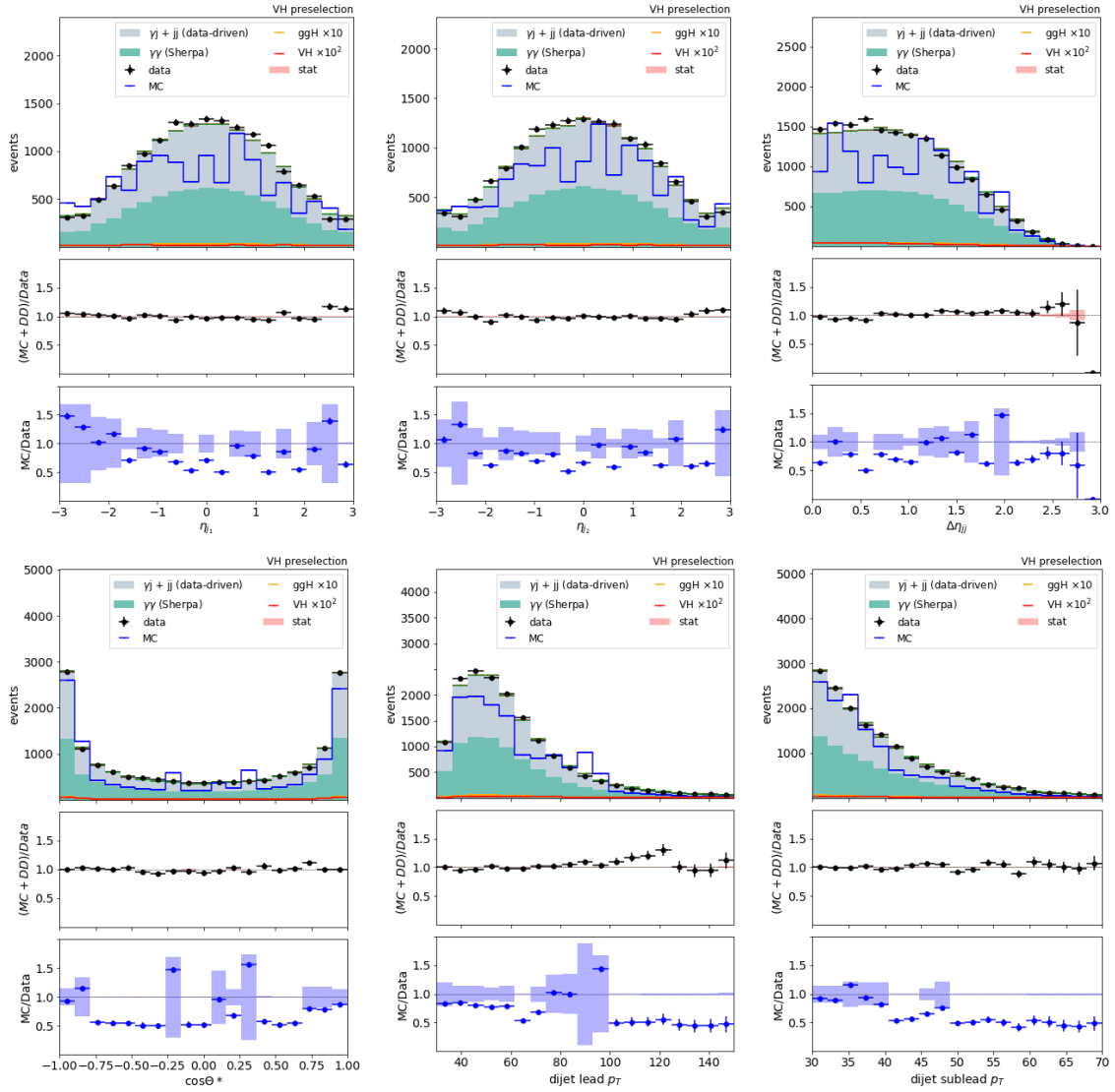

Figure C.18: 2016 validation of the data-driven method on various kinematics variables relevant to the VH BDT. The data points represent data outside the Higgs boson mass window (115-125 GeV and satisfying the VH preselection criteria. The DD+MC method is compared to data in the ratio plot with black dots while the MC-only method is compared to data in the ratio plot with blue dots.

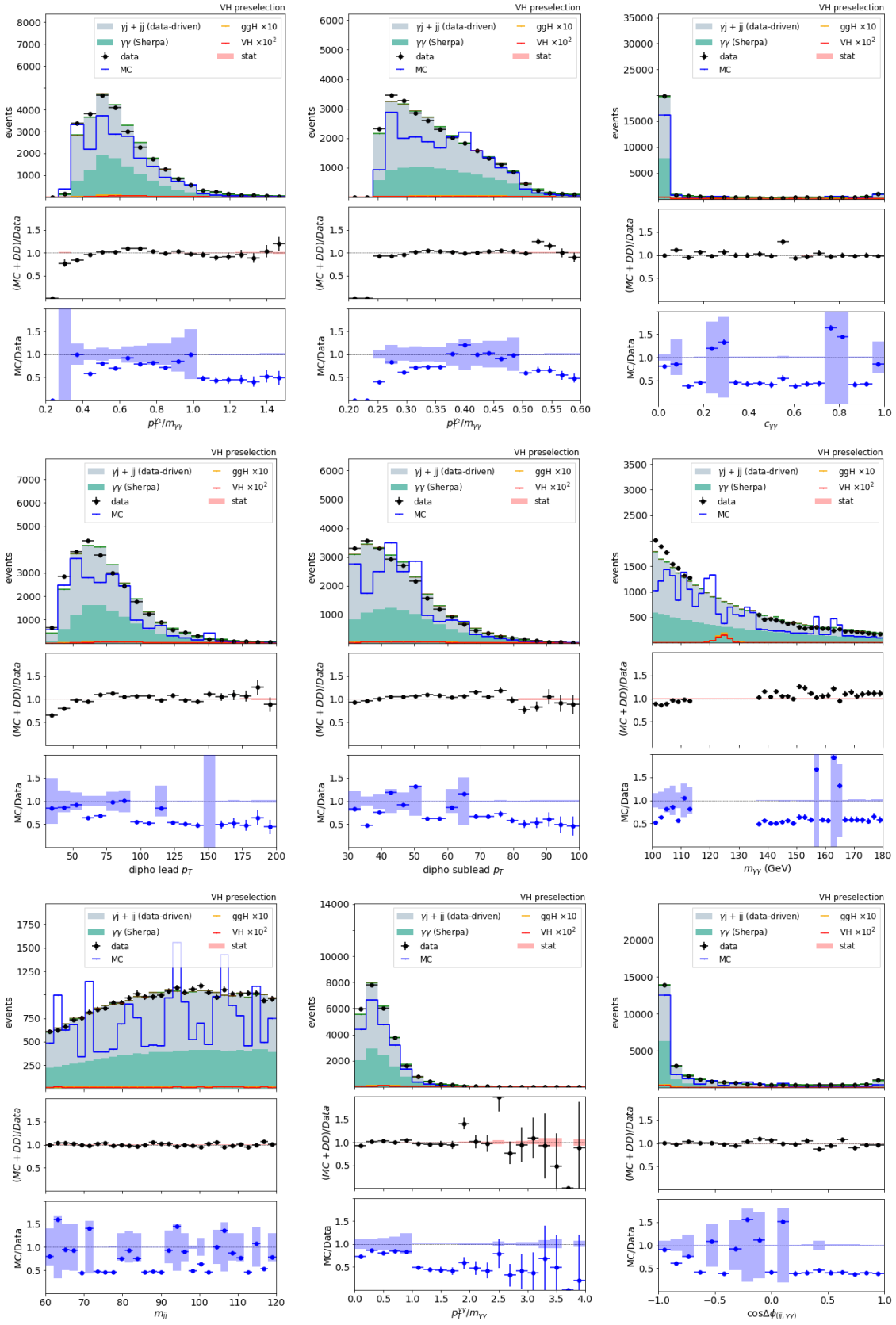

Figure C.19: 2017 validation of the data-driven method on various kinematics variables relevant to the VH BDT.

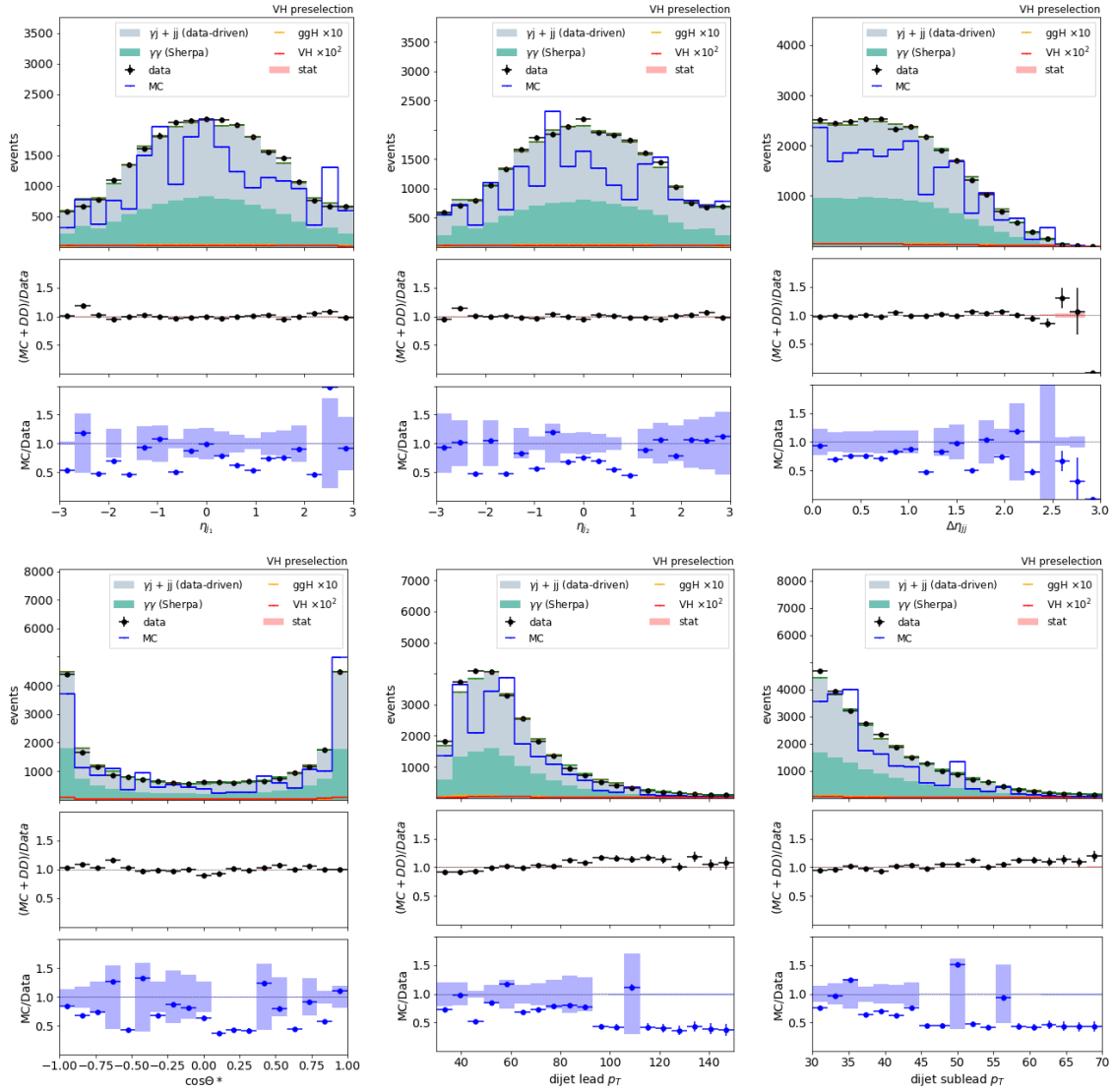

Figure C.20: 2017 validation of the data-driven method on various kinematics variables relevant to the VH BDT. The data points represent data outside the Higgs boson mass window (115-125 GeV and satisfying the VH preselection criteria. The DD+MC method is compared to data in the ratio plot with black dots while the MC-only method is compared to data in the ratio plot with blue dots.

C.4 VH BDT signal validation

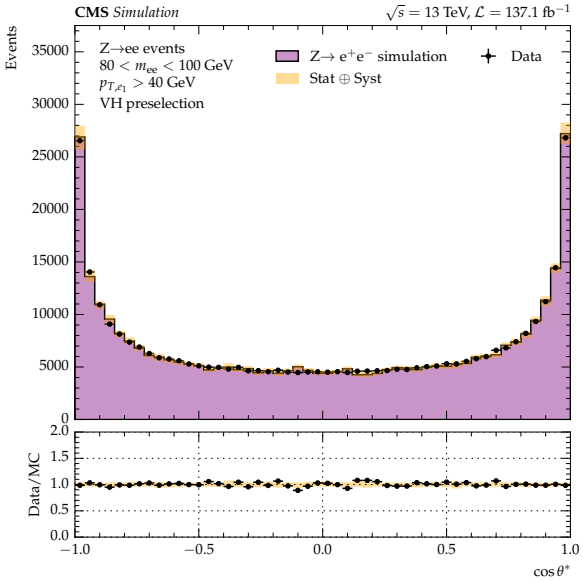

Figure C.21: VH BDT signal validation in the $Z \to ee$ control region. The DY simulation is compared to data taken in 2016, 2017, and 2018 (black points) for each variable.

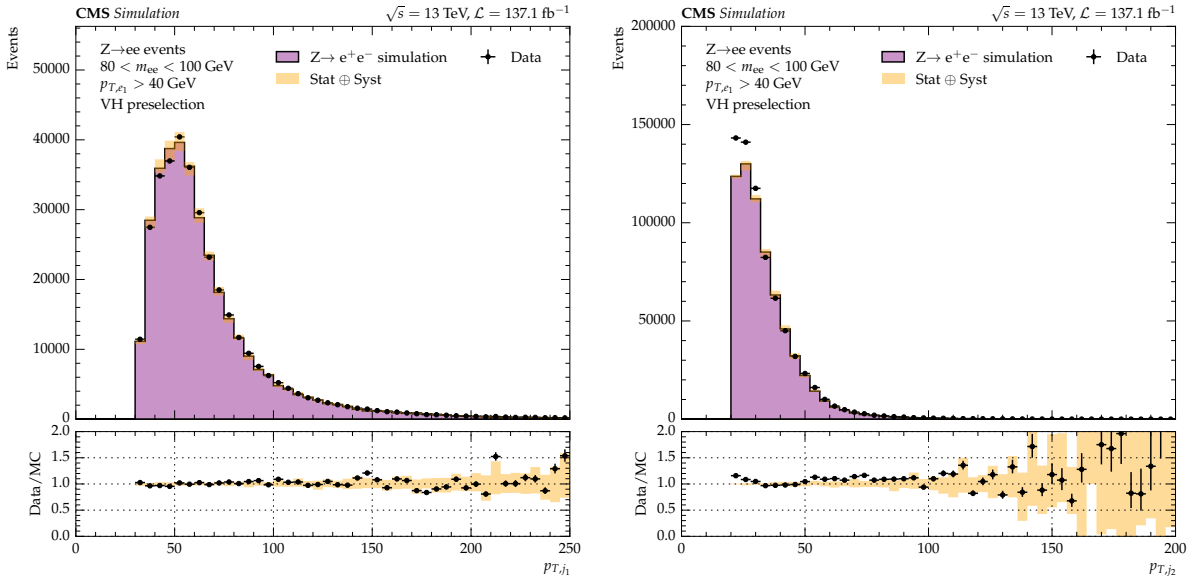

Figure C.22: VH BDT signal validation in the $Z \to ee$ control region. The DY simulation is compared to data taken in 2016, 2017, and 2018 (black points) for each variable.

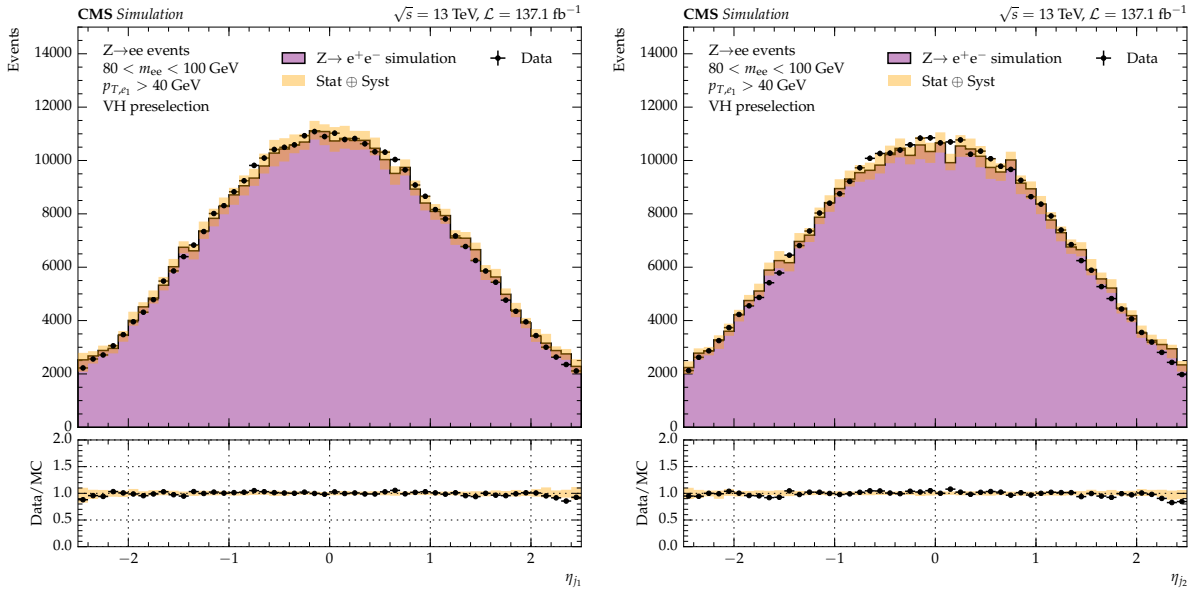

Figure C.23: VH BDT signal validation in the $Z \to ee$ control region. The DY simulation is compared to data taken in 2016, 2017, and 2018 (black points) for each variable.

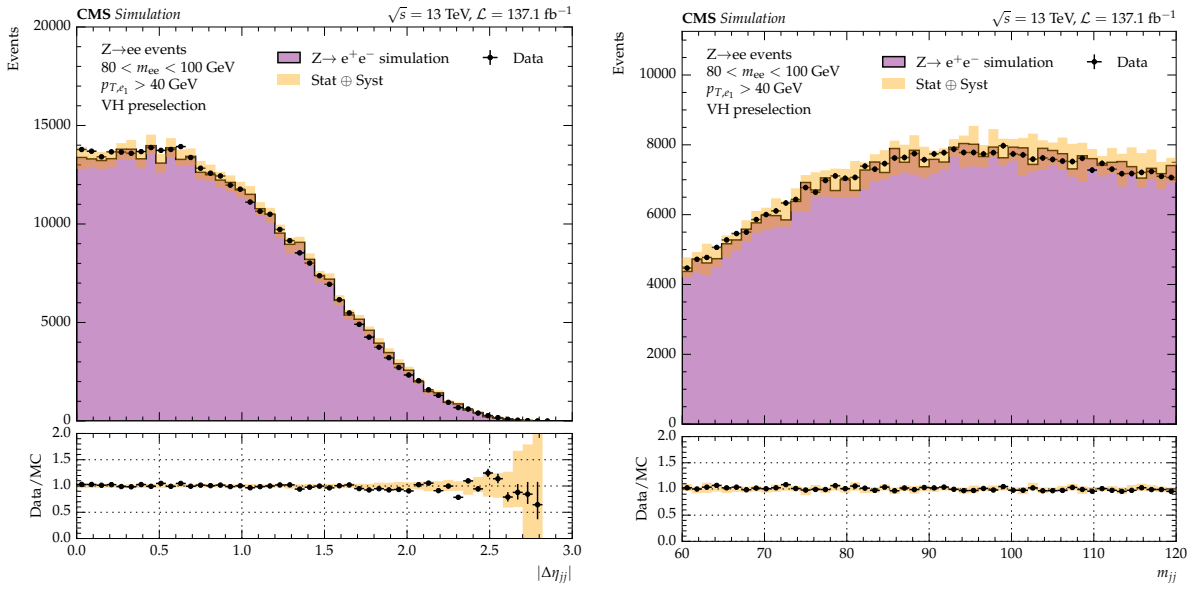

Figure C.24: VH BDT signal validation in the $Z \to ee$ control region. The DY simulation is compared to data taken in 2016, 2017, and 2018 (black points) for each variable.

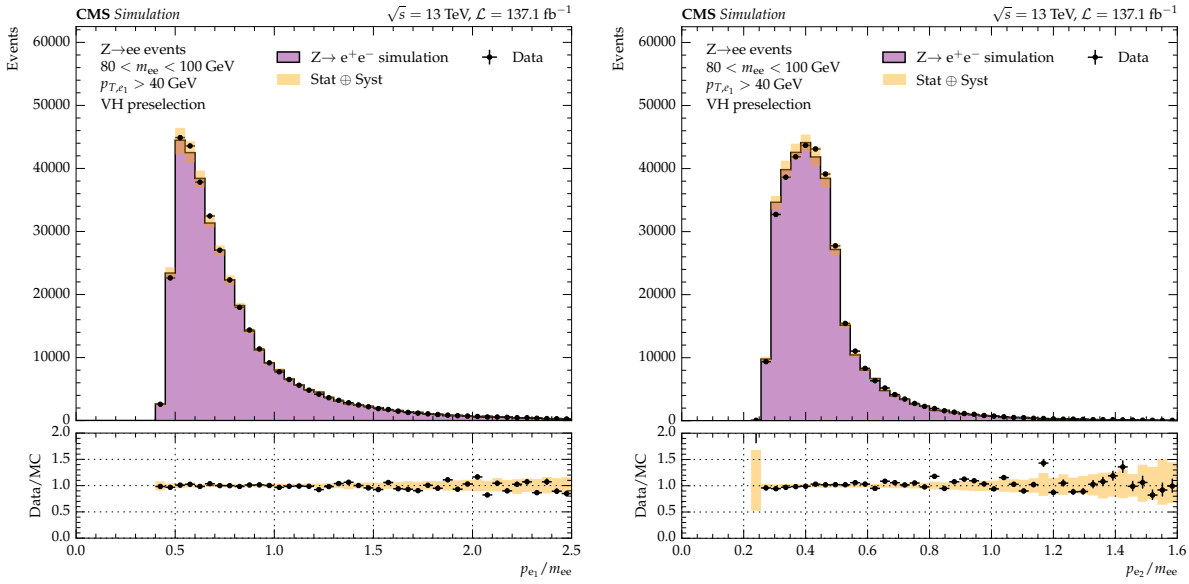

Figure C.25: VH BDT signal validation in the $Z \to ee$ control region. The DY simulation is compared to data taken in 2016, 2017, and 2018 (black points) for each variable.

Appendix D

D.1 tHq hadronic BDT signal validation

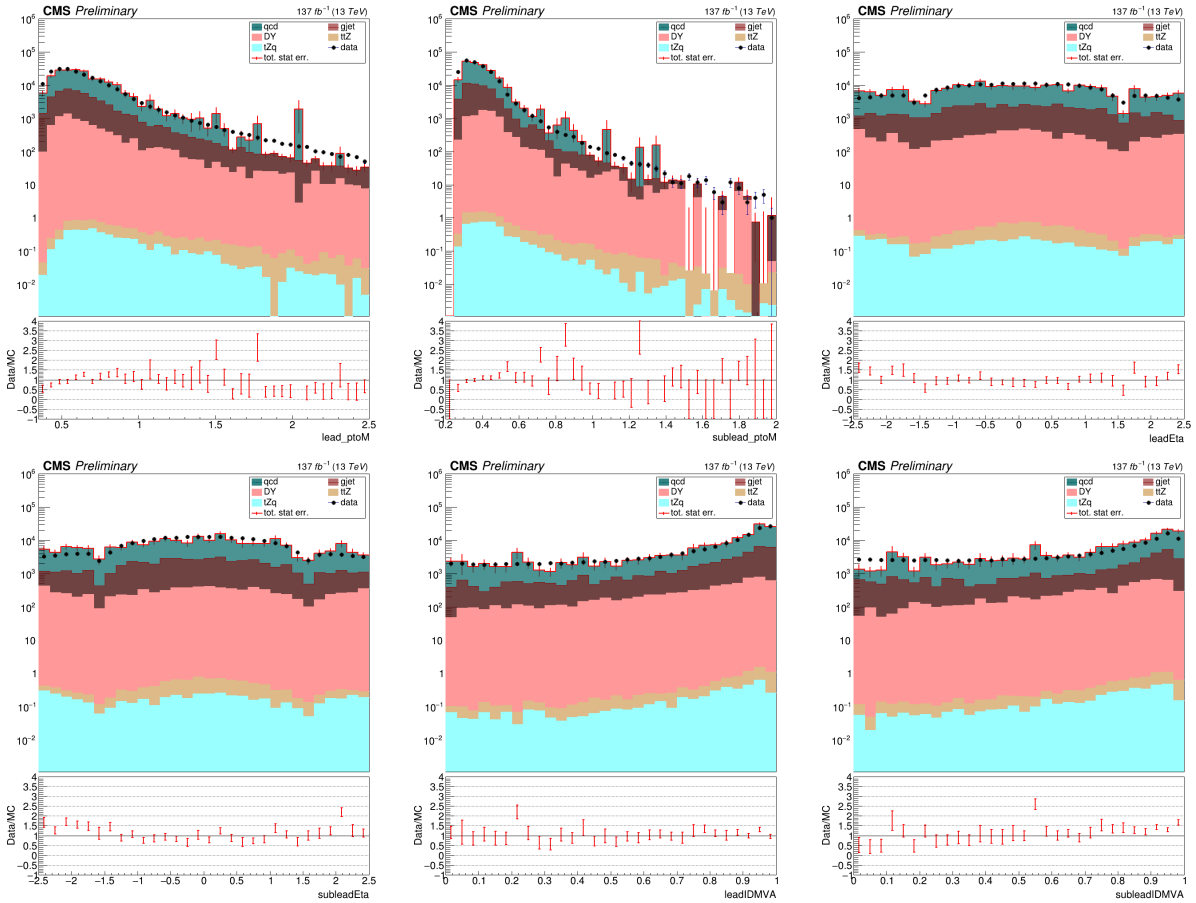

Figure D.1: tHq hadronic BDT signal validation in the $Z \to ee$ control region. The simulation (stacked coloured histograms) is compared to the combination of data taken in 2016, 2017, and 2018 (black points).

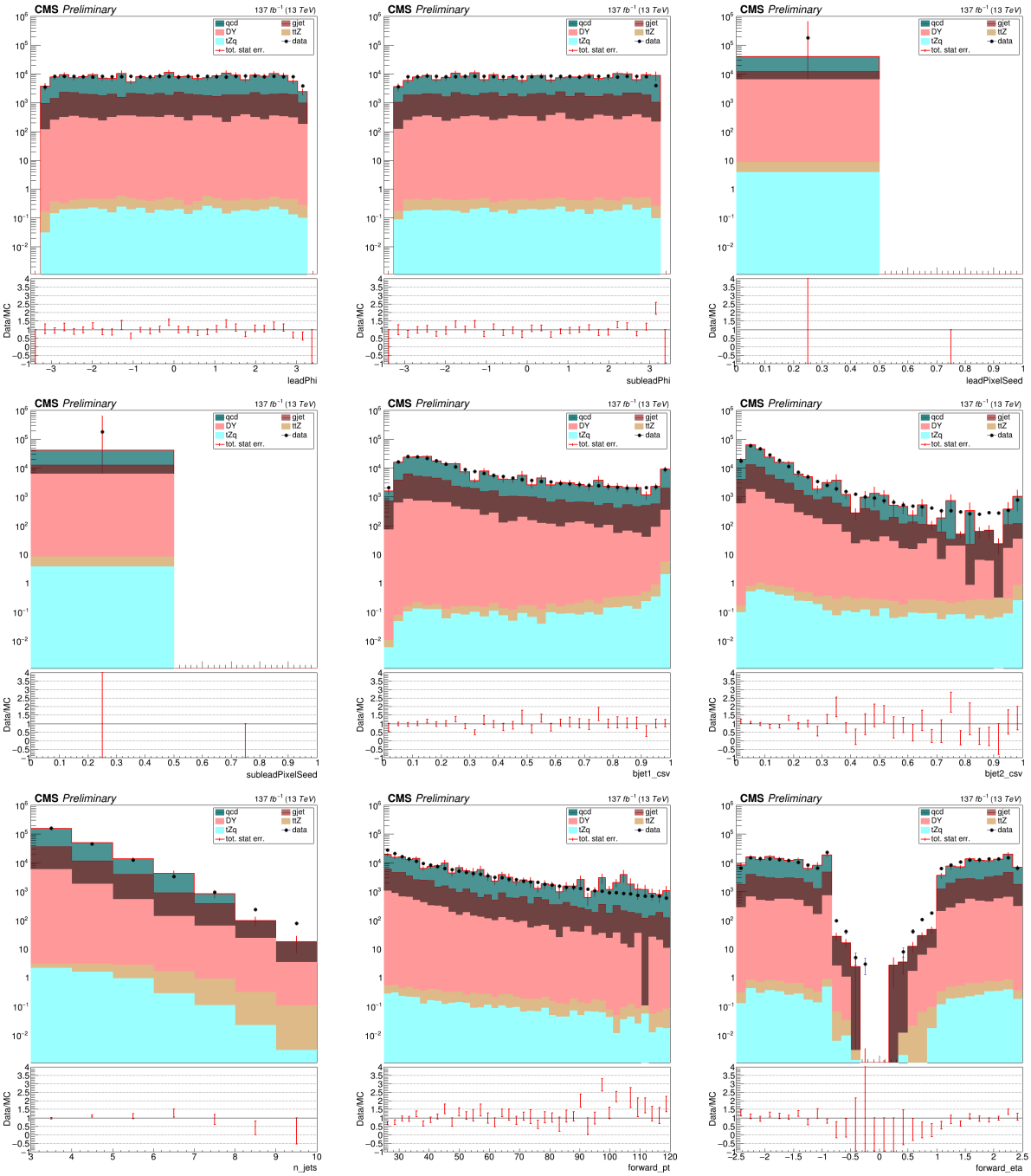

Figure D.2: tHq hadronic BDT signal validation in the $Z \rightarrow ee$ control region. The simulation (stacked coloured histograms) is compared to the combination of data taken in 2016, 2017, and 2018 (black points).

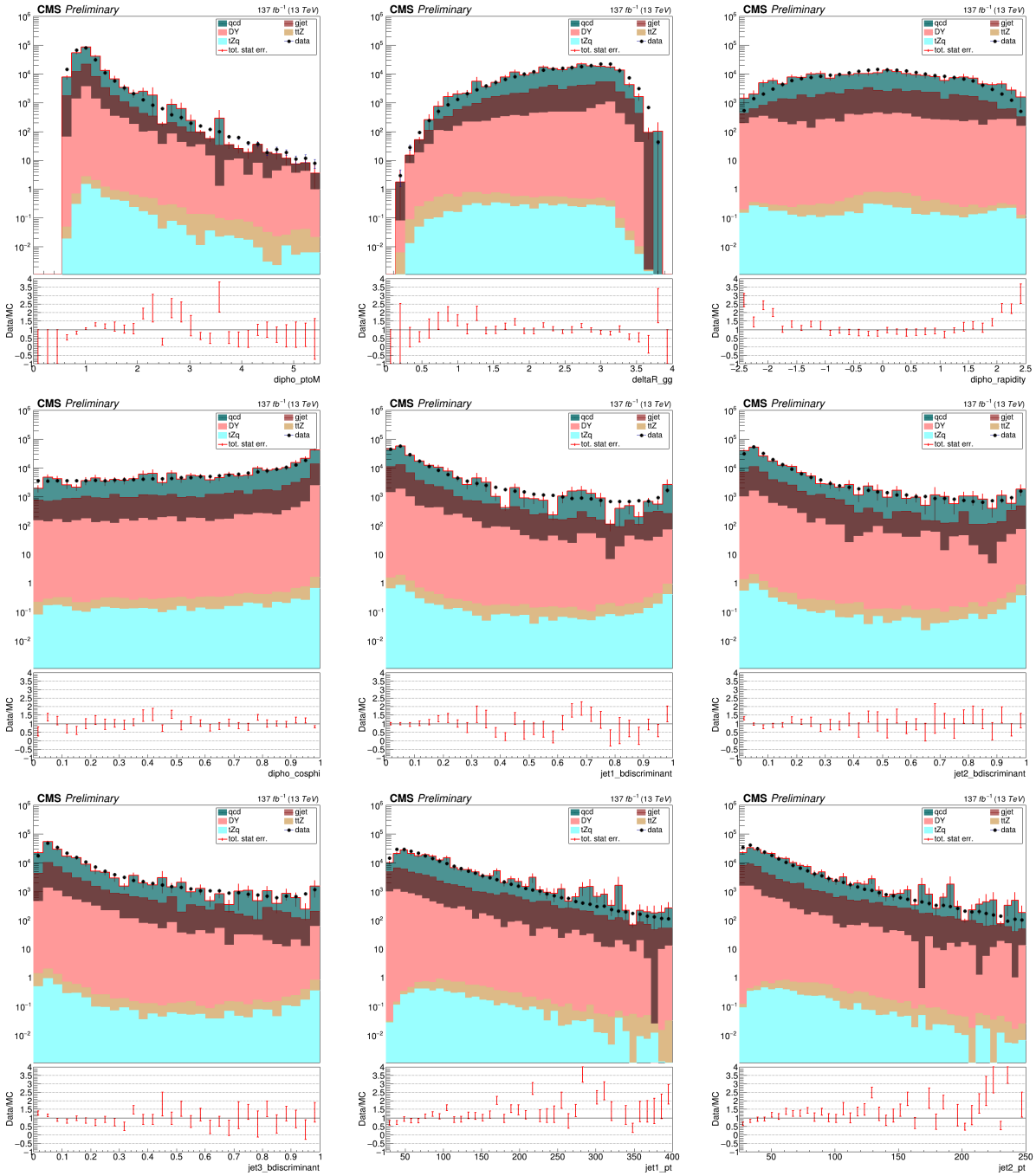

Figure D.3: tHq hadronic BDT signal validation in the $Z \to ee$ control region. The simulation (stacked coloured histograms) is compared to the combination of data taken in 2016, 2017, and 2018 (black points).

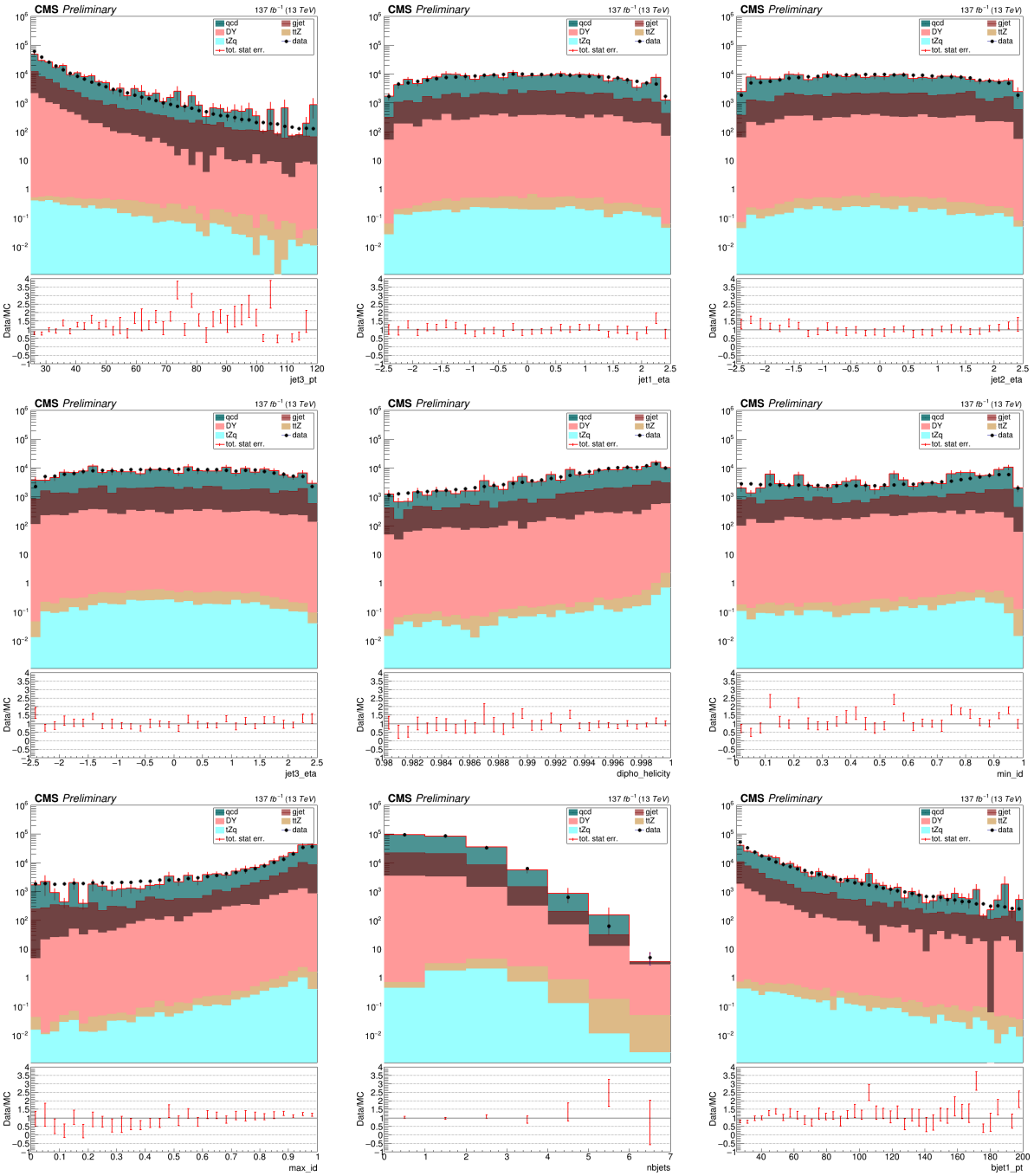

Figure D.4: tHq hadronic BDT signal validation in the $Z \to ee$ control region. The simulation (stacked coloured histograms) is compared to the combination of data taken in 2016, 2017, and 2018 (black points).

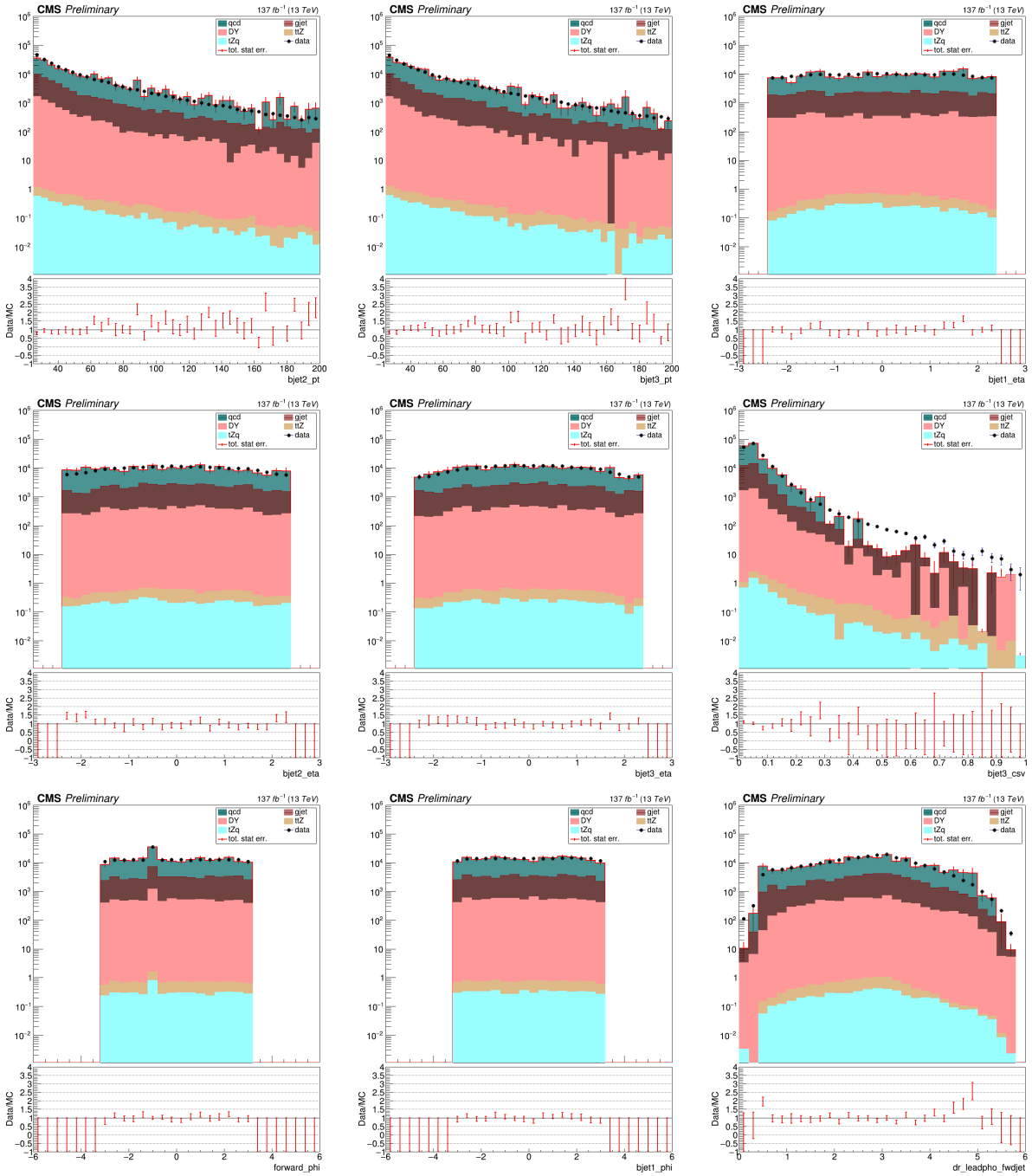

Figure D.5: tHq hadronic BDT signal validation in the $Z \to ee$ control region. The simulation (stacked coloured histograms) is compared to the combination of data taken in 2016, 2017, and 2018 (black points).

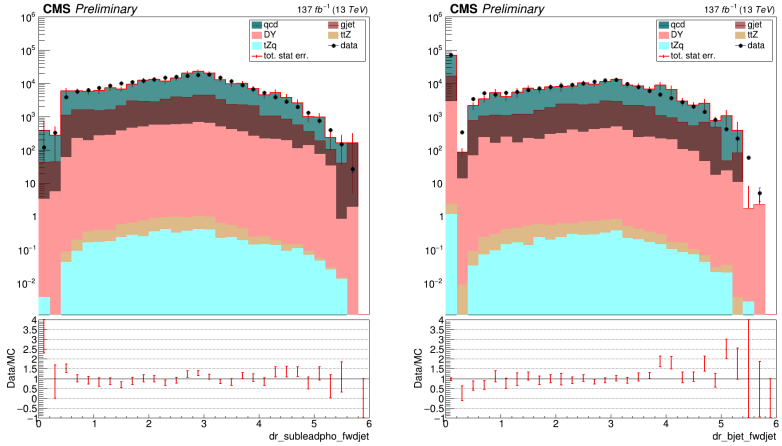

Figure D.6: tHq hadronic BDT signal validation in the $Z \to ee$ control region. The simulation (stacked coloured histograms) is compared to the combination of data taken in 2016, 2017, and 2018 (black points).

Appendix E

E.1 Signal models

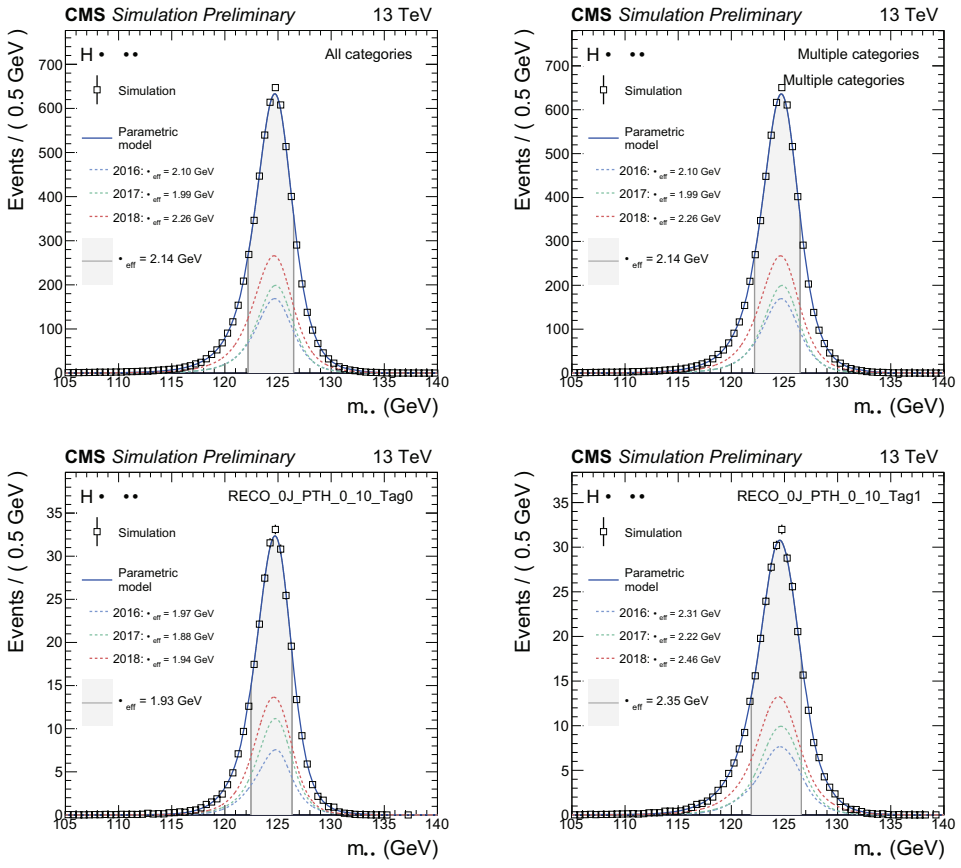

Figure E.1: Signal models for the STXS Stage 1.2 analysis categories.

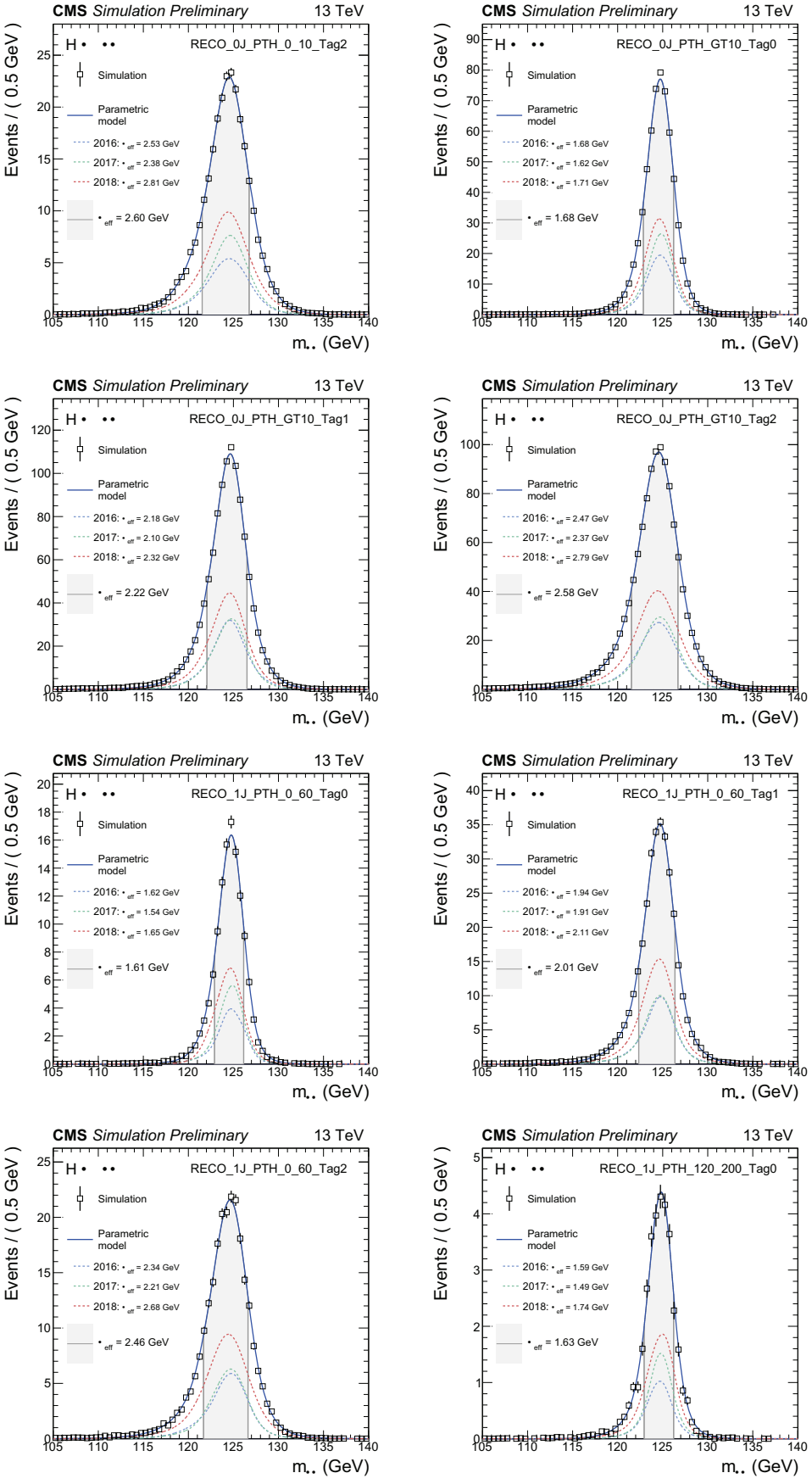

Figure E.2: Signal models for the STXS Stage 1.2 analysis categories.

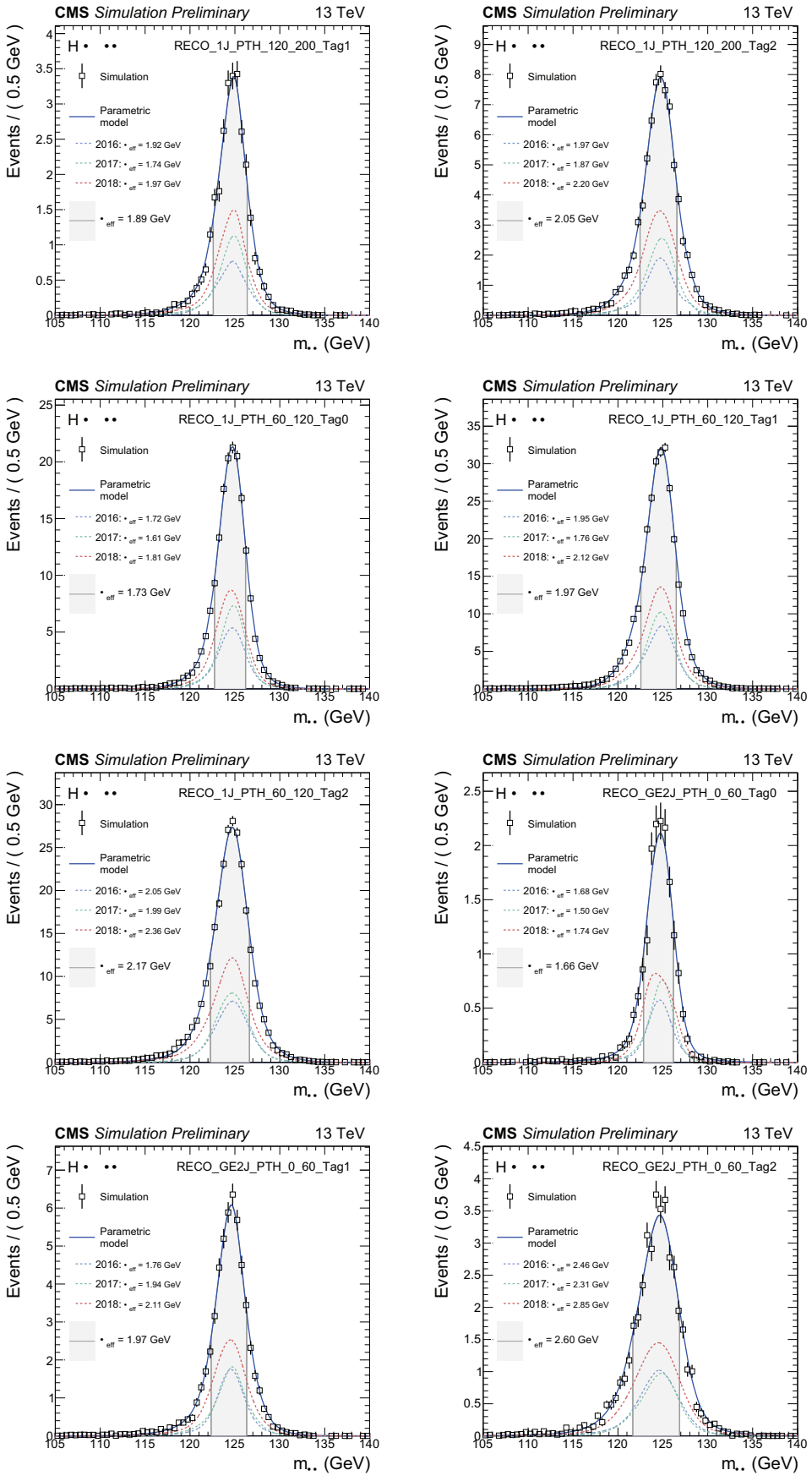

Figure E.3: Signal models for the STXS Stage 1.2 analysis categories.

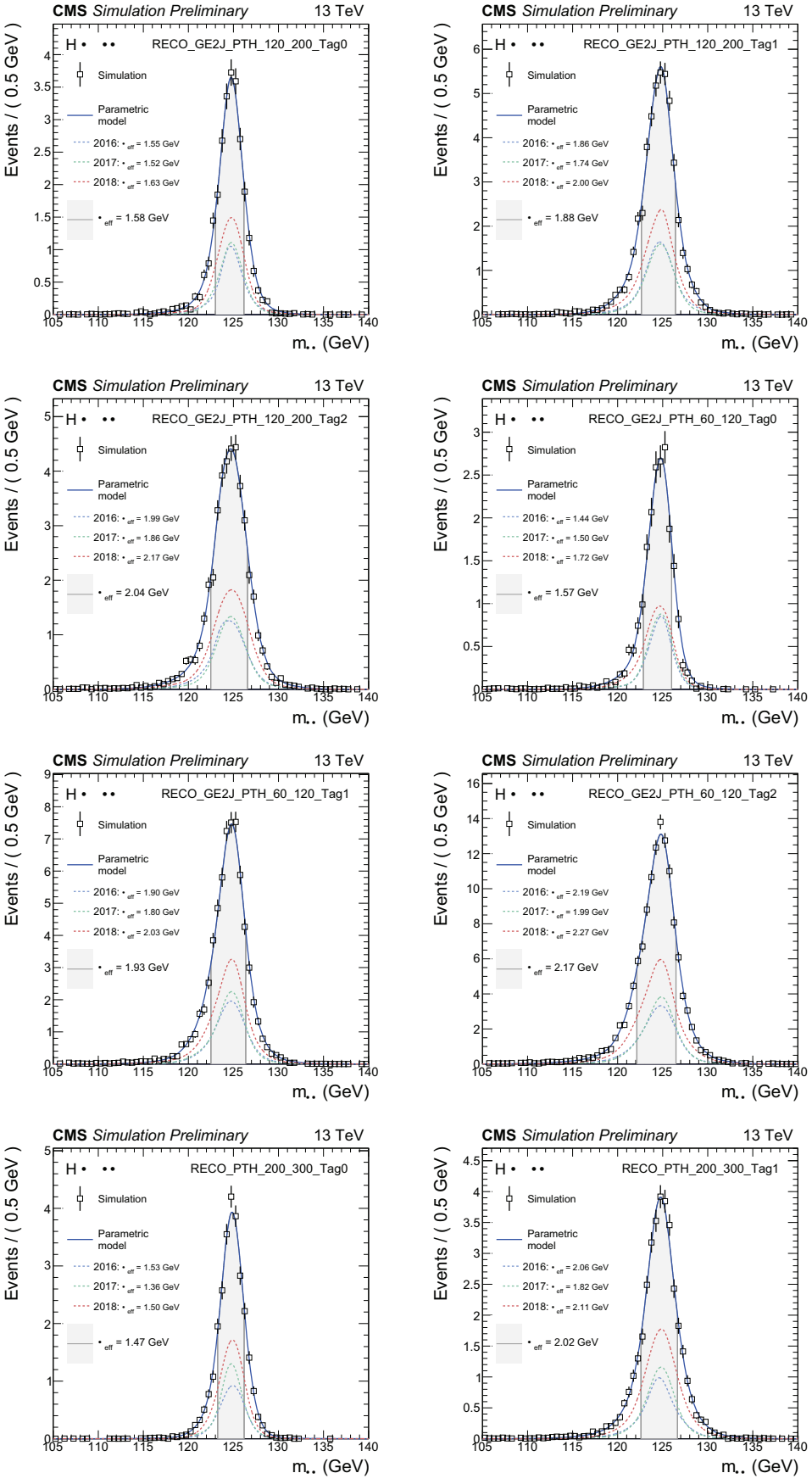

Figure E.4: Signal models for the STXS Stage 1.2 analysis categories.

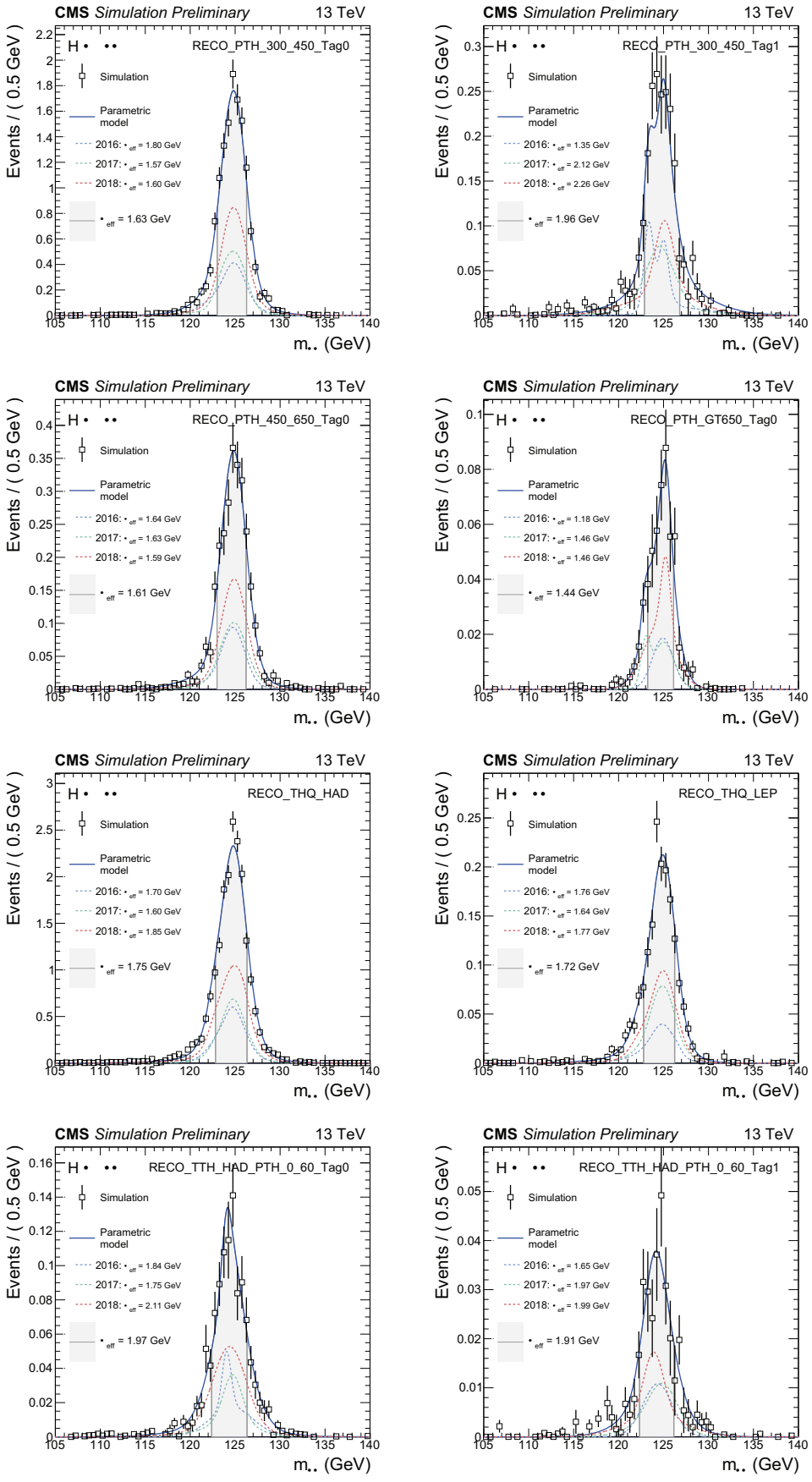

Figure E.5: Signal models for the STXS Stage 1.2 analysis categories.

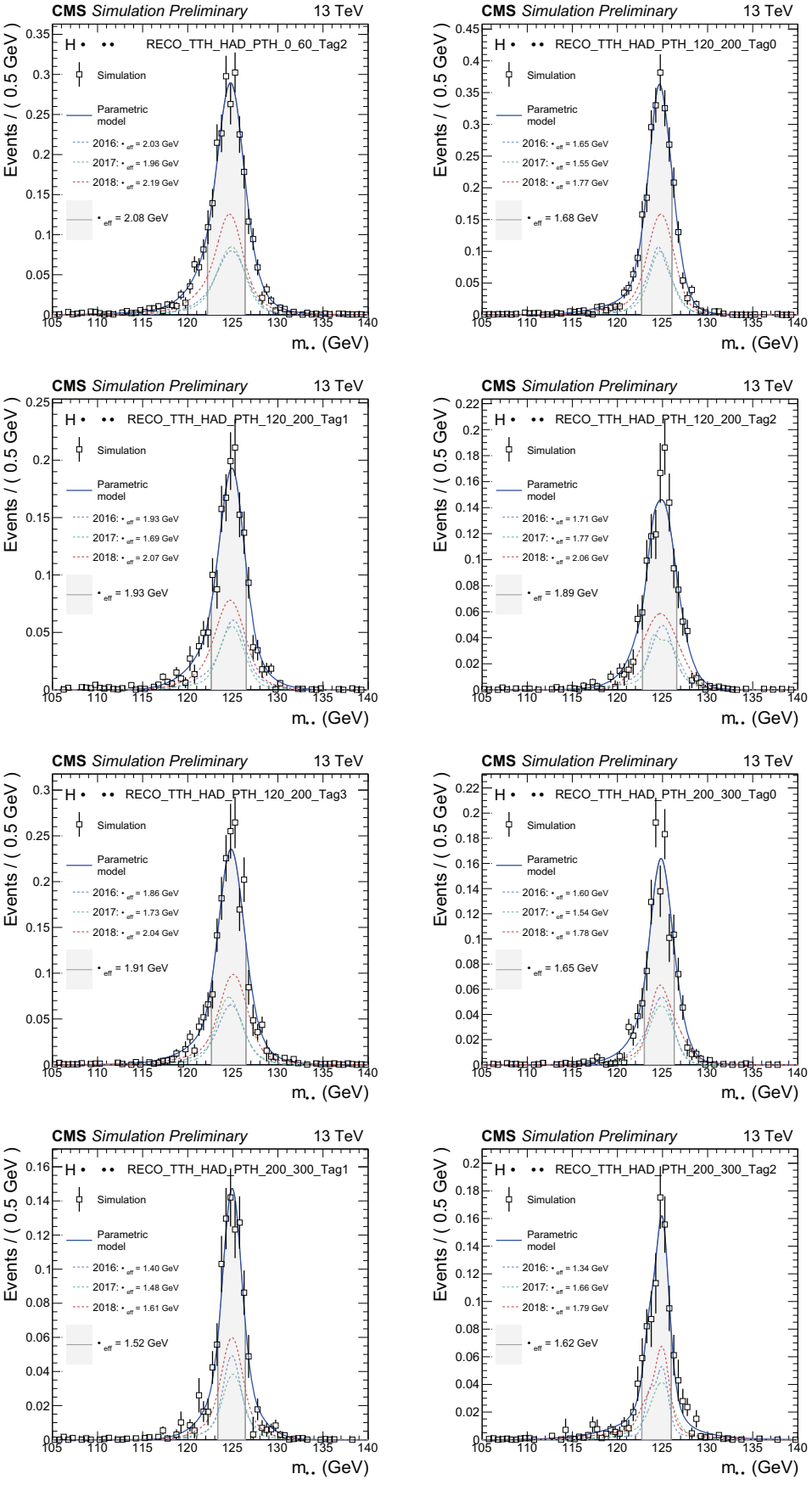

Figure E.6: Signal models for the STXS Stage 1.2 analysis categories.

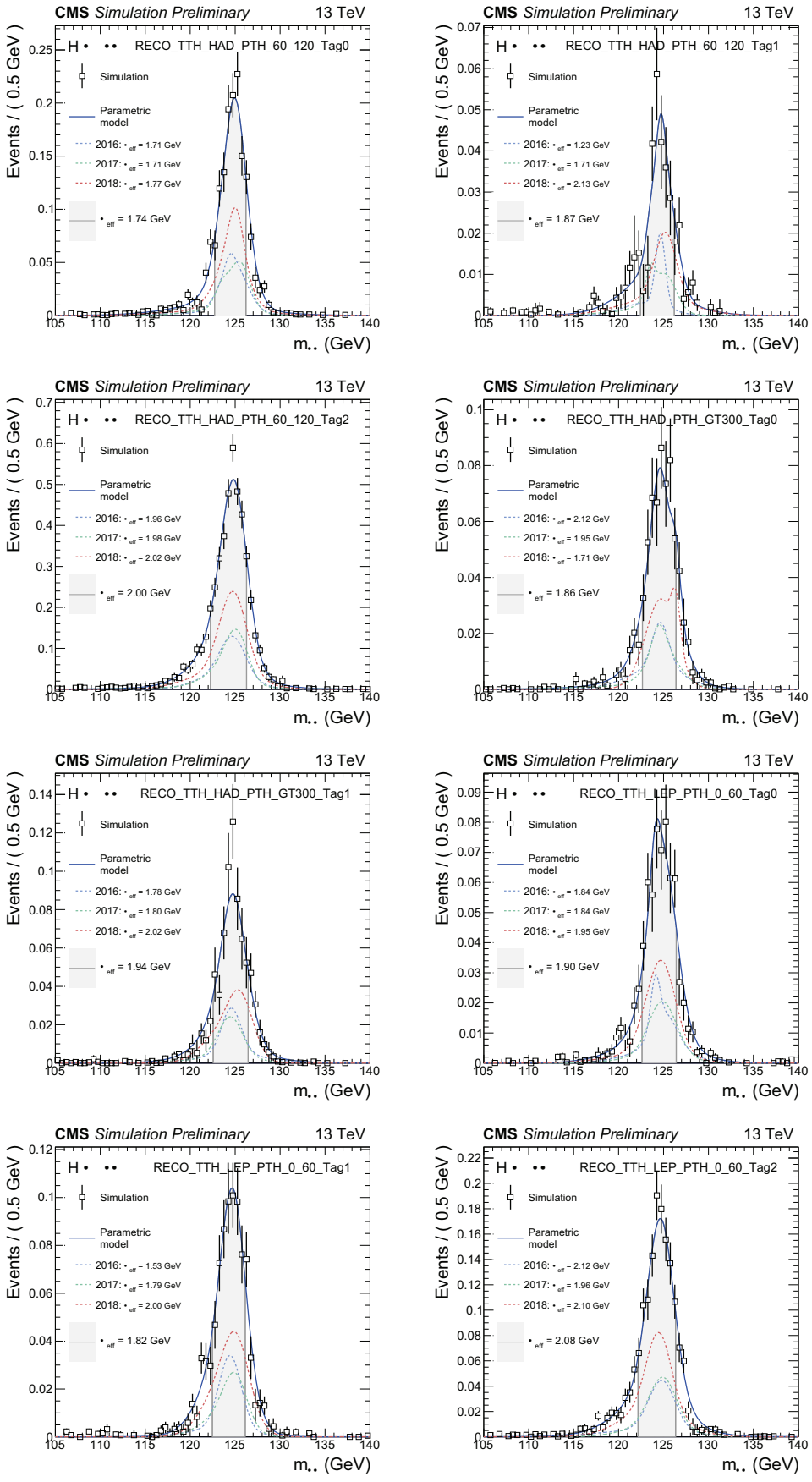

Figure E.7: Signal models for the STXS Stage 1.2 analysis categories.

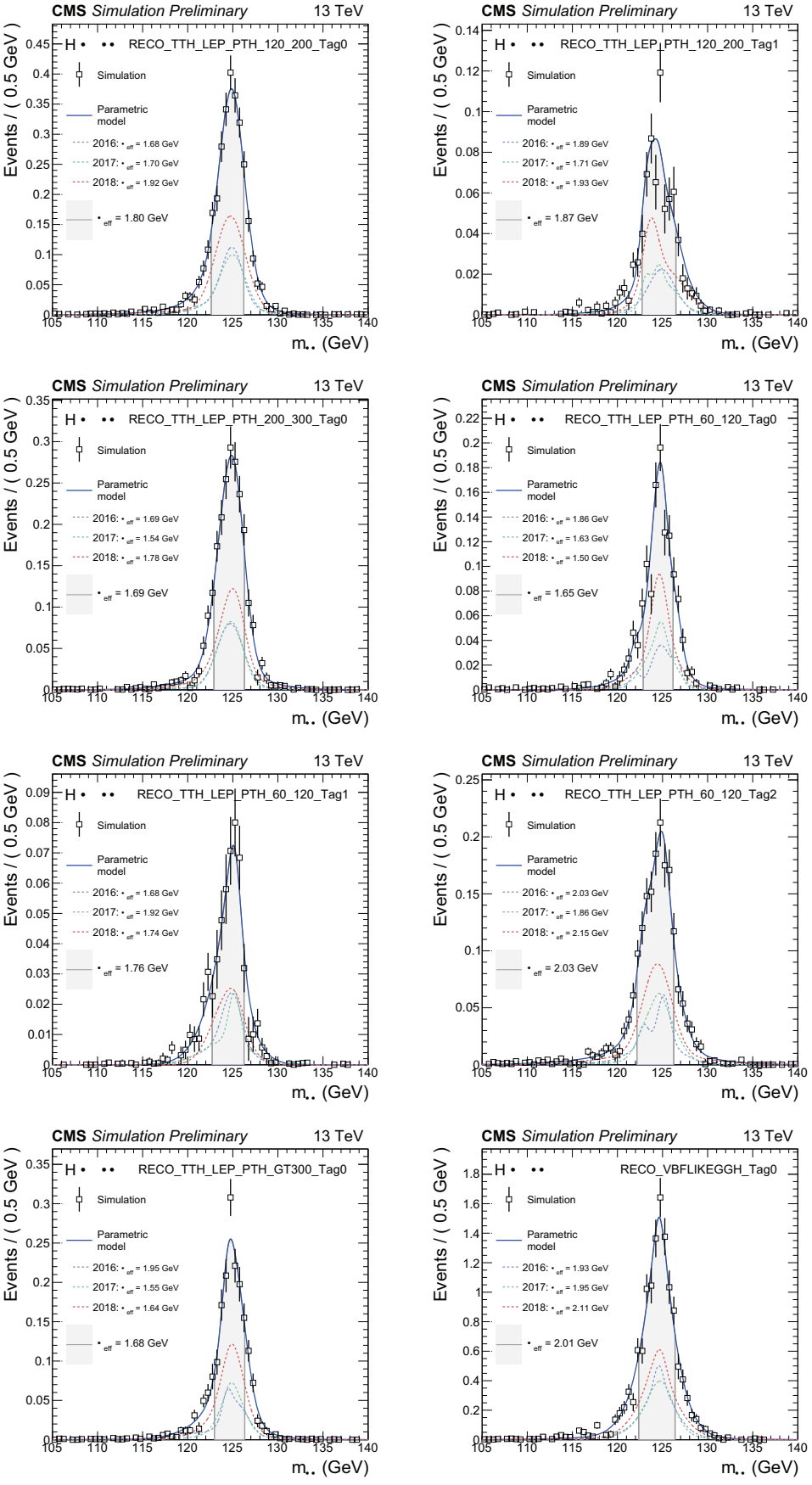

Figure E.8: Signal models for the STXS Stage 1.2 analysis categories.

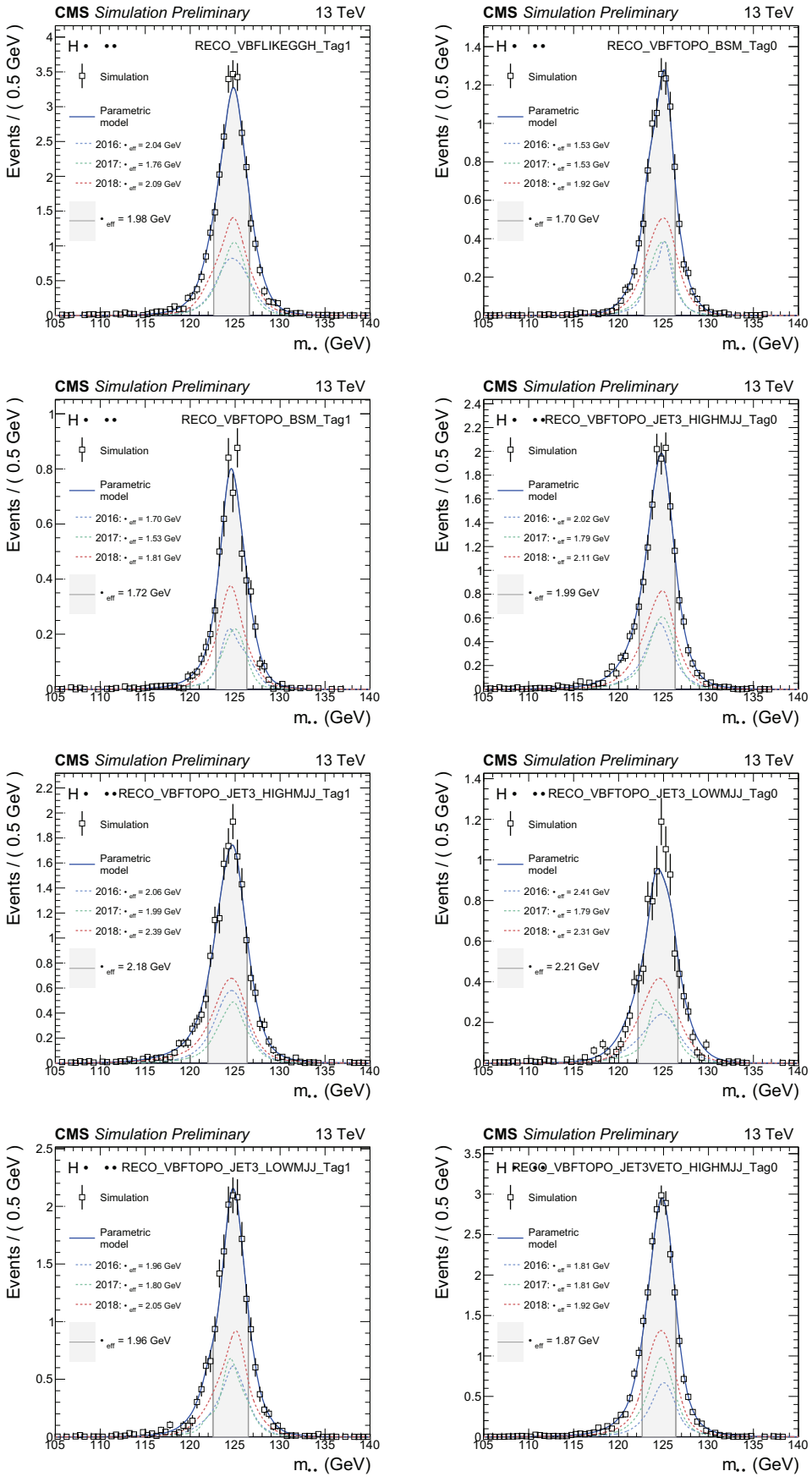

Figure E.9: Signal models for the STXS Stage 1.2 analysis categories.

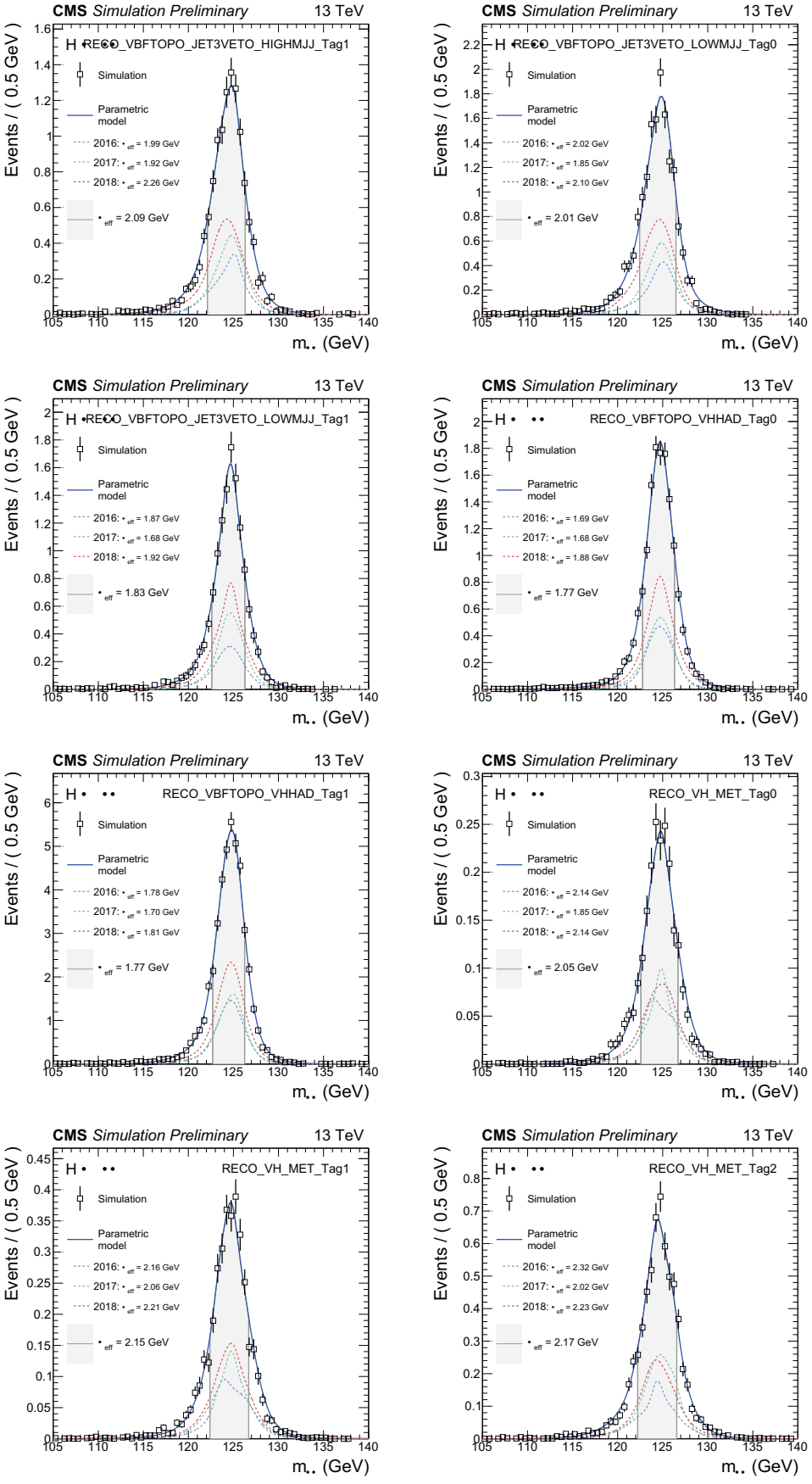

Figure E.10: Signal models for the STXS Stage 1.2 analysis categories.

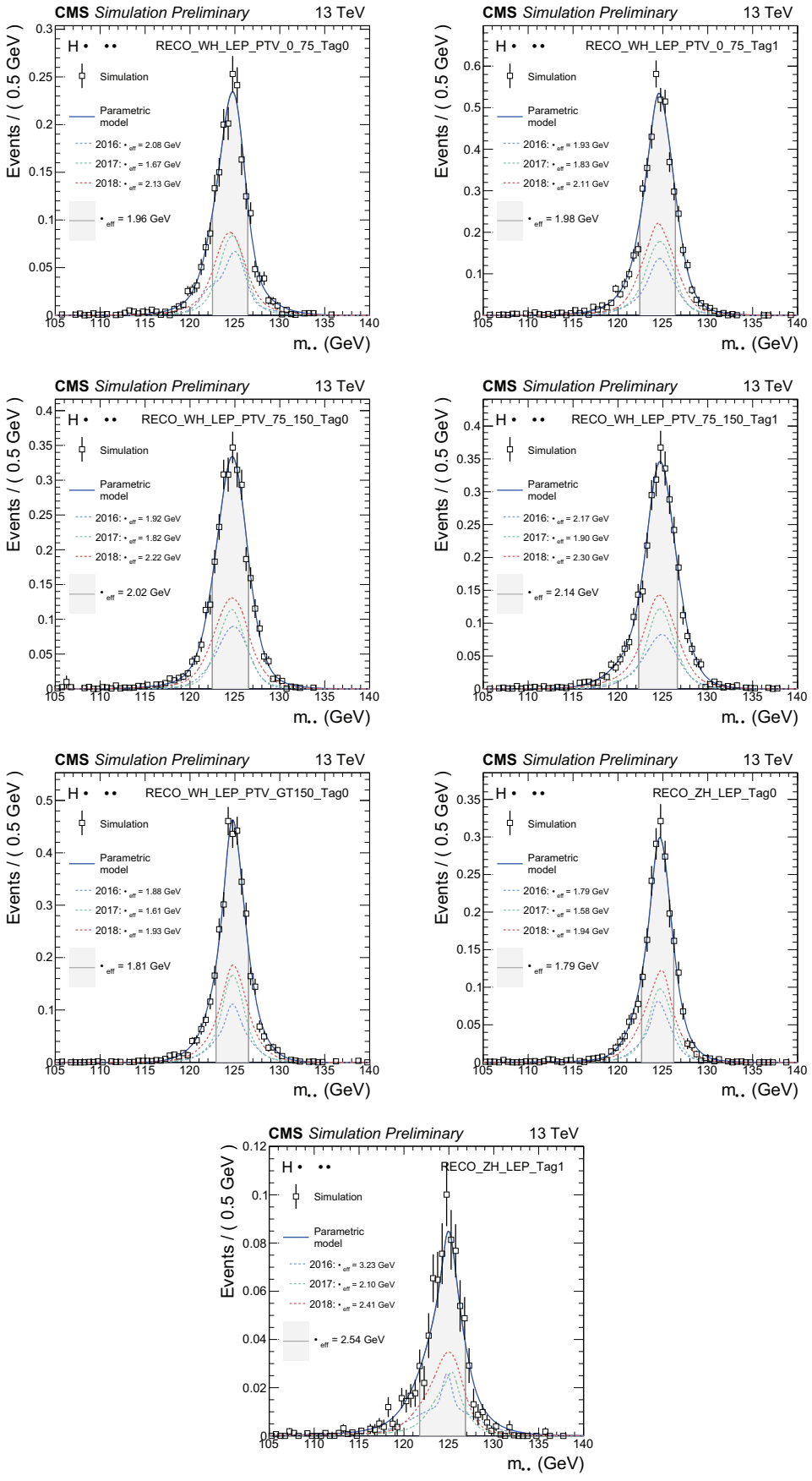

Figure E.11: Signal models for the STXS Stage 1.2 analysis categories.

Appendix F

F.1 Background models

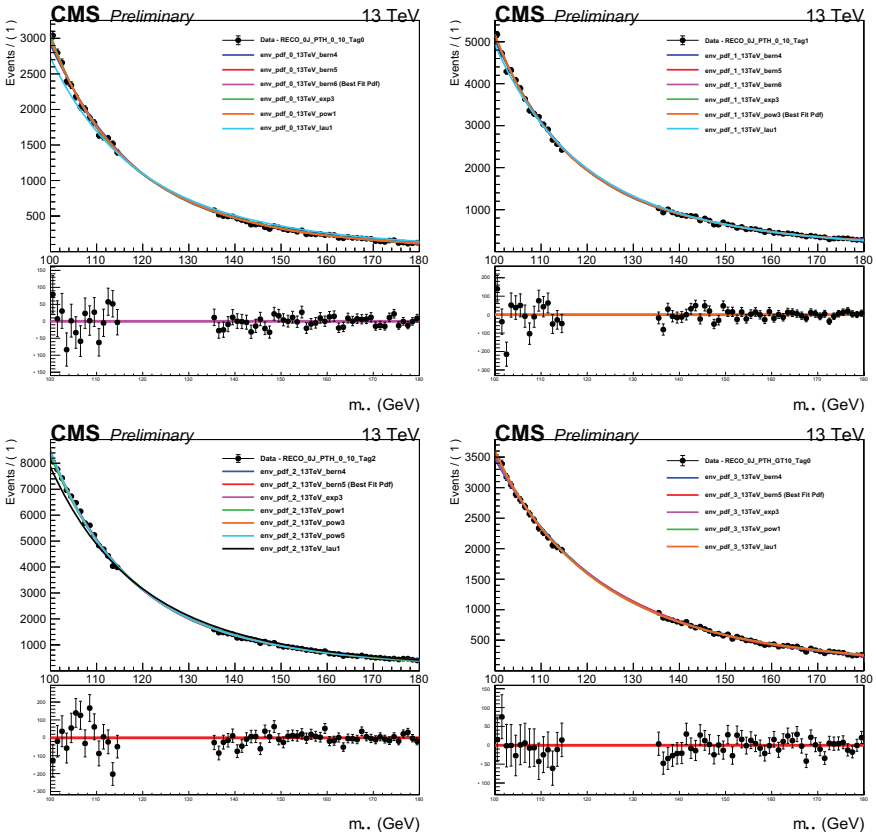

Figure F.1: Set of functions chosen to fit the background in STXS Stage 1.2 analysis categories using the discrete profiling method.

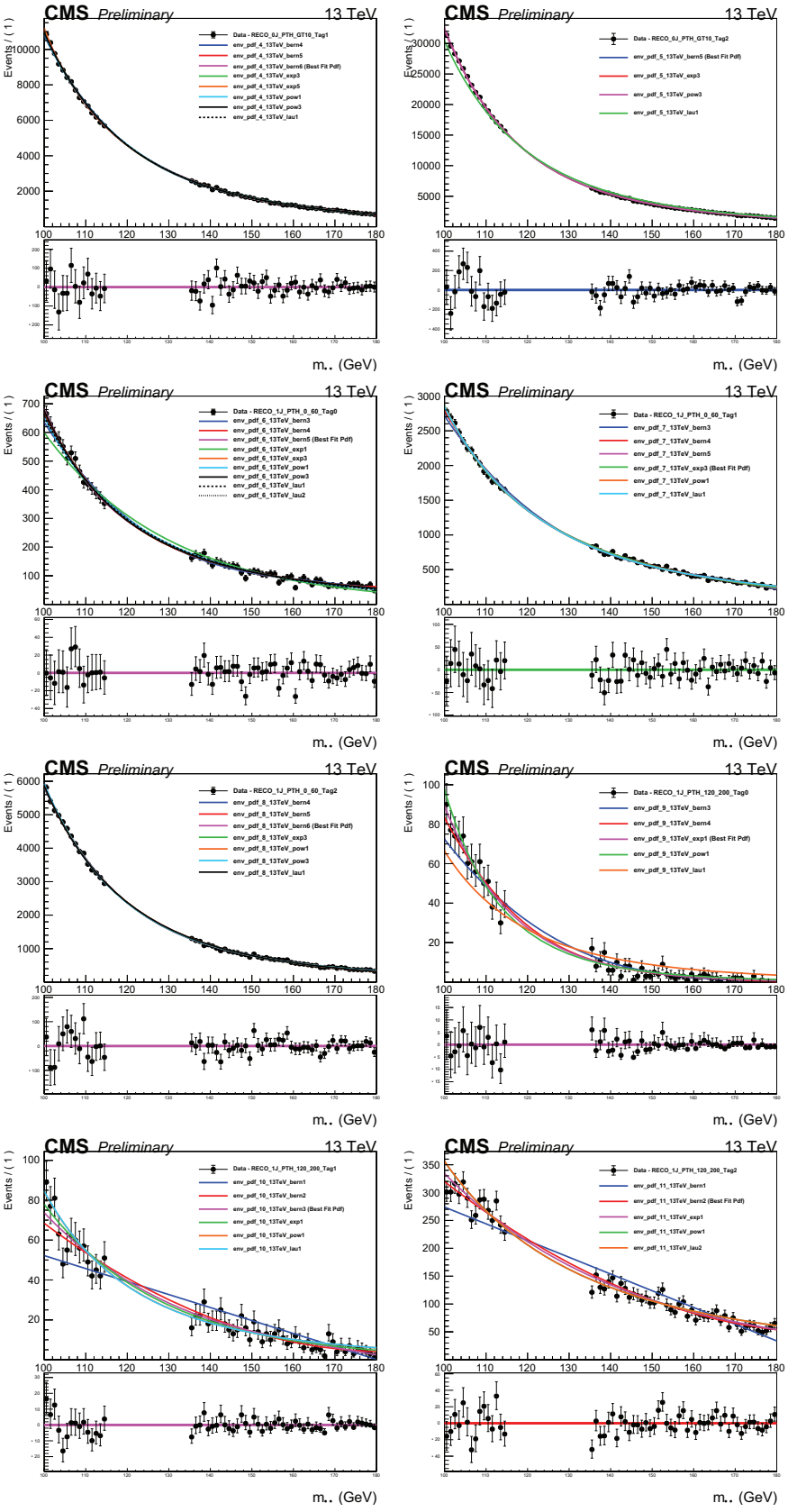

Figure F.2: Set of functions chosen to fit the background in STXS Stage 1.2 analysis categories using the discrete profiling method.

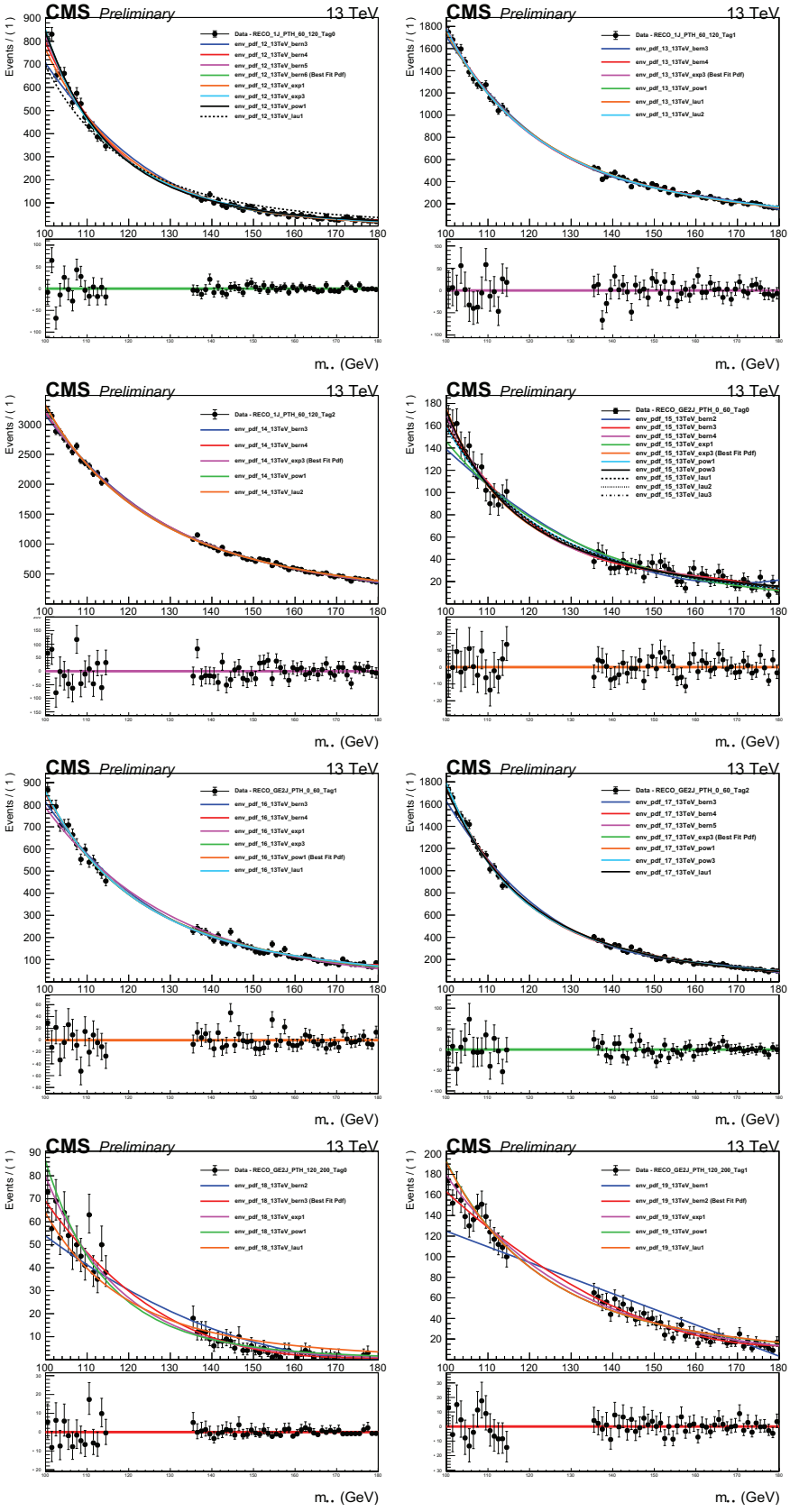

Figure F.3: Set of functions chosen to fit the background in STXS Stage 1.2 analysis categories using the discrete profiling method.

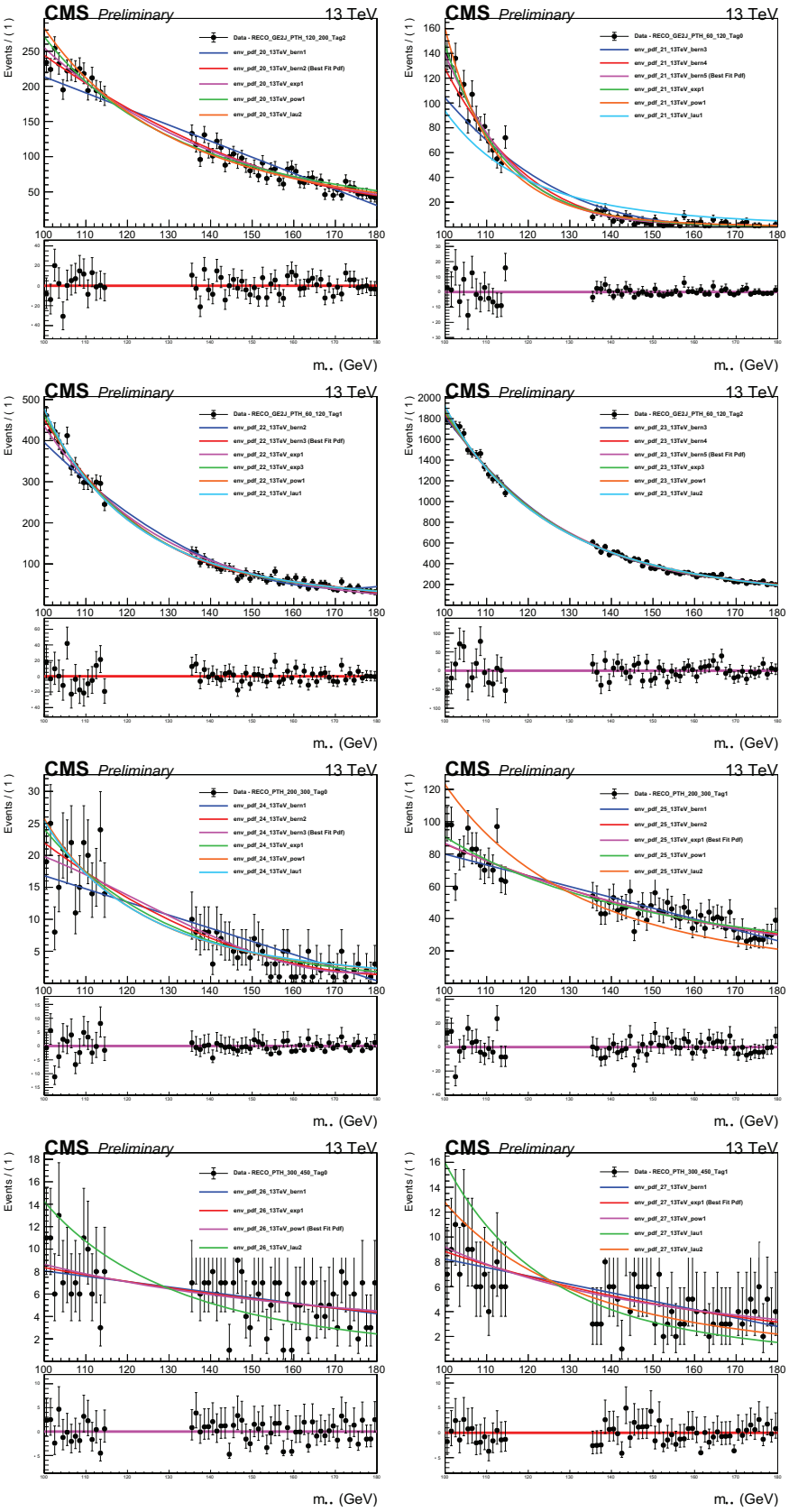

Figure F.4: Set of functions chosen to fit the background in STXS Stage 1.2 analysis categories using the discrete profiling method.

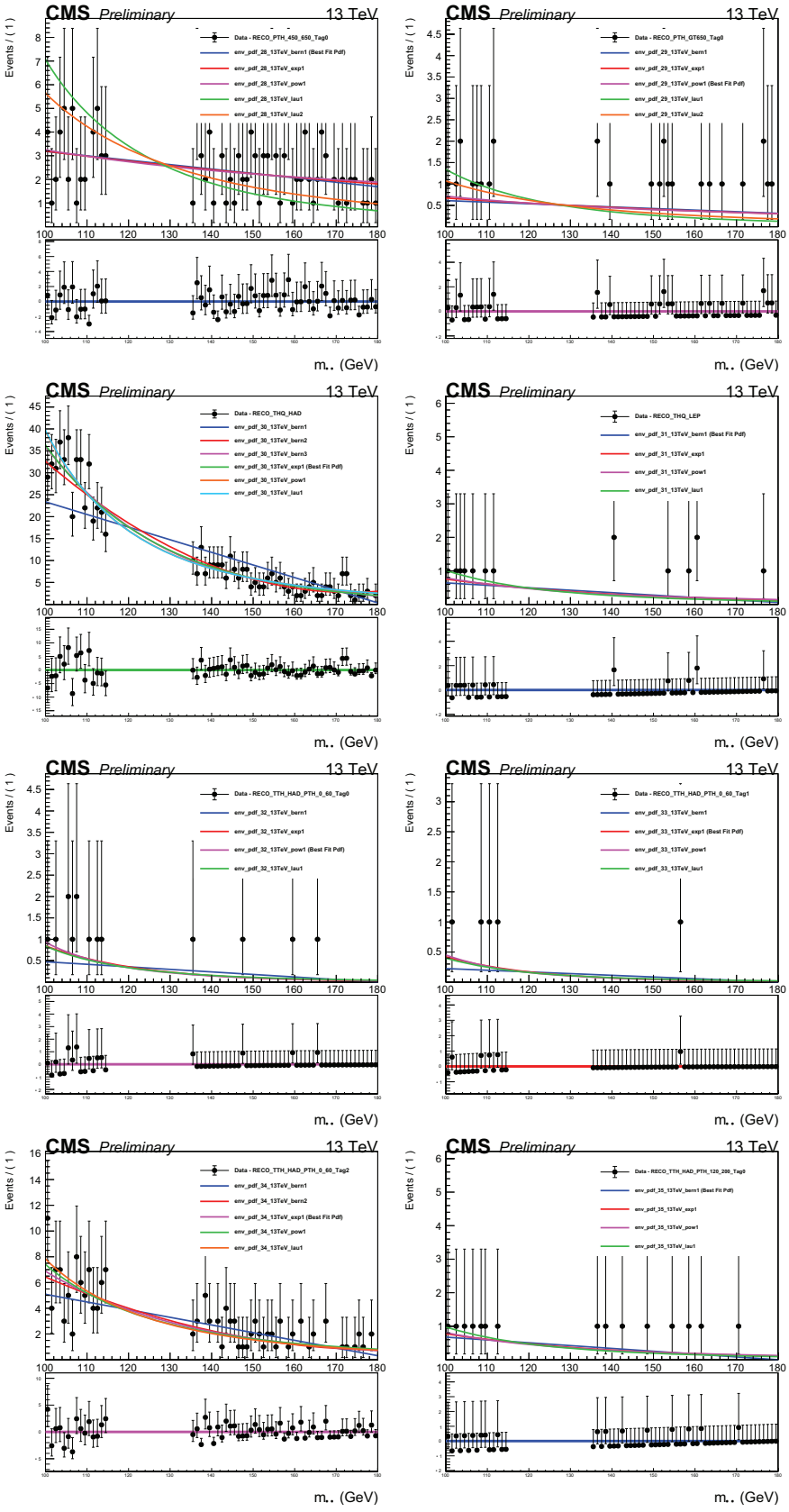

Figure F.5: Set of functions chosen to fit the background in STXS Stage 1.2 analysis categories using the discrete profiling method.

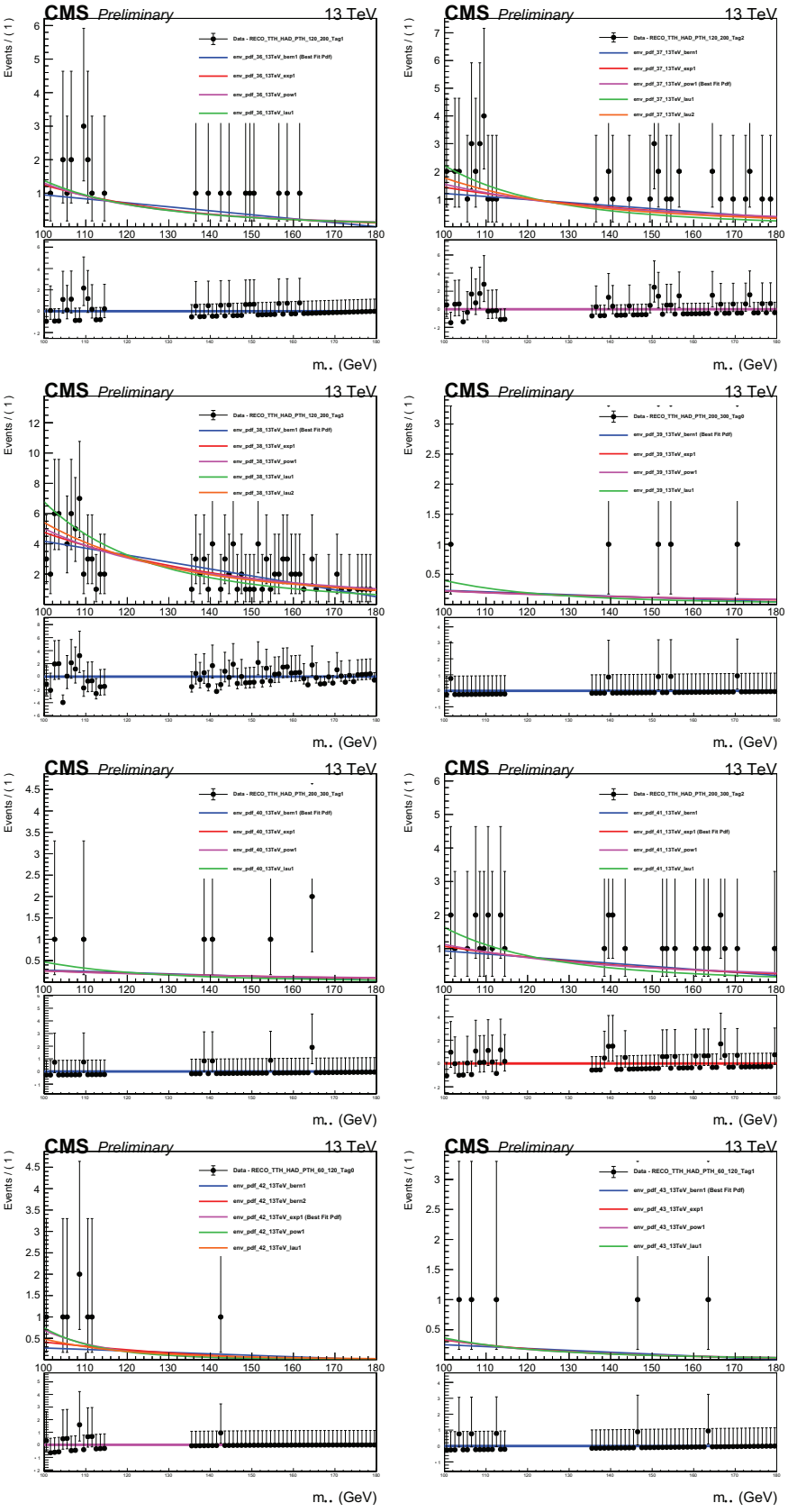

Figure F.6: Set of functions chosen to fit the background in STXS Stage 1.2 analysis categories using the discrete profiling method.

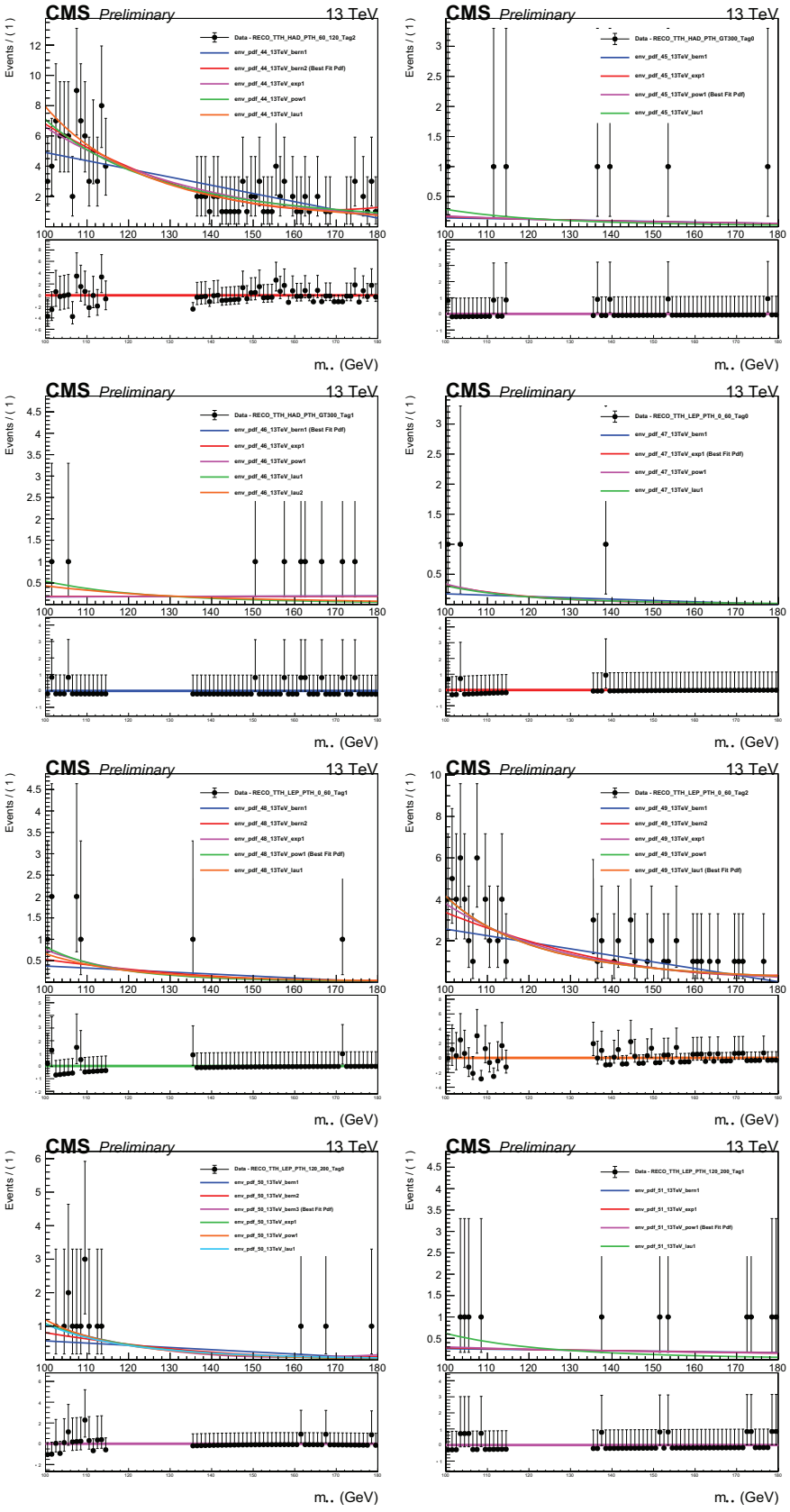

Figure F.7: Set of functions chosen to fit the background in STXS Stage 1.2 analysis categories using the discrete profiling method.

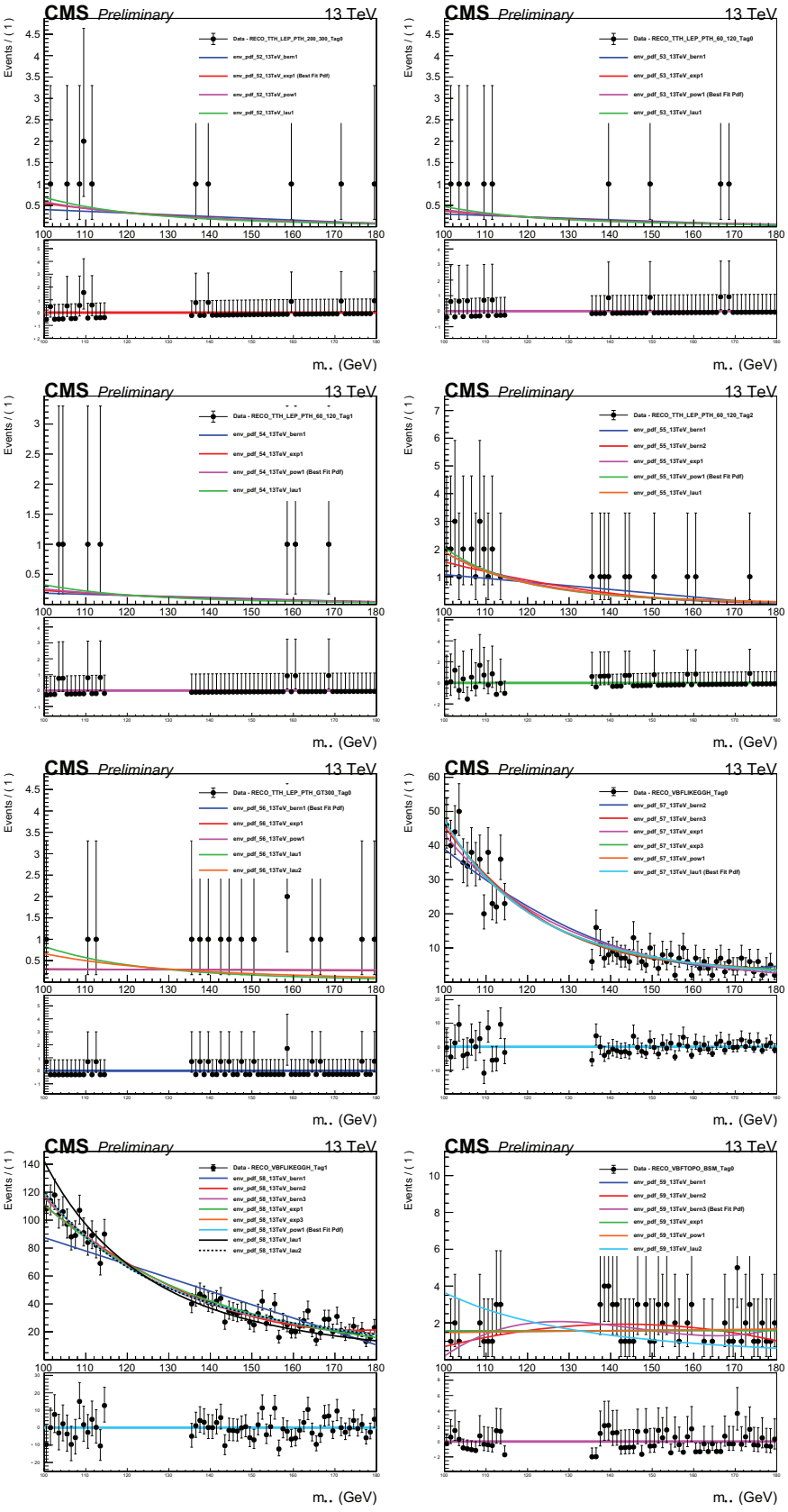

Figure F.8: Set of functions chosen to fit the background in STXS Stage 1.2 analysis categories using the discrete profiling method.

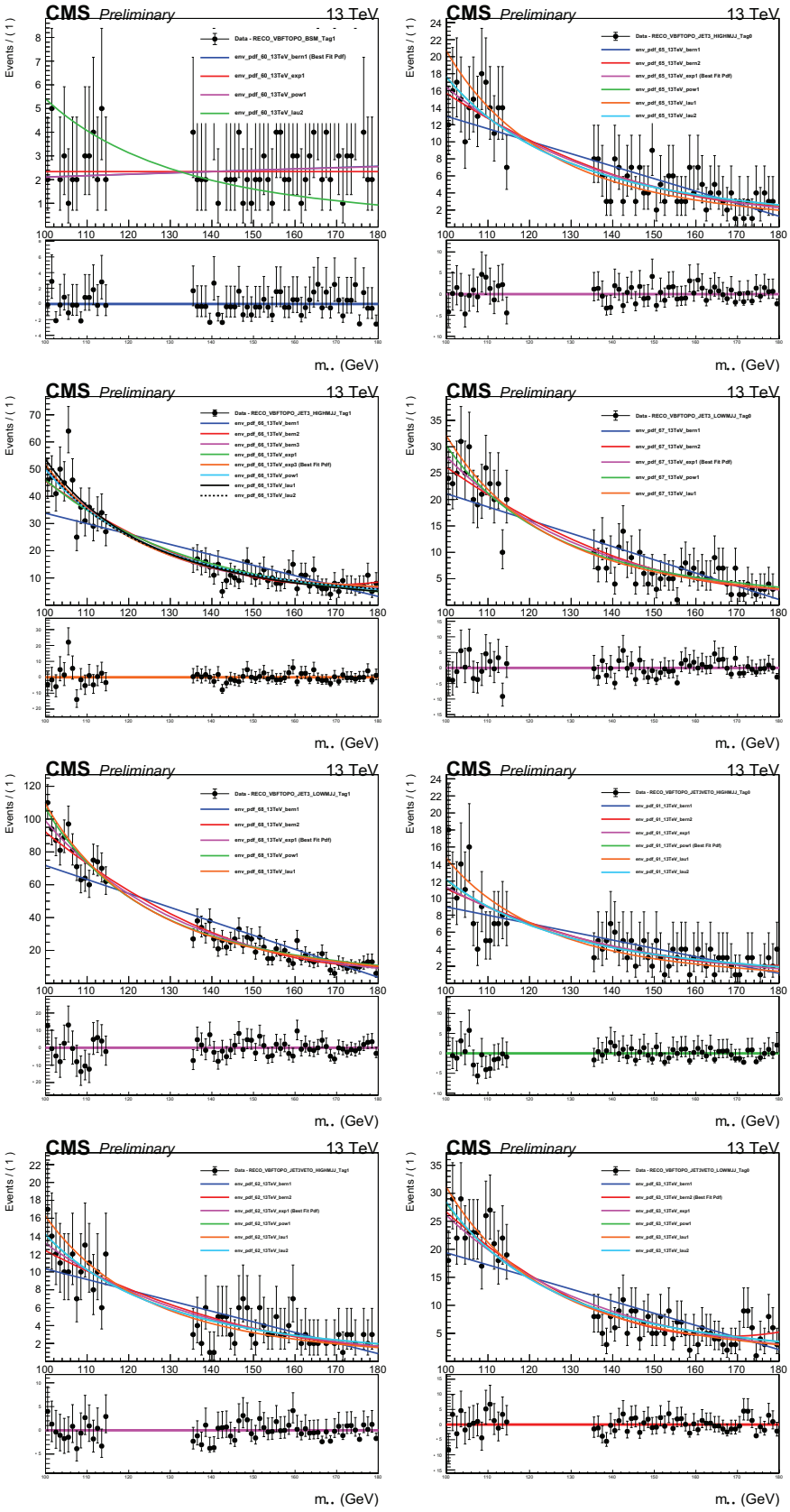

Figure F.9: Set of functions chosen to fit the background in STXS Stage 1.2 analysis categories using the discrete profiling method.

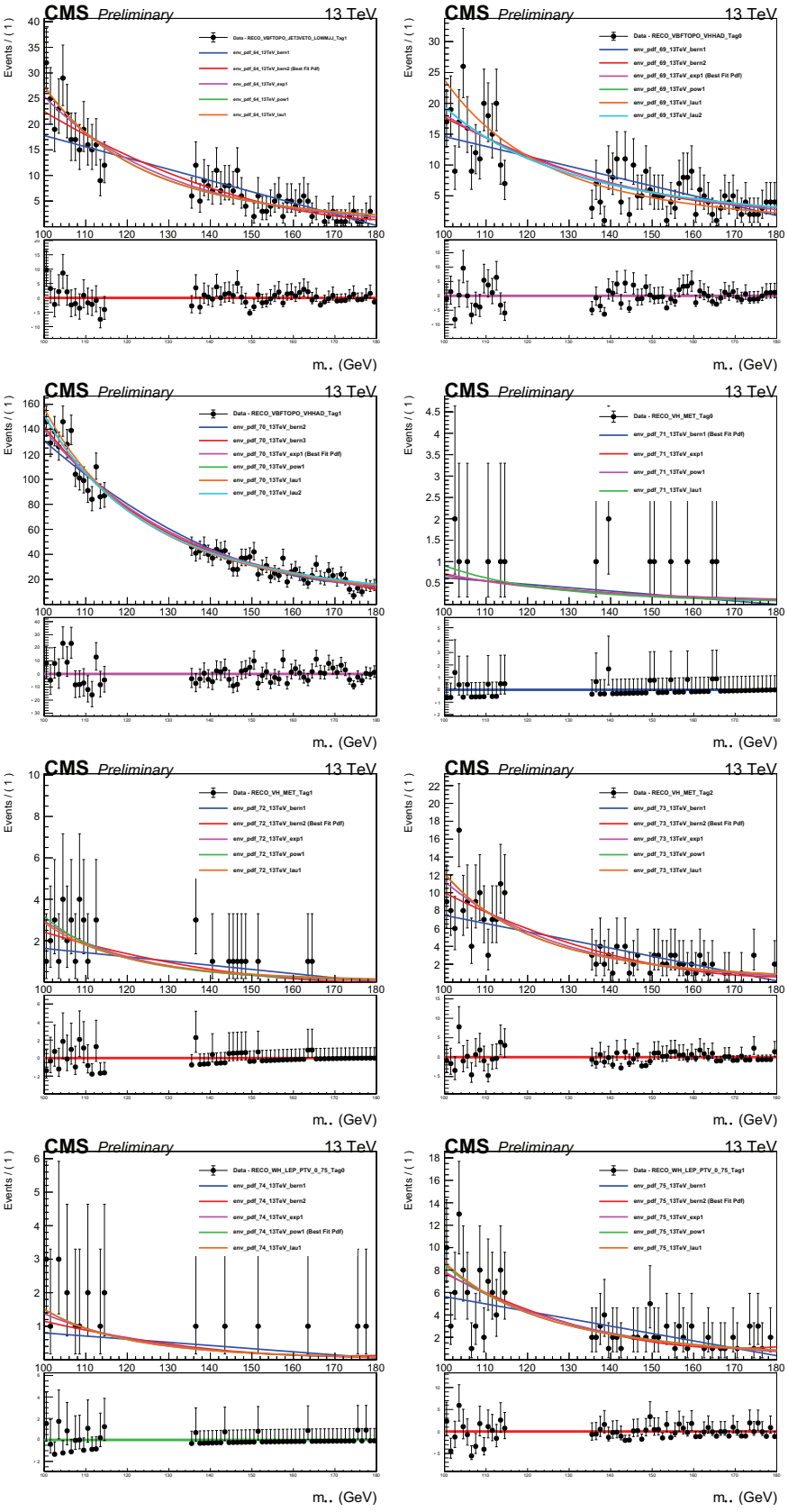

Figure F.10: Set of functions chosen to fit the background in STXS Stage 1.2 analysis categories using the discrete profiling method.

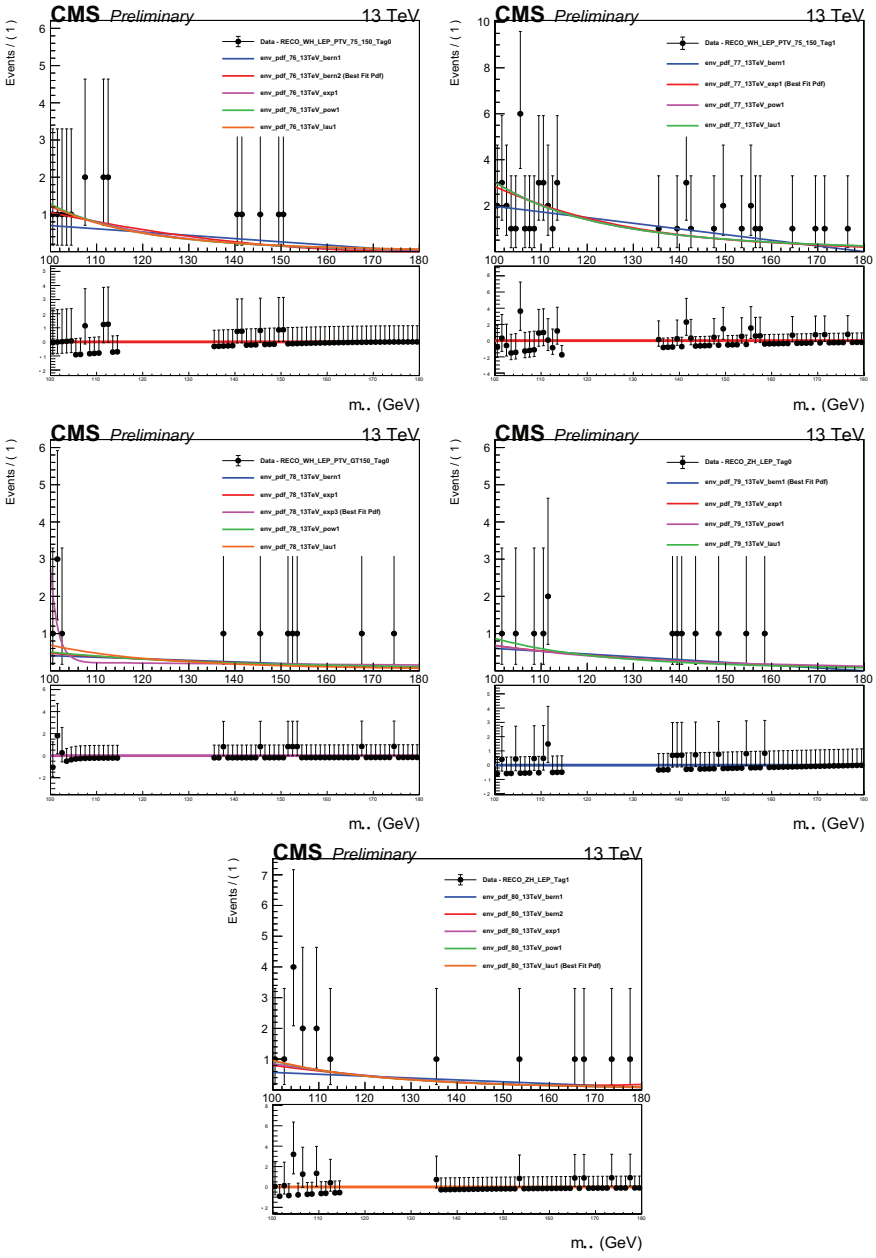

Figure F.11: Set of functions chosen to fit the background in STXS Stage 1.2 analysis categories using the discrete profiling method.

Appendix G

G.1 Signal-plus-background models

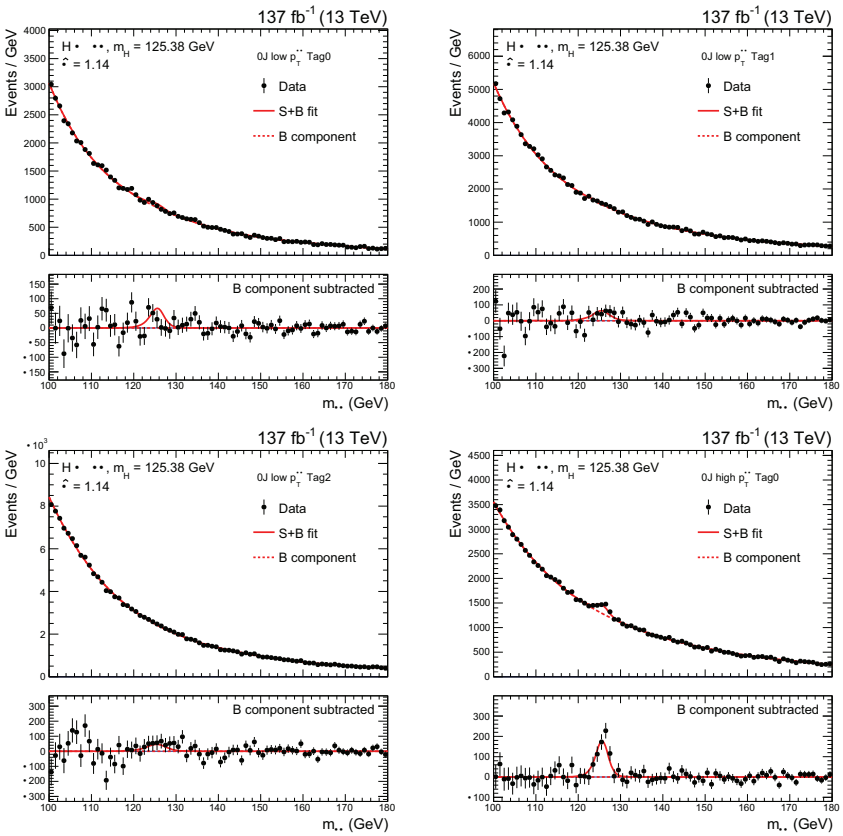

Figure G.1: Data points (black) and signal-plus-background model fit for STXS Stage 1.2 analysis categories.

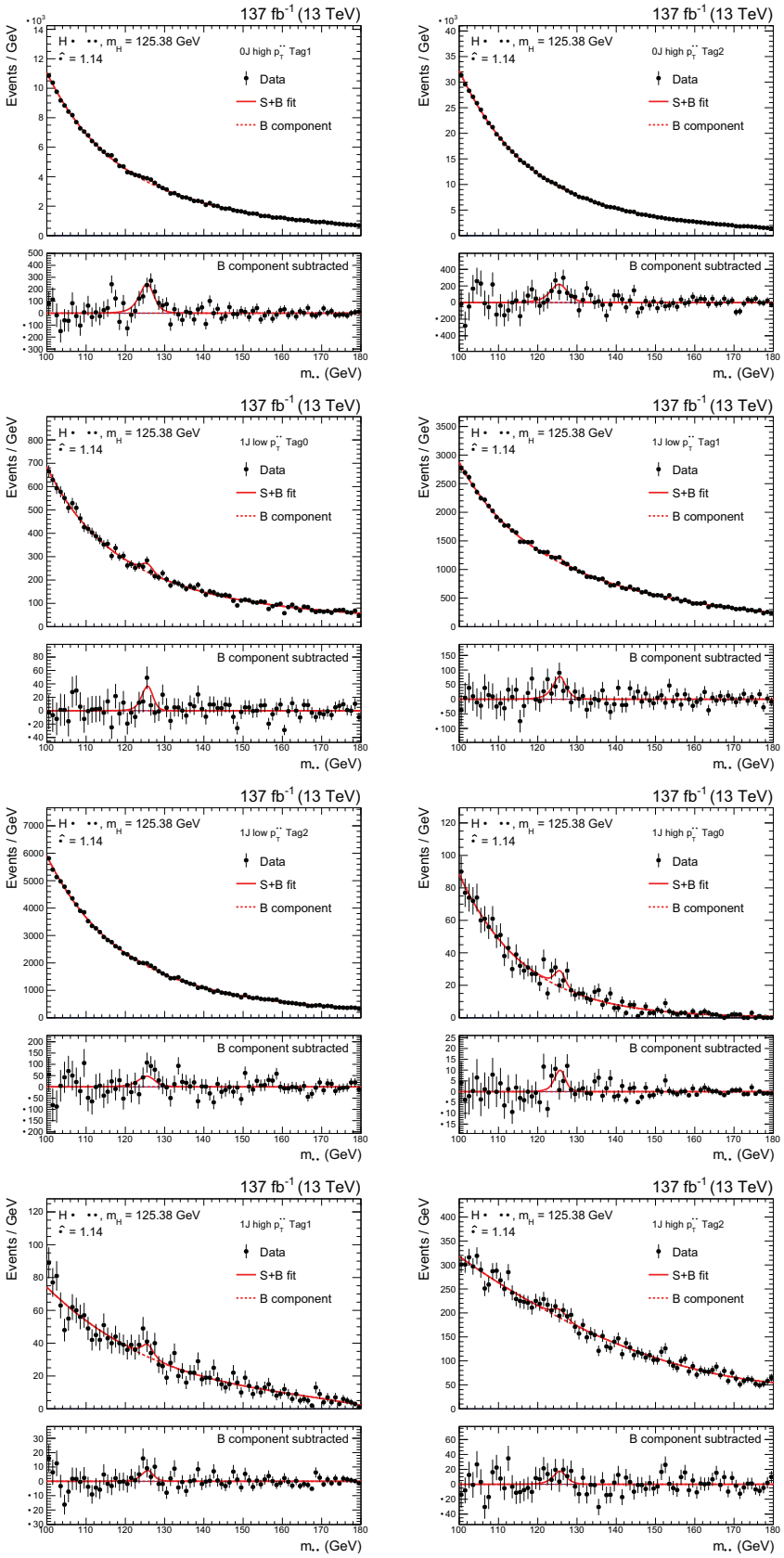

Figure G.2: Data points (black) and signal-plus-background model fit for STXS Stage 1.2 analysis categories.

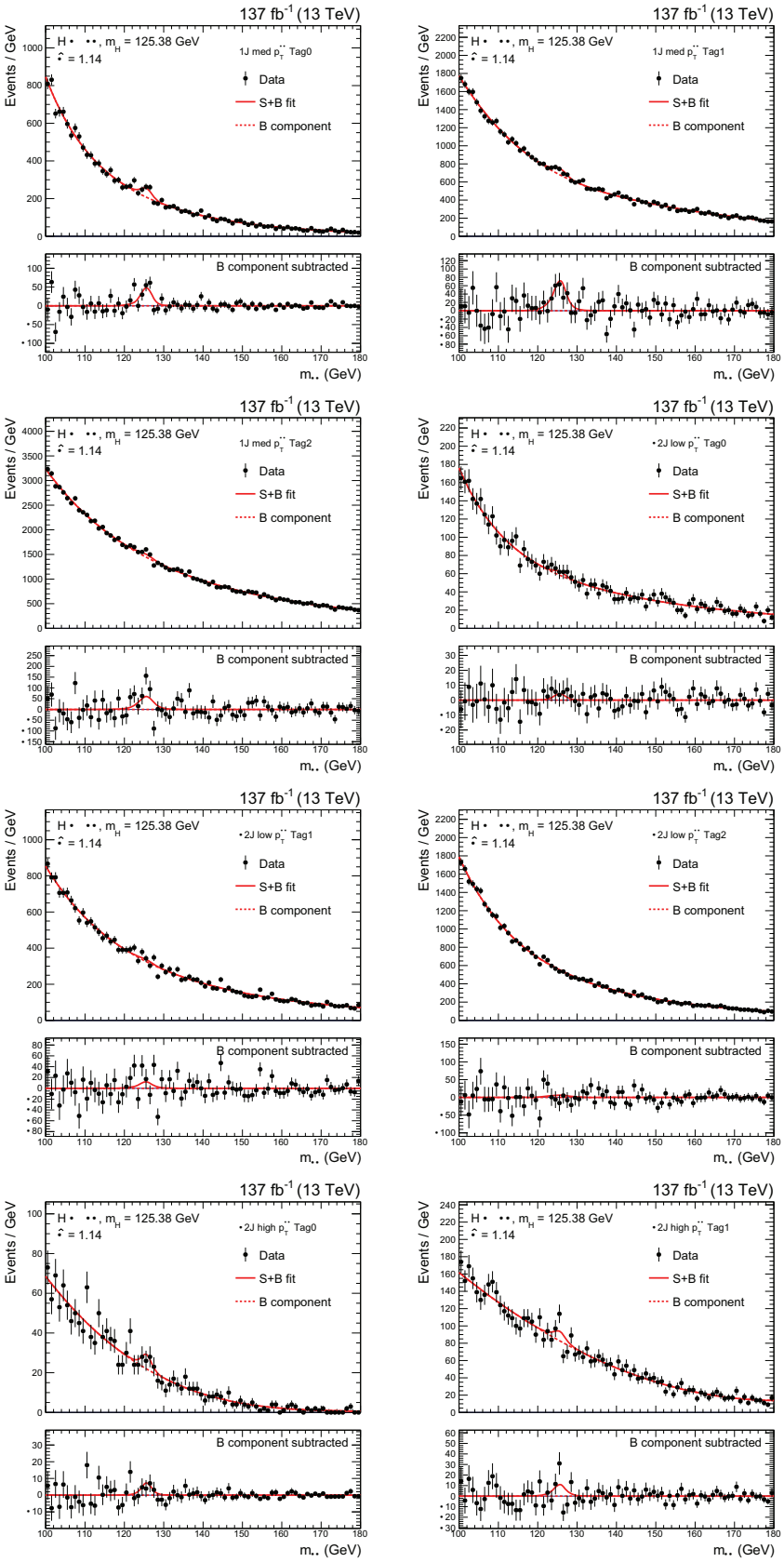

Figure G.3: Data points (black) and signal-plus-background model fit for STXS Stage 1.2 analysis categories.

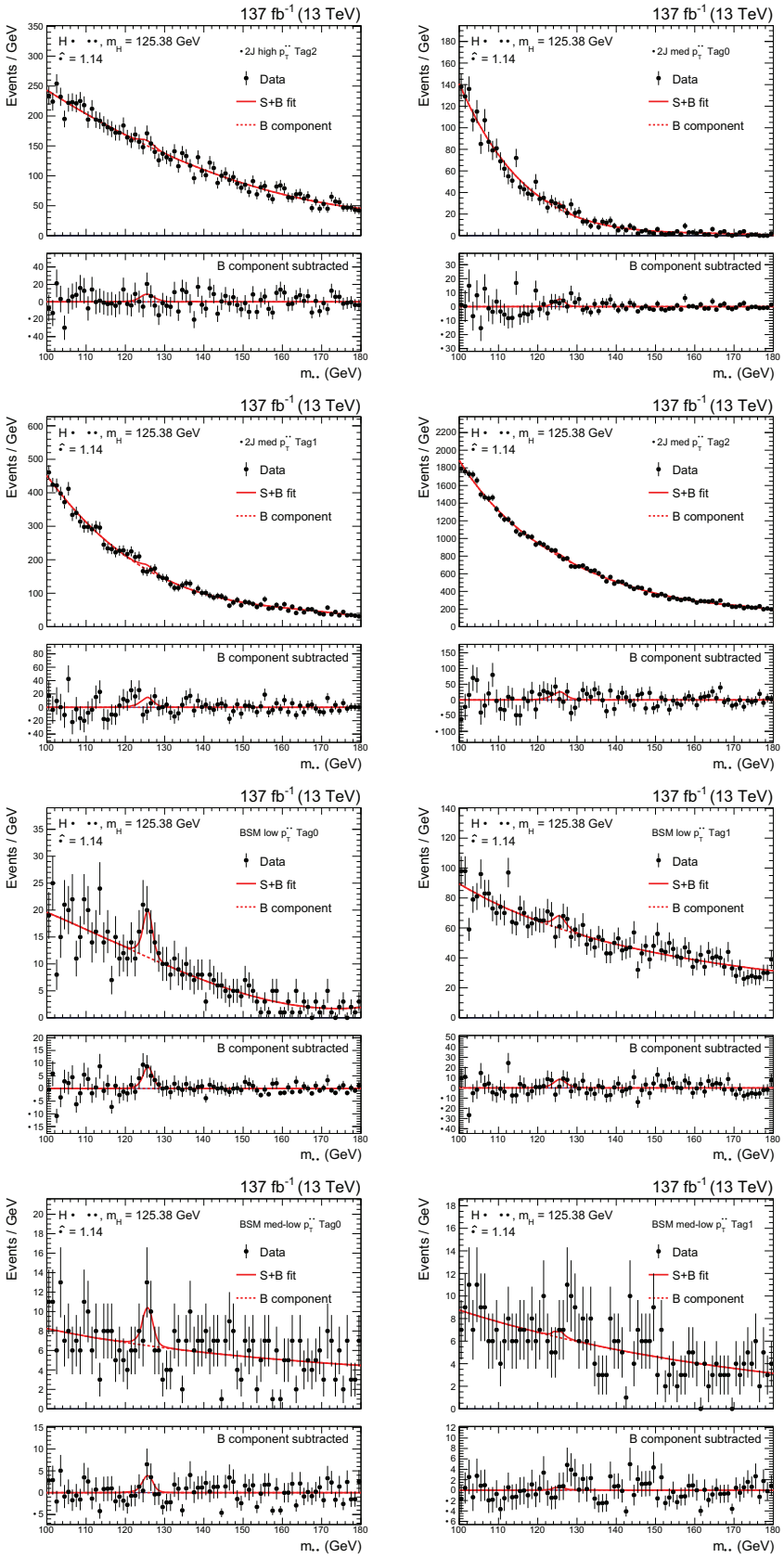

Figure G.4: Data points (black) and signal-plus-background model fit for STXS Stage 1.2 analysis categories.

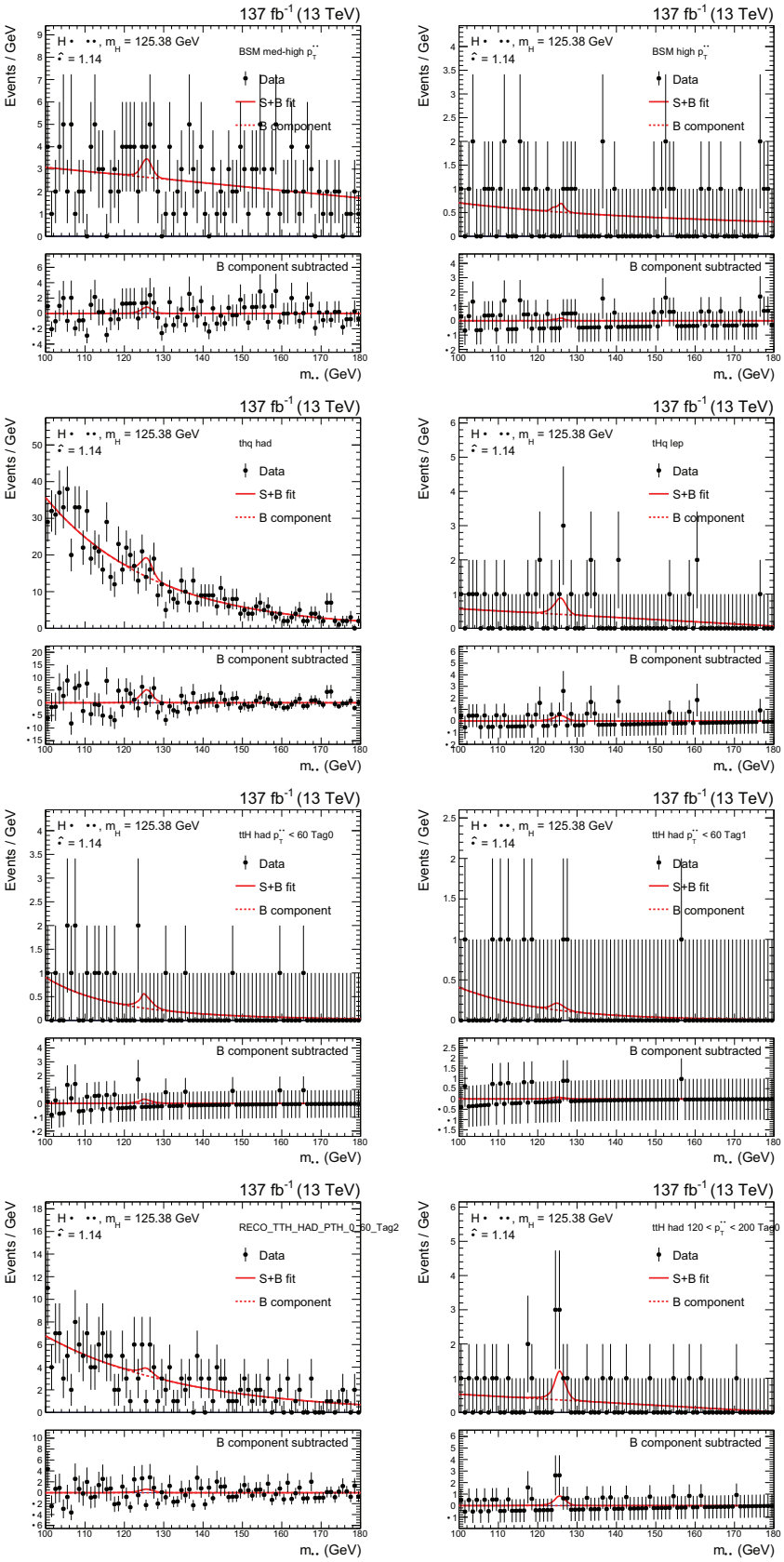

Figure G.5: Data points (black) and signal-plus-background model fit for STXS Stage 1.2 analysis categories.

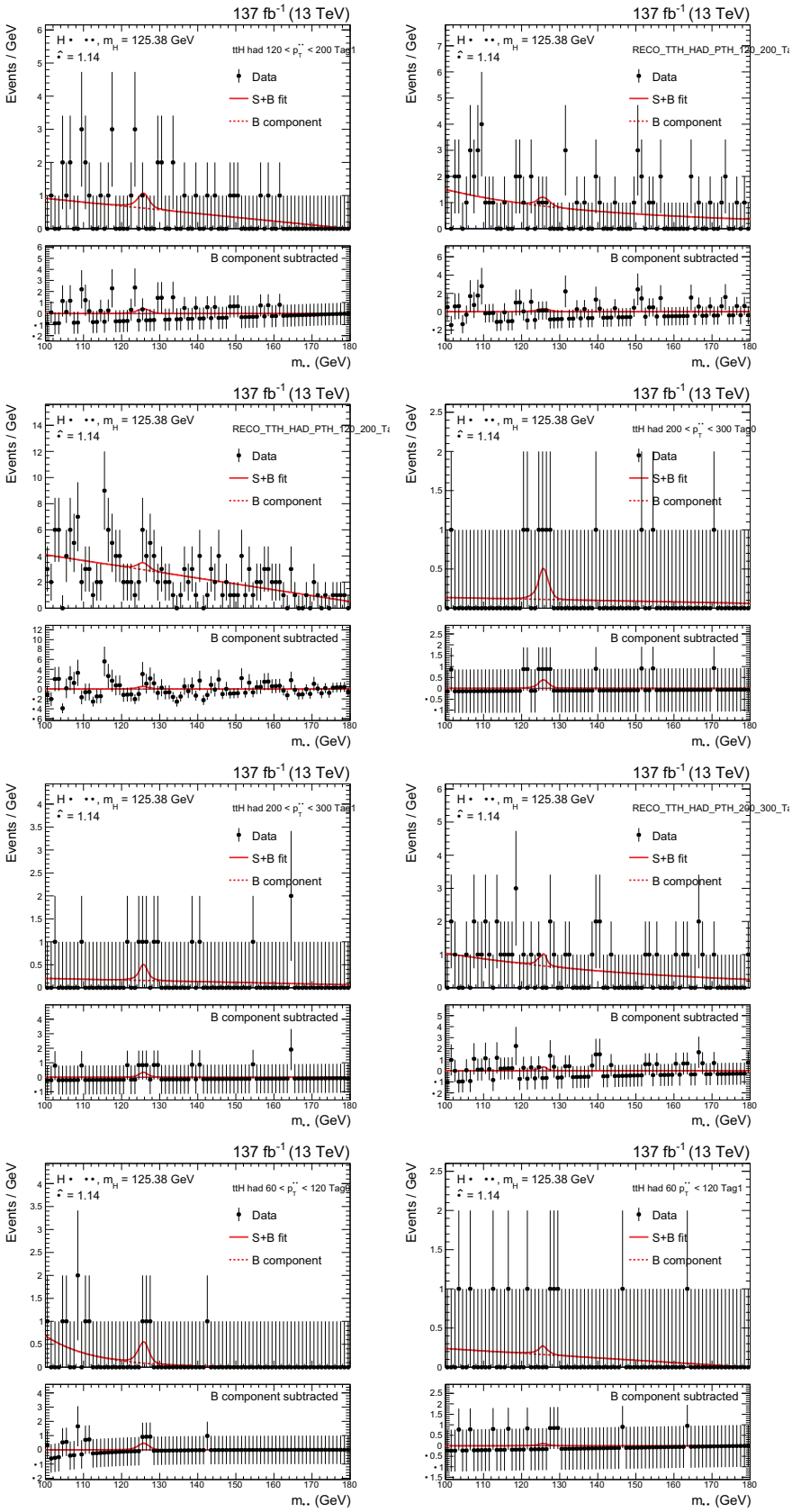

Figure G.6: Data points (black) and signal-plus-background model fit for STXS Stage 1.2 analysis categories.

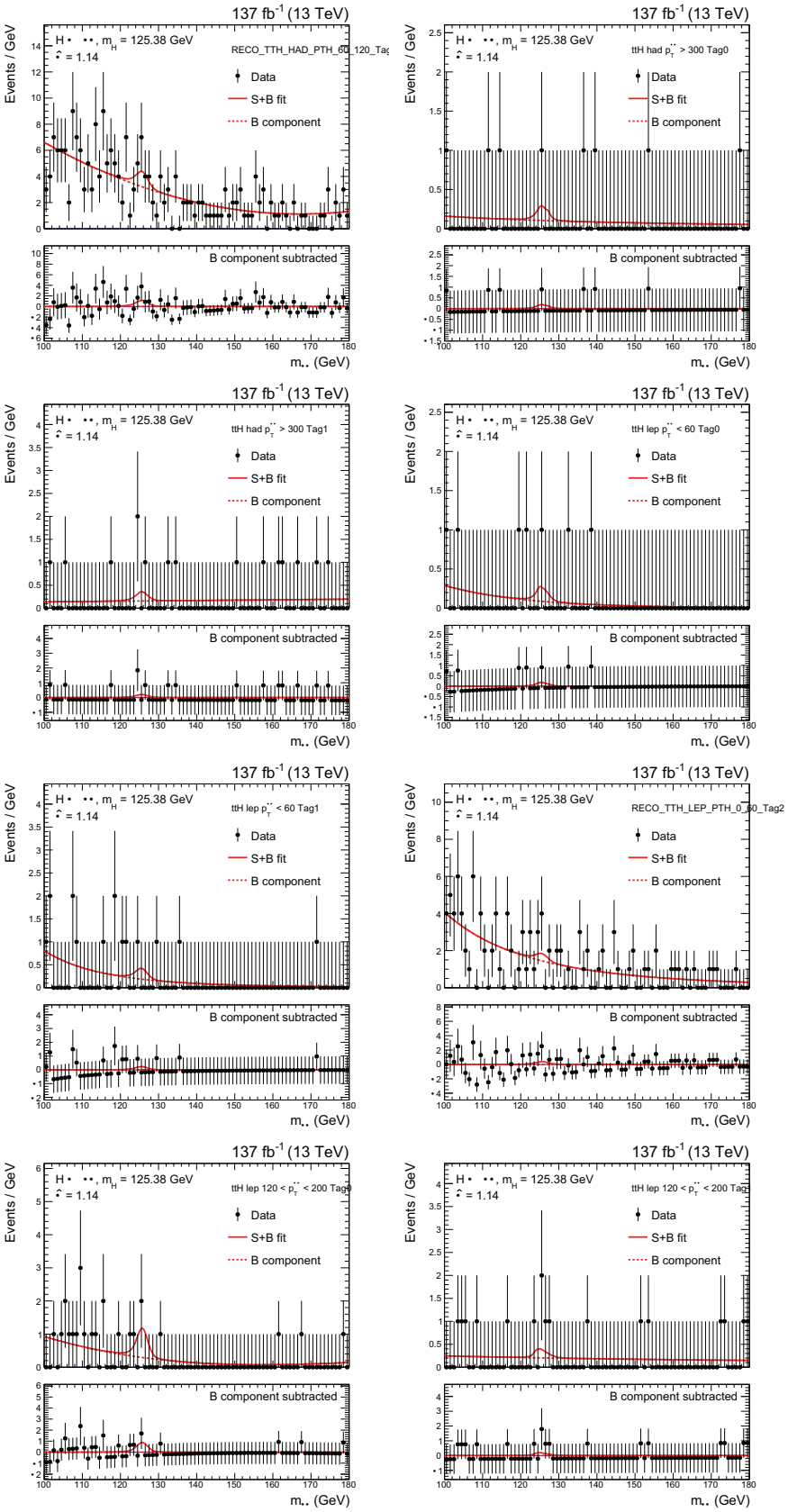

Figure G.7: Data points (black) and signal-plus-background model fit for STXS Stage 1.2 analysis categories.

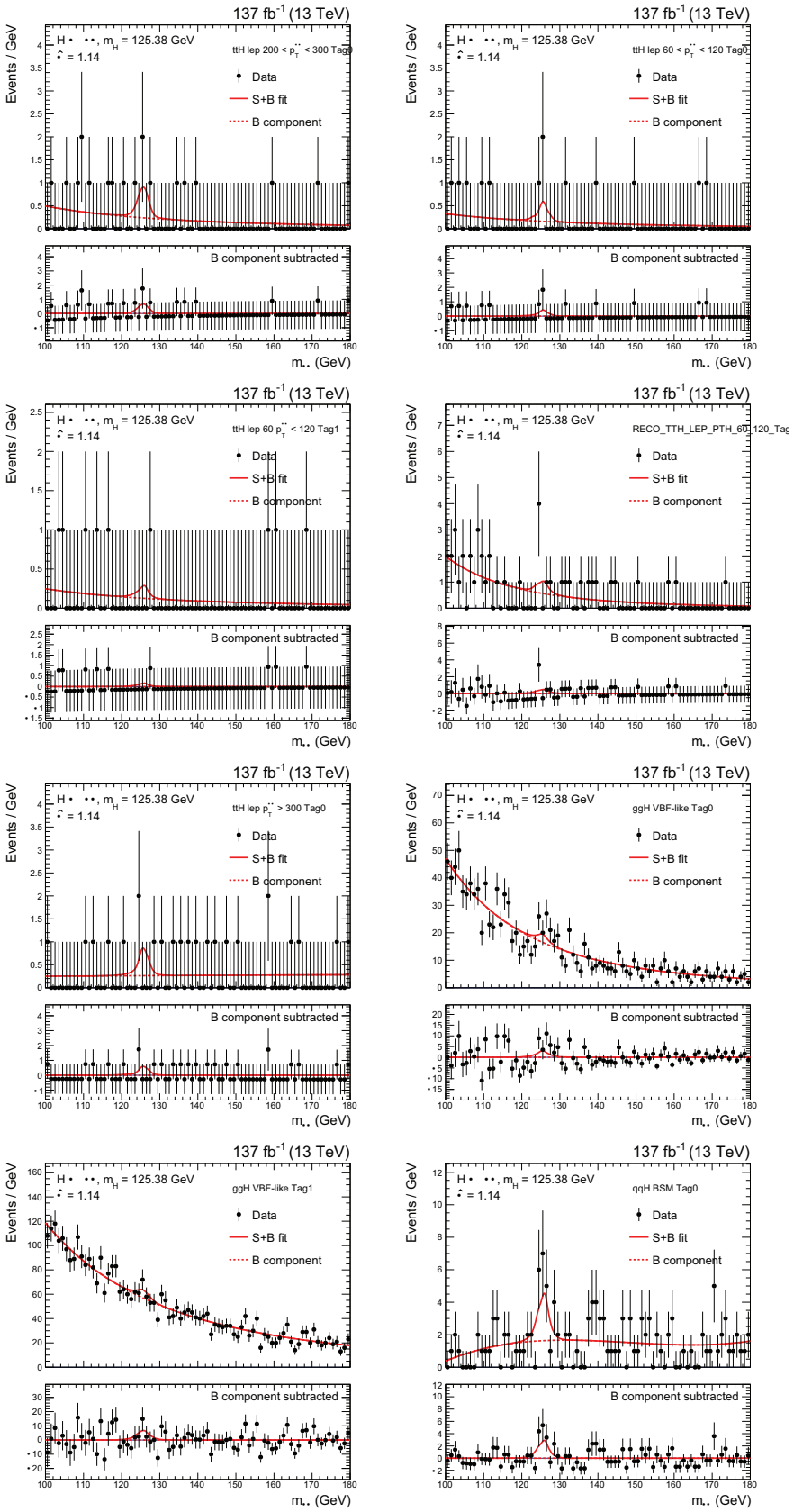

Figure G.8: Data points (black) and signal-plus-background model fit for STXS Stage 1.2 analysis categories.

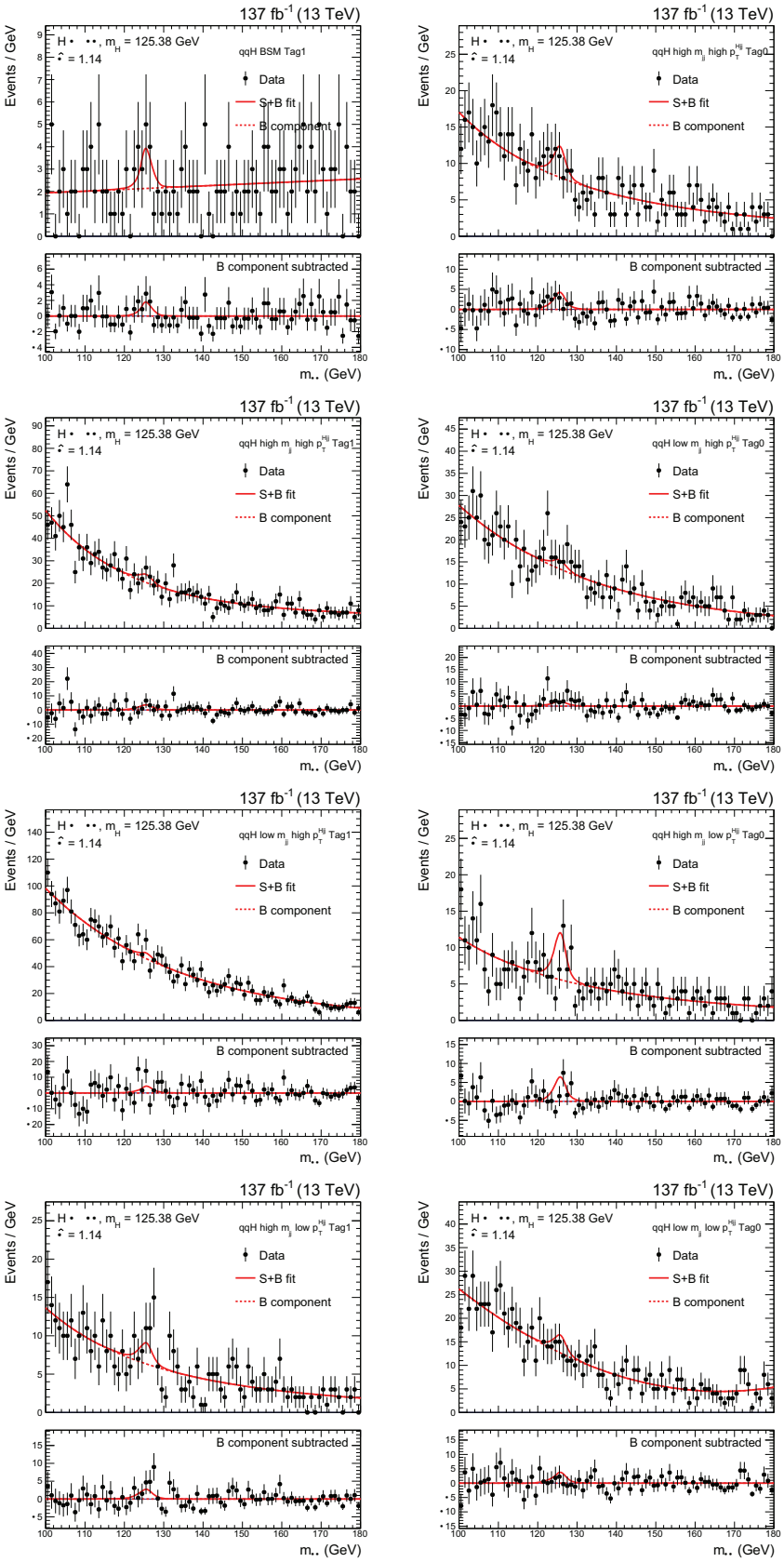

Figure G.9: Data points (black) and signal-plus-background model fit for STXS Stage 1.2 analysis categories.

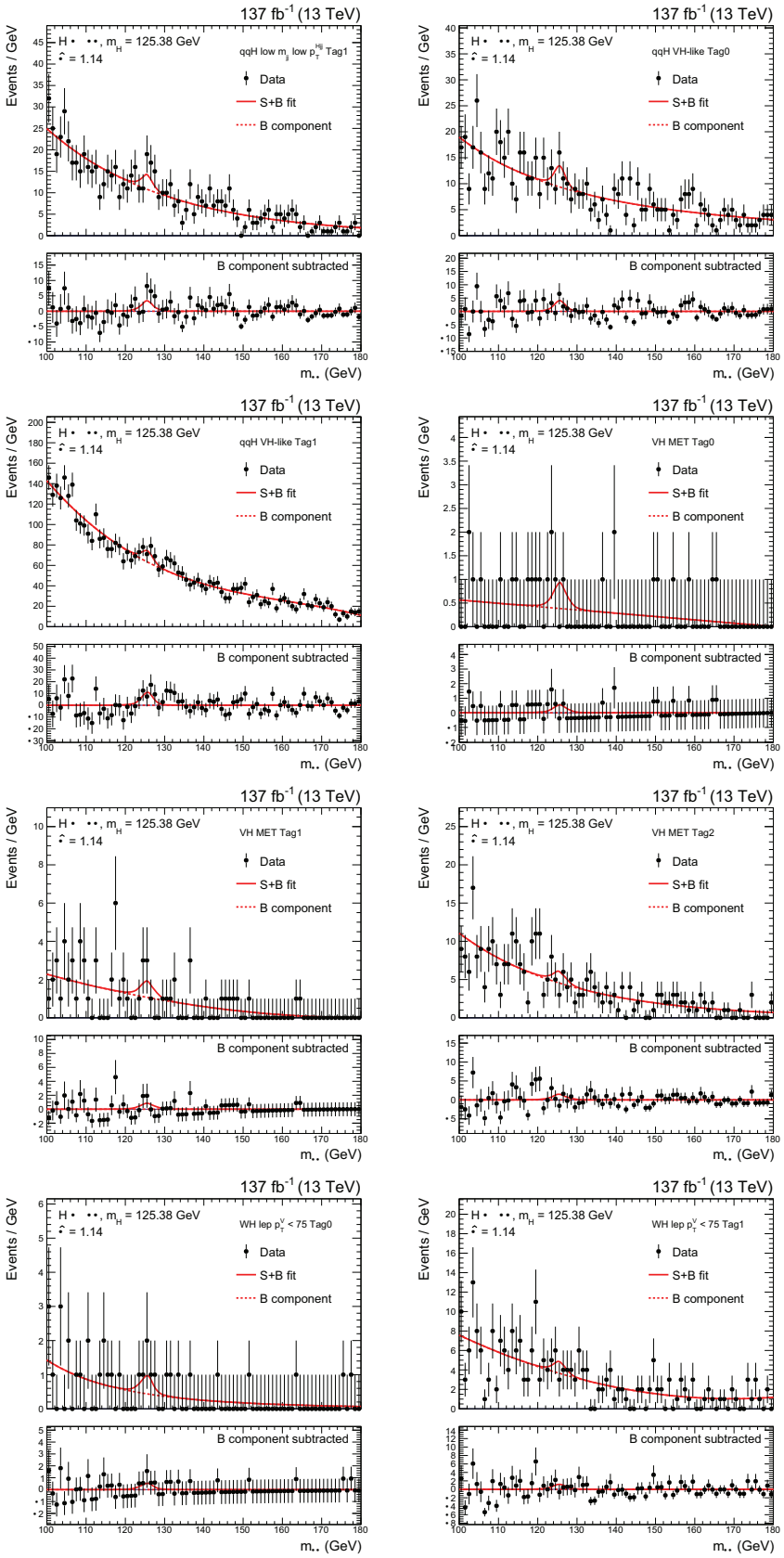

Figure G.10: Data points (black) and signal-plus-background model fit for STXS Stage 1.2 analysis categories.

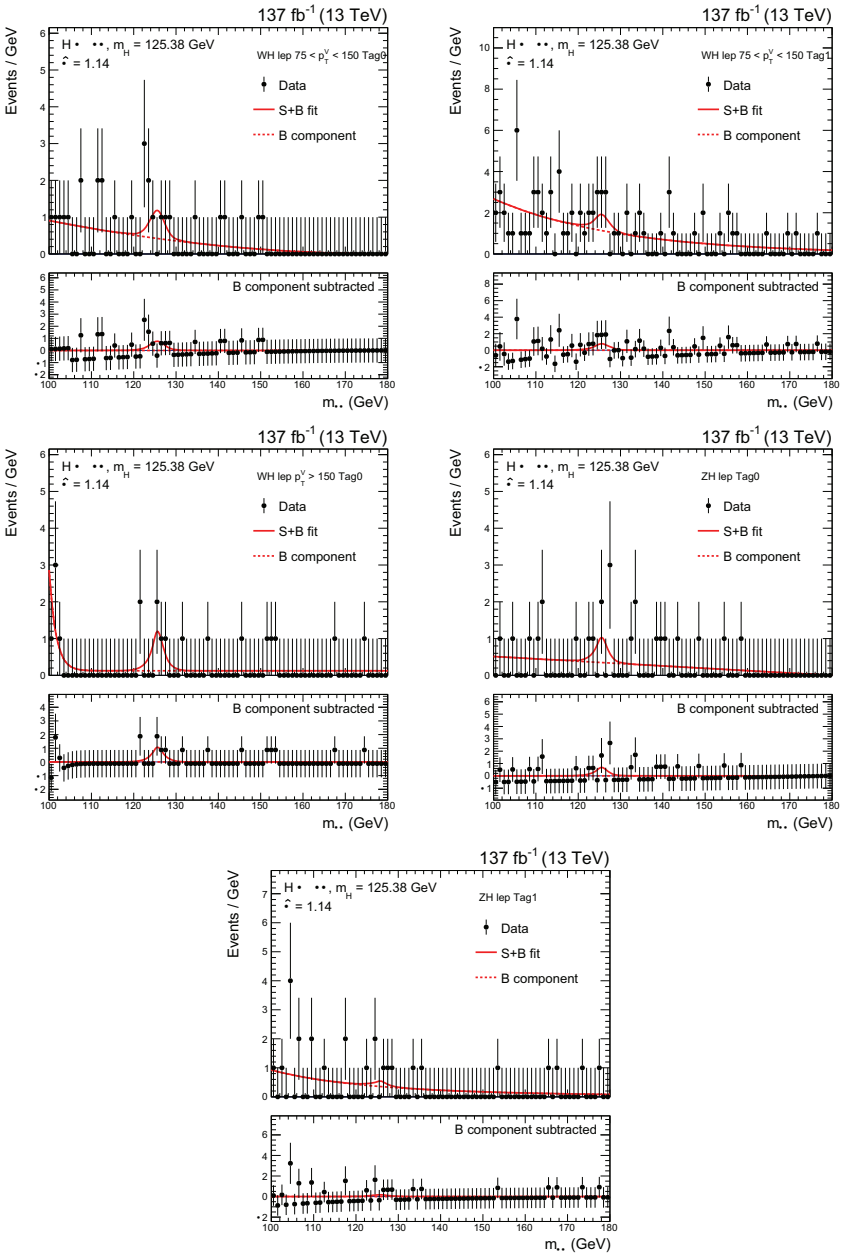

Figure G.11: Data points (black) and signal-plus-background model fit for STXS Stage 1.2 analysis categories.

Appendix H

H.1 Likelihood scans

H.1.1 Expected likelihood scans per production mode

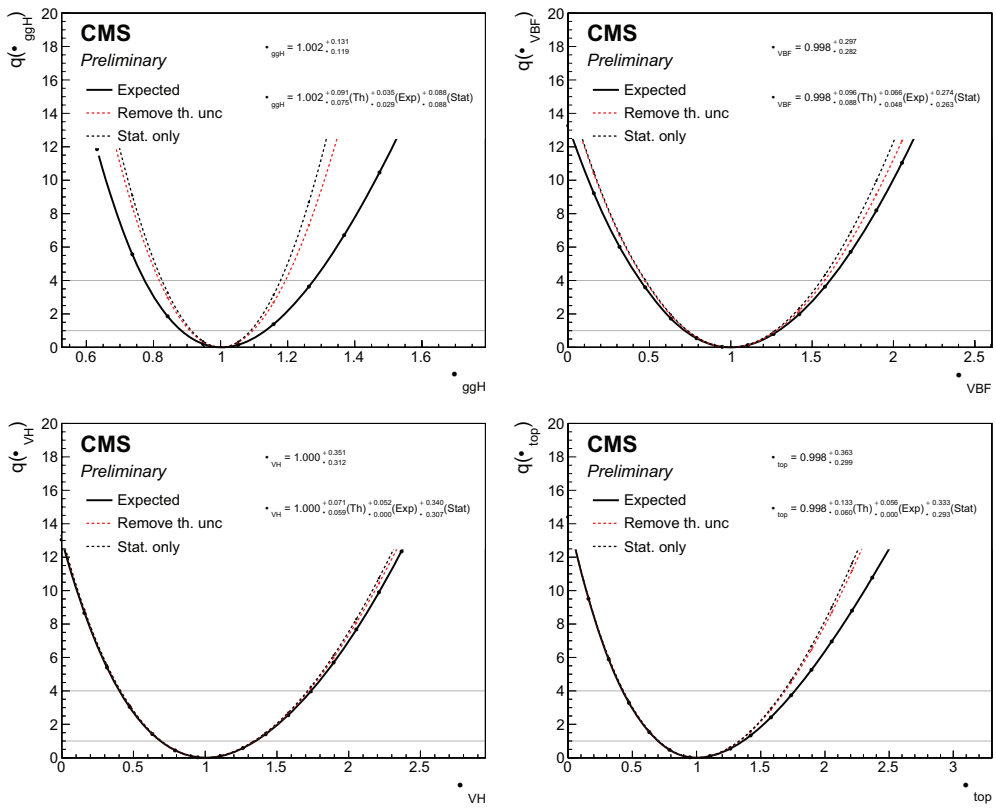

Figure H.1: Expected likelihood scans in the per-production mode signal strength fit.

H.1.2 Observed likelihood scans per production mode

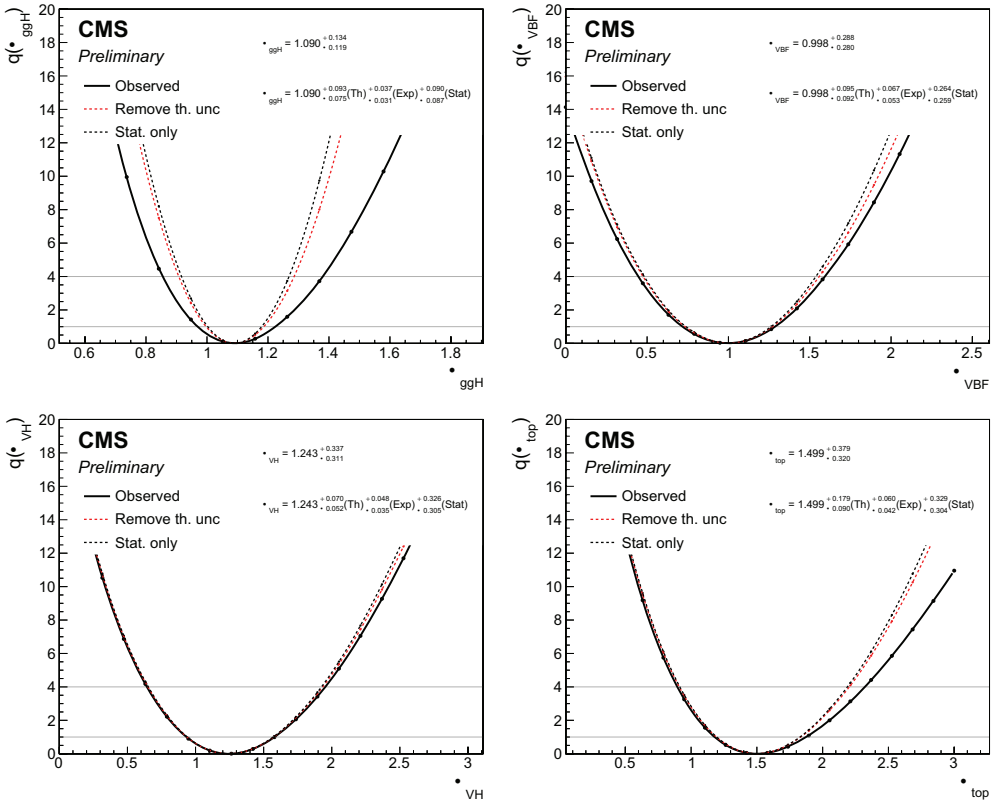

Figure H.2: Observed likelihood scans in the per-production mode signal strength fit.

H.1.3 Expected likelihood scans in the STXS maximal merging scheme

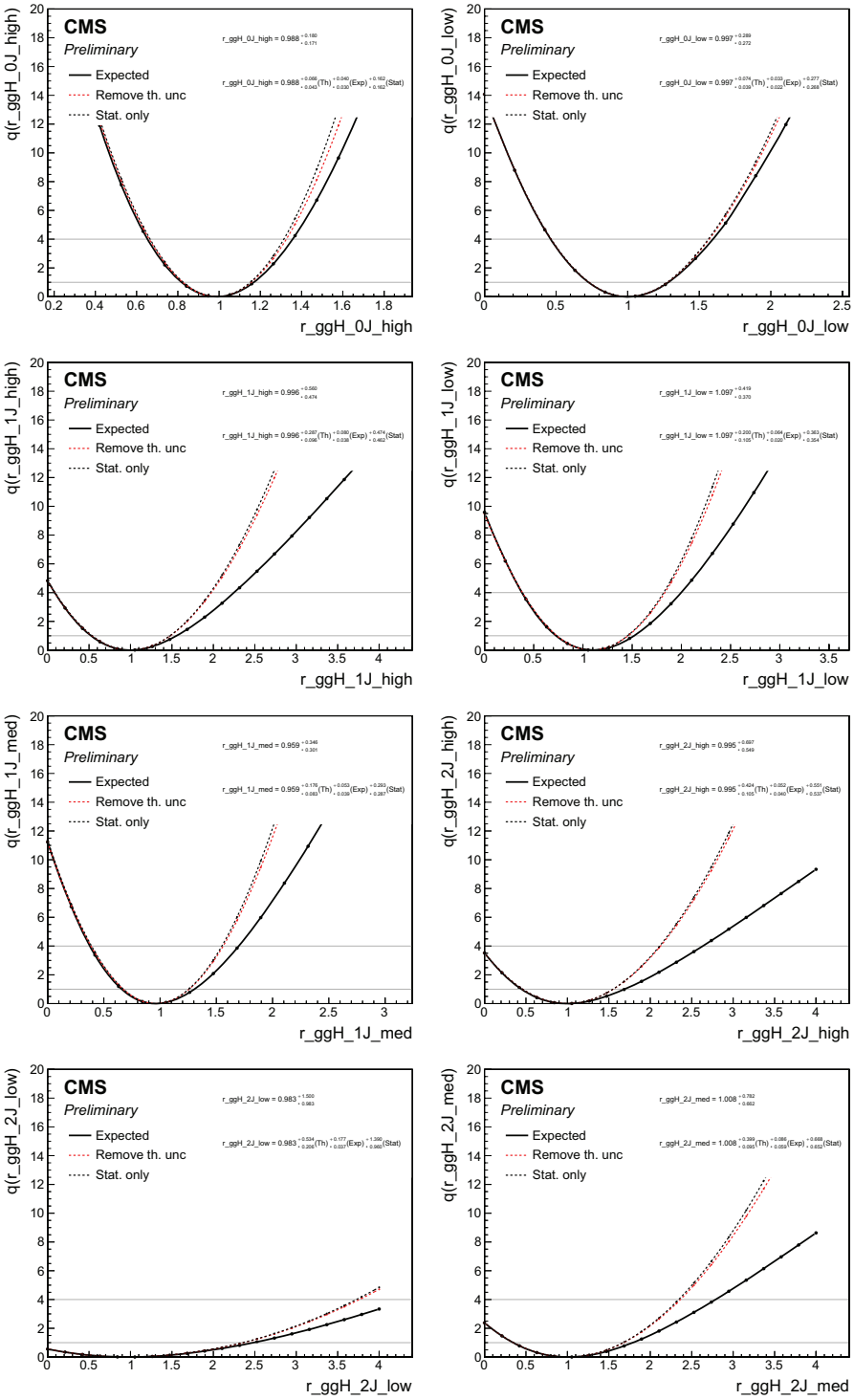

Figure H.3: Expected likelihood scans in the 17 parameter maximal merging STXS Stage 1.2 fit.

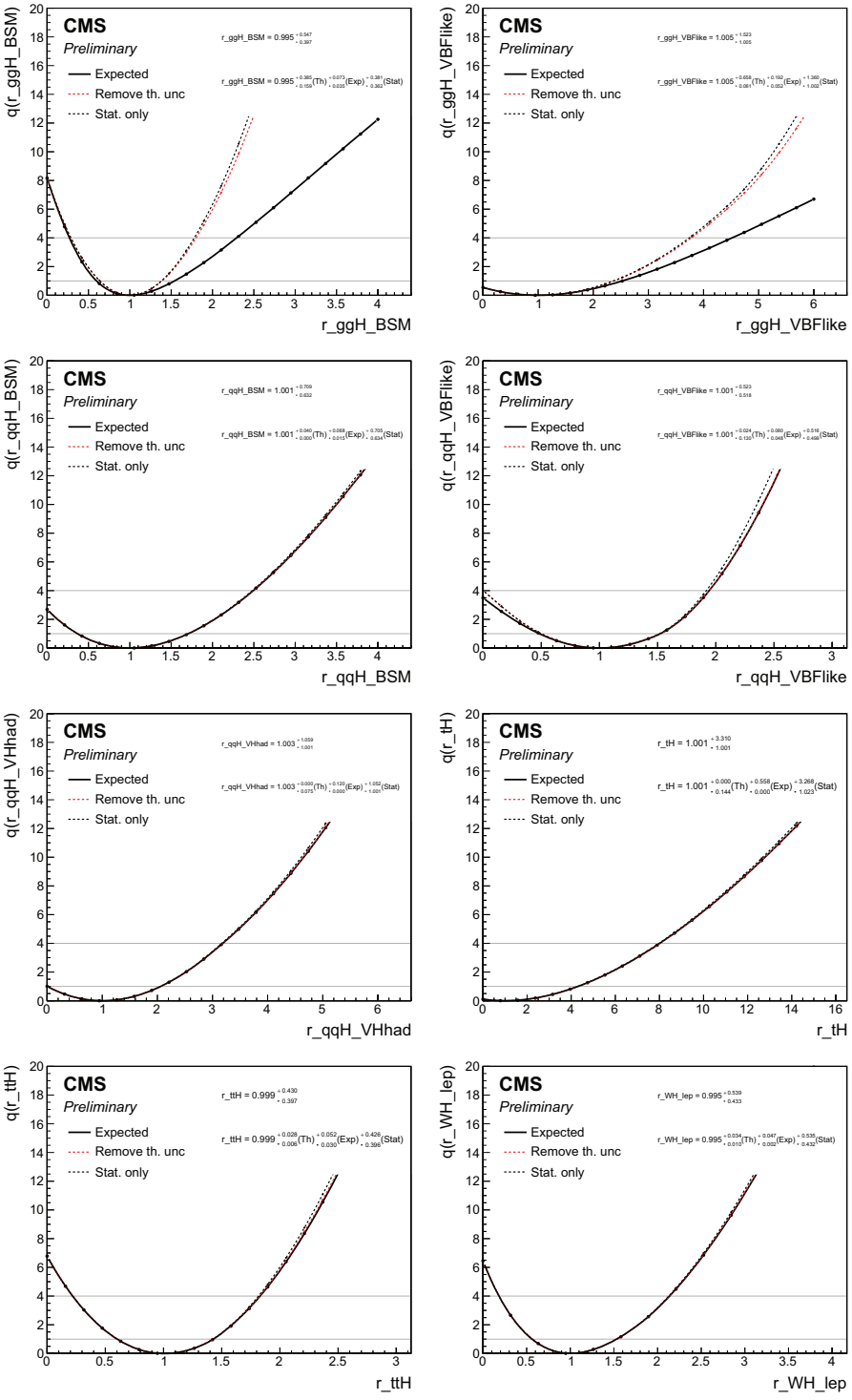

Figure H.4: Expected likelihood scans in the 17 parameter maximal merging STXS Stage 1.2 fit.

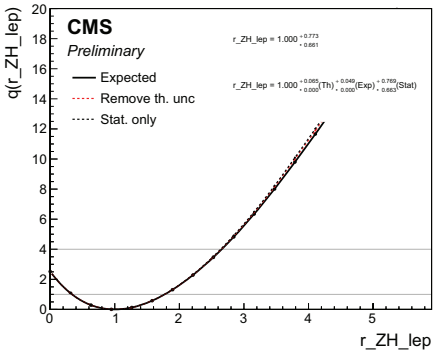

Figure H.5: Expected likelihood scans in the 17 parameter maximal merging STXS Stage 1.2 fit.

H.1.4 Observed likelihood scans in the STXS maximal merging scheme

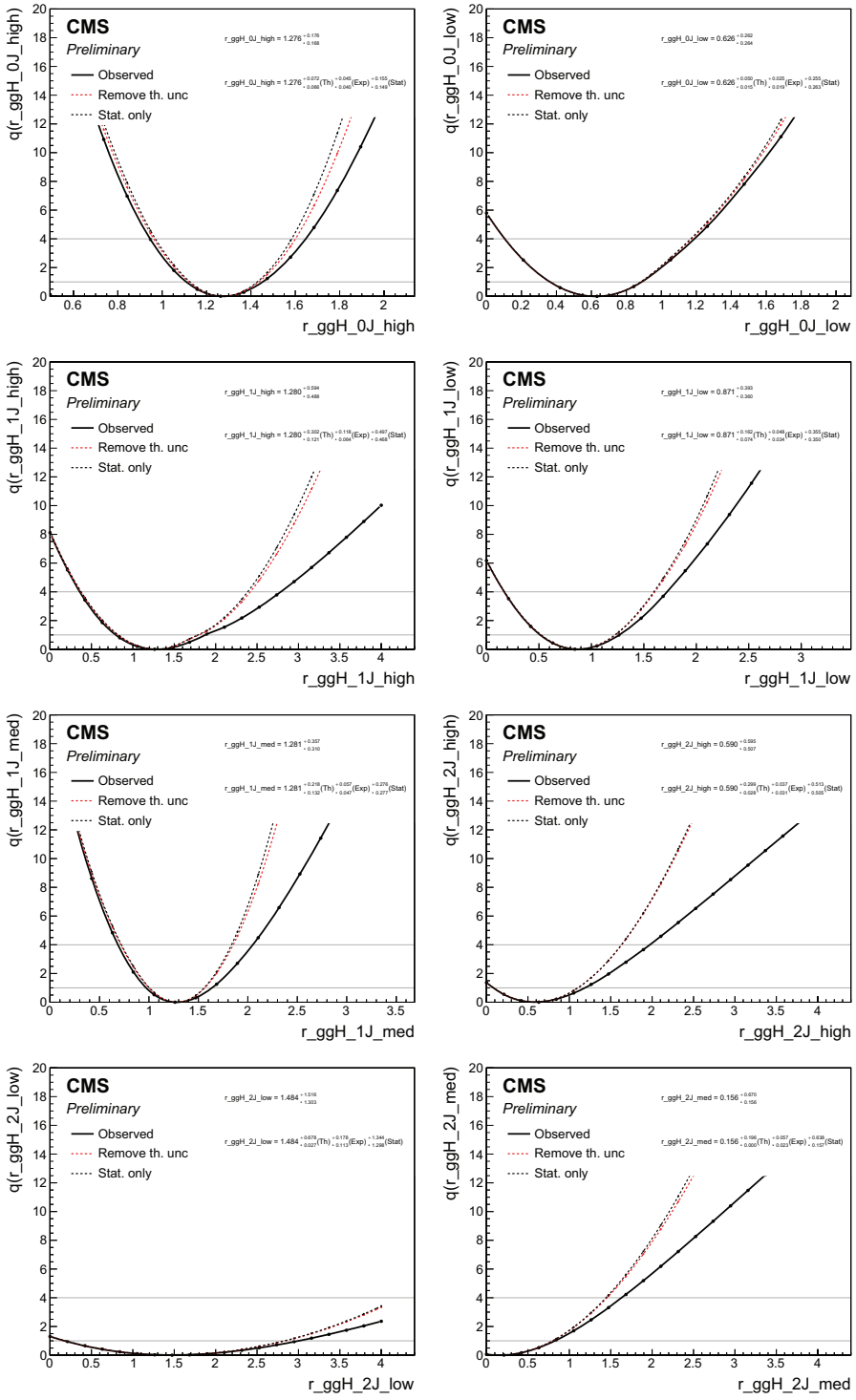

Figure H.6: Observed likelihood scans in the 17 parameter maximal merging STXS Stage 1.2 fit.

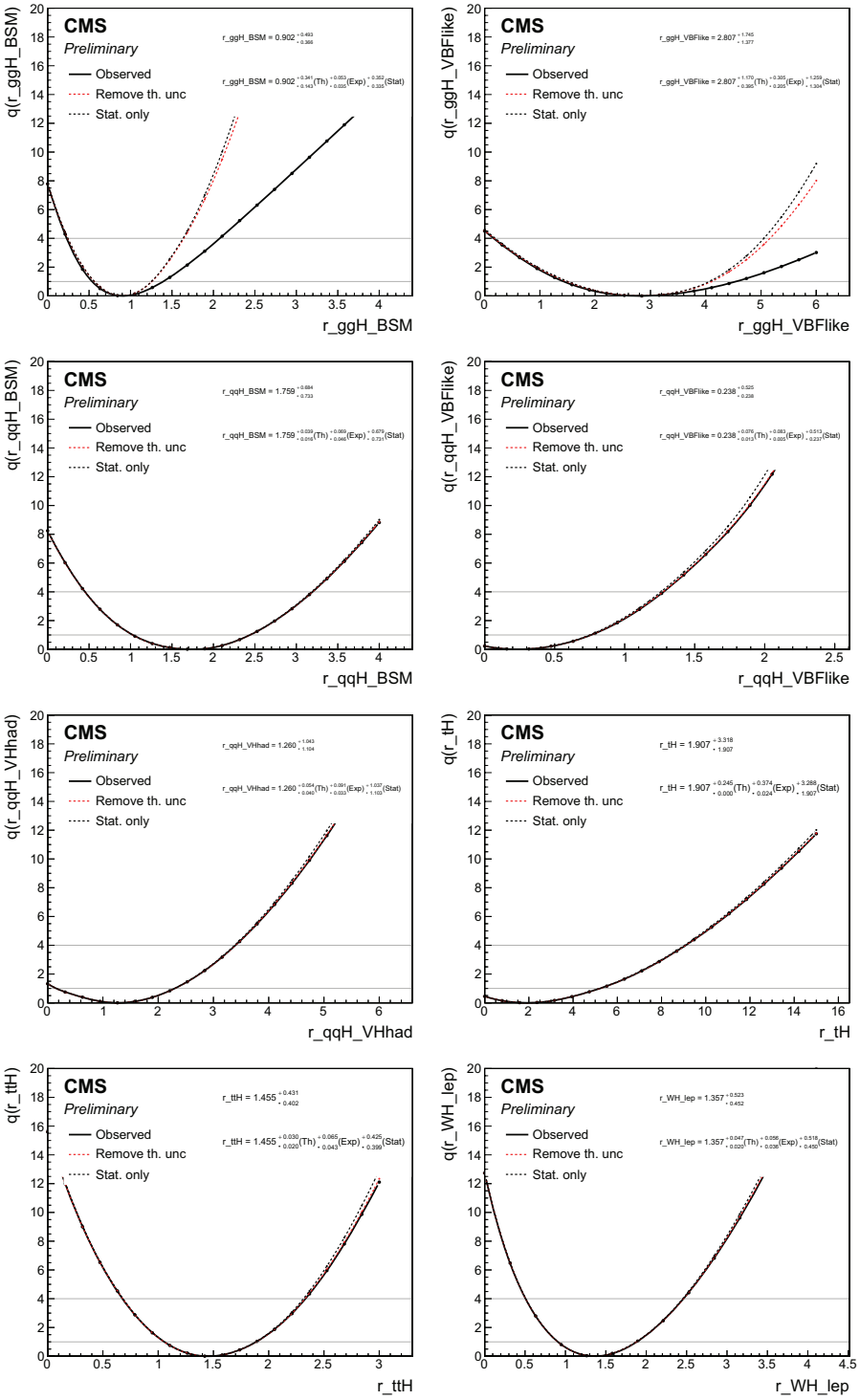

Figure H.7: Observed likelihood scans in the 17 parameter maximal merging STXS Stage 1.2 fit.

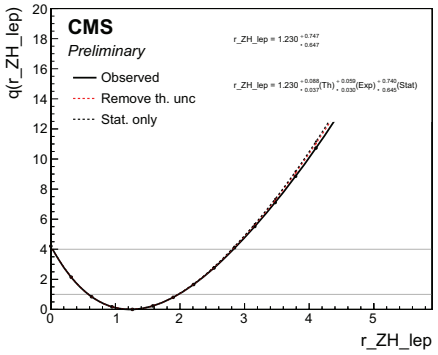

Figure H.8: Observed likelihood scans in the 17 parameter maximal merging STXS Stage 1.2 fit.

H.1.5 Expected likelihood scans in the STXS minimal merging scheme

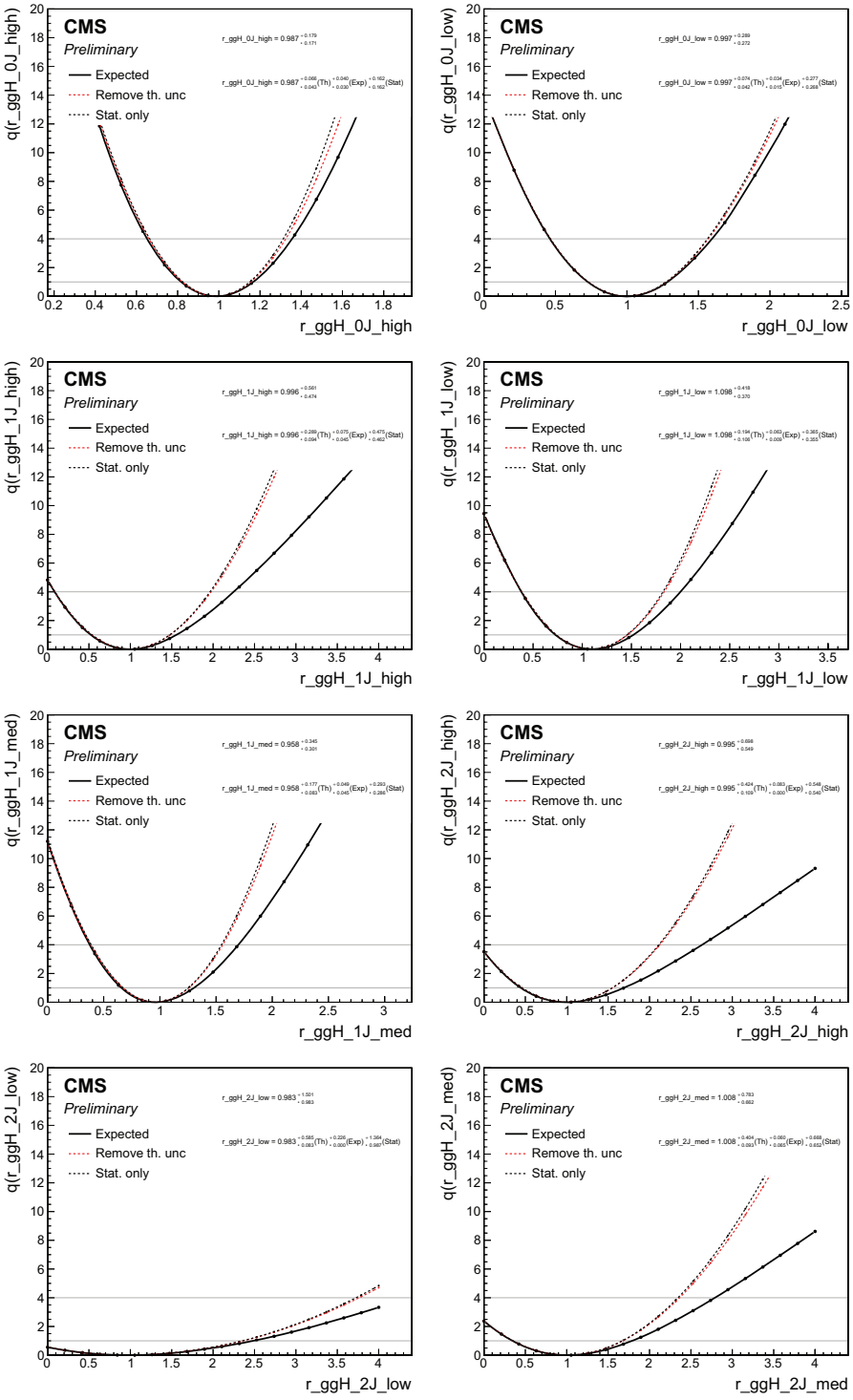

Figure H.9: Expected likelihood scans in the 27 parameter minimal merging STXS Stage 1.2 fit.

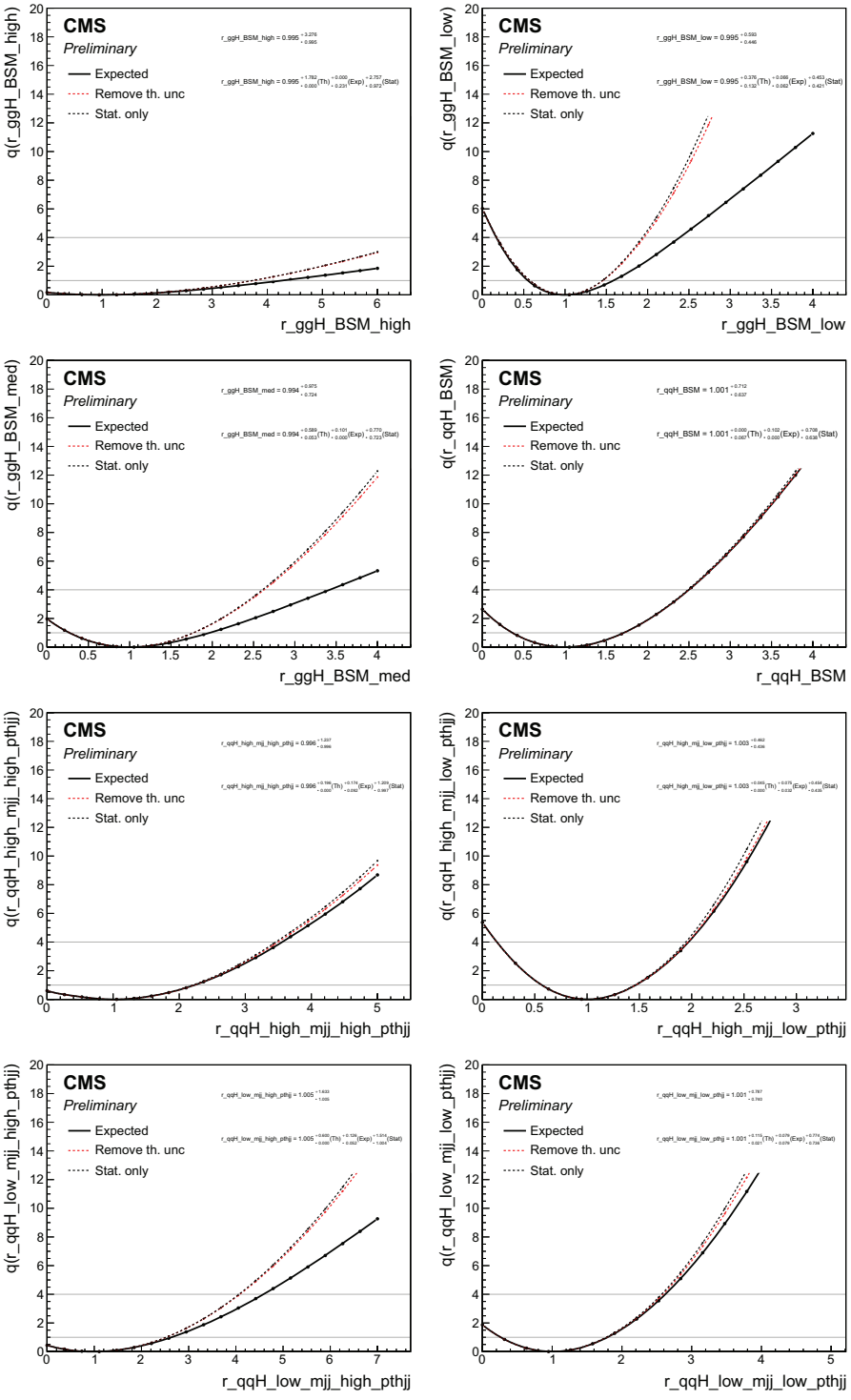

Figure H.10: Expected likelihood scans in the 27 parameter minimal merging STXS Stage 1.2 fit.

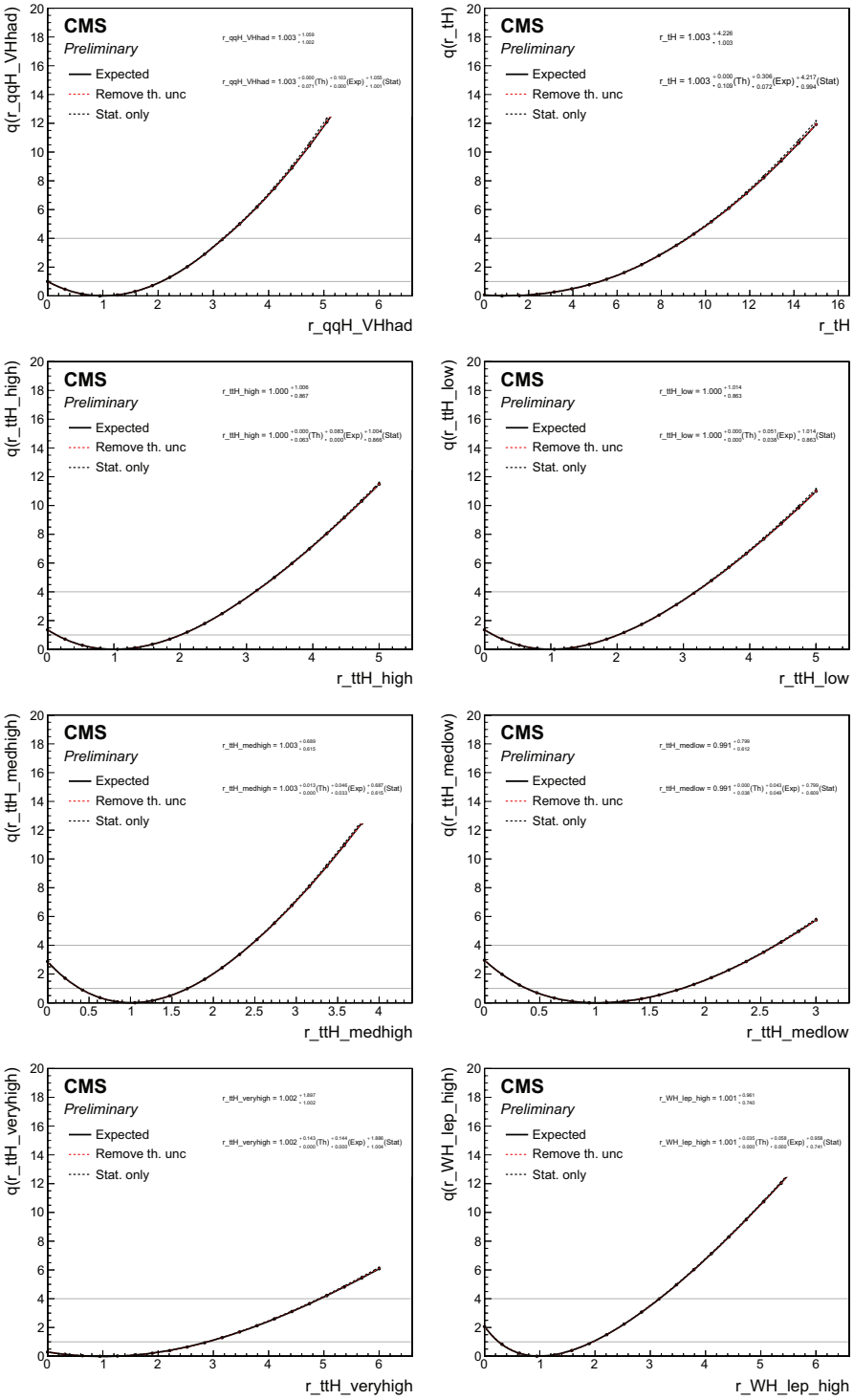

Figure H.11: Expected likelihood scans in the 27 parameter minimal merging STXS Stage 1.2 fit.

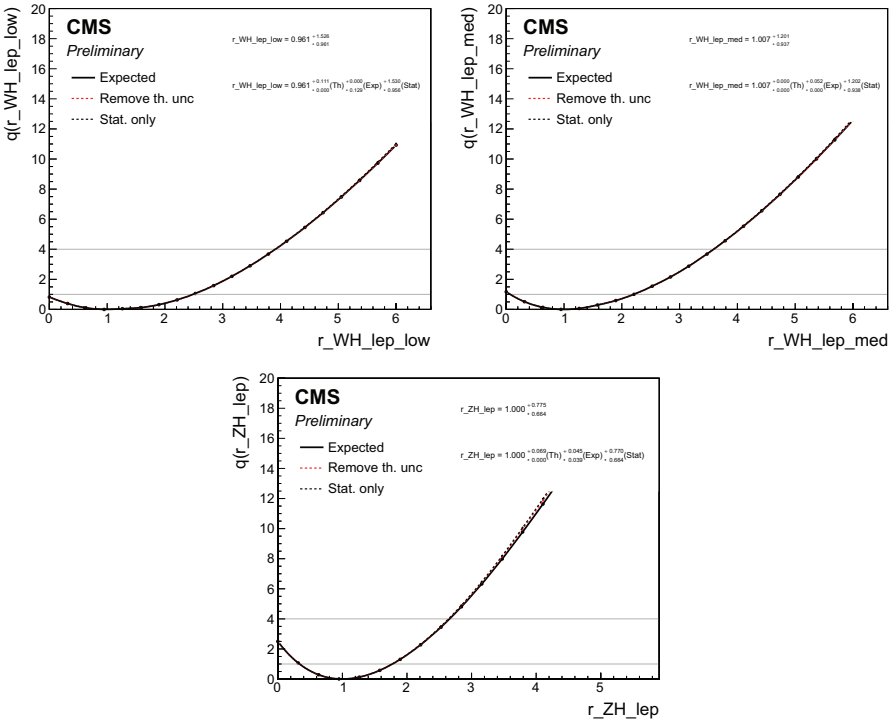

Figure H.12: Expected likelihood scans in the 27 parameter minimal merging STXS Stage 1.2 fit.

H.1.6 Observed likelihood scans in the STXS minimal merging scheme

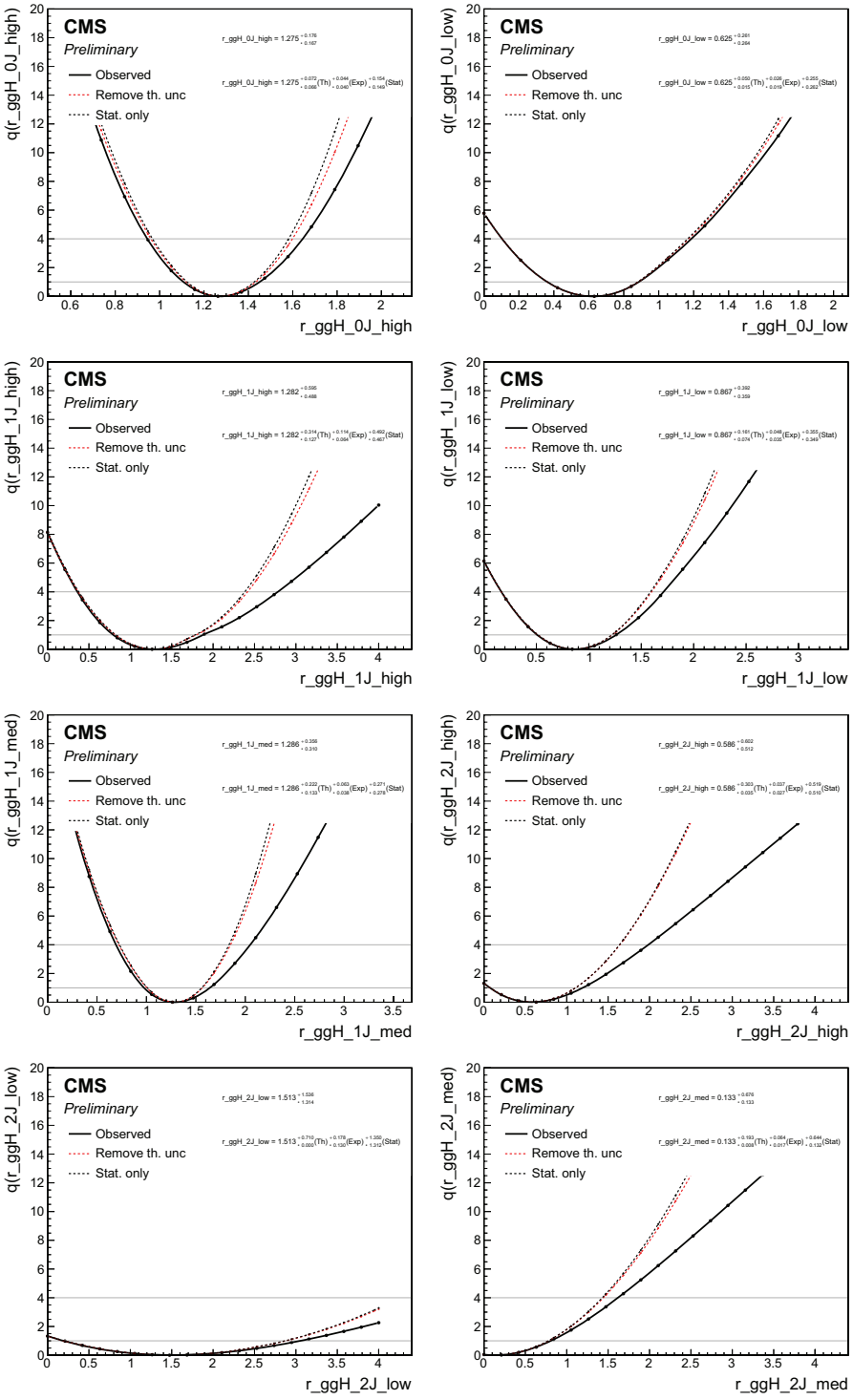

Figure H.13: Observed likelihood scans in the 27 parameter minimal merging STXS Stage 1.2 fit.

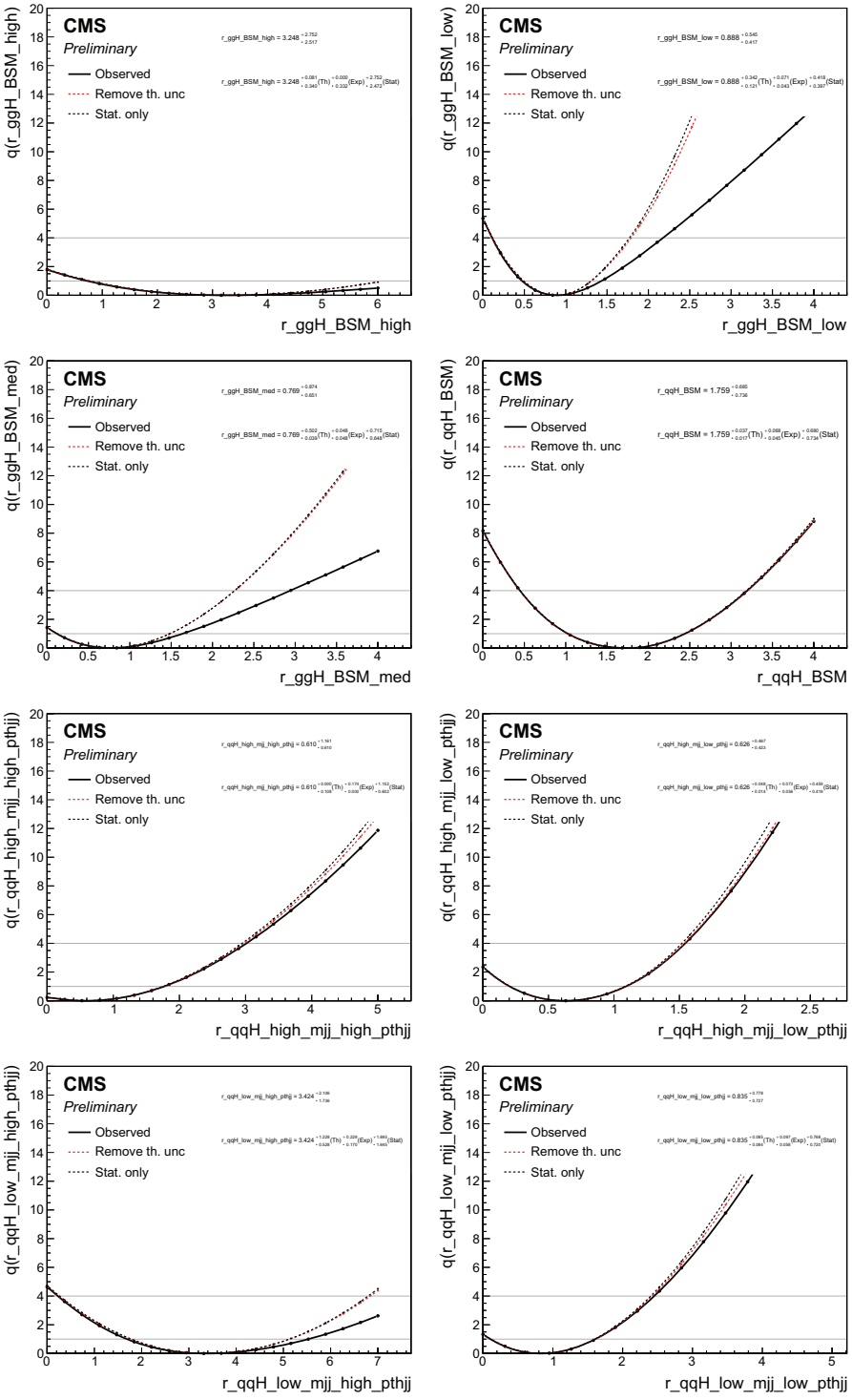

Figure H.14: Observed likelihood scans in the 27 parameter minimal merging STXS Stage 1.2 fit.

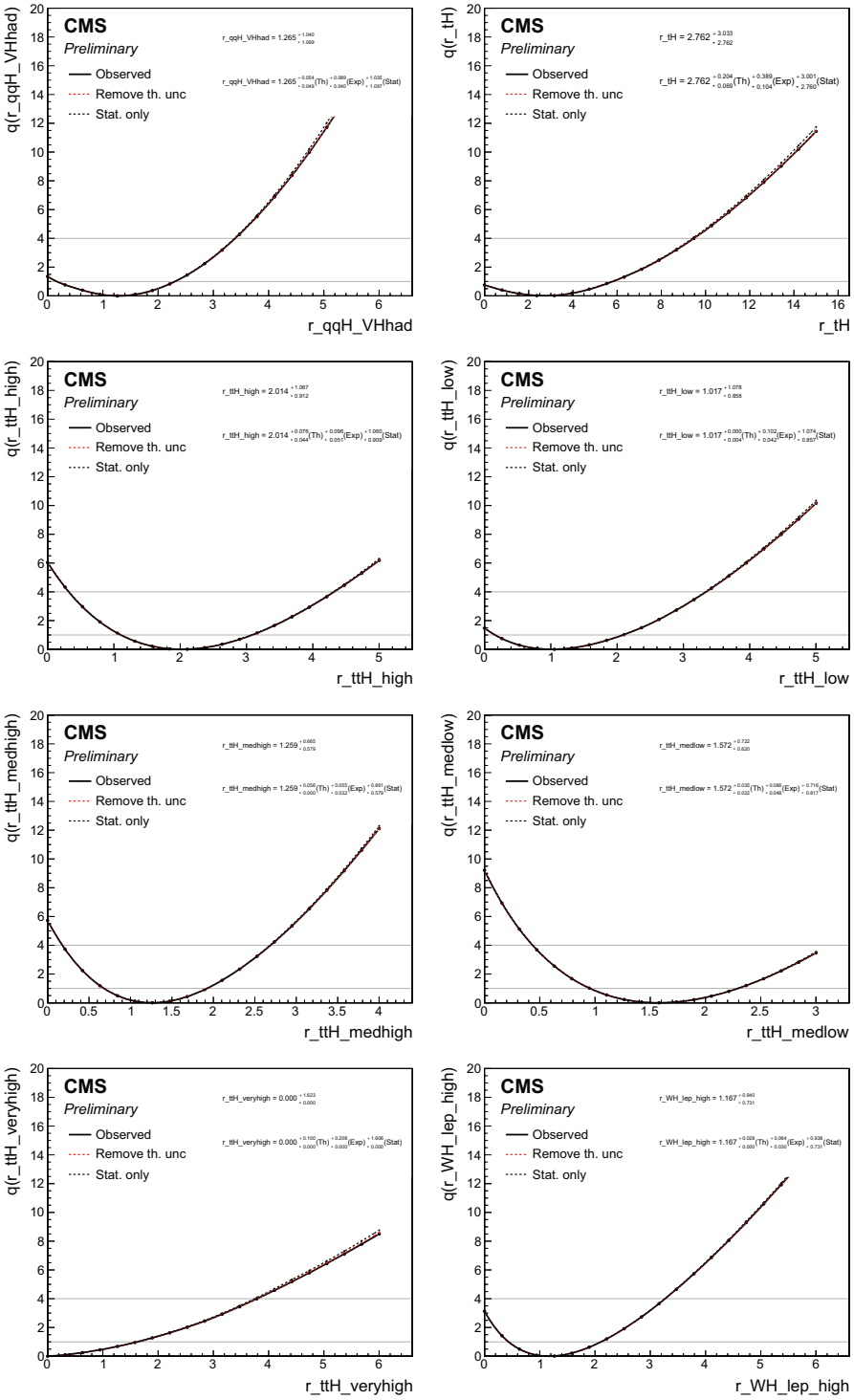

Figure H.15: Observed likelihood scans in the 27 parameter minimal merging STXS Stage 1.2 fit.

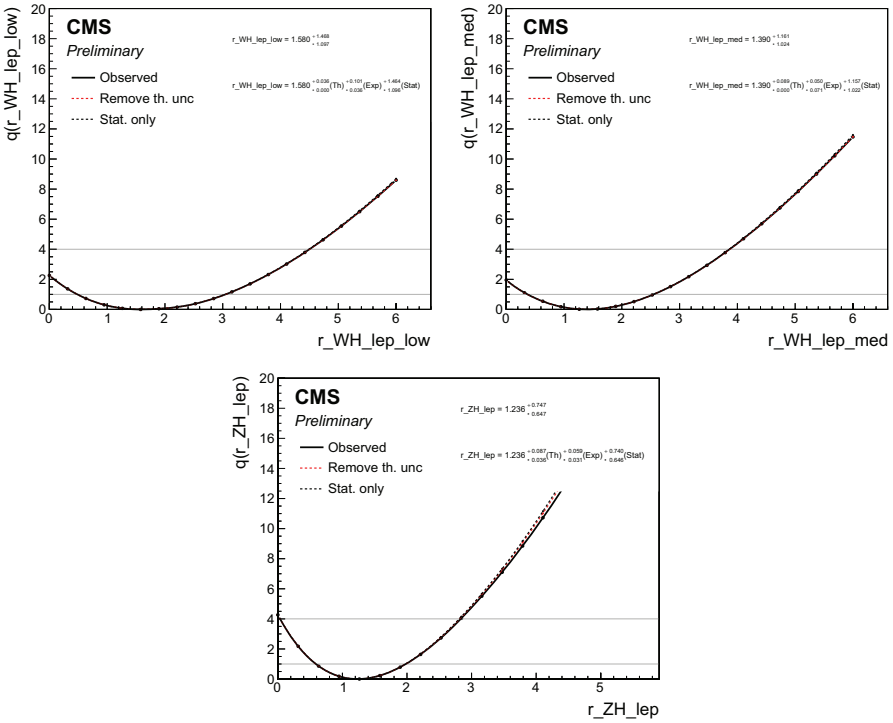

Figure H.16: Observed likelihood scans in the 27 parameter minimal merging STXS Stage 1.2 fit.

Appendix I

I.1 Impacts for per-process signal strengths

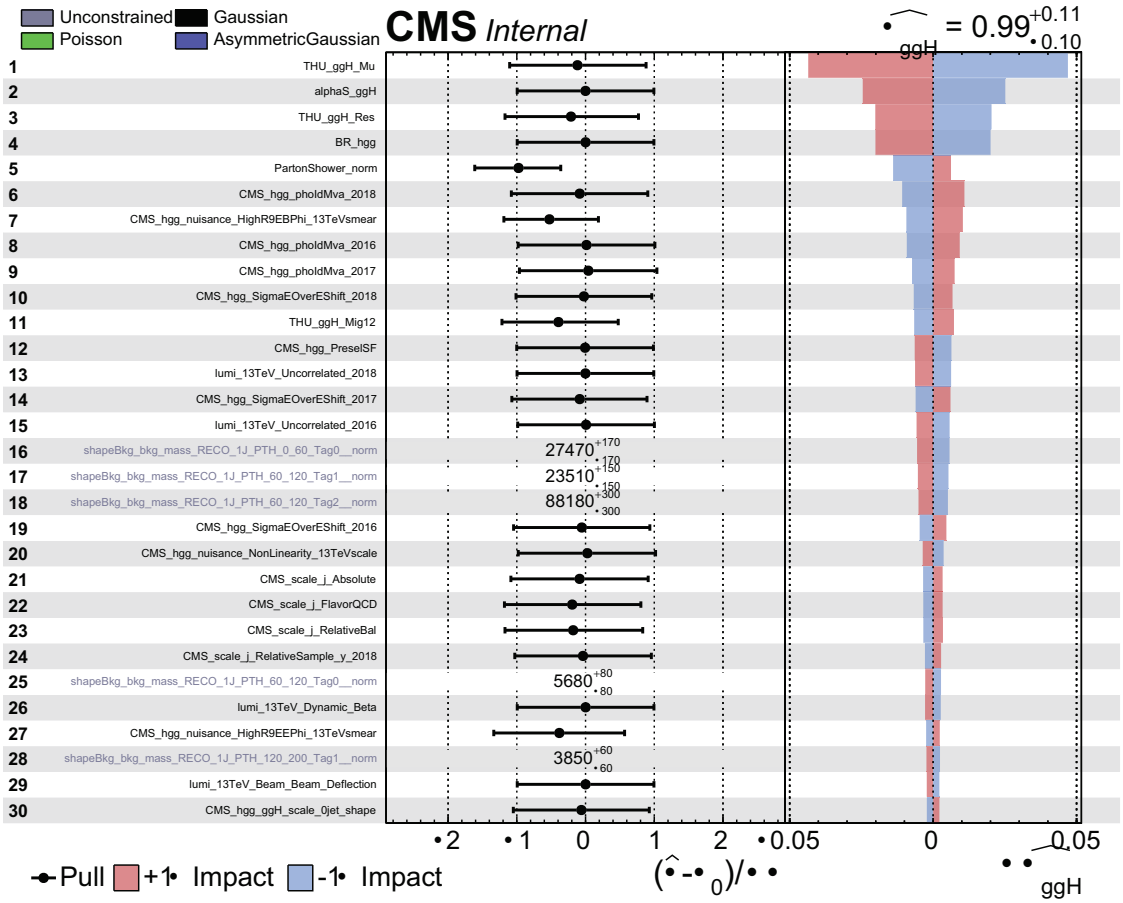

Figure I.1: Impacts for the ggH signal strength.

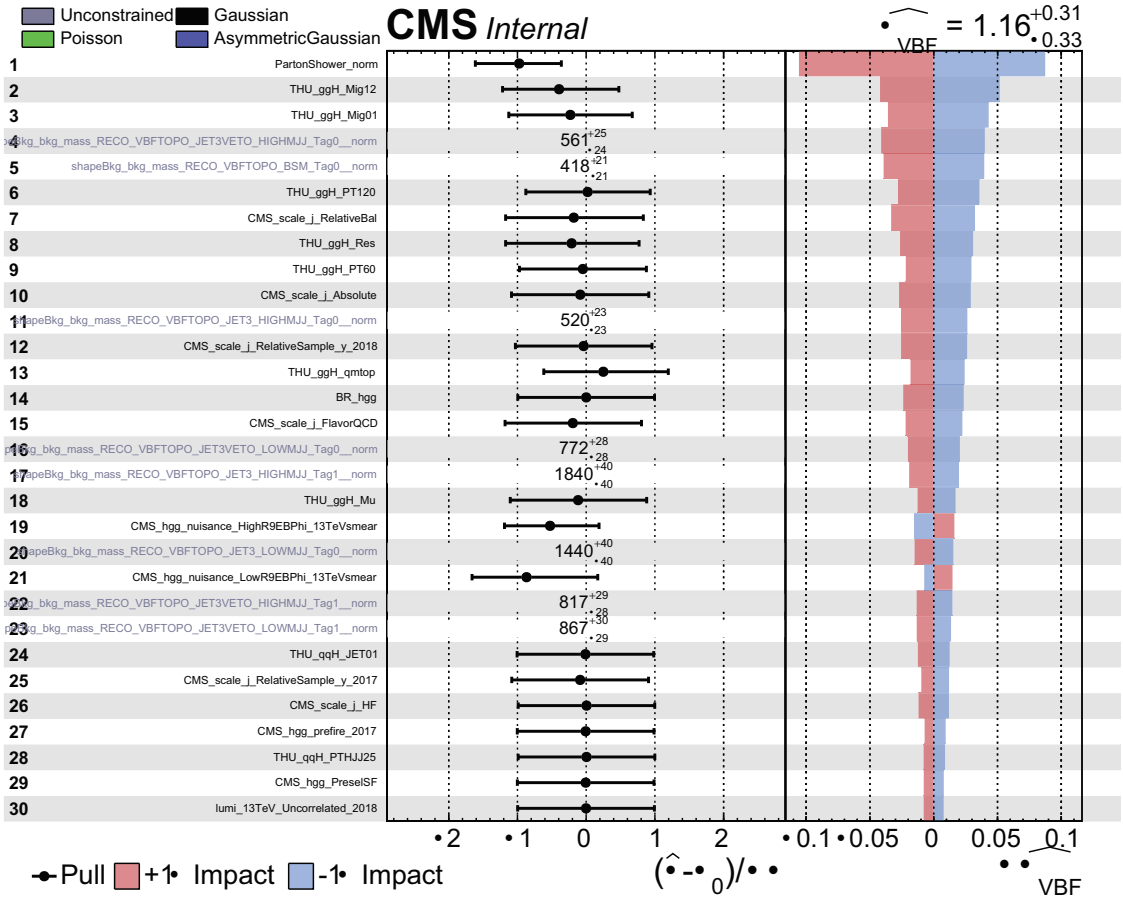

Figure I.2: Impacts for the VBF signal strength.

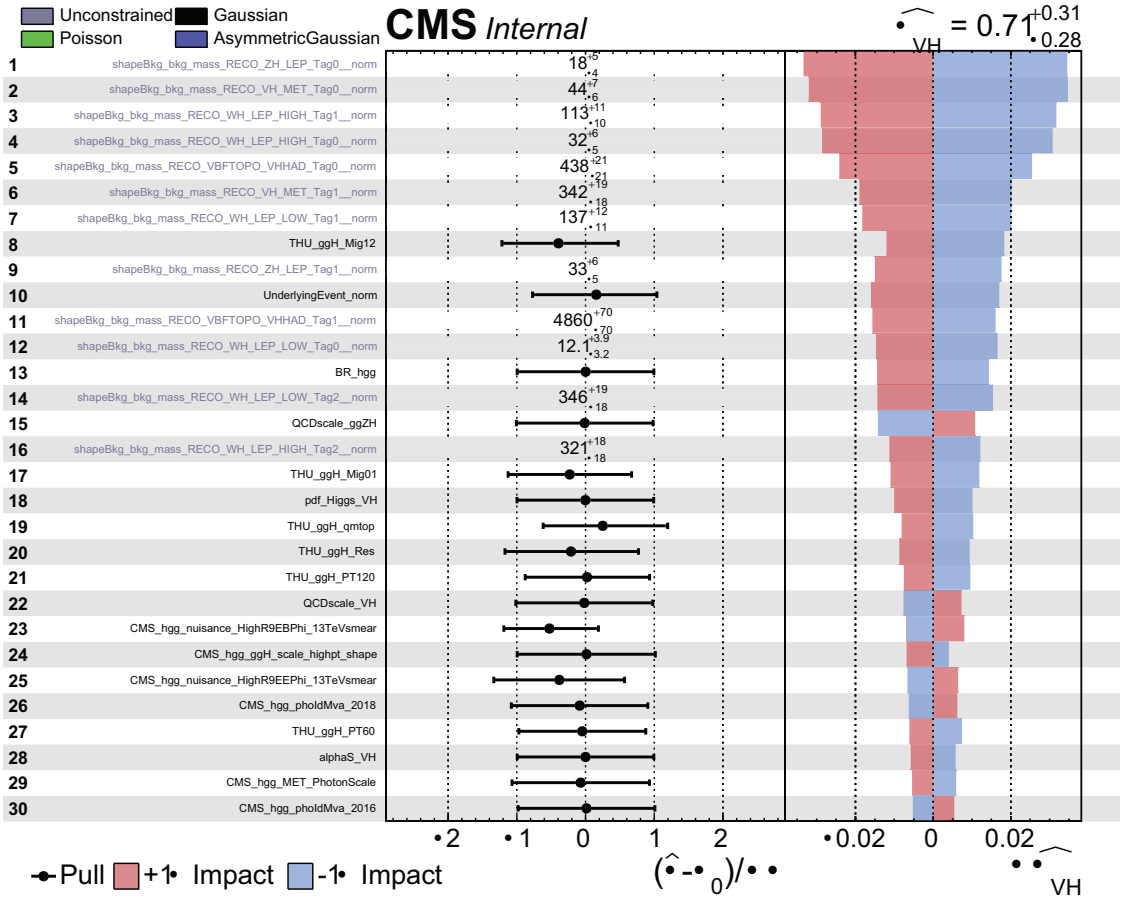

Figure I.3: Impacts for the VH signal strength.

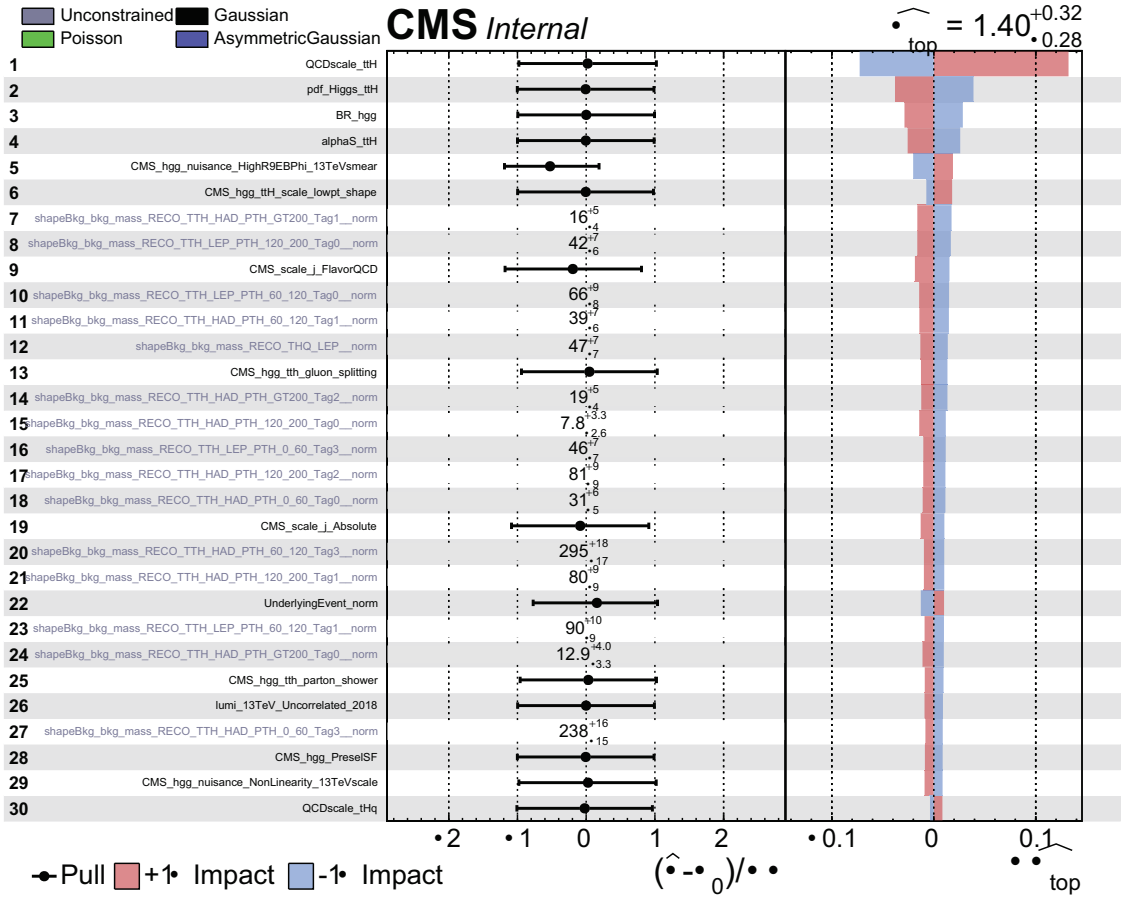

Figure I.4: Impacts for the top signal strength.